Imaging of Biomarkers and Brain Circuits Involved in Parkinson's Disease

Dissertation

der Mathematisch-Naturwissenschaftlichen Fakultät
der Eberhard Karls Universität Tübingen
zur Erlangung des Grades eines
Doktors der Naturwissenschaften
(Dr. rer. nat.)

vorgelegt von
M.Sc. Sabrina Haas (geb. Buß)
aus Friedrichshafen

Tübingen
2024

Gedruckt mit Genehmigung der Mathematisch-Naturwissenschaftlichen Fakultät der Eberhard Karls Universität Tübingen.

Tag der mündlichen Qualifikation:	07.04.2025
Dekan:	Prof. Dr. Thilo Stehle
1. Berichterstatter/-in:	Prof. Dr. Kristina Herfert
2. Berichterstatter/-in:	Prof. Dr. Steffen Hage

Für meine Familie

Contents

List of figures

List of tables

List of abbreviations

AAV	adeno-associated virus
ATP	adenosine triphosphate
B_0	main magnetic field MR scanner
B_{max}	amount of available binding sites
BOLD	blood oxygenation level-dependent
cAMP	cyclic adenosine monophosphate
CBF	cerebral blood flow
CBV	cerebral blood volume
ChR2	channelrhodopsin-2
$CMRO_2$	cerebral metabolic rate of oxygen
cpm	counts per minute
cryo-EM	cryo-electron microscopy
CTX	cortex
D1R/D2R	D1/D2 dopamine receptor
DAT	dopamine transporter
DTBZ	dihydrotetrabenazine
EPI	echo planar imaging
FBP	filtered back projection
[^{18}F]FDG	[^{18}F]2-fluoro-2-deoxy-D-glucose
fMRI	functional MRI
fPET	functional PET
FoV	field of view
GABA	γ-aminobutyric acid
GFP	green fluorescent protein
GLUT	glucose transporter
GPi/e	globus pallidus internus/externus
HPLC	high performance liquid chromatography
IC_{50}	half maximal inhibitory concentration
K_d	equilibrium dissociation constant
K_i	inhibition constant
lipos.	liposomes

L-DOPA	L-dihydroxyphenylalanine
LOR	line of response
MAO-B	monoamine oxidase-B
MB	midbrain
MDMA	3,4-methylenedioxymethamphetamine
mitoch.	mitochondria
MRI	magnetic resonance imaging
MSA	multiple system atrophy
M_{xy}	transverse magnetization
M_z	longitudinal magnetization
NAC	non-amyloid-β component
NSB	non-specific binding
OSEM	ordered subset expectation maximization
PET	positron emission tomography
P-gp	P-glycoprotein
prom.	promoter
REM	rapid eye movement
s	source
$Ser129^P$	phosphorylated serine-129
SNc/r	substantia nigra pars compacta/reticulata
STN	subthalamic nucleus
STR	striatum
TAC	time activity curve
TH	tyrosine hydroxylase
THA	thalamus
VOI	volume of interest

Summary

This work, titled "*Imaging of Biomarkers and Brain Circuits Involved in Parkinson's Disease*", aims to advance early diagnosis of Parkinson's disease and deepen our understanding of the basal ganglia circuit. By employing a range of imaging techniques, the study seeks to provide non-invasive insights into brain structures and mechanisms associated with Parkinson´s disease.

The dopaminergic nigrostriatal projections, a key component of the basal ganglia circuit, have been extensively studied since their degeneration was linked to the symptoms of Parkinson's disease. This neurodegenerative disorder affects nearly 2% of the European population over the age of 65 and is gaining significance as life expectancy rises in industrialized nations. Early diagnosis remains challenging, as a clinical diagnosis is typically made only after motor symptoms emerge. However, pathological changes at the cellular, molecular, and functional level often begin decades before these symptoms become apparent.

Toxic species of misfolded α-synuclein protein are known to cause the progressive loss of dopaminergic neurons in the substantia nigra pars compacta. Detecting aggregated α-synuclein could aid in monitoring disease progression, evaluating treatment response, and enabling early diagnosis for more timely medical intervention. Additionally, misfolded α-synuclein is implicated in several other neurodegenerative diseases collectively referred to as synucleinopathies.

The **first part** of this work focuses on developing and validating a workflow to test low molecular weight compounds as potential positron emission tomography (PET) tracers for aggregated α-synuclein. Emrusolmin (anle138b) is a promising therapeutic compound, which has shown preclinical efficacy in inhibiting α-synuclein aggregation and is currently in a phase 2 clinical trial. Two derivatives of Emrusolmin, MODAG-001 and MODAG-005, were selected for further investigation as PET tracers. *In vitro* and *in vivo* studies assessed the specificity and selectivity of [^{3}H]MODAG-001 and [^{3}H]MODAG-005 for α-synuclein aggregates, with saturation and competition binding assays performed using recombinant human α-synuclein, tau and amyloid-β fibrils. Both tracers demonstrated high affinity for α-synuclein fibrils ($K_{\text{d-MODAG-001}}$ = 0.6 ± 0.1 nM/$K_{\text{d-MODAG-005}}$ = 0.2 ± 0.03 nM) and good selectivity over other amyloids, including tau and amyloid-β, which often co-localize with α-synuclein pathology in neurodegenerative diseases. A detailed evaluation of binding parameters revealed high selectivity, with MODAG-005 showing particularly strong binding to α-synuclein fibrils and lower affinity for tau and amyloid-β.

Following successful carbon-11 labeling, dynamic PET scans were conducted in healthy rats and mice to evaluate the delivery and clearance of both tracers. [^{11}C]MODAG-001 and [^{11}C]MODAG-005 demonstrated effective blood-brain barrier penetration and rapid tracer washout from the brain. Radiometabolite analysis in brain tissue and plasma identified two radiometabolites penetrating the blood-brain barrier after [^{11}C]MODAG-001 injection, which was only slightly reduced after the deuteration of the compound. After [^{11}C]MODAG-005 injection, only one metabolite was detected in the rodent brain with lower non-specific binding.

The **second part** of this thesis focuses on deepening our knowledge of the functional, metabolic, and biochemical processes in the dopaminergic system. A precise characterization of the dopaminergic system is crucial for enhancing our understanding of disease mechanisms, improving diagnostics, and developing targeted therapies. A reliable protocol was developed for simultaneous [^{18}F]FDG-functional PET (fPET)/blood oxygenation level-dependent functional magnetic resonance imaging (BOLD-fMRI) to study the basal ganglia circuitry during optogenetic stimulation of the substantia nigra pars compacta.

Building on previous work by Wehrl *et al.* who used hybrid PET/MR imaging to investigate hemodynamic changes in small animals using fMRI while measuring changes in brain metabolism with fPET (Wehrl et al., 2013), this study aimed to improve data comparability by implementing a fully simultaneous data acquisition approach with an identical stimulation paradigm. Despite some overlap in activation patterns between fPET and fMRI, spatial and geometric discrepancies were observed, which were attributed to different physiological readouts of each modality. Additionally, an overshoot in the BOLD signal was detected in dopaminergic regions immediately after light stimulation during the resting period and only a modest positive BOLD response occurred during stimulation. This phenomenon may be explained by active inhibitory feedback mechanisms or vascular effects triggered by neurotransmitter release. Additionally, negative BOLD signal changes were observed in the motor and sensory cortices possibly attributed to increased dopamine binding to D2 receptors following tonic stimulation, leading to predominant activation of the indirect pathway and a subsequent reduction in cortical excitation.

In conclusion, this work advances both molecular imaging techniques and the understanding of basal ganglia circuitry contributing to the development of more effective diagnostic and therapeutic approaches for Parkinson’s disease.

German summary

Diese Arbeit mit dem Titel „*Imaging of Biomarkers and Brain Circuits Involved in Parkinson's Disease*“ (Bildgebung von Biomarkern und Gehirnschaltkreisen, die an der Parkinson-Krankheit beteiligt sind) zielt darauf ab, die Frühdiagnose der Parkinson-Krankheit zu verbessern und unser Verständnis der Basalganglienschleife zu vertiefen. Durch den Einsatz verschiedener bildgebender Verfahren soll die Studie nicht-invasive Einblicke in Gehirnstrukturen und Mechanismen im Zusammenhang mit der Parkinson-Krankheit liefern.

Die dopaminergen nigrostriatalen Projektionen, eine Schlüsselkomponente der Basalganglienschleife, wurden eingehend untersucht seit deren Degeneration mit den Symptomen der Parkinson-Krankheit in Verbindung gebracht wurde. Diese neurodegenerative Störung betrifft fast 2% der europäischen Bevölkerung über 65 Jahre und gewinnt mit der steigenden Lebenserwartung in den Industrieländern zunehmend an Bedeutung. Die Frühdiagnose ist nach wie vor schwierig, da die klinische Diagnose in der Regel erst nach dem Auftreten von motorischen Symptomen gestellt wird. Allerdings beginnen die pathologischen Veränderungen auf zellulärer, molekularer und funktioneller Ebene oft schon Jahrzehnte vor dem Auftreten der Symptome.

Es ist bekannt, dass toxische Spezies von fehlgefaltetem α-Synuklein-Protein den fortschreitenden Verlust von dopaminergen Neuronen in der Substantia nigra pars compacta verursachen. Der Nachweis von aggregiertem α-Synuklein könnte dabei helfen, das Fortschreiten der Krankheit zu überwachen, das Ansprechen auf die Behandlung zu bewerten und eine frühzeitige Diagnose für eine rechtzeitige medizinische Intervention zu ermöglichen. Darüber hinaus ist fehlgefaltetes α-Synuklein an mehreren anderen neurodegenerativen Erkrankungen beteiligt, die unter dem Begriff Synukleinopathien zusammengefasst werden.

Der **erste Teil** dieser Arbeit konzentriert sich auf die Entwicklung und Validierung eines Protokolls zur Prüfung niedermolekularer Verbindungen, welche als potenzielle Positronen-Emissions-Tomographie (PET)-Tracer für aggregiertes α-Synuklein relevant sind. Emrusolmin (anle138b) ist ein vielversprechender therapeutischer Wirkstoff, der präklinische Wirksamkeit bei der Hemmung der α-Synuklein-Aggregation gezeigt hat und sich derzeit in einer klinischen Studie der Phase 2 befindet. Zwei Derivate von Emrusolmin, MODAG-001 und MODAG-005, wurden für weitere Untersuchungen als PET-Tracer ausgewählt. *In vitro*- und *in vivo*-Studien untersuchten die Spezifität und Selektivität von [^{3}H]MODAG-001 und [^{3}H]MODAG-005 für α-Synuklein-Aggregate. Hierbei wurden Sättigungs- und Kompetitions-Bindungstests mit rekombinanten humanen α-Synuklein, Tau und

Amyloid-β-Fibrillen durchgeführt. Beide Tracer zeigten eine hohe Affinität für α-Synuklein-Fibrillen ($K_{d\text{-}MODAG\text{-}001}$ =0,6 ± 0,1 nM/$K_{d\text{-}MODAG\text{-}005}$ = 0,2 ± 0,03 nM) und eine gute Selektivität gegenüber anderen Amyloiden, einschließlich Tau und Amyloid-β, die bei neurodegenerativen Erkrankungen häufig gemeinsam mit α-Synuklein lokalisiert sind. Eine detaillierte Bestimmung der Bindungsparameter zeigte eine hohe Selektivität, wobei MODAG-005 eine besonders starke Bindung an α-Synuklein-Fibrillen zeigte und eine geringere Affinität für Tau und Amyloid-β.

Nach erfolgreicher Kohlenstoff-11-Markierung wurden dynamische PET-Messungen an gesunden Ratten und Mäusen durchgeführt, um die Anreicherung und Ausscheidung beider Tracer zu beurteilen. [^{11}C]MODAG-001 und [^{11}C]MODAG-005 zeigten eine effektive Durchdringung der Blut-Hirn-Schranke und eine rasche Ausschwemmung des Tracers aus dem Gehirn. Bei der Analyse der Radiometaboliten im Hirngewebe und Blutplasma wurden zwei Radiometaboliten identifiziert, die nach der Injektion von [^{11}C]MODAG-001 die Blut-Hirn-Schranke durchdrungen haben. Dies wurde durch Deuterierung der Verbindung nur geringfügig reduziert. Bei [^{11}C]MODAG-005 wurde nur ein Metabolit nachgewiesen, der eine geringere unspezifische Bindung im Nagetierhirn aufwies.

Der **zweite Teil** dieser Arbeit konzentriert sich auf die Vertiefung unserer Kenntnisse über die funktionellen, metabolischen und biochemischen Vorgänge im dopaminergen System. Eine genaue Charakterisierung des dopaminergen Systems ist entscheidend für ein besseres Verständnis der Krankheitsmechanismen, eine bessere Diagnostik und die Entwicklung gezielter Therapien. Es wurde ein zuverlässiges, simultanes [^{18}F]FDG-fPET/BOLD-fMRI (funktionelle [^{18}F]FDG-PET/BOLD (von englisch blood oxygenation level-dependent) funktionelle Magnetresonanztomographie) Protokoll entwickelt um die Basalganglienschleife während der optogenetischen Stimulation der Substantia nigra pars compacta zu untersuchen.

Aufbauend auf der Arbeit von Wehrl *et al*., die eine hybride PET/MR-Bildgebung verwendeten um hämodynamische Veränderungen bei Kleintieren mit fMRI zu untersuchen und gleichzeitig Veränderungen des Hirnstoffwechsels mit fPET zu messen (Wehrl et al., 2013), zielte diese Studie darauf ab, die Vergleichbarkeit der Daten zu verbessern, indem ein vollständig simultanes Messprotokoll zur Datenerfassung mit einem identischen Stimulationsparadigma implementiert wurde. Trotz einiger Überschneidungen in den Aktivierungsmustern zwischen fPET und fMRI wurden räumliche und geometrische Diskrepanzen beobachtet, die auf unterschiedliche physiologische Messparameter der beiden Modalitäten zurückgeführt werden. Darüber hinaus wurde in dopaminergen Regionen in der

Ruhephase unmittelbar nach der Lichtstimulation ein Überschießen des BOLD-Signals festgestellt. Während der Stimulation trat nur eine bescheidene positive BOLD-Antwort auf. Dieses Phänomen könnte durch aktive hemmende Rückkopplungsmechanismen oder vaskuläre Effekte erklärt werden, die durch die Freisetzung von Neurotransmittern ausgelöst werden. Darüber hinaus wurden negative BOLD-Signaländerungen im motorischen und sensorischen Kortex beobachtet, die möglicherweise auf eine erhöhte Dopaminbindung an D2-Rezeptoren nach tonischer Stimulation zurückzuführen sind, was zu einer überwiegenden Aktivierung des indirekten Weges und einer anschließenden Verringerung der kortikalen Erregung führt.

Zusammenfassend lässt sich sagen, dass diese Arbeit sowohl die molekularen Bildgebungsverfahren als auch das Verständnis der Basalganglienschleife voranbringt und zu der Entwicklung wirksamer diagnostischer und therapeutischer Ansätze für die Parkinson-Krankheit beiträgt.

List of publications

a) Accepted publications included in the dissertation

I. **Haas, S.***, Bravo, F.*, Ionescu, T., Gonzalez-Menendez, I., Quintanilla-Martinez, L., Dunkel, G., Kuebler, L., Hahn, A., Lanzenberger, R., Weigelin, B., Reischl, G., Pichler, B.J., Herfert, K., 2024. Functional PET/MRI reveals active inhibition of neuronal activity during optogenetic activation of the nigrostriatal pathway. Science Advances, 10, eadn2776. ***contributed equally**. IF (2023): 11.7

II. Kuebler, L.*, **Buss, S.***, Leonov, A. *, Ryazanov, S. *, Schmidt, F. *, Maurer, A., Weckbecker, D., Landau, A.M., Lillethorup, T.P., Bleher, D., Saw, R., Pichler, B.J., Griesinger, C., Giese, A., Herfert, K., 2020. [^{11}C]MODAG-001 – towards a PET tracer targeting α-synuclein aggregates. European Journal of Nuclear Medicine and Molecular Imaging, 48, 1759– 1772. ***contributed equally**. IF (2020): 9.236

b) Submitted publications included in the dissertation

III. Saw, R.*, **Haas, S.***, Schmidt, F.*, Ryazanov, S.*, Leonov, A.*, Kuebler, L., Bleher, D., Papadopoulos, I., Roeben, B., Schmidt, F., Reimold, M., Bonanno, F., Grotegerd, A., Ruf, V.C., Dahl, B., Sandiego, C.M., Henry, K.E., Fehrenbacher, B., Schaller M., Kahle, P., Gasser, T., Brockmann, K., Reischl, G., la Fougère, C., Pichler, B.J., Maurer, A., Griesinger, C., Giese, A., Herfert, K.. [^{11}C]MODAG-005 – a novel PET tracer targeting alpha-synuclein aggregates in the brain. Preprint (2024). ***contributed equally**.

c) Further submitted or accepted publications created in the context of this dissertation

IV. Stotz, S., Dunkel, G., **Haas, S.**, Kinzler, J., Schaller, M., Weigelin, B., Herfert, K., Pichler, B.J., Maurer, A.. A Versatile PET Reporter System to Visualize Gene Transfer to the Murine Brain. *In revision in Nature Biomedical Engineering*. IF (2023): 26.8

V. Ma, Y., Kuebler, L., **Haas, S.**, Maurer, A., Herfert, K., 2024. Impact of Mechanical Ventilation and Anesthesia on PET Tracer Kinetics for Combined PET/fMRI Studies in Rats. Preprint (2024). *In revision in Molecular Imaging and Biology.* IF (2023): 3.0

VI. Bowden, G., Stotz, S., Dunkel, G., **Haas, S.**, Kimmerle, E., Schaller, M., Weigelin, B., Herfert, K., Pichler, B.J., Maurer, A., 2024. [^{18}F] *p* FBC, a Covalent CLIP-Tag Radiotracer for Detection of Viral Reporter Gene Transfer in the Murine Brain. Bioconjugate Chemistry, 35(2):254-264. IF (2023): 4.0

VII. Zizmare, L., Boyle, C.N., **Buss, S.**, Louis, S., Kuebler, L., Mulay, K., Krüger, R., Steinhauer, L., Mack, I., Gomez, M.R., Herfert, K., Ritze, Y., and Trautwein, C., 2022. Roux-En-Y Gastric Bypass (RYGB) Surgery during High Liquid Sucrose Diet Leads to

Gut Microbiota-Related Systematic Alterations. International Journal of Molecular Sciences, 23, no. 3: 1126. IF (2022): 5.6

VIII. Maurer, A., Leonov, A., Ryazanov, S., Herfert, K., Kuebler, L., **Buss, S.**, Schmidt, F., Weckbecker, D., Linder, R., Bender, D., Giese, A., Pichler, B.J., Griesinger, C., 2020. ^{11}C Radiolabeling of anle253b: a Putative PET Tracer for Parkinson's Disease That Binds to α-Synuclein Fibrils in vitro and Crosses the Blood-Brain Barrier. ChemMedChem, 15(5):411-415. IF (2020): 3.466

IX. *Book chapter:* Herfert, K., Marciano, S., Kuebler, L., **Buss, S.**, Landeck, N., Mannheim, J., Napieczynska, H., 2019. Radioparmaceutical Chemistry, Editors: Lewis J.S., Windhorst A.D., Zeglis B.M.. Preclinical Experimentation in Neurology pages 583-606

Declaration of contributions

The projects demonstrated in this thesis were designed by Kristina Herfert, Bernd J. Pichler, Christian Griesinger and Armin Giese.

The experiments comprising the first publication *[^{11}C]MODAG-001 – towards a PET tracer targeting α-synuclein aggregates* were performed by **Sabrina Haas** (*in vitro* binding assays on fibrils and brain homogenate, mouse PET, mouse MRI, metabolite analysis), Laura Kuebler (*in vitro* autoradiography, mouse PET, mouse MRI, metabolite analysis), Andrei Leonov (compound synthesis), Sergey Ryazanov (compound synthesis), Felix Schmidt (α-synuclein fibril production), Andreas Maurer (radiochemical labeling), Daniel Weckbecker (tau fibril production), Anne M. Landau (autoradiography), Thea P. Lillethorup (autoradiography), Daniel Bleher (amyloid-β fibril production) and Ran Sing Saw (fibril inoculations, rat PET).

Sabrina Haas analyzed all datasets on *in vitro* binding assays, metabolite analysis, *in vivo* mouse PET, and MRI, Laura Kuebler analyzed all data sets on *in vitro* autoradiography. Ran Sing Saw analyzed all data sets on fibril injected rats. Daniel Bleher analyzed all data sets on electron microscopy.

Sabrina Haas and Laura Kuebler wrote the manuscript. Dr. Andrei Leonov, Sergey Ryazanov, Felix Schmidt, Andreas Maurer, Daniel Weckbecker, Anne M. Landau, Thea P. Lillethorup, Daniel Bleher, Ran Sing Saw, Bernd J. Pichler, Christian Griesinger, Armin Giese and Kristina Herfert supported the interpretation of the data and corrected the manuscript.

The experiments comprising the second manuscript *[^{11}C]MODAG-005 – a novel PET tracer targeting alpha-synuclein aggregates in the brain* were performed by **Sabrina Haas** (*in vitro* binding assays on fibrils, mouse PET, mouse MRI, metabolite analysis), Ran Sing Saw (*in vitro* autoradiography, fibril inoculations, rat PET, *in vivo* PET and *in vitro* autoradiography in A30P mice, immunohistochemistry), Felix Schmidt (α-synuclein fibril production), Sergey Ryazanov (compound synthesis), Andrei Leonov (compound synthesis), Laura Kuebler (mouse PET, mouse MRI, metabolite analysis), Daniel Bleher (amyloid-β and tau fibril production), Ioannis Papadopoulos (microautoradiography), Benjamin Roeben (patient recruitment, clinical monitoring), Fabian Schmidt (human data reconstruction), Matthias Reimold (human PET data acquisition), Federica Bonanno (radiochemical labeling), Ann-Kathrin Grotegerd (*in vitro* autoradiography, immunofluorescence), Viktoria C. Ruf (provided human brain tissue), Bernadette Dahl (screening of A30P mice), Christine M. Sandiego (non-human primate

experiments), Kelly E. Henry (non-human primate experiments), Birgit Fehrenbacher (electron microscopy), Martin Schaller (electron microscopy), Philipp Kahle (provided A30P mice), Thomas Gasser (patient recruitment, clinical monitoring), Kathrin Brockmann (patient recruitment, clinical monitoring), Gerald Reischl (GMP tracer synthesis for human scans), Christian la Fougère (human PET data acquisition), Andreas Maurer (radiochemical labeling) and Kristina Herfert (funding).

Sabrina Haas analyzed all datasets on *in vitro* binding assays, metabolite analysis, *in vivo* mouse and rat PET and MRI, in part also macaques. Ran Sing Saw analyzed the data sets on fibril injected rats, *in vitro* (micro)autoradiography and immunohistochemistry, A30P mouse PET and autoradiography. Daniel Bleher analyzed data sets on electron microscopy. Kelly E. Henry analyzed non-human primate experiments. Kristina Herfert analyzed human data.

Sabrina Haas, Laura Kuebler, Ran Sing Saw and Kristina Herfert wrote the manuscript. Felix Schmidt, Sergey Ryazanov, Andrei Leonov, Daniel Bleher, Federica Bonanno, Ann-Kathrin Grotegerd, Viktoria C. Ruf, Kelly E. Henry, Christine M. Sandiego, Bernd J. Pichler, Andreas Maurer, Christian Griesinger, Armin Giese, and Kristina Herfert supported the interpretation of the data and corrected the manuscript. Matthias Reimold and Christian la Fougère supported data interpretation.

For both publications support was given by the Werner Siemens Imaging Center for PET and metabolite analysis (Linda Schramm, Dennis Haupt, Maren Harant, Sandro Aidone, Natalie Hermann) and by the Radiopharmacy department of the Werner Siemens Imaging Center for radiochemical labeling (Ramona Stumm, Ramona Stremme, Elena Kimmerle, Johannes Kinzler).

The experiments comprising the third publication *Functional PET/MRI Reveals Active Inhibition of Neuronal Activity During Optogenetic Activation of the Nigrostriatal Pathway* were performed by **Sabrina Haas** (adeno-associated virus injections, *in vitro* fPET/BOLD-fMRI), Gina Dunkel (GFP/YFP staining), Helga Pertsch, technical assistant of the mouse pathology core facility of the University of Tuebingen (cFos and TH staining) and Gina Dunkel (IF staining).

Tudor Ionescu and Fernando Bravo preprocessed and analyzed all PET and fMRI datasets.

Sabrina Haas and Fernando Bravo wrote this manuscript. Tudor Ionescu, Laura Kuebler, Gina Dunkel, Irene Gonzalez-Menendez, Leticia Quintanilla-Martinez de Fend and Kristina Herfert supported the interpretation of the data and revised the manuscript.

For this publication support was given by the Werner Siemens Imaging Center for simultaneous fPET/BOLD-fMRI (Linda Schramm, Maren Harant, Miriam Owczorz) and by the Radiopharmacy department of the Werner Siemens Imaging Center for radiochemical labeling (Tatjana Kloster, Ender Özdemir, Oliver Zeiler).

The tracers used in the experiments were provided by the Radiopharmacy department of the Werner Siemens Imaging Center.

Prof. Dr. Kristina Herfert supervised all projects.

1 Introduction

Parkinson's disease, multiple system atrophy, and dementia with Lewy bodies form a diverse group of neurodegenerative disorders characterized by the accumulation of insoluble, misfolded α-synuclein protein deposits (Stefanis, 2012). In Parkinson's disease, motor symptoms like resting tremor, bradykinesia, and rigidity, along with non-motor symptoms such as psychiatric issues, cognitive deficits, and olfactory dysfunction, are commonly observed. This disease affects nearly 2% of the European population over the age of 65 (de Rijk et al., 2000; Lang & Lozano, 1998; Lee & Koh, 2015). Histologically, the progressive loss of dopaminergic neurons and the formation of Lewy bodies – aggregates containing insoluble, misfolded α-synuclein – can be detected in the substantia nigra pars compacta, locus coeruleus, amygdala, and hypothalamus (Yang & Yu, 2017). Since misfolded α-synuclein and its precursors play a central role in Parkinson's disease pathogenesis, they hold potential as biomarkers for monitoring disease progression and facilitating early diagnosis, even before the onset of motor symptoms (Gibb et al., 1987; Gomez-Tortosa et al., 2000). The loss of dopaminergic neurons in the substantia nigra pars compacta disrupts the basal ganglia circuitry essential for motor control (Blandini et al., 2000). However, the precise organization and mechanisms of the basal ganglia circuit remain poorly understood, and further research could help identify new treatment strategies.

1.1 The neurotransmitter dopamine

Dopamine is a catecholamine involved in regulating movement, attention, and mood (Schultz, 2007). The enzyme tyrosine hydroxylase initiates dopamine synthesis by converting the amino acid L-tyrosine into levodopa or L-dihydroxyphenylalanine (L-DOPA), which is also used therapeutically to treat Parkinson’s disease symptoms (see **Fig. 1**). Tyrosine hydroxylase activity, the rate-limiting step in this process, is regulated by signals within the cytosol of axon terminals. Reduced dopamine release from axon terminals increases cytosolic dopamine levels, thereby inhibiting tyrosine hydroxylase, while large dopamine release enhances its activity. In the next step, dopamine is synthesized from L-DOPA by the enzyme dopa decarboxylase. The newly synthesized dopamine is then transported into synaptic vesicles via vesicular monoamine transporters for temporary storage. When an action potential arrives, dopamine is released into the synaptic cleft through vesicle fusion with the presynaptic membrane. It can be reabsorbed into the presynapse via dopamine transporters or degraded directly in the synaptic cleft

(Daubner et al., 2011). Dopamine plays a crucial role in the functioning of the basal ganglia, among other processes.

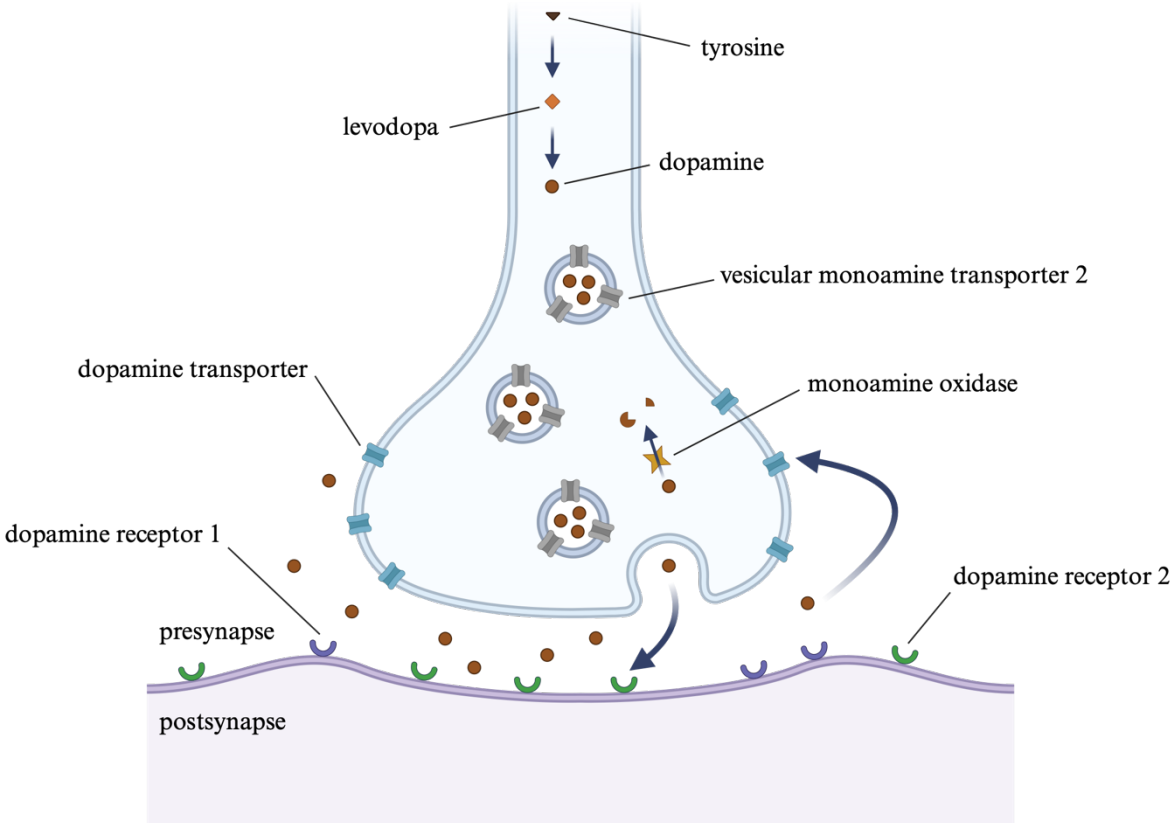

Fig. 1: Dopamine synapse. Tyrosine is converted into levodopa by the enzyme tyrosine hydroxylase. Levodopa is then transformed into dopamine by the enzyme aromatic L-amino acid decarboxylase. Once synthesized, dopamine is packaged into vesicles for storage and future release, facilitated by the protein vesicular monoamine transporter 2. The dopamine transporter is a membrane protein that regulates dopamine levels by reabsorbing it from the synaptic cleft back into the presynaptic neuron for recycling or degradation. Figure created in BioRender.com (Haas, 2024b)

1.2 The basal ganglia circuit

The basal ganglia circuit, depicted in **Fig. 2**, is an extensively studied brain region primarily involved in voluntary motor control, as well as in emotional and cognitive functions (Lanciego et al., 2012). This circuit comprises the globus pallidus, striatum, subthalamic nucleus, substantia nigra, thalamus, and cortex, which interact in a distinct and coordinated manner:

The basal ganglia circuit is divided into two pathways: the direct pathway and the indirect pathway.

The *direct* pathway: The cerebral cortex sends excitatory glutamatergic projections to the striatum, which in turn exerts an inhibitory (γ-aminobutyric acid-ergic (GABAergic)) effect on the globus pallidus internus and substantia nigra pars reticulata, both of which normally inhibit

the thalamus. Activation of the direct pathway reduces this inhibition of the thalamus, allowing it to activate motor cortex areas (including the primary motor cortex, premotor cortex, and supplementary motor cortex). This overall process facilitates movement through the *direct* pathway (Rommelfanger & Wichmann, 2010).

The *indirect* pathway: The cerebral cortex projects to the striatum, which inhibits the globus pallidus externus. This inhibition leads to disinhibition of the subthalamic nucleus, allowing it to activate the globus pallidus internus and substantia nigra pars reticulata. This activation then inhibits the thalamus, and consequently the cerebral cortex. Overall, the *indirect* pathway results in the suppression of unwanted movements (Rommelfanger & Wichmann, 2010).

In an alternative pathway, the cerebral cortex directly activates the subthalamic nucleus, which in turn stimulates the globus pallidus internus. This activation results in the inhibition of the thalamus, allowing for the immediate suppression of movements that have already begun.

The substantia nigra pars compacta projects dopaminergic fibers to the dorsal striatum. Dopamine's effect on neurons can be either excitatory or inhibitory, depending on the type of receptor present at the postsynapse (see also **Fig. 1**). There are five identified types of dopamine receptors (D1 to D5), which fall into two families of G protein-coupled receptors: D1 and D2. D1 and D5 receptors belong to the D1 family and are coupled with stimulatory G proteins, leading to neuronal activation. Conversely, D2, D3, and D4 receptors, part of the D2 family, are coupled with inhibitory G proteins, resulting in neuronal inhibition (Mishra et al., 2018; Rommelfanger & Wichmann, 2010).

In the *direct* pathway, neurons primarily possess excitatory D1 receptors, which promote movement by activating GABAergic neurons. In the *indirect* pathway, neurons mainly have inhibitory D2 receptors, which also promote movement by inhibiting GABAergic neurons – resulting in an overall excitatory effect (Mishra et al., 2018; Rommelfanger & Wichmann, 2010).

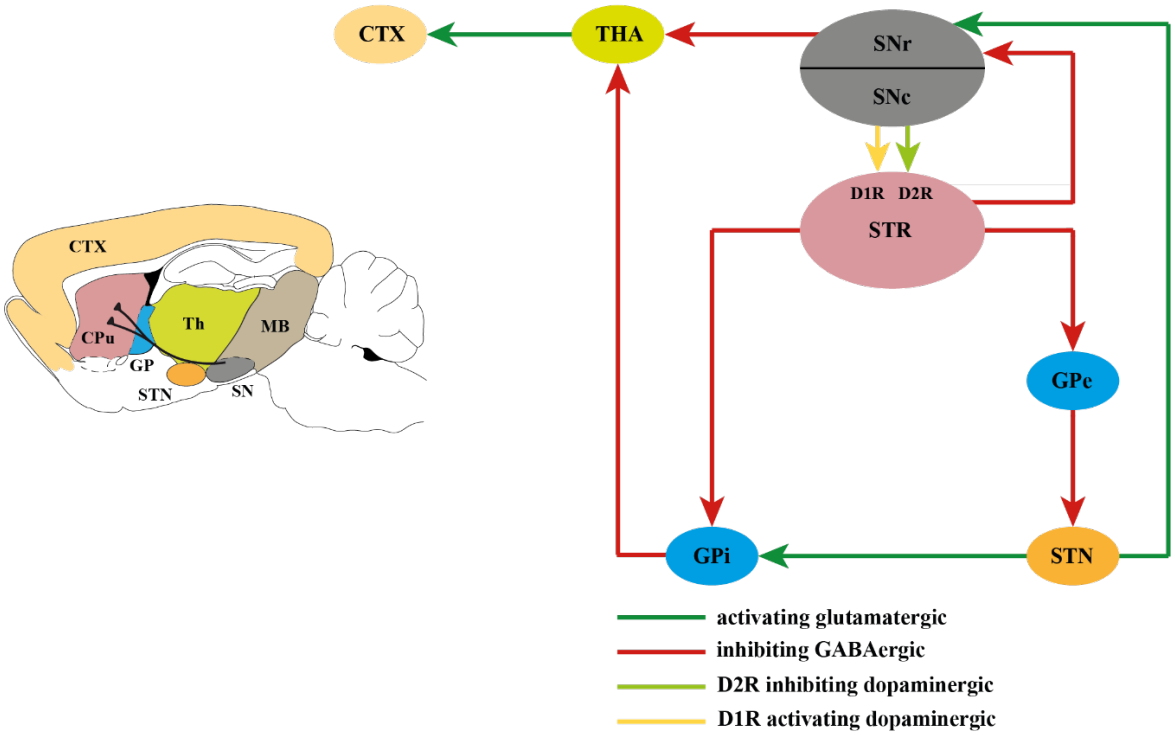

Fig. 2: The basal ganglia loop. A schematic depiction of the anatomical relationships within the basal ganglia system is provided, illustrating the direct and indirect projection pathways originating from the striatum. Abbreviations: CTX, cortex; D1R/D2R, D1/D2 dopamine receptor; GPe/GPi, globus pallidus externus/internus; MB, midbrain; SNc/r, substantia nigra pars compacta/reticulata; STN, subthalamic nucleus; STR, striatum; THA, thalamus

The precise mechanisms governing the interaction between the direct and indirect pathways of the basal ganglia remain controversial and not yet fully understood, with various theories put forward:

A classic theory posits that the basal ganglia's direct and indirect pathways serve opposing functions, with the direct pathway facilitating movement and the indirect pathway inhibiting it, forming the basis of the ‘Go/No-go’ model (Albin et al., 1989; DeLong, 1990; Kravitz et al., 2010). Kravitz *et al.* conducted a study that reinforced the earlier 'Go/No-go' model by using Cre-mice engineered to express either direct or indirect pathway medium spiny neurons exclusively. Optogenetic stimulation of the direct pathway medium spiny neurons led to a reduction in freezing behavior and an increase in locomotion, supporting the idea that this pathway facilitates movement. Conversely, stimulation of the indirect pathway neurons induced parkinsonian-like symptoms, including heightened freezing, bradykinesia, and reduced initiation of movement, underscoring the pathway's role in inhibiting motor activity.

A more recent theory challenges the traditional view, suggesting that the direct pathway plays a role in selecting the intended action, while the indirect pathway simultaneously suppresses competing actions to sharpen and emphasize the chosen movement. This is known

as the 'Co-activation' model (Cui et al., 2013; Hikosaka et al., 2000; Mink, 1996). Cui *et al.* provided evidence challenging the classical model and supporting the 'Co-activation' model by measuring the activity of direct and indirect pathway spiny projection neurons. The researchers employed viral expression in the dorsal striatum of mice specifically engineered to target either the direct or indirect pathways – D1-Cre mice for the direct pathway and A2A-Cre mice for the indirect pathway. By integrating fiber optics with time-correlated single-photon counting, the researchers identified brief surges in neural activity in both direct and indirect pathway spiny projection neurons that occurred exclusively at the onset of actions. Notably, these neurons remained inactive during periods of rest. Moreover, *in vivo* electrophysiological and imaging studies have shown that both the direct and indirect striatal pathways are simultaneously activated during action initiation, aligning with the predictions of the 'Co-activation' model (Barbera et al., 2016; Geddes et al., 2018; Markowitz et al., 2018; Nonomura et al., 2018).

A novel but still emerging functional model, known as the 'Triple-Control' model of the basal ganglia, posits that action selection is dynamically regulated by interactions among the direct pathway and two components of the indirect pathway (Li & Jin, 2023).

Beyond the existing theories on the direct and indirect pathways, the complexity increases with the varying affinities of dopamine receptors for dopamine. Specifically, the D2 receptor has a much higher affinity for dopamine (K_d = 25 nM) compared to the D1 receptor (K_d = 1.6 μM). This difference in affinity implies that these receptors may respond differently to tonic and phasic dopamine release, influencing their roles in basal ganglia function. Tonic dopamine release is believed to activate D2 receptors, whereas phasic dopamine release – characterized by bursts and pauses – is thought to primarily activate D1 receptors (Dreyer et al., 2010; Richfield et al., 1989; Surmeier et al., 2007). In other studies, it was shown that low dopamine levels activate D1 receptors, thereby increasing inhibitory activity in the prefrontal cortex, by increasing GABA release via the direct pathway. High dopamine levels decrease inhibition via D2 receptor activation and subsequent GABA decrease via the indirect pathway. This happens through two separate signaling pathways (Trantham-Davidson et al., 2004). In contrast, a computational study proposed that both types of receptors respond to both phasic and tonic dopamine firing (Hunger et al., 2020). This theory is partly supported by research from Yapo *et al.*, which demonstrates that phasic dopamine release can also activate D2 receptors (Yapo et al., 2017).

Beyond postsynaptic receptors, presynaptic dopamine autoreceptors located in the substantia nigra pars compacta play a crucial role in modulating dopamine release in the

striatum. These autoreceptors, similar to D2 receptors, are found on dendrites, the soma, and terminal boutons. When dopamine binds to these autoreceptors, it inhibits tyrosine hydroxylase activity, leading to decreased dopamine synthesis and, consequently, reduced dopamine release per vesicle. Binding to autoreceptors can also increase dopamine reuptake through the dopamine transporter. Thus, these autoreceptors function as a negative feedback mechanism, regulating the neuron's own activity and controlling the release of neurotransmitters (Ford, 2014). In addition to dopamine-mediated autoinhibition, these neurons have also been shown to release glutamate and GABA (Hnasko et al., 2010; Tecuapetla et al., 2010; Tritsch et al., 2012). Patel *et al.* demonstrated that GABA also plays an autoinhibitory role by inhibiting dopamine release through binding to presynaptic GABA receptors. This inhibition occurs both after a single stimulation impulse and following multiple pulses (Melani & Tritsch, 2022; Patel et al., 2024). Moreover, this inhibition of dopamine release is significant because dopamine autoinhibition is a relatively slow process.

Motor impairments can arise from an imbalance in these pathways and are linked to progressive movement disorders like multiple system atrophy and Parkinson's disease (Alberico et al., 2015; Damier et al., 1999; Hacker et al., 2012; Salvesen et al., 2015; Zheng et al., 2020). In Parkinson's disease, for instance, reduced dopamine release from the substantia nigra disrupts these pathways, leading to diminished motor activity and the hallmark symptoms of the disease, including bradykinesia, tremors, and muscle rigidity. Additionally, certain parts of the basal ganglia are involved in decision-making. Currently, there is no cure for these disorders, as the mechanisms underlying neuronal degeneration remain unclear, though α-synuclein aggregation may be a crucial factor.

1.3 The protein α-synuclein: Structure, function, and its role in neurodegenerative diseases

Physiologically, α-synuclein exists in the cytosol as an unfolded, monomeric, and soluble protein (Kotzbauer et al., 2012). This presynaptic protein plays a crucial role in maintaining the size of the presynaptic vesicle pool (Murphy et al., 2000). It is involved in neurotransmitter release and provides protection against neurodegeneration (Sidhu et al., 2004). Additionally, α-synuclein is thought to be significant in learning and synaptic plasticity, and it likely plays a regulatory role in dopamine release, which could explain its higher concentration in the substantia nigra (Burré, 2015). Pathologically, α-synuclein is linked to the formation of Lewy bodies – insoluble, misfolded protein inclusions found in conditions such as Parkinson's disease and dementia with Lewy bodies (Srinivasan et al., 2021; Yang & Yu, 2017).

Parkinson's disease ranks as the second most prevalent neurodegenerative disorder, following Alzheimer's disease, affecting approximately 1% of individuals aged 60 and older. The disease often begins with subtle symptoms such as constipation, loss of smell, and rapid eye movement (REM) sleep disorders. The hallmark of Parkinson's disease is motor impairment, which includes bradykinesia (slowness of movement), progressively smaller movements, muscle stiffness (rigidity), tremors at rest, and postural instability. Additional non-motor symptoms may involve the autonomic nervous system, such as frequent urination, and psychological issues, including depression (Kouli et al., 2018; Tysnes & Storstein, 2017). The disease is characterized by the degeneration of nerve cells in the substantia nigra, leading to a deficiency in dopamine. This degeneration is partly due to the accumulation of misfolded α-synuclein, which forms Lewy bodies in the dopamine-producing neurons of the substantia nigra. Contributing factors may include environmental exposures to pesticides (e.g., paraquat) and chemicals (e.g., trichloroethylene), which are known to negatively impact the nervous system structures affected in Parkinson's disease (Kouli et al., 2018; Tysnes & Storstein, 2017). Currently, there is no cure for Parkinson's disease; treatment focuses on symptom management. Dopamine replacement therapy remains a cornerstone of treatment, primarily involving the use of levodopa, a dopamine precursor. This is complemented by other antiparkinsonian medications that enhance levodopa's effectiveness and dopamine agonists (Kouli et al., 2018; Tysnes & Storstein, 2017).

Dementia with Lewy bodies is marked by the accumulation of α-synuclein aggregates within nerve cell bodies, known as Lewy bodies, and in neuronal processes, called Lewy neurites, with a characteristic distribution pattern, particularly in the neocortex and brainstem. Clinically, the condition primarily presents as dementia, with cognitive decline affecting attention, executive functions, and visuospatial abilities, which significantly impact daily life. Neuropsychological testing is essential for identifying early visuospatial disturbances, language disorders such as naming and word fluency issues, and executive dysfunction (Galasko, 2017).

Multiple system atrophy is a progressive neurological disorder characterized by the presence of α-synuclein aggregates in the brain. These aggregates, known as glial cytoplasmic inclusions, are found in oligodendrocytes and are predominantly located in the cerebellum, pons, and basal ganglia (Spillantini et al., 1998). The condition manifests through a variety of clinical syndromes. Multiple system atrophy parkinsonian type, occurring in approximately 60% of cases, is characterized by bradykinesia, rigidity, tremor, and postural instability. Cerebellar multiple system atrophy, present in about 40% of cases, involves gait ataxia, cerebellar dysarthria, limb ataxia, and cerebellar oculomotor dysfunction. Some patients exhibit

features of both multiple system atrophy parkinsonian type and cerebellar multiple system atrophy. A distinguishing feature of multiple system atrophy is its low response to levodopa, which helps differentiate it from Parkinson's disease. Treatment for multiple system atrophy focuses on symptom management, including medications to address motor symptoms and other related issues (Palma et al., 2018; Roncevic et al., 2014).

The 14 kDa protein α-synuclein is structured into three distinct regions (see **Fig. 3a**). It features an α-helical NH_2-terminus, which may harbor inherited Parkinson's disease mutations such as A30P or A53T. The acidic COOH-terminus, found in 90% of Lewy bodies, is commonly phosphorylated. The middle region contains a hydrophobic non-amyloid-β component, which is implicated in protein aggregation (Gallegos et al., 2015; Uéda et al., 1993). Research has shown a correlation between the severity of Parkinson's disease and the number of mutations in the SNCA gene, which encodes α-synuclein. This raises the question of whether disease severity is linked to the concentration of α-synuclein (Singleton & Gwinn-Hardy, 2004; van den Berge et al., 2012). There are three isoforms of α-synuclein – α-synuclein 140, 126, and 112 – produced through alternative splicing. This process occurs through two mechanisms: the shortening of mRNA or the deletion of in-frame segments. These alterations result in substantial changes to the protein's secondary structure, which can lead to functional changes due to the selective deletion of critical protein domains (Beyer, 2006; Zhang et al., 2019).

The primary structure of α-synuclein contains several sites that are prone to posttranslational modifications, with phosphorylation at serine-129 (Ser129) being the most prevalent and potentially the most critical. In brains affected by dementia with Lewy bodies, over 90% of insoluble α-synuclein is phosphorylated at this site, compared to only about 4% of normal α-synuclein. This suggests that widespread phosphorylation of α-synuclein is a key event in disease pathogenesis. Additionally, immunohistochemical studies have revealed extensive accumulation of Ser129 phosphorylated α-synuclein in both glial and neuronal cells in the brains of individuals with multiple system atrophy (Beyer, 2006).

Research on the potential toxicity of α-synuclein primarily centers on its aggregation process. Under specific physiological conditions, native α-synuclein can begin to aggregate. Initially, monomeric, insoluble, and misfolded α-synuclein is believed to aggregate into a disordered, unstable oligomeric state (**Fig. 3b**). As this process continues, these oligomers reorganize into more stable structures characterized by β-sheet formations. Further reorganization, through the incorporation of additional monomers or ordered self-association, leads to the formation of fibrils and, ultimately, Lewy bodies (Chiti & Dobson, 2017). The

specific stage of α-synuclein aggregation responsible for toxicity remains debated. Identifying early aggregation states could be crucial for initiating early treatment and managing disease progression. Moreover, since the location of pathology varies across different synucleinopathies, differential diagnosis may be feasible (Kao et al., 2009).

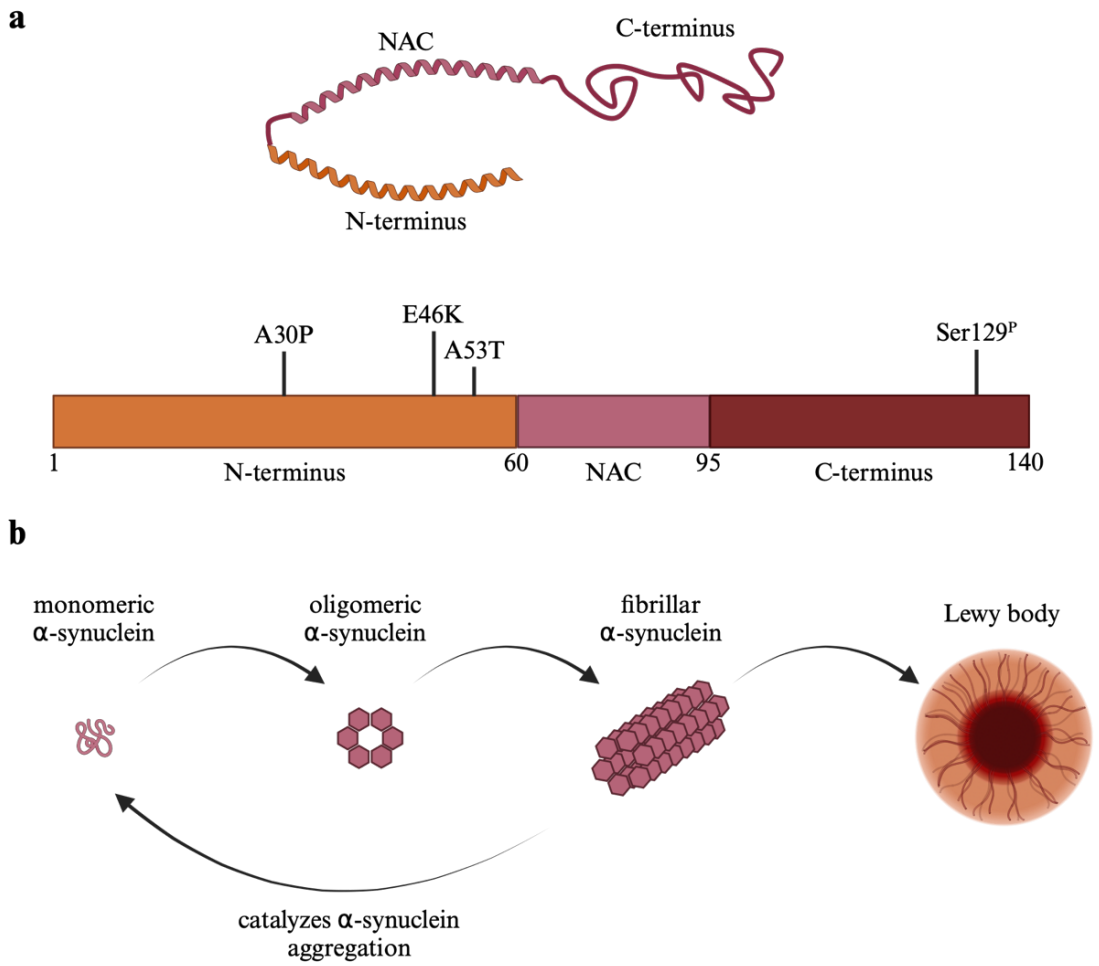

Fig. 3: The protein α-synuclein (a) and Lewy body formation (b). (**a**) The protein α-synuclein is divided into functional domains: the amphipathic N-terminus, the central NAC domain, and the acidic C-terminus. Mutations that cause familial Parkinson's disease are located at the N-terminus, the NAC region tends to aggregate, and post-translational phosphorylations such as serine-129 are located in the C-terminus. The N-terminus and NAC domain form α-helical structures, while the C-terminus remains disordered. (**b**) Under certain physiological conditions, native α-synuclein can aggregate. It starts as monomeric, misfolded α-synuclein, which forms unstable oligomers. These oligomers then stabilize into β-sheet-rich structures. As more monomers are added or through self-association, fibrils form, eventually leading to the development of Lewy bodies. Figure created in BioRender.com (Haas, 2024c); adapted from (Gallegos et al., 2015). Abbreviations: NAC, non-amyloid-β component; Ser129^{P}, phosphorylated serine-129; term, terminus

Cryo-electron microscopy (cryo-EM) has emerged as a powerful tool for visualizing protein structures at near-atomic resolution, offering detailed insights into protein folding, interactions, and aggregation. Two "multiple system atrophy folds" are specifically linked to multiple system atrophy and are characterized by a tightly packed arrangement of β-sheets, forming a compact and stable fibril core (**Fig. 4**). In contrast, the "Lewy fold," associated with

Parkinson's disease and dementia with Lewy bodies, features β-sheets arranged in a less compact core with different twisting patterns and orientations (**Fig. 4**).

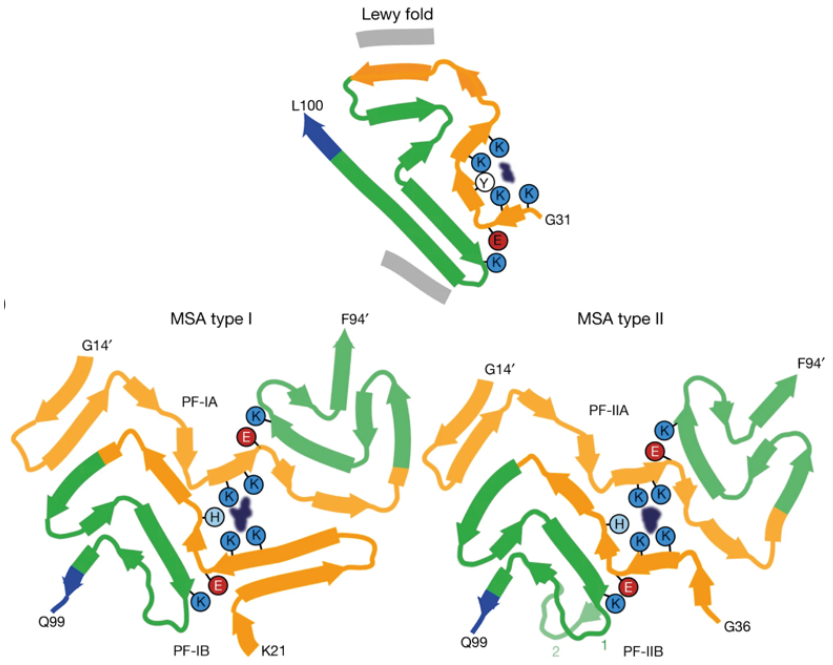

Fig. 4: Lewy and multiple system atrophy filamentous folds. Two unique "multiple system atrophy folds" are linked to multiple system atrophy, featuring tightly packed β-sheets forming a stable fibril core. In contrast, the "Lewy fold," associated with Parkinson's disease and dementia with Lewy bodies, has a less compact β-sheet structure with different twisting patterns and orientations. Figure from (Yang et al., 2022). Abbreviations: MSA, multiple system atrophy

Despite those folds being composed of the same protein, their structural differences contribute to the distinct pathological features observed in each disease. The multiple system atrophy fold is associated with the rapid progression of neurodegeneration seen in multiple system atrophy, whereas the Lewy fold is linked to the slower progression of Parkinson's disease and the mixed symptomatology of dementia with Lewy bodies. Additionally, a newly identified α-synuclein structure associated with juvenile-onset synucleinopathy shares similarities only with the multiple system atrophy folds (Guerrero-Ferreira et al., 2020; Schweighauser et al., 2020; Yang et al., 2023; Yang et al., 2022).

In addition to the synucleinopathies mentioned earlier, pathological α-synuclein is also present in several other neurodegenerative diseases, often co-localizing with other amyloids such as tau and amyloid-β. The Lewy body variant of Alzheimer's disease, for example, includes Lewy bodies containing α-synuclein aggregates. Moreover, α-synuclein aggregates have been identified in Lewy bodies in familial Alzheimer's disease and Down's syndrome (Hamilton, 2000; Lippa et al., 1998; Lippa et al., 1999). Progressive supranuclear palsy, a tauopathy with symptoms similar to Parkinson's disease, also features Lewy bodies containing

misfolded α-synuclein in the substantia nigra, locus coeruleus, and raphe nuclei. Additionally, tau aggregates have been found in dementia with Lewy bodies. Notably, amyloid-β pathology is observed across all synucleinopathies; for instance, amyloid-β deposits are detected in dementia with Lewy bodies (Forrest & Kovacs, 2023; Kon et al., 2024; Kovacs et al., 2013; Mihaescu et al., 2022).

1.4 Imaging modalities

Non-invasive imaging techniques like positron emission tomography (PET) and magnetic resonance imaging (MRI) are valuable for studying biological targets and physiological processes. As both modalities are featured in publications I to III, their technical details and capabilities are outlined in the following sections.

1.4.1 Positron emission tomography

PET is a non-invasive imaging technique used to visualize metabolic processes, neurotransmission, and protein expression, among other things. Here, a trace amount of a radioactively labeled substance, known as a "tracer," is injected into the bloodstream. The radiation emitted by the tracer is detected by a PET scanner, which then generates images based on this data. The most commonly used PET radionuclides and their half-lives are listed in

Table 1 (Pimlott & Sutherland, 2011).

Table 1: Typical positron emitters and their half-lives

Radionuclide	Half-life
Carbon-11	20.3 minutes
Nitrogen-13	10.0 minutes
Oxygen-15	2.07 minutes
Fluorine-18	110 minutes
Cupper-64	12.7 hours
Gallium-68	68 minutes

Radioactive nuclides are produced in a cyclotron through the acceleration of protons (**Fig. 5a**). A cyclotron consists of two hollow, D-shaped metal electrodes known as "dees." A high-frequency alternating current is applied to these dees, creating an electric field that alternates between positive and negative. This electric field is concentrated in the gap between

the dees. Above and below the dees are electromagnets that generate a constant, uniform magnetic field. Inside the cyclotron, a particle source emits free ions, such as positively charged protons, into the gap. These protons are accelerated towards the negatively charged dee. When the protons enter the dee, they leave the electric field, and the magnetic field causes them to follow a circular path due to the Lorentz force. As the polarity of the dees reverses, the protons are accelerated towards the other dee, following a similar circular path. With each pass, the protons gain speed and the radius of their circular path increases. Eventually, the protons are deflected from the dee by an additional electric field produced by a deflection electrode and are directed at a target to initiate a nuclear reaction.

A simplified illustration of the $^{14}N(p, \alpha)^{11}C$ nuclear reaction is shown in **Fig. 5b**. Accelerated protons bombard a ^{14}N-target, resulting in the production of an unstable, β^+-emitting ^{11}C-nuclide and an α particle. The radionuclide is then transferred to a hot cell, where it is combined with a suitable substance to form a radiopharmaceutical (Cherry et al., 2012).

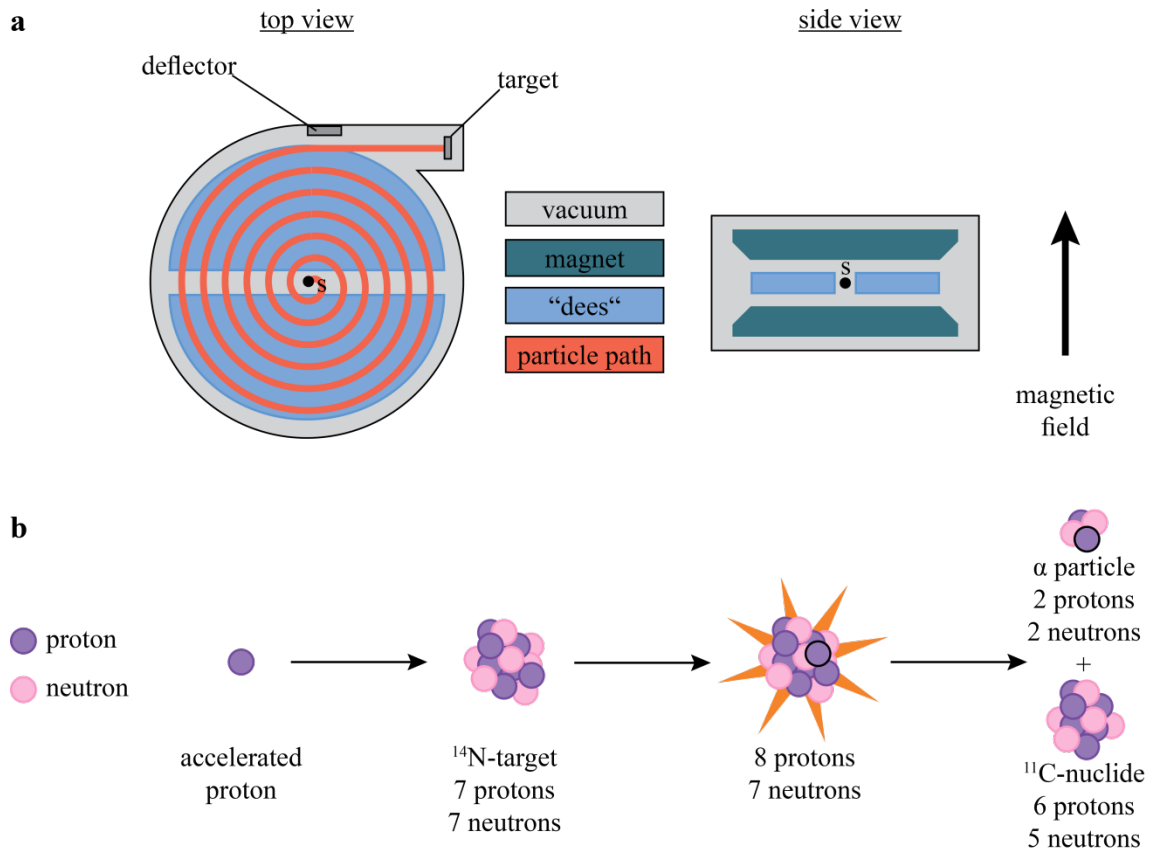

Fig. 5: Proton acceleration in a cyclotron (a) and nuclear reaction (b). In a cyclotron, alternating electric fields and a static magnetic field guide protons along a circular path to accelerate them (**a**). The accelerated particles are then directed towards a target. The simplified $^{14}N(p, \alpha)^{11}C$ nuclear reaction that occurs upon bombardment of the target is shown in (**b**). Fig. a adapted from (Cherry et al., 2012), Fig. a, b adapted from (Buss, 2018). Abbreviations: s, source

The molar activity and carrier content are crucial parameters for assessing the quality of a radiopharmaceutical. Molar activity refers to the activity of the radiolabeled molecules (e.g., ^{11}C-labeled molecules) relative to the total number of isotopic molecules. In radiopharmacology, this is categorized into three types: carrier-free, no carrier added, and carrier-added.

"Carrier-free" conditions are not achievable with natural elements, so "no carrier added" is used instead. This term indicates that while no additional carrier was intentionally included, some unavoidable mixing with stable isotopes occurs. In some production processes, adding inactive carriers in a controlled manner is necessary, and such cases are termed "carrier-added." Generally, adding carriers is undesirable because it significantly reduces the maximum achievable molar activity. Radiopharmaceuticals made from no carrier added radionuclides are typically dosed in the submicrogram range, minimizing the likelihood of pharmacodynamic effects (Cherry et al., 2012; de Goeij & Bonardi, 2005).

PET imaging captures γ-photons generated by the annihilation of a positron (**Fig. 6a**). These photons are emitted by a radiopharmaceutical tagged with a β^+ emitter. When the emitted positron encounters an electron in the tissue, it forms a positronium and subsequently undergoes annihilation. This process produces two γ-photons with an energy of 511 keV, which travel in nearly opposite directions. To detect these γ-photons, detectors are arranged in a circular array around the subject. Only pairs of photons detected by two different detectors within a brief time window are considered, as they must originate from the same annihilation event and thus align along a straight line (**Fig. 6b**) between the detectors (coincidence event) (Raichle, 1983).

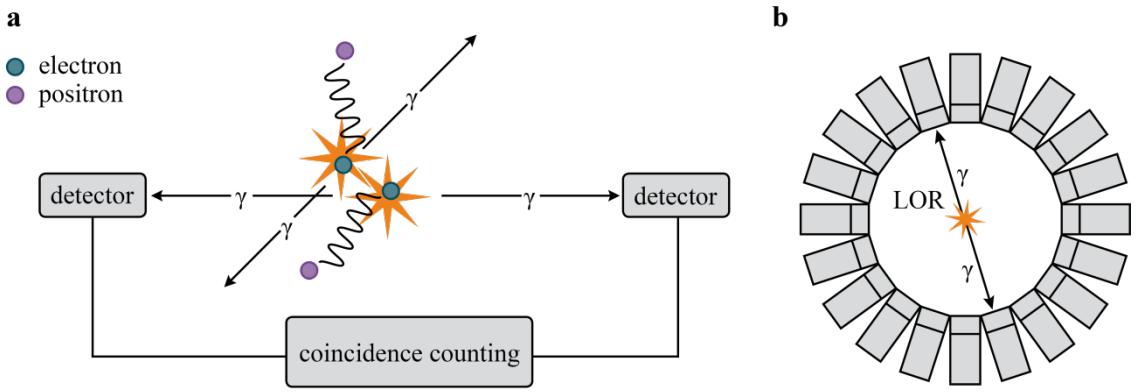

Fig. 6: Coincidence counting. Positron-electron annihilation results in the emission of two γ-photons traveling in opposite directions (**a**). An event is recorded when these γ-photons strike two detectors within a specific energy and time window (**b**). Figure adapted from (Buss, 2018) and (Raichle, 1983). Abbreviations: LOR, line of response

The assumption that an event occurs along the line of response is not always accurate. Unlike a true event (**Fig. 7a**), photons may scatter, leading to a mislocated emission (**Fig. 7b**). By measuring pulse heights, which should correspond to photon energy, these scattered events can be minimized. Additionally, two photons from separate annihilation events can sometimes be detected as a single event (**Fig. 7c**) but using a shorter detection window can reduce such occurrences. Photon attenuation may also cause an event to be entirely missed (**Fig. 7d**) (Lewellen, 2008).

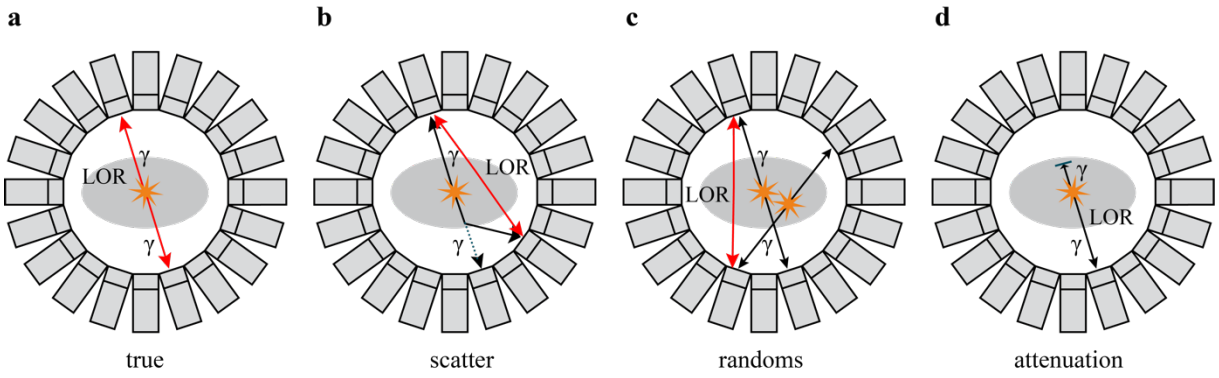

Fig. 7: Coincidence events and attenuation. The red line of response represents true coincidences (**a**), scatter coincidences (**b**), and random coincidences (**c**). Attenuation can result in missed coincidences (**d**). Figure adapted from (Buss, 2018) and partially adapted from (Lewellen, 2008). Abbreviations: line of response, LOR

Scintillation crystals, commonly composed of bismuth germanate or lutetium oxyorthosilicate, detect γ-photons by converting 511 keV photons into visible light. For effective photon detection, the crystals must have high material density. Additionally, a short signal decay time is preferred to minimize random events. Photomultipliers then convert the visible light into electrons, which are amplified to produce a digital signal (Lewellen, 2008).

During PET acquisition, the coincidence data are initially recorded in a list mode file (**Fig. 8a**). This file includes details about each coincidence, such as time, angle, detector position, and distance from the origin. This data is then processed into a sinogram, which depicts parallel projections of the tracer distribution (**Fig. 8b**). Each point in a sinogram represents the summed activity concentrations along the line of response, with each line corresponding to a one-dimensional projection of activity concentrations from various angles (Reader & Zaidi, 2007).

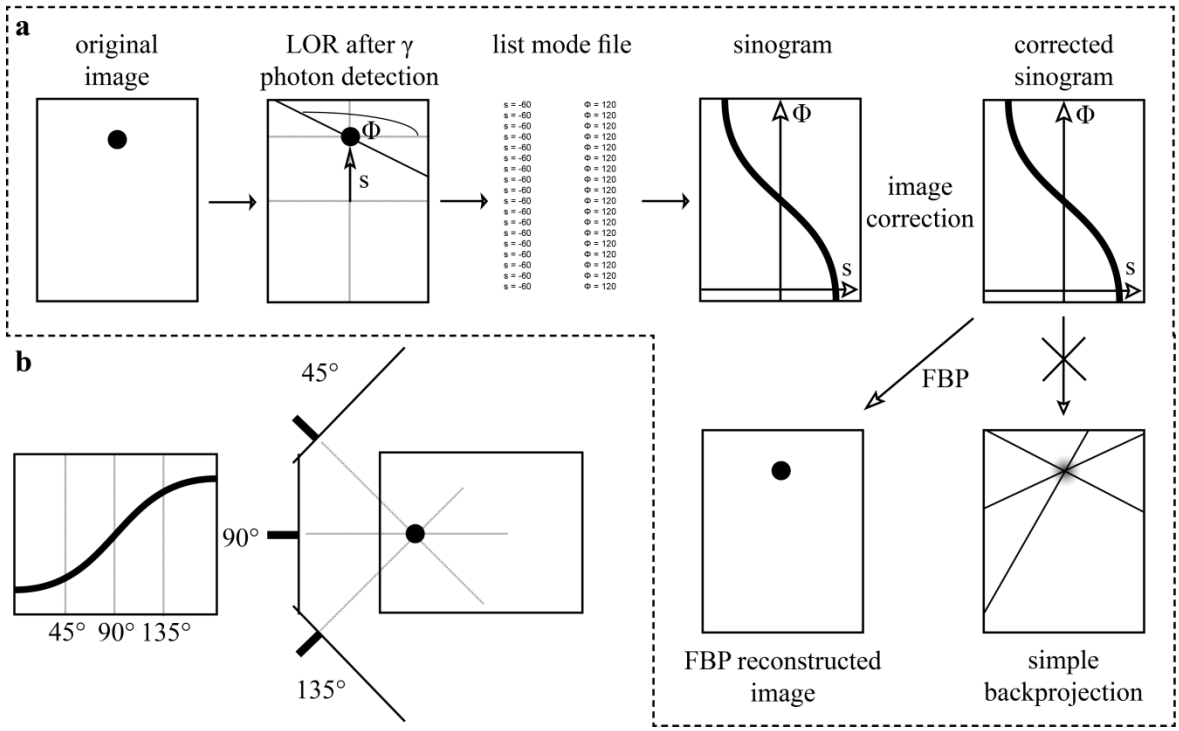

Fig. 8: PET image reconstruction. A list mode file records details such as time, the distance to the γ-photon origin (s), and the angle (ϕ) (**a**). A sinogram is a graphical representation of this data. To create an image from the corrected sinogram, a filtered back projection is used. After applying various image correction techniques, the corrected sinogram is reconstructed using filtered back projection. The resulting image, which contains a sinusoidal waveform, is generated by aggregating projections from all directions through the subject (**b**). Figure from (Buss, 2018), adapted from (Reader & Zaidi, 2007). Abbreviations: FBP, filtered back projection; LOR, line of response

Filtered back projection is a commonly used method for reconstructing PET data due to its relatively quick analytical approach. After correcting the sinogram, each point is back-projected onto a line of response with a uniform activity concentration. To prevent blurring caused by this approximation, each projection is filtered before being back-projected into the image space. This filtering process corresponds to multiplication in the frequency domain and acts as low-pass filtering (Kinahan et al., 2004).

Iterative correction methods, such as ordered-subsets-expectation maximization, first attempt to reach an acceptable solution through a sequence of approximations. Starting from an initial estimate, the algorithm tries to achieve a better and better approximation to the truth (for further information see Lalush, 2004).

1.4.1.1 PET imaging of synucleinopathies

Imaging procedures are primarily used for confirming diagnoses or assisting in differential diagnosis. In Parkinson's disease, [^{18}F]FDG-PET scans can reveal a range of hypometabolism patterns, from minimal cortical involvement to extensive hypometabolism in the

parieto-temporo-occipital regions. These patterns are often accompanied by relative hypermetabolism in areas such as the striatal nuclei, globus pallidus, midbrain, thalamus, cerebellum, and primary sensory-motor cortex (Arnone et al., 2022). For dementia with Lewy bodies, [^{18}F]FDG-PET may show hypometabolism in the occipital lobe, while in multiple system atrophy, hypometabolism might be observed in the putamen, brainstem, or cerebellum (Galasko, 2017; Palma et al., 2018).

Striatal [^{18}F]DOPA-PET imaging is a definitive method for diagnosing Parkinson's disease *in vivo*, providing a direct measure of nigrostriatal dopamine synthesis. Reduced [^{18}F]DOPA uptake in the putamen is commonly observed in nearly all Parkinson's patients, even at early stages. In dementia with Lewy bodies, [^{18}F]DOPA-PET typically shows striatal dopaminergic denervation, whereas multiple system atrophy is characterized by symmetrical striatal dopaminergic denervation (Depierreux et al., 2021; Galasko, 2017; Palma et al., 2018). Additionally, [^{18}F]dihydrotetrabenazine ([^{18}F]DTBZ) or [^{11}C]DTBZ, which binds to the vesicular monoamine transporter type 2, serves as a reliable marker for assessing dopaminergic neuron integrity. Decreased binding in the striatum and substantia nigra can be detected in Parkinson's disease patients (Wood, 2014).

1.4.2 Magnetic resonance imaging

A magnetic field can be generated by the movement of electric charges through a coiled wire. In an MRI system, this principle is applied using a large coil, or magnet, which is maintained in a superconducting state by cooling with liquid helium. The MRI magnet is supplemented with additional coils: shim coils, gradient coils, and high-frequency coils. Shim coils enhance the uniformity of the magnetic field, correcting for any distortions caused by objects within the scanner. High-frequency coils transmit pulses to excite the sample and receive the emitted signals. Gradient coils produce a linear variation in magnetic field strength, enabling slice selection and spatial encoding (Mahesh, 2013). A simplified cross-section of the MR scanner is shown in **Fig. 9**.

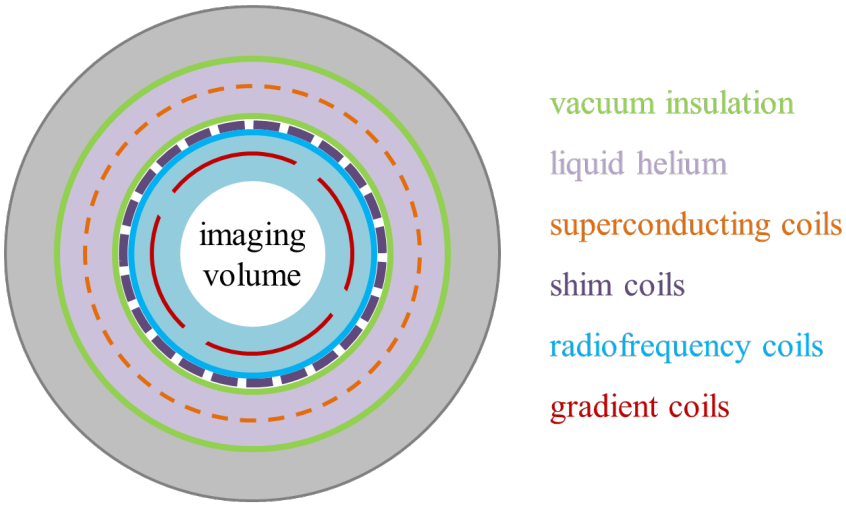

Fig. 9: Cross-section of an MR scanner. A simplified cross-section illustrates the superconducting coil, which is cooled by helium, and shows the shim, high-frequency, and gradient coils positioned within the main coil. Figure adapted from (Mahesh, 2013)

Hydrogen protons exhibit a property known as nuclear spin or intrinsic angular momentum, which causes them to rotate around their axis. This rotation makes the proton behave like a small magnet with dipole characteristics. In an MR scanner, the strong magnetic field, denoted as B_0, aligns the proton's rotation axis either parallel or antiparallel to the B_0 field. As the field strength increases, more nuclei align with B_0 generating a magnetic field, M (see **Fig. 10a**). M consists of two components: longitudinal magnetization (M_z), aligned parallel to B_0, and transverse magnetization (M_{xy}), oriented perpendicular to B_0 (see **Fig. 10b**). The transverse magnetization rotates at a frequency known as the Larmor frequency, which is determined by the type of nucleus and the magnetic field strength. This rotating magnetization produces a high-frequency voltage in a nearby receiving coil, which is detected as a signal. In contrast, longitudinal magnetization remains static and does not generate measurable signals (Grover et al., 2015; Mahesh, 2013).

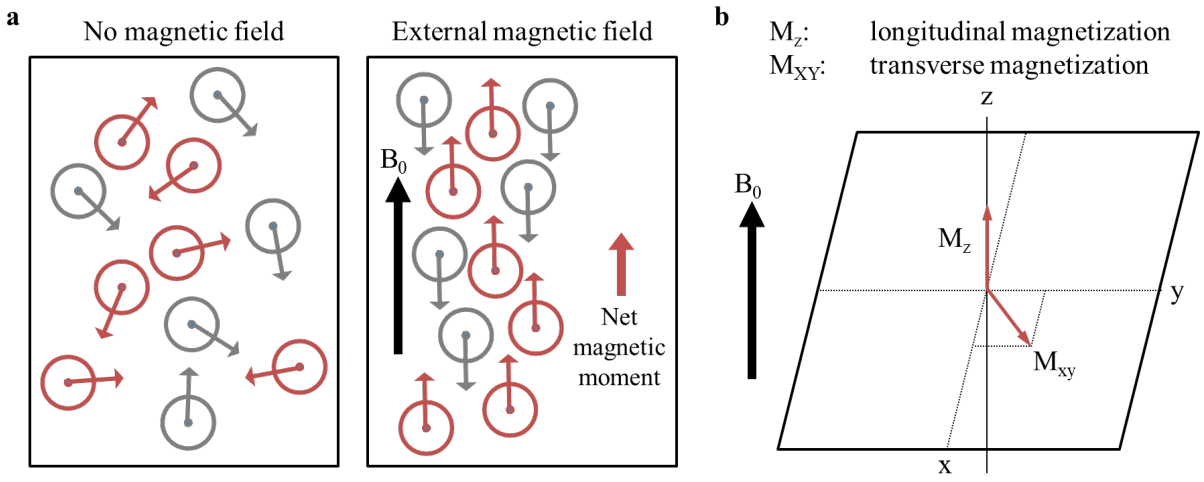

Fig. 10: Proton alignment in a magnetic field and magnetization vectors. In the absence of an external magnetic field, protons are randomly oriented. However, when an external magnetic field B_0 is applied, the protons align either parallel or antiparallel to this field, resulting in a net magnetic moment aligned with B_0 (**a**). The component of this magnetic moment vector that aligns along the z-axis is known as longitudinal magnetization M_z. The component that aligns in the xy plane is referred to as transverse magnetization M_{xy} (**b**). Figure adapted from (Mahesh, 2013). Abbreviations: B_0, main magnetic field in MR scanner; M_{xy}, transverse magnetization; M_z, longitudinal magnetization; x, y, z, geometric axis orientations

In the absence of external intervention, the magnetic field M is not measurable because it only exhibits longitudinal magnetization. To detect this magnetization, it must first be shifted into a transverse magnetization by applying an external high-frequency pulse. This shift occurs when the Larmor frequency of the protons matches closely with the frequency of the applied pulse. The degree to which the magnetization moves away from its initial position is determined by the strength and duration of the radiofrequency pulse (Grover et al., 2015).

Relaxation is the process by which the magnetization M returns to its original alignment after the radiofrequency pulse is turned off. This process occurs at varying rates in different tissues and involves both longitudinal and transverse directions. As a result, the relaxation properties contribute to tissue contrast, complementing the spatial density of protons (Grover et al., 2015).

The flip angle defines the amount of longitudinal magnetization that remains after a high-frequency pulse. For a 90° pulse, this magnetization is effectively eliminated, while a 180° pulse reverses it to -M. By using flip angles ranging from 0° to 180°, intermediate values between M and -M can be achieved. The time constant T1 represents the duration needed for a tissue to return to 37% (1/e) of its original longitudinal magnetization. Different tissues relax at varying rates, with adipose tissue relaxing more quickly than brain, muscle, or liver tissue, and free fluid relaxing the slowest (Mahesh, 2013).

The flip angle following a high-frequency pulse also affects the transverse magnetization. A 90° pulse achieves the maximum transverse magnetization. Relaxation in the transverse direction follows an exponential decay, with the transverse magnetization approaching zero over time. The time constant T2 measures the time required for a tissue's transverse magnetization to decay to 37% (1/e) of its initial value. As previously noted, different tissues have varying relaxation rates: tendons and bones relax the fastest, followed by brain, muscle, and liver tissues, with free fluid relaxing the slowest (Grover et al., 2015; Mahesh, 2013).

The MR signal obtained corresponds to the electrical voltage induced in the receiver coil at each measurement point. This voltage is influenced by the interaction of all transverse magnetization components within the region of interest. To achieve accurate spatial encoding, each location within the tissue must be assigned its own magnetization vector, as these vectors respond differently depending on the external influences present in various areas. Additionally, the tissue's diamagnetic or paramagnetic properties can cause variations in the static magnetic field, leading to local inhomogeneities that affect the local Larmor frequency (Mahesh, 2013).

To selectively excite a single layer of the subject, a gradient along the B_0 direction is applied during the radiofrequency pulse. This process, known as slice selection, ensures that only the signal from the slice where the Larmor frequency matches the frequency of the radiofrequency pulse is sampled. Signals from adjacent slices are excluded because their Larmor frequencies are either too high or too low (Mahesh, 2013).

The origin of the measured signal is encoded by applying a read gradient and a phase gradient. When the read gradient is active, it alters the Larmor frequency in a spatially dependent manner, causing transverse magnetizations in the examination area to rotate at different speeds according to their respective Larmor frequencies. The data collected during this phase are represented as lines in k-space.

Phase encoding is performed in a direction perpendicular to the frequency encoding. The phase encoding gradient momentarily alters the Larmor frequency based on the position along the phase encoding direction, leading to spatially varying phase shifts in the transverse magnetization components. This gradient defines the vertical position in k-space. A two-dimensional Fourier transform of the k-space data generates an image, revealing the spatial distribution of signal intensities (Mahesh, 2013).

In certain scenarios, rapid image acquisition is highly beneficial. For instance, it enables dynamic tracking of contrast agent distribution or allows for imaging while the patient holds breath to minimize breathing artifacts. The echo planar imaging sequence, also used in this

study, offers the advantage of extremely fast acquisition times. This makes it particularly well-suited for dynamic and functional imaging, such as observing temporal changes associated with brain activation.

The echo planar imaging technique generates echoes by alternately switching the gradient in one direction and then reversing it. This process causes the dispersed components of the transverse magnetization to re-align during gradient reversal, resulting in a measurable signal known as an "echo" (Mahesh, 2013).

1.5 PET tracer development

1.5.1 Requirements for a successful central nervous system PET tracer for misfolded α-synuclein

Creating a successful PET tracer for the central nervous system requires meeting several specific criteria (**Fig. 11**) (Zhang et al., 2013).

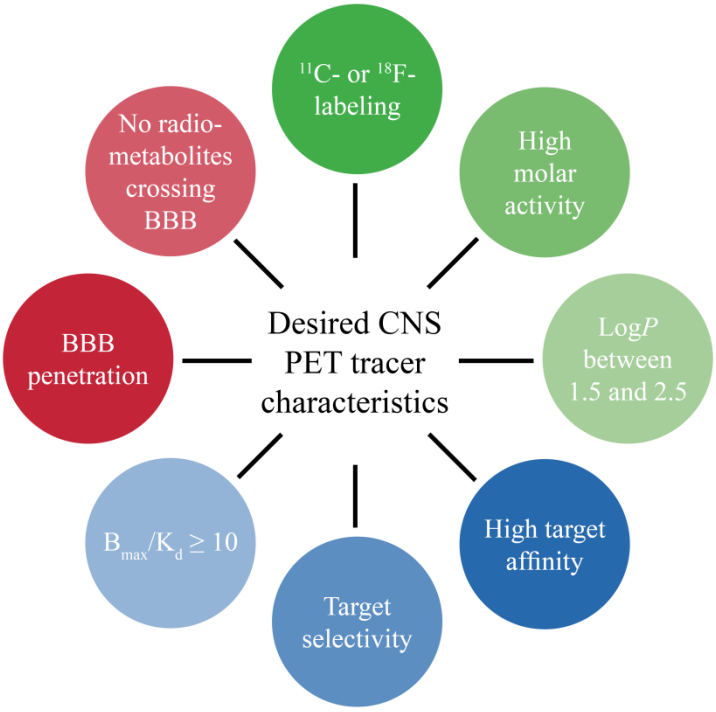

Fig. 11: Desired properties of a PET tracer for the central nervous system. Radiochemical requirements are marked in green, pharmacological properties in blue, and *in vivo* examinations in red. Figure adapted from (Buss, 2018). Abbreviations: BBB, blood-brain barrier; CNS, central nervous system; PET, positron emission tomography

For PET tracers, using carbon-11 or fluorine-18 is preferred due to their short half-lives, which facilitates quick patient discharge from the hospital or radiology department. Consequently, both ^{11}C- and ^{18}F-labeling options should be considered.

To ensure effective membrane penetration and minimal non-specific binding to blood proteins and lipids, the log*P* value of the tracer should fall between 1.5 and 2.5. The log*P* value, or the n-octanol/water partition coefficient, represents the logarithm of the concentration ratio between these two phases. It can be either measured or calculated and indicates the hydrophilicity of the compound. The ability of a molecule to cross the blood-brain barrier is influenced not only by its charge and size but also by its lipophilicity. Highly hydrophilic molecules struggle to cross membranes, while excessively lipophilic molecules may adhere to lipids and blood proteins, which reduces the free plasma fraction and increases non-specific binding in tissues, thus affecting the signal-to-noise ratio.

Furthermore, a high molar activity is crucial for small animal studies, particularly when target densities are low. Since both the carrier and the radioligand compete for the same binding site and are chemically identical, a higher carrier fraction can lead to increased occupancy of binding sites by non-signal-contributing molecules (Saha, 2010; Seddon et al., 2009).

The affinity of a ligand for its target is dictated by its chemical structure. Ideally, the ligand should exhibit minimal off-target binding, demonstrating high specificity and selectivity for its intended target. The equilibrium dissociation constant K_d quantifies the ratio between the unbound ligand and the target-ligand complex, with a lower K_d value indicating a higher affinity. *In vitro* saturation binding experiments, detailed in the following section, offer a swift method to experimentally determine the K_d value for a compound. In addition, with these assays the B_{max} can be calculated. This value represents the total number of available binding sites. The binding potential, expressed as $B_{max}/K_d \geq 10$ is often used as a benchmark to indicate an optimal balance between ligand affinity and binding site availability (Zhang et al., 2013).

For an effective PET tracer, high target selectivity is crucial. This challenge is especially pronounced when developing a tracer for oligomeric or aggregated α-synuclein. α-Synuclein is part of a broader group of amyloid-forming proteins, each with distinct structural patterns. Due to these structural similarities, off-target binding to related sites may contribute to the PET signal, complicating the tracer's specificity (Zhang et al., 2013).

Metabolism of the tracer can produce radiometabolites that also cross the blood-brain barrier, adding to the PET signal and complicating data interpretation. This issue is particularly problematic if the tracer is metabolized rapidly, before reaching equilibrium. The liver enzymes are responsible for metabolizing substances into more hydrophilic forms to facilitate their excretion from the body (Pike, 2009).

1.5.2 Challenges in the development of a PET tracer for aggregated α-synuclein

Fig. 12 outlines the challenges encountered by chemists and structural biologists in developing a PET tracer for misfolded α-synuclein. One major challenge is the target's structural diversity. During Lewy body formation, α-synuclein transitions from small, soluble oligomers to larger β-sheet-containing oligomers and eventually to insoluble fibrils that aggregate into Lewy bodies. Identifying the most toxic molecular species of misfolded α-synuclein and selecting the optimal target for small molecule compounds remains unresolved. Furthermore, α-synuclein's structure may vary among patients due to environmental factors and posttranslational modifications. The species of α-synuclein also differs between multiple system atrophy, Parkinson's disease, and dementia with Lewy bodies, which could potentially aid in distinguishing these diseases (Brundin et al., 2017; Chiti & Dobson, 2017; Martel & Gatti McArthur, 2020). An example of a successful PET tracer is [^{11}C]PIB, which is used for imaging amyloid-β in Alzheimer's disease. Unlike amyloid-β, which is found in extracellular plaques, misfolded α-synuclein is present in much lower concentrations and is located intracellularly within Lewy bodies. Thus, a PET tracer must not only cross the blood-brain barrier but also penetrate cell membranes to reach its target. This requires the tracer to possess adequate lipophilicity. However, excessive lipophilicity can lead to increased non-specific binding to lipids or blood proteins. While aggregated amyloids share β-sheet structures, dyes such as Thioflavin-T used by pathologists do not specifically target individual amyloid types. A PET tracer must be able to differentiate between various amyloid strains to accurately identify neurological diseases associated with amyloidosis (Mathis et al., 2017). Additionally, reaching the target within Lewy bodies presents further challenges. Recent studies have shown that Lewy bodies are densely packed with lysosomal structures, mitochondria, and lipids, in addition to aggregated α-synuclein (Shahmoradian et al., 2019). These dense components may impede the tracer's ability to bind effectively.

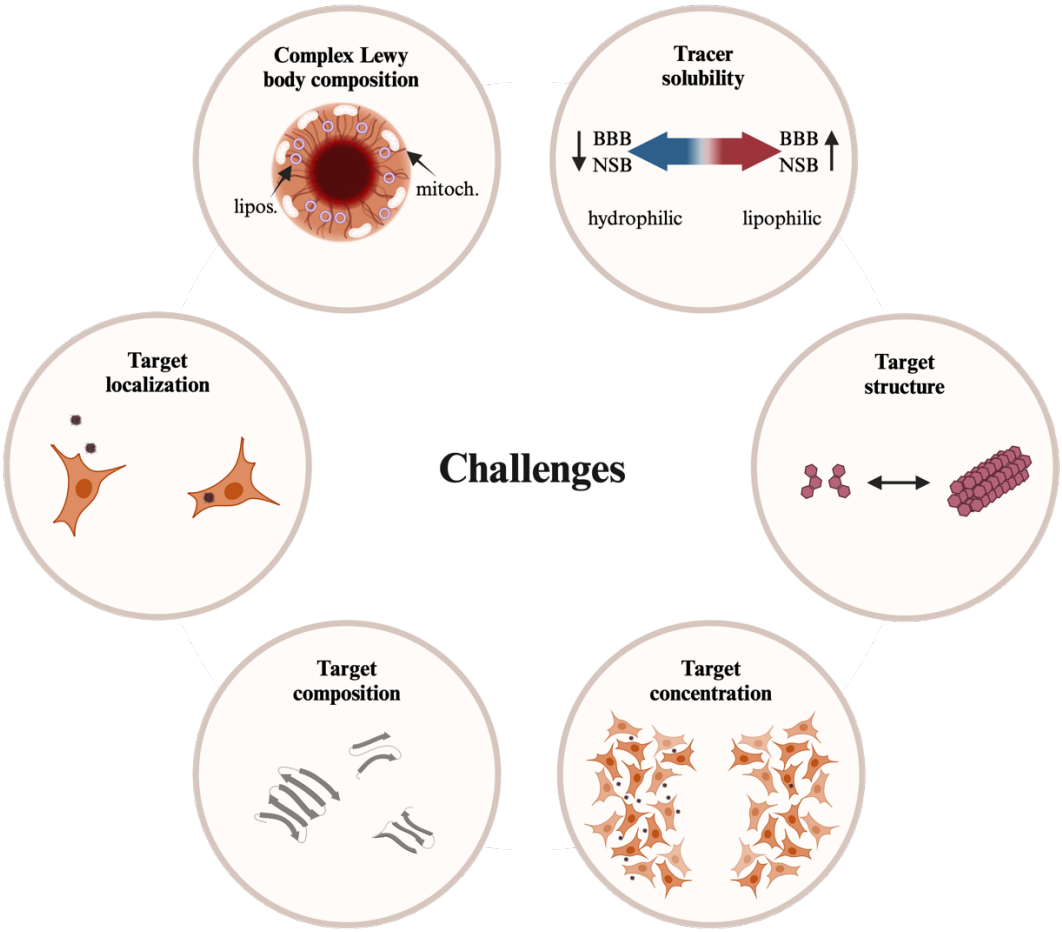

Fig. 12: Challenges in the development of PET tracers for misfolded α-synuclein. Challenges in developing PET tracers for pathological α-synuclein include the various forms of misfolded α-synuclein, low target concentration, localisation of pathological depositions, expected solubility of the tracer, structural similarities with other amyloids, and complex composition of Lewy body depositions that complicate tracer penetration. Figure created in part with BioRender.com (Haas, 2024a), adapted in part from (Lonati et al., 2014; Shahmoradian et al., 2019). Abbreviations: BBB, blood-brain barrier; lipos., liposomes; mitoch., mitochondria; NSB, non-specific binding

1.5.3 Tracer development pipeline

The development pipeline for new PET tracers involves several stages, as illustrated in (**Fig. 13**). The process begins with modifying a lead compound that has demonstrated binding to aggregated α-synuclein, resulting in a diverse library of new compounds. Testing each compound *in vivo* would be prohibitively expensive and time-consuming. To streamline this process, *in vitro* screening assays using recombinant proteins are employed to identify promising candidates more efficiently.

Initially, compounds are evaluated through competition binding assays against the lead structure. Compounds that show strong binding to the target are then selected for further testing. These promising candidates are tritiated to assess their binding affinity for α-synuclein aggregates and their selectivity over tau and amyloid-β. Binding studies are conducted on both

recombinant fibrils and human brain slices using (micro)autoradiography. To differentiate between specific and non-specific binding, immunohistochemistry is performed on the same or adjacent tissue sections. Compounds that demonstrate high affinity, selectivity, and specificity are subsequently labeled with carbon-11. These labeled tracers are then injected into rodents or non-human primates to evaluate their pharmacokinetic properties, biodistribution, and metabolism, as described by (Bigott-Hennkens et al., 2008). Finally, the *in vivo* binding of the tracer to fibrils is validated after stereotaxic injection into animal models, such as mice, rats, or non-human primates, followed by PET imaging. This comprehensive approach ensures that only the most promising tracers advance through the development pipeline.

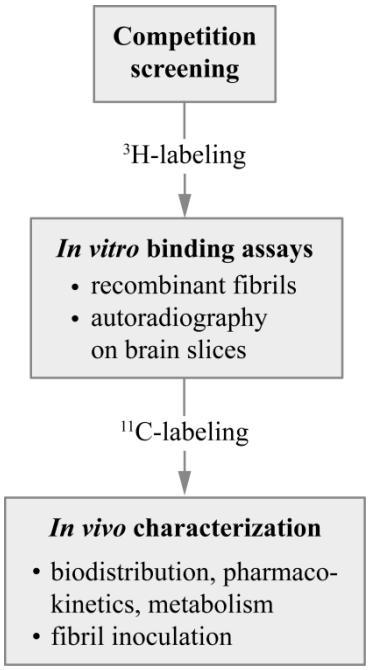

Fig. 13: PET tracer development process for misfolded α-synuclein. A library of molecules is first screened for their ability to compete with a lead compound to narrow down the selection. After tritiation, binding characteristics are determined and high-affinity compounds with promising selectivity are subsequently labeled with carbon-11 or fluorine-18. *In vivo* studies are conducted to assess their biodistribution, pharmacokinetics, metabolism and ability to bind fibrils *in vivo*

1.5.3.1 *In vitro* binding assays

A preliminary and cost-effective assessment of a molecule's binding affinity and selectivity can be achieved through competition binding assays (**Fig. 14**). In this assay, decreasing concentrations of a non-radioactive competitor are incubated with fixed concentrations of a radiolabeled ligand ($\leq K_d$) and the target molecule. The resulting competition curve, generated by plotting radioactivity against competitor concentration, is used to estimate the IC_{50} value. The inflection point represents the concentration of the competitor required to displace 50% of the radioligand from the target. The IC_{50} value is then used to calculate the K_i value, which is

the equilibrium dissociation constant of the inhibitor, provided the K_d value of the radioligand is known (Auld et al., 2004). Compounds showing promising results are then selected for tritiation to further evaluate their affinity and selectivity.

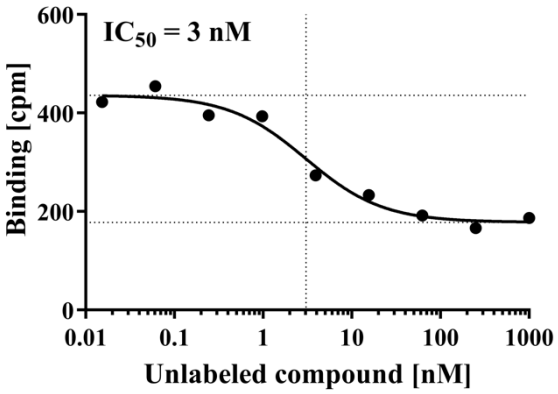

Fig. 14: Competition binding curve for IC_{50} determination. To determine the concentration of an inhibitor needed to occupy or displace 50% of the target (IC_{50}), a single concentration of radiotracer is used while varying the concentrations of a non-radioactive competitor. The IC_{50} is identified as the inflection point of the resulting competition curve. Figure adapted from (Herfert et al., 2019). Abbreviations: cpm, counts per minute

A saturation binding experiment is conducted to determine a compound's target affinity (**Fig. 15**). In this process, a constant concentration of the target molecule is incubated with varying concentrations of the radioligand. Plotting the activity of the bound fraction (counted activity/target concentration) against the radioligand concentrations yields a saturation curve. However, true saturation is not achieved because the ligand also binds non-specifically to other sites. Non-specific binding sites can be present on both biological (tissue sections) and artificial (consumables) materials. For example, ligands forming hydrogen bonds may weakly interact with proteins in tissue preparations, while lipophilic ligands might bind to lipids commonly found in membrane preparations. Additionally, materials used in the experiment (e.g., well plates, filters) can act as potential binding sites for radioligands. To characterize non-specific binding, an excess of the non-radioactive compound is used to displace specific binding. The total binding observed is a combination of specific and non-specific binding. Typically, the radiotracer concentration ranges from 1/10 of the estimated K_d to 10 times K_d, while the competitor concentration is maintained at 1000 times K_d. Linear regression analysis is then employed to estimate the K_d and B_{max} values (Auld et al., 2004). The available binding sites B_{max}, largely determine the required affinity K_d (Zhang et al., 2013). If the tissue contains a low concentration of binding sites, a very high affinity is necessary to generate a detectable signal.

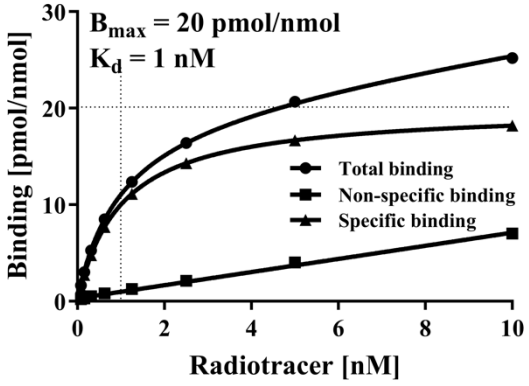

Fig. 15: Saturation binding curve for B_{max} and K_d determination. Total binding (target + radioligand) and non-specific binding (target + radioligand + excess non-radioactive compound) are measured after incubating various concentrations of radioligand. The specific binding curve is then derived by subtracting non-specific binding from total binding. B_{max}, representing the maximum number of target, is indicated by the horizontal dotted line, which converges with the specific binding curve at saturation. The dissociation constant K_d is marked by the vertical dotted line and is defined as the concentration of radiotracer required to reach half-maximum binding ($B_{max}/2$). Figure adapted from (Herfert et al., 2019)

Two primary assay formats for testing ligand-target interactions can be distinguished (**Fig. 16**): the scintillation proximity assay (**Fig. 16a**) and the filter binding assay (**Fig. 16b**). In the scintillation proximity assay, radioactive decay occurring near the scintillator-coated surface of a well plate generates scintillation, which is then detected by photomultipliers. In the filter binding assay, tracer molecules and the target are incubated in a filter well plate, followed by filtration. After filtration, scintillator is added, and the emitted light is detected by photomultipliers (Huhtala, 2013). Alternatively, a filter membrane can be used instead of a filter plate.

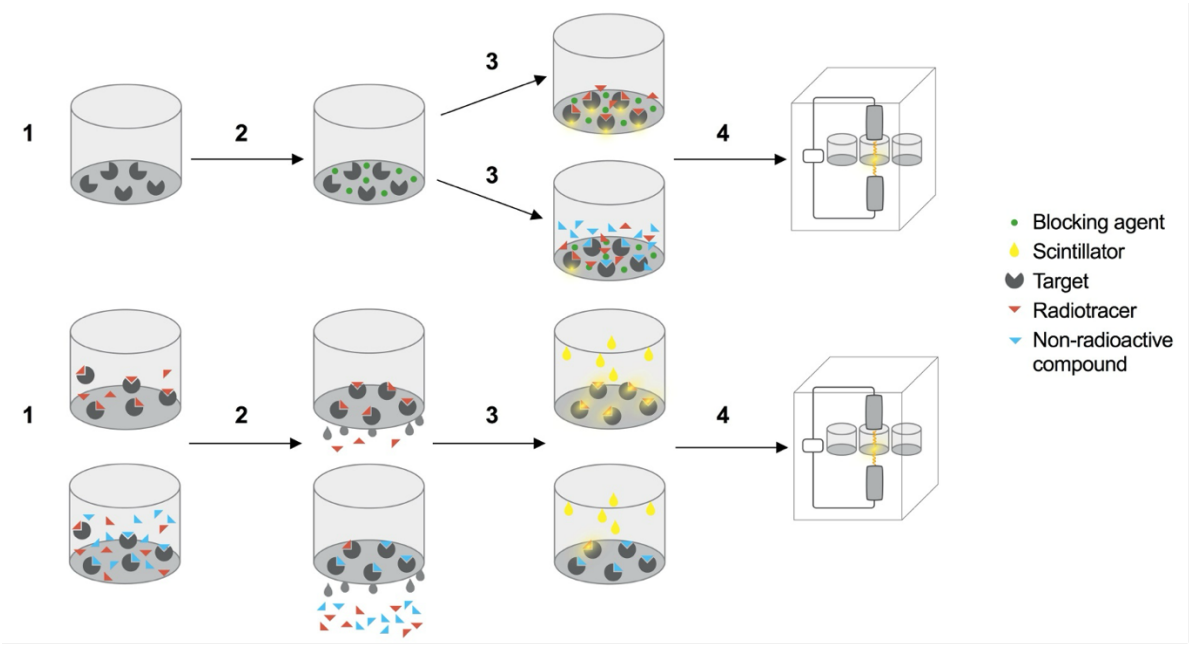

Fig. 16: Types of ligand-target interaction assays. (**a**) Scintillation proximity assay: (1) The target molecule is first incubated on a scintillator-coated plate. (2) A blocking step follows, using a non-reactive protein or blocking agent like bovine serum albumin to reduce non-specific binding to the plate. (3) To measure total binding, the radiotracer is dissolved in assay buffer and added to the wells. For assessing non-specific binding, the radiotracer is combined with an excess of the non-radioactive compound and added to a separate set of plates. (4) The proximity of the low-energy β-emitters to the scintillator-coated plate generates light, which is detected by a liquid scintillation counter. (**b**) Filter binding assay: (1) The radiotracer and target protein are incubated in solution on a filter plate to determine total binding. For non-specific binding assessment, an excess of the non-radioactive compound is added to a separate set of filter plates. (2) Vacuum filtration is performed to separate the bound radiotracer from the unbound radiotracer, followed by several washing steps to remove non-specifically bound radiotracer. (3) The scintillator is then added to each well of the filter plate. (4) The emitted light from the scintillator is detected by a scintillation counter. Figure extracted from (Herfert et al., 2019). Abbreviations: PTM, photomultiplier

K_d determination can also be carried out through *in vitro* autoradiography using healthy or diseased brain sections. This approach not only allows for the estimation of the dissociation constant K_d but also provides insight into the local distribution of the target within the tissue. Similar to a saturation binding experiment with recombinant proteins, brain tissue sections are incubated with increasing concentrations of the radioligand, with a parallel set incubated in the presence of an excess of the non-radioactive ligand. After washing away the unbound fraction, the sections are exposed to phosphor imaging screens, which are then analyzed using a phosphor imager (Johnstrom & Davenport, 2005). To further distinguish between specific and non-specific binding, immunohistochemistry can be performed on the same or adjacent sections. Compounds demonstrating favorable binding properties *in vitro* are subsequently selected for radiolabeling.

To date, various i*n vitro* methods have been developed to assess the binding affinity of compounds to α-synuclein fibrils. However, it remains uncertain whether these assays accurately reflect the pathophysiological conditions found in human-derived tissues. Using

cryo-EM, researchers have identified distinct conformations of α-synuclein fibrils associated with different synucleinopathies, revealing that these conformations differ from synthetic fibrils (Schweighauser et al., 2020).

1.5.3.2 *In vivo* characterization

In the subsequent phase of tracer development, the behavior of the tracer within the body and brain of wild-type rodents is closely examined. Various physiological factors, including liver metabolism, molecular size, the phagocytic system, and immune response, all contribute to the *in vivo* metabolism of the tracer (Huhtala, 2013). To monitor the tracer's distribution, samples are taken from organs such as the kidneys, muscles, blood, liver, lymph nodes, bones, heart, lungs, and brain at different time intervals following radiotracer injection. The radioactivity within these sampled organs is measured using a gamma counter. Additionally, whole-body PET imaging offers a non-invasive means to track tracer distribution over time.

In vivo metabolism can be further assessed through metabolite analysis, which involves identifying radiolabeled metabolites in plasma and homogenized brain samples at various time points post-injection. This is typically done using radio high performance liquid chromatography (HPLC). The presence of brain metabolites is particularly problematic, as they are indistinguishable from the parent tracer in imaging, potentially confounding the interpretation of the PET scan results (Hashimoto et al., 2014).

The tracer's binding to fibrils is ultimately confirmed *in vivo* by performing stereotaxic injections in mice, rats, or non-human primates, and subsequently conducting PET imaging.

1.5.4 Compound selection

Screening over 20,000 compounds revealed 3,5-diphenylpyrazole as a highly effective scaffold for detecting aggregated α-synuclein inclusions (Wagner et al., 2013). Compounds based on 3,5-diphenylpyrazole effectively inhibited pathological aggregation of α-synuclein by binding to α-synuclein fibrils, as shown by fluorescence spectroscopy. Among these, anle138b (**Fig. 17a**) demonstrated significant inhibition of both prion protein and α-synuclein aggregates with strong effectiveness against various prion strains. It also prevented oligomer formation *in vitro* and *in vivo*, reduced oligomer accumulation, neuronal degeneration, and disease progression in mouse models of prion disease and Parkinson’s disease, all without detectable toxicity. Additionally, anle138b exhibited excellent oral bioavailability and effective blood-brain barrier penetration. Fluorescence studies revealed that anle138b increased fluorescence specifically when bound to fibrillar α-synuclein, not to its monomeric form, and

showed a high binding affinity (K_d = 190 ± 120 nM) for hydrophobic pockets in fibrils (Deeg et al., 2015). Subsequent research expanded anle138b's application to tauopathies, multiple system atrophy, and Alzheimer's disease with tau pathology. Anle138b was shown to bind aggregated tau, as revealed by fluorescence spectrometry, inhibit tau aggregation *in vitro* and *in vivo*, and improve disease progression, symptoms, and cognition in tau transgenic mice (Wagner et al., 2015). In a model of multiple system atrophy, treatment with anle138b reduced α-synuclein oligomer accumulation and improved motor function (Heras-Garvin et al., 2019). Additionally, in a tau transgenic mouse model, anle138b treatment reduced tau pathology when administered after the onset of initial symptoms (Brendel et al., 2019). These findings suggest that oligomer modulators like anle138b could offer a new disease-modifying approach for neurodegenerative diseases, as they target structural features common to pathological oligomers across different protein aggregation diseases.

To effectively develop and validate a therapy, it is crucial to have a method for assessing its success *in vivo*, with PET tracers being a suitable option. However, anle138b (now Emrusolmin) cannot be labeled with carbon-11 or fluorine-18. As a solution, anle253b (**Fig. 17b**), a derivative of anle138b, was synthesized and tested. This compound was labeled with carbon-11 and evaluated *in vivo* using PET imaging in mice (Maurer et al., 2020). *In vitro* competition using [^{3}H]anle138b as lead compound revealed high affinity binding to α-synuclein fibrils (IC_{50} = 1.6 nM). However, *in vivo*, [^{11}C]anle253b PET showed unfavorable distribution in mouse brain, likely caused by a relatively high clog*P* value of 4.55.

The log*P* value measures lipophilicity and is critical in determining a PET tracer's ability to cross the blood-brain barrier while avoiding excessive binding to lipid tissues, which can compromise the signal-to-noise ratio. The optimal log*P*/log*D* range for PET tracers, as identified by Cunningham *et al.* and van de Waterbeemd *et al.,* is between 1.5 to 2.5/1 to 3 at a pH of 7.4 (Cunningham et al., 2005; van de Waterbeemd et al., 1998). To find suitable PET tracers, new derivatives were developed and selected from a synthesized compound library based on their log*P* values. Among these, MODAG-001 (**Fig. 17c**) (clog*P* = 3.63) and its de-methylated derivative MODAG-005 (**Fig. 17d**) (clog*P* = 3.38) were identified for further evaluation.

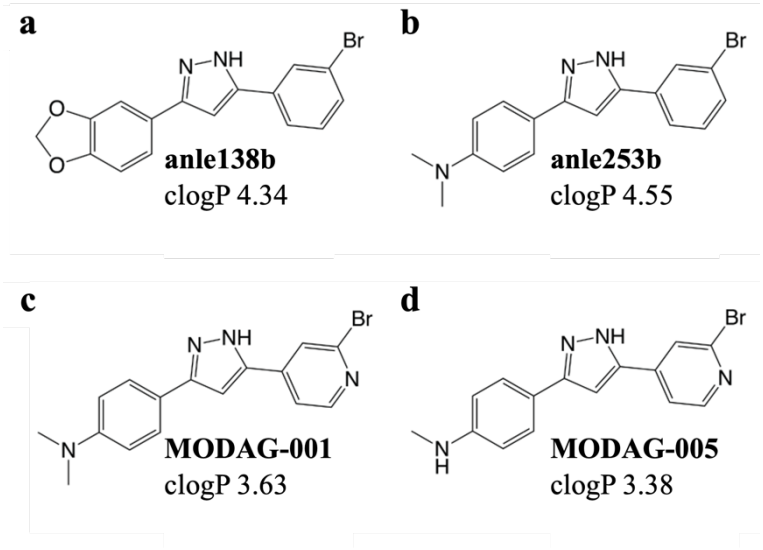

Fig. 17: Compounds based on 3,5-diphenylpyrazole. (**a**) anle138b (Emrusolmin), (**b**) anle253b, (**c**) MODAG-001 and (**d**) MODAG-005 and their respective clog*P* values. Figure created in ChemDraw

1.5.5 Current progress in developing α-synuclein aggregate binding ligands for PET imaging

The first molecules identified for binding to α-synuclein fibrils were derived from the fluorescent dye Thioflavin-T (Naiki et al., 1989). Subsequently, several other dyes were developed and tested, including derivatives of N-arylaminonaphthalene sulfonate, mono-, tri-, and pentamethine, cyanine. However, these dyes either exhibited low affinities (in the micromolar range) or non-selective binding (Celej et al., 2008; Kovalska et al., 2012; Volkova et al., 2008). Nile Red and Nile Blue have been shown to bind to Lewy bodies in human brain tissue sections from patients with Parkinson's disease and dementia with Lewy bodies (Neal et al., 2013). These dyes also demonstrated selectivity over tau and amyloid-β in human brain tissue from Alzheimer's disease patients. However, it is unclear whether further investigations have been conducted to explore these findings in more detail.

One of the most well-known α-synuclein ligands is SIL23, a phenothiazine analogue (Bagchi et al., 2013). SIL23 was identified from a set of compounds that demonstrated strong affinity for α-synuclein fibrils following several structural modifications. Although its selectivity over tau and amyloid-β was limited, SIL23 remains useful for screening purposes. SIL5 and SIL26, derivatives of SIL23, were selected for PET imaging studies (Zhang et al., 2014). However, the slow washout of these tracers poses a challenge, leading to high binding values that may obscure specific binding to pathological α-synuclein. Further investigation using transgenic animals or animals injected with α-synuclein fibrils could help address this issue.

Benzothiazole derivatives have been developed from the tau-binding compound [^{11}C]PBB-3, known for its high affinity for α-synuclein fibrils and good selectivity over tau and amyloid-β (Miranda-Azpiazu et al., 2020). Among these, the C05 family stands out, with [^{3}H]C05-01 binding to α-synuclein fibrils at an affinity of approximately 25 nM. Interestingly, this compound also showed very high affinity in homogenates from dementia with Lewy bodies and tissue sections from Alzheimer's disease, indicating a need for further optimization. Additionally, the related thiazolium compounds RB1 and RB2 have been developed, with RB1 exhibiting an improved K_d value of 30 nM (Gaur et al., 2021). However, these fluorescent probes also bind to various amyloid fibrils including insulin.

Ferrie *et al.* employed an *in silico* screening approach to identify compounds for competition and saturation binding studies (Ferrie et al., 2020). Their most successful compound [^{125}I]61, selected from a series of 2-phenoxy-N-(3-phenylisoxazol-5-yl)acetamide analogues, demonstrated a K_d value of 1.06 nM toward α-synuclein fibrils. However, it showed only a five-fold selectivity over amyloid-β. While binding to pathological regions was confirmed in an A53T mouse model of Parkinson's disease, the compounds ultimately failed due to high non-specific binding.

Several other studies have described potential tracers that faced various challenges, such as insufficient affinity (C.-J. Hsieh et al., 2018), lack of selectivity (Bagchi et al., 2013; Josephson et al., 2018; Yue et al., 2018), failure to bind to rodent or human brain tissue (Verdurand et al., 2018), unfavorable *in vivo* kinetics, or lack of sufficient data (Chu et al., 2015; Kaide et al., 2022; Kaide et al., 2020; Ono et al., 2016; Watanabe et al., 2017).

Recent research has made significant progress toward identifying a suitable PET tracer for pathological α-synuclein. Four promising ligands have been proposed: [^{18}F]ACI-12589 (Capotosti et al., 2021; Smith et al., 2023), [^{18}F]C05-05 (Endo et al., 2024; Ono et al., 2020), [^{18}F]SPAL-T-06 (Matsuoka et al., 2022), and the recently published benzothiazole derivative [^{18}F]-F0502B (Xiang et al., 2023).

The PBB3 derivative [^{18}F]C05-05 was identified through *in vitro* screenings and demonstrated binding to brain sections from patients with dementia with Lewy bodies, Parkinson's disease dementia, and multiple system atrophy via autoradiography. In a competition assay using dementia with Lewy bodies homogenates, it showed eight-fold higher binding compared to Alzheimer's disease homogenates. However, while longitudinal studies have tracked its binding in α-synuclein fibril inoculated mice and marmosets, comprehensive PET quantification of the tracer is still lacking. Additionally, detailed *in vivo* and *in vitro*

evaluations, including fibril affinity, radiometabolite formation and *in vivo* blocking effects, remain unreported (Endo et al., 2024; Ono et al., 2020).

The evaluation of [^{18}F]ACI-12589 lacks data on fibril binding assays. The authors report that their compound has low nanomolar affinity (17 nM to 33.5 ± 17.4 nM) for brain sections from familial and sporadic Parkinson's disease, as well as a case of multiple system atrophy, based on autoradiography. They also suggest a more than 30-fold selectivity over tau and amyloid-β. However, it is unclear how well the brain tissue was characterized to determine if binding co-localized with α-synuclein aggregates. Notably, [^{18}F]ACI-12589 shows strong binding to the cerebellum of multiple system atrophy patients in PET imaging compared to controls. Autoradiography revealed binding in cases of multiple system atrophy, Lewy body variant of Alzheimer's disease, Parkinson's disease, and Parkinson's disease dementia. Despite claims of selectivity over tau and amyloid-β, no data on Alzheimer's disease patients were presented (Capotosti et al., 2021; Smith et al., 2023).

Preclinical *in vitro* and *in vivo* data for [^{18}F]SPAL-T-06 have not been published, leaving gaps in understanding regarding off-target binding, selectivity, kinetics, and metabolism. However, a PET study with [^{18}F]SPAL-T-06 did show promising results, with good binding observed in two cases of multiple system atrophy (one cerebellar type and one Parkinsonian type). The third case (Parkinsonian type) showed only minor differences in uptake compared to healthy controls. Additionally, autoradiography demonstrated blockable binding in multiple system atrophy (Parkinsonian type). [^{18}F]SPAL-T-06 exhibited high affinity (K_i = 2.49 nM) in homogenates of the putamen from a multiple system atrophy patient (Matsuoka et al., 2022).

The benzothiazole derivative F0502B, demonstrated a K_d value of 10.97 nM for preformed α-synuclein fibrils and between 4.26 nM and 7.32 nM for α-synuclein deposits in Parkinson's disease brains. The authors conducted a study involving [^{18}F]-F0502B PET scans in macaques, showing higher binding in subjects injected with α-synuclein preformed fibrils compared to controls, though with a notably low SUV (lower than 1). Evidence supporting the use of [^{18}F]-F0502B as a PET tracer for misfolded α-synuclein in humans is still lacking. Moreover, a comprehensive *in vitro* validation, including detailed histology and autoradiography, has not been provided. Limitations of this compound include the need for investigation of off-target binding and concerns regarding whether the recombinant fibrils truly resemble those found in the brains of Parkinson's disease patients (Xiang et al., 2023).

1.6 Imaging brain activation

1.6.1 BOLD-fMRI

The blood oxygenation level-dependent (BOLD) signal has been used in functional MRI (fMRI) studies to describe neuronal activity indirectly and non-invasively with high spatial and temporal resolution at rest and during stimulation-evoked activation in the brain (Bandettini et al., 1992; Biswal et al., 1995; Kwong et al., 1992; Ogawa, Lee, Kay, et al., 1990). Furthermore, the recognized activated areas can be easily assigned to the corresponding anatomical structures. The vascular-driven BOLD contrast is a convoluted signal composed of contributions from cerebral blood volume (CBV), cerebral blood flow (CBF), and cerebral metabolic rate of oxygen ($CMRO_2$) (Belliveau et al., 1991; Kim & Ogawa, 2012). Changes in MRI signal intensity in affected voxels occur when the ratio of oxygenated (diamagnetic) to deoxygenated (paramagnetic) blood in the circulation changes (Ogawa & Lee, 1990; Ogawa, Lee, Nayak, et al., 1990).

When specific cells are activated or stimulated by a task, they require more oxygen, leading to a rapid, slight increase in $CMRO_2$ and consequently higher oxygen consumption along with a higher concentration of deoxygenated blood. Following this, a slower but more pronounced response occurs: an increase in CBF which leads to a significant reduction in deoxygenated blood concentration as fresh, oxygenated blood replaces the deoxygenated blood. Therefore, the BOLD signal does not directly measure brain activity; instead, it reflects changes in blood flow and oxygenation. These hemodynamic changes can be measured in the affected network, allowing activity analysis within the respective task or stimulation period (Logothetis et al., 2001; Raichle, 2001)

These processes shape the characteristic hemodynamic response function (see **Fig. 18a**). Initially, a slight decrease in signal intensity, known as the "initial dip," occurs before the positive BOLD signal. This dip is due to increased oxygen uptake in the brain, leading to a brief local drop in blood oxygen levels as oxygen delivery lags by one to two seconds. Following this, an oversupply of oxygen reduces the proportion of deoxygenated hemoglobin in the blood, producing the actual BOLD signal, which peaks with a delay of four to six seconds. After the stimulation ends, brain oxygen consumption decreases, leading to a brief post-stimulus undershoot that can last up to 30 seconds, a phenomenon still under debate (Magistretti & Allaman, 2015; Siero et al., 2013).

With a prolonged series of stimuli, the dominant peak evolves into a broad plateau that persists until the stimulation ceases (**Fig. 18b**).

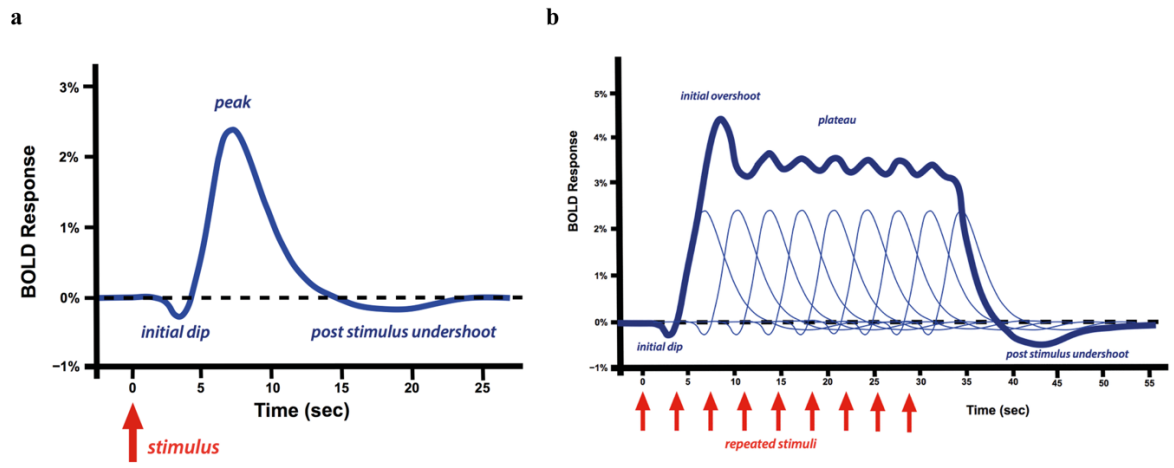

Fig. 18: Typical hemodynamic response function (a) and hemodynamic response function after repeated stimuli (b). (**a**) A brief initial dip is noted before the primary positive BOLD response, which is followed by a post-stimulus undershoot. (**b**) Following the initial dip, successive stimuli lead to a plateau in the BOLD response. Courtesy of Allen D. Elster, MRIquestions.com (Elster, 2024) (lastly browsed on 2nd of September 2024). Abbreviations: BOLD, blood oxygen level-dependent

The BOLD signal is influenced by factors beyond neuronal activity, including the vascular geometry, blood hemoglobin concentration, blood volume, and blood oxygenation. Oxygenation levels in the brain are regulated by the balance between oxygen extraction for metabolism (neurometabolic coupling) and the delivery of oxygenated blood to active regions (neurovascular coupling). In an average adult human, the brain constitutes roughly 2% of total body weight. Despite its small size, it consumes approximately 20% of the body's oxygen and, consequently, a significant portion of its caloric intake (Howarth et al., 2012; Kadekaro et al., 1985; Shu et al., 2016).

In the cerebral cortex, most energy is used by the sodium-potassium ATPase (adenosine triphosphate-ase) to maintain ionic gradients after neuronal activity. The brain has limited glycogen storage, so it relies on a continuous supply of oxygen and glucose for ATP production via oxidative phosphorylation. *Neurovascular coupling* ensures this supply during neuronal activity, though the oxygen provided often exceeds what is consumed. This suggests that neurovascular coupling may serve other roles than increasing oxygen supply, such as maintaining glucose levels, clearing waste products, or regulating temperature. Understanding which cells control blood flow and oxygen consumption is key to interpreting BOLD signals accurately (Attwell et al., 2010; Brown & Ransom, 2007; Hall et al., 2012; Howarth et al., 2012; Howarth et al., 2021). Neuronal activity triggers the BOLD signal, which is often thought to reflect the combined activity of excitatory neurons within a specific brain region. In fact,

task-related BOLD signals typically increase in brain areas where excitatory activity is anticipated to rise (Logothetis et al., 2001; Marota et al., 1999; Silva et al., 1999). In contrast, negative BOLD responses in human subjects have been noted in regions with increased GABAergic activity, indicating a drop in neuronal activity below baseline levels (Harel et al., 2002; Walter et al., 2016). *Neuromodulators* such as noradrenaline, acetylcholine, dopamine (see introduction), and serotonin can individually influence the activity of excitatory neurons, astrocytes, and the vasculature. This variability can complicate the interpretation of BOLD signals (Lecrux et al., 2017; Zaldivar et al., 2014). *Astrocytes* play a crucial role in bridging neuronal activity and blood flow regulation. They directly provide essential metabolites like lactate to neurons and influence blood vessel function through their involvement in neurovascular coupling. When neurons become active, this can lead to an increase in calcium levels within astrocytes, prompting them to release vasoactive substances that affect blood flow dynamics (Attwell et al., 2010). Beyond the signals originating from neurons and astrocytes, the intrinsic properties of the *vasculature* also play a significant role in shaping the BOLD response in various ways. Blood vessel constriction and dilation in response to signals from the brain or blood are directly controlled by contractile *smooth muscle cells* and *pericytes*. Traditionally, smooth muscle cells on arterioles have been seen as the primary mediators of the vascular changes underlying neurovascular coupling. However, recent research has highlighted the crucial role of pericytes, particularly those on capillaries and precapillary arterioles. These pericytes, which express smooth muscle actin, are now recognized for their ability to actively constrict or dilate in response to neuronal signals (Hall et al., 2014; Peppiatt et al., 2006). Hill *et al.* challenge this view, arguing that pericytes do not express smooth muscle actin and are not contractile *in vivo.* Instead, they suggest that neurovascular coupling is primarily driven by the contractility of smooth muscle cells in arterioles (Hill et al., 2015). *Endothelial cells* play a crucial role in modulating the vascular response to neuronal activity, and thus the BOLD signal, by transmitting vasodilatory signals along the vasculature. This process amplifies the hemodynamic response by causing dilation of blood vessels upstream of the site of local neural activity (Iadecola et al., 1997).

However, the BOLD response reflects not just the influx of oxygenated blood but also the balance between this supply and the rate at which nearby cells consume oxygen.

Brain oxygen consumption largely reflects excitatory and inhibitory neuronal activity, glial and vascular cells also play a role. The consumption of oxygen by active neurons can diminish positive BOLD signals, making it challenging to accurately interpret these signals as indicators of neuronal activity. Calibrated BOLD studies, which measure $CMRO_2$, might offer a more

precise representation of net neuronal activity due to their enhanced spatial specificity to active regions. However, since the most metabolically active cells (such as excitatory neurons or parvalbumin interneurons) are often not the same as those responsible for signaling blood vessel dilation (inhibitory neurons or astrocytes), $CMRO_2$ measurements provide different insights compared to positive BOLD signals regarding cellular activity (Attwell & Laughlin, 2001; Howarth et al., 2012; Howarth et al., 2021; Kann, 2016).

Although the brain has evolved to minimize energy expenditure, BOLD-fMRI measurements of brain activity are closely linked to stimulation-induced aerobic glycolysis, a less energy-efficient metabolic process. This pathway consumes more glucose but produces less ATP compared to the more efficient cellular respiration via oxidative phosphorylation. Theriault *et al.* propose that aerobic glycolysis serves as a trade-off between energy efficiency and information processing: by sacrificing metabolic efficiency, the brain optimizes the informational efficiency of thin axons and potentially other small neural and glial structures (Theriault et al., 2023).

1.6.2 [^{18}F]FDG-fPET

Another imaging technique for monitoring regional brain activity *in vivo* in both humans and rodents is PET known for its high sensitivity and specificity. PET imaging of glucose metabolism is conducted using the radiolabeled glucose analog [^{18}F]2-fluoro-2-deoxy-D-glucose ([^{18}F]FDG), following an uptake period after a bolus injection (Phelps et al., 1979; Reivich et al., 1979). Unlike glucose, [^{18}F]FDG is phosphorylated by hexokinase but cannot proceed through the glycolytic pathway, leading to its accumulation in the cell. Consequently, cells with increased activity accumulate more [^{18}F]FDG over time. To differentiate between increased regional activation during tasks or stimuli (such as finger tapping or checkerboard patterns) and resting state brain activity, two separate PET scans are typically performed: one for baseline measurement and one during stimulation (Kushner et al., 1988; Pietrini et al., 2000; Vlassenko et al., 2006). Additionally, two separate [^{18}F]FDG-PET scans have been used in rats to visualize brain metabolic connectivity following optogenetic stimulation of nucleus accumbens neurons (Thanos et al., 2013). To reduce within-subject variability from repeated scans, a constant infusion of [^{18}F]FDG has been employed. This approach maintains stable [^{18}F]FDG levels in plasma and tissue throughout the scan, allowing for the detection of regional changes in tracer uptake during task or stimulus-induced brain activation (**Fig. 19**) (Hahn et al., 2016; Rischka et al., 2018; Villien, 2015).

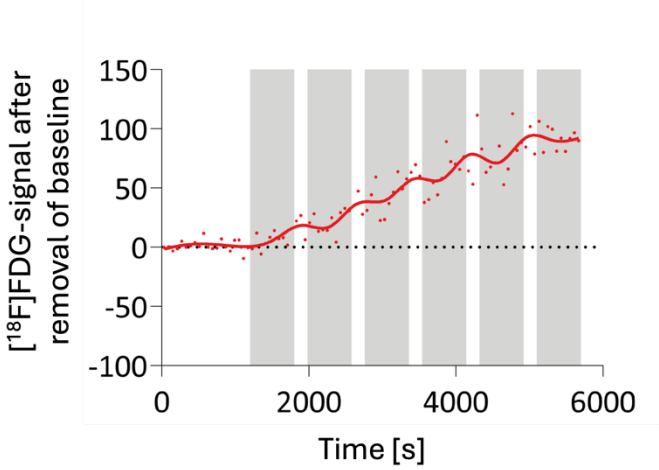

Fig. 19: Uptake pattern in stimulation experiments during constant [^{18}F]FDG infusion. A constant infusion of [^{18}F]FDG can be used to maintain stable levels of the tracer throughout the acquisition. This method facilitates the detection of regional changes in tracer uptake (red) associated with brain activation during tasks or stimulation (grey bars)

The accumulation of the tracer [^{18}F]FDG is primarily facilitated by the glucose transporter (GLUT) family. The human brain consumes about 20% of the D-glucose we ingest. For glucose to reach brain cells, it must pass through several barriers, most notably the blood-brain barrier, which is made up of tightly connected endothelial cells that restrict the entry of many substances. Because D-glucose is hydrophilic, it requires the aid of specific glucose transporters to move across these barriers and enter brain cells, including neurons, astrocytes, oligodendrocytes, and microglia. To meet the brain's diverse metabolic demands, different glucose transporters are expressed in various brain regions and cell types. The primary transporter responsible for moving D-glucose across the blood-brain barrier is GLUT1, a high-affinity transporter found abundantly in endothelial cells. Additional transporters such as GLUT3, GLUT4, and SGLT1 are also present in smaller brain vessels. Astrocytes, which surround brain capillaries with their end-feet, also express the high-affinity GLUT1 transporter and play a crucial role in glucose metabolism. These cells additionally express low-affinity transporters like GLUT2, GLUT3, and the insulin-sensitive GLUT4. Most of the D-glucose that exits the capillaries is absorbed by astrocytes, where it is either converted into L-lactate or passed along to neurons. Neurons primarily rely on the high-affinity GLUT3 transporter for glucose uptake, although GLUT2 and GLUT4 also contribute to their glucose absorption (Koepsell, 2020; Meyer et al., 2019).

The contribution of different cell types to the PET signal following [^{18}F]FDG injection is still debated:

Several studies suggest that *astrocytes* are the primary contributors to the PET signal (Carter et al., 2019; Magistretti & Pellerin, 1996; Stoessl, 2017; Zimmer et al., 2017). Neurons, which have limited metabolic reserves, rely on a continuous energy supply. Astrocytes, which store energy as glycogen, increase glycolysis in response to heightened neuronal activity. Their endfeet, which interact with blood vessels, are equipped with GLUT1 to facilitate glucose uptake, thus meeting the energy demands of active neurons. Additionally, astrocytes produce and release lactate to support neuronal function. Although the lactate transfer from astrocytes to neurons is well-established as crucial for neuronal energy support, the precise mechanisms through which astrocytes sense and respond to neuronal metabolic needs, and the signaling pathways regulating their glucose metabolism, are not fully understood (Beard et al., 2021; Theparambil et al., 2024; Turner & Adamson, 2011). Theparambil *et al.* propose that adenosine, via A2B receptor activation and cAMP (cyclic adenosine monophosphate) signaling, regulates astrocytic glucose metabolism in response to neuronal activity. Astrocytes also help clear neurotransmitters from the synaptic cleft using ATP produced through glycolysis (Beard et al., 2021).

Contrary to the view that astrocytes are the primary contributors, a study examining isolated neurons, astrocytes, and microglia following [^{18}F]FDG injection in mice suggests that *microglia* might be the major contributors to the PET signal (Xiang et al., 2021). This finding, though controversial and requiring further investigation, highlights ongoing debates and the need for more research in this area.

Several studies have suggested that neurons directly import glucose in culture (Díaz-García et al., 2021; Koepsell, 2020; Pathak et al., 2015; Rangaraju et al., 2014). However, confirming this directly has been challenging due to the presence of glia in primary rodent neuron cultures, which makes it difficult to separate glial from neuronal glucose uptake. Li *et al.* addressed this by using nearly homogeneous human neuron cultures, demonstrating that GLUT3, a glucose transporter, is exclusively expressed in neurons and is essential for normal glucose uptake at physiological brain levels. Their findings confirmed that human neurons metabolize glucose via glycolysis and derive most of their tricarboxylic acid cycle metabolites from glucose (Boado et al., 1994; Li et al., 2023).

1.7 Optogenetic stimulation

In September 1979, Crick published an article in Scientific American, asserting that despite the ongoing accumulation of detailed knowledge, the functioning of the human brain remains deeply mysterious. He proposed that it would be beneficial to have *"... a method that would*

make it possible to inject one neuron with a substance that would then clearly stain all the neurons connected to it, and no others, would be invaluable. So would a method by which all neurons of just one type could be inactivated, leaving the others more or less unaltered" (Crick, 1979). Manipulating neural activity through methods like extracellular electrical manipulation or pharmacological and genetic techniques is challenging, as these approaches either lack cell-type specificity or temporal precision. The need for a technique that combines both high temporal and cellular precision led to the development of optogenetics.

Optogenetics enables a temporally precise cell-type-specific activation or inhibition of neurons, allowing for the manipulation of specific networks of functionally, metabolically, and structurally connected neurons. This capability is possible *in vivo* thanks to Karl Deisseroth's research group, which successfully transferred the light-activated ion channel channelrhodopsin-2 (ChR2) into neurons (Boyden et al., 2005) (**Fig. 20a**). These channels are seven transmembrane domain proteins that provide the algae *Chlamydomonas reinhardtii* with visible light perception to optimize their positioning in water. When exposed to blue light, the protein undergoes a conformational change, causing the ChR2 to open and allowing cations, such as H^+, Ca^+ and Na^+, to enter, consequently depolarizing the membrane (**Fig. 20b**). In contrast, halorhodopsin, another type of opsin, allows Cl^- ions to flow into the cytoplasm when exposed to yellow light. Opsins can be distinguished by various characteristics, including the light spectra that activate them, their light sensitivity, and their rates of opening and closing. For instance, ChR2 (specifically the H134R variant used in our experiments) is optimally stimulated by blue light at 450 nm and requires an illumination intensity of at least 1.07 mW/mm². At a higher light intensity of 19.8 mW/mm², the channel takes approximately 1.92 ms to open and 17.9 ms to close (Delbeke et al., 2017; Lin, 2011; Lin et al., 2009). When using prolonged stimulation with ChR2, caution is needed to avoid desensitization of the channel. Desensitization means that after the channel closes, there is a period of about two seconds during which it cannot be reactivated. Additionally, synapses may become exhausted and require time to recover. Kittelmann *et al.* investigated the detailed spatiotemporal patterns of synaptic vesicle recycling and recovery in *C. elegans* motoneurons under conditions of vigorous optogenetic stimulation. Both morphological and physiological assessments revealed a surprisingly slow recovery process, taking up to 20 seconds (Kittelmann et al., 2013; Nagel et al., 2003). However, these values are likely to vary with changes in stimulation duration, intensity, and frequency.

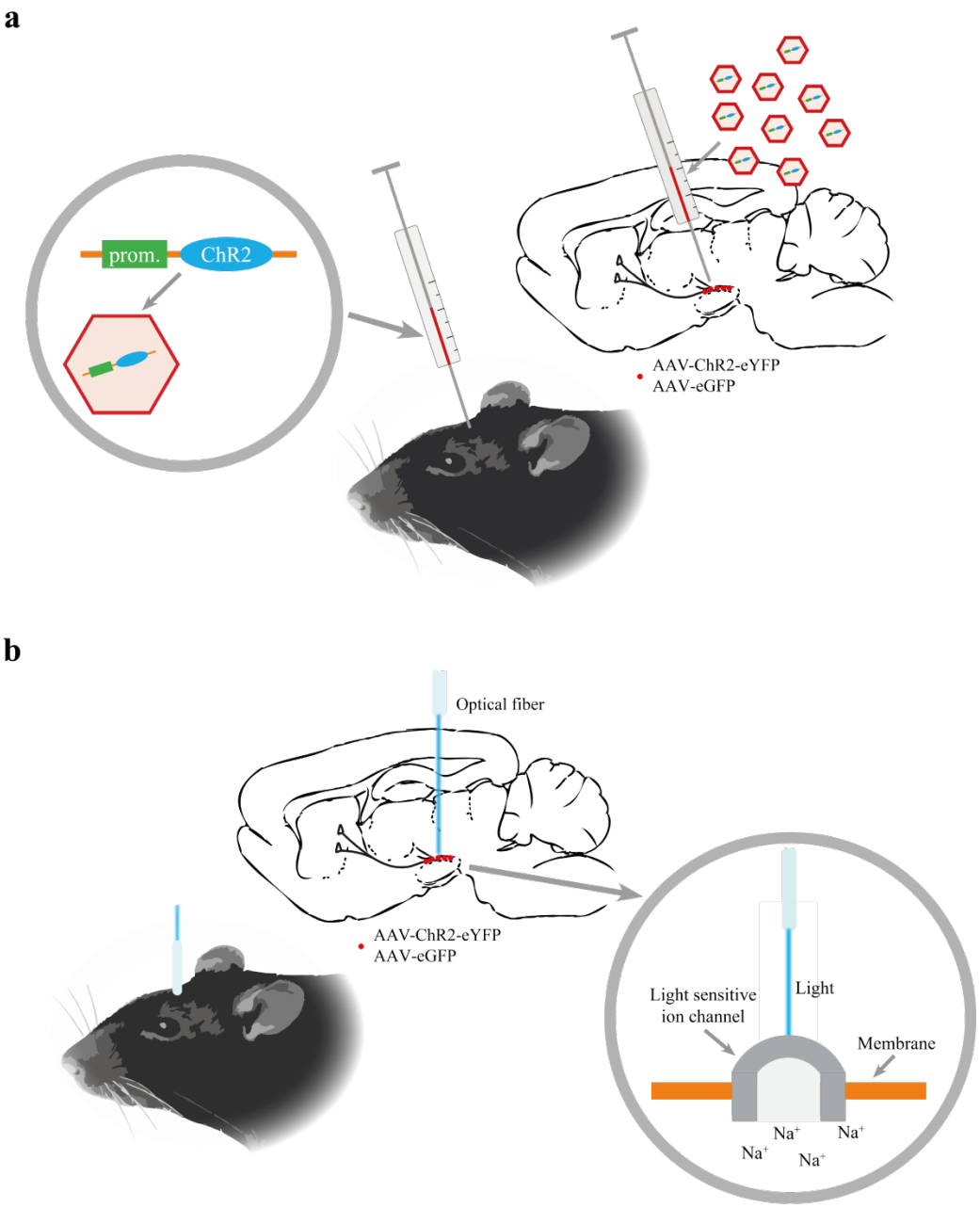

Fig. 20: Optogenetic stimulation of neurons expressing ChR2. Genes encoding the channel protein ChR2 along with a suitable promoter, are incorporated into a viral vector. Following injection into the target area, this genetic construct integrates the ChR2 into the neuronal cell membrane (**a**). When the expression reaches its peak, an optical fiber connected to a controlled light source is implanted at the injection site. Upon illumination, the ChR2, which features seven transmembrane helices, undergoes a conformational change that opens the central pore. This allows cations to enter the cell, causing membrane depolarization and triggering an action potential.(**b**). Abbreviations: ChR2, channelrhodopsin-2; prom., promoter

1.7.1 Strategies and challenges in targeting neuronal populations

To determine how to target (specific) neuronal populations with genetic methods, several factors must be considered. Viruses, such as the adeno-associated virus (AAV), herpes simplex virus or the lentivirus are highly effective gene delivery systems. They can infect host cells, hijack their metabolism for replication and have a protective shell called a capsid.

Advancements in viral vector technology allow for the precise modification of these viruses. By editing their genomes to remove pathogenic genes and replace them with therapeutic ones, researchers create viral vectors that do not replicate but still retain their ability to deliver genetic material to target cells. These vectors are typically assembled using multiple plasmids that include components such as ChR2 and the promoter, among others, and are selected for their specificity. There are several AAV serotypes, ranging from AAV 1 to 9, with serotype 2 being the most frequently used for targeting neurons. A key observation in adenoviral-mediated gene transfer to the brain is that dopaminergic neurons in the substantia nigra do not support long-term expression of adenoviral vectors. Remarkably, these neurons seem to specifically reduce transgene expression by eliminating the adenoviral genome (Haggerty et al., 2020; Kügler et al., 2003). Another crucial factor is the choice of promoter on the plasmid. For example, ChR2 is often placed downstream of powerful promoters such as human synapsin or human cytomegalovirus. The selected promoter influences the level of opsin expression in the targeted cells, which can vary by brain region, ensuring robust expression where the construct is implemented (Albert et al., 2017; Delbeke et al., 2017). AAVs are traditionally injected into the brain via stereotactic methods, which can cause needle tracts, skull perforations, inflammation at the injection site, and the unintended spread of the virus when withdrawing the needle. However, Wang's group has proposed a novel non-invasive technique to deliver AAVs into target tissues. Their team was the first to show that focused ultrasound can facilitate viral gene delivery by temporarily opening the blood-brain barrier after systemic AAV administration. Using this approach, they successfully achieved optogenetic activation of blue-sensitive ChR2 following intravenous AAV delivery, combining functional ultrasound with circulating microbubbles to target gene delivery through the blood-brain barrier opening (Pouliopoulos et al., 2022; Wang et al., 2017; Wang et al., 2015).

To achieve more precise activation or inactivation of specific neuronal cell types, researchers developed opsin-delivering viruses that rely on Cre recombinase for opsin expression, using a double-floxed inverted open-reading-frame approach. In this system, the opsin gene is initially in a nonfunctional orientation and is only flipped into the correct position in the presence of Cre, enabling strong and targeted opsin expression (Atasoy et al., 2008). This technique is combined with the use of bacterial artificial chromosome vectors in transgenic animals, which allows for efficient, reproducible, and cell-specific protein expression *in vivo*. For example, neurons can be targeted based on their neurotransmitter phenotype, such as creating a rat line that expresses Cre exclusively in dopaminergic neurons, ensuring only those neurons express the opsin (Gong et al., 2007).

Alongside advancements in viral vector technology, non-viral gene delivery methods have also been developed. These alternatives include techniques such as electroporation, which uses electrical pulses to facilitate transfection, as well as laser photoporation, which utilizes light-based approaches to introduce genetic material into cells (Antkowiak et al., 2013; Nomura et al., 2016). Animals have been genetically engineered to directly express opsins but using transgenic or knock-in mouse lines for optogenetic research comes with significant challenges. These include the considerable time, expense, and effort needed to generate and validate such animal models, making the process less efficient and more resource-intensive (Arenkiel et al., 2007).

Optogenetics depends on advanced light delivery systems to precisely control neural activity in both research and live animal environments. As light travels through materials, including biological tissues, it is absorbed and scattered, which reduces its effectiveness. Blue light can activate neurons at depths of up to 1.4 mm, though higher light power can increase tissue temperature. Shifting to near-infrared light extends the penetration to about 5 mm, but this is still insufficient for deep brain regions. Consequently, effective optogenetic activation often requires the implantation of a light-delivering fiber connected to a laser or LED (Aravanis et al., 2007; Chen et al., 2018).

1.7.2 Application of optogenetics in neurobiology

Optogenetics is a cutting-edge technique used to investigate neural circuits associated with psychiatric and neurological conditions. By delivering light-sensitive proteins into specific brain cells via gene transfer, researchers can precisely control neural activity. This method enables both activation and inhibition of neurons within extensive networks, such as the cortex, allowing for sophisticated manipulation of neural circuits. Optogenetics can be utilized in three primary ways:

First, to allow for precise control over the activation and inhibition of neurons. By generating and analyzing various firing patterns, researchers can explore their impact on postsynaptic neurons and related behaviors. Second, optogenetics is used to selectively modulate specific types of neurons to investigate neural circuits associated with mental disorders, to uncover insights into these conditions and identify potential therapeutic targets. Third, to facilitate the creation of reversible models of neurological disorders, enabling researchers to test and refine new treatments (Chen et al., 2022).

Deep brain stimulation is a prominent therapeutic approach for treating severe neurological and psychiatric disorders, such as Parkinson's disease. However, due to the diverse nature of brain tissues where deep brain stimulation electrodes are implanted, pinpointing the precise target cell types and understanding the underlying mechanisms have been challenging. To address this, recent research employed optogenetics and solid-state optics to selectively modulate neural circuits in freely moving rodents with Parkinson's disease. The study revealed that effective therapeutic outcomes in the subthalamic nucleus result from stimulating the afferent axons that project to this area, rather than directly altering the subthalamic nucleus neurons themselves. These insights underscore the potential of optogenetics in accurately defining neural circuits and evaluating the effects of targeted stimulation on behavior (Gradinaru et al., 2009).

Research into Parkinson's disease has highlighted the roles of the direct and indirect pathways in motor symptomatology. Kravitz *et al.* employed optogenetics to explore these pathways in mice with ChR2 expression driven by D1-Cre or D2-Cre recombinase in medium spiny neurons. Their study revealed that activation of the D2 neurons in the indirect pathway led to symptoms such as freezing, bradykinesia, and decreased movement. Conversely, activation of the D1 neurons in the direct pathway resulted in reduced freezing and increased movement. Additionally, stimulating the direct pathway effectively mitigated motor deficits induced by 6-hydroxydopamine lesions. These findings emphasize the crucial interplay between these pathways and open avenues for developing targeted treatments to improve motor function in Parkinson's disease (Kravitz et al., 2010).

1.7.3 Application of optogenetics in fMRI and PET

Research integrating optogenetic stimulation with PET or fMRI is still quite limited. Here, several pivotal studies in this field are outlined that have (partially) played a crucial role in shaping our own research efforts.

Thanos *et al.* utilized [^{18}F]FDG-PET to measure brain glucose metabolism in awake rats undergoing optogenetic stimulation of the nucleus accumbens with ChR2. The results revealed increased brain glucose metabolism not only in the nucleus accumbens but also in interconnected regions such as the ipsilateral striatum, somatosensory cortex, periaqueductal gray and contralateral amygdala, globus pallidus, ventral pallidum and hippocampus. In contrast, brain glucose metabolism decreased in areas associated with the default mode network and the secondary motor cortex. This study underscores the utility of PET imaging for tracking brain connectivity and regional activity in live animals (Thanos et al., 2013). A limitation of

this study is that PET scans were conducted sequentially, with one scan at baseline and a second scan a week later after stimulation.

Panic disorder is a debilitating anxiety condition with unknown underlying mechanisms, especially concerning the involvement of the dorsal periaqueductal gray. In a study by He *et al.*, panic-like behaviors were induced by optogenetic stimulation of the dorsal periaqueductal gray. [^{18}F]FDG-PET revealed notable increased uptake in regions such as the dorsal periaqueductal gray, primary visual cortex, cingulate cortex, cuneiform nucleus and cerebellum, while decreases were observed in the frontal cortex, basal ganglia and primary somatosensory cortex. These results highlight PET imaging's effectiveness in capturing the neurofunctional shifts linked to panic attacks triggered by dorsal periaqueductal gray stimulation, offering new insights into the disorder's neural pathways. As in the study above, a limitation of this study is that PET scans were conducted sequentially (He et al., 2019).

A recent study by Kim *et al.* investigated how specific neuronal types contribute to stroke recovery by employing optogenetic stimulation in a rat model. Researchers targeted distinct neuronal populations, including pyramidal neurons, inhibitory parvalbumin-expressing neurons, and a general pan-neuronal group. The results showed that stimulating inhibitory neurons led to markedly improved motor recovery compared to the other groups. [^{18}F]FDG-PET imaging further revealed that this group experienced reduced cortical diaschisis and heightened activity in the corticostriatal network, closely mirroring the observed improvements in motor function and behavior (Kim et al., 2024).

Unlike PET, which has been less commonly combined with optogenetic stimulation, fMRI has seen numerous studies integrating these techniques, with early research dating back over a decade. At that time, it was still uncertain whether BOLD signals truly reflected the activation of local excitatory neurons. Lee *et al.* addressed this question by demonstrating that optogenetic stimulation of CaMKIIα-expressing excitatory neurons in the neocortex or thalamus produced positive BOLD signals. Their optogenetic fMRI approach provided insights into how specific neuronal subtypes influence BOLD signal changes, including effects observed in downstream brain regions (Lee et al., 2010).

Desai *et al.* advanced optogenetic fMRI by applying it to awake mice, allowing for the examination of complex neural circuit dynamics in a context that reflects natural behavior. With the expression of ChR2 in pyramidal cells of the primary somatosensory barrel cortex, they successfully mapped both cortical and striatal regions linked to this sensory area. Additionally, their study demonstrates the utility of optogenetic fMRI in exploring how the common

anesthetic isoflurane influences the activation and connectivity of neural networks downstream from specific cell types (Desai et al., 2011).

2 Objectives

This work focuses on two distinct projects aimed at advancing the early diagnosis of Parkinson's disease and enhancing our understanding of the basal ganglia circuit's organization and mechanisms to support the development of new treatment strategies:

Currently, PET tracers to detect α-synuclein pathology are still lacking, making the ability to non-invasively diagnose and monitor disease progression difficult. The two small molecule compounds MODAG-001 and MODAG-005, identified in previous studies, have shown high binding affinity to α-synuclein fibrils. Therefore, the goal of the first project was to optimize *in vitro* binding assays using recombinant fibrils to systematically evaluate these compounds for their specificity to α-synuclein aggregates and selectivity over tau and amyloid-β fibrils. Additionally, this thesis aimed to assess the pharmacokinetic profile and metabolism of these compounds *in vivo* in healthy mice and rats to determine their potential as PET tracers for α-synuclein pathology.

The second project focused on developing a protocol to detect neural activity triggered by optogenetic stimulation using simultaneous fPET/fMRI. PET is known for its high sensitivity and specificity in studying biochemical and functional processes in the body, while fMRI offers superior spatial and temporal resolution for investigating brain function in both humans and rodents. Previous studies in our lab using hybrid PET/MR imaging demonstrated that it is possible to visualize hemodynamic changes in small animals with fMRI while measuring brain metabolism changes with fPET during the same session, utilizing a whisker stimulation model (Wehrl et al., 2013). However, discrepancies in the signals detected by each modality were likely due to the different stimulation protocols used. The goal of the current study was to advance this research by establishing a fully simultaneous [^{18}F]FDG-fPET/BOLD-fMRI approach in rats, enabling the concurrent acquisition of both fPET and fMRI data during the same stimulation paradigm. By leveraging optogenetics, which allows for precise *in vivo* stimulation of neuronal pathways, this project aimed to stimulate the nigrostriatal pathway, which is involved in motor behavior, and to study the resulting impact on BOLD-fMRI and [^{18}F]FDG-fPET activation patterns in the brain.

3 Results

This dissertation comprises three original publications focused on imaging biomarkers and brain circuits associated with synucleinopathies. The first two publications investigate the potential of two small molecule compounds as PET tracers for α-synuclein aggregates, utilizing both *in vitro* and *in vivo* methods (Kuebler et al., 2020). The third publication examines the basal ganglia circuit through simultaneous fPET/fMRI, with light-induced activation of dopaminergic neurons (Haas et al., 2024).

3.1 Publication I

[^{11}C]MODAG-001 – towards a PET tracer targeting α-synuclein aggregates

Kuebler L.*, **Buss S.***, Leonov A., Ryazanov S., Schmidt F., Maurer A., Weckbecker D., Landau A.M., Lillethorup T.P., Bleher D., Saw R., Pichler B.J., Griesinger C., Giese A., Herfert K., 2020.

European Journal of Nuclear Medicine and Molecular Imaging. 2020. 48, 1759– 1772. IF (2020): 9.236

***contributed equally**

This first publication presents a comprehensive *in vitro* and preclinical *in vivo* characterization of the small molecule compound MODAG-001. The study demonstrates that MODAG-001 exhibits very high affinity for α-synuclein fibrils and good selectivity over structurally similar tau and amyloid-β fibrils, as shown by filter binding assays using tritiated MODAG-001. Additionally, *in vivo* PET studies in mice with [^{11}C]MODAG-001 revealed its ability to cross the blood-brain barrier, with favorable pharmacokinetics and biodistribution. Metabolite analysis identified two brain metabolites, and deuteration of the parent compound improved its stability. Furthermore, (d_3)-[^{11}C]MODAG-001 successfully detected injected α-synuclein fibrils in rats. Despite these encouraging findings, future studies need to address the issue of high non-specific background binding.

Contributions first publication:

- experimental: *in vitro* binding assays on recombinant fibrils and brain homogenates, mouse tracer kinetics with PET, mouse MRI, mouse metabolite analysis
- data analysis: *in vitro* binding assays, metabolite analysis, *in vivo* mouse PET and MRI

- paper draft writing and figures: 50%
- paper revision: 100%

3.2 Publication II

[^{11}C]MODAG-005 – a novel PET tracer targeting alpha-synuclein aggregates in the brain

Saw, R.*, **Haas, S.***, Schmidt, F.*, Ryazanov, S.*, Leonov, A.*, Kuebler, L., Bleher, D., Papadopoulos, I., Roeben, B., Schmidt, F., Reimold, M., Bonanno, F., Grotegerd, A., Ruf, V.C., Dahl, B., Sandiego, C.M., Henry, K.E., Fehrenbacher, B., Schaller M., Kahle, P., Gasser, T., Brockmann, K., Reischl, G., la Fougère, C., Pichler, B.J., Maurer, A., Griesinger, C., Giese, A., Herfert, K..

Preprint. (2024)

***contributed equally**

The second publication presents a comprehensive *in vitro* and preclinical and clinical *in vivo* characterization of MODAG-005, the de-methylated form of MODAG-001. This compound demonstrated exceptionally high affinity for α-synuclein fibrils, along with excellent selectivity over structurally similar tau and amyloid-β fibrils, as shown through filter binding assays using tritiated MODAG-005. Additionally, it exhibited strong binding affinity to human multiple system atrophy brain sections with confirmed pathology, as validated by immunofluorescence. *In vivo* PET studies with [^{11}C]MODAG-005 in mice and rats revealed that the radiopharmaceutical effectively crossed the blood-brain barrier, with favorable pharmacokinetics and biodistribution, and showed reduced non-specific binding. Specific binding to α-synuclein was confirmed in a rat model with injected fibrils and in a transgenic mouse model with the A30P mutation, which overexpresses α-synuclein. Off-target binding to monoamine oxidase-B (MAO-B) and glial fibrillary acidic protein was ruled out. Injection of [^{11}C]MODAG-005 into non-human primates corroborated the findings observed in mice and rats. A first-in-human study further validated these results, showing increased tracer retention in regions of expected pathology in a case of mixed multiple system atrophy.

Contributions second publication:

- experimental: *in vitro* binding assays on fibrils, wildtype mouse and rat PET, wildtype mouse and rat MRI, mouse and rat metabolite analysis
- data analysis: *in vitro* binding assays, metabolite analysis, *in vivo* mouse and rat PET and MRI, metabolite analysis macaques, PET analysis macaques

- paper draft writing and figures: 50%

3.3 Publication III

Functional PET/MRI reveals active inhibition of neuronal activity during optogenetic activation of the nigrostriatal pathway

Haas, S.*, Bravo, F.*, Ionescu, T., Gonzalez-Menendez, I., Quintanilla-Martinez, L., Dunkel, G., Kuebler, L., Hahn, A., Lanzenberger, R., Weigelin, B., Reischl, G., Pichler, B.J., Herfert, K., 2024.

Science Advances. 10, eadn2776. 2024. IF (2023): 11.7

***contributed equally**

In the third publication, the basal ganglia circuit was explored by simultaneously employing [^{18}F]FDG-fPET and BOLD-fMRI to measure activity patterns following optogenetic stimulation of the substantia nigra pars compacta. Overlapping activated areas were identified, although these did not align spatially and geometrically, and regions that were exclusively activated by one of the modalities were uncovered. Notably, a BOLD signal overshoot was observed in dopaminergic regions during the resting period immediately after light stimulation. Additionally, negative BOLD signal changes in both bilateral cortical regions and dopaminergic regions on the contralateral side of the stimulation were detected.

Contributions third publication:

- experimental: adeno-associated virus injections, *in vivo* fPET/BOLD-fMRI measurements, establishment of optogenetics in the lab
- paper draft writing and figures: 80%

4 Discussion

The early diagnosis of Parkinson's disease remains a major challenge, as its only reliable *in vivo* after the onset of symptoms. However, brain changes occur at cellular, molecular, and functional level long before. Identifying an early biomarker could greatly enhance monitoring of disease progression, treatment efficacy, and enable timely medical intervention. Parkinson's disease is characterized by the progressive loss of dopaminergic neurons in the substantia nigra pars compacta, a critical input to the basal ganglia circuit, which is essential for movement control. This work, titled "*Imaging of Biomarkers and Brain Circuits Involved in Parkinson's Disease*" aimed to contribute to earlier diagnosis and a better understanding of basal ganglia function through two approaches:

First, two related small molecule compounds were evaluated as potential PET tracers for imaging aggregated α-synuclein, a protein associated with the degeneration of dopaminergic neurons and found in brain inclusions in patients with Parkinson's disease, multiple system atrophy, and Lewy body dementia. Second, a simultaneous [^{18}F]FDG-fPET/BOLD-fMRI protocol with optogenetic stimulation of nigrostriatal projections was implemented to explore the potential for a more precise characterization of the dopaminergic system, with the goal of improving diagnosis and targeted therapy in the future.

4.1 Evaluation of the two small molecule compounds MODAG-001 and MODAG-005 as potential PET tracers for aggregated α-synuclein

The first and second publication in this body of work present a comprehensive *in vitro* and *in vivo* evaluation of the small molecule compounds MODAG-001 and MODAG-005 as PET tracers for aggregated α-synuclein (Kuebler et al., 2020).

MODAG-001 and its de-methylated form MODAG-005 – introduced at a later stage of the study – exhibited the most favorable binding properties to recombinant α-synuclein fibrils. This was determined through our internally developed *in vitro* filter competition and saturation binding assays, yielding highly desirable subnanomolar K_d values of 0.6 ± 0.1 nM for MODAG-001 and 0.2 ± 0.03 nM for MODAG-005 (Kuebler et al., 2020). To our knowledge, these K_d values are superior to all compounds reported in the literature thus far, including the recently published compound [^{18}F]ACI-12589, with a mean K_d of 33.5 ± 17.4 nM (Smith et al., 2023), and other notable tracers like [^{3}H]4i ($K_d = 3.0 \pm 1.4$ nM) (Kim et al., 2023), [^{18}F]-SPAL-T-06 ($K_i = 2.49$ nM – on homogenate) (Matsuoka et al., 2022), [^{3}H]/[^{18}F]BF-227 ($K_d = 46.0$ nM/9.6 nM) (Fodero-Tavoletti et al., 2009), [^{125}I]SIL23 ($K_d = 148$ nM) (Bagchi et

al., 2013), 25 quinolinyl analogues (best K_i = 15 nM) (Yue et al., 2018), the most promising ^{18}F-labeled 3-(benzylidine)indolin-2-one derivative 46a (K_d = 8.9 nM) (Chu et al., 2015), [^{18}F]2FBox (K_d = 3.3 nM) (Verdurand et al., 2018), [^{18}F]-F0502B (K_d for preformed fibrils = 10.97 nM) (Xiang et al., 2023), [^{125}I]61 (K_d = 1.06 nM) (Ferrie et al., 2020), [^{125}I]PHNP-3 (K_d = 6.9 nM) (Kaide et al., 2022), the first generation tau tracer [^{11}C]PBB3 (K_d = 58 nM) (Korat et al., 2021), and its derivative [^{3}H]C05-01 (K_d = 25 nM) (Miranda-Azpiazu et al., 2020), to name a few. While IC_{50} values are not directly comparable to K_d values, as they need to be converted into K_i values, it is noteworthy that [^{18}F]C05-05 demonstrated a high binding affinity in dementia with Lewy bodies tissue samples, with an IC_{50} of 1.5 nM (Endo et al., 2024).

In addition to evaluating the compounds' affinity for α-synuclein fibrils, their selectivity against recombinant tau and amyloid-β fibrils was assessed. This assessment is crucial because amyloid fibrils can have similar structural features, such as β-sheet secondary structures (Breydo & Uversky, 2015). Zhang *et al.* suggested that the binding affinity of α-synuclein fibrils should be more than 30 to 100-fold higher compared to other amyloids (Zhang et al., 2013). Our results showed that [^{3}H]MODAG-001 has an approximately 30-fold lower affinity for tau (19 ± 6.4 nM) and amyloid-β fibrils (20 ± 10 nM) compared to α-synuclein. Similarly, [^{3}H]MODAG-005 demonstrated about 36-fold lower affinity for tau (7.1 ± 0.7 nM) and more than 100-fold lower affinity for amyloid-β fibrils (21 ± 7.7 nM) (Kuebler et al., 2020).

To achieve a B_{max}/K_d ratio greater than 10, a high number of binding sites is necessary. For MODAG-001 a B_{max} of 9.7 ± 0.4 pmol/nmol for α-synuclein fibrils was observed, resulting in a B_{max}/K_d ratio of 16.2. MODAG-005 showed a B_{max} of 6.6 ± 0.7 pmol/nmol, yielding a B_{max}/K_d ratio of 33. In contrast, more than 200-fold and more than 1600-fold lower B_{max}/K_d ratios were observed for tau and amyloid-β fibrils, respectively: 0.08 for MODAG-001 (B_{max} = 1.5 ± 0.4 pmol/nmol) and 0.17 for MODAG-005 (B_{max} = 1.2 ± 0.2 pmol/nmol) on tau; and 0.01 for MODAG-001 (B_{max} = 0.2 ± 0.1 pmol/nmol) and 0.005 for MODAG-005 (B_{max} = 0.11 ± 0.03 pmol/nmol) on amyloid-β fibrils, reflecting their lower affinity and fewer binding sites. Thus, MODAG-001 (16.2) and MODAG-005 (33) achieve the desired B_{max}/K_d ratio greater than 10 (Kuebler et al., 2020).

The exact mechanism by which the MODAG compounds bind to α-synuclein aggregates remains unclear. To investigate the binding site of [^{3}H]MODAG-001 on α-synuclein, a competition assay was conducted using SIL26. SIL26 has been shown to bind to site 3/13 on recombinant α-synuclein fibrils, as determined by "*in silico* docking, photoaffinity labeling, and radioligand binding studies" (C. J. Hsieh et al., 2018). The results indicated that SIL26

displaced [^{3}H]MODAG-001 in a dose-dependent manner, with a K_i of 21 nM. This suggests that SIL26 has a lower affinity than MODAG-001 and likely binds to the same site.

Structural differences between recombinant fibrils and fibrils from human brain extracts have been documented (Burger et al., 2024; Schweighauser et al., 2020; Strohäker et al., 2019; Yang et al., 2023; Yang et al., 2022). Therefore, it is important to consider whether recombinant fibrils are suitable for use in screening assays or for affinity determination. Using cryo-EM, Schweighauser *et al.* demonstrated that recombinant α-synuclein fibrils differ significantly from those found in multiple system atrophy (Schweighauser et al., 2020). As a result, a PET compound that binds to recombinant fibrils may not necessarily bind to the pathological fibrils present in patient tissue. Additionally, variations in α-synuclein structures from patients with multiple system atrophy, Parkinson's disease, Parkinson's disease dementia and dementia with Lewy bodies further complicate the selection of suitable test subjects for *in vitro* assays (Van der Perren et al., 2020; Yang et al., 2022). Yang *et al.* identified two distinct types of α-synuclein filaments in multiple system atrophy brains, each consisting of two distinct protofilaments, using cryo-EM (Schweighauser et al., 2020). In contrast, cryo-EM analysis by Yang *et al.* revealed that α-synuclein filaments in dementia with Lewy bodies, Parkinson's disease and Parkinson's disease dementia brains are composed of a single protofilament (Lewy fold), differing significantly from those in multiple system atrophy (Yang et al., 2022). A case of synucleinopathy with onset at 13 years of age and death two years later, termed early-onset dementia with Lewy bodies, was reported (Takao et al., 2004). Cryo-EM analysis revealed that the filament's core structure showed no resemblance to the Lewy fold observed in dementia with Lewy bodies and Parkinson's disease, and only partially resembled the filament structure seen in multiple system atrophy (Yang et al., 2023). Therefore, efforts should be directed toward producing fibrils that accurately mimic those found in each specific synucleinopathy. It is suggested that employing protein amplification techniques, such as those used in protein misfolding cyclic amplification assays, may improve the resemblance of fibrils to those found in the specific synucleinopathies. These techniques involve producing α-synuclein fibrils through repeated cycles of sonication and rest, where sonication fragments the seed (e.g., from brain homogenates of multiple system atrophy) into shorter pieces, thereby amplifying it and serving as a template for monomer addition during resting phases (Saborio et al., 2001). Recently, Burger *et al.* successfully performed and identified the seeding of 1B fibrils – a strain resembling those found in multiple system atrophy – in the mouse brain using correlative light-electron microscopy (Burger et al., 2024). In this case, the histopathologic pattern closely resembled that observed after seeding with multiple system atrophy brain homogenate.

Therefore, employing a fibril strain that closely mimics the human version could be valuable for screening assays or in the development of animal models. Nonetheless, in our studies K_d values of the same magnitude in fibril binding assays and human brain tissue of multiple system atrophy cases were observed, which could be an indication that the recombinant fibrils used in the present study are very similar to those from human multiple system atrophy tissue.

An alternative method for screening compounds in human tissue is to use brain homogenates from patient samples. These assays offer the advantage of enabling high-throughput screening in tissue that contains actual pathology. However, a significant limitation is that these homogenates often contain co-pathologies, and they do not provide information about the distribution of pathology within the tissue. Therefore, using well-characterized tissues and comparing them with control samples is crucial. To determine the minimum concentration required for detecting α-synuclein fibrils with [^{3}H]MODAG-001, a sensitivity assay was performed. Wild-type mouse brain homogenate was inoculated with varying concentrations of α-synuclein fibrils and [^{3}H]MODAG-001 saturation binding assays were conducted. The results showed that [^{3}H]MODAG-001 could detect fibrils at concentrations as low as 5 nM in 100 µg protein/mL. However, it was unable to detect α-synuclein fibrils at the lower concentration of 4 nM in 830 µg protein/mL found in our human Parkinson's disease brain homogenate, likely due to low target availability or high non-specific binding (Kuebler et al., 2020).

To our knowledge, only four studies have successfully determined the K_d values for α-synuclein fibrils in crude human brain homogenates. These include: [^{11}C]PBB3 in an amygdala homogenate of a case of dementia with Lewy bodies (K_d = 58 nM), [^{125}I]SIL23 in the insoluble fraction of a brain homogenate of Parkinson's disease dementia (K_d = 119 nM to 168 nM across four samples), [^{18}F]-F0502B in a crude homogenate of a Parkinson's disease patient (K_d = 3.68 nM), and [^{18}F]-SPAL-T-06 (K_i = 2.49 nM) in homogenates of the putamen of a multiple system atrophy patient (Bagchi et al., 2013; Matsuoka et al., 2022; Miranda-Azpiazu et al., 2020; Xiang et al., 2023). For homogenate assays, it is essential to use highly purified tissue, such as samples containing only α-synuclein pathology, to minimize off-target binding. However, obtaining such pure tissue samples is extremely challenging. Still, homogenate binding assays are fundamentally valuable because, like fibril binding assays, they can be conducted in 96-well plates and allow for high throughput screening. However, they lack the ability to provide local resolution of tissue pathology. In contrast, autoradiography can precisely identify the location of the pathology using immunohistochemistry and can be performed on the same tissue slide.

In fibril saturation binding assays, [^{3}H]MODAG-001 and [^{3}H]MODAG-005 exhibited adequate *in vitro* selectivity (more than 200-fold and more than 1600-fold lower B_{max}/K_d ratios for tau and amyloid-β fibrils) but still showed some binding to tau and amyloid-β in human brain sections (Kuebler et al., 2020). To further enhance specificity, one approach could be the development of PET ligands based on larger molecules, such as antibodies, antibody fragments, or nanobodies, which may offer improved target specificity and selectivity. However, antibody-based radioligands are typically more effective for imaging peripheral targets due to their limited ability to cross the blood-brain barrier and less favorable *in vivo* kinetics. Moreover, the intracellular location of pathological α-synuclein inclusions adds another barrier, making it difficult for antibodies to reach their target. This issue is not unique to antibodies; for instance, the well-known ligand raclopride can enter the brain but struggles to cross cell membranes (Sun et al., 2003). A study further demonstrated this limitation: a bispecific α-synuclein-TfR antibody radiolabeled with iodine-124 did not show increased retention in a transgenic Parkinson's disease mouse model compared to wild-type mice, although it successfully visualized α-synuclein fibrils several days after intrastriatal injection (Roshanbin et al., 2022). In contrast, Sehlin *et al.* developed an antibody-based PET ligand for amyloid-β pathology, which was tested in two transgenic Alzheimer's disease mouse models. By fusing an amyloid-β protofibril antibody with a transferrin receptor antibody, they achieved better blood-brain barrier penetration and could track the progression of amyloid-β pathology over time (Sehlin et al., 2016). Subsequently, Hultqvist *et al.* created a blood-brain barrier shuttle by fusing a transferrin receptor fragment with an antibody targeting amyloid-β fibrils. This shuttle enabled a nine-fold higher uptake into the brains of transgenic Alzheimer's disease mice compared to wild-type mice, and a three-fold increase in uptake compared to their previous method (Hultqvist et al., 2017; Sehlin et al., 2016). Moreover, the extended washout time of antibodies lowers the signal-to-noise ratio. Employing antibody fragments could result in shorter biological half-lives (de Lucas Á et al., 2023). In summary, given the current limitations of these approaches, small molecule tracers continue to be the most promising option for imaging intracellular targets in the brain, such as α-synuclein inclusions.

In subsequent experiments, [^{11}C]MODAG-001 and [^{11}C]MODAG-005 were injected into healthy mice and rats to assess their pharmacokinetic profile and biodistribution using PET. A peak standardized uptake value of greater than 1.5 is anticipated for a sufficient signal to noise ratio. Both tracers demonstrated good uptake in the mouse brain, with peak standardized uptake values reaching up to 1.4 for [^{11}C]MODAG-001 and 1.9 for [^{11}C]MODAG-005, respectively, and exhibited rapid washout from the brain (Kuebler et al., 2020). A standardized uptake value

of one represents the radiotracer concentration after uniform distribution throughout the body. Values exceeding one in the brain indicate tracer entry and are visually distinguishable from the mean (*Central Nervous System Radiotracer Development: Bench to Bedside*, 2024; Korat et al., 2021; Pike, 2009).

Quantification of PET tracer kinetics assumes that metabolism does not produce radiometabolites that cross the blood-brain barrier and contribute to the detected PET signal. Our radiometabolite analysis in mice revealed two metabolites of [^{11}C]MODAG-001 in the brain. Approximately 3% and 7% of metabolite-1 and about 6% and 12% of metabolite-2 were observed at five and 15 minutes post-injection. Conversely, 91% and 81% of the parent compound remained present at five and 15 minutes post-injection, respectively, and may thus not be a major concern for the quantification (Kuebler et al., 2020).

Metabolism can be reduced by deuterating the compound (Pirali et al., 2019). Deuterium, with its greater atomic mass compared to hydrogen, requires more energy to break covalent bonds to carbon. To minimize metabolism, the NMe_2 group of [^{11}C]MODAG-001 was deuterated, which was identified as the primary site of metabolism, by replacing three hydrogen atoms with three deuterium atoms. Injections into healthy mice showed similar pharmacokinetics and biodistribution in PET, with peak standardized uptake values reaching up to 1.7. However, similar to [^{11}C]MODAG-001, 5% of metabolite-1 remained at five and 15 minutes post-injection, and about 2% and 8% of metabolite-2, was still present at the same time points (Kuebler et al., 2020). Thus, the metabolism was not significantly reduced, likely because only a single methyl group was deuterated, leading to a minimal impact on the overall metabolic rate.

Following the injection of [^{11}C]MODAG-005, the de-methylated form of [^{11}C]MODAG-001, in mice, only one metabolite was detected in the brain with 96 ± 1.1% and 79 ± 3.1% of the parent compound present in the brain (Kuebler et al., 2020). The metabolite's structure has not been identified but based on plasma HPLC analysis showing one polar and one less polar metabolite, it is hypothesized that the metabolite unable to cross the blood-brain barrier is the de-methylated form of [^{11}C]MODAG-005, while the other corresponds to the cleaved methyl group. However, it is unlikely that this cleaved group binds to the target.

In healthy rats, (d_3)-[^{11}C]MODAG-001 and [^{11}C]MODAG-005 exhibited pharmacokinetic profiles similar to those observed in mice, with peak standardized uptake values reaching 2.1 and 3.2, respectively (Kuebler et al., 2020). Radiometabolite analysis of [^{11}C]MODAG-005 identified a metabolite that crosses the blood-brain barrier, with 9% of the metabolite present

at five minutes and 36% at 15 minutes post-injection. This suggests a slightly faster metabolism in rats compared to mice. However, the chromatogram at the 15-minute time point is quite noisy, with only a small detectable peak, leading to a greater margin of error in the calculation.

Despite the detection of blood-brain barrier-penetrating radiometabolites in mice and rats, even after deuteration of the compound, metabolism in rodents should not be a reason to exclude a PET ligand for human use. First, the amount of metabolite is relatively low (more than 80% parent compound in mice, more than 64% parent compound in rats). Second, blood-brain barrier penetration of the radiometabolite or metabolism of the compound itself may vary between species. Studies have shown that species differences in the distribution and specificity of transporters, such as the P-glycoprotein (P-gp), complicate predictions of drug pharmacokinetics and PET tracers (Chu et al., 2013). For instance, Syvänen *et al.* demonstrated P-gp-dependent species differences in the brain-to-plasma ratios of [^{11}C]verapamil, [^{11}C]GR205171, and [^{18}F]altanserin in rats, guinea pigs, minipigs, monkeys, and humans (Syvanen et al., 2009). They observed a nine-fold higher brain-to-plasma ratio of [^{11}C]GR205171 in humans, monkeys, and minipigs compared to rats and guinea pigs, likely due to higher P-gp levels resulting in increased efflux transport in rodents (Syvanen et al., 2009). Consequently, greater efflux in rodents leads to a higher amount of the compound available for metabolism, which can result in faster generation of radiometabolites. In addition, [^{11}C]PIB, the gold standard for amyloid PET imaging in Alzheimer's disease, showed significant radiometabolite formation in rat brains, whereas minimal to no amounts of radiometabolite were observed in mouse, human, and baboon brains (Mathis et al., 2004).

In addition to the research presented in this thesis, further studies were conducted using MODAG-001 and MODAG-005 to assess their specificity both *in vitro* and *in vivo*. These investigations included (micro)autoradiography in human brain tissue and animal models of synucleinopathies, which confirmed the high binding specificity of MODAG-005 for α-synuclein pathology in multiple system atrophy and demonstrated its binding in animal models exhibiting both extracellular and intracellular α-synuclein pathology. Furthermore, *in vivo* pharmacokinetic evaluations in non-human primates aligned with the results observed in mice and rats. Notably, a recent first-in-human PET scan was performed under compassionate use conditions, revealing favorable pharmacokinetics in the human brain and significant retention in regions associated with synuclein pathology. Although these experiments fall outside the scope of this thesis and are not discussed in detail, they reinforce the findings presented herein.

In conclusion, a promising PET tracer for aggregated α-synuclein has been identified. Among all the small molecule compounds presented, [^{11}C]MODAG-005 offers the most comprehensive evaluation, with the best published K_d value for α-synuclein fibrils, and a corresponding K_d value for α-synuclein pathology in human brain sections of multiple system atrophy. Low non-specific tracer binding was observed, which allows imaging with a high signal-to-noise ratio, along with excellent pharmacokinetics and biodistribution, even in non-human primates.

4.2 Establishment of a simultaneous optogenetic [^{18}F]FDG-fPET/BOLD-fMRI protocol to shed light on basal ganglia function in rats

The third publication highlights the benefits of a newly established simultaneous multimodal approach, which offers insights into brain activation patterns and enhances our understanding of basal ganglia function (Haas et al., 2024).

This study builds on the work by Wehrl *et al.*, who first presented simultaneously acquired [^{18}F]FDG-PET and BOLD-fMRI data on brain activation in response to whisker pad stimulation in rats (Wehrl et al., 2013). Wehrl *et al.* demonstrated the complementary nature of these methods and emphasized their combined value for investigating brain networks. However, a limitation of their study was the non-simultaneous data acquisition; PET and fMRI measurements were performed sequentially with different stimulation paradigms. Using the previously established fPET approach, our aim was to enhance the comparability of the data sets by implementing a full simultaneous data acquisition approach with the same stimulation paradigm.

Increased metabolic and hemodynamic activity was observed across regions, but the spatial extent, location of activation centers, proportion of overlapping voxels, and significance of activated regions differed between the two modalities. BOLD-fMRI within-group analysis identified 15 brain regions with BOLD signal increases and nine regions with negative BOLD responses. In contrast, [^{18}F]FDG-PET within-group (independent component) analysis revealed 16 activated brain regions, with no regions showing reduced [^{18}F]FDG uptake. Among these, nine regions showed activation in both modalities, but overlapping voxels were found in only six regions: the ipsilateral (right) nucleus accumbens, striatum, thalamus, insular cortex, somatosensory cortex, and hypothalamus (Haas et al., 2024).

4.2.1 Understanding geometric discrepancies between fPET and fMRI: physiological and technical considerations

CBF and the cerebral metabolic rate of glucose are typically interconnected during task-based stimulation, suggesting that increases in local glucose consumption correspond with rises in CBF. Consequently, both BOLD-fMRI and [^{18}F]FDG-PET imaging are expected to reflect these signal increases (Theriault et al., 2023).

However, our findings of both overlaps and discrepancies in activated areas, which align with Wehrl *et al.'s* observations of spatial differences at the group level between brain regions identified by fPET and fMRI, do not meet our initial expectations (Haas et al., 2024; Wehrl et al., 2013). Wehrl *et al.* attributed these discrepancies to variations in stimulus duration between the two modalities. Since our study utilized simultaneous fPET and fMRI, differences in stimulus duration are not a factor here.

Instead, the discrepancies are likely due to the distinct physiological readouts of each modality – fPET directly measures glucose consumption, reflecting long-term metabolic activity in the brain by using a radioactive glucose analog that accumulates in regions of high energy demand. This makes it particularly effective in detecting overall metabolic activity, including slower processes like synaptic transmission. BOLD-fMRI, on the other hand, tracks changes in blood oxygenation, which directly relates to short-term neural activity and blood flow, providing a faster and more dynamic measure of brain function. This difference can cause the two modalities to highlight different regions, especially when studying tasks or states with rapid changes in brain activity.

One might expect that heightened brain activity would lead to increased oxygen consumption and glucose metabolism. Research shows that when the brain is engaged in tasks, it tends to adopt a less efficient energy production strategy, consuming more glucose relative to oxygen (Theriault et al., 2023). Aerobic glycolysis in the brain refers to a process where, during task-based stimulation, the brain prefers an energy-inefficient method of metabolism. Instead of fully utilizing oxygen for energy, glucose is consumed at a higher rate than oxygen, leading to the production of lactate. This occurs in response to various stimuli. Normally, oxygen, provided by increased blood flow, is used to maximize energy from glucose, but during these tasks, this balance, or "coupling", between glucose and oxygen consumption is disrupted – a phenomenon called "glucose-oxygen decoupling”. The inefficiency in meeting the brain’s energy demands arises from its structural constraints. To transmit large amounts of information, a vast number of axons is required. However, to accommodate them, these axons must be

extremely thin, leaving insufficient space for mitochondria, the cell's main energy producers. As a result, these thin axons rely on ATP produced through aerobic glycolysis, which takes up less space but is less efficient than mitochondrial respiration.

In addition, BOLD-fMRI offers finer resolution, typically around 1 mm to 2 mm (in our study, EPI-BOLD voxel size was 0.27×0.27 mm^2), whereas [^{18}F]FDG-PET has a coarser spatial resolution of approximately 4 mm (with spatial resolution limits depending on crystal size 1.5×1.5 mm^2) (Delso et al., 2011; Wehrl et al., 2013). Given that certain brain regions are close to the resolution limit of the scanner, it becomes clear that detecting subtle changes in these areas is particularly challenging. The small size of these structures can blur the boundaries between regions, making it difficult for the modality to differentiate and accurately capture localized activity or metabolic shifts. Consequently, the resolution constraint can lead to underrepresentation of changes that may still be biologically significant but remain undetected within these smaller, harder-to-resolve regions.

Wehrl *et al.* suggested that PET might have higher sensitivity, though other studies propose the opposite (Hahn et al., 2018; Savio et al., 2017). It is rather that [^{18}F]FDG-PET might detect more overall metabolic processes, including slower biochemical events. In contrast, BOLD-fMRI is highly sensitive to rapid changes in blood flow and neuronal firing, which can result in different regions being activated in each imaging technique.

BOLD-fMRI is influenced by vascular factors, and the relationship between blood flow and neural activity (neurovascular coupling) may vary across brain regions. This variability can cause discrepancies between BOLD-fMRI and [^{18}F]FDG-PET results, as some areas might exhibit blood flow changes without corresponding increases in glucose metabolism. Also, vascular responses can occur at a distance from the actual site of neural activation. These widespread vascular effects can limit spatial resolution, potentially leading to misinterpretation of the true location of the activation center (X. Yu et al., 2012).

Thus, several factors could collectively contribute to the observed discrepancies in our findings. Moreover, biological factors add further complexity to the interpretation, which will be explored in greater detail in the following sections.

4.2.2 Exploring BOLD signal changes in dopaminergic regions: autoreceptor function or vasoactive effects

A notable observation emerged when analyzing the BOLD signal patterns in specific regions. In dopaminergic areas such as the right striatum, nucleus accumbens, and amygdala,

an unusual BOLD signal shape was identified. For instance, in the right striatum, the BOLD signal was slightly elevated (0.91%) during the 60-second stimulation period, but a robust overshoot (2.06%) occurred immediately after termination of the stimulus (Haas et al., 2024). It is hypothesized that this may be related to an active suppression during stimulation. [^{18}F]FDG-PET data further showed significantly increased activity in all three regions, which receive dopaminergic inputs, suggesting that dopamine may play a key role.

To validate the increased activity in the dorsal striatum and substantia nigra pars compacta observed in fMRI, *ex vivo* cFos staining was conducted. Consistent with the fMRI data, heightened cFos levels in the right dorsal striatum were detected compared to the contralateral side, but no differences between the right and left sides in the substantia nigra pars compacta, which projects to the striatum. This suggests again that dopamine may have an influence on these observations. Dopaminergic neurons can regulate their own dopamine synthesis and release through D2 auto- and heteroreceptors (Anzalone et al., 2012; Benoit-Marand et al., 2001; Ford, 2014; L. Yu et al., 2012). It is hypothesized that these neurons actively suppress their activity to modulate dopamine levels at the synapse, leading to a suppressed positive BOLD signal and an overshoot after the laser is turned off.

The release of neurotransmitters like serotonin or dopamine can trigger vascular responses that influence the BOLD signal (Edvinsson et al., 1985; Hadi et al., 2012; Northoff et al., 2007; Shih et al., 2009; Van Nueten et al., 1985). As a result, regions of activation may exhibit a negative or diminished BOLD response due to decreased CBV caused by neurotransmitter-induced vasoconstriction. It has been suggested that this mechanism could also account for the negative BOLD signals observed following pain induction (Morrow et al., 1998; Zhao et al., 2008).

Additional studies that might clarify how GABA influences the suppressed BOLD signal are detailed in the following section: One study suggested that dopaminergic neurons from the substantia nigra pars compacta may release GABA in the striatum, resulting in inhibition (Tritsch et al., 2012). Patel *et al.* demonstrated that GABA co-release can regulate dopamine release through GABA autoreceptors on dopamine neurons, as the autoinhibitory feedback mechanism of dopamine on its own autoreceptors operates more slowly (Patel et al., 2024). Striatal cholinergic interneurons have been shown to leverage dopamine terminals to initiate GABA release, resulting in the rapid inhibition of striatal output neurons (Koos & Tepper, 1999; Nelson et al., 2014). As previously mentioned, the substantia nigra contains GABA-releasing neurons, with parvalbumin neurons being the largest population (González-Hernández &

Rodríguez, 2000). A study on optogenetic stimulation of parvalbumin neurons demonstrated initial vasoconstriction followed by vasodilation at a 20 Hz stimulation frequency mediated by substance P (Vo et al., 2023). Since parvalbumin neurons are also present in the substantia nigra pars reticulata, which is very close to our stimulation site, it may be possible that the BOLD signal overshoot observed in our study originates from a similar effect. In contrast to the vasodilatory effect observed by Vo *et al*., which occurred over several seconds, the overshoot observed in our study was notably brief in the striatum, nucleus accumbens and amygdala, lasting approximately eight to fifteen seconds. Interestingly, the substantia nigra exhibited a more prolonged positive BOLD response, similar to what Vo *et al*. reported, but without preceding vasoconstriction. To clarify these findings, further research using selective stimulation in TH-Cre (tyrosine hydroxylase) or DAT-Cre (dopamine transporter) rats is needed to avoid stimulation of non-dopaminergic cells. Additionally, experiments incorporating pharmacological inhibition of dopamine and GABA autoreceptors could offer deeper insights.

A recent study by Cerrie *et al.* demonstrated negative striatal CBV-fMRI responses in rats following optogenetic stimulation of both cortical (motor cortex – glutamatergic) and subcortical (parafascicular thalamus – glutamatergic, globus pallidus externus – GABAergic, and striatal terminals or cell bodies – GABAergic) regions, which project to dorsal striatal neurons (Cerri et al., 2024). These vasoconstrictive responses were notable as they occurred even when striatal neuronal activity increased, as confirmed by electrophysiological recordings and spectral fiber-photometry. In contrast, positive CBV responses were consistently observed at the stimulation site. Interestingly and in line with our results, stimulation of the substantia nigra pars compacta produced positive CBV responses in the striatum but no response at the stimulation site itself. High-resolution fast-scan cyclic voltammetry revealed dopamine release in the striatum, along with increased oxygen levels during substantia nigra pars compacta stimulation. Conversely, stimulation of the parafascicular thalamus and substantia nigra pars reticulata resulted in only minimal dopamine release and reduced oxygen levels. The study provides a plausible explanation for the findings observed in our research: a possible co-stimulation of non-dopaminergic cells in the substantia nigra pars reticulata is suggested, potentially leading to a positive CBV response at the stimulation site and vasoconstriction in the striatum. The distinct positive striatal CBV response to substantia nigra pars compacta stimulation, with no response at the stimulation site, could explain the overall reduced positive BOLD response observed in the striatum in this study, alongside the positive BOLD response at the site of stimulation.

4.2.3 Dopamine receptor subtypes and their influence on BOLD signals: effects of direct and indirect pathway activation

As mentioned in the introduction, the effect of dopamine on neurons is determined by the receptor type: D1 receptors are excitatory, activating neurons via stimulatory G proteins, while D2 receptors are inhibitory, linked to inhibitory G proteins. Direct pathway neurons primarily express D1 receptors, and indirect pathway neurons mainly express D2 receptors (Mishra et al., 2018; Rommelfanger & Wichmann, 2010). Moreover, there are various theories about the functioning of the direct and indirect pathways. Dopamine exhibits higher affinity for the D2 receptor (K_d = 25 nM) compared to the D1 receptor (K_d = 1.6 μM), suggesting different responses to tonic versus phasic dopamine release (Dreyer et al., 2010; Richfield et al., 1989; Surmeier et al., 2007). PET/MR imaging studies indicate that both receptor types contribute to the fMRI signal (Mandeville et al., 2013; Sander et al., 2013). A model by Hunger *et al.* proposes that D1 receptors, with their lower affinity, detect high-amplitude phasic dopamine increases, while D2 receptors detect low-amplitude tonic increases (Hunger et al., 2020). The negative BOLD response in the contralateral motor cortex observed in our study supports this model, potentially due to increased inhibition of thalamic output from predominant indirect pathway activation, which reduces cortical excitation (Haas et al., 2024). In contrast, recent research also shows D2 receptor activation during phasic dopamine release (Marcott et al., 2014; Yapo et al., 2017). Further clarification could be achieved through selective dopamine receptor stimulation.

4.2.4 Understanding negative BOLD signals in contralateral regions and the absence of [^{18}F]FDG responses

BOLD signal decreases were observed predominantly in the contralateral striatum, nucleus accumbens, amygdala, entorhinal cortex, hippocampus anterior, insular cortex, motor cortex, orbitofrontal cortex and somatosensory cortex, without corresponding changes in [^{18}F]FDG-fPET uptake (Haas et al., 2024). The physiological origin of these negative BOLD signals remains unclear and has been discussed in several studies (Allison et al., 2000; Harel et al., 2002; Ionescu et al., 2022; Shmuel et al., 2006; Stefanovic et al., 2004; Wehrl et al., 2013). Various theories have been proposed to explain these observations:

Unlike the well-known initial dip in the BOLD signal, which is attributed to increased oxygen consumption outpacing the CBF response at the onset of a stimulus, prolonged negative BOLD responses are thought to result from elevated concentrations of deoxyhemoglobin (Malonek et al., 1997; Vanzetta & Grinvald, 1999). These deoxyhemoglobin increases arise

when oxygen consumption surpasses a constant CBF or when CBF decreases while oxygen consumption remains high, stable, or only slightly reduced.

A possible explanation for these findings is the "vascular steal" effect, which posits that regions of strong activation demand more blood flow. This increased demand could reduce blood flow and oxygen levels in nearby regions served by the same vascular system (Harel et al., 2002; Woolsey et al., 1996). However, this theory does not seem to account for our results. The negative BOLD responses are primarily observed on the contralateral side of the stimulation, and are not in close proximity to these areas. Additionally, these regions do not share the same vascular supply (Scremin, 2004). The bilateral occurrence of cortical negative BOLD signals further suggests that the vascular steal effect is unlikely.

Another hypothesis, known as “vascular sharing”, proposes that remote negative BOLD responses arise from the regulation of CBF by the autonomic nervous system, which influences pericytes and smooth muscle cells near the blood vessels (Liu et al., 2011; Moraschi et al., 2012; Rodriguez-Baeza et al., 1998). Although this system is controversial and not extensively researched, it could account for our findings. According to this hypothesis, one would observe negative BOLD responses due to reduced CBF, while [^{18}F]FDG uptake remains stable, as glucose metabolism would be unaffected.

A third theory suggests that negative BOLD responses arise from extremely high regional oxygen consumption due to intense neuronal activity, which cannot be compensated by an increase in CBF (Harel et al., 2002). This theory is supported by studies on seizures, where negative BOLD signals were associated with increased metabolism and decreased oxygen levels (Pereira de Vasconcelos et al., 2002; van Eijsden et al., 2004). However, since our studies do not anticipate high neuronal activity on the contralateral side of the stimulation – which would be reflected by increased [^{18}F]FDG uptake – this explanation does not apply to our findings.

Stiernman *et al.* detected similar negative BOLD signals, which were not linked to changes in metabolism (Stiernman et al., 2021). They were unable to provide a definitive explanation for this phenomenon, indicating a need for further research. In 2023, Godbersen *et al.* investigated this phenomenon within the default mode network and found that two distinct types of BOLD deactivations occur. One type involves a metabolically demanding deactivation process, which would likely lead to increased [^{18}F]FDG uptake, while the other type involves a downregulation of metabolism, resulting in decreased uptake. However, if this process has only slight metabolic activity, [^{18}F]FDG might not be sensitive enough to detect positive

changes. The occurrence of each type depended on the nature of the task: one requiring an external focus of attention, and the other involving cognitive control during working memory tasks (Godbersen et al., 2023). At present, this hypothesis seems the most likely.

4.2.5 Strengths and limitations

4.2.5.1 Advantages of simultaneous fPET and fMRI

A key strength was the use of a functional [^{18}F]FDG-PET study design, conducted simultaneously with BOLD-fMRI. Generally, fPET offers superior temporal resolution compared to traditional PET, enabling the identification of regional dynamic changes in tracer uptake over time during task-induced brain activation within a single PET session using a constant infusion of [^{18}F]FDG (Hahn et al., 2016; Jamadar et al., 2020; Rischka et al., 2018; Villien, 2015). While [^{18}F]FDG-fPET has been previously used in humans to study induced neuronal activity, Ionescu *et al.* recently extended its application to rodents to examine the effects of MDMA (3,4-methylenedioxymethamphetamine; “Ecstasy”) (Ionescu et al., 2022).

4.2.5.2 Activation patterns in the ipsilateral striatum and nucleus accumbens: implications of mesocorticolimbic system involvement

Activation was observed in the ipsilateral striatum and nucleus accumbens in both PET and fMRI (Haas et al., 2024). This may be attributed to the involvement of the mesocorticolimbic system, potentially due to the spread of the ChR2 virus to the ventral tegmental area (Beier et al., 2015; Douma & de Kloet, 2020). To prevent this, selective stimulation of dopamine neurons could be achieved by using DAT-Cre or TH-Cre rats, thereby avoiding unintended activation of ventral tegmental area neurons. Since the ventral tegmental area has projections to the substantia nigra pars reticulata, it is possible that this region was also indirectly stimulated.

4.2.5.3 Limitations due to coil configuration

A limitation of our study was the use of a single-loop coil, which restricted our ability to capture signals from the entire brain and resulted in weaker signals from more distant and deeper structures (Haas et al., 2024). This may explain the lower percentage of activated voxels in the substantia nigra in the BOLD-fMRI data compared to the PET data. Additionally, artifacts observed in BOLD-fMRI slices near the fiber may have been caused by fluid movement along the fiber, necessitating cautious interpretation of these data. To address these issues, a green

fluorescent protein (GFP) control group was included to account for artifacts and weaker signals.

4.2.5.4 Impact of anesthesia on stimulation response and imaging

A notable limitation of this study is the use of anesthesia, which could influence both the responsiveness to optogenetic stimulation and the outcomes of BOLD-fMRI and [^{18}F]FDG-PET imaging. Anesthesia can significantly influence neural activity, impacting physiological responses, brain metabolism, neurovascular coupling, and the functionality of brain circuits and networks as measured by both imaging techniques. In this study, a combination of α-chloralose with pancuronium bromide and a low concentration (0.5%) of isoflurane was selected (Haas et al., 2024).

Pancuronium bromide was specifically chosen to minimize animal movement, which is particularly critical for BOLD-fMRI imaging. Controlled chest movements, regulated by the ventilator, generate consistent and repetitive changes leading to magnetic field inhomogeneities. By using a repetition time that aligns with this consistent movement (e.g., one, two, or three seconds rather than 2.5 seconds with a respiration rate of 60 per minute), artifacts related to breathing can be effectively minimized, improving the overall quality of the fMRI data.

α-Chloralose was chosen for its suitability across both BOLD-fMRI and [^{18}F]FDG-fPET imaging informed by research from Paasonen *et al*., which compared six different anesthesia protocols (propofol, urethane, α-chloralose, isoflurane + medetomidine, isoflurane, and medetomidine) to the awake state (Paasonen et al., 2018). Their findings showed that propofol and urethane resulted in functional connectivity patterns most closely resembling those in awake rats. However, propofol has been linked to reduced glucose metabolism and CBF in humans, limiting its use for [^{18}F]FDG-PET (glucose equivalent) studies (Kaisti et al., 2003). Urethane is known to be carcinogenic and mutagenic, also for humans, which is why this volatile anesthetic was not used in this work (Field & Lang, 1988). While α-chloralose and isoflurane + medetomidine displayed moderate similarity to awake-state functional patterns, the combination of isoflurane + medetomidine was excluded from our study due to findings by Wehrl *et al.*, who observed a 45% increase in blood glucose levels under medetomidine, complicating [^{18}F]FDG-PET imaging (Wehrl et al., 2013). Also, Grandjean *et al.* proposed the isoflurane + medetomidine combination for fMRI studies, but its effect on glucose regulation made it unsuitable for our dual-modality imaging approach (Grandjean et al., 2014).

In contrast, α-chloralose has proven to be particularly effective for functional imaging due to its strong coupling between metabolic activity and neuronal function. Even with relatively mild stimulations, it consistently generates robust BOLD signals, making it an optimal anesthetic for studies involving both [^{18}F]FDG-PET and BOLD-fMRI (Ueki et al., 1992). However, α-chloralose does have limitations, as it is generally a terminal anesthetic, precluding its use in repeated imaging sessions. That said, some protocols, such as those published by Alonso *et al.*, show potential for repeated scanning under this anesthetic (Alonso Bde et al., 2011).

In the Paasonen *et al*. study, isoflurane and medetomidine anesthesia exhibited the most substantial deviations from the awake-state functional connectivity patterns, with isoflurane significantly altering [^{18}F]FDG uptake, both regionally and globally (Paasonen et al., 2018; Spangler-Bickell et al., 2016).

These findings underscore the complexity of anesthesia choice in functional imaging studies, with α-chloralose providing the best balance for our research objectives.

4.2.5.5 Considerations regarding the stimulation paradigm

Unlike other optogenetic studies (Bass et al., 2010; Chen et al., 2019; Chen et al., 2020), an intense and prolonged stimulation paradigm was employed to capture both BOLD-fMRI changes and variations in [^{18}F]FDG uptake. Tests conducted with a few animals indicated that shorter stimulation intervals or lower light intensities, such as 30 seconds *on* followed by 30 seconds *off* or 15 seconds *on* followed by 60 seconds *off*, did not yield changes in the [^{18}F]FDG signal. This phenomenon can be attributed to the inherent characteristics of [^{18}F]FDG-PET. While BOLD-fMRI has superior temporal resolution, capable of capturing changes in brain activity within seconds, [^{18}F]FDG-PET provides excellent spatial resolution for identifying metabolic changes across brain regions but has slower temporal resolution due to the integration of data over longer periods. Using shorter or less intense stimulation protocols may lead to the oversight of subtle changes in regions where smaller effects have been observed, such as the thalamus, amygdala, or nucleus accumbens.

It is crucial to acknowledge that our stimulation protocol does not mimic typical physiological conditions, warranting careful interpretation of the results. The observed exaggerated dopaminergic responses could be a potential consequence of this approach. Moreover, intense stimulation can lead to heat artifacts, which may damage tissue or affect metabolism and vascular function. Additionally, artifacts caused by fluid movement can occur

at the site of fiber implantation. However, incorporating the GFP control group into our study effectively mitigates the impact of these technical artifacts, such as those resulting from excessive heat generated by strong stimulation or complications associated with fiber implantation.

4.2.6 Impact of the study

Our research, in line with findings by Cerri *et al.*, demonstrates that fMRI alone cannot serve as a definitive indicator of neural activity (Cerri et al., 2024). Instead, the shape and polarity of hemodynamic responses are influenced by both neural activity and neurotransmitter release within specific circuits. This understanding is critical for interpreting fMRI data in conditions such as Parkinson's disease, where dopamine signaling is disrupted or altered by treatment interventions. In contrast, [^{18}F]FDG-PET offers a more holistic view, identifying metabolic changes across the brain without being influenced by local neurochemical changes. This comprehensive view is valuable in assessing the effects of nigrostriatal dysfunction, as seen in Parkinson's disease.

For example, while [^{11}C]DTBZ is a tracer that binds to vesicular monoamine transporter 2 to assess dopaminergic neuron status, its utility is largely confined to the striatal region, potentially missing broader network disruptions. [^{18}F]FDG-PET, on the other hand, captures these widespread effects, offering a more thorough examination of brain metabolism and thereby enriching current diagnostic approaches (Houssein et al., 2023; Meyer et al., 2017).

When combined with techniques like fast-scan cyclic voltammetry and models such as TH-Cre or DAT-Cre rodents, this multimodal approach can address gaps in understanding negative hemodynamic responses and neurotransmitter release. This can deepen our knowledge of metabolic and hemodynamic changes linked to dopamine and possibly GABA release, leading to the identification of novel therapeutic targets.

Furthermore, simultaneous [^{18}F]FDG-PET/BOLD-fMRI may reveal specific brain activation patterns, such as the effects of deep brain stimulation in Parkinson's disease. While deep brain stimulation has long been beneficial in treating Parkinson's disease, its underlying mechanisms remain poorly understood. This approach could fine-tune deep brain stimulation by identifying optimal stimulation settings or target areas, potentially reducing medication reliance. Another promising development is near real-time [^{18}F]FDG-fPET imaging, which could allow for dynamic adjustments to deep brain stimulation settings during scans, further enhancing patient care.

In 2014, the goal of a study, funded by The Michael J. Fox Foundation, was to assess whether available optogenetic tools could reverse movement abnormalities in pre-clinical models of Parkinson's disease. Two opsins successfully reversed many of the parkinsonian abnormalities in experimental models. These results provide critical support for further development of optogenetics as a novel therapeutic strategy that combines the benefits of deep brain stimulation and gene therapy, offering a promising, but not yet applicable alternative for treating Parkinson's disease in humans (*Optogenetic Restoration of Basal Ganglia Function to Treat Parkinson's Disease*, 2024). By applying a multimodal approach in conjunction with a similar study design, deeper insights can be obtained into how effectively brain circuit function can be restored.

5 Conclusion

In conclusion, this work contributes significantly to the early diagnosis and comprehension of Parkinson's disease by leveraging two innovative approaches: the development of potential PET tracers for imaging α-synuclein aggregates and the implementation of a simultaneous [^{18}F]FDG-fPET/BOLD-fMRI protocol with optogenetic stimulation to study basal ganglia function.

The first approach involved the successful evaluation of [^{11}C]MODAG-001 and [^{11}C]MODAG-005 as potential PET tracers targeting α-synuclein aggregates, which are central to Parkinson's disease pathology. Both compounds demonstrated high affinity and selectivity for α-synuclein fibrils, outperforming previously reported tracers. In particular MODAG-005 showed excellent pharmacokinetics and minimal non-specific binding, making it a promising candidate for future imaging applications in diagnosing Parkinson's disease and related synucleinopathies.

The second approach involved the successful establishment of a simultaneous [^{18}F]FDG-fPET/BOLD-fMRI protocol to examine activity patterns following optogenetic stimulation of the basal ganglia circuit. A complex interplay between hemodynamic and metabolic processes was observed, improving our comprehension of the brain's neurotransmitter system. Although additional research is required to untangle the complexities of central nervous system circuits and neurotransmitter interactions, this approach may also improve deep brain stimulation outcomes by refining target region identification.

In conclusion, this research represents a significant step toward enhancing diagnostic methodologies and developing more effective treatments for Parkinson's disease.

Bibliography

Alberico, S. L., Cassell, M. D., & Narayanan, N. S. (2015). The Vulnerable Ventral Tegmental Area in Parkinson's Disease. *Basal Ganglia*, *5*(2-3), 51-55. https://doi.org/10.1016/j.baga.2015.06.001

Albert, K., Voutilainen, M. H., Domanskyi, A., & Airavaara, M. (2017). AAV Vector-Mediated Gene Delivery to Substantia Nigra Dopamine Neurons: Implications for Gene Therapy and Disease Models. *Genes (Basel)*, *8*(2). https://doi.org/10.3390/genes8020063

Albin, R. L., Young, A. B., & Penney, J. B. (1989). The functional anatomy of basal ganglia disorders. *Trends in Neurosciences*, *12*(10), 366-375. https://doi.org/https://doi.org/10.1016/0166-2236(89)90074-X

Allison, J. D., Meador, K. J., Loring, D. W., Figueroa, R. E., & Wright, J. C. (2000). Functional MRI cerebral activation and deactivation during finger movement. *Neurology*, *54*(1), 135-142. https://doi.org/10.1212/wnl.54.1.135

Alonso Bde, C., Makarova, T., & Hess, A. (2011). On the use of α-chloralose for repeated BOLD fMRI measurements in rats. *J Neurosci Methods*, *195*(2), 236-240. https://doi.org/10.1016/j.jneumeth.2010.12.010

Antkowiak, M., Torres-Mapa, M. L., Witts, E. C., Miles, G. B., Dholakia, K., & Gunn-Moore, F. J. (2013). Fast targeted gene transfection and optogenetic modification of single neurons using femtosecond laser irradiation. *Sci Rep*, *3*, 3281. https://doi.org/10.1038/srep03281

Anzalone, A., Lizardi-Ortiz, J. E., Ramos, M., De Mei, C., Hopf, F. W., Iaccarino, C., Halbout, B., Jacobsen, J., Kinoshita, C., Welter, M., Caron, M. G., Bonci, A., Sulzer, D., & Borrelli, E. (2012). Dual control of dopamine synthesis and release by presynaptic and postsynaptic dopamine D2 receptors. *J Neurosci*, *32*(26), 9023-9034. https://doi.org/10.1523/jneurosci.0918-12.2012

Aravanis, A. M., Wang, L. P., Zhang, F., Meltzer, L. A., Mogri, M. Z., Schneider, M. B., & Deisseroth, K. (2007). An optical neural interface: in vivo control of rodent motor cortex with integrated fiberoptic and optogenetic technology. *J Neural Eng*, *4*(3), S143-156. https://doi.org/10.1088/1741-2560/4/3/s02

Arenkiel, B. R., Peca, J., Davison, I. G., Feliciano, C., Deisseroth, K., Augustine, G. J., Ehlers, M. D., & Feng, G. (2007). In vivo light-induced activation of neural circuitry in transgenic mice expressing channelrhodopsin-2. *Neuron*, *54*(2), 205-218. https://doi.org/10.1016/j.neuron.2007.03.005

Arnone, A., Allocca, M., Di Dato, R., Puccini, G., Laghai, I., Rubino, F., Nerattini, M., Ramat, S., Lombardi, G., Ferrari, C., Bessi, V., Sorbi, S., De Cristofaro, M. T., Polito, C., & Berti, V. (2022). FDG PET in the differential diagnosis of degenerative parkinsonian disorders: usefulness of voxel-based analysis in clinical practice. *Neurol Sci*, *43*(9), 5333-5341. https://doi.org/10.1007/s10072-022-06166-w

Atasoy, D., Aponte, Y., Su, H. H., & Sternson, S. M. (2008). A FLEX switch targets Channelrhodopsin-2 to multiple cell types for imaging and long-range circuit mapping. *J Neurosci*, *28*(28), 7025-7030. https://doi.org/10.1523/jneurosci.1954-08.2008

Attwell, D., Buchan, A. M., Charpak, S., Lauritzen, M., Macvicar, B. A., & Newman, E. A. (2010). Glial and neuronal control of brain blood flow. *Nature*, *468*(7321), 232-243. https://doi.org/10.1038/nature09613

Attwell, D., & Laughlin, S. B. (2001). An Energy Budget for Signaling in the Grey Matter of the Brain. *Journal of Cerebral Blood Flow & Metabolism*, *21*(10), 1133-1145. https://doi.org/10.1097/00004647-200110000-00001

Auld, D. S., Farmen, M. W., Kahl, S. D., Kriauciunas, A., McKnight, K. L., Montrose, C., & Weidner, J. R. (2004). Receptor Binding Assays for HTS and Drug Discovery. In G. S. Sittampalam, N. P. Coussens, K. Brimacombe, A. Grossman, M. Arkin, D. Auld, C. Austin, J. Baell, B. Bejcek, T. D. Y. Chung, J. L. Dahlin, V. Devanaryan, T. L. Foley, M. Glicksman, M. D. Hall, J. V. Hass, J. Inglese, P. W. Iversen, S. D. Kahl, S. C. Kales, M. Lal-Nag, Z. Li, J. McGee, O. McManus, T. Riss, O. J. Trask, Jr., J. R. Weidner, M. Xia, & X. Xu (Eds.), *Assay Guidance Manual*. https://www.ncbi.nlm.nih.gov/pubmed/22553864

Bagchi, D. P., Yu, L., Perlmutter, J. S., Xu, J., Mach, R. H., Tu, Z., & Kotzbauer, P. T. (2013). Binding of the radioligand SIL23 to alpha-synuclein fibrils in Parkinson disease brain tissue establishes feasibility and screening approaches for developing a Parkinson disease imaging agent. *PLoS One*, *8*(2), e55031. https://doi.org/10.1371/journal.pone.0055031

Bandettini, P. A., Wong, E. C., Hinks, R. S., Tikofsky, R. S., & Hyde, J. S. (1992). Time course EPI of human brain function during task activation. *Magn Reson Med*, *25*(2), 390-397. https://doi.org/10.1002/mrm.1910250220

Barbera, G., Liang, B., Zhang, L., Gerfen, Charles R., Culurciello, E., Chen, R., Li, Y., & Lin, D.-T. (2016). Spatially Compact Neural Clusters in the Dorsal Striatum Encode Locomotion Relevant Information. *Neuron*, *92*(1), 202-213. https://doi.org/10.1016/j.neuron.2016.08.037

Bass, C. E., Grinevich, V. P., Vance, Z. B., Sullivan, R. P., Bonin, K. D., & Budygin, E. A. (2010). Optogenetic control of striatal dopamine release in rats. *J Neurochem*, *114*(5), 1344-1352. https://doi.org/10.1111/j.1471-4159.2010.06850.x

Beard, E., Lengacher, S., Dias, S., Magistretti, P. J., & Finsterwald, C. (2021). Astrocytes as Key Regulators of Brain Energy Metabolism: New Therapeutic Perspectives. *Front Physiol*, *12*, 825816. https://doi.org/10.3389/fphys.2021.825816

Beier, K. T., Steinberg, E. E., DeLoach, K. E., Xie, S., Miyamichi, K., Schwarz, L., Gao, X. J., Kremer, E. J., Malenka, R. C., & Luo, L. (2015). Circuit Architecture of VTA Dopamine Neurons Revealed by Systematic Input-Output Mapping. *Cell*, *162*(3), 622-634. https://doi.org/10.1016/j.cell.2015.07.015

Belliveau, J. W., Kennedy, D. N., Jr., McKinstry, R. C., Buchbinder, B. R., Weisskoff, R. M., Cohen, M. S., Vevea, J. M., Brady, T. J., & Rosen, B. R. (1991). Functional mapping of the human visual cortex by magnetic resonance imaging. *Science*, *254*(5032), 716-719. https://doi.org/10.1126/science.1948051

Benoit-Marand, M., Borrelli, E., & Gonon, F. (2001). Inhibition of dopamine release via presynaptic D2 receptors: time course and functional characteristics in vivo. *J Neurosci*, *21*(23), 9134-9141. https://doi.org/10.1523/jneurosci.21-23-09134.2001

Beyer, K. (2006). α-Synuclein structure, posttranslational modification and alternative splicing as aggregation enhancers. *Acta Neuropathologica*, *112*(3), 237-251. https://doi.org/10.1007/s00401-006-0104-6

Bigott-Hennkens, H. M., Dannoon, S., Lewis, M. R., & Jurisson, S. S. (2008). In vitro receptor binding assays: general methods and considerations. *Q J Nucl Med Mol Imaging*, *52*(3), 245-253. https://www.ncbi.nlm.nih.gov/pubmed/18475249

Biswal, B., Yetkin, F. Z., Haughton, V. M., & Hyde, J. S. (1995). Functional connectivity in the motor cortex of resting human brain using echo-planar MRI. *Magn Reson Med*, *34*(4), 537-541. https://doi.org/10.1002/mrm.1910340409

Blandini, F., Nappi, G., Tassorelli, C., & Martignoni, E. (2000). Functional changes of the basal ganglia circuitry in Parkinson's disease. *Prog Neurobiol*, *62*(1), 63-88. https://doi.org/10.1016/s0301-0082(99)00067-2

Boado, R. J., Black, K. L., & Pardridge, W. M. (1994). Gene expression of GLUT3 and GLUT1 glucose transporters in human brain tumors. *Brain Res Mol Brain Res*, *27*(1), 51-57. https://doi.org/10.1016/0169-328x(94)90183-x

Boyden, E. S., Zhang, F., Bamberg, E., Nagel, G., & Deisseroth, K. (2005). Millisecond-timescale, genetically targeted optical control of neural activity. *Nat Neurosci*, *8*(9), 1263-1268. https://doi.org/10.1038/nn1525

Brendel, M., Deussing, M., Blume, T., Kaiser, L., Probst, F., Overhoff, F., Peters, F., von Ungern-Sternberg, B., Ryazanov, S., Leonov, A., Griesinger, C., Zwergal, A., Levin, J., Bartenstein, P., Yakushev, I., Cumming, P., Boening, G., Ziegler, S., Herms, J.,…Rominger, A. (2019). Late-stage Anle138b treatment ameliorates tau pathology and metabolic decline in a mouse model of human Alzheimer's disease tau. *Alzheimers Res Ther*, *11*(1), 67. https://doi.org/10.1186/s13195-019-0522-z

Breydo, L., & Uversky, V. N. (2015). Structural, morphological, and functional diversity of amyloid oligomers. *FEBS Lett*, *589*(19 Pt A), 2640-2648. https://doi.org/10.1016/j.febslet.2015.07.013

Brown, A. M., & Ransom, B. R. (2007). Astrocyte glycogen and brain energy metabolism. *Glia*, *55*(12), 1263-1271. https://doi.org/10.1002/glia.20557

Brundin, P., Dave, K. D., & Kordower, J. H. (2017). Therapeutic approaches to target alpha-synuclein pathology. *Exp Neurol*, *298*(Pt B), 225-235. https://doi.org/10.1016/j.expneurol.2017.10.003

Burger, D., Kashyrina, M., Lewis, A., De Nuccio, F., Mohammed, I., de La Seiglière, H., van den Heuvel, L., Verchère, J., Feuillie, C., Berbon, M., Arotçarena, M.-L., Retailleau, A., Bezard, E., Laferrière, F., Loquet, A., Bousset, L., Baron, T., Lofrumento, D. D., De Giorgi, F.,…Ichas, F. (2024). 1.94 Å structure of synthetic α-synuclein fibrils seeding MSA neuropathology. In: bioRxiv.

Burré, J. (2015). The Synaptic Function of α-Synuclein. *J Parkinsons Dis*, *5*(4), 699-713. https://doi.org/10.3233/jpd-150642

Buss, S. (2018). *Evaluation of a Potential New PET Tracer to Image Synucleinopathies* [Masterthesis, University of Tuebingen].

Capotosti, F., Vokali, E., Molette, J., Ravache, M., Delgado, C., Kocher, J., Pittet, L., Dimitrakopoulos, I. K., Di-Bonaventura, I., Touilloux, T., Piorkowska, K., Chauhan, M., Kroth, H., Hliva, V., Sol, O., Pfeifer, A., & Kosco-Vilbois, M. (2021). The development of [18F]ACI-12589, a high affinity and selective alpha-synuclein radiotracer, as a biomarker for Parkinson's disease and other synucleinopathies. *17*(S5), e053943. https://doi.org/https://doi.org/10.1002/alz.053943

Carter, S. F., Herholz, K., Rosa-Neto, P., Pellerin, L., Nordberg, A., & Zimmer, E. R. (2019). Astrocyte Biomarkers in Alzheimer's Disease. *Trends Mol Med*, *25*(2), 77-95. https://doi.org/10.1016/j.molmed.2018.11.006

Celej, M. S., Jares-Erijman, E. A., & Jovin, T. M. (2008). Fluorescent N-arylaminonaphthalene sulfonate probes for amyloid aggregation of alpha-synuclein. *Biophys J*, *94*(12), 4867-4879. https://doi.org/10.1529/biophysj.107.125211

Central Nervous System Radiotracer Development: Bench to Bedside. (2024). INTERNATIONAL ATOMIC ENERGY AGENCY. https://doi.org/https://www.iaea.org/publications/15528/central-nervous-system-radiotracer-development-bench-to-bedside

Cerri, D. H., Albaugh, D. L., Walton, L. R., Katz, B., Wang, T.-W., Chao, T.-H. H., Zhang, W., Nonneman, R. J., Jiang, J., Lee, S.-H., Etkin, A., Hall, C. N., Stuber, G. D., & Shih, Y.-Y. I. (2024). Distinct neurochemical influences on fMRI response polarity in the striatum. *Nature Communications*, *15*(1), 1916. https://doi.org/10.1038/s41467-024-46088-z

Chen, S., Weitemier, A. Z., Zeng, X., He, L., Wang, X., Tao, Y., Huang, A. J. Y., Hashimotodani, Y., Kano, M., Iwasaki, H., Parajuli, L. K., Okabe, S., Teh, D. B. L., All, A. H., Tsutsui-Kimura, I., Tanaka, K. F., Liu, X., & McHugh, T. J. (2018). Near-infrared deep brain stimulation via upconversion nanoparticle-mediated optogenetics. *Science*, *359*(6376), 679-684. https://doi.org/10.1126/science.aaq1144

Chen, W., Li, C., Liang, W., Li, Y., Zou, Z., Xie, Y., Liao, Y., Yu, L., Lin, Q., Huang, M., Li, Z., & Zhu, X. (2022). The Roles of Optogenetics and Technology in Neurobiology: A Review. *Front Aging Neurosci*, *14*, 867863. https://doi.org/10.3389/fnagi.2022.867863

Chen, X., Sobczak, F., Chen, Y., Jiang, Y., Qian, C., Lu, Z., Ayata, C., Logothetis, N. K., & Yu, X. (2019). Mapping optogenetically-driven single-vessel fMRI with concurrent neuronal calcium recordings in the rat hippocampus. *Nature Communications*, *10*(1), 5239. https://doi.org/10.1038/s41467-019-12850-x

Chen, Y., Sobczak, F., Pais-Roldán, P., Schwarz, C., Koretsky, A. P., & Yu, X. (2020). Mapping the Brain-Wide Network Effects by Optogenetic Activation of the Corpus Callosum. *Cereb Cortex*, *30*(11), 5885-5898. https://doi.org/10.1093/cercor/bhaa164

Cherry, S. R., Sorenson, J. A., & Phelps, M. E. (2012). Radionuclide and Radiopharmaceutical Production. In *Physics in Nuclear Medicine* (pp. 43-61). https://doi.org/10.1016/B978-1-4160-5198-5.00005-8

Chiti, F., & Dobson, C. M. (2017). Protein Misfolding, Amyloid Formation, and Human Disease: A Summary of Progress Over the Last Decade. *86*(1), 27-68. https://doi.org/10.1146/annurev-biochem-061516-045115

Chu, W., Zhou, D., Gaba, V., Liu, J., Li, S., Peng, X., Xu, J., Dhavale, D., Bagchi, D. P., D'Avignon, A., Shakerdge, N. B., Bacskai, B. J., Tu, Z., Kotzbauer, P. T., & Mach, R. H. (2015). Design, Synthesis, and Characterization of 3-(Benzylidene)indolin-2-one Derivatives as Ligands for α-Synuclein Fibrils. *Journal of Medicinal Chemistry*, *58*, 6002-6017. https://doi.org/10.1021/acs.jmedchem.5b00571

Chu, X., Bleasby, K., & Evers, R. (2013). Species differences in drug transporters and implications for translating preclinical findings to humans. *Expert Opin Drug Metab Toxicol*, *9*(3), 237-252. https://doi.org/10.1517/17425255.2013.741589

Crick, F. H. (1979). Thinking about the brain. *Sci Am*, *241*(3), 219-232. https://doi.org/10.1038/scientificamerican0979-219

Cui, G., Jun, S. B., Jin, X., Pham, M. D., Vogel, S. S., Lovinger, D. M., & Costa, R. M. (2013). Concurrent activation of striatal direct and indirect pathways during action initiation. *Nature*, *494*(7436), 238-242. https://doi.org/10.1038/nature11846

Cunningham, V. J., Parker, C. A., Rabiner, E. A., Gee, A. D., & Gunn, R. N. (2005). PET studies in drug development: Methodological considerations. *Drug Discovery Today: Technologies*, *2*(4), 311-315. https://doi.org/https://doi.org/10.1016/j.ddtec.2005.11.003

Damier, P., Hirsch, E. C., Agid, Y., & Graybiel, A. M. (1999). The substantia nigra of the human brain. II. Patterns of loss of dopamine-containing neurons in Parkinson's disease. *Brain*, *122 (Pt 8)*, 1437-1448. https://doi.org/10.1093/brain/122.8.1437

Daubner, S. C., Le, T., & Wang, S. (2011). Tyrosine hydroxylase and regulation of dopamine synthesis. *Arch Biochem Biophys*, *508*(1), 1-12. https://doi.org/10.1016/j.abb.2010.12.017

de Goeij, J. J. M., & Bonardi, M. L. (2005). How do we define the concepts specific activity, radioactive concentration, carrier, carrier-free and no-carrier-added? *Journal of Radioanalytical and Nuclear Chemistry*, *263*(1), 13-18. https://doi.org/10.1007/s10967-005-0004-6

de Lucas Á, G., Lamminmäki, U., & López-Picón, F. R. (2023). ImmunoPET Directed to the Brain: A New Tool for Preclinical and Clinical Neuroscience. *Biomolecules*, *13*(1). https://doi.org/10.3390/biom13010164

de Rijk, M. C., Launer, L. J., Berger, K., Breteler, M. M., Dartigues, J. F., Baldereschi, M., Fratiglioni, L., Lobo, A., Martinez-Lage, J., Trenkwalder, C., & Hofman, A. (2000). Prevalence of Parkinson's disease in Europe: A collaborative study of population-based cohorts. Neurologic Diseases in the Elderly Research Group. *Neurology*, *54*(11 Suppl 5), S21-23.

Deeg, A. A., Reiner, A. M., Schmidt, F., Schueder, F., Ryazanov, S., Ruf, V. C., Giller, K., Becker, S., Leonov, A., Griesinger, C., Giese, A., & Zinth, W. (2015). Anle138b and related compounds are aggregation specific fluorescence markers and reveal high affinity binding to alpha-synuclein aggregates. *Biochim Biophys Acta*, *1850*(9), 1884-1890. https://doi.org/10.1016/j.bbagen.2015.05.021

Delbeke, J., Hoffman, L., Mols, K., Braeken, D., & Prodanov, D. (2017). And Then There Was Light: Perspectives of Optogenetics for Deep Brain Stimulation and Neuromodulation. *Front Neurosci*, *11*, 663. https://doi.org/10.3389/fnins.2017.00663

DeLong, M. R. (1990). Primate models of movement disorders of basal ganglia origin. *Trends in Neurosciences*, *13*(7), 281-285. https://doi.org/https://doi.org/10.1016/0166-2236(90)90110-V

Delso, G., Fürst, S., Jakoby, B., Ladebeck, R., Ganter, C., Nekolla, S. G., Schwaiger, M., & Ziegler, S. I. (2011). Performance Measurements of the Siemens mMR Integrated Whole-Body PET/MR Scanner. *Journal of Nuclear Medicine*, *52*(12), 1914-1922. https://doi.org/10.2967/jnumed.111.092726

Depierreux, F., Parmentier, E., Mackels, L., Baquero, K., Degueldre, C., Balteau, E., Salmon, E., Phillips, C., Bahri, M. A., Maquet, P., & Garraux, G. (2021). Parkinson's disease multimodal imaging: F-DOPA PET, neuromelanin-sensitive and quantitative iron-sensitive MRI. *npj Parkinson's Disease*, *7*(1), 57. https://doi.org/10.1038/s41531-021-00199-2

Desai, M., Kahn, I., Knoblich, U., Bernstein, J., Atallah, H., Yang, A., Kopell, N., Buckner, R. L., Graybiel, A. M., Moore, C. I., & Boyden, E. S. (2011). Mapping brain networks in awake mice using combined optical neural control and fMRI. *J Neurophysiol*, *105*(3), 1393-1405. https://doi.org/10.1152/jn.00828.2010

Díaz-García, C. M., Meyer, D. J., Nathwani, N., Rahman, M., Martínez-François, J. R., & Yellen, G. (2021). The distinct roles of calcium in rapid control of neuronal glycolysis and the tricarboxylic acid cycle. *eLife*, *10*. https://doi.org/10.7554/eLife.64821

Douma, E. H., & de Kloet, E. R. (2020). Stress-induced plasticity and functioning of ventral tegmental dopamine neurons. *Neurosci Biobehav Rev*, *108*, 48-77. https://doi.org/10.1016/j.neubiorev.2019.10.015

Dreyer, J. K., Herrik, K. F., Berg, R. W., & Hounsgaard, J. D. (2010). Influence of phasic and tonic dopamine release on receptor activation. *J Neurosci*, *30*(42), 14273-14283. https://doi.org/10.1523/JNEUROSCI.1894-10.2010

Edvinsson, L., McCulloch, J., & Sharkey, J. (1985). Vasomotor responses of cerebral arterioles in situ to putative dopamine receptor agonists. *British journal of pharmacology*, *85*(2), 403-410. https://doi.org/10.1111/j.1476-5381.1985.tb08875.x

Elster, A. D. (2024). *MRI Questions*. Retrieved 03.09.2024 from https://mriquestions.com/does-boldbrain-activity.html

Endo, H., Ono, M., Takado, Y., Matsuoka, K., Takahashi, M., Tagai, K., Kataoka, Y., Hirata, K., Takahata, K., Seki, C., Kokubo, N., Fujinaga, M., Mori, W., Nagai, Y., Mimura, K., Kumata, K., Kikuchi, T., Shimozawa, A., Mishra, S. K.,…Higuchi, M. (2024). Imaging α-synuclein pathologies in animal models and patients with Parkinson's and

related diseases. *Neuron*, *112*(15), 2540-2557.e2548. https://doi.org/10.1016/j.neuron.2024.05.006

Ferrie, J. J., Lengyel-Zhand, Z., Janssen, B., Lougee, M. G., Giannakoulias, S., Hsieh, C.-J., Pagar, V. V., Weng, C.-C., Xu, H., Graham, T. J. A., Lee, V. M. Y., Mach, R. H., & Petersson, E. J. (2020). Identification of a nanomolar affinity α-synuclein fibril imaging probe by ultra-high throughput in silico screening [10.1039/D0SC02159H]. *Chemical Science*, *11*(47), 12746-12754. https://doi.org/10.1039/D0SC02159H

Field, K. J., & Lang, C. M. (1988). Hazards of urethane (ethyl carbamate): a review of the literature. *Lab Anim*, *22*(3), 255-262. https://doi.org/10.1258/002367788780746331

Fodero-Tavoletti, M. T., Mulligan, R. S., Okamura, N., Furumoto, S., Rowe, C. C., Kudo, Y., Masters, C. L., Cappai, R., Yanai, K., & Villemagne, V. L. (2009). In vitro characterisation of BF227 binding to α-synuclein/Lewy bodies. *European Journal of Pharmacology*, *617*, 54-58. https://doi.org/10.1016/j.ejphar.2009.06.042

Ford, C. P. (2014). The role of D2-autoreceptors in regulating dopamine neuron activity and transmission. *Neuroscience*, *282*, 13-22. https://doi.org/https://doi.org/10.1016/j.neuroscience.2014.01.025

Forrest, S. L., & Kovacs, G. G. (2023). Current Concepts of Mixed Pathologies in Neurodegenerative Diseases. *Canadian Journal of Neurological Sciences / Journal Canadien des Sciences Neurologiques*, *50*(3), 329-345. https://doi.org/10.1017/cjn.2022.34

Galasko, D. (2017). Lewy Body Disorders. *Neurol Clin*, *35*(2), 325-338. https://doi.org/10.1016/j.ncl.2017.01.004

Gallegos, S., Pacheco, C., Peters, C., Opazo, C. M., & Aguayo, L. G. (2015). Features of alpha-synuclein that could explain the progression and irreversibility of Parkinson's disease. *Front Neurosci*, *9*, 59. https://doi.org/10.3389/fnins.2015.00059

Gaur, P., Galkin, M., Kurochka, A., Ghosh, S., Yushchenko, D. A., & Shvadchak, V. V. (2021). Fluorescent Probe for Selective Imaging of α-Synuclein Fibrils in Living Cells. *ACS Chemical Neuroscience*, *12*(8), 1293-1298. https://doi.org/10.1021/acschemneuro.1c00090

Geddes, C. E., Li, H., & Jin, X. (2018). Optogenetic Editing Reveals the Hierarchical Organization of Learned Action Sequences. *Cell*, *174*(1), 32-43.e15. https://doi.org/10.1016/j.cell.2018.06.012

Gibb, W. R., Esiri, M. M., & Lees, A. J. (1987). Clinical and pathological features of diffuse cortical Lewy body disease (Lewy body dementia). *Brain*, *110 (Pt 5)*, 1131-1153. https://doi.org/10.1093/brain/110.5.1131

Godbersen, G. M., Klug, S., Wadsak, W., Pichler, V., Raitanen, J., Rieckmann, A., Stiernman, L., Cocchi, L., Breakspear, M., Hacker, M., Lanzenberger, R., & Hahn, A. (2023). Task-evoked metabolic demands of the posteromedial default mode network are shaped by dorsal attention and frontoparietal control networks. *eLife*, *12*. https://doi.org/10.7554/eLife.84683

Gomez-Tortosa, E., Newell, K., Irizarry, M. C., Sanders, J. L., & Hyman, B. T. (2000). alpha-Synuclein immunoreactivity in dementia with Lewy bodies: morphological staging and comparison with ubiquitin immunostaining. *Acta Neuropathol*, *99*(4), 352-357. https://doi.org/10.1007/s004010051135

Gong, S., Doughty, M., Harbaugh, C. R., Cummins, A., Hatten, M. E., Heintz, N., & Gerfen, C. R. (2007). Targeting Cre recombinase to specific neuron populations with bacterial artificial chromosome constructs. *J Neurosci*, *27*(37), 9817-9823. https://doi.org/10.1523/jneurosci.2707-07.2007

González-Hernández, T., & Rodríguez, M. (2000). Compartmental organization and chemical profile of dopaminergic and GABAergic neurons in the substantia nigra of the rat. *J*

Comp Neurol, *421*(1), 107-135. https://doi.org/10.1002/(sici)1096-9861(20000522)421:1<107::aid-cne7>3.3.co;2-6

Gradinaru, V., Mogri, M., Thompson, K. R., Henderson, J. M., & Deisseroth, K. (2009). Optical deconstruction of parkinsonian neural circuitry. *Science*, *324*(5925), 354-359. https://doi.org/10.1126/science.1167093

Grandjean, J., Schroeter, A., Batata, I., & Rudin, M. (2014). Optimization of anesthesia protocol for resting-state fMRI in mice based on differential effects of anesthetics on functional connectivity patterns. *NeuroImage*, *102*, 838-847. https://doi.org/https://doi.org/10.1016/j.neuroimage.2014.08.043

Grover, V. P., Tognarelli, J. M., Crossey, M. M., Cox, I. J., Taylor-Robinson, S. D., & McPhail, M. J. (2015). Magnetic Resonance Imaging: Principles and Techniques: Lessons for Clinicians. *J Clin Exp Hepatol*, *5*(3), 246-255. https://doi.org/10.1016/j.jceh.2015.08.001

Guerrero-Ferreira, R., Kovacik, L., Ni, D., & Stahlberg, H. (2020). New insights on the structure of alpha-synuclein fibrils using cryo-electron microscopy. *Current Opinion in Neurobiology*, *61*, 89-95. https://doi.org/https://doi.org/10.1016/j.conb.2020.01.014

Haas, S. (2024a). Challenges in the development of PET tracers for misfolded alpha-synuclein. In: BioRender.com.

Haas, S. (2024b). Dopamine synapse. In: BioRender.com.

Haas, S. (2024c). The protein alpha-synuclein and Lewy body formation. In: BioRender.com.

Haas, S., Bravo, F., Ionescu, T. M., Gonzalez-Menendez, I., Quintanilla-Martinez, L., Dunkel, G., Kuebler, L., Hahn, A., Lanzenberger, R., Weigelin, B., Reischl, G., Pichler, B. J., & Herfert, K. (2024). Functional PET/MRI reveals active inhibition of neuronal activity during optogenetic activation of the nigrostriatal pathway. *Science Advances*, *10*(43), eadn2776. https://doi.org/doi:10.1126/sciadv.adn2776

Hacker, C. D., Perlmutter, J. S., Criswell, S. R., Ances, B. M., & Snyder, A. Z. (2012). Resting state functional connectivity of the striatum in Parkinson's disease. *Brain*, *135*(Pt 12), 3699-3711. https://doi.org/10.1093/brain/aws281

Hadi, S., Siadat, M., & Babajani-Feremi, A. (2012). *Negative BOLD response and serotonin concentration within rostral subgenual portion of the anterior cingulate cortex for long-allele carriers during perceptual processing of emotional tasks* (Vol. 8317). SPIE. https://doi.org/10.1117/12.905188

Haggerty, D. L., Grecco, G. G., Reeves, K. C., & Atwood, B. (2020). Adeno-Associated Viral Vectors in Neuroscience Research. *Mol Ther Methods Clin Dev*, *17*, 69-82. https://doi.org/10.1016/j.omtm.2019.11.012

Hahn, A., Gryglewski, G., Nics, L., Hienert, M., Rischka, L., Vraka, C., Sigurdardottir, H., Vanicek, T., James, G. M., Seiger, R., Kautzky, A., Silberbauer, L., Wadsak, W., Mitterhauser, M., Hacker, M., Kasper, S., & Lanzenberger, R. (2016). Quantification of Task-Specific Glucose Metabolism with Constant Infusion of ¹⁸F-FDG. *57*(12), 1933-1940. https://doi.org/10.2967/jnumed.116.176156 %J Journal of Nuclear Medicine

Hahn, A., Gryglewski, G., Nics, L., Rischka, L., Ganger, S., Sigurdardottir, H., Vraka, C., Silberbauer, L., Vanicek, T., Kautzky, A., Wadsak, W., Mitterhauser, M., Hartenbach, M., Hacker, M., Kasper, S., & Lanzenberger, R. (2018). Task-relevant brain networks identified with simultaneous PET/MR imaging of metabolism and connectivity. *Brain Struct Funct*, *223*(3), 1369-1378. https://doi.org/10.1007/s00429-017-1558-0

Hall, C. N., Klein-Flügge, M. C., Howarth, C., & Attwell, D. (2012). Oxidative Phosphorylation, Not Glycolysis, Powers Presynaptic and Postsynaptic Mechanisms Underlying Brain Information Processing. *The Journal of Neuroscience*, *32*(26), 8940-8951. https://doi.org/10.1523/jneurosci.0026-12.2012

Hall, C. N., Reynell, C., Gesslein, B., Hamilton, N. B., Mishra, A., Sutherland, B. A., O'Farrell, F. M., Buchan, A. M., Lauritzen, M., & Attwell, D. (2014). Capillary pericytes regulate cerebral blood flow in health and disease. *Nature*, *508*(7494), 55-60. https://doi.org/10.1038/nature13165

Hamilton, R. L. (2000). Lewy bodies in Alzheimer's disease: a neuropathological review of 145 cases using alpha-synuclein immunohistochemistry. *Brain Pathol*, *10*(3), 378-384. https://doi.org/10.1111/j.1750-3639.2000.tb00269.x

Harel, N., Lee, S. P., Nagaoka, T., Kim, D. S., & Kim, S. G. (2002). Origin of negative blood oxygenation level-dependent fMRI signals. *J Cereb Blood Flow Metab*, *22*(8), 908-917. https://doi.org/10.1097/00004647-200208000-00002

Hashimoto, H., Kawamura, K., Igarashi, N., Takei, M., Fujishiro, T., Aihara, Y., Shiomi, S., Muto, M., Ito, T., Furutsuka, K., Yamasaki, T., Yui, J., Xie, L., Ono, M., Hatori, A., Nemoto, K., Suhara, T., Higuchi, M., & Zhang, M. R. (2014). Radiosynthesis, photoisomerization, biodistribution, and metabolite analysis of 11C-PBB3 as a clinically useful PET probe for imaging of tau pathology. *J Nucl Med*, *55*(9), 1532-1538. https://doi.org/10.2967/jnumed.114.139550

He, X., Jin, C., Ma, M., Zhou, R., Wu, S., Huang, H., Li, Y., Chen, Q., Zhang, M., Zhang, H., & Tian, M. (2019). PET imaging on neurofunctional changes after optogenetic stimulation in a rat model of panic disorder. *Frontiers of Medicine*, *13*(5), 602-609. https://doi.org/10.1007/s11684-019-0704-x

Heras-Garvin, A., Weckbecker, D., Ryazanov, S., Leonov, A., Griesinger, C., Giese, A., Wenning, G. K., & Stefanova, N. (2019). Anle138b modulates α-synuclein oligomerization and prevents motor decline and neurodegeneration in a mouse model of multiple system atrophy. *Mov Disord*, *34*(2), 255-263. https://doi.org/10.1002/mds.27562

Herfert, K., Marciano, S., Kuebler, L., Buss, S., Landeck, N., Mannheim, J. G., & Napieczynska, H. (2019). Preclinical Experimentation in Neurology. In J. S. Lewis, A. D. Windhorst, & B. M. Zeglis (Eds.), *Radiopharmaceutical Chemistry* (pp. 583-606). Springer International Publishing. https://doi.org/10.1007/978-3-319-98947-1_34

Hikosaka, O., Takikawa, Y., & Kawagoe, R. (2000). Role of the Basal Ganglia in the Control of Purposive Saccadic Eye Movements. *Physiological Reviews*, *80*(3), 953-978. https://doi.org/10.1152/physrev.2000.80.3.953

Hill, Robert A., Tong, L., Yuan, P., Murikinati, S., Gupta, S., & Grutzendler, J. (2015). Regional Blood Flow in the Normal and Ischemic Brain Is Controlled by Arteriolar Smooth Muscle Cell Contractility and Not by Capillary Pericytes. *Neuron*, *87*(1), 95-110. https://doi.org/10.1016/j.neuron.2015.06.001

Hnasko, T. S., Chuhma, N., Zhang, H., Goh, G. Y., Sulzer, D., Palmiter, R. D., Rayport, S., & Edwards, R. H. (2010). Vesicular glutamate transport promotes dopamine storage and glutamate corelease in vivo. *Neuron*, *65*(5), 643-656. https://doi.org/10.1016/j.neuron.2010.02.012

Houssein, N. J., Henriksen, A. C., Hejl, A.-M., & Marner, L. (2023). Diagnostic accuracy of cerebral [18F]FDG PET in atypical parkinsonism. *EJNMMI Research*, *13*(1), 74. https://doi.org/10.1186/s13550-023-01025-x

Howarth, C., Gleeson, P., & Attwell, D. (2012). Updated energy budgets for neural computation in the neocortex and cerebellum. *J Cereb Blood Flow Metab*, *32*(7), 1222-1232. https://doi.org/10.1038/jcbfm.2012.35

Howarth, C., Mishra, A., & Hall, C. N. (2021). More than just summed neuronal activity: how multiple cell types shape the BOLD response. *Philos Trans R Soc Lond B Biol Sci*, *376*(1815), 20190630. https://doi.org/10.1098/rstb.2019.0630

Hsieh, C.-J., Xu, K., Lee, I., Graham, T. J. A., Tu, Z., Dhavale, D., Kotzbauer, P., & Mach, R. H. (2018). Chalcones and Five-Membered Heterocyclic Isosteres Bind to Alpha

Synuclein Fibrils in Vitro. *ACS Omega*, *3*(4), 4486-4493. https://doi.org/10.1021/acsomega.7b01897

Hsieh, C. J., Ferrie, J. J., Xu, K., Lee, I., Graham, T. J. A., Tu, Z., Yu, J., Dhavale, D., Kotzbauer, P., Petersson, E. J., & Mach, R. H. (2018). Alpha Synuclein Fibrils Contain Multiple Binding Sites for Small Molecules. *ACS Chem Neurosci*, *9*(11), 2521-2527. https://doi.org/10.1021/acschemneuro.8b00177

Huhtala, T. (2013). *Biodistribution Studies in Small Animal Models Using Pre-Clinical SPECT/CT Imaging* [Dissertation]. [73]. University of Eastern Finland, Kuopio. http://www.uef.fi/kirjasto

Hultqvist, G., Syvanen, S., Fang, X. T., Lannfelt, L., & Sehlin, D. (2017). Bivalent Brain Shuttle Increases Antibody Uptake by Monovalent Binding to the Transferrin Receptor. *Theranostics*, *7*(2), 308-318. https://doi.org/10.7150/thno.17155

Hunger, L., Kumar, A., & Schmidt, R. (2020). Abundance Compensates Kinetics: Similar Effect of Dopamine Signals on D1 and D2 Receptor Populations. *J Neurosci*, *40*(14), 2868-2881. https://doi.org/10.1523/jneurosci.1951-19.2019

Iadecola, C., Yang, G., Ebner, T. J., & Chen, G. (1997). Local and Propagated Vascular Responses Evoked by Focal Synaptic Activity in Cerebellar Cortex. *Journal of Neurophysiology*, *78*(2), 651-659. https://doi.org/10.1152/jn.1997.78.2.651

Ionescu, T. M., Amend, M., Watabe, T., Hatazawa, J., Maurer, A., Reischl, G., Pichler, B. J., Wehrl, H. F., & Herfert, K. (2022). Neurovascular Uncoupling: Multimodal Imaging Delineates the Acute Effects of MDMA. *bioRxiv*, 2022.2002.2014.480365. https://doi.org/10.1101/2022.02.14.480365

Jamadar, S. D., Ward, P. G. D., Close, T. G., Fornito, A., Premaratne, M., O'Brien, K., Stäb, D., Chen, Z., Shah, N. J., & Egan, G. F. (2020). Simultaneous BOLD-fMRI and constant infusion FDG-PET data of the resting human brain. *Scientific Data*, *7*(1), 363. https://doi.org/10.1038/s41597-020-00699-5

Johnstrom, P., & Davenport, A. P. (2005). Imaging and characterization of radioligands for positron emission tomography using quantitative phosphor imaging autoradiography. *Methods Mol Biol*, *306*, 203-216. https://doi.org/10.1385/1-59259-927-3:203

Josephson, L., Stratman, N., Liu, Y., Qian, F., Liang, S. H., Vasdev, N., & Patel, S. (2018). The Binding of BF-227-Like Benzoxazoles to Human α-Synuclein and Amyloid β Peptide Fibrils. *Mol Imaging*, *17*, 1536012118796297. https://doi.org/10.1177/1536012118796297

Kadekaro, M., Crane, A. M., & Sokoloff, L. (1985). Differential effects of electrical stimulation of sciatic nerve on metabolic activity in spinal cord and dorsal root ganglion in the rat. *Proc Natl Acad Sci U S A*, *82*(17), 6010-6013. https://doi.org/10.1073/pnas.82.17.6010

Kaide, S., Watanabe, H., Iikuni, S., Hasegawa, M., Itoh, K., & Ono, M. (2022). Chalcone Analogue as New Candidate for Selective Detection of alpha-Synuclein Pathology. *ACS Chem Neurosci*, *13*(1), 16-26. https://doi.org/10.1021/acschemneuro.1c00441

Kaide, S., Watanabe, H., Shimizu, Y., Iikuni, S., Nakamoto, Y., Hasegawa, M., Itoh, K., & Ono, M. (2020). Identification and Evaluation of Bisquinoline Scaffold as a New Candidate for alpha-Synuclein-PET Imaging. *ACS Chem Neurosci*, *11*(24), 4254-4261. https://doi.org/10.1021/acschemneuro.0c00523

Kaisti, K. K., Långsjö, J. W., Aalto, S., Oikonen, V., Sipilä, H., Teräs, M., Hinkka, S., Metsähonkala, L., & Scheinin, H. (2003). Effects of sevoflurane, propofol, and adjunct nitrous oxide on regional cerebral blood flow, oxygen consumption, and blood volume in humans. *Anesthesiology*, *99*(3), 603-613. https://doi.org/10.1097/00000542-200309000-00015

Kann, O. (2016). The interneuron energy hypothesis: Implications for brain disease. *Neurobiol Dis*, *90*, 75-85. https://doi.org/10.1016/j.nbd.2015.08.005

Kao, A. W., Racine, C. A., Quitania, L. C., Kramer, J. H., Christine, C. W., & Miller, B. L. (2009). Cognitive and neuropsychiatric profile of the synucleinopathies: Parkinson disease, dementia with Lewy bodies, and multiple system atrophy. *Alzheimer Dis Assoc Disord*, *23*(4), 365-370. https://doi.org/10.1097/WAD.0b013e3181b5065d

Kim, H. Y., Chia, W. K., Hsieh, C. J., Saturnino Guarino, D., Graham, T. J. A., Lengyel-Zhand, Z., Schneider, M., Tomita, C., Lougee, M. G., Kim, H. J., Pagar, V. V., Lee, H., Hou, C., Garcia, B. A., Petersson, E. J., O'Shea, J., Kotzbauer, P. T., Mathis, C. A., Lee, V. M.,…Mach, R. H. (2023). A Novel Brain PET Radiotracer for Imaging Alpha Synuclein Fibrils in Multiple System Atrophy. *J Med Chem*, *66*(17), 12185-12202. https://doi.org/10.1021/acs.jmedchem.3c00779

Kim, R. G., Cho, J., Park, J.-Y., Kim, Y. R., Lee, M.-C., & Kim, H.-I. (2024). Neuron type-specific optogenetic stimulation for differential stroke recovery in chronic capsular infarct. *Experimental & Molecular Medicine*, *56*(6), 1439-1449. https://doi.org/10.1038/s12276-024-01253-8

Kim, S. G., & Ogawa, S. (2012). Biophysical and physiological origins of blood oxygenation level-dependent fMRI signals. *J Cereb Blood Flow Metab*, *32*(7), 1188-1206. https://doi.org/10.1038/jcbfm.2012.23

Kinahan, P. E., Defrise, M., & Clackdoyle, R. (2004). Analytic image reconstruction methods. In *Emission Tomography* (pp. 421-442). https://doi.org/10.1016/B978-012744482-6.50023-5

Kittelmann, M., Liewald, J. F., Hegermann, J., Schultheis, C., Brauner, M., Steuer Costa, W., Wabnig, S., Eimer, S., & Gottschalk, A. (2013). In vivo synaptic recovery following optogenetic hyperstimulation. *Proc Natl Acad Sci U S A*, *110*(32), E3007-3016. https://doi.org/10.1073/pnas.1305679110

Koepsell, H. (2020). Glucose transporters in brain in health and disease. *Pflügers Archiv - European Journal of Physiology*, *472*(9), 1299-1343. https://doi.org/10.1007/s00424-020-02441-x

Kon, T., Ichimata, S., Di Luca, D. G., Martinez-Valbuena, I., Kim, A., Yoshida, K., Alruwaita, A. A., Kleiner, G., Strafella, A. P., Forrest, S. L., Sato, C., Rogaeva, E., Fox, S. H., Lang, A. E., & Kovacs, G. G. (2024). Multiple system atrophy with amyloid-β-predominant Alzheimer's disease neuropathologic change. *Brain Communications*, *6*(3). https://doi.org/10.1093/braincomms/fcae141

Koos, T., & Tepper, J. M. (1999). Inhibitory control of neostriatal projection neurons by GABAergic interneurons. *Nat Neurosci*, *2*(5), 467-472. https://doi.org/10.1038/8138

Korat, Š., Shalina, N., Bidesi, R., Bonanno, F., Di Nanni, A., Nguyễn, Á., Hoàng, N., Herfert, K., Maurer, A., Battisti, U., Bowden, G., Thonon, D., Vugts, D., Windhorst, A., & Herth, M. (2021). pharmaceuticals Alpha-Synuclein PET Tracer Development-An Overview about Current Efforts. *Pharmaceuticals*, *14*. https://doi.org/10.3390/ph14090847

Kotzbauer, P. T., Cairns, N. J., Campbell, M. C., Willis, A. W., Racette, B. A., Tabbal, S. D., & Perlmutter, J. S. (2012). Pathologic accumulation of α-synuclein and Aβ in Parkinson disease patients with dementia. *Arch Neurol*, *69*(10), 1326-1331. https://doi.org/10.1001/archneurol.2012.1608

Kouli, A., Torsney, K. M., & Kuan, W. L. (2018). Parkinson's Disease: Etiology, Neuropathology, and Pathogenesis. In T. B. Stoker & J. C. Greenland (Eds.), *Parkinson's Disease: Pathogenesis and Clinical Aspects*. Codon PublicationsCopyright: The Authors. https://doi.org/10.15586/codonpublications.parkinsonsdisease.2018.ch1

Kovacs, G. G., Milenkovic, I., Wöhrer, A., Höftberger, R., Gelpi, E., Haberler, C., Hönigschnabl, S., Reiner-Concin, A., Heinzl, H., Jungwirth, S., Krampla, W., Fischer, P., & Budka, H. (2013). Non-Alzheimer neurodegenerative pathologies and their

combinations are more frequent than commonly believed in the elderly brain: a community-based autopsy series. *Acta Neuropathologica*, *126*(3), 365-384. https://doi.org/10.1007/s00401-013-1157-y

Kovalska, V. B., Losytskyy, M. Y., Tolmachev, O. I., Slominskii, Y. L., Segers-Nolten, G. M., Subramaniam, V., & Yarmoluk, S. M. (2012). Tri- and pentamethine cyanine dyes for fluorescent detection of α-synuclein oligomeric aggregates. *J Fluoresc*, *22*(6), 1441-1448. https://doi.org/10.1007/s10895-012-1081-x

Kravitz, A. V., Freeze, B. S., Parker, P. R. L., Kay, K., Thwin, M. T., Deisseroth, K., & Kreitzer, A. C. (2010). Regulation of parkinsonian motor behaviours by optogenetic control of basal ganglia circuitry. *Nature*, *466*(7306), 622-626. https://doi.org/10.1038/nature09159

Kuebler, L., Buss, S., Leonov, A., Ryazanov, S., Schmidt, F., Maurer, A., Weckbecker, D., Landau, A. M., Lillethorup, T. P., Bleher, D., Saw, R. S., Pichler, B. J., Griesinger, C., Giese, A., & Herfert, K. (2020). [(11)C]MODAG-001-towards a PET tracer targeting alpha-synuclein aggregates. *Eur J Nucl Med Mol Imaging*. https://doi.org/10.1007/s00259-020-05133-x

Kügler, S., Kilic, E., & Bähr, M. (2003). Human synapsin 1 gene promoter confers highly neuron-specific long-term transgene expression from an adenoviral vector in the adult rat brain depending on the transduced area. *Gene Therapy*, *10*(4), 337-347. https://doi.org/10.1038/sj.gt.3301905

Kushner, M. J., Rosenquist, A., Alavi, A., Rosen, M., Dann, R., Fazekas, F., Bosley, T., Greenberg, J., & Reivich, M. (1988). Cerebral metabolism and patterned visual stimulation: A positron emission tomographic study of the human visual cortex. *Neurology*, *38*(1), 89-95. https://doi.org/10.1212/WNL.38.1.89

Kwong, K. K., Belliveau, J. W., Chesler, D. A., Goldberg, I. E., Weisskoff, R. M., Poncelet, B. P., Kennedy, D. N., Hoppel, B. E., Cohen, M. S., Turner, R., & et al. (1992). Dynamic magnetic resonance imaging of human brain activity during primary sensory stimulation. *Proc Natl Acad Sci U S A*, *89*(12), 5675-5679. https://doi.org/10.1073/pnas.89.12.5675

Lalush, D. S. (2004). Iterative image reconstruction. In *Emission Tomography* (pp. 443-472). https://doi.org/10.1016/B978-012744482-6.50024-7

Lanciego, J. L., Luquin, N., & Obeso, J. A. (2012). Functional neuroanatomy of the basal ganglia. *Cold Spring Harb Perspect Med*, *2*(12), a009621. https://doi.org/10.1101/cshperspect.a009621

Lang, A. E., & Lozano, A. M. (1998). Parkinson's Disease. *339*(15), 1044-1053. https://doi.org/10.1056/nejm199810083391506

Lecrux, C., Sandoe, C. H., Neupane, S., Kropf, P., Toussay, X., Tong, X.-K., Lacalle-Aurioles, M., Shmuel, A., & Hamel, E. (2017). Impact of Altered Cholinergic Tones on the Neurovascular Coupling Response to Whisker Stimulation. *The Journal of Neuroscience*, *37*(6), 1518-1531. https://doi.org/10.1523/jneurosci.1784-16.2016

Lee, H. M., & Koh, S. B. (2015). Many Faces of Parkinson's Disease: Non-Motor Symptoms of Parkinson's Disease. *J Mov Disord*, *8*(2), 92-97. https://doi.org/10.14802/jmd.15003

Lee, J. H., Durand, R., Gradinaru, V., Zhang, F., Goshen, I., Kim, D.-S., Fenno, L. E., Ramakrishnan, C., & Deisseroth, K. (2010). Global and local fMRI signals driven by neurons defined optogenetically by type and wiring. *Nature*, *465*(7299), 788-792. https://doi.org/10.1038/nature09108

Lewellen, T. K. (2008). Recent developments in PET detector technology. *Phys Med Biol*, *53*(17), R287-317. https://doi.org/10.1088/0031-9155/53/17/R01

Li, H., Guglielmetti, C., Sei, Y. J., Zilberter, M., Le Page, L. M., Shields, L., Yang, J., Nguyen, K., Tiret, B., Gao, X., Bennett, N., Lo, I., Dayton, T. L., Kampmann, M., Huang, Y., Rathmell, J. C., Vander Heiden, M., Chaumeil, M. M., & Nakamura, K.

(2023). Neurons require glucose uptake and glycolysis in vivo. *Cell Rep*, *42*(4), 112335. https://doi.org/10.1016/j.celrep.2023.112335

Li, H., & Jin, X. (2023). Multiple dynamic interactions from basal ganglia direct and indirect pathways mediate action selection. *eLife*, *12*, RP87644. https://doi.org/10.7554/eLife.87644

Lin, J. Y. (2011). A user's guide to channelrhodopsin variants: features, limitations and future developments. *Exp Physiol*, *96*(1), 19-25. https://doi.org/10.1113/expphysiol.2009.051961

Lin, J. Y., Lin, M. Z., Steinbach, P., & Tsien, R. Y. (2009). Characterization of engineered channelrhodopsin variants with improved properties and kinetics. *Biophys J*, *96*(5), 1803-1814. https://doi.org/10.1016/j.bpj.2008.11.034

Lippa, C. F., Fujiwara, H., Mann, D. M., Giasson, B., Baba, M., Schmidt, M. L., Nee, L. E., O'Connell, B., Pollen, D. A., St George-Hyslop, P., Ghetti, B., Nochlin, D., Bird, T. D., Cairns, N. J., Lee, V. M., Iwatsubo, T., & Trojanowski, J. Q. (1998). Lewy bodies contain altered alpha-synuclein in brains of many familial Alzheimer's disease patients with mutations in presenilin and amyloid precursor protein genes. *Am J Pathol*, *153*(5), 1365-1370. https://doi.org/10.1016/s0002-9440(10)65722-7

Lippa, C. F., Schmidt, M. L., Lee, V. M., & Trojanowski, J. Q. (1999). Antibodies to alpha-synuclein detect Lewy bodies in many Down's syndrome brains with Alzheimer's disease. *Ann Neurol*, *45*(3), 353-357. https://doi.org/10.1002/1531-8249(199903)45:3<353::aid-ana11>3.0.co;2-4

Liu, Y., Shen, H., Zhou, Z., & Hu, D. (2011). Sustained negative BOLD response in human fMRI finger tapping task. *PLoS One*, *6*(8), e23839. https://doi.org/10.1371/journal.pone.0023839

Logothetis, N. K., Pauls, J., Augath, M., Trinath, T., & Oeltermann, A. (2001). Neurophysiological investigation of the basis of the fMRI signal. *Nature*, *412*(6843), 150-157. https://doi.org/10.1038/35084005

Lonati, E., Sala, G., & Bulbarelli, A. (2014). Protein Misfolding and Accumulation as Root Cause in Neurodegeneration [Review Article]. *Austin Alzheimer's and Parkinson's Disease*, *1*(3).

Magistretti, Pierre J., & Allaman, I. (2015). A Cellular Perspective on Brain Energy Metabolism and Functional Imaging. *Neuron*, *86*(4), 883-901. https://doi.org/https://doi.org/10.1016/j.neuron.2015.03.035

Magistretti, P. J., & Pellerin, L. (1996). The contribution of astrocytes to the 18F-2-deoxyglucose signal in PET activation studies. *Mol Psychiatry*, *1*(6), 445-452.

Mahesh, M. (2013). The Essential Physics of Medical Imaging, Third Edition. *Med Phys*, *40*(7). https://doi.org/10.1118/1.4811156

Malonek, D., Dirnagl, U., Lindauer, U., Yamada, K., Kanno, I., & Grinvald, A. (1997). Vascular imprints of neuronal activity: relationships between the dynamics of cortical blood flow, oxygenation, and volume changes following sensory stimulation. *Proc Natl Acad Sci U S A*, *94*(26), 14826-14831. https://doi.org/10.1073/pnas.94.26.14826

Mandeville, J. B., Sander, C. Y. M., Jenkins, B. G., Hooker, J. M., Catana, C., Vanduffel, W., Alpert, N. M., Rosen, B. R., & Normandin, M. D. (2013). A receptor-based model for dopamine-induced fMRI signal. *Neuroimage*, *75*, 46-57. https://doi.org/10.1016/j.neuroimage.2013.02.036

Marcott, P. F., Mamaligas, A. A., & Ford, C. P. (2014). Phasic dopamine release drives rapid activation of striatal D2-receptors. *Neuron*, *84*(1), 164-176. https://doi.org/10.1016/j.neuron.2014.08.058

Markowitz, J. E., Gillis, W. F., Beron, C. C., Neufeld, S. Q., Robertson, K., Bhagat, N. D., Peterson, R. E., Peterson, E., Hyun, M., Linderman, S. W., Sabatini, B. L., & Datta, S.

R. (2018). The Striatum Organizes 3D Behavior via Moment-to-Moment Action Selection. *Cell*, *174*(1), 44-58.e17. https://doi.org/10.1016/j.cell.2018.04.019

Marota, J. J. A., Ayata, C., Moskowitz, M. A., Weisskoff, R. M., Rosen, B. R., & Mandeville, J. B. (1999). Investigation of the early response to rat forepaw stimulation. *Magnetic Resonance in Medicine*, *41*(2), 247-252. https://doi.org/https://doi.org/10.1002/(SICI)1522-2594(199902)41:2<247::AID-MRM6>3.0.CO;2-U

Martel, J. C., & Gatti McArthur, S. (2020). Dopamine Receptor Subtypes, Physiology and Pharmacology: New Ligands and Concepts in Schizophrenia [Review]. *11*. https://doi.org/10.3389/fphar.2020.01003

Mathis, C. A., Holt, D., Wang, Y., Huang, G.-F., Debnath, M., Shao, L., & Klunk, W. E. (2004). Species-dependent formation and identification of the brain metabolites of the amyloid imaging agent [11C]PIB. Neurobiology of Aging,

Mathis, C. A., Lopresti, B. J., Ikonomovic, M. D., & Klunk, W. E. (2017). Small-molecule PET Tracers for Imaging Proteinopathies. *Seminars in Nuclear Medicine*, *47*(5), 553-575. https://doi.org/https://doi.org/10.1053/j.semnuclmed.2017.06.003

Matsuoka, K., Ono, M., Takado, Y., Hirata, K., Endo, H., Ohfusa, T., Kojima, T., Yamamoto, T., Onishi, T., Orihara, A., Tagai, K., Takahata, K., Seki, C., Shinotoh, H., Kawamura, K., Shimizu, H., Shimada, H., Kakita, A., Zhang, M.-R.,…Higuchi, M. (2022). High-Contrast Imaging of α-Synuclein Pathologies in Living Patients with Multiple System Atrophy. *37*(10), 2159-2161. https://doi.org/https://doi.org/10.1002/mds.29186

Maurer, A., Leonov, A., Ryazanov, S., Herfert, K., Kuebler, L., Buss, S., Schmidt, F., Weckbecker, D., Linder, R., Bender, D., Giese, A., Pichler, B. J., & Griesinger, C. (2020). (11) C Radiolabeling of anle253b: a Putative PET Tracer for Parkinson's Disease That Binds to α-Synuclein Fibrils in vitro and Crosses the Blood-Brain Barrier. *ChemMedChem*, *15*(5), 411-415. https://doi.org/10.1002/cmdc.201900689

Melani, R., & Tritsch, N. X. (2022). Inhibitory co-transmission from midbrain dopamine neurons relies on presynaptic GABA uptake. *Cell Reports*, *39*(3), 110716. https://doi.org/https://doi.org/10.1016/j.celrep.2022.110716

Meyer, H.-J., Wienke, A., & Surov, A. (2019). Associations between GLUT expression and SUV values derived from FDG-PET in different tumors—A systematic review and meta analysis. *PLoS One*, *14*(6), e0217781. https://doi.org/10.1371/journal.pone.0217781

Meyer, P. T., Frings, L., Rücker, G., & Hellwig, S. (2017). ¹⁸F-FDG PET in Parkinsonism: Differential Diagnosis and Evaluation of Cognitive Impairment. *Journal of Nuclear Medicine*, *58*(12), 1888-1898. https://doi.org/10.2967/jnumed.116.186403

Mihaescu, A. S., Valli, M., Uribe, C., Diez-Cirarda, M., Masellis, M., Graff-Guerrero, A., & Strafella, A. P. (2022). Beta amyloid deposition and cognitive decline in Parkinson's disease: a study of the PPMI cohort. *Molecular Brain*, *15*(1), 79. https://doi.org/10.1186/s13041-022-00964-1

Mink, J. W. (1996). THE BASAL GANGLIA: FOCUSED SELECTION AND INHIBITION OF COMPETING MOTOR PROGRAMS. *Progress in Neurobiology*, *50*(4), 381-425. https://doi.org/https://doi.org/10.1016/S0301-0082(96)00042-1

Miranda-Azpiazu, P., Svedberg, M., Higuchi, M., Ono, M., Jia, Z., Sunnemark, D., Elmore, C. S., Schou, M., & Varrone, A. (2020). Identification and in vitro characterization of C05-01, a PBB3 derivative with improved affinity for alpha-synuclein. *Brain Res*, *1749*, 147131. https://doi.org/10.1016/j.brainres.2020.147131

Mishra, A., Singh, S., & Shukla, S. (2018). Physiological and Functional Basis of Dopamine Receptors and Their Role in Neurogenesis: Possible Implication for Parkinson's

disease. *J Exp Neurosci*, *12*, 1179069518779829. https://doi.org/10.1177/1179069518779829

Moraschi, M., DiNuzzo, M., & Giove, F. (2012). On the origin of sustained negative BOLD response. *108*(9), 2339-2342. https://doi.org/10.1152/jn.01199.2011

Morrow, T. J., Paulson, P. E., Danneman, P. J., & Casey, K. L. (1998). Regional changes in forebrain activation during the early and late phase of formalin nociception: analysis using cerebral blood flow in the rat. *Pain*, *75*(2-3), 355-365. https://doi.org/10.1016/s0304-3959(98)00016-5

Murphy, D. D., Rueter, S. M., Trojanowski, J. Q., & Lee, V. M. (2000). Synucleins are developmentally expressed, and alpha-synuclein regulates the size of the presynaptic vesicular pool in primary hippocampal neurons. *J Neurosci*, *20*(9), 3214-3220. https://doi.org/10.1523/jneurosci.20-09-03214.2000

Nagel, G., Szellas, T., Huhn, W., Kateriya, S., Adeishvili, N., Berthold, P., Ollig, D., Hegemann, P., & Bamberg, E. (2003). Channelrhodopsin-2, a directly light-gated cation-selective membrane channel. *Proc Natl Acad Sci U S A*, *100*(24), 13940-13945. https://doi.org/10.1073/pnas.1936192100

Naiki, H., Higuchi, K., Hosokawa, M., & Takeda, T. (1989). Fluorometric determination of amyloid fibrils in vitro using the fluorescent dye, thioflavin T1. *Anal Biochem*, *177*(2), 244-249. https://doi.org/10.1016/0003-2697(89)90046-8

Neal, K. L., Shakerdge, N. B., Hou, S. S., Klunk, W. E., Mathis, C. A., Nesterov, E. E., Swager, T. M., McLean, P. J., & Bacskai, B. J. (2013). Development and Screening of Contrast Agents for In Vivo Imaging of Parkinson's Disease. *Molecular Imaging and Biology*, *15*(5), 585-595. https://doi.org/10.1007/s11307-013-0634-y

Nelson, A. B., Hammack, N., Yang, C. F., Shah, N. M., Seal, R. P., & Kreitzer, A. C. (2014). Striatal cholinergic interneurons Drive GABA release from dopamine terminals. *Neuron*, *82*(1), 63-70. https://doi.org/10.1016/j.neuron.2014.01.023

Nomura, T., Nishimura, Y., Gotoh, H., & Ono, K. (2016). Rapid and efficient gene delivery into the adult mouse brain via focal electroporation. *Sci Rep*, *6*, 29817. https://doi.org/10.1038/srep29817

Nonomura, S., Nishizawa, K., Sakai, Y., Kawaguchi, Y., Kato, S., Uchigashima, M., Watanabe, M., Yamanaka, K., Enomoto, K., Chiken, S., Sano, H., Soma, S., Yoshida, J., Samejima, K., Ogawa, M., Kobayashi, K., Nambu, A., Isomura, Y., & Kimura, M. (2018). Monitoring and Updating of Action Selection for Goal-Directed Behavior through the Striatal Direct and Indirect Pathways. *Neuron*, *99*(6), 1302-1314.e1305. https://doi.org/10.1016/j.neuron.2018.08.002

Northoff, G., Walter, M., Schulte, R. F., Beck, J., Dydak, U., Henning, A., Boeker, H., Grimm, S., & Boesiger, P. (2007). GABA concentrations in the human anterior cingulate cortex predict negative BOLD responses in fMRI. *Nat Neurosci*, *10*(12), 1515-1517. https://doi.org/10.1038/nn2001

Ogawa, S., & Lee, T. M. (1990). Magnetic resonance imaging of blood vessels at high fields: in vivo and in vitro measurements and image simulation. *Magn Reson Med*, *16*(1), 9-18. https://doi.org/10.1002/mrm.1910160103

Ogawa, S., Lee, T. M., Kay, A. R., & Tank, D. W. (1990). Brain magnetic resonance imaging with contrast dependent on blood oxygenation. *Proc Natl Acad Sci U S A*, *87*(24), 9868-9872. https://doi.org/10.1073/pnas.87.24.9868

Ogawa, S., Lee, T. M., Nayak, A. S., & Glynn, P. (1990). Oxygenation-sensitive contrast in magnetic resonance image of rodent brain at high magnetic fields. *Magn Reson Med*, *14*(1), 68-78. https://doi.org/10.1002/mrm.1910140108

Ono, M., Doi, Y., Watanabe, H., Ihara, M., Ozaki, A., & Saji, H. (2016). Structure–activity relationships of radioiodinated diphenyl derivatives with different conjugated double

bonds as ligands for α-synuclein aggregates [10.1039/C6RA02710E]. *RSC Advances*, *6*(50), 44305-44312. https://doi.org/10.1039/C6RA02710E

Ono, M., Takahashi, M., Shimozawa, A., Fujinaga, M., Mori, W., Nagai, Y., Mimura, K., Minamihisamatsu, T., Uchida, S., Shimojo, M., Takado, Y., Takuwa, H., Sahara, N., Zhang, M.-R., Minamimoto, T., Hasegawa, M., & Higuchi, M. (2020). In vivo visualization of propagating α-synuclein pathologies in mouse and marmoset models by a bimodal imaging probe, C05-05. 2020.2010.2023.349860. https://doi.org/10.1101/2020.10.23.349860 %J bioRxiv

Optogenetic Restoration of Basal Ganglia Function to Treat Parkinson's Disease. (2024). Michael J. Fox Foundation. Retrieved 03.10.2024 from https://www.michaeljfox.org/grant/optogenetic-restoration-basal-ganglia-function-treat-parkinsons-disease

Paasonen, J., Stenroos, P., Salo, R. A., Kiviniemi, V., & Gröhn, O. (2018). Functional connectivity under six anesthesia protocols and the awake condition in rat brain. *NeuroImage*, *172*, 9-20. https://doi.org/https://doi.org/10.1016/j.neuroimage.2018.01.014

Palma, J. A., Norcliffe-Kaufmann, L., & Kaufmann, H. (2018). Diagnosis of multiple system atrophy. *Auton Neurosci*, *211*, 15-25. https://doi.org/10.1016/j.autneu.2017.10.007

Patel, J. C., Sherpa, A. D., Melani, R., Witkovsky, P., Wiseman, M. R., O'Neill, B., Aoki, C., Tritsch, N. X., & Rice, M. E. (2024). GABA co-released from striatal dopamine axons dampens phasic dopamine release through autoregulatory GABA(A) receptors. *Cell Rep*, *43*(3), 113834. https://doi.org/10.1016/j.celrep.2024.113834

Pathak, D., Shields, L. Y., Mendelsohn, B. A., Haddad, D., Lin, W., Gerencser, A. A., Kim, H., Brand, M. D., Edwards, R. H., & Nakamura, K. (2015). The role of mitochondrially derived ATP in synaptic vesicle recycling. *J Biol Chem*, *290*(37), 22325-22336. https://doi.org/10.1074/jbc.M115.656405

Peppiatt, C. M., Howarth, C., Mobbs, P., & Attwell, D. (2006). Bidirectional control of CNS capillary diameter by pericytes. *Nature*, *443*(7112), 700-704. https://doi.org/10.1038/nature05193

Pereira de Vasconcelos, A., Ferrandon, A., & Nehlig, A. (2002). Local cerebral blood flow during lithium-pilocarpine seizures in the developing and adult rat: role of coupling between blood flow and metabolism in the genesis of neuronal damage. *J Cereb Blood Flow Metab*, *22*(2), 196-205. https://doi.org/10.1097/00004647-200202000-00007

Phelps, M. E., Huang, S. C., Hoffman, E. J., Selin, C., Sokoloff, L., & Kuhl, D. E. (1979). Tomographic measurement of local cerebral glucose metabolic rate in humans with (F-18)2-fluoro-2-deoxy-D-glucose: validation of method. *Ann Neurol*, *6*(5), 371-388. https://doi.org/10.1002/ana.410060502

Pietrini, P., Alexander, G. E., Furey, M. L., Dani, A., Mentis, M. J., Horwitz, B., Guazzelli, M., Shapiro, M. B., & Rapoport, S. I. (2000). Cerebral metabolic response to passive audiovisual stimulation in patients with Alzheimer's disease and healthy volunteers assessed by PET. *J Nucl Med*, *41*(4), 575-583.

Pike, V. W. (2009). PET radiotracers: crossing the blood-brain barrier and surviving metabolism. *Trends Pharmacol Sci*, *30*(8), 431-440. https://doi.org/10.1016/j.tips.2009.05.005

Pimlott, S., & Sutherland, A. (2011). Molecular tracers for the PET and SPECT imaging of disease. *Chemical Society reviews*, *40*, 149-162. https://doi.org/10.1039/b922628c

Pirali, T., Serafini, M., Cargnin, S., & Genazzani, A. A. (2019). Applications of Deuterium in Medicinal Chemistry. *Journal of Medicinal Chemistry*, *62*(11), 5276-5297. https://doi.org/10.1021/acs.jmedchem.8b01808

Pouliopoulos, A. N., Murillo, M. F., Noel, R. L., Batts, A. J., Ji, R., Kwon, N., Yu, H., Tong, C. K., Gelinas, J. N., Araghy, D. K., Hussaini, S. A., & Konofagou, E. E. (2022). Non-

invasive optogenetics with ultrasound-mediated gene delivery and red-light excitation. *Brain Stimul*, *15*(4), 927-941. https://doi.org/10.1016/j.brs.2022.06.007

Raichle, M. E. (1983). Positron Emission Tomography. *Annual Review Neuroscience*, *6*, 249-267. https://doi.org/10.1146/annurev.ne.06.030183.001341

Raichle, M. E. (2001). Bold insights. *Nature*, *412*(6843), 128-130. https://doi.org/10.1038/35084300

Rangaraju, V., Calloway, N., & Ryan, T. A. (2014). Activity-driven local ATP synthesis is required for synaptic function. *Cell*, *156*(4), 825-835. https://doi.org/10.1016/j.cell.2013.12.042

Reader, A. J., & Zaidi, H. (2007). Advances in PET Image Reconstruction. *PET Clin*, *2*(2), 173-190. https://doi.org/10.1016/j.cpet.2007.08.001

Reivich, M., Kuhl, D., Wolf, A., Greenberg, J., Phelps, M., Ido, T., Casella, V., Fowler, J., Hoffman, E., Alavi, A., Som, P., & Sokoloff, L. (1979). The [18F]fluorodeoxyglucose method for the measurement of local cerebral glucose utilization in man. *Circ Res*, *44*(1), 127-137. https://doi.org/10.1161/01.res.44.1.127

Richfield, E. K., Penney, J. B., & Young, A. B. (1989). Anatomical and affinity state comparisons between dopamine D1 and D2 receptors in the rat central nervous system. *Neuroscience*, *30*(3), 767-777. https://doi.org/10.1016/0306-4522(89)90168-1

Rischka, L., Gryglewski, G., Pfaff, S., Vanicek, T., Hienert, M., Klöbl, M., Hartenbach, M., Haug, A., Wadsak, W., Mitterhauser, M., Hacker, M., Kasper, S., Lanzenberger, R., & Hahn, A. (2018). Reduced task durations in functional PET imaging with [(18)F]FDG approaching that of functional MRI. *NeuroImage*, *181*, 323-330. https://doi.org/10.1016/j.neuroimage.2018.06.079

Rodriguez-Baeza, A., Reina-De La Torre, F., Ortega-Sanchez, M., & Sahuquillo-Barris, J. (1998). Perivascular structures in corrosion casts of the human central nervous system: a confocal laser and scanning electron microscope study. *Anat Rec*, *252*(2), 176-184. https://doi.org/https://doi.org/10.1002/(sici)1097-0185(199810)252:2<176::Aid-ar3>3.0.Co;2-1

Rommelfanger, K., & Wichmann, T. (2010). Extrastriatal Dopaminergic Circuits of the Basal Ganglia [Review]. *4*. https://doi.org/10.3389/fnana.2010.00139

Roncevic, D., Palma, J. A., Martinez, J., Goulding, N., Norcliffe-Kaufmann, L., & Kaufmann, H. (2014). Cerebellar and parkinsonian phenotypes in multiple system atrophy: similarities, differences and survival. *J Neural Transm (Vienna)*, *121*(5), 507-512. https://doi.org/10.1007/s00702-013-1133-7

Roshanbin, S., Xiong, M., Hultqvist, G., Söderberg, L., Zachrisson, O., Meier, S., Ekmark-Lewén, S., Bergström, J., Ingelsson, M., Sehlin, D., & Syvänen, S. (2022). In vivo imaging of alpha-synuclein with antibody-based PET. *Neuropharmacology*, *208*, 108985. https://doi.org/10.1016/j.neuropharm.2022.108985

Saborio, G. P., Permanne, B., & Soto, C. (2001). Sensitive detection of pathological prion protein by cyclic amplification of protein misfolding. *Nature*, *411*(6839), 810-813. https://doi.org/10.1038/35081095

Saha, G. B. (2010). Basics of PET Imaging. https://doi.org/10.1007/978-1-4419-0805-6

Salvesen, L., Ullerup, B. H., Sunay, F. B., Brudek, T., Løkkegaard, A., Agander, T. K., Winge, K., & Pakkenberg, B. (2015). Changes in total cell numbers of the basal ganglia in patients with multiple system atrophy - A stereological study. *Neurobiol Dis*, *74*, 104-113. https://doi.org/10.1016/j.nbd.2014.11.008

Sander, C. Y., Hooker, J. M., Catana, C., Normandin, M. D., Alpert, N. M., Knudsen, G. M., Vanduffel, W., Rosen, B. R., & Mandeville, J. B. (2013). Neurovascular coupling to D2/D3 dopamine receptor occupancy using simultaneous PET/functional MRI. *Proc Natl Acad Sci U S A*, *110*(27), 11169-11174. https://doi.org/10.1073/pnas.1220512110

Savio, A., Fünger, S., Tahmasian, M., Rachakonda, S., Manoliu, A., Sorg, C., Grimmer, T., Calhoun, V., Drzezga, A., Riedl, V., & Yakushev, I. (2017). Resting-State Networks as Simultaneously Measured with Functional MRI and PET. *J Nucl Med*, *58*(8), 1314-1317. https://doi.org/10.2967/jnumed.116.185835

Schultz, W. (2007). Multiple dopamine functions at different time courses. *Annu Rev Neurosci*, *30*, 259-288. https://doi.org/10.1146/annurev.neuro.28.061604.135722

Schweighauser, M., Shi, Y., Tarutani, A., Kametani, F., Murzin, A. G., Ghetti, B., Matsubara, T., Tomita, T., Ando, T., Hasegawa, K., Murayama, S., Yoshida, M., Hasegawa, M., Scheres, S. H. W., & Goedert, M. (2020). Structures of α-synuclein filaments from multiple system atrophy. *Nature*, *585*(7825), 464-469. https://doi.org/10.1038/s41586-020-2317-6

Scremin, O. U. (2004). CHAPTER 33 - Cerebral Vascular System. In G. Paxinos (Ed.), *The Rat Nervous System (Third Edition)* (pp. 1167-1202). Academic Press. https://doi.org/https://doi.org/10.1016/B978-012547638-6/50034-1

Seddon, A. M., Casey, D., Law, R. V., Gee, A., Templer, R. H., & Ces, O. (2009). Drug interactions with lipid membranes [10.1039/B813853M]. *Chemical Society reviews*, *38*(9), 2509-2519. https://doi.org/10.1039/B813853M

Sehlin, D., Fang, X. T., Cato, L., Antoni, G., Lannfelt, L., & Syvanen, S. (2016). Antibody-based PET imaging of amyloid beta in mouse models of Alzheimer's disease. *Nat Commun*, *7*, 10759. https://doi.org/10.1038/ncomms10759

Shahmoradian, S. H., Lewis, A. J., Genoud, C., Hench, J., Moors, T. E., Navarro, P. P., Castaño-Díez, D., Schweighauser, G., Graff-Meyer, A., Goldie, K. N., Sütterlin, R., Huisman, E., Ingrassia, A., Gier, Y. d., Rozemuller, A. J. M., Wang, J., Paepe, A. D., Erny, J., Staempfli, A.,…Lauer, M. E. (2019). Lewy pathology in Parkinson's disease consists of crowded organelles and lipid membranes. *Nature Neuroscience*, *22*(7), 1099-1109. https://doi.org/10.1038/s41593-019-0423-2

Shih, Y. Y., Chen, C. C., Shyu, B. C., Lin, Z. J., Chiang, Y. C., Jaw, F. S., Chen, Y. Y., & Chang, C. (2009). A new scenario for negative functional magnetic resonance imaging signals: endogenous neurotransmission. *J Neurosci*, *29*(10), 3036-3044. https://doi.org/10.1523/jneurosci.3447-08.2009

Shmuel, A., Augath, M., Oeltermann, A., & Logothetis, N. K. (2006). Negative functional MRI response correlates with decreases in neuronal activity in monkey visual area V1. *Nat Neurosci*, *9*(4), 569-577. https://doi.org/10.1038/nn1675

Shu, C. Y., Sanganahalli, B. G., Coman, D., Herman, P., & Hyder, F. (2016). New horizons in neurometabolic and neurovascular coupling from calibrated fMRI. *Prog Brain Res*, *225*, 99-122. https://doi.org/10.1016/bs.pbr.2016.02.003

Sidhu, A., Wersinger, C., Moussa, C. E., & Vernier, P. (2004). The role of alpha-synuclein in both neuroprotection and neurodegeneration. *Ann N Y Acad Sci*, *1035*, 250-270. https://doi.org/10.1196/annals.1332.016

Siero, J. C., Bhogal, A., & Jansma, J. M. (2013). Blood Oxygenation Level-dependent/Functional Magnetic Resonance Imaging: Underpinnings, Practice, and Perspectives. *PET Clin*, *8*(3), 329-344. https://doi.org/10.1016/j.cpet.2013.04.003

Silva, A. C., Lee, S.-P., Yang, G., Iadecola, C., & Kim, S.-G. (1999). Simultaneous Blood Oxygenation Level-Dependent and Cerebral Blood Flow Functional Magnetic Resonance Imaging during Forepaw Stimulation in the Rat. *Journal of Cerebral Blood Flow & Metabolism*, *19*(8), 871-879. https://doi.org/10.1097/00004647-199908000-00006

Singleton, A., & Gwinn-Hardy, K. (2004). Parkinson's disease and dementia with Lewy bodies: a difference in dose? *Lancet*, *364*(9440), 1105-1107. https://doi.org/10.1016/s0140-6736(04)17117-1

Smith, R., Capotosti, F., Schain, M., Ohlsson, T., Vokali, E., Molette, J., Touilloux, T., Hliva, V., Dimitrakopoulos, I. K., Puschmann, A., Jögi, J., Svenningsson, P., Andréasson, M., Sandiego, C., Russell, D. S., Miranda-Azpiazu, P., Halldin, C., Stomrud, E., Hall, S.,…Hansson, O. (2023). The α-synuclein PET tracer [18F] ACI-12589 distinguishes multiple system atrophy from other neurodegenerative diseases. *Nature Communications*, *14*(1), 6750. https://doi.org/10.1038/s41467-023-42305-3

Spangler-Bickell, M. G., de Laat, B., Fulton, R., Bormans, G., & Nuyts, J. (2016). The effect of isoflurane on (18)F-FDG uptake in the rat brain: a fully conscious dynamic PET study using motion compensation. *EJNMMI Res*, *6*(1), 86. https://doi.org/10.1186/s13550-016-0242-3

Spillantini, M. G., Crowther, R. A., Jakes, R., Cairns, N. J., Lantos, P. L., & Goedert, M. (1998). Filamentous alpha-synuclein inclusions link multiple system atrophy with Parkinson's disease and dementia with Lewy bodies. *Neurosci Lett*, *251*(3), 205-208. https://doi.org/10.1016/s0304-3940(98)00504-7

Srinivasan, E., Chandrasekhar, G., Chandrasekar, P., Anbarasu, K., Vickram, A. S., Karunakaran, R., Rajasekaran, R., & Srikumar, P. S. (2021). Alpha-Synuclein Aggregation in Parkinson's Disease [Review]. *8*. https://doi.org/10.3389/fmed.2021.736978

Stefanis, L. (2012). α-Synuclein in Parkinson's disease. *Cold Spring Harb Perspect Med*, *2*(2), a009399. https://doi.org/10.1101/cshperspect.a009399

Stefanovic, B., Warnking, J. M., & Pike, G. B. (2004). Hemodynamic and metabolic responses to neuronal inhibition. *Neuroimage*, *22*(2), 771-778. https://doi.org/10.1016/j.neuroimage.2004.01.036

Stiernman, L. J., Grill, F., Hahn, A., Rischka, L., Lanzenberger, R., Panes Lundmark, V., Riklund, K., Axelsson, J., & Rieckmann, A. (2021). Dissociations between glucose metabolism and blood oxygenation in the human default mode network revealed by simultaneous PET-fMRI. *118*(27), e2021913118. https://doi.org/doi:10.1073/pnas.2021913118

Stoessl, A. J. (2017). Glucose utilization: still in the synapse. *Nature Neuroscience*, *20*(3), 382-384. https://doi.org/10.1038/nn.4513

Strohäker, T., Jung, B. C., Liou, S. H., Fernandez, C. O., Riedel, D., Becker, S., Halliday, G. M., Bennati, M., Kim, W. S., Lee, S. J., & Zweckstetter, M. (2019). Structural heterogeneity of α-synuclein fibrils amplified from patient brain extracts. *Nat Commun*, *10*(1), 5535. https://doi.org/10.1038/s41467-019-13564-w

Sun, W., Ginovart, N., Ko, F., Seeman, P., & Kapur, S. (2003). In vivo evidence for dopamine-mediated internalization of D2-receptors after amphetamine: differential findings with [3H]raclopride versus [3H]spiperone. *Mol Pharmacol*, *63*(2), 456-462. https://doi.org/10.1124/mol.63.2.456

Surmeier, D. J., Ding, J., Day, M., Wang, Z., & Shen, W. (2007). D1 and D2 dopamine-receptor modulation of striatal glutamatergic signaling in striatal medium spiny neurons. *Trends Neurosci*, *30*(5), 228-235. https://doi.org/10.1016/j.tins.2007.03.008

Syvanen, S., Lindhe, O., Palner, M., Kornum, B. R., Rahman, O., Langstrom, B., Knudsen, G. M., & Hammarlund-Udenaes, M. (2009). Species differences in blood-brain barrier transport of three positron emission tomography radioligands with emphasis on P-glycoprotein transport. *Drug Metab Dispos*, *37*(3), 635-643. https://doi.org/10.1124/dmd.108.024745

Takao, M., Ghetti, B., Yoshida, H., Piccardo, P., Narain, Y., Murrell, J. R., Vidal, R., Glazier, B. S., Jakes, R., Tsutsui, M., Spillantini, M. G., Crowther, R. A., Goedert, M., & Koto, A. (2004). Early-onset dementia with Lewy bodies. *Brain Pathol*, *14*(2), 137-147. https://doi.org/10.1111/j.1750-3639.2004.tb00046.x

Tecuapetla, F., Patel, J. C., Xenias, H., English, D., Tadros, I., Shah, F., Berlin, J., Deisseroth, K., Rice, M. E., Tepper, J. M., & Koos, T. (2010). Glutamatergic signaling by mesolimbic dopamine neurons in the nucleus accumbens. *J Neurosci*, *30*(20), 7105-7110. https://doi.org/10.1523/jneurosci.0265-10.2010

Thanos, P. K., Robison, L., Nestler, E. J., Kim, R., Michaelides, M., Lobo, M.-K., & Volkow, N. D. (2013). Mapping Brain Metabolic Connectivity in Awake Rats with μPET and Optogenetic Stimulation. *33*(15), 6343-6349. https://doi.org/10.1523/JNEUROSCI.4997-12.2013 %J The Journal of Neuroscience

Theparambil, S. M., Kopach, O., Braga, A., Nizari, S., Hosford, P. S., Sagi-Kiss, V., Hadjihambi, A., Konstantinou, C., Esteras, N., Gutierrez Del Arroyo, A., Ackland, G. L., Teschemacher, A. G., Dale, N., Eckle, T., Andrikopoulos, P., Rusakov, D. A., Kasparov, S., & Gourine, A. V. (2024). Adenosine signalling to astrocytes coordinates brain metabolism and function. *Nature*, *632*(8023), 139-146. https://doi.org/10.1038/s41586-024-07611-w

Theriault, J. E., Shaffer, C., Dienel, G. A., Sander, C. Y., Hooker, J. M., Dickerson, B. C., Barrett, L. F., & Quigley, K. S. (2023). A functional account of stimulation-based aerobic glycolysis and its role in interpreting BOLD signal intensity increases in neuroimaging experiments. *Neurosci Biobehav Rev*, *153*, 105373. https://doi.org/10.1016/j.neubiorev.2023.105373

Trantham-Davidson, H., Neely, L. C., Lavin, A., & Seamans, J. K. (2004). Mechanisms underlying differential D1 versus D2 dopamine receptor regulation of inhibition in prefrontal cortex. *J Neurosci*, *24*(47), 10652-10659. https://doi.org/10.1523/jneurosci.3179-04.2004

Tritsch, N. X., Ding, J. B., & Sabatini, B. L. (2012). Dopaminergic neurons inhibit striatal output through non-canonical release of GABA. *Nature*, *490*(7419), 262-266. https://doi.org/10.1038/nature11466

Turner, D. A., & Adamson, D. C. (2011). Neuronal-astrocyte metabolic interactions: understanding the transition into abnormal astrocytoma metabolism. *J Neuropathol Exp Neurol*, *70*(3), 167-176. https://doi.org/10.1097/NEN.0b013e31820e1152

Tysnes, O. B., & Storstein, A. (2017). Epidemiology of Parkinson's disease. *J Neural Transm (Vienna)*, *124*(8), 901-905. https://doi.org/10.1007/s00702-017-1686-y

Uéda, K., Fukushima, H., Masliah, E., Xia, Y., Iwai, A., Yoshimoto, M., Otero, D. A., Kondo, J., Ihara, Y., & Saitoh, T. (1993). Molecular cloning of cDNA encoding an unrecognized component of amyloid in Alzheimer disease. *Proc Natl Acad Sci U S A*, *90*(23), 11282-11286. https://doi.org/10.1073/pnas.90.23.11282

Ueki, M., Mies, G., & Hossmann, K. A. (1992). Effect of alpha-chloralose, halothane, pentobarbital and nitrous oxide anesthesia on metabolic coupling in somatosensory cortex of rat. *Acta Anaesthesiol Scand*, *36*(4), 318-322. https://doi.org/10.1111/j.1399-6576.1992.tb03474.x

van de Waterbeemd, H., Camenisch, G., Folkers, G., Chretien, J. R., & Raevsky, O. A. (1998). Estimation of blood-brain barrier crossing of drugs using molecular size and shape, and H-bonding descriptors. *J Drug Target*, *6*(2), 151-165. https://doi.org/10.3109/10611869808997889

van den Berge, S. A., Kevenaar, J. T., Sluijs, J. A., & Hol, E. M. (2012). Dementia in Parkinson's Disease Correlates with alpha-Synuclein Pathology but Not with Cortical Astrogliosis. *Parkinsons Dis*, *2012*, 420957. https://doi.org/10.1155/2012/420957

Van der Perren, A., Gelders, G., Fenyi, A., Bousset, L., Brito, F., Peelaerts, W., Van den Haute, C., Gentleman, S., Melki, R., & Baekelandt, V. (2020). The structural differences between patient-derived α-synuclein strains dictate characteristics of Parkinson's disease, multiple system atrophy and dementia with Lewy bodies. *Acta Neuropathol*, *139*(6), 977-1000. https://doi.org/10.1007/s00401-020-02157-3

van Eijsden, P., Notenboom, R. G., Wu, O., de Graan, P. N., van Nieuwenhuizen, O., Nicolay, K., & Braun, K. P. (2004). In vivo 1H magnetic resonance spectroscopy, T2-weighted and diffusion-weighted MRI during lithium-pilocarpine-induced status epilepticus in the rat. *Brain Res*, *1030*(1), 11-18. https://doi.org/10.1016/j.brainres.2004.09.025

Van Nueten, J. M., Janssens, W. J., & Vanhoutte, P. M. (1985). Serotonin and vascular reactivity. *Pharmacol Res Commun*, *17*(7), 585-608. https://doi.org/10.1016/0031-6989(85)90067-0

Vanzetta, I., & Grinvald, A. (1999). Increased cortical oxidative metabolism due to sensory stimulation: implications for functional brain imaging. *Science*, *286*(5444), 1555-1558. https://doi.org/10.1126/science.286.5444.1555

Verdurand, M., Levigoureux, E., Zeinyeh, W., Berthier, L., Mendjel-Herda, M., Cadarossanesaib, F., Bouillot, C., Iecker, T., Terreux, R., Lancelot, S., Chauveau, F., Billard, T., & Zimmer, L. (2018). In Silico, in Vitro, and in Vivo Evaluation of New Candidates for alpha-Synuclein PET Imaging. *Mol Pharm*, *15*(8), 3153-3166. https://doi.org/10.1021/acs.molpharmaceut.8b00229

Villien, M. (2015). Simultaneous functional imaging using fPET and fMRI. *EJNMMI Physics*, *2*(1), A66. https://doi.org/10.1186/2197-7364-2-S1-A66

Vlassenko, A. G., Rundle, M. M., & Mintun, M. A. (2006). Human brain glucose metabolism may evolve during activation: findings from a modified FDG PET paradigm. *Neuroimage*, *33*(4), 1036-1041. https://doi.org/10.1016/j.neuroimage.2006.06.065

Vo, T. T., Im, G. H., Han, K., Suh, M., Drew, P. J., & Kim, S. G. (2023). Parvalbumin interneuron activity drives fast inhibition-induced vasoconstriction followed by slow substance P-mediated vasodilation. *Proc Natl Acad Sci U S A*, *120*(18), e2220777120. https://doi.org/10.1073/pnas.2220777120

Volkova, K. D., Kovalska, V. B., Balanda, A. O., Losytskyy, M. Y., Golub, A. G., Vermeij, R. J., Subramaniam, V., Tolmachev, O. I., & Yarmoluk, S. M. (2008). Specific fluorescent detection of fibrillar alpha-synuclein using mono- and trimethine cyanine dyes. *Bioorg Med Chem*, *16*(3), 1452-1459. https://doi.org/10.1016/j.bmc.2007.10.051

Wagner, J., Krauss, S., Shi, S., Ryazanov, S., Steffen, J., Miklitz, C., Leonov, A., Kleinknecht, A., Göricke, B., Weishaupt, J. H., Weckbecker, D., Reiner, A. M., Zinth, W., Levin, J., Ehninger, D., Remy, S., Kretzschmar, H. A., Griesinger, C., Giese, A., & Fuhrmann, M. (2015). Reducing tau aggregates with anle138b delays disease progression in a mouse model of tauopathies. *Acta Neuropathologica*, *130*(5), 619-631. https://doi.org/10.1007/s00401-015-1483-3

Wagner, J., Ryazanov, S., Leonov, A., Levin, J., Shi, S., Schmidt, F., Prix, C., Pan-Montojo, F., Bertsch, U., Mitteregger-Kretzschmar, G., Geissen, M., Eiden, M., Leidel, F., Hirschberger, T., Deeg, A. A., Krauth, J. J., Zinth, W., Tavan, P., Pilger, J.,…Giese, A. (2013). Anle138b: a novel oligomer modulator for disease-modifying therapy of neurodegenerative diseases such as prion and Parkinson's disease. *Acta Neuropathol*, *125*(6), 795-813. https://doi.org/10.1007/s00401-013-1114-9

Walter, S. A., Forsgren, M., Lundengård, K., Simon, R., Torkildsen Nilsson, M., Söderfeldt, B., Lundberg, P., & Engström, M. (2016). Positive Allosteric Modulator of GABA Lowers BOLD Responses in the Cingulate Cortex. *PLoS One*, *11*(3), e0148737. https://doi.org/10.1371/journal.pone.0148737

Wang, S., Kugelman, T., Buch, A., Herman, M., Han, Y., Karakatsani, M. E., Hussaini, S. A., Duff, K., & Konofagou, E. E. (2017). Non-invasive, Focused Ultrasound-Facilitated Gene Delivery for Optogenetics. *Sci Rep*, *7*, 39955. https://doi.org/10.1038/srep39955

Wang, S., Olumolade, O. O., Sun, T., Samiotaki, G., & Konofagou, E. E. (2015). Noninvasive, neuron-specific gene therapy can be facilitated by focused ultrasound and recombinant adeno-associated virus. *Gene Ther*, *22*(1), 104-110. https://doi.org/10.1038/gt.2014.91

Watanabe, H., Ariyoshi, T., Ozaki, A., Ihara, M., Ono, M., & Saji, H. (2017). Synthesis and biological evaluation of novel radioiodinated benzimidazole derivatives for imaging alpha-synuclein aggregates. *Bioorg Med Chem*, *25*(24), 6398-6403. https://doi.org/10.1016/j.bmc.2017.10.010

Wehrl, H. F., Hossain, M., Lankes, K., Liu, C. C., Bezrukov, I., Martirosian, P., Schick, F., Reischl, G., & Pichler, B. J. (2013). Simultaneous PET-MRI reveals brain function in activated and resting state on metabolic, hemodynamic and multiple temporal scales. *Nat Med*, *19*(9), 1184-1189. https://doi.org/10.1038/nm.3290

Wood, H. (2014). 18F-DTBZ PET tracks dopaminergic degeneration in patients with Parkinson disease. *Nature Reviews Neurology*, *10*(6), 305-305. https://doi.org/10.1038/nrneurol.2014.81

Woolsey, T. A., Rovainen, C. M., Cox, S. B., Henegar, M. H., Liang, G. E., Liu, D., Moskalenko, Y. E., Sui, J., & Wei, L. (1996). Neuronal units linked to microvascular modules in cerebral cortex: response elements for imaging the brain. *Cereb Cortex*, *6*(5), 647-660. https://doi.org/10.1093/cercor/6.5.647

Xiang, J., Tao, Y., Xia, Y., Luo, S., Zhao, Q., Li, B., Zhang, X., Sun, Y., Xia, W., Zhang, M., Kang, S. S., Ahn, E. H., Liu, X., Xie, F., Guan, Y., Yang, J. J., Bu, L., Wu, S., Wang, X.,…Ye, K. (2023). Development of an α-synuclein positron emission tomography tracer for imaging synucleinopathies. *Cell*, *186*(16), 3350-3367.e3319. https://doi.org/10.1016/j.cell.2023.06.004

Xiang, X., Wind, K., Wiedemann, T., Blume, T., Shi, Y., Briel, N., Beyer, L., Biechele, G., Eckenweber, F., Zatcepin, A., Lammich, S., Ribicic, S., Tahirovic, S., Willem, M., Deussing, M., Palleis, C., Rauchmann, B. S., Gildehaus, F. J., Lindner, S.,…Brendel, M. (2021). Microglial activation states drive glucose uptake and FDG-PET alterations in neurodegenerative diseases. *Sci Transl Med*, *13*(615), eabe5640. https://doi.org/10.1126/scitranslmed.abe5640

Yang, W., & Yu, S. (2017). Synucleinopathies: common features and hippocampal manifestations. *Cell Mol Life Sci*, *74*(8), 1485-1501. https://doi.org/10.1007/s00018-016-2411-y

Yang, Y., Garringer, H. J., Shi, Y., Lövestam, S., Peak-Chew, S., Zhang, X., Kotecha, A., Bacioglu, M., Koto, A., Takao, M., Spillantini, M. G., Ghetti, B., Vidal, R., Murzin, A. G., Scheres, S. H. W., & Goedert, M. (2023). New SNCA mutation and structures of α-synuclein filaments from juvenile-onset synucleinopathy. *Acta Neuropathol*, *145*(5), 561-572. https://doi.org/10.1007/s00401-023-02550-8

Yang, Y., Shi, Y., Schweighauser, M., Zhang, X., Kotecha, A., Murzin, A. G., Garringer, H. J., Cullinane, P. W., Saito, Y., Foroud, T., Warner, T. T., Hasegawa, K., Vidal, R., Murayama, S., Revesz, T., Ghetti, B., Hasegawa, M., Lashley, T., Scheres, S. H. W., & Goedert, M. (2022). Structures of α-synuclein filaments from human brains with Lewy pathology. *Nature*, *610*(7933), 791-795. https://doi.org/10.1038/s41586-022-05319-3

Yapo, C., Nair, A. G., Clement, L., Castro, L. R., Hellgren Kotaleski, J., & Vincent, P. (2017). Detection of phasic dopamine by D1 and D2 striatal medium spiny neurons. *J Physiol*, *595*(24), 7451-7475. https://doi.org/10.1113/jp274475

Yu, L., Cui, J., Padakanti, P. K., Engel, L., Bagchi, D. P., Kotzbauer, P. T., & Tu, Z. (2012). Synthesis and in vitro evaluation of α-synuclein ligands. *Bioorganic and Medicinal Chemistry*, *20*, 4625-4634. https://doi.org/10.1016/j.bmc.2012.06.023

Yu, X., Glen, D., Wang, S., Dodd, S., Hirano, Y., Saad, Z., Reynolds, R., Silva, A. C., & Koretsky, A. P. (2012). Direct imaging of macrovascular and microvascular contributions to BOLD fMRI in layers IV-V of the rat whisker-barrel cortex. *NeuroImage*, *59*(2), 1451-1460. https://doi.org/10.1016/j.neuroimage.2011.08.001

Yue, X., Dhavale, D. D., Li, J., Luo, Z., Liu, J., Yang, H., Mach, R. H., Kotzbauer, P. T., & Tu, Z. (2018). Design, synthesis, and in vitro evaluation of quinolinyl analogues for α-synuclein aggregation. *Bioorg Med Chem Lett*, *28*(6), 1011-1019. https://doi.org/10.1016/j.bmcl.2018.02.031

Zaldivar, D., Rauch, A., Whittingstall, K., Logothetis, Nikos K., & Goense, J. (2014). Dopamine-Induced Dissociation of BOLD and Neural Activity in Macaque Visual Cortex. *Current Biology*, *24*(23), 2805-2811. https://doi.org/10.1016/j.cub.2014.10.006

Zhang, J., Li, X., & Li, J. D. (2019). The Roles of Post-translational Modifications on α-Synuclein in the Pathogenesis of Parkinson's Diseases. *Front Neurosci*, *13*, 381. https://doi.org/10.3389/fnins.2019.00381

Zhang, L., Villalobos, A., Beck, E. M., Bocan, T., Chappie, T. A., Chen, L., Grimwood, S., Heck, S. D., Helal, C. J., Hou, X., Humphrey, J. M., Lu, J., Skaddan, M. B., McCarthy, T. J., Verhoest, P. R., Wager, T. T., & Zasadny, K. (2013). Design and selection parameters to accelerate the discovery of novel central nervous system positron emission tomography (PET) ligands and their application in the development of a novel phosphodiesterase 2A PET ligand. *J Med Chem*, *56*(11), 4568-4579. https://doi.org/10.1021/jm400312y

Zhang, X., Jin, H., Padakanti, P. K., Li, J., Yang, H., Fan, J., Mach, R. H., Kotzbauer, P., & Tu, Z. (2014). Radiosynthesis and in Vivo Evaluation of Two PET Radioligands for Imaging alpha-Synuclein. *Appl Sci (Basel)*, *4*(1), 66-78. https://doi.org/10.3390/app4010066

Zhao, F., Zhao, T., Zhou, L., Wu, Q., & Hu, X. (2008). BOLD study of stimulation-induced neural activity and resting-state connectivity in medetomidine-sedated rat. *Neuroimage*, *39*(1), 248-260. https://doi.org/10.1016/j.neuroimage.2007.07.063

Zheng, W., Ge, Y., Ren, S., Ran, W., Zhang, X., Tian, W., Chen, Z., Dou, W., & Wang, Z. (2020). Abnormal static and dynamic functional connectivity of resting-state fMRI in multiple system atrophy. *Aging (Albany NY)*, *12*(16), 16341-16356. https://doi.org/10.18632/aging.103676

Zimmer, E. R., Parent, M. J., Souza, D. G., Leuzy, A., Lecrux, C., Kim, H. I., Gauthier, S., Pellerin, L., Hamel, E., & Rosa-Neto, P. (2017). [(18)F]FDG PET signal is driven by astroglial glutamate transport. *Nat Neurosci*, *20*(3), 393-395. https://doi.org/10.1038/nn.4492

Attachments

a) Accepted publications included in the dissertation

European Journal of Nuclear Medicine and Molecular Imaging (2021) 48:1759–1772
https://doi.org/10.1007/s00259-020-05133-x

ORIGINAL ARTICLE

[^{11}C]MODAG-001—towards a PET tracer targeting α-synuclein aggregates

Laura Kuebler[1] · Sabrina Buss[1] · Andrei Leonov[2,3] · Sergey Ryazanov[2,3] · Felix Schmidt[2] · Andreas Maurer[1] · Daniel Weckbecker[2] · Anne M. Landau[4,5] · Thea P. Lillethorup[5] · Daniel Bleher[1] · Ran Sing Saw[1] · Bernd J. Pichler[1] · Christian Griesinger[3,6] · Armin Giese[2] · Kristina Herfert[1]

Received: 9 July 2020 / Revised: 25 September 2020 / Accepted: 20 October 2020 / Published online: 28 December 2020

Abstract

Purpose Deposition of misfolded alpha-synuclein (αSYN) aggregates in the human brain is one of the major hallmarks of synucleinopathies. However, a target-specific tracer to detect pathological aggregates of αSYN remains lacking. Here, we report the development of a positron emission tomography (PET) tracer based on anle138b, a compound shown to have therapeutic activity in animal models of neurodegenerative diseases.

Methods Specificity and selectivity of [^{3}H]MODAG-001 were tested in in vitro binding assays using recombinant fibrils. After carbon-11 radiolabeling, the pharmacokinetic and metabolic profile was determined in mice. Specific binding was quantified in rats, inoculated with αSYN fibrils and using in vitro autoradiography in human brain sections of Lewy body dementia (LBD) cases provided by the Neurobiobank Munich (NBM).

Results [^{3}H]MODAG-001 revealed a very high affinity towards pure αSYN fibrils ($K_d = 0.6 \pm 0.1$ nM) and only a moderate affinity to hTau46 fibrils ($K_d = 19 \pm 6.4$ nM) as well as amyloid-β_{1-42} fibrils ($K_d = 20 \pm 10$ nM). [^{11}C]MODAG-001 showed an excellent ability to penetrate the mouse brain. Metabolic degradation was present, but the stability of the parent compound improved after selective deuteration of the precursor. (d_3)-[^{11}C]MODAG-001 binding was confirmed in fibril-inoculated rat striata using in vivo PET imaging. In vitro autoradiography showed no detectable binding to aggregated αSYN in human brain sections of LBD cases, most likely, because of the low abundance of aggregated αSYN against background protein.

Conclusion MODAG-001 provides a promising lead structure for future compound development as it combines a high affinity and good selectivity in fibril-binding assays with suitable pharmacokinetics and biodistribution properties.

Keywords Alpha-synuclein · Parkinson's disease · PET imaging · Tracer development

Laura Kuebler, Sabrina Buss, Andrei Leonov, Sergey Ryazanov and Felix Schmidt contributed equally to this work.

This article is part of the Topical Collection on Preclinical Imaging

✉ Christian Griesinger
cigr@nmr.mpibpc.mpg.de

✉ Armin Giese
giese@modag.net

✉ Kristina Herfert
kristina.herfert@med.uni-tuebingen.de

[1] Werner Siemens Imaging Center, Department of Preclinical Imaging and Radiopharmacy, Eberhard Karls University of Tübingen, Röntgenweg 13, 72076 Tübingen, Germany

[2] MODAG GmbH, Mikroforum Ring 3, 55234 Wendelsheim, Germany

[3] Department of NMR-based Structural Biology, Max Planck Institute for Biophysical Chemistry, Am Faßberg 11, 37077 Göttingen, Germany

[4] Translational Neuropsychiatry Unit, Aarhus University, Norrebrogade 44, 8000 Aarhus, Denmark

[5] Department of Nuclear Medicine and PET-Centre, Aarhus University, Palle Juul-Jensens 165, J109, 8200 Aarhus, Denmark

[6] University Göttingen, Cluster of Excellence Multiscale Bioimaging Molecular Machines, 37077 Göttingen, Germany

Introduction

The molecular pathogenesis of all common neurodegenerative diseases is associated with the disease-specific aggregation of misfolded proteins. Aggregation of α-synuclein (αSYN) has been shown to play a crucial role in the pathogenesis of Parkinson's disease (PD) [1], Lewy body dementia (LBD), and multiple system atrophy (MSA) [2, 3]. In PD and LBD [4, 5], αSYN-containing inclusions accumulate in Lewy bodies (LBs) [6] and Lewy neurites (LNs).

Noninvasive imaging technologies such as magnetic resonance imaging (MRI) and positron emission tomography (PET) could serve as a valuable tool for the early and differential diagnosis of neurodegenerative diseases. Furthermore, they would allow for the monitoring of disease progression as well as evaluation of disease-modifying therapies. Whereas PET imaging of amyloid-β (Aβ) in Alzheimer's disease (AD) is well established [7–9], PET tracers to detect pathologically aggregated αSYN in synucleinopathies are still missing despite intensive research.

Challenges complicating their identification might be (i) the target structure, as pathological αSYN might be present mainly in an oligomeric form rather than as fibrillar structures; (ii) the target concentration, as the amount of aggregated protein in condensed fibrillar αSYN aggregates (LBs, LNs) are by far less abundant than, for example, Aβ plaques; (iii) the target localization, as pathological αSYN is located intracellularly, making the cell membrane an additional physical barrier for tracer accessibility; (iv) the target composition, as β-sheet-binding motifs might be shared between different pathological protein aggregates, therefore complicating differential diagnosis or leading to unselective binding in the case of common co-pathologies; (v) the highly complex LB and LN composition comprising lipid membrane fragments and distorted organelles as recently shown by [10], which may hamper binding to αSYN fibrils; and (vi) the tracer structure, as lipophilic compounds that efficiently cross the blood-brain barrier (BBB) might show high nonspecific binding, reducing the signal-to-noise ratio (SNR) [11–13].

Here, we aimed to develop a PET tracer starting from the lead structure anle138b (Fig. 1a), a compound that has been shown to have therapeutic activity in animal models of PD [15, 16] and MSA [17] based on specific structure-dependent binding to aggregated αSYN [18]. A previous derivative of anle138b, anle253b (Fig. 1b), was suited for ^{11}C-labeling and showed high affinity towards αSYN aggregates in vitro; however, it showed suboptimal pharmacokinetics in vivo [14]. Therefore, we further modified the chemical structure of anle253b by exchanging the bromophenyl moiety with bromopyridine to reduce lipophilicity and improve the pharmacokinetic properties while keeping or even improving binding affinity (Fig. 1c). The resulting compound—MODAG-001—was evaluated in the current study using in vitro binding experiments on recombinant fibrils; autoradiography (AR) of human brain tissue with confirmed αSYN, Tau, and Aβ pathology [19]; pharmacokinetic analysis in vivo using mice; and the detection of stereotactically inoculated αSYN aggregates in vivo in a rat model.

Material and methods

Precursor and standard synthesis of MODAG-001 and (d_3)-MODAG-001

The synthesis of MODAG-001, (d_3)-MODAG-001, and the respective precursors for radiosynthesis is described in the supplementary material and methods section. The chemical structures are shown in Supplemental Fig. S1.

MODAG-001 tritiation

MODAG-001 (Fig. 1c) was tritiated (RC Tritec AG, Teufen Switzerland), dissolved in ethanol and stored at − 80 °C until further usage. Its molar activity (A_m) was 2.6 GBq/μmol, and its radiochemical purity was > 99% determined by high-performance liquid chromatography (HPLC).

Fibril-binding experiments

Preparation and characterization of recombinant αSYN, hTau46, and $Aβ_{1–42}$ fibrils are described in the supplementary material and methods section.

For saturation binding assays, the optimal fibril concentrations were determined according to Auld et al. [20] using a concentration determination assay (see supplementary material and methods section). Sonicated human recombinant αSYN (15 nM), hTau46 (250 nM), and $Aβ_{1–42}$ (1 μM) fibrils diluted in phosphate-buffered saline (PBS) were incubated in low-binding plates (96-well micro test plate, Ratiolab GmbH, Dreieich, Germany) with [^{3}H]MODAG-001 at increasing concentrations (0.05–12 nM/24 nM) in 30 mM Tris-HCl, 10% ethanol, 0.05% Tween20, pH 7.4 in a total volume of 200 μL/well. Nonspecific binding of the radiotracer was determined by coincubation with 400 nM nonlabeled MODAG-001 dissolved in DMSO (final DMSO concentration 0.04%). To determine the potential binding site of MODAG-001, a competition binding assay using SIL26 previously evaluated by Bagchi et al. [24] was performed. Recombinant αSYN fibrils (sonicated, 15 nM/) were incubated with 1 nM [^{3}H]MODAG-001 and decreasing concentrations of a 1:4 serial dilution of nonlabeled SIL26 (4 μM-0.06 nM) in 30 mM Tris-HCl, 10% ethanol, 0.05% Tween20, pH 7.4 in a total volume of 200 μL/well.

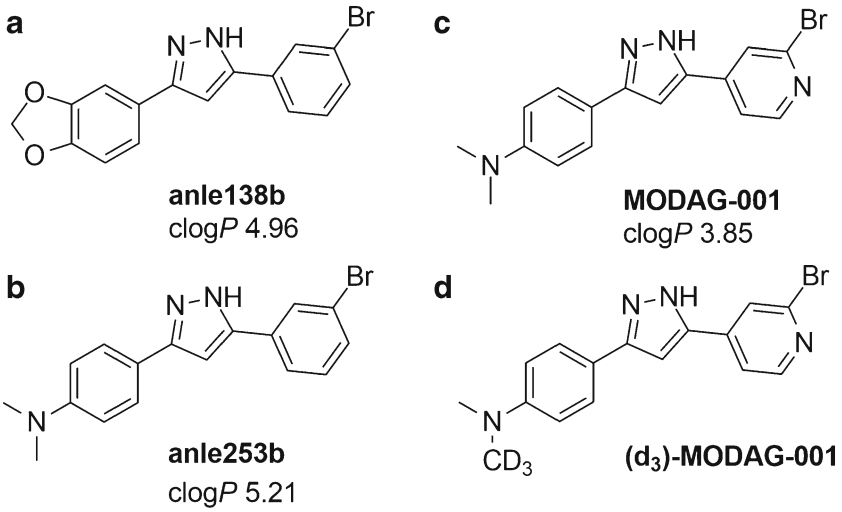

Fig. 1 Chemical structures and calculated log*P* values (clog*P*) of anle138b (**a**), anle253b (**b**) MODAG-001 (**c**), and (d_3)-MODAG-001 (**d**) [14]

Filtration and readout of competition and saturation binding experiments were performed as described in the supplementary material and methods section.

Sensitivity analysis in mouse brain homogenates

To determine the limit of detection of [^{3}H]MODAG-001 for αSYN fibrils in brain homogenates, one C57BL/6 mouse was sacrificed with CO_2, and its brain was surgically removed. PBS containing one tablet each of phosphatase inhibitors (PhosSTOP™ phosphatase inhibitor tablets, Hoffmann-La Roche, Basel, Switzerland) and proteinase inhibitors (cOmplete™ protease inhibitor cocktail, Hoffmann-La Roche) per 5 mL was added to the brain to reach a protein concentration of approximately 200 mg/mL. The brain was sequentially homogenized using large and small clearance pestles (approximately ten strokes per pestle), contained in a tissue grinder set (2 mL, DWK Life Sciences Inc., Kimble Chase, Vineland, NJ, USA), and the homogenate was stored at − 80 °C until further use. The protein concentration was determined using a BCA kit (Micro BCA™ Protein Assay Kit, Thermo Fisher Scientific). Saturation assays were performed as described above. Homogenates were diluted in PBS to reach final protein concentrations of 0.5 mg/mL, 0.1 mg/mL, and 0.05 mg/mL, and fibrils were added to reach concentrations of 125 nM, 25 nM, and 5 nM.

Radiosynthesis of [^{11}C]MODAG-001 and (d_3)-[^{11}C]MODAG-001

Radiolabeling was performed in a manner analogous to [^{11}C]anle253b radiolabeling [14]. For a detailed description, see supplementary material and methods section.

Animals

All animal experiments were conducted in compliance with the European directives on the protection and use of laboratory animals (Council Directive 2010/63/UE) and in addition with the German animal protection law and with the approval of the local authorities (*Regierungspräsidium Tübingen*). Twenty-two female C57BL/6 mice (25 ± 6 g) and four female Sprague-Dawley rats (278 ± 25 g) were obtained from Charles River Laboratories (Sulzfeld, Germany). All animals were maintained in our vivarium on a 12:12 h light-dark cycle at a temperature of 22 °C with 40–60% humidity and given free access to a standard diet and tap water.

In vivo PET imaging and metabolite analysis

PET imaging was performed on a dedicated small animal Inveon PET scanner (Siemens Healthcare, Knoxville (TN), USA). Mice and rats were anesthetized with 1.5–1.7% isoflurane evaporated in 100% oxygen at a flow rate of 0.8 L/min, which was maintained during the entire experiment. After a tail vein catheter was placed, the animal was positioned in the center of the field of view (FOV) on an MR-compatible PET bed that was connected to a feedback temperature control unit set to 37 °C. Mice were injected intravenously (i.v.) with 17 ± 2 MBq [^{11}C]MODAG-001 (n = 3) or 12 ± 1 MBq (d_3)-[^{11}C]MODAG-001 (n = 5) 5 s after the start of the PET acquisition.

Rats were inoculated with αSYN fibrils (4 μL, 30 μM) into the right striatum (see supplementary material and methods section for a detailed description) and scanned 4 days post-inoculation with 23 ± 1 MBq of (d_3)-[^{11}C]MODAG-001.

Data acquisition, correction, framing and reconstruction, volume of interest (VOI) definition, and determination of

binding parameters are described in detail in the supplementary material and methods section.

For metabolite analysis, mice were i.v. injected with 91 ± 24 MBq of [^{11}C]MODAG-001 ($n = 4$ per time point) or 120 ± 41 MBq of (d_3)-[^{11}C]MODAG-001 ($n = 3$ per time point) using a tail vein catheter. Five and 15 min after injection, plasma and brain homogenates were analyzed using radio-HPLC (for detailed information see supplemental material and methods section).

In vitro autoradiography in human brain tissue sections and continuous sucrose gradient centrifugation of human PD brain homogenates

Fresh-frozen 20 μm slices of the cortices from one AD case (Braak & Braak 5-6, CERAD C), two LBD cases (with pronounced αSYN and no to low Aβ and Tau pathology), one progressive supranuclear palsy (PSP) case, and one control case were kindly provided by Neurobiobank Munich [19], and stored at − 80 °C. PD brain tissue for preparation of homogenates was kindly provided by NBM [19]. Autoradiography, preparation of PD brain homogenates, and their analysis by continuous sucrose gradient centrifugation experiments are described in the supplementary material and methods section.

Results

Fibril characterization and in vitro binding assays

Quality control of in vitro-formed fibrils using negative stain electron microscopy (EM) (Fig. 2a–f and Supplemental Fig. S2) confirmed the presence of typical amyloid fibrils. In saturation binding assays, [^{3}H]MODAG-001 showed a very high affinity towards αSYN fibrils ($K_d = 0.6 \pm 0.1$ nM) with low nonspecific binding (Fig. 2g). Compared to the affinity towards αSYN fibrils, a 30-fold lower affinity was observed towards hTau46 fibrils ($K_d = 19 \pm 6.4$ nM) (Fig. 2h) and $A\beta_{1–42}$ fibrils ($K_d = 20 \pm 10$ nM) (Fig. 2i). Of note, also B_{max} was almost 7 and 50-fold higher for αSYN fibrils than for hTau46 fibrils and $A\beta_{1–42}$ fibrils, respectively.

To further characterize the potential binding site of [^{3}H]MODAG-001, a competition assay with SIL26 was performed. SIL26 displaced [^{3}H]MODAG-001 binding in a dose-dependent manner with a K_i of 21 nM, indicating lower affinity for SIL26 than for MODAG-001 (see Supplemental Fig. S3).

Determination of the limit of detection in brain homogenates

To determine the limit of detection of αSYN fibrils by [^{3}H]MODAG-001 in brain tissue homogenates, a saturation binding assay was performed in mouse brain homogenates spiked with αSYN fibrils at different concentrations (Fig. 3). Separation of the total binding (TB) and nonspecific binding (NSB) curves to calculate specific binding (SB) in the presence of 100 μg protein/mL mouse brain homogenate was possible at αSYN concentrations down to 5 nM (limit of detection). At a 5-fold higher homogenate concentration of 500 μg protein/mL, SB was undetectable, as the SB curve was superposed by the NSB curve, but SB was detectable when the fibril concentration was increased to 25 nM.

Using sucrose gradient centrifugation to determine the amount of aggregated αSYN in a human PD brain homogenate, we observed an αSYN aggregate concentration of approximately 4 nM and 830 μg protein/mL in a 1% homogenate, which is slightly below the limit of detection by [^{3}H]MODAG-001 (Supplemental Fig. S5).

^{11}C-labeling of MODAG-001 and optimization of the molar activity for in vivo applications

MODAG-001 was readily radiolabeled by reductive methylation using in situ-generated formaldehyde with a radiochemical yield of 11.4 ± 3.7% ($n = 18$, decay-corrected from [^{11}C]MeI) (Fig. 4). These preparations were suitable for the first in vivo studies (similar to anle253b [14]), but the A_m was low (31.3 ± 6.4 GBq/μmol), prompting us to switch to direct methylation for subsequent experiments. Here, we achieved a A_m of 98.6 ± 24.7 GBq/μmol but a radiochemical yield of only 3.6 ± 1.1% (final product: 266 ± 113 MBq instead of 1003 ± 247 MBq), a yield sufficient for our animal studies.

Pharmacokinetic and metabolic profile of [^{11}C]MODAG-001 in mice

Figure 5 shows whole-body sagittal [^{11}C]MODAG-001 PET/MR images and time activity curves (TACs) of selected organs from one exemplary animal at different time points after i.v. injection, which resulted in rapid brain uptake with an SUV of 1.4 (radioactivity normalized to injected dose and body weight) with only small regional differences across multiple brain regions and fast washout from the brain (Fig. 5a–c).

Radio-metabolite formation of [^{11}C]MODAG-001 in the mouse brain and plasma was determined 5 min and 15 min after tracer injection (Fig. 5d). A full quantitative analysis of two exemplary mice revealed two metabolites in the mouse brain and three metabolites in the plasma with 91% and 81% of the parent compound present in the brain at 5 min and 15 min after injection, respectively. Quantitative values determined by brain and plasma analyses are summarized in Table 1.

As we hypothesize that the NMe_2 group is the major target of metabolism for [^{11}C]MODAG-001, we deuterated [^{11}C]MODAG-001, as previous studies have shown the utility of this method by enhancing the in vivo stability of

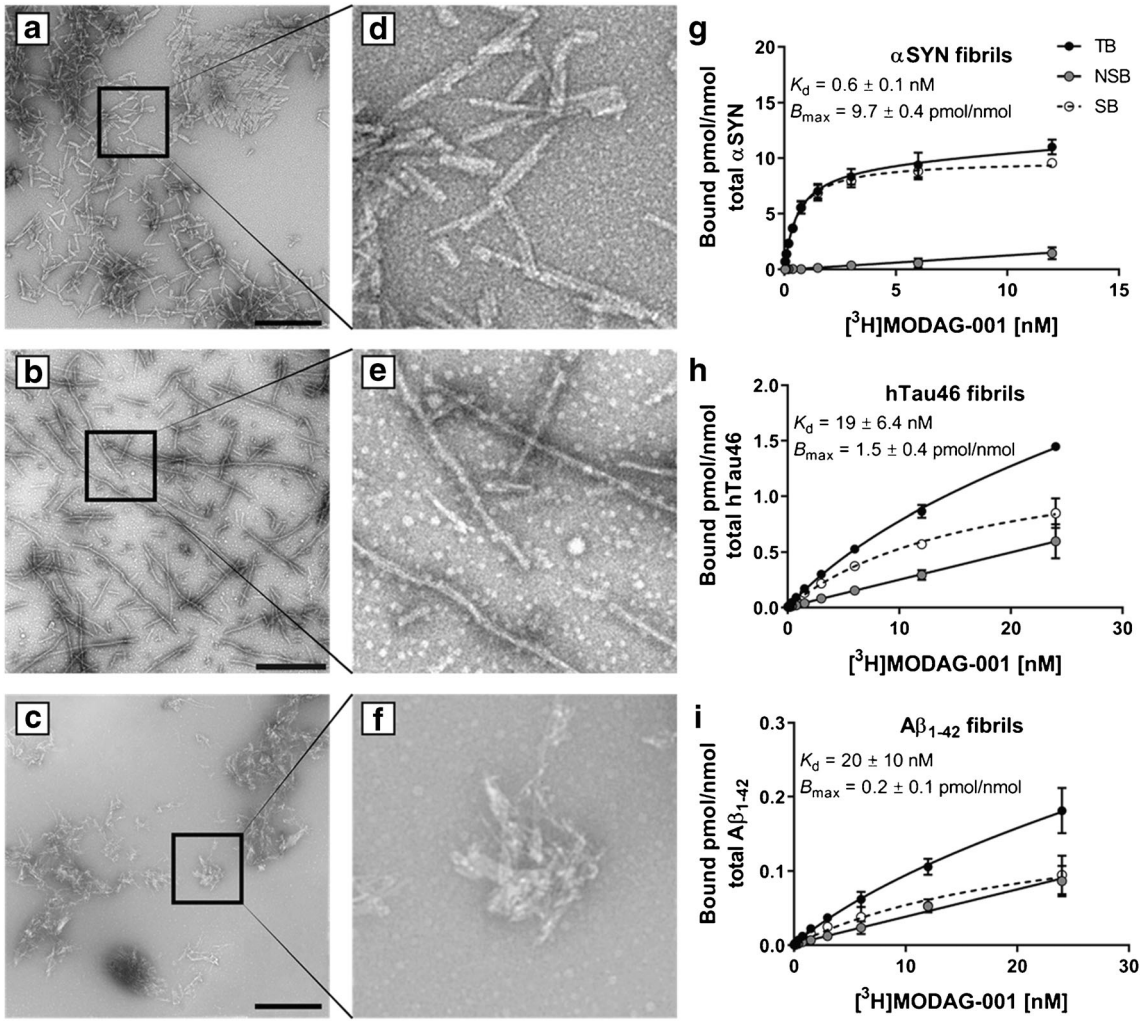

Fig. 2 [^{3}H]MODAG-001 binding experiments using recombinant human fibrils. Negative stain electron microscopy images and 4.7-fold magnification of α-synuclein (**a**, **d**), hTau46 (**b**, **e**), and amyloid-$\beta_{1–42}$ (**c**, **f**) fibrils used in the binding experiments. Total and nonspecific binding curves of [^{3}H]MODAG-001 to α-synuclein (**g**), hTau46 (**h**), and amyloid-$\beta_{1–42}$ (**i**) fibrils. Scale bar 500 nm. TB, total binding; NSB, nonspecific binding; SB, specific binding; αSYN, α-synuclein; $A\beta_{1–42}$, amyloid-$\beta_{1–42}$

compounds and drugs injected into animals as well as humans [22]. Therefore, a deuterium-substituted analog of [^{11}C]MODAG-001 was designed by full deuteration of the nonradioactive methyl group (Fig. 1d).

Pharmacokinetic and metabolic profile of (d_3)-[^{11}C]MODAG-001 in mice

After the successful synthesis of (d_3)-[^{11}C]MODAG-001, dynamic whole-body PET scans were performed in mice. Figure 6 a–c shows sagittal whole-body PET/MR images and TACs of selected organs from one exemplary mouse at different time points after systemic administration of (d_3)-[^{11}C]MODAG-001, which resulted in rapid brain uptake with an SUV of 1.7 (radioactivity normalized to injected dose and body weight) with only small regional differences across multiple brain regions.

Chromatograms showed similar results of all metabolite experiments (Fig. 6d). Quantitative analysis of two exemplary mice revealed two radio-metabolites in the brain and three radio-metabolites in the plasma at 5 and 15 min after tracer injection, with 93% and 87% of the parent compound present in the brain at 5 and 15 min after injection, respectively. Quantitative values determined by brain and plasma analyses are summarized in Table 2.

Binding of (d_3)-[^{11}C]MODAG-001 to αSYN in a fibril-inoculated rat brain

Figure 7 a shows coregistered PET/MR images of three fibril-inoculated rats and one non-injected rat. Thioflavin S staining

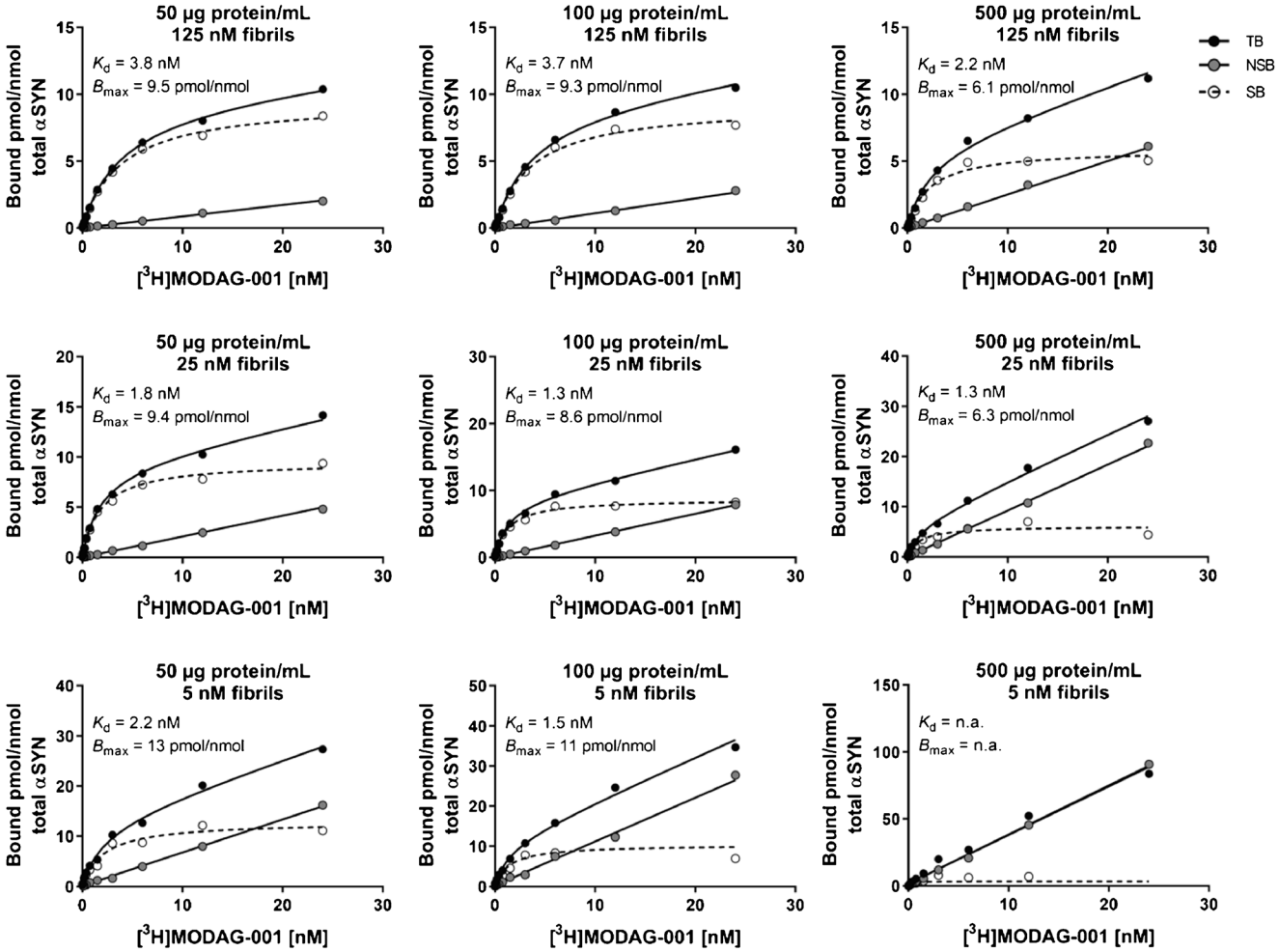

Fig. 3 [^{3}H]MODAG-001 sensitivity analysis. Determination of total binding and nonspecific binding of [^{3}H]MODAG-001 in mouse brain homogenates spiked with recombinant α-synuclein (αSYN) fibrils. Increasing homogenate protein concentrations (left to right) were inoculated with decreasing fibril concentrations (top to bottom). At smallest concentrations of 5 nM fibrils, total binding and nonspecific curves were still separated to calculate specific binding at a homogenate concentration of 100 µg/mL, but indistinguishable at a protein concentration of 500 µg/mL. A 5-fold increase of the αSYN fibril concentration increased the total binding curve, enabling the calculation of specific binding. TB, total binding; NSB, nonspecific binding; SB, specific binding; αSYN, α-synuclein; $A\beta_{1–42}$, amyloid-$\beta_{1–42}$

confirmed the presence of fibrils at the site of inoculation in the right striatum (Fig. 7b). Using a SUV threshold of 0.8 to 1.2 to remove background binding, a better visualization of the tracer binding to the inoculated fibrils was possible from the images (see Supplemental Fig. S4). (d_3)-[^{11}C]MODAG-001 injection resulted in rapid brain uptake, with peak SUV values of 2.1 ± 0.1 in the left striatum of inoculated rats (radioactivity normalized to injected dose and body weight) and

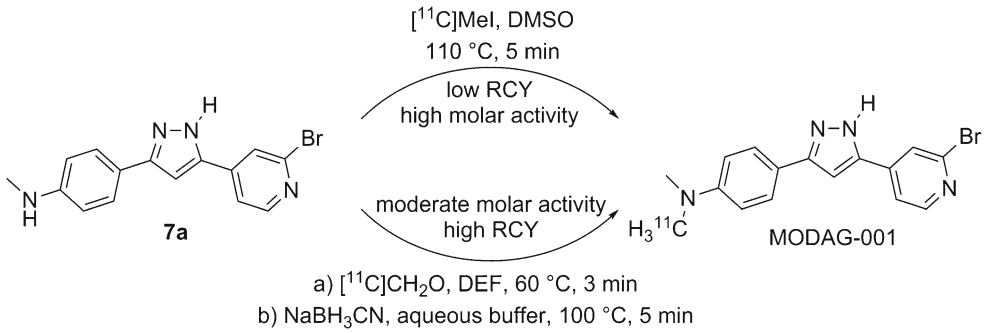

Fig. 4 Radiolabeling of [^{11}C]MODAG-001. Depending on the required molar radioactivity, two different strategies were used. Direct methylation (upper reaction conditions) gave lower radiochemical yields but a high molar radioactivity (266 ± 113 MBq, 98.6 ± 24.7 GBq/µmol) while reductive methylation (lower reaction arrow) gave better yields but lower molar radioactivities (1003 ± 247 MBq, 31.3 ± 6.4 GBq/µmol)

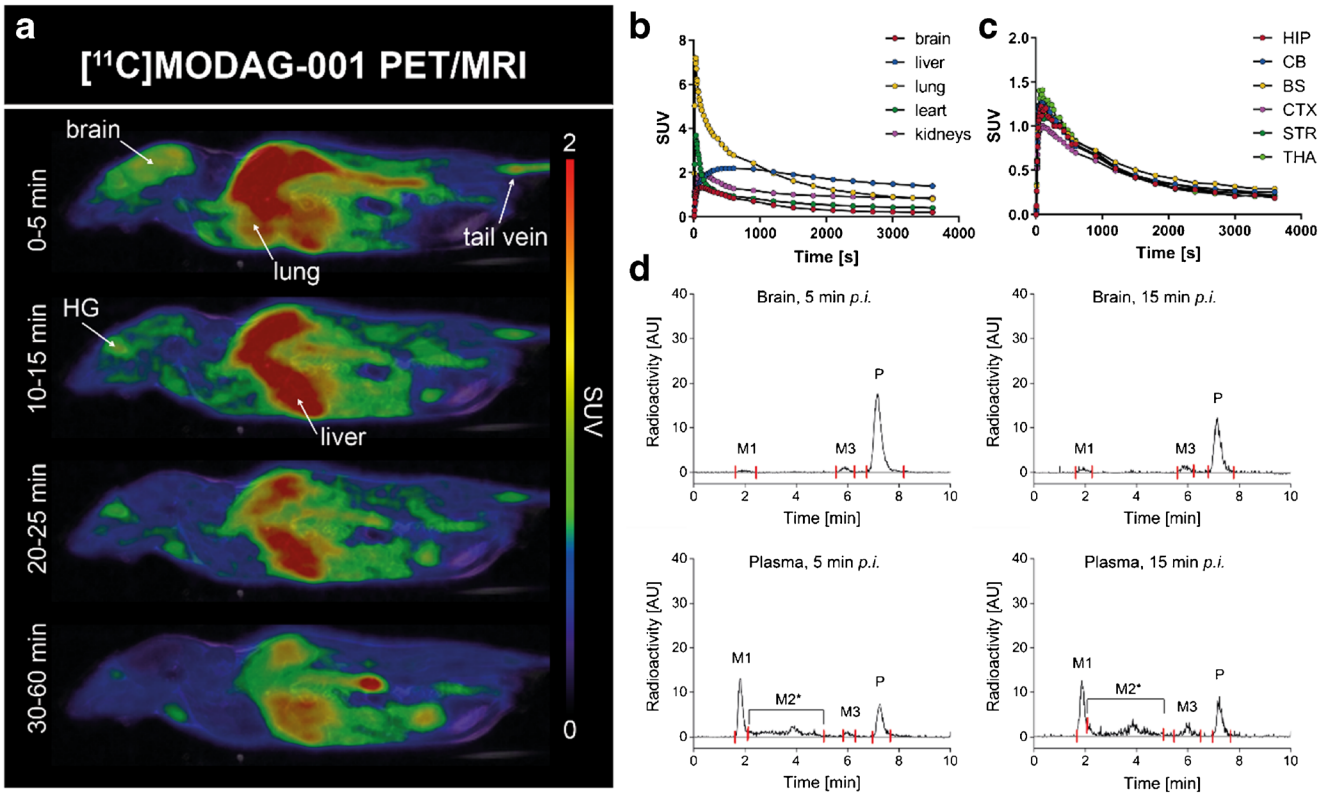

Fig. 5 Pharmacokinetic profile of [^{11}C]MODAG-001 in the mouse. Whole-body PET/MR images of one exemplary mouse at different time points after i.v. injection (**a**) and corresponding time activity curves of different organs and brain regions (**b**, **c**). Images show a good brain uptake with a peak standardized uptake value of 1.4. Metabolite analysis of [^{11}C]MODAG-001 revealed two detectable metabolites M1 and M3 present in the brain (**d**). PET, positron emission tomography; MRI, magnetic resonance imaging; SUV, standardized uptake value; HG, harderian glands; HIP, hippocampus; CB, cerebellum; BS, brainstem; CTX, cortex; STR, striatum; THA, thalamus; AU, arbitrary units; M1, metabolite 1; M2*, mixture of various metabolites; M3, metabolite 3; P, parent compound; *p.i.*, *post iniectio*

2.1 in the non-injected rat, and fast washout from the brain (Fig. 7c–e) with higher tracer retention in the right, fibril-inoculated striatum compared to the contralateral, vehicle-injected striatum. Using a conservative analytical approach with the whole striatum as the reference region, a mean distribution volume ratio (DVR)-$1_{40\text{-}60min}$ of 0.14 ± 0.1 was calculated, while a mean DVR-$1_{40\text{-}60min}$ of 0.44 ± 0.21 was calculated using 70% automatic isocontour detection at the location of fibril accumulation. The mean $SUV_{40\text{-}60min}$ of the right, fibril-inoculated striatum and contralateral, vehicle-injected striatum significantly differed ($p = 0.03$ with the whole striatum as the VOI). The non-injected rat showed no difference in mean $SUV_{40\text{-}60min}$ between the right and left striatum, with brain uptake comparable to that in the inoculated rats. In all rat brains, nonspecific binding was also observed in brain regions without fibrils, reducing the SNR in the inoculated striatum.

Table 1 Quantification of radio-metabolites in plasma and brain samples 5 and 15 min after [^{11}C]MODAG-001 injection

	M1		M2*		M3		P	
	%	%ID	%	%ID	%	%ID	%	%ID
Brain, 5 min	3	0.4*	–	–	6	0.7*	91	10.5*
Brain, 15 min	7	0.4*	–	–	12	0.7*	81	5.3*
Plasma, 5 min	34	1.0#	37	1.1#	3	0.1#	26	0.8#
Plasma, 15 min	29	0.8#	36	1.0#	11	0.3#	24	0.7#

M1, metabolite 1; *M2**, mixture of various metabolites; *M3*, metabolite 3; *P*, parent compound; *%ID*, % injected dose; * per g brain tissue, # per plasma in 1 mL blood

In vitro binding of [^{3}H]MODAG-001 to human brain tissue

Figure 8 a shows [^{3}H]MODAG-001 AR images of the cortex of two LBD cases, one AD case and one PSP case, and one control case. In all cases, [^{3}H]MODAG-001 showed a non-specific blocking effect, which was likely related to the high concentration of MODAG-001 (50 μM) used for blocking. For the AD case, clear binding of [^{3}H]MODAG-001 in the cortex was observed. Binding values for the LBD 1 (80.5 ± 8.7 pmol/mg), LBD 2 (64.4 ± 9.8 pmol/mg), PSP (79.0 ± 13.3 pmol/mg), and AD (167.7 ± 40.0 pmol/mg) cases and

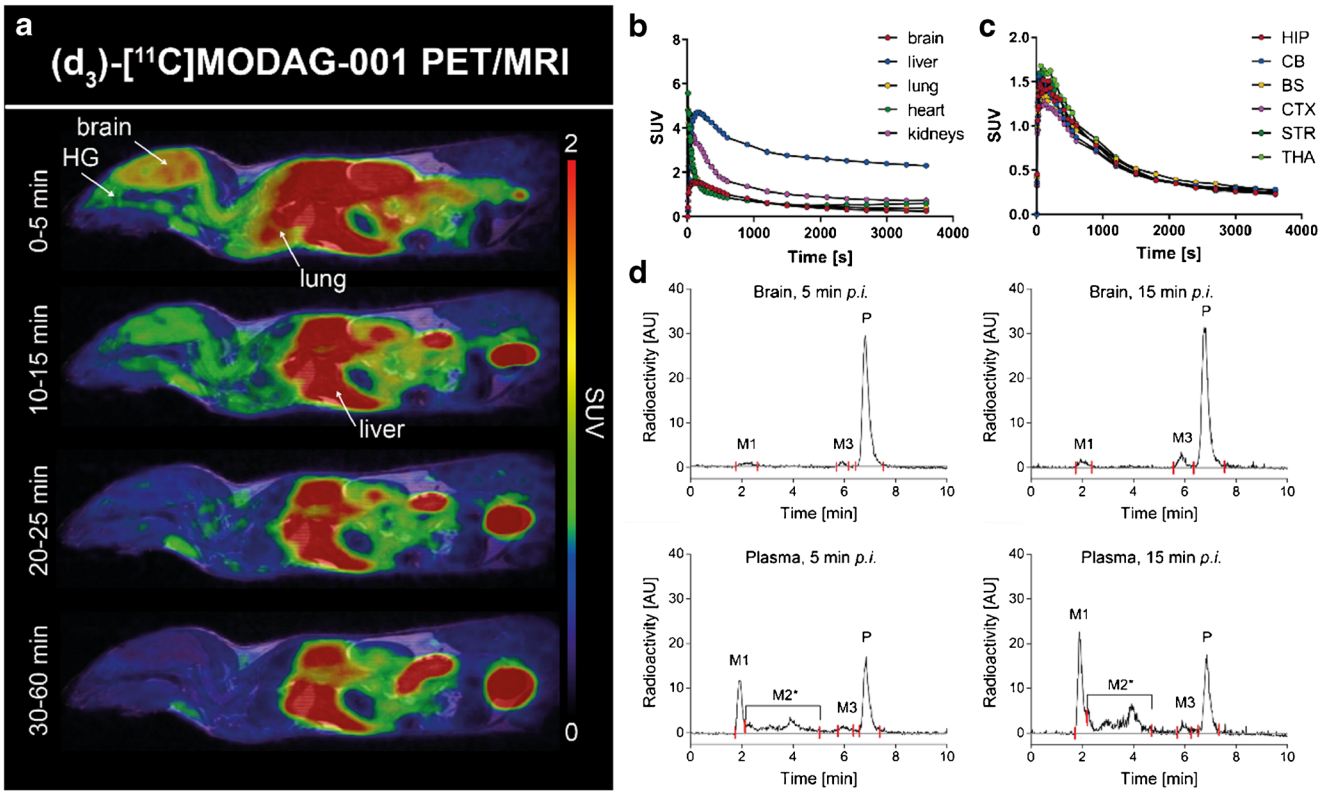

Fig. 6 Pharmacokinetic profile of (d_3)-[^{11}C]MODAG-001 in the mouse. Whole-body tracer accumulation over time is shown (**a**, **b**). (d_3)-[^{11}C]MODAG-001 rapidly entered the brain with peak standardized uptake values of 1.7 (**c**) followed by a fast washout. HPLC chromatograms of (d_3)-[^{11}C]MODAG-001 in plasma and brain homogenates revealed two detectable metabolites M1 and M3 present in the brain (**d**). HPLC, high-performance liquid chromatography, PET, positron emission tomography; MRI, magnetic resonance imaging; SUV, standardized uptake value; HG, harderian glands; HIP, hippocampus; CB, cerebellum; BS, brain stem; CTX, cortex; STR, striatum; THA, thalamus; AU, arbitrary units; M1, metabolite 1; M2*, mixture of various metabolites; M3, metabolite 3; P, parent compound; *p.i.*, *post iniectio*

the control (64.1 ± 19.1 pmol/mg) are shown in Fig. 8b. At high magnification, labeling of plaque-like structures was evident in the AD case (Fig. 8c). Comparison with the results of immunohistochemical staining in consecutive sections confirmed that this signal colocalized with Aβ-positive AD plaques (Fig. 8d).

Table 2 Quantification of radio-metabolites in plasma and brain samples 5 and 15 min after (d_3)-[^{11}C]MODAG-001 injection

	M1		M2*		M3		P	
	%	%ID	%	%ID	%	%ID	%	%ID
Brain, 5 min	5	0.4*	–	–	2	0.2*	93	8.8*
Brain, 15 min	5	0.4*	–	–	8	0.7*	87	7.2*
Plasma, 5 min	21	0.6#	34	0.9#	6	0.1#	39	1.0#
Plasma, 15 min	30	0.8#	36	1.0#	4	0.1#	30	0.8#

M1, metabolite 1; *M2**, mixture of various metabolites; *M3*, metabolite 3; *P*, parent compound; *%ID*, % injected dose; * per g brain tissue, # per plasma in 1 mL blood

Discussion

Since the discovery in 1997 that the protein αSYN can be found in Lewy bodies in PD [1], much research on αSYN has been conducted. The aggregation of αSYN seems to be the central driver of the pathogenesis of synucleinopathies; however, the relationship between αSYN misfolding and cellular dysfunction or cell death is far from fully understood. The removal of αSYN aggregates holds considerable promise as a therapeutic strategy. In this context, imaging biomarkers are desperately needed for early and differential diagnosis, to follow disease progression and to determine the efficacy of potential disease-modifying treatments. An αSYN PET tracer would unquestionably be of high importance and a game-changing tool for diagnosis and therapy development.

Here, we aimed to develop a PET tracer based on the lead structure of anle138b by further modifying anle253b, which was previously reported by our group to have a good affinity towards human recombinant αSYN fibrils but poor pharmacokinetics in vivo, presumably caused by high lipophilicity with a calculated log*P* (clog*P*) of 5.21 [14]. Ishikawa et al.

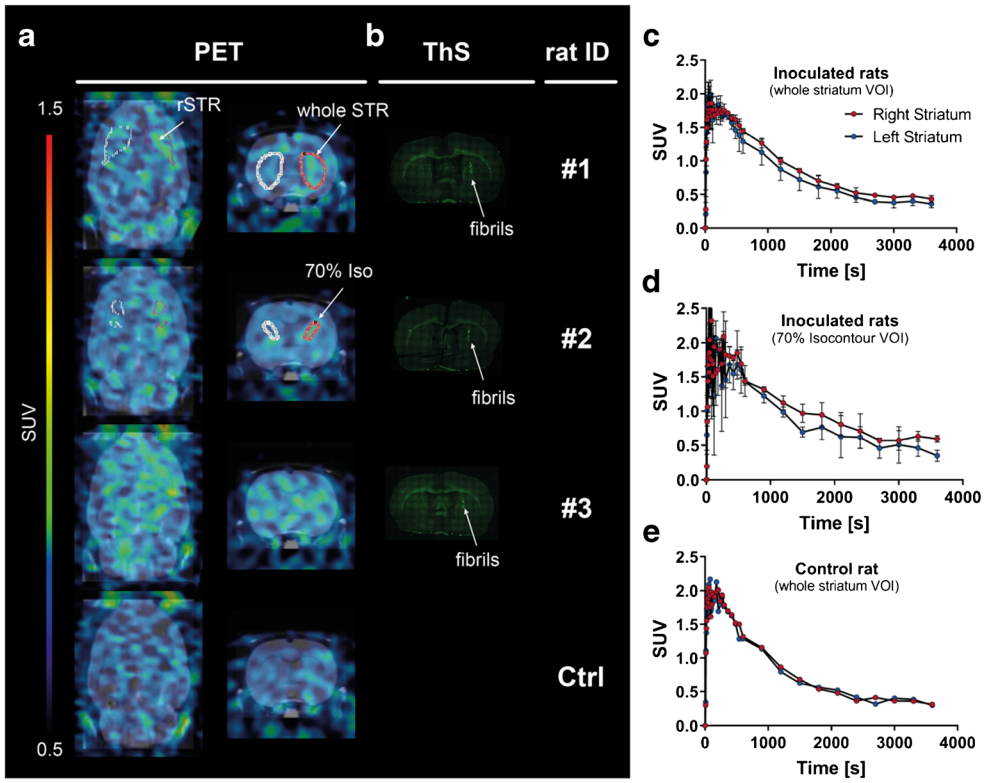

Fig. 7 In vivo binding of (d_3)-[^{11}C]MODAG-001 in α-synuclein-inoculated rats. Coronal and transversal PET images summed up from 2.5 to 60 min of three rats (#1–3) 4 days *post inoculation* and one non-injected control rat (**a**). Images show increased tracer accumulation in the αSYN fibril-inoculated right striatum compared to the vehicle-injected contralateral striatum (**a**, row 1–3). Thioflavin S staining (**b**) confirmed the location of αSYN fibrils (white arrow) in the right striatum of fibril-inoculated rats (#1–3) (**b**). Time activity curves of (d_3)-[^{11}C]MODAG-001 show a rapid brain uptake with peak standardized uptake values of 2.1 ± 0.1 in the left striatum and a difference between the right (injected) and left (vehicle injected) striatum (**c**, **d**, **e**). The binding potential (DVR-$1_{40\text{-}60min}$) was 0.14 ± 0.1 for the whole striatum VOI analysis and 0.44 ± 0.21 for the 70% isocontour VOI analysis, using the contralateral side as reference region (**c**), while no difference was observed in the non-inoculated control rat (**d**). PET, positron emission tomography; αSYN, α-synuclein; rSTR, right striatum; ThS, thioflavin S; Ctrl, control; SUV, standardized uptake value, DVR-1, distribution volume ratio-1; VOI, voxel of interest

performed studies on the improvement in polarity of drug candidates. They showed that exchange of the phenyl group with pyridine largely improved polarity in phosphate buffer at physiological pH, which consequently reduced the log*P* value [23]. We designed a chemical derivative of anle253b, MODAG-001, in which one of the phenyl groups was exchanged with pyridine to reduce the lipophilicity of the compound to a clog*P* value of 3.85. After tritiation, [^{3}H]MODAG-001 was tested in saturation binding experiments against human recombinant fibrils and showed very high affinity to αSYN fibrils, with a K_d value of 0.6 nM in vitro. Compared to [^{3}H]MODAG-001, all the compounds, which have been described in the literature as potential αSYN PET ligands, showed an at least one order of magnitude lower binding affinity (higher K_d values) in vitro towards recombinant αSYN fibrils [14, 21, 24–31]. These compounds comprise [^{125}I]SIL23, (K_d = 148 nM) and its derivative SIL26 (K_i = 15.5 nM), [24] [^{18}F]BF-227 (K_d = 9.6 nM) [26], several fluorescent probes (K_ds in the micromolar and elevated nanomolar range) [32, 33], and the ^{18}F-labeled 3-(benzylidine)indolin-2-one derivative [^{18}F]46a (K_d = 8.9 nM) [25].

Furthermore, we observed 30-fold selectivity over hTau46 and A$\beta_{1–42}$ fibrils, which was suggested for an ideal CNS PET tracer, as both structurally similar proteins have also been shown to be highly abundant in many patients with synucleinopathies [34]. However, the selectivity is determined not only by a lower K_d, but also by the difference of available binding sites. B_{max} was approximately 7- and 50-fold higher for αSYN fibrils compared to hTau46 fibrils and A$\beta_{1–42}$ fibrils, respectively. The measured fibril length of hTau46 (453.4 ± 261.9 nm) was three times larger compared to αSYN (152.5 ± 76.6 nm) and A$\beta_{1–42}$ (139.4 ± 77.3 nm), which were very similar in size. Of note, not only the fibril length, but especially the amount of available binding sites per fibril length, which might differ due to differences in the 3D structure, may play an important role.

These encouraging in vitro binding data were the prerequisite for further ^{11}C-labeling and in vitro and in vivo characterization of MODAG-001. The pharmacokinetic and metabolic profiles of [^{11}C]MODAG-001 after i.v. injection into healthy mice revealed good BBB penetration with high uptake into the brain (SUV = 1.4) and relatively fast clearance

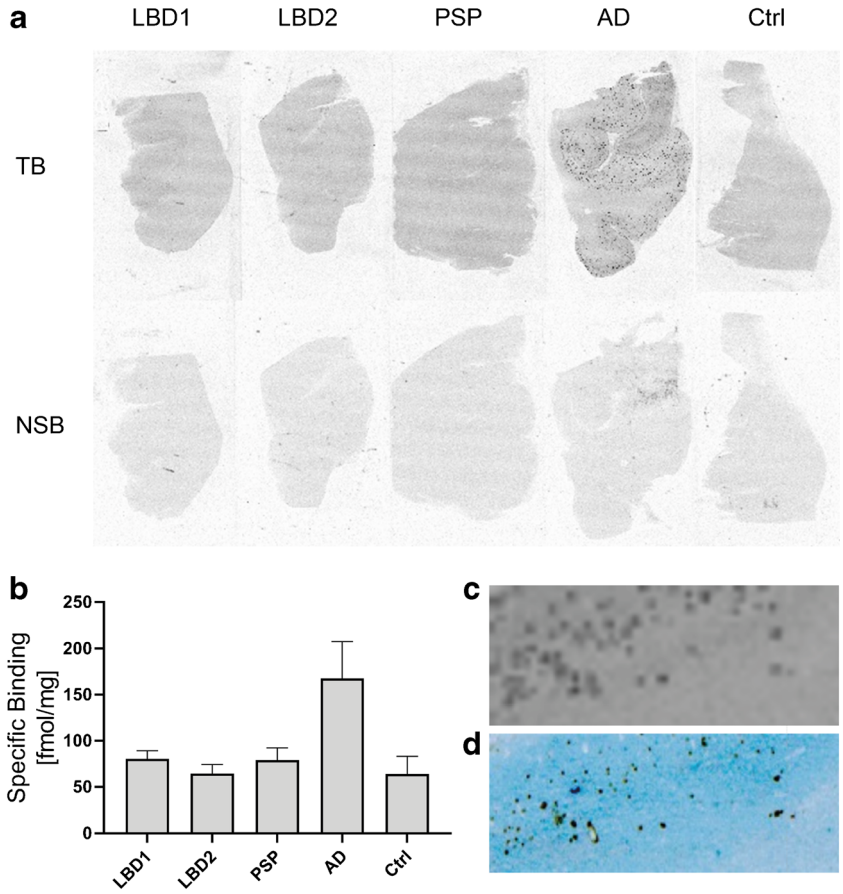

Fig. 8 **a** [^{3}H]MODAG-001 in vitro autoradiography (AR) on human brain slices with different pathologies: Lewy body dementia (LBD), progressive supranuclear palsy (PSP), Alzheimer's disease (AD), healthy control (Ctrl). Images show total (TB) and non-specific binding (NSB) of [^{3}H]MODAG-001. **b** Quantification of specific tracer binding in respective brain slices in fmol/mg is shown. **c** Magnification of a pathological region in the AR of an AD case counterstained for Aβ plaques (**d**)

from the brain. Our metabolite analysis revealed that [^{11}C]MODAG-001 was degraded into the three metabolites, two of which were detectable in the brain, with 81% of the parent compound remaining at 15 min. We hypothesize that metabolite M3 might be the demethylated form of MODAG-001, as demethylation is a very common form of metabolic degradation. Fast metabolism resulting in BBB-penetrating radio-metabolites hampers tracer quantification. Previous studies have shown that improved metabolic stability can be obtained by incorporating deuterium into the molecule. In comparison to carbon-hydrogen bonds, carbon-deuterium bonds potentially decelerate metabolism by cytochrome P450 enzymes due to the primary kinetic isotopic effect [22]. Since the NMe_2 group of MODAG-001 is considered the main target of metabolism (M3 corresponds to the monodemethylated metabolite of MODAG-001), we fully deuterated the nonradioactive methyl group to reduce the formation of radio-metabolites and improve the metabolic stability of the tracer in vivo. Comparison of the pharmacokinetic and metabolic profiles of (d_3)-[^{11}C]MODAG-001 and [^{11}C]MODAG-001 revealed that formation of the monodemethylated radio-metabolite M3 was reduced and that the ratio of M3 to M1 (which hypothetically represents the cleaved ^{11}C-methyl group) was increased for (d_3)-[^{11}C]MODAG-001. Moreover, total metabolism of the parent compound was reduced, resulting in increased levels of the parent compound in the brain at 15 min. This is emphasized in Table 1 and Table 2 showing that the injected dose per gram for [^{11}C]MODAG-001 was reduced from 10.5% at 5 min to 5.3% at 15 min, whereas the injected dose per gram for (d_3)-[^{11}C]MODAG-001 was reduced to a lower extent from 8.8% at 5 min to 7.2% at 15 min.

We next asked whether (d_3)-[^{11}C]MODAG-001 can detect aggregated αSYN in the brain and thus inoculated the right striatum in rats with the same batch of αSYN fibrils used for the in vitro binding experiments. (d_3)-[^{11}C]MODAG-001 binding properties in three fibril-inoculated rats and one non-injected control rat were assessed using in vivo PET imaging. In the three fibril-inoculated rats, we observed higher binding in the right striatum compared to the vehicle-inoculated contralateral side, with mean DVR-$1_{40\text{-}60\text{min}}$ of 0.14 ± 0.1 (whole striatum) and 0.44 ± 0.21 (70% automatic isocontour detection) 4 days after injection, respectively, indicating in vivo binding of (d_3)-[^{11}C]MODAG-001 to inoculated αSYN fibrils. Furthermore, similar overall brain uptake was observed in fibril-inoculated rats (peak SUV, 2.1 ± 0.1) and the non-injected rat (peak SUV, 2.1), demonstrating that potential disruption of the BBB from the intracranial injection

is unlikely to account for higher uptake into the inoculated striatum. A similar rat model was also used by Verdurand et al. [30] to select potential αSYN PET tracer candidates. Notably, they were able to detect the binding of [^{18}F]BF227, [^{18}F]2FBox, and [^{18}F]4FBox to αSYN and Aβ$_{1–42}$ fibrils using in vitro AR; however, no binding was observed in vivo despite good uptake into the cerebral tissue and high A_m (68–543 GBq/μmol).

To further test binding of MODAG-001 in human brain slices with confirmed αSYN pathology, we performed in vitro AR using [^{3}H]MODAG-001 in LBD, PSP, AD, and control cases [19]. The advantage of using tritium AR over carbon-11 AR is its 10-fold higher spatial resolution of approximately 50 μm^2 compared to the spatial resolution of carbon-11 AR of approximately 566 μm^2 due to the positron range of the radionuclide [35, 36].

Despite the high affinity of [^{3}H]MODAG-001 for recombinant αSYN fibrils and good selectivity for αSYN fibrils over hTau46 and Aβ$_{1–42}$ fibrils, no strong binding was observed in brain sections from LBD cases. We observed slightly more intense binding in the cortical gray matter compared to the white matter, which could be blocked by the nonlabeled compound, but this signal was not significantly stronger than that in controls. Interestingly, clear, blockable binding corresponding to the distribution of Aβ plaques was observed in AD brain tissue. Whether this represents binding to Aβ fibrils or binding to aggregated αSYN species, which have been described in AD plaques, remains to be determined [37–40]. Notably, no evidence of binding to aggregated Tau was observed in the PSP and AD cases. A high SNR is an important requirement in brain binding studies with low target abundancy. Possible explanations why we did not observe stronger binding in LBD brain sections are likely related to low target availability in the brains of LBD patients, high nonspecific binding, and/or structural differences between the αSYN fibrils used in the screening assays and those in human brain tissue.

We determined the limit of detection of [^{3}H]MODAG-001 using fibrils and brain homogenate at different concentrations. Quantification of specific binding was still possible at αSYN concentrations down to 5 nM in the presence of 100 μg protein/mL mouse brain homogenate, but not at higher homogenate concentrations of 500 μg protein/mL. When we used sucrose gradient centrifugation of human PD brain tissue to quantify aggregated αSYN, we found approximately 400 nM aggregated αSYN, corresponding to 4 nM aggregated αSYN and 830 μg protein/mL in homogenate at a 1:100 dilution (Supplemental Fig. S5c). At this fibril concentration, the homogenate concentration was approximately 8-fold higher than the limit for a similar fibril concentration determined in our assay. Therefore, we hypothesize that the nonspecific binding of [^{3}H]MODAG-001 is likely responsible for the low signal-to-noise ratio in pathological human brain tissue. For MODAG-001, we calculated a clog*P* value of 3.85, which is rather high compared to the values calculated for successfully established PET ligands.

Structural differences between recombinant fibrils obtained in vitro and fibrils in the LB and LN of LBD patients may also account for the different binding behaviors of MODAG-001. Such structural differences were identified in a study in which αSYN fibrils from LBD patients were amplified from in vivo aggregates by protein misfolding cyclic amplification (PMCA) [41]. The same study also revealed the heterogeneity of αSYN fibrils in different synucleinopathies using solution-state NMR spectroscopy and fluorescent probes. Furthermore, structural differences were also observed in cryo-EM studies in which artificially produced Tau fibrils were compared with Tau extracted from AD or Pick's disease patients with Tau pathology [42–45].

Despite the presence of structural differences between recombinant fibrils and those found in human brain slices, homogenates, or αSYN brain extracts, the availability of the latter is very limited; as such, recombinant fibrils remain a widely used screening tool for the preselection of compounds before PET radiolabeling.

Many studies have shown that a large percentage of AD patients exhibit significant LB pathology in addition to Aβ plaques and neurofibrillary tangles (NFTs) and vice versa [46–50]. As an example, Hamilton et al. [47] investigated the *postmortem* tissue of 145 sporadic AD cases using immunohistochemistry for αSYN and observed LBs in 60.7% of all cases. Colo-Cadena et al. [48] found that Aβ deposition positively correlated with LBD pathogenesis. However, direct comparison of the results of AR and immunohistochemistry in the same AD brain slice revealed the clear colocalization of Aβ-positive plaques and bound MODAG-001. Therefore, the binding is either related to cross-β-sheet structures, a common feature shared by Aβ, Tau, and αSYN [51–53], or to the non-amyloid-β component (NAC) domain identified by Ueda et al., which is part of the αSYN protein in AD plaques [40]. However, as we cannot provide experimental evidence for the latter, this remains speculative.

Determination of the αSYN fibril-binding sites of novel compounds is crucial for PET tracer development. Hsieh and Ferrie et al. identified three putative binding sites for fibrillar αSYN using a combination of in silico docking, photoaffinity labeling, and radiotracer binding studies [54]. While styrene- and piperazine-based analogs showed a preference for sites 2 and 9, tricyclic compounds and an indolinone-diene analog showed a preference for site 3/13. We performed a [^{3}H]MODAG-001 competition assay using the tricyclic compound SIL26 as a competitor and observed a K_i value of 21 nM, indicating preferential binding to site 3/13 at fibrillar αSYN. However, the interpretation needs to be done with care, as preference to sites 2 and 9 were not tested.

Conclusion

Over the past years, several attempts have been made to develop an αSYN-specific PET tracer [14, 21, 24–31]. However, the low abundance of αSYN inclusions and high similarity to structurally related proteins present in pathological brain regions [51, 55] made its discovery very challenging. MODAG-001 fulfills several important criteria needed for a CNS PET tracer targeting αSYN. Its nonspecific binding needs to be reduced to achieve a higher SNR in human brain tissue with synuclein pathology, which is currently being addressed in further optimization experiments. To the best of our knowledge, none of the compounds available so far has been shown to have a comparably high affinity towards recombinant αSYN fibrils in the picomolar range. In addition, MODAG-001 showed high brain uptake and favorable in vivo kinetics and biodistribution in rats and mice.

Supplementary Information The online version contains supplementary material available at https://doi.org/10.1007/s00259-020-05133-x.

Acknowledgments We thank Anna Ohmayer for her support in acquiring the microscope images, Adriana Di Nanni for the synthesis of SIL26, and Birgit Fehrenbacher from the Department of Dermatology for acquiring the electron microscopy images. We also thank the technical assistants at the Department of Preclinical Imaging and Radiopharmacy, University of Tuebingen. Human brain tissue was kindly provided by Neurobiobank Munich, which was established with funding provided by the German Federal Ministry of Education and Research. The samples and corresponding scientific documentation were prepared by Dr. Viktoria Ruf and colleagues.

Authors' contributions Laura Kuebler and Sabrina Buss—data acquisition and analysis, drafting of the manuscript.

Andrei Leonov, Sergey Ryazanov, Felix Schmidt, Andreas Maurer, Daniel Weckbecker, Anne M Landau, Thea P Lillethorup, Daniel Bleher, Ran Sing Saw—data acquisition and analysis, reviewed the manuscript.

Bernd J Pichler, Christian Griesinger, Armin Giese Kristina Herfert—development and conceptual design, supervised experiments, drafting and reviewed the manuscript.

Funding Open Access funding enabled and organized by Projekt DEAL. This research project received funding from the European Union's Seventh Framework Programme (FP7/2007 2013, Multisyn) under REA grant agreement No. 602646, the European Union's Horizon 2020 Research and Innovative Programme under the Marie Skłodowska-Curie grant agreement No. 813528, and the Michael J Fox Foundation for Parkinson's Research under grant No. MJFF16008 and the Max Planck Society and the Deutsche Forschungsgemeinschaft (DFG, German Research Foundation) under Germany's Excellence Strategy—EXC 2067/1-390729940.

Data availability The data can be made available upon request.

Compliance with ethical standards

Conflict of interest A patent has been filed.

Armin Giese, Felix Schmidt, Daniel Weckbecker, Andrei Leonov, and Sergey Ryazanov are employed by MODAG GmbH, which retains ownership of MODAG-001, and Armin Giese and Christian Griesinger are shareholders of MODAG GmbH.

Ethics approval The questionnaire and methodology for this study was approved by the Human Research Ethics committee of the University of Munich (Ethics approval number: 813/2018BO2).

All animal experiments were conducted in compliance with the German animal protection law and with the approval of the local authorities (Regierungspräsidium Tübingen).

Consent for publication All authors agree with the submitted version of the manuscript. The material submitted for publication has not been previously reported and is not under consideration for publication elsewhere.

References

1. Spillantini MG, Schmidt ML, Lee VM, Trojanowski JQ, Jakes R, Goedert M. Alpha-synuclein in Lewy bodies. Nature. 1997;388(6645):839–40. https://doi.org/10.1038/42166.
2. Fanciulli A, Wenning GK. Multiple-system atrophy. N Engl J Med. 2015;372(14):1375–6. https://doi.org/10.1056/NEJMc1501657.
3. Graham JG, Oppenheimer DR. Orthostatic hypotension and nicotine sensitivity in a case of multiple system atrophy. J Neurol Neurosurg Psychiatry. 1969;32(1):28–34. https://doi.org/10.1136/jnnp.32.1.28.
4. Gibb WR, Esiri MM, Lees AJ. Clinical and pathological features of diffuse cortical Lewy body disease (Lewy body dementia). Brain. 1987;110(Pt 5):1131–53. https://doi.org/10.1093/brain/110.5.1131.
5. Gomez-Tortosa E, Newell K, Irizarry MC, Sanders JL. Hyman BT. alpha-Synuclein immunoreactivity in dementia with Lewy bodies: morphological staging and comparison with ubiquitin immunostaining. Acta Neuropathol. 2000;99(4):352–7. https://doi.org/10.1007/s004010051135.
6. Lewandowsky MAG, Bumke O. Handbuch der Neurologie. Springer-Verlag Berlin Heidelberg; 1910.
7. Clark CM, Schneider JA, Bedell BJ, Beach TG, Bilker WB, Mintun MA, et al. Use of florbetapir-PET for imaging beta-amyloid pathology. JAMA. 2011;305(3):275–83. https://doi.org/10.1001/jama.2010.2008.
8. Klunk WE, Engler H, Nordberg A, Wang Y, Blomqvist G, Holt DP, et al. Imaging brain amyloid in Alzheimer's disease with Pittsburgh Compound-B. Ann Neurol. 2004;55(3):306–19. https://doi.org/10.1002/ana.20009.
9. Villemagne VL, Ong K, Mulligan RS, Holl G, Pejoska S, Jones G, et al. Amyloid imaging with (18)F-florbetaben in Alzheimer disease and other dementias. J Nucl Med. 2011;52(8):1210–7. https://doi.org/10.2967/jnumed.111.089730.

10. Shahmoradian SH, Lewis AJ, Genoud C, Hench J, Moors TE, Navarro PP, et al. Lewy pathology in Parkinson's disease consists of crowded organelles and lipid membranes. Nat Neurosci. 2019;22(7):1099–109. https://doi.org/10.1038/s41593-019-0423-2.
11. Kotzbauer PT, Tu Z, Mach RH. Current status of the development of PET radiotracers for imaging alpha synuclein aggregates in Lewy bodies and Lewy neurites. Clin Transl Imaging. 2017;5(1):3–14. https://doi.org/10.1007/s40336-016-0217-4.
12. Mathis CA, Lopresti BJ, Ikonomovic MD, Klunk WE. Small-molecule PET tracers for imaging proteinopathies. Semin Nucl Med. 2017;47(5):553–75. https://doi.org/10.1053/j.semnuclmed.2017.06.003.
13. Pike VW. Considerations in the development of reversibly binding PET radioligands for brain imaging. Curr Med Chem. 2016;23(18):1818–69. https://doi.org/10.2174/0929867323666160418114826.
14. Maurer A, Leonov A, Ryazanov S, Herfert K, Kuebler L, Buss S, et al. (11) C Radiolabeling of anle253b: a putative PET tracer for Parkinson's disease that binds to alpha-synuclein fibrils in vitro and crosses the blood-brain barrier. ChemMedChem. 2019. https://doi.org/10.1002/cmdc.201900689.
15. Wagner J, Ryazanov S, Leonov A, Levin J, Shi S, Schmidt F, et al. Anle138b: a novel oligomer modulator for disease-modifying therapy of neurodegenerative diseases such as prion and Parkinson's disease. Acta Neuropathol. 2013;125(6):795–813. https://doi.org/10.1007/s00401-013-1114-9.
16. Wegrzynowicz M, Bar-On D, Calo L, Anichtchik O, Iovino M, Xia J, et al. Depopulation of dense alpha-synuclein aggregates is associated with rescue of dopamine neuron dysfunction and death in a new Parkinson's disease model. Acta Neuropathol. 2019;138(4):575–95. https://doi.org/10.1007/s00401-019-02023-x.
17. Heras-Garvin A, Weckbecker D, Ryazanov S, Leonov A, Griesinger C, Giese A, et al. Anle138b modulates alpha-synuclein oligomerization and prevents motor decline and neurodegeneration in a mouse model of multiple system atrophy. Mov Disord. 2019;34(2):255–63. https://doi.org/10.1002/mds.27562.
18. Reiner AM, Schmidt F, Ryazanov S, Leonov A, Weckbecker D, Deeg AA, et al. Photophysics of diphenyl-pyrazole compounds in solutions and alpha-synuclein aggregates. Biochim Biophys Acta Gen Subj. 2018;1862(4):800–7. https://doi.org/10.1016/j.bbagen.2017.12.007.
19. Neurobiobank Munich, Germany (NBM). Ludwig Maximilians University Munich [BIORESOURCE]. https://www.neuropathologie.med.uni-muenchen.de/neurobiobank_muenchen/index.html
20. Auld DS, Farmen MW, Kahl SD, Kriauciunas A, McKnight KL, Montrose C, et al. Receptor Binding Assays for HTS and Drug Discovery. In: Sittampalam GS, Grossman A, Brimacombe K, Arkin M, Auld D, Austin CP, et al., editors. Assay Guidance Manual. Bethesda; 2004.
21. Zhang X, Jin H, Padakanti PK, Li J, Yang H, Fan J, et al. Radiosynthesis and in vivo evaluation of two PET radioligands for imaging alpha-synuclein. Appl Sci (Basel). 2014;4(1):66–78. https://doi.org/10.3390/app4010066.
22. Pirali T, Serafini M, Cargnin S, Genazzani AA. Applications of deuterium in medicinal chemistry. J Med Chem. 2019;62(11):5276–97. https://doi.org/10.1021/acs.jmedchem.8b01808.
23. Ishikawa M, Hashimoto Y. Improvement in aqueous solubility in small molecule drug discovery programs by disruption of molecular planarity and symmetry. J Med Chem. 2011;54(6):1539–54. https://doi.org/10.1021/jm101356p.
24. Bagchi DP, Yu L, Perlmutter JS, Xu J, Mach RH, Tu Z, et al. Binding of the radioligand SIL23 to alpha-synuclein fibrils in Parkinson disease brain tissue establishes feasibility and screening approaches for developing a Parkinson disease imaging agent. PLoS One. 2013;8(2):e55031. https://doi.org/10.1371/journal.pone.0055031.
25. Chu W, Zhou D, Gaba V, Liu J, Li S, Peng X, et al. Design, synthesis, and characterization of 3-(Benzylidene)indolin-2-one derivatives as ligands for alpha-synuclein fibrils. J Med Chem. 2015;58(15):6002–17. https://doi.org/10.1021/acs.jmedchem.5b00571.
26. Fodero-Tavoletti MT, Mulligan RS, Okamura N, Furumoto S, Rowe CC, Kudo Y, et al. In vitro characterisation of BF227 binding to alpha-synuclein/Lewy bodies. Eur J Pharmacol. 2009;617(1–3):54–8. https://doi.org/10.1016/j.ejphar.2009.06.042.
27. Hsieh CJ, Xu K, Lee I, Graham TJA, Tu Z, Dhavale D, et al. Chalcones and five-membered heterocyclic isosteres bind to alpha synuclein fibrils in vitro. ACS Omega. 2018;3(4):4486–93. https://doi.org/10.1021/acsomega.7b01897.
28. Kikuchi A, Takeda A, Okamura N, Tashiro M, Hasegawa T, Furumoto S, et al. In vivo visualization of alpha-synuclein deposition by carbon-11-labelled 2-[2-(2-dimethylaminothiazol-5-yl)ethenyl]-6-[2-(fluoro)ethoxy]benzoxazole positron emission tomography in multiple system atrophy. Brain. 2010;133(Pt 6):1772–8. https://doi.org/10.1093/brain/awq091.
29. Verdurand M, Levigoureux E, Lancelot S, Zeinyeh W, Billard T, Quadrio I, et al. Amyloid-beta radiotracer [(18)F]BF-227 does not bind to cytoplasmic glial inclusions of postmortem multiple system atrophy brain tissue. Contrast Media Mol Imaging. 2018;2018:9165458. https://doi.org/10.1155/2018/9165458.
30. Verdurand M, Levigoureux E, Zeinyeh W, Berthier L, Mendjel-Herda M, Cadarossanesaib F, et al. In silico, in vitro, and in vivo evaluation of new candidates for alpha-synuclein PET imaging. Mol Pharm. 2018;15(8):3153–66. https://doi.org/10.1021/acs.molpharmaceut.8b00229.
31. Yue X, Dhavale DD, Li J, Luo Z, Liu J, Yang H, et al. Design, synthesis, and in vitro evaluation of quinolinyl analogues for alpha-synuclein aggregation. Bioorg Med Chem Lett. 2018;28(6):1011–9. https://doi.org/10.1016/j.bmcl.2018.02.031.
32. Celej MS, Jares-Erijman EA, Jovin TM. Fluorescent N-arylaminonaphthalene sulfonate probes for amyloid aggregation of alpha-synuclein. Biophys J. 2008;94(12):4867–79. https://doi.org/10.1529/biophysj.107.125211.
33. Volkova KD, Kovalska VB, Balanda AO, Losytskyy MY, Golub AG, Vermeij RJ, et al. Specific fluorescent detection of fibrillar alpha-synuclein using mono- and trimethine cyanine dyes. Bioorg Med Chem. 2008;16(3):1452–9. https://doi.org/10.1016/j.bmc.2007.10.051.
34. Zhang L, Villalobos A, Beck EM, Bocan T, Chappie TA, Chen L, et al. Design and selection parameters to accelerate the discovery of novel central nervous system positron emission tomography (PET) ligands and their application in the development of a novel phosphodiesterase 2A PET ligand. J Med Chem. 2013;56(11):4568–79. https://doi.org/10.1021/jm400312y.
35. Strome EM, Jivan S, Doudet DJ. Quantitative in vitro phosphor imaging using [3H] and [18F] radioligands: the effects of chronic desipramine treatment on serotonin 5-HT2 receptors. J Neurosci Methods. 2005;141(1):143–54. https://doi.org/10.1016/j.jneumeth.2004.06.008.
36. Sihver W, Sihver S, Bergstrom M, Murata T, Matsumura K, Onoe H, et al. Methodological aspects for in vitro characterization of receptor binding using 11C-labeled receptor ligands: a detailed study with the benzodiazepine receptor antagonist [11C]Ro 15–1788. Nucl Med Biol. 1997;24(8):723–31. https://doi.org/10.1016/s0969-8051(97)00113-3.
37. Iwai A, Masliah E, Yoshimoto M, Ge N, Flanagan L, de Silva HA, et al. The precursor protein of non-A beta component of Alzheimer's disease amyloid is a presynaptic protein of the central nervous system. Neuron. 1995;14(2):467–75. https://doi.org/10.1016/0896-6273(95)90302-x.
38. Masliah E, Iwai A, Mallory M, Ueda K, Saitoh T. Altered presynaptic protein NACP is associated with plaque formation and

neurodegeneration in Alzheimer's disease. Am J Pathol. 1996;148(1):201–10.
39. Twohig D, Nielsen HM. Alpha-synuclein in the pathophysiology of Alzheimer's disease. Mol Neurodegener. 2019;14(1):23. https://doi.org/10.1186/s13024-019-0320-x.
40. Ueda K, Fukushima H, Masliah E, Xia Y, Iwai A, Yoshimoto M, et al. Molecular cloning of cDNA encoding an unrecognized component of amyloid in Alzheimer disease. Proc Natl Acad Sci U S A. 1993;90(23):11282–6. https://doi.org/10.1073/pnas.90.23.11282.
41. Strohaker T, Jung BC, Liou SH, Fernandez CO, Riedel D, Becker S, et al. Structural heterogeneity of alpha-synuclein fibrils amplified from patient brain extracts. Nat Commun. 2019;10(1):5535. https://doi.org/10.1038/s41467-019-13,564-w.
42. Falcon B, Zhang W, Murzin AG, Murshudov G, Garringer HJ, Vidal R, et al. Structures of filaments from Pick's disease reveal a novel tau protein fold. Nature. 2018;561(7721):137–40. https://doi.org/10.1038/s41586-018-0454-y.
43. Falcon B, Zivanov J, Zhang W, Murzin AG, Garringer HJ, Vidal R, et al. Novel tau filament fold in chronic traumatic encephalopathy encloses hydrophobic molecules. Nature. 2019;568(7752):420–3. https://doi.org/10.1038/s41586-019-1026-5.
44. Fitzpatrick AWP, Falcon B, He S, Murzin AG, Murshudov G, Garringer HJ, et al. Cryo-EM structures of tau filaments from Alzheimer's disease. Nature. 2017;547(7662):185–90. https://doi.org/10.1038/nature23002.
45. Zhang W, Falcon B, Murzin AG, Fan J, Crowther RA, Goedert M, et al. Heparin-induced tau filaments are polymorphic and differ from those in Alzheimer's and Pick's diseases. Elife. 2019;8. https://doi.org/10.7554/eLife.43584.
46. Bergeron C, Pollanen M. Lewy bodies in Alzheimer disease—one or two diseases? Alzheimer Dis Assoc Disord. 1989;3(4):197–204.
47. Hamilton RL. Lewy bodies in Alzheimer's disease: a neuropathological review of 145 cases using alpha-synuclein immunohistochemistry. Brain Pathol. 2000;10(3):378–84.
48. Colom-Cadena M, Gelpi E, Charif S, Belbin O, Blesa R, Marti MJ, et al. Confluence of alpha-synuclein, tau, and beta-amyloid pathologies in dementia with Lewy bodies. J Neuropathol Exp Neurol. 2013;72(12):1203–12. https://doi.org/10.1097/Nen.0000000000000018.
49. Irwin DJ, Lee VM, Trojanowski JQ. Parkinson's disease dementia: convergence of alpha-synuclein, tau and amyloid-beta pathologies. Nat Rev Neurosci. 2013;14(9):626–36. https://doi.org/10.1038/nrn3549.
50. Robinson JL, Lee EB, Xie SX, Rennert L, Suh E, Bredenberg C, et al. Neurodegenerative disease concomitant proteinopathies are prevalent, age-related and APOE4-associated. Brain. 2018;141:2181–93. https://doi.org/10.1093/brain/awy146.
51. Flores-Fernandez JM, Rathod V, Wille H. Comparing the folds of prions and other pathogenic amyloids. Pathogens. 2018;7(2). https://doi.org/10.3390/pathogens7020050.
52. Harada R, Okamura N, Furumoto S, Yanai K. Imaging protein misfolding in the brain using beta-sheet ligands. Front Neurosci. 2018;12:585. https://doi.org/10.3389/fnins.2018.00585.
53. Serpell LC, Berriman J, Jakes R, Goedert M, Crowther RA. Fiber diffraction of synthetic alpha-synuclein filaments shows amyloid-like cross-beta conformation. Proc Natl Acad Sci U S A. 2000;97(9):4897–902. https://doi.org/10.1073/pnas.97.9.4897.
54. Hsieh CJ, Ferrie JJ, Xu K, Lee I, Graham TJA, Tu Z, et al. Alpha synuclein fibrils contain multiple binding sites for small molecules. ACS Chem Neurosci. 2018;9(11):2521–7. https://doi.org/10.1021/acschemneuro.8b00177.
55. Breydo L, Uversky VN. Structural, morphological, and functional diversity of amyloid oligomers. FEBS Lett. 2015;589(19 Pt A):2640–8. https://doi.org/10.1016/j.febslet.2015.07.013.

Supplemental Material:

[^{11}C]MODAG-001 – Towards a PET Tracer Targeting α-Synuclein Aggregates

Laura Kuebler[1*], Sabrina Buss[1*], Andrei Leonov[2,3*], Sergey Ryazanov[3*†], Felix Schmidt[2*], Andreas Maurer[1], Daniel Weckbecker[2], Anne M Landau[4,5], Thea P Lillethorup[5], Daniel Bleher[1], Ran Sing Saw[1], Bernd J Pichler[1], Christian Griesinger[3,6#], Armin Giese[2#], Kristina Herfert[1#]

[*]contributed equally

[#]corresponding authors

[†]present address also MODAG

[1]Werner Siemens Imaging Center, Department of Preclinical Imaging and Radiopharmacy, Eberhard Karls University, Tuebingen, Germany

[2]MODAG GmbH, Wendelsheim, Germany

[3]Department of NMR-based Structural Biology, Max Planck Institute for Biophysical Chemistry, Göttingen, Germany

[4]Translational Neuropsychiatry Unit, Aarhus University, Aarhus, Denmark

[5]Department of Nuclear Medicine and PET, Aarhus University, Aarhus, Denmark

[6]University Göttingen, Cluster of Excellence Multiscale Bioimaging molecular machines, 37077 Göttingen, Germany

Material and methods

Compound Synthesis

All starting materials and solvents were of commercial grade and used as received unless noted otherwise. Thin layer chromatography (TLC): Macherey-Nagel precoated sheets, 0.25 mm ALUGRAM® SIL G/UV254 plates, detection with UV and/or by charring with 10 wt % ethanolic phosphomolybdic acid reagent followed by heating at 200 °C. Flash column chromatography was performed by using Merck silica gel 60 (0.063-0.100 mm). Analytical high performance liquid chromatography (HPLC) was performed by using a Waters HPLC system with a Waters 996 Photodiode Array Detector. All separations involved a mobile phase of 0.1 % trifluoroacetic acid (TFA) (v/v) in water and 0.1 % TFA in acetonitrile. Unless otherwise specified, a gradient 50 % CH_3CN /50 % H_2O $\rightarrow$100 % CH_3CN in 30 minutes was used. HPLC was performed by using a reversed-phase (RP) column Eurospher RP 18, 100 Å, 5 µm, 250 $\times$ 4.6 mm at flow rate of 1 mL/min. Electrospray ionization mass spectrometry (ESI-MS) and liquid chromatography/ mass spectrometry (LC/MS) analyses were obtained by using a Waters Micromass ZQ 4000 mass spectrometer in conjunction with the Waters HPLC apparatus described above. NMR spectra were recorded by using a 400 MHz Bruker Avance spectrometer (Bruker AG, Rheinstetten, Germany) equipped with a TXI HCN z-gradient probe. All spectra were processed by using TOPSPIN 3.1 (Bruker AG, Karlsruhe, Germany). ^{1}H-NMR chemical shifts (δ) are reported in parts per million (ppm) relative to $CHCl_3$, DMSO-d_5 and TFA-d_1 as internal standards. Data are reported as follows: chemical shift, multiplicity (s = singlet, d = doublet, t = triplet, q = quartet, qi = quintet, dd = doublet of doublets, dt = doublet of triplets, b = broadened, m = multiplet, sept = septet), coupling constants (J, given in Hz), integration. ^{13}C-NMR chemical shifts (δ) are reported in parts per million (ppm) relative to $CDCl_3$, DMSO-d_6 and TFA-d_1 as internal standards. The following experiments were used to record the resonances of the compounds: ^{1}H-1D, ^{13}C-1D-NMR spectra and ^{13}C-APT (attached proton test with a single J-evolution time of 1/145 seconds, spectra are processed such that quaternary and methylene groups have positive sign and methyl and methine groups negative sign). To resolve overlap of resonances and recover undetectable resonances in ^{1}H and APT spectra, 2D-[^{13}C,^{1}H]-HSQC (heteronuclear single quantum coherence), 2D-[^{13}C,^{1}H]-HMBC (heteronuclear multiple bond correlation) and 2D-NOESY were recorded for some compounds.

Experimental procedures and characterization of compounds

MODAG-001: 4-[3-(4-Dimethylaminophenyl)-1*H*-pyrazol-5-yl]-2-bromopyridine

To a solution of 1-[4-(dimethylamino)phenyl]ethanone (490 mg, 3.00 mmol) and methyl 2-bromopyridine-4-carboxylate (843 mg, 3.9 mmol) in DMSO (7.5 mL) and THF (1.9 mL) sodium hydride (60 % in oil, 3.9 mmol, 156 mg) was added, and the reaction mixture was stirred at 20 °C for 15 hours. The reaction mixture was poured into 50 mL of an ice water and 1 M phosphate buffer, p*H* 7 (10 mL), stirred for one hour, the resulting precipitate was filtered off, washed with water (2 ×10 mL), methanol (10 mL), hexane (10 mL), and dried on the air to obtain a crude intermediate 1-(2-bromopyridin-4-yl)-3-[4-(dimethylamino)phenyl]propane-1,3-dione (964 mg) as an orange solid. To a suspension of this crude intermediate in THF (20 mL) hydrazine hydrate (292 µL, 300 mg, 6 mmol) was added. The reaction mixture was stirred at 70 °C for five hours, cooled and concentrated *in vacuo*. The residue was suspended in methanol (10 mL), filtered off, washed with cold methanol (2×5 mL), recrystallized from *n*-butanol (10 mL) and *N*,*N*-dimethylformamide (0.2 mL), and dried in high vacuo at 20 °C for 15 hours afforded the product 4-[3-(4-dimethylaminophenyl)-1*H*-pyrazol-5-yl]-2-bromopyridine (715 mg, 2.08 mmol, 69 % over two steps) as a light pink solid. ^{1}H-NMR (400 MHz, DMSO-d_6 + 1 % DCl) δ = 8.42 (d, *J*= 5.2 Hz, 1H), 8.05 (d, *J*= 1.4 Hz, 1H), 7.93 (d, *J*= 8.7 Hz, 2H), 7.87 (dd, *J*= 5.2, 1.4 Hz, 1H), 7.66 (bd, *J*= 7.8 Hz, 2H), 7.51 (s, 1H), 3.11 (s, 6H). ^{13}C-NMR (100.6 MHz, DMSO + 1 % DCl) δ = 151.0, 145.4, 144.6 (2C), 142.5, 142.3, 127.9, 126.5 (2C), 123.2, 119.6 (2C), 119.1, 101.8, 44.2 (2C). LC MS (RP18-100Å, gradient 50 % CH_3CN /50 % H_2O →100 % CH_3CN in 30 minutes), RT 4.8 minutes and mass 343.1 (100 %), 345.2 (97 %), $[M+H]^+$. TLC (SiO_2, *n*-hexane/EtOAc = 2/1) R_f 0.36, m.p.: 224-226 °C.

tert-Butyl *N*-(4-acetylphenyl)-*N*-($^{2}H_3$)methylcarbamate **4b**

A mixture of *tert*-butyl *N*-(4-acetylphenyl)carbamate **3** (FW 235.28, 2.35 g, 10 mmol) and Cs_2CO_3 (FW 325.82, 6.52 g, 20 mmol) in diglyme (20 mL) was stirred at room temperature for ten minutes. CD_3I (FW 144.96, d 2.33, b.p. 42 °C; 933 µL, 2.17 g, 15 mmol) was added and stirring was continued for 20 hours. The reaction mixture was quenched with 1 M phosphate buffer, p*H* 7 (20 mL), ethyl acetate (30 mL) was added, the organic phase was separated, washed with water (3 × 20 mL), dried over Na_2SO_4 and evaporated. The oily residue (2.67 g) was purified on silica gel (*n*-hexane/EtOAc = 3/1 R_f 0.38) to give 2.1 g (8.3 mmol, 83 %) of pure product as a slightly yellow oil. ^{1}H NMR (400 MHz, $CDCl_3$, 298K) δ = 7.91 (d, *J* = 8.6 Hz, 2H), 7.35 (d, *J* = 8.6 Hz, 2H), 2.57 (s, 3H), 1.47 (s, 9H). ^{13}C NMR (100.6 MHz, $CDCl_3$, 298K) δ = 197.1, 154.1, 148.0, 133.4, 128.8 (2C), 124.2 (2C), 81.1, 40.0 (sept, J_{D-C} = 21.3 Hz), 28.2 (3C), 26.5. LC MS (RP18-100 Å, gradient 50 % CH_3CN /50 %

$H_2O \rightarrow$ 100 % CH_3CN in 30 minutes), RT 10.0 minutes and mass 253.2 (5 %), $[M+H]^+$, 238.1 (14 %), $[M+H\text{-}CH_3]^+$. 196.8 (100 %), $[M+H\text{-}C_4H_9]^+$.

tert-Butyl *N*-(4-acetylphenyl)-*N*-methylcarbamate **4a**

The title compound was prepared analogously to **4b** using CH_3I as an educt to give the compound **4a** in 94 % yield. This compound has been reported previously [1], CAS [907209-80-7]. ^1H NMR data match those reported in the literature [1].

tert-Butyl {4-[3-(2-bromopyridin-4-yl)-3-oxopropanoyl]phenyl}methylcarbamate **5a**

To a solution of *tert*-butyl *N*-(4-acetylphenyl)-*N*-methylcarbamate **4a** (498 mg, 2.00 mmol) and methyl 2-bromopyridine-4-carboxylate **2** (518 mg, 2.4 mmol) in DMSO (5 mL) and THF (1.3 mL) sodium hydride (60 % in oil, 2.4 mmol, 96 mg) was added, and the mixture was stirred at 20 °C for 15 hours. TLC analysis of sampled 20 µL aliquot showed incompleteness of reaction (*n*-hexane/EtOAc = 3:1, carbamate R_f 0.5; product R_f 0.35). Methyl 2-bromopyridine-4-carboxylate (43 mg, 0.2 mmol) and sodium hydride (60 % in oil, 0.4 mmol, 16 mg) were added additionally, and the stirring was continued for 15 hours. The reaction mixture was poured into ice water (20 mL) and 1 M phosphate buffer p*H* 7 (10 mL), stirred for 30 minutes, and extracted with chloroform (3 × 10 mL). The solution was washed with brine, dried over Na_2SO_4 and concentrated *in vacuo*. The resulting oil was purified on 90 g silica gel (*n*-hexane/EtOAc = 3:1, R_f 0.39) to afford the *tert*-butyl {4-[3-(2-bromopyridin-4-yl)-3-oxopropanoyl]phenyl}methylcarbamate (580 mg, 1.34 mmol, 67 %) as a yellow glass. ^1H NMR (400 MHz, $CDCl_3$, 298K) δ = 8.53 (d, *J* = 5.1 Hz, 1H), 7.97 (m, 3H), 7.73 (dd, *J* = 5.1, 1.4 Hz, 1H), 7.44 (m, 2H), 6.80 (s, 1H), 3.34 (s, 3H), 1.50 (s, 9H). ^{13}C NMR (100.6 MHz, $CDCl_3$, 298K) δ = 187.6, 178.7, 153.8, 150.7, 148.3, 144.8, 142.9, 130.5, 127.9 (2C), 124.9, 124.2 (2C), 119.3, 93.9, 81.1, 36.6, 28.1 (3C). LC-MS (RP18-100 Å, gradient 50 % CH_3CN /50 % $H_2O \rightarrow$ 100 % CH_3CN in 30 minutes), RT 24.1 min and mass 433.1 (100%), 435.3 (98%) $[M+H]^+$.

tert-Butyl {4-[3-(2-bromopyridin-4-yl)-3-oxopropanoyl]phenyl}($^2H_3$)methylcarbamate **5b**

The title compound was prepared analogously to **5a** using **4b** as an educt to give the compound **5b** in 65 % yield. ^1H NMR (400 MHz, $CDCl_3$, 298K) δ = 8.52 (d, *J* = 5.1 Hz, 1H), 7.96 (m, 3H), 7.72 (dd, *J* = 5.1, 1.4 Hz, 1H), 7.43 (m, 2H), 6.79 (s, 1H), 1.50 (s, 9H). ^{13}C NMR (100.6 MHz, $CDCl_3$, 298K) δ = 187.6, 178.7, 153.8, 150.7, 148.2, 144.9, 142.9, 130.5, 127.9 (2C), 124.9, 124.1 (2C), 119.3, 93.9, 81.2, 35.9 (sept, $J_{D\text{-}C}$ = 21.2 Hz), 28.1 (3C). LC-MS (RP18-100 Å, gradient 50 % CH_3CN /50 % $H_2O \rightarrow$ 100 % CH_3CN in 30 minutes), RT 24.2

min and mass 436.3 (100%), 438.3 (98%) $[M+H]^+$. TLC (SiO_2, *n*-hexane/EtOAc = 3:1) R_f = 0.39.

tert-Butyl { 4-[5-(2-bromopyridin-4-yl)-1*H*-pyrazol-3-yl]phenyl }($^2H_3$)methylcarbamate **6b**

To a solution of the *tert*-butyl {4-[3-(2-bromopyridin-4-yl)-3-oxopropanoyl]phenyl}($^2H_3$)methylcarbamate **5b** (873 mg, 2 mmol) in THF (10 mL) was added hydrazine monohydrate (194 µL, 200 mg, 4 mmol). After being stirred at 60 °C for 15 hours the reaction mixture was cooled to room temperature, concentrated *in vacuo* and evaporated with methanol (10 mL). The residue (900 mg) was purified on silica gel ($CHCl_3$/MeOH = 95:5, R_f 0.31) to give 830 mg (1.9 mmol, 96 %) of the product as a beige foam. ^{1}H NMR (400 MHz, $CDCl_3$, 298K) δ = 11.68 (bs, 1H), 8.36 (d, *J* = 5.2 Hz, 1H), 7.88 (s, 1H), 7.63 (d, *J* = 5.2 Hz, 1H), 7.54 (d, *J* = 8.5 Hz, 2H), 7.31 (d, *J* = 8.5 Hz, 2H), 6.84 (s, 1H), 1.50 (s, 9H). ^{13}C NMR (100.6 MHz, $CDCl_3$, 298K) δ = 154.7, 150.2, 147.0, 145.9, 144.0, 142.5, 142.4, 125.7 (3C), 125.5 (2C), 124.0, 119.0, 100.9, 80.9, 36.4 (sept, $J_{D\text{-}C}$ = 21.2 Hz), 28.3 (3C). LC-MS (RP18-100 Å, gradient 50 % CH_3CN /50 % H_2O $\rightarrow$ 100 % CH_3CN in 30 minutes), RT 15.3 min and mass 432.3 (100%), 434.3 (98%) $[M+H]^+$.

tert-Butyl { 4-[5-(2-bromopyridin-4-yl)-1*H*-pyrazol-3-yl]phenyl }methylcarbamate **6a**

The title compound was prepared analogously to **6b** using **5a** as an educt to give the compound **6a** in 96 % yield. ^{1}H NMR (400 MHz, $CDCl_3$, 298K) δ = 8.36 (d, *J* = 5.2 Hz, 1H), 7.88 (m, 1H), 7.63 (dd, *J* = 5.2, 1.4 Hz, 1H), 7.54 (d, *J* = 8.5 Hz, 2H), 7.32 (d, *J* = 8.5 Hz, 2H), 6.84 (s, 1H), 3.29 (s, 3H), 1.50 (s, 9H). ^{13}C NMR (100.6 MHz, $CDCl_3$, 298K) δ = 154.7, 150.3, 147.3, 145.9, 143.9, 142.6 (2C), 126.0, 125.6 (4C), 124.0, 119.0, 100.8, 80.9, 37.1, 28.3 (3C). LC-MS (RP18-100 Å, gradient 50 % CH_3CN /50 % H_2O $\rightarrow$ 100 % CH_3CN in 30 minutes), RT 15.5 min and mass 429.3 (100%), 431.3 (98%) $[M+H]^+$. TLC (SiO_2, $CHCl_3$/MeOH = 95:5) R_f = 0.31.

4-[5-(2-Bromopyridin-4-yl)-1*H*-pyrazol-3-yl]-*N*-($^2H_3$)methylaniline **7b**

To a solution of *tert*-butyl {4-[5-(2-bromopyridin-4-yl)-1*H*-pyrazol-3-yl]phenyl}($^2H_3$)methylcarbamate **6b** (810 mg, 1.87 mmol) in CH_2Cl_2 (15 mL) trifluoroacetic acid (2 mL, 2.96 g, 26 mmol) was added. The mixture was stirred at room temperature for 15 hours and concentrated *in vacuo*. 1 M phosphate buffer, p*H* 7 (20 mL) was added, the resulting precipitate was filtered off, washed with water (2 $\times$ 10 mL) and air dried for 15 hours to give 559 mg (1.68 mmol, 90 %) of product as a beige-colored solid with HPLC purity 99 %+ (sample 0.5 mg/mL in CH_3CN; 5 µL injection volume; column: Eurospher RP18 100Å, 5 µm, 250×4.6 mm, solvents: water (+0.1 % TFA, A) and CH_3CN (+0.1 % TFA, B), gradient:

B 0 % ®100 % in 30 minutes, detector UV 260 nm, peak RT 17.7 minutes). ^{1}H NMR (400 MHz, TFA-d_1, 298K) δ = 8.46 (d, *J* = 6.4 Hz, 1H), 8.31 (s, 1H), 8.12 (d, *J* = 6.4 Hz, 1H), 7.70 (d, *J* = 8.6 Hz, 2H), 7.43 (d, *J* = 8.6 Hz, 2H), 7.22 (s, 1H). ^{13}C NMR (100.6 MHz, TFA-d_1, 298K) δ = 151.0, 148.9, 146.4, 146.2, 139.3, 137.2, 131.5, 131.0 (2C), 130.5, 125.1 (2C), 124.1, 108.1, 40.0 (m, J_{D-C} = 21.1 Hz). LC MS (RP18-100 Å, gradient 0 % CH_3CN /100 % H_2O $\rightarrow$ 100 % CH_3CN in 30 minutes), RT 17.7 minutes and mass 329.1 (98 %), 331.1 (100 %), $[M+H]^+$. TLC (SiO_2, *n*-hexane/EtOAc = 1/1) R_f 0.40, m.p.: 224-225 °C.

4-[5-(2-Bromopyridin-4-yl)-1*H*-pyrazol-3-yl]-*N*-methylaniline **7a**

The title compound was prepared analogously to **7b** using **6a** as an educt to give the compound **6a** in 74 % yield as a beige-colored solid with HPLC purity 98.3 % (sample 0.1 mg/mL in CH_3CN; 5 µL injection volume; column: Eurospher RP18 100 Å, 5 µm, 250 × 4.6 mm, solvents: water (+0.1 % TFA, A) and CH_3CN (+0.1 % TFA, B), gradient: B 0 % $\rightarrow$ 100 % in 30 minutes, detector UV 254 nm, peak RT 17.7 min). ^{1}H NMR (400 MHz, DMSO-d_6 + 1 % DCl, 313K) δ = 8.41 (d, *J* = 5.2 Hz, 1H), 8.04 (d, *J* = 1.1 Hz, 1H), 7.93 (d, *J* = 8.6 Hz, 2H), 7.86 (dd, *J* = 5.2, 1.4 Hz, 1H), 7.57 (d, *J* = 8.6 Hz, 2H), 7.48 (s, 1H), 2.92 (s, 3H). ^{13}C NMR (400 MHz, DMSO-d_6 + 1 % DCl, 313K) δ = 150.8, 145.5, 145.0, 142.2, 142.1, 138.7, 129.0, 126.5 (2C), 123.1, 121.6 (2C), 119.0, 101.9, 35.0. LC MS (RP18-100 Å, gradient 0 % CH_3CN /100 % H_2O $\rightarrow$ 100 % CH_3CN in 30 minutes), RT 17.7 minutes and mass 329.1 (98 %), 331.1 (100 %), $[M+H]^+$. TLC (SiO_2, *n*-hexane/EtOAc = 1/1) R_f 0.40, m.p.: 225-226 °C.

Preparation and characterization of recombinant αSYN fibrils and hTau46 fibrils

Expression and purification of recombinant wild-type αSYN was performed as previously described [2]. Briefly, pET-5a/α-synuclein (136TAT) plasmid (wt plasmid provided by Philipp Kahle, Hertie Institute for Clinical Brain Research, Tübingen; 136-TAC/TAT-Mutation provided by Matthias Habeck, LMU Munich) was used to transform *E. coli* BL21(DE3)pLys cells (Novagen, Madison, WI, USA), and expression was induced with isopropyl-β-D-thiogalactopyranose (IPTG, Peqlab, Erlangen, Germany). Cells were lysed by boiling after heat inactivation of proteases. After centrifugation, the supernatant was filtered through a Filtropur S 0.2 µm filter (Sarstedt, Nümbrecht, Germany), loaded on a HiTrap Q HP anion exchange column (5 mL, GE Healthcare, Munich, Germany) and eluted with a linear gradient of 25 mM to 500 mM NaCl. Fractions containing αSYN were pooled and further purified by gel filtration via a Superdex 75 prep-grade column (25 mL, GE Healthcare). The protein concentration was adjusted to 1 mg/mL in 50 mM Tris-HCl, p*H* 7.0. After freezing in

liquid nitrogen, the protein was stored at -80 °C. Fibrilization was induced by constant agitation at high protein concentrations as described previously [3, 2]. Briefly, 50 µM αSYN in 50 mM Tris-HCl containing 100 mM NaCl and 0.02 % NaN_3, p*H* 7.0, was incubated for 96 hours at 37 °C and 1400 rpm using an Eppendorf Thermomixer Comfort (Eppendorf, Hamburg, Germany). To purify the fibrils from nonaggregated monomeric αSYN, the fibril preparations were ultracentrifuged at 135,000 × g at 4 °C for 30 minutes in a Beckman Optima Max-XP centrifuge (Beckman Coulter, Krefeld, Germany). The pellet was resuspended in aggregation buffer, and the concentration was determined using a BCA assay. After freezing in liquid nitrogen, fibrils were stored at -80 °C. Recombinant hTau46 was purchased lyophilized from Bio-Techne GmbH (Wiesbaden, Germany) and was solved in 50 mM Tris-base, p*H* 7.0. Fibrillization was induced by heparin under constant agitation, as described previously [4]. Briefly, 10 µM hTau46 was incubated in presence of 0.02 % NaN_3 and 0.03 mg/mL heparin (sodium salt, Sigma Aldrich, Taufkirchen, Germany) for 72 h at 37 °C and 1,000 rpm. Fibril formation was verified using Thioflavin (Th)T-fluorescence and sucrose density centrifugation. ThT-fluorescence was measured using a LS55 Luminescence Spectrometer (Perkin Elmer, Hamburg, Germany) with 0.5 µM protein and 20 µM ThT (Sigma Aldrich, Taufkirchen, Germany) in 50 mM Tris-HCl, p*H* 7.5. Spectra were recorded at wavelengths ranging from 460 nm to 560 nm. A continuous sucrose gradient assay was performed as described previously [3, 2]. Briefly, solutions containing 50 mM Tris-Base, p*H* 7.5, 0.1 % NP-40 (Roche, Mannheim, Germany) and sucrose (10 %, 20 %, 30 %, 40 %, 50 % and 60 %, respectively) were filled into a 4 mL 11 × 60 mm polyallomer tube (Beckman Coulter), with 200 µL of the 60 % sucrose solution first loaded into the bottom, followed by 400 µL of the 50 % solution to the 10 % sucrose solution. Finally, 200 µL of 5 µM protein in 1x TBS (p*H* 7.5) containing 0.1 % NP-40 was loaded on the top of the gradient. Ultracentrifugation at 40,000 x g and 4 °C for one hour was performed in a Sorvall WX Ultra 90 centrifuge using a Sw60Ti rotor (Beckman Coulter). The resulting continuous gradients were fractionated in volumes of 200 µL. Twenty microliters per fraction were analyzed by denaturing SDS-PAGE and Western blot analysis using a monoclonal antibody against human αSYN (4B12, Biolegend, San Diego, CA, USA), and human Tau46, respectively (Cell Signaling Technology, Leiden, Netherlands).

Preparation and characterization of $A\beta_{1-42}$ fibrils

$A\beta_{1-42}$ fibril production was adapted from Bagchi *et al.* [5]. One milligram of synthetic lyophilized human $A\beta_{1-42}$ peptide with >90 % purity (EMC Microcollections, Tuebingen, Germany) was dissolved in 44.3 µL of DMSO. Deionized water (820 µL) and 1 M Tris-HCl (22.2 µL, p*H* 7.6) were added to reach a final monomer concentration of 250 µM (1.13 mg/mL). Aggregation was induced by shaking at 800 rpm in an Eppendorf

Thermomixer for 65 hours at 37 °C. Fibrils were sonicated in a water bath (Elmasonic S 60 H, Elma Schmidbauer GmbH, Singen, Germany) at 37 °C for three minutes. The presence of β-helical secondary structure was confirmed via an increase in ThT (AB 137040, abcr GmbH, Karlsruhe, Germany) fluorescence determined by obtaining an emission spectrum. To this end, $A\beta_{1-42}$ was diluted in 50 mM glycine/NaOH, p*H* 8.5, with 10 µM ThT to a final concentration of 2.5 µM as described previously [6, 7].

Negative staining transmission electron microscopy

Different fibril suspensions were placed directly onto a glow-discharged electron microscopy (EM) grid. After adsorption, the grid was washed in double distilled water and negatively stained with 1 % uranyl acetate. The grids were examined using a Zeiss LIBRA 120 transmission electron microscope (Carl Zeiss, Oberkochen, Germany) operating at 120 kV.

Fibril concentration determination

To avoid radioligand depletion in binding experiments, the radioligand needs to be added in access. The concentration of human recombinant αSYN, hTau46 and $A\beta_{1-42}$ fibrils at which ≤ 10 % of the added ligand binds to the target molecule was determined for saturation and competition experiments, according to [8]. Briefly, decreasing fibril concentrations were incubated with 1 nM [^{3}H]MODAG-001 for two hours at 37 °C. Washing and harvesting of fibrils was performed as described in the next paragraph. Radioactivity converted into % total bound/added radioligand was plotted against increasing fibril concentrations.

Binding assays – filtration and read-out

Plates covered by removable sealing tape (PerkinElmer, Waltham, MA, USA) were incubated on a shaker (MaxQ™ 6000, orbit diameter 1.9 cm, Thermo Fisher Scientific Inc., Marietta, OH, USA) at 45 rpm for two hours at 37 °C. After incubation, bound and free radioligands were separated by vacuum filtration through glassfiber filtermat B (PerkinElmer) using a filtermat harvester (PerkinElmer). To harvest plates containing αSYN and $A\beta_{1-42}$ fibrils, the filtermat was additionally incubated with 5 mg/mL polyethylenimine for 30 minutes at 4 °C prior to harvesting. The filter was washed three times with 100 mL (approximately 1 mL/well) of ice cold incubation buffer and subsequently dried in a microwave for 2.5 minutes at medium power. Melt on scintillator sheets (MeltiLex™ B/HS, PerkinElmer) were melted into the filter using a heating plate set to 120 °C. After hardening at room temperature, the filter was sealed in a plastic sample bag (PerkinElmer). Accumulation of tritium was immediately counted in a Wallac MicroBeta® TriLux liquid scintillation counter (PerkinElmer). Radioactivity was plotted against ^{3}H-labeled compound concentration. Data points were fitted

using nonlinear regression analysis in GraphPad Prism (GraphPad Software, Inc., version 7.03, La Jolla (CA), USA). Saturation binding experiments were performed as three independent experiments using three technical replicates for TB and NSB in each experiment.

Radiosynthesis of [^{11}C]MODAG-001 and (d_3)-[^{11}C]MODAG-001

[^{11}C]CO_2 was produced on a PETtrace 860 cyclotron (GE Healthcare, Uppsala, Sweden) and reacted to [^{11}C]MeI using a Tracerlab FX MeI module (GE Healthcare) according to the manufacturer's recommendations. A Tracerlab FX M module (GE Healthcare) was used for radiomethylation, HPLC purification and formulation. Depending on the required tracer amount and A_m, either direct methylation (high A_m) or reductive methylation (high yield) was applied. For direct methylation, the alkylating reagent was bubbled through a solution of 1 mg of precursor **7a** (nondeuterated or deuterated) in 500 µL of DMSO at 18 °C. The methylation reaction was performed for five minutes at 110 °C. For reductive methylation, the alkylating reagent was bubbled through a solution of 5 mg of Me_3NO and 1 mg of precursor in 350 µL of diethyl formamide at -25 °C. The mixture was heated to 60 °C for three minutes and subsequently cooled to 40 °C. $NaBH_3CN$ (7.6 mg) in a mixture of 60 µL of diethyl formamide and 1.2 mL of 100 mM citrate-phosphate buffer (p*H* 5) was added and heated to 100 °C for five minutes. After labeling, the reaction was subjected to semipreparative HPLC on a Synergi Max-RP column (4 µm, 80 Å, 250 mm × 10 mm, Phenomenex, Aschaffenburg, Germany) with 55 % MeCN in water at a flow rate of 6 mL/min. The HPLC fraction containing the product was diluted with 30 mL of water and loaded onto a Sep-Pak C8 Plus Light cartridge (Waters, Milford, MA, USA). The product was eluted with 0.3 mL of ethanol and diluted with 3 mL of PBS.

Quality control and measurement of A_m were performed on a 1260 Infinity HPLC system (Agilent Technologies, Waldbronn, Germany). An analytical Luna Phenyl-Hexyl column (5 µm, 100 Å, 300 mm × 4.6 mm, Phenomenex) was used for separation, with 30 % MeCN in 0.1 % aqueous trifluoroacetic acid at an isocratic flow rate of 1.5 mL/min. The carrier content was calculated from linear regression of a calibration curve of the nonradioactive standard molecule.

Fibril inoculation into the rat brain

Rats were allowed to adapt for two weeks in the animal facility before fibril injection. Three adult female rats were anaesthetized with an intraperitoneal (i.p.) injection of a mixture of fentanyl (0.005 mg/kg), midazolam (2 mg/kg), and medetomidine (0.15 mg/kg) at 1 mL/kg. The head of each rat was shaved, and the animal was placed into a stereotaxic frame. A

central incision was made to expose the bregma and lambda. A 5 µL syringe needle (Hamilton Company, Reno (NV), USA) was enclosed with a glass capillary (inner diameter, 50 µm, Hilgenberg GmbH, Malsfeld, Germany). αSYN fibrils (4 µL, 30 µM) were injected using a stereotaxic injector (Stoelting, Wood Lane, IL, USA) through a drill hole into the right striatum (ML= -3.2 mm, AP = 0.0 mm, DV = -4.8 mm) according to the stereotaxic atlas of Paxinos and Watson [9][. Based on the volume of the right striatum (0.04 cm^3), the concentration of inoculated fibrils was calculated as 2.8 µM. As a negative control, 4 µL of vehicle (50 mM Tris base, 100 mM sodium chloride, 0.02 % sodium azide, p*H* 7.0) were injected into the contralateral striatum. A total fibril volume of 4 µL was obtained by the injection of 0.4 µL every 60 seconds. To allow for diffusion of the fibrils into the tissue, the needle was left in this position for five minutes. Before slowly retracting the needle from the brain (0.5 mm/10 s), it was withdrawn 0.2 mm (DV) and maintained for another minute. The incision was closed, and a subcutaneous antidote injection of atipamezole (0.75 mg/kg) and flumazenil (0.2 mg/kg) was administered.

PET data acquisition and analysis

Dynamic PET data were acquired for 60 minutes and divided into 39 time frames (12×5 s, 6×10 s, 6×30 s, 5×60 s and 10×300 s). A transmission measurement using a cobalt-57 point source was performed for 13 minutes after PET data acquisition for attenuation correction. The data were reconstructed into a dynamic PET image using the reconstruction algorithm OSEM3D.

Whole body mouse PET scans were coregistered to the whole body MR scan, which was sequentially acquired after the PET scan, and the volumes of interest (VOIs) of the lung, liver, heart, brain, and kidneys were drawn by hand based on the MR anatomical information using PMOD software (version 3.2; PMOD Technologies, Zürich, Switzerland). VOIs of different brain regions were extracted using the mouse or rat brain atlas provided by PMOD [10-12], and tissue time activity curves (TACs) were calculated and are expressed as standardized uptake values (SUVs), which were calculated as follows: SUV(t) = radioactivity concentration (kBq/mL of the organ)/(injected dose [kBq]/body weight [g]). For inoculated rats, an additional VOI was placed over the right striatum using the isocontour tool adjusted to 70 % of the peak counts of hot spots, which was copied to the left control striatum with the mirroring tool. Distribution volume ratio 1 (DVR-1) values were calculated from individual TACs from 40 to 60 minutes, using the vehicle-injected striatum as a reference region, with the following formula: activity in fibril inoculated right striatum/activity in vehicle injected left striatum) - 1. The mean SUV from 40 to 60 minutes between the right, fibril inoculated striatum and contralateral, vehicle injected striatum was tested for significance using a two

sided t test. All fibril-inoculated rats were sacrificed under CO_2 after PET acquisition and subsequently perfused with 100 mL of cold PBS. Brains were dissected and immediately frozen in 2-methybutane on dry ice.

Thioflavin S staining

Coronal cryosections (30 µm) of fibril-inoculated rats were air-dried at room temperature and stored at -20 °C until further use. For thioflavin S staining, sections were allowed to thaw for 30 minutes at room temperature, fixed for 15 minutes in 4.5 % formaldehyde, washed three times for five minutes each in PBS and rinsed for one minute in 60 % and then 80 % ethanol. Sections were subsequently incubated for 15 minutes in 0.1 % thioflavin S (Sigma-Aldrich Chemie GmbH) dissolved in 80 % ethanol. After one-minute rinses in 80 % ethanol and 60 % ethanol and two washes in PBS for five minutes each, the slides were mounted with Eukitt quick-hardening mounting medium (Sigma-Aldrich Chemie GmbH) and allowed to dry overnight. Whole-brain images of the stained sections were captured using the FITC filter settings (excitation, 460 nm-500 nm; emission, 512 nm-542 nm) of a Leica DMi8 microscope interfaced with Leica LAS X software (Leica Microsystems CMS GmbH, Wetzlar, Germany).

Metabolite analysis

A 400 µL blood sample was collected by heart puncture five or 15 minutes after tracer injection. The blood was centrifuged at 17,000 x g and 4 °C for two minutes, and the plasma was transferred to a 1.5 mL reaction tube on ice for further analysis. After blood collection, mice were transcardially perfused (10 mL/min) with 20 mL of ice-cold PBS, and the brain of each mouse was removed from the skull. The brain was transferred to a glass tube (2 mL Dounce tissue grinder set, Sigma Aldrich Chemie GmbH) containing 0.5 mL of ice-cold PBS, sequentially homogenized using large and small clearance pestles and transferred to a 1.5 mL reaction tube on ice for further analysis. Plasma or brain homogenate was mixed 1:1 with acetonitrile and briefly centrifuged. After two minutes of incubation on ice, each mixture was centrifuged at room temperature for 1.5 minutes at 12,000 x g (MiniSpin®, Eppendorf AG) to remove precipitated proteins. The supernatant was subjected to reversed-phase HPLC on a Luna Phenyl Hexyl column (5 µm, 100 Å, 300 mm x 4.6 mm, Phenomenex) equipped with a radioactivity detector with 0.1 % trifluoroacetic acid in water/acetonitrile (70:30) at an isocratic flow rate of 1.5 mL/min.

For data analysis, the median of ten consecutive data points was calculated to remove noise; data were corrected for radioactive decay to time zero, defined as start of the HPLC of the five minute brain sample. This time zero radioactivity was plotted against time using Origin software (OriginLab Corporation, version 9.1G, Northampton, MA, USA). The area under the

curve was calculated in % using the peak analyzer function and scaled up that the peaks add up to 100 %. The area under the curve was transformed into radioactivity values using a standard of [^{11}C]MODAG-001 with known radioactivity also corrected for decay and expressed as % injected radioactivity dose (%ID) per gram of brain tissue or per plasma in one mL of blood.

MRI

Whole-body anatomical MR images of the mice were acquired on a 7T small animal MRI scanner (Bruker BioSpin GmbH, Ettlingen, Germany) following PET data acquisition. Anesthetization of the animals was maintained with 1.5 % isoflurane evaporated in 100 % oxygen at a flow rate of 0.8 L/min. A rat whole-body coil (Bruker BioSpin GmbH) was used for MR measurements in mice. After the mouse was positioned in the center of the FOV, a Turbo RARE T2 (TR/TE 800 ms/35.1 ms; FoV, 37.4 mm $\times$ 85.8 mm $\times$ 22.8 mm; matrix, 144 $\times$ 256 $\times$ 92) sequence was used to acquire the anatomical image of the body.

In vitro autoradiography

The defrosted human sections were preincubated in incubation buffer (50 mM Tris-base, 10 % ethanol, 0.05 % Tween80, p*H* 7.4) for 25 minutes at room temperature. Subsequently, the sections were incubated in 3 nM [^{3}H]MODAG-001 for total binding (TB). Nonspecific binding (NSB) of the radiotracer was determined by coincubation of consecutive slices with 50 µM nonradioactive MODAG-001 dissolved in DMSO (final concentration 0.5 %). After incubation for 60 minutes at room temperature, the sections were washed three times for ten minutes in ice-cold incubation buffer and dipped for three seconds in deionized water. The sections were dried overnight in a desiccator filled with powdered paraformaldehyde at room temperature. Slides were then exposed to phosphor imaging plates (BAS-IP TR2025, Fuji Imaging Plate, VWR, Denmark) with a tritium standard (American Radiolabeled Chemicals, St. Louis, MO, USA) for seven days and scanned in a phosphor imager (BAS-5000, FUJIFILM Life Science, Stamford, CT, USA), and the images were displayed with Image Gauge version 4.0 (Science Lab 2001, FUJIFILM Life Science, Stamford, CT, USA). For data quantification, rectangular regions of interest (ROIs) were placed over the tritium standards to obtain a standard curve for the quantification of radioactivity concentrations. Next, four rectangular ROIs per slice were placed into the cortex of each case to calculate TB and NSB. Specific binding (SB) values were calculated by subtracting the calculated NSB values from the TB values interpolated from the standard curve and converted to pmol/mg.

Continuous sucrose gradient centrifugation

For continuous sucrose gradient centrifugation 10 % (w/v) brain homogenates were prepared in 50 mM Tris-base, 175 mM NaCl, 1 mM $MgCl_2$, 0.1 mM PMSF, 1 mM NEM, 0.1 % Nonidet P-40 Substitute (Sigma-Aldrich, Taufkirchen, Germany), protease inhibitor (cOmplete, Mini, EDTA-free Protease Inhibitor Cocktail, Hoffmann-La Roche, Basel, Switzerland), p*H* 7.5. Aliquots of the homogenate were frozen in liquid nitrogen and stored at -80 °C. Total protein concentration was determined by BCA assay (Sigma-Aldrich, Taufkirchen, Germany). For the sucrose gradient analysis 50 µL of the homogenate were used. To this end, the brain homogenate was thawed on ice and diluted in 50 mM Tris-base, 175 mM NaCl, 0.1 % *N*-lauroylsarcosine sodium salt (sarcosyl), 0.1 % Nonidet P-40 Substitute (Sigma-Aldrich), p*H* 7.5. The samples were agitated at 1,200 rpm (ThermoMixer C, Eppendorf) and 4 °C for 30 minutes. Sucrose gradients were prepared in 4-mL 11 × 60 mm polyallomer tube (Beckman Coulter, Krefeld, Germany). 200 µL of 60 % sucrose solution in 50 mM Tris-base, 0.1 % sarcosyl, p*H* 7.5 were pipetted into the tube followed by 400 µL of 50, 40, 30, 20 and 10 % sucrose solutions in 50 mM Tris-base, 0.1 % sarcosyl, p*H* 7.5. Then, 200 µL of the homogenate samples were pipetted as uppermost layer onto the gradient. The samples were ultracentrifuged in a SW 60 Ti rotor (Beckman Coulter, Krefeld, Germany) at 40,000 rpm and 4 °C for one hour. Twelve fractions of 200 µL each were collected from the top to the bottom of each tube and subjected to trichloroacetic acid (TCA) precipitation (10 % TCA) overnight at -20 °C. After thawing, samples were centrifuged at 25,000 g and 4 °C for 15 minutes. The precipitates were washed once with acetone (-20 °C), centrifuged at 25,000 × g and 4 °C for 15 minutes, and finally resuspended in Laemmli sample buffer. Samples were boiled at 96 °C for five minutes and subjected to SDS-PAGE and Western Blotting. A primary antibody against αSYN (4B12, BioLegend, San Diego, CA, USA), a secondary HRP-coupled antibody (Cell Signaling Technology, Inc., Danvers, MA, USA), and Clarity ECL substrate (Bio-Rad Laboratories, Hercules, CA, USA) were used for protein detection. Signals were quantified with ImageJ (US National Institutes of Health, Bethesda, MD, USA).

Supplemental Results

Fibril characterization

αSYN fibrils were straight and arranged in bundles with an average length of 152.5 ± 76.6 nm (n = 135). In contrast, hTau46 fibrils showed less clustering or stacking and an average length of 453.4 ± 261.9 nm (n = 154). $A\beta_{1-42}$ fibrils had an average length of 139.4 ± 77.3 nm (n = 71) and were arranged mainly in clusters (Supplemental Fig. S 2).

Supplemental figures

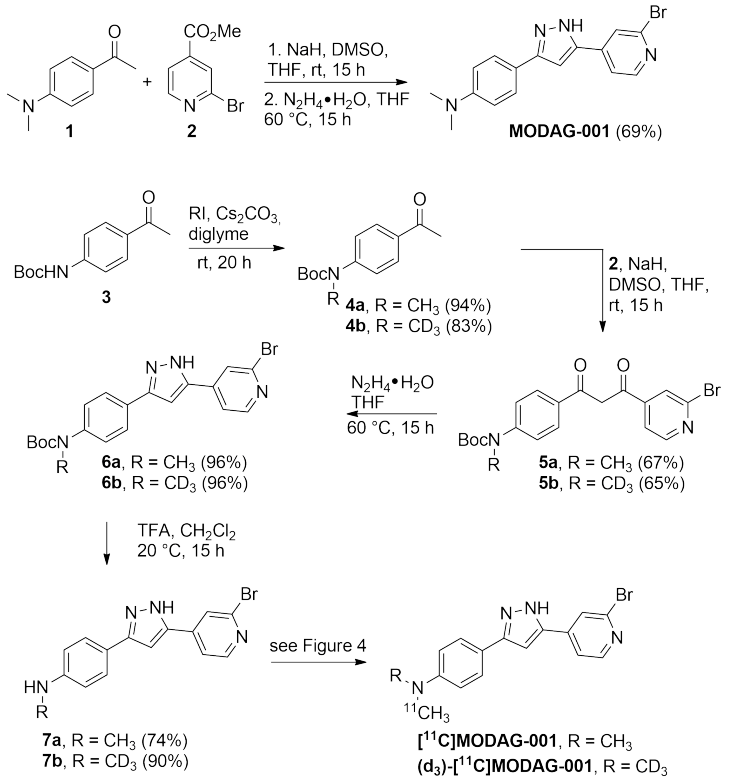

Supplemental Fig. S 1 Synthesis of MODAG-001 and (d_3)-MODAG-001

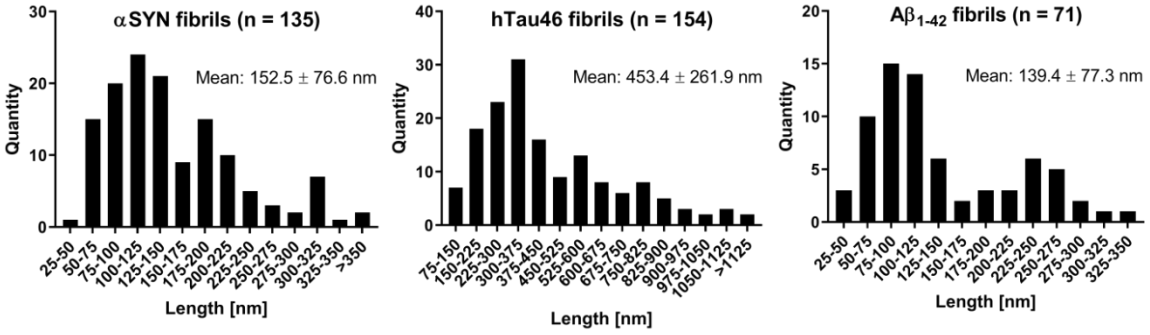

Supplemental Fig. S 2 Quantification of αSYN (a), hTau46 (b) and $A\beta_{1-42}$ (c) fibril length using negative stain electron microscopy

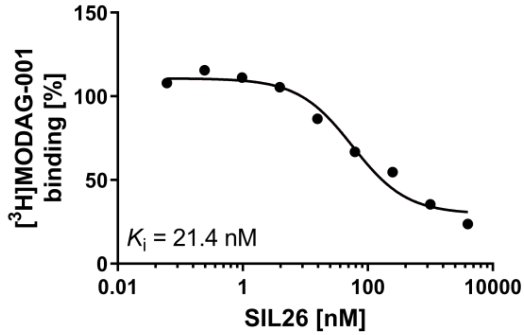

Supplemental Fig. S 3 SIL26 competition assay using 1 nM [^{3}H]MODAG-001. Non-linear regression analysis revealed a K_i of 21.4 nM

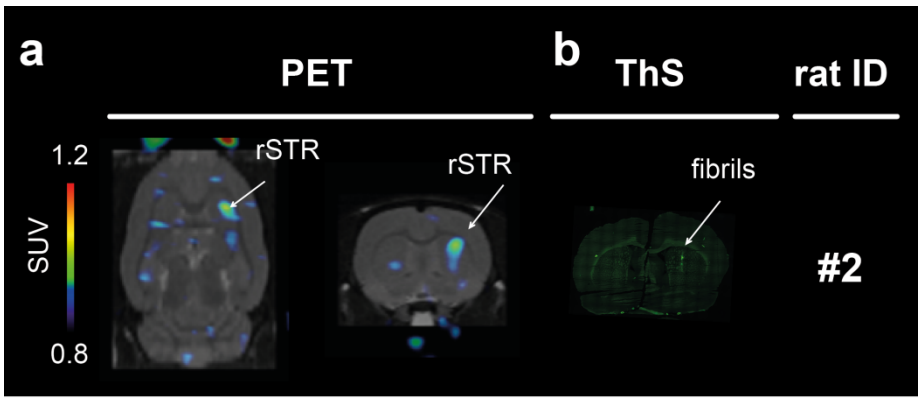

Supplemental Fig. S 4: *In vivo* binding of (d_3)-[^{11}C]MODAG-001 in the α-synuclein-inoculated rat #2 shown in figure 7 of the manuscript (a). Coronal and transversal PET images are shown using a SUV of 0.8 to 1.2 of the PET images to remove the unspecific signal for a better visualization of the specific binding signal. Images are summed up from 2.5 to 60 minutes. Thioflavin S staining (b) confirmed the location of αSYN fibrils (white arrow) in the right striatum of the fibril inoculated rat.

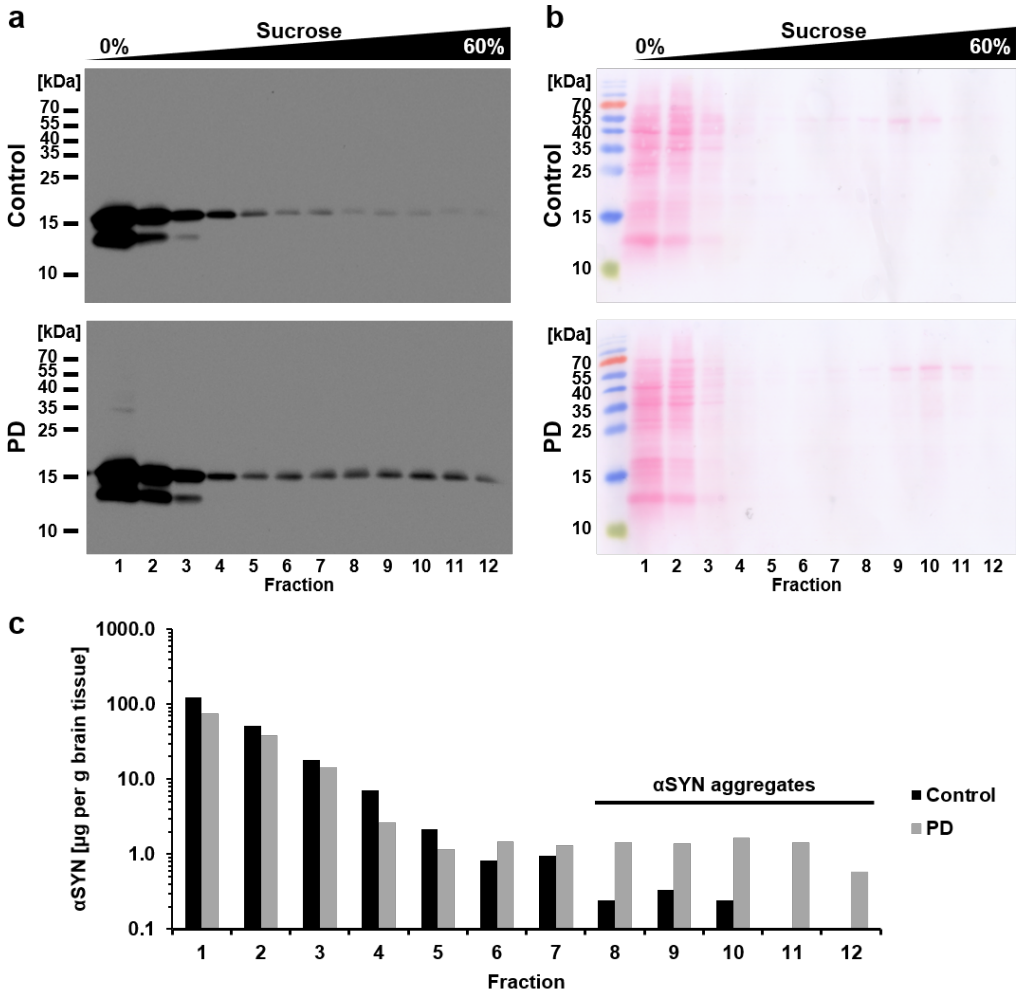

Supplemental Fig. S 5 Quantification of the amount of aggregated αSYN in a PD brain using sucrose gradient centrifugation. αSYN was detected by Western blotting using the 4B12 antibody (a) and quantified (c). Total protein was stained with Ponceau S (Carl Roth, Karlsruhe, Germany) (b)

References

1. Tago T, Furumoto S, Okamura N, Harada R, Ishikawa Y, Arai H et al. Synthesis and preliminary evaluation of 2-arylhydroxyquinoline derivatives for tau imaging. J Labelled Comp Radiopharm. 2014;57(1):18-24. doi:10.1002/jlcr.3133.

2. Maurer A, Leonov A, Ryazanov S, Herfert K, Kuebler L, Buss S et al. (11) C Radiolabeling of anle253b: a Putative PET Tracer for Parkinson's Disease That Binds to alpha-Synuclein Fibrils in vitro and Crosses the Blood-Brain Barrier. ChemMedChem. 2019. doi:10.1002/cmdc.201900689.

3. Deeg AA, Reiner AM, Schmidt F, Schueder F, Ryazanov S, Ruf VC et al. Anle138b and related compounds are aggregation specific fluorescence markers and reveal high affinity binding to alpha-synuclein aggregates. Biochim Biophys Acta. 2015;1850(9):1884-90. doi:10.1016/j.bbagen.2015.05.021.

4. Goedert M, Jakes R, Spillantini MG, Hasegawa M, Smith MJ, Crowther RA. Assembly of microtubule-associated protein tau into Alzheimer-like filaments induced by sulphated glycosaminoglycans. Nature. 1996;383(6600):550-3. doi:10.1038/383550a0.

5. Bagchi DP, Yu L, Perlmutter JS, Xu J, Mach RH, Tu Z et al. Binding of the radioligand SIL23 to alpha-synuclein fibrils in Parkinson disease brain tissue establishes feasibility and screening approaches for developing a Parkinson disease imaging agent. PLoS One. 2013;8(2):e55031. doi:10.1371/journal.pone.0055031.

6. Hudson SA, Ecroyd H, Kee TW, Carver JA. The thioflavin T fluorescence assay for amyloid fibril detection can be biased by the presence of exogenous compounds. FEBS J. 2009;276(20):5960-72. doi:10.1111/j.1742-4658.2009.07307.x.

7. Zhang X, Tian Y, Li Z, Tian X, Sun H, Liu H et al. Design and synthesis of curcumin analogues for in vivo fluorescence imaging and inhibiting copper-induced cross-linking of amyloid beta species in Alzheimer's disease. J Am Chem Soc. 2013;135(44):16397-409. doi:10.1021/ja405239v.

8. Auld DS, Farmen MW, Kahl SD, Kriauciunas A, McKnight KL, Montrose C et al. Receptor Binding Assays for HTS and Drug Discovery. In: Sittampalam GS, Grossman A, Brimacombe K, Arkin M, Auld D, Austin CP et al., editors. Assay Guidance Manual. Bethesda (MD)2004.

9. Paxinos G, Watson CR, Emson PC. AChE-stained horizontal sections of the rat brain in stereotaxic coordinates. J Neurosci Methods. 1980;3(2):129-49. doi:10.1016/0165-0270(80)90021-7.

10. Ma Y, Hof PR, Grant SC, Blackband SJ, Bennett R, Slatest L et al. A three-dimensional digital atlas database of the adult C57BL/6J mouse brain by magnetic resonance microscopy. Neuroscience. 2005;135(4):1203-15. doi:10.1016/j.neuroscience.2005.07.014.

11. Mirrione MM, Schiffer WK, Fowler JS, Alexoff DL, Dewey SL, Tsirka SE. A novel approach for imaging brain-behavior relationships in mice reveals unexpected metabolic patterns during seizures in the absence of tissue plasminogen activator. Neuroimage. 2007;38(1):34-42. doi:10.1016/j.neuroimage.2007.06.032.

12. Schiffer WK, Mirrione MM, Biegon A, Alexoff DL, Patel V, Dewey SL. Serial microPET measures of the metabolic reaction to a microdialysis probe implant. J Neurosci Methods. 2006;155(2):272-84. doi:10.1016/j.jneumeth.2006.01.027.

NEUROSCIENCE

Functional PET/MRI reveals active inhibition of neuronal activity during optogenetic activation of the nigrostriatal pathway

Sabrina Haas[1]†, Fernando Bravo[1]†, Tudor M. Ionescu[1], Irene Gonzalez-Menendez[2,3], Leticia Quintanilla-Martinez[2,3], Gina Dunkel[1,3], Laura Kuebler[1], Andreas Hahn[4,5], Rupert Lanzenberger[4,5], Bettina Weigelin[1,3], Gerald Reischl[1,3], Bernd J. Pichler[1,3], Kristina Herfert[1]*

The dopaminergic system is a central component of the brain's neurobiological framework, governing motor control and reward responses and playing an essential role in various brain disorders. Within this complex network, the nigrostriatal pathway represents a critical circuit for dopamine neurotransmission from the substantia nigra to the striatum. However, stand-alone functional magnetic resonance imaging is unable to study the intricate interplay between brain activation and its molecular underpinnings. In our study, the use of a functional [fluorine-18]2-fluor-2-deoxy-D-glucose positron emission tomography approach, simultaneously with blood oxygen level–dependent functional magnetic resonance imaging, provided an important insight that demonstrates an active suppression of the nigrostriatal activity during optogenetic stimulation. This result increases our understanding of the molecular mechanisms of brain function and provides an important perspective on how dopamine influences hemodynamic responses in the brain.

INTRODUCTION

The dopaminergic circuitry is instrumental in numerous essential functions within the nervous system, orchestrating processes related to motor control, reward processing, cognitive functions, and emotional regulation. Its dysfunction has been implicated in a variety of neurological and psychiatric disorders, including Parkinson's disease (PD), schizophrenia, drug abuse, and attention-deficit hyperactivity syndrome (*1*). As one of the principal neuromodulatory systems in the brain, the dopaminergic system is subject of intense studies, and understanding this complex circuitry is pivotal for elucidating the underlying mechanism of these diseases and for developing targeted therapies. Consequently, the accurate characterization of this circuitry, including its biochemical, structural, and functional aspects, has become vital for both basic research and clinical applications, offering prospects for improved diagnostics and tailored interventions.

In vivo imaging technologies have greatly advanced our understanding of neuronal circuits at the whole-brain level. Two powerful noninvasive tools that have emerged in this field are positron emission tomography (PET) and functional magnetic resonance imaging (fMRI). Recent developments have led to the integration of PET and MRI into hybrid systems offering remarkable opportunities for comprehensive investigations (*2*–*7*). By integrating [^{18}F]2-fluor-2-deoxy-D-glucose (FDG)–PET with blood oxygen level–dependent (BOLD)–fMRI, our approach leverages the strengths of both modalities to offer a perspective on the dynamic interactions within the dopaminergic system under optogenetic manipulation. This integration enables us to map out the metabolic and hemodynamic responses, providing a multifaceted view of the neuronal and physiological processes that underlie the functioning of the dopaminergic system, addressing some limitations of existing methods such as microdialysis, fast-scan cyclic voltammetry, fiber photometry, and [^{11}C]raclopride PET. Microdialysis, while effective in measuring neurotransmitter levels in brain interstitial fluid, is hampered by low temporal resolution and spatial restriction to a single target area. Techniques such as fast-scan cyclic voltammetry and fiber photometry excel in real-time monitoring of dopamine release with high temporal resolution but are limited to small, localized regions. In contrast, our integrated [^{18}F]FDG-PET/BOLD-fMRI approach provides noninvasive, whole-brain coverage, capturing dynamic changes of the dopaminergic system without disrupting tissue integrity. This method elucidates their impact on overall brain energy metabolism and blood flow, offering a holistic understanding of brain function. In addition, while [^{11}C]raclopride, [^{18}F]fluoro–L-dopa, and [^{11}C]methylphenidate effectively assess dopamine receptor/transporter availability (*8*, *9*) and extracellular dopamine release (*10*), the tracers fall short in detailing downstream regional responses. By combining [^{18}F]FDG-PET glucose metabolism measurements with BOLD-fMRI blood flow assessments, our approach elucidates the energetic and vascular underpinnings of dopaminergic neurotransmission, providing unprecedented detail and enhancing our understanding of the dopaminergic system. The insights gained from this research could advance our understanding of the molecular and systemic mechanisms of the dopaminergic system, with important implications for diagnosing and treating neuropsychiatric disorders.

There is a growing body of evidence suggesting a potential decoupling between metabolic and hemodynamic signals using

[1]Department of Preclinical Imaging and Radiopharmacy, Werner Siemens Imaging Center, Eberhard Karls University Tuebingen, Tuebingen, Germany. [2]Institute of Pathology and Neuropathology, Comprehensive Cancer Center, Eberhard Karls University of Tuebingen, Tuebingen, Germany. [3]Cluster of Excellence iFIT (EXC 2180) "Image Guided and Functionally Instructed Tumor Therapies", Eberhard Karls University of Tuebingen, Tuebingen, Germany. [4]Department of Psychiatry and Psychotherapy, Medical University of Vienna, Vienna, Austria. [5]Comprehensive Center for Clinical Neurosciences and Mental Health (C3NMH), Medical University of Vienna, Vienna, Austria.
*Corresponding author. Email: Kristina.herfert@med.uni-tuebingen.de
†These authors contributed equally to this work.

simultaneously acquired PET/fMRI (*5*, *11*), implying that conventional imaging methods may fail to provide a comprehensive or completely accurate representation of the neuronal activity within the brain. This raises the fundamental question whether we can capture the complete picture of dopaminergic activity and its downstream pathways using stand-alone imaging techniques.

To explore this compelling question, we initiated a study using optogenetic stimulation (OGS), a cutting-edge method for precisely manipulating neuronal activity (*12*). We hypothesized that this approach might unveil hidden dimensions of neuronal functioning, including potential silencing mechanisms, which have been reported by other techniques (*13*), and that stand-alone imaging methods might overlook. BOLD-fMRI, with its superior spatial and temporal resolution compared to [^{18}F]FDG-PET, which has been improved to study task-related brain activation in a single functional PET (fPET) session (*14*), each provides unique insights. Previous studies combining [^{18}F]FDG-PET and BOLD-fMRI in rats during an electrical whisker stimulation paradigm revealed regional overlaps and mismatches in brain activation pattern between the two modalities (*15*, *16*). However, these data were not simultaneously acquired, as different stimulation paradigms and time points were used for PET and fMRI.

Here, we introduce an innovative approach, fusing OGS with fully simultaneous fPET/fMRI measurements in rats. Our findings not only enhance our understanding of inhibitory mechanisms during neuronal activation but also underscore the efficacy of hybrid PET/MRI systems in studying brain function. These insights offer an important contribution to the field, encouraging further exploration and refining our comprehension of the dopaminergic system.

RESULTS

BOLD signal suppression in dopamine-innervated brain regions during substantia nigra pars compacta stimulation

To delineate the nigrostriatal system and investigate selective dopaminergic modulatory effects on neuronal activity and glucose metabolism, we performed simultaneous in vivo BOLD-fMRI/[^{18}F]FDG-fPET scans in rats, overexpressing either channelrhodopsin-2 (ChR2) or green fluorescent protein (GFP) control virus in the right substantia nigra (SN) pars compacta (SNc), during OGS (Fig. 1, A and B). To allow for a within-group fPET data analysis, we applied [^{18}F]FDG as a bolus plus constant infusion to maintain constant activity concentrations in the brain. This technique was first applied to identify task-relevant brain networks in human studies but has not been applied in rodent brain imaging yet (*16*, *17*). We started laser stimulation 20 min after beginning the simultaneous fPET/fMRI acquisition using a block design with 10-min stimulation blocks and 3-min rest between the blocks. We further divided each stimulation block into 60-s light-on and 15-s light-off periods.

fMRI data analysis was performed in ChR2- and GFP-injected animals by modeling each of the 10-min stimulation blocks using a canonical hemodynamic response function. For between-group analysis, a comparison between ChR2 and GFP animals was performed to control for nonspecific effects of the OGS. For the

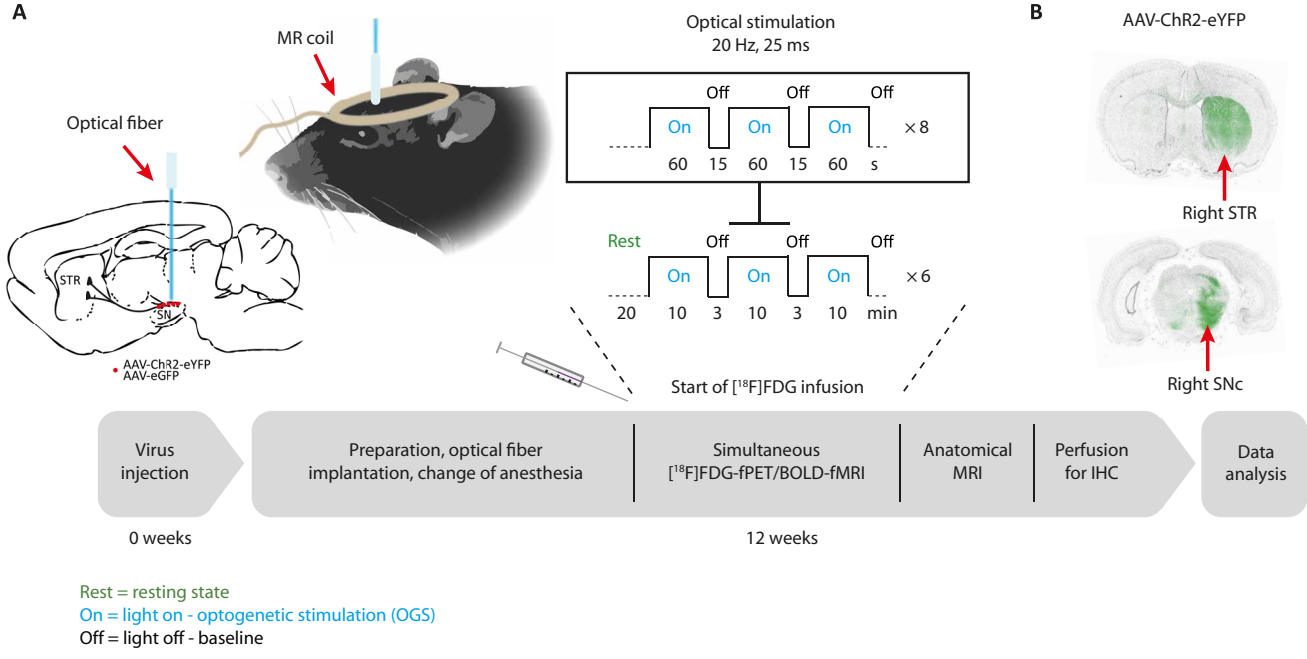

Fig. 1. The time course and study protocol of simultaneous optogenetic [^{18}F]FDG-fPET/BOLD-fMRI experiments are illustrated. (**A**) Adeno-associated virus (AAV)–ChR2 or AAV-GFP control virus was injected into the right SNc. Twelve weeks after viral vector injection, rats were catheterized and intubated. After fiber implantation, the [^{18}F]FDG-fPET/BOLD-fMRI experiments were acquired using an [^{18}F]FDG bolus-infusion protocol during optical stimulation of the SNc over 90 min using 6× 10-min stimulations and 3-min rest. Each 10-min stimulation block consisted of eight light-on and light-off phases. Within the on phase, a frequency of 20 Hz was set with a duty cycle of 50%, resulting in a pulse duration of 25 ms. After acquisition of an anatomical sequence, the rat brain was transcardially perfused for in vitro immunohistochemistry (IHC). (**B**) ChR2 and GFP control virus expression in the striatum (STR) and SNc was confirmed by fluorescence microscopy of ChR2–enhanced yellow fluorescent protein (eYFP) and enhanced GFP (eGFP).

within-group analysis, the 10-min stimulation blocks were compared against 3-min baseline blocks.

OGS of nigrostriatal neurons resulted in positive BOLD-signal changes in brain regions of the basal ganglia, namely, the right striatum, nucleus accumbens, amygdala, thalamus, and midbrain, as well as negative responses in the left striatum and right and left somatosensory cortex (S1). Figure 2 (A and B) shows activated voxels presented as colored *t* maps overlaid on an MRI rat brain atlas after between-group (n_{ChR2} = 18 and n_{GFP} = 12) and within-group (n_{ChR2} = 18) analysis [at thresholds of $P < 0.001$ voxel level–uncorrected and $P < 0.05$ cluster-level family-wise error (FWE)–corrected]. A list reporting mean *t* values and the percentage of activated voxels within a region after cluster-level FWE correction at $P < 0.05$ is shown in Table 1 for between- and within-group analyses.

Mean % BOLD signal changes are shown over a period of 400 s for selected brain regions (Fig. 2C). Sixty-second stimulation blocks are highlighted in gray. We found positive BOLD signal changes in several areas of the basal ganglia including in the ipsilateral (right) striatum, nucleus accumbens, amygdala, and midbrain during the 60-s stimulation periods (on phase). However, the BOLD signal increase was rather low during stimulation, while we observed a robust BOLD signal overshoot after termination of the stimulation in the ipsilateral (right) striatum, nucleus accumbens, and amygdala, which went back to baseline within the 15-s rest period (off phase).

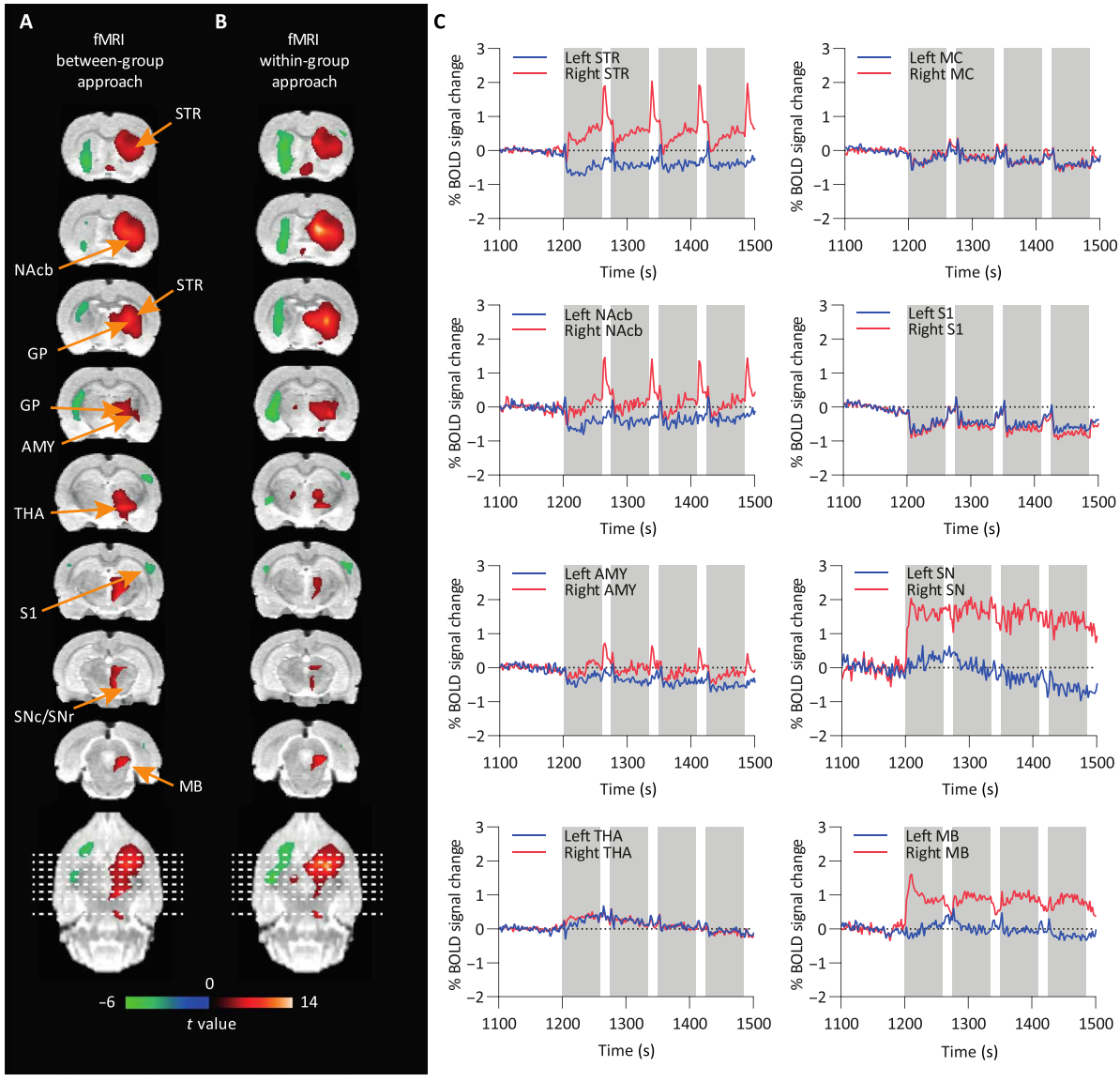

Fig. 2. BOLD-fMRI *t*-activation maps reveal significant neuronal responses following OGS of the SNc. (**A**) Between-group [ChR2 (n = 18) versus GFP (n = 12)] and (**B**) within-group comparisons (ChR2, stimulation versus rest, n = 18) are shown. Positive (red) and negative (green) BOLD responses are shown (FWE-corrected $P < 0.05$ for cluster-level inference). (**C**) BOLD signal time courses from different brain regions. Gray bars indicate 60-s stimulation on periods. STR, striatum; AMY, amygdala; MB, midbrain; MC, motor cortex; S1, somatosensory cortex; NAcb, nucleus accumbens; THA, thalamus; GP, globus pallidus, SNc/SNr, substantia nigra pars compacta/pars reticulata.

Table 1. Percentage of significant voxels per ROI and mean *t* values in fMRI. Results shown at uncorrected $P < 0.001$ with cluster-level FWE-corrected $P < 0.05$. Asterisk markings show areas with significant signal changes at voxel-level FWE-corrected $P < 0.05$. EC, entorhinal cortex; HIP, hippocampus; INS, insular cortex; OC, olfactory cortex; OFC, orbitofrontal cortex; PAG, periaqueductal gray; SC, superior colliculus; Sep, septum.

	Between-group approach positive BOLD		Between-group approach negative BOLD		Within-group approach positive BOLD in ChR2		Within-group approach negative BOLD in ChR2	
Brain region (ROI)	**Activated voxels (%)**	**Mean *t***	**Activated voxels (%)**	**Mean *t***	**Activated voxels (%)**	**Mean *t***	**Activated voxels (%)**	**Mean *t***
R AMY	2.0	3.9 ± 0.3			3.6	4.1 ± 0.4		
L AMY			0.2	3.4 ± 0.02			6.0	4.0 ± 0.2
R EC					0.01	3.7 ± 0.0		
L EC			0.1	3.6 ± 0.2			0.4	3.9 ± 0.2
L HIP anterior			0.9	3.6 ± 0.1			0.2	3.8 ± 0.1
R HIP posterior	0.4	4.2 ± 0.7						
R HYP	17*	4.9 ± 1.3			15*	4.5 ± 0.6		
R INS					0.1	3.9 ± 0.1		
L INS							0.3	4.1 ± 0.2
R MB	3.4*	4.7 ± 0.6			22*	5.3 ± 1.0		
L MC			0.1	3.5 ± 0.04			0.3	3.8 ± 0.1
R NAcb	2.2	3.7 ± 0.2			4.0	4.1 ± 0.3		
L NAcb			18	4.0 ± 0.3			18	4.4 ± 0.4
L OC			0.9	3.6 ± 0.2				
R OFC	0.2	3.6 ± 0.1			0.2	4.0 ± 0.2		
L OFC							1.1	4.1 ± 0.2
PAG	2.4	3.7 ± 0.2			2.7	4.1 ± 0.4		
R S1					0.02	4.1 ± 0.1		
L S1							1.1	3.9 ± 0.2
R SC					2.7*	4.9 ± 0.9		
Sep	17*	4.8 ± 1.0			33*	6.2 ± 2.1		
R SN	3.6*	5.0 ± 0.9			2.3	4.3 ± 0.4		
R STR	67*	5.0 ± 1.2			66*	5.3 ± 1.5		
L STR			31	3.9 ± 0.4			58	4.3 ± 0.4
R THA	53*	4.7 ± 0.7			40*	5.1 ± 1.2		
L THA					0.9	4.3 ± 0.5		

Negative BOLD signal changes appeared in the contralateral (left) striatum, nucleus accumbens, amygdala, ipsi- and contralateral motor cortex, and S1. Mean BOLD signal time courses of all ChR2 rats are shown over the whole scan time for selected regions in fig. S1. In GFP control rats, we did not observe responses to stimulation in the BOLD signal time courses (fig. S2A). The BOLD signal time course of one exemplary ChR2 and GFP rat is further plotted over the whole scan time in fig. S3A.

Activation of the nigrostriatal pathway revealed by [^{18}F]FDG-fPET within-group analysis

To directly compare hemodynamic responses from fMRI with metabolic responses from fPET, we established a within-animal PET analysis that allows us to compare activation versus baseline in the same animal. For this, we applied both the general linear model (GLM) described previously (*16*, *18*) and the independent component analysis (ICA) approach as within-sample methods to examine the OGS data. ICA has already been applied to [^{18}F]FDG-fPET data to investigate brain glucose metabolism and connectivity during task-related designs (*17*, *19*). We used the aforementioned strategy (*19*) and further performed an automatic sorting of the resulting components based on spatial kurtosis (i.e., spatial sparseness), an approach that proved effective in isolating task-related components without the use of stimulus timing information (*20*–*22*). The OGS component map appeared as the first-ranked component with the highest kurtosis value (9.47), revealing significant [^{18}F]FDG uptake during stimulation in the right SN, right midbrain, right thalamus, right hypothalamus, and right striatum. Additional parameters derived from component's voxel value distribution, including skewness (a measure of the asymmetry of the distribution), spatial variability (a widespread/clustering measure), and frequency (the center of mass in spectral power), are shown in Table 2 (see table S1 for descriptive measures for all 20 components). Alternatively, the OGS component can also be identified for its lowest frequency content, following the power spectrum ranking method (*23*).

Figure 3 shows activated voxels as colored *t* maps overlaid on an MRI atlas using between-group (Fig. 3A), GLM within-group (Fig. 3B), and ICA within-group (Fig. 3C) analyses ($n_{ChR2} = 16$ and $n_{GFP} = 14$) of

Table 2. ICA. Descriptive measures derived from the independent component's voxel value distribution.

Component	Kurtosis	Skewness	Variability	Frequency
OGS (via highest kurtosis sorting)	9.4702	1.5296	0.89649	0.015126

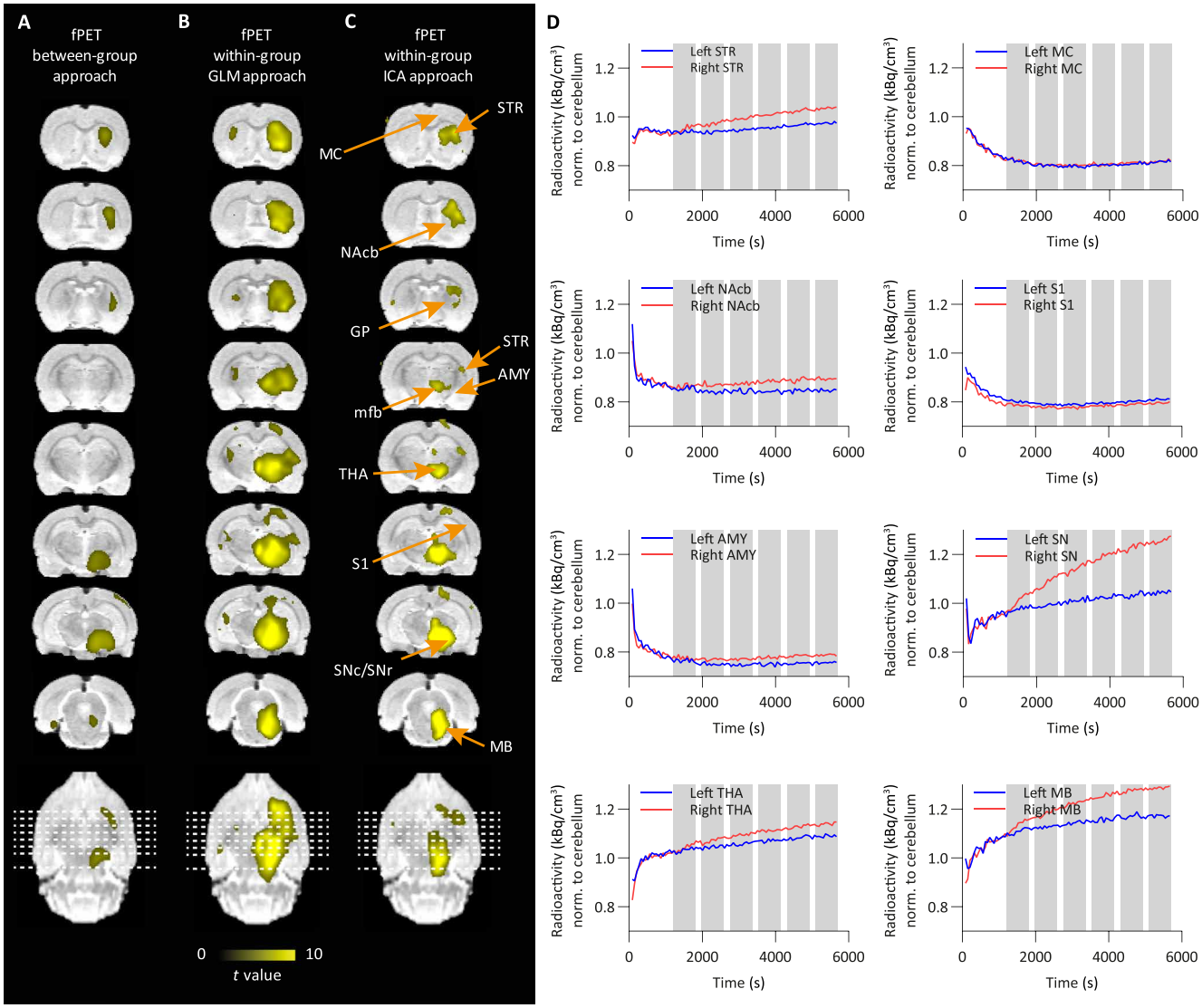

Fig. 3. [^{18}F]FDG-fPET *t* activation maps display metabolic responses following optogenetic SNc stimulation. (**A**) Between-group [ChR2 ($n = 16$) versus GFP ($n = 14$)], (**B**) GLM within-group (ChR2, stimulation versus rest, $n = 16$), and (**C**) ICA within-group (ChR2, stimulation versus rest, $n = 16$) comparisons are shown. Positive responses (yellow) are shown (FWE-corrected $P < 0.05$ for cluster-level inference). (**D**) [^{18}F]FDG time-activity curves from different brain regions (gray bars indicate 10-min stimulation blocks). Right, ipsilateral; left, contralateral.

[^{18}F]FDG-fPET data (at thresholds of $P < 0.001$ voxel level–uncorrected and $P < 0.05$ cluster-level FWE-corrected). In contrast to MRI, we did not observe any negative signal changes in the [^{18}F]FDG-fPET data. A list reporting mean *t* values and the percentage of activated voxels within a region is shown in Table 3.

During OGS, the GLM approach yielded increased [^{18}F]FDG uptake in similar areas as after using the between-group and ICA within-group approaches (right SN, right midbrain, right hypothalamus, and right striatum). In addition, the GLM strategy showed strong uptake in the right insular cortex, thalamus, right hippocampus posterior, left hypothalamus, right orbitofrontal cortex, pituitary gland, and right amygdala.

Mean normalized time-activity curves of all ChR2-expressing rats are shown over the whole scan time for selected brain regions.

Table 3. Percentage of significant voxels per ROI and mean *t* values in fPET. Results shown at uncorrected $P < 0.001$ with cluster-level FWE-corrected $P < 0.05$. Asterisk markings show areas with significant signal changes at voxel-level FWE-corrected $P < 0.05$. AUD, auditory cortex; PG, pituitary gland; RS, retrosplenial cortex; V1, visual cortex.

	Between-group approach		Within-group GLM approach		Within-group ICA approach	
Brain region (ROI)	**Activated voxels (%)**	**Mean *t***	**Activated voxels (%)**	**Mean *t***	**Activated voxels (%)**	**Mean *t***
R AMY	9.7*	4.6 ± 0.8	11*	5.0 ± 1.0	0.8	5.1 ± 0.9
R AUD			2.5	4.5 ± 0.6		
R EC	0.5	3.9 ± 0.4	1.0	4.4 ± 0.6		
R HIP anterior			5.0	4.2 ± 0.4	0.7	3.9 ± 0.2
L HIP anterior			6.1	4.1 ± 0.3		
R HIP posterior	13*	4.6 ± 0.8	34*	5.6 ± 1.2	6.0	4.8 ± 0.8
L HIP posterior			5.8	4.2 ± 0.4		
R HYP	24*	4.5 ± 0.7	48*	7.2 ± 2.3	36*	7.5 ± 3.0
L HYP			3.4*	5.4 ± 1.4	4.4	4.5 ± 0.5
R INS			10*	5.6 ± 1.8	2.7	4.8 ± 1.0
R MB	21.2*	4.4 ± 0.8	97*	7.7 ± 2.1	68*	7.1 ± 2.1
R MC			0.6	4.1 ± 0.3		
R NAcb			12	4.9 ± 0.8	2.3	4.3 ± 0.5
R OFC			7.1*	5.3 ± 1.2		
PG	3.9	3.9 ± 0.3	7.7*	5.2 ± 1.1	16	4.9 ± 1.0
R PAR			29	4.3 ± 0.4		
PAG	0.4	3.7 ± 0.2	26	5.0 ± 0.8	9.8*	5.1 ± 1.0
R RS			1.1	4.0 ± 0.3		
R S1			3.3	4.4 ± 0.5	0.5	4.4 ± 0.6
R SC			7.0	4.4 ± 0.6		
Sep			0.9	4.1 ± 0.3		
R SN	87*	5.8 ± 1.0	100*	10.0 ± 1.2	98*	9.8 ± 2.8
L SN			11	4.7 ± 0.7	1.9	4.8 ± 0.5
R STR	27*	4.3 ± 0.6	94*	6.5 ± 1.5	50*	4.9 ± 0.9
L STR			6.6	4.2 ± 0.3		
R THA	0.7	3.8 ± 0.3	74*	6.7 ± 2.0	24*	5.3 ± 1.3
L THA			4.1*/3.6	4.7 ± 0.8/3.9 ± 0.2	0.3	4.0 ± 0.1
R V1			2.7	3.9 ± 0.1		

Ten-minute stimulation blocks are highlighted in gray (Fig. 3D). We observed a gradual increase of [^{18}F]FDG during the stimulation in the ipsilateral (right) striatum nucleus accumbens, thalamus, SN, and midbrain compared to the contralateral side, while little to no changes were observed in the amygdala, motor cortex, and S1. Mean normalized time-activity curves of all GFP-expressing rats are shown over 95 min for selected regions (fig. S2B). No changes between the left and right hemisphere of the selected brain regions were observed in the GFP group.

[^{18}F]FDG activity of one exemplary ChR2 and GFP rat is plotted over the whole scan time in fig. S3B. [^{18}F]FDG showed an increased accumulation in the ipsilateral (right) striatum compared to the contralateral (left) striatum in the ChR2 rat, while no differences between the ipsilateral (right) and contralateral (left) striatum were found in the GFP rat, confirming a stimulation-induced increase in [^{18}F]FDG metabolism.

Uncoupling of hemodynamic and metabolic responses to SNc stimulation

After validation of the within-group fPET analysis, we next aimed to compare hemodynamic and metabolic responses induced by nigrostriatal pathway activation. Figure 4 (A and B) shows a comparison of activated voxels from BOLD-fMRI and [^{18}F]FDG-fPET as colored *t* maps overlaid on an MRI atlas (between- and within-group comparisons) (at threshold $P < 0.001$ voxel level–uncorrected and $P < 0.05$ cluster-level FWE-corrected). For within-group fPET, we show the results from the data-driven ICA approach (ICA with kurtosis/frequency sorting), which does not require a priori information, as is the case for the GLM fPET approach. Figure 4C shows a comparative analysis of the BOLD-fMRI and [^{18}F]FDG-PET responses across five key regions during OGS of the SNc. This analysis offers insights into the distinct patterns of neural activation and suppression induced by dopaminergic modulation. PET and fMRI data

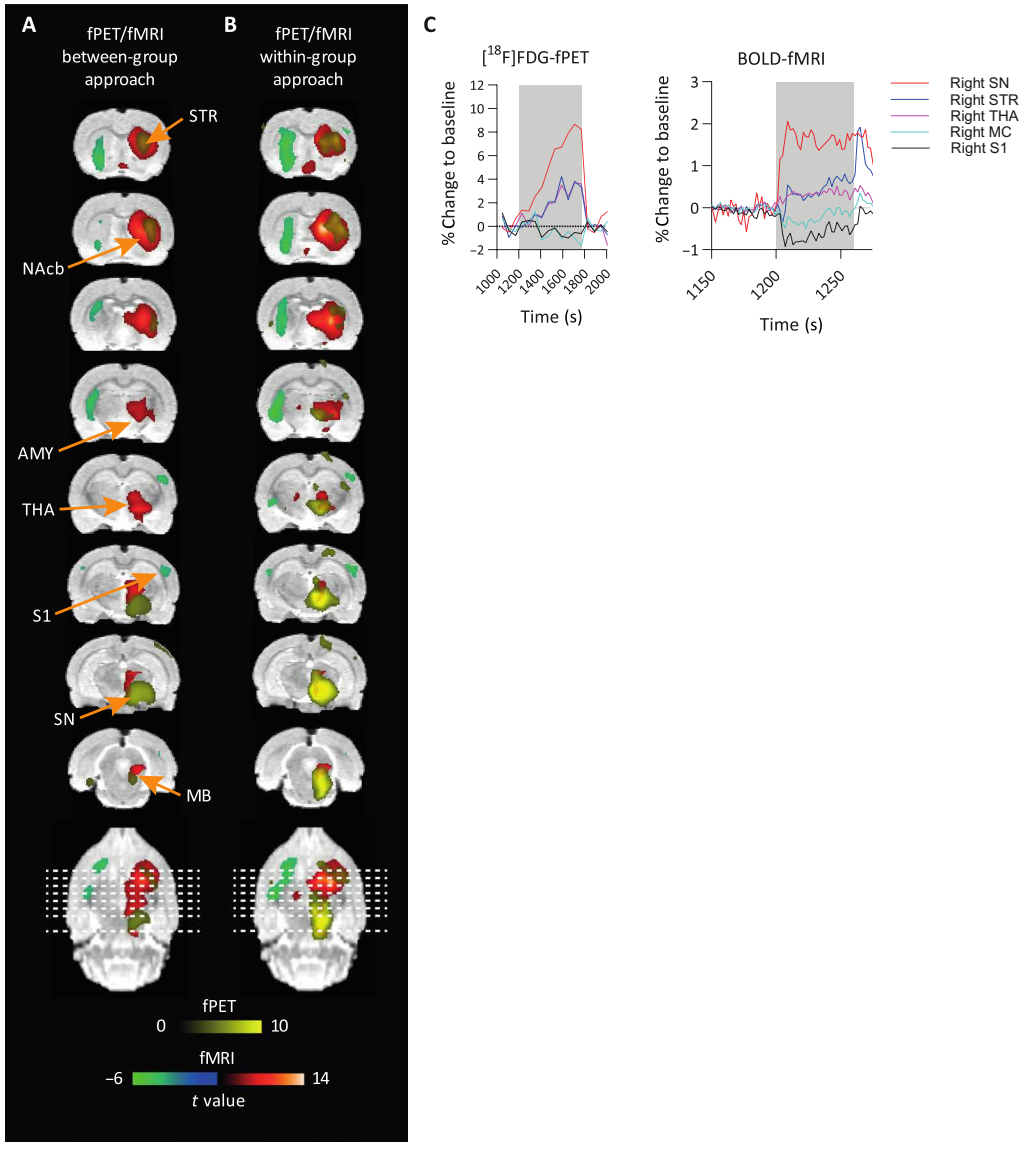

Fig. 4. Overlay of [^{18}F]FDG-fPET and BOLD-fMRI activation maps highlights the spatial and temporal differences in neuronal responses following OGS of SNc. (**A** and **B**) An overlay of significantly activated and deactivated areas (FWE-corrected $P < 0.05$ for cluster-level inference) after OGS of the SNc in fPET and fMRI is shown in colored overlays on a rat brain atlas. Activated areas in fMRI are depicted in red, deactivated areas in fMRI are depicted in green, and activated areas in fPET are depicted in yellow. The spatial extension of activated areas between modalities differs. (**C**) BOLD and [^{18}F]FDG time courses in percent change from baseline, shown as mean values. A small stimulation block of 60-s on/15-s off for fMRI and a 10-min stimulation block for fPET are shown.

revealed an immediate signal increase at the side of the stimulation in the SN, followed by delayed activations in the striatum and thalamus, contrasting with a negative BOLD-fMRI response in the primary motor cortex and S1.

Dice similarity coefficients were calculated to quantify overlapping voxels of both modalities (table S2). Within-group analysis revealed six overlapping regions: right striatum, right nucleus accumbens, right insular cortex, right thalamus, right S1, and right hypothalamus. Largest differences were observed in the spatial extension, most predominantly in the right striatum and right SN. Independent of the approach, BOLD-fMRI activation maps of the striatum show a larger spatial extension than fPET activation maps, while the opposite was observed in the SN. This is also confirmed when comparing the percentage of activated voxels per region presented in Tables 1 and 3 (within-group approach: striatum, 66% versus 50%; SN, 2.3% versus 98%). Coordinates of peak *t* values were extracted from regions of interest (ROIs) activated in both modalities to quantify the distance of the respective activation centers (table S2).

Predictive neuronal activity in the SN revealed by multivariate pattern analysis

Following the minimal BOLD response in the SN yielded by the univariate within-sample analysis, we used multivariate pattern analysis (MVPA) to test whether sufficient information about the neural response to the OGS (versus baseline) would be contained in

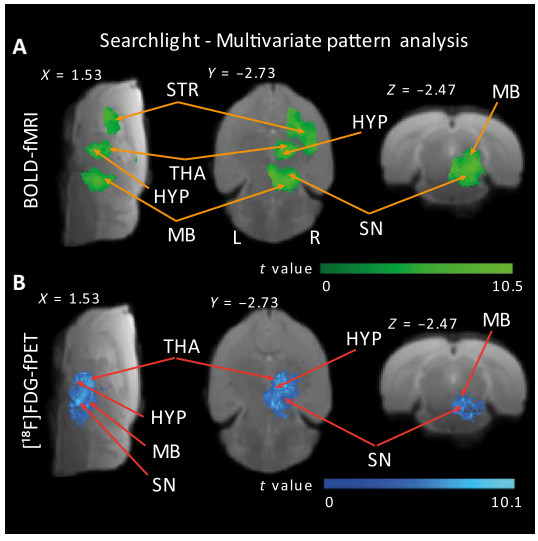

Fig. 5. Classification searchlight analysis identifies brain regions where OGS is distinguishable from baseline activity across the whole brain. Colored voxels indicate centers of searchlights for the fMRI (**A**) and fPET (**B**) datasets, where the classifier could successfully discriminate between OGS and baseline signal patterns. Searchlight classification of >65% and whole-brain cluster-corrected $P < 0.05$ via comparison with 1000 random permutations. Sagittal, axial, and coronal views were selected to highlight the largest clusters containing information maps; for detailed results, see table S6. HYP, hypothalamus; L, left; R, right.

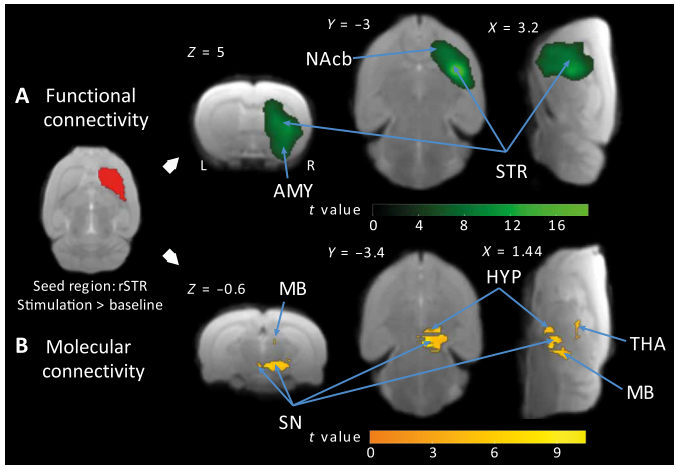

Fig. 6. OGS of the SNc modulates functional and molecular connectivity within key brain regions. (**A**) Green color identifies voxels in the right striatum, nucleus accumbens, and amygdala, which exhibited stronger functional connectivity with the seed region (right striatum) for the contrast OGS versus baseline. (**B**) Yellow color identifies voxels upstream the nigrostriatal pathway showing a stronger metabolic coupling with the seed region for the contrast OGS versus baseline (results shown at FWE-corrected $P < 0.05$ for cluster-level inference).

signal patterns of voxels within the SN. MVPA allows to evaluate differences between conditions with higher sensitivity than conventional univariate analysis by focusing on the analysis and comparison of distributed patterns of activity (*24*, *25*). We performed MVPA at a whole-brain level using SpaceNet classifiers (*26*) and searchlight (*27*) on both the fMRI and the fPET datasets. In addition, we conducted an ROI MVPA analysis that specifically targeted the SN. We tested the statistical significance of the prediction accuracy using a permutation test: Assuming that there is no class information in the data, the labels defining the conditions can be permuted without altering the expected accuracy using a given classifier and number of features (i.e., this would equal chance level). We performed 1000 permutations of a leave-one-subject-out cross-validated MVPA (*28*). The whole-brain fMRI and fPET MVPA results showed that information maps were distributed across right-lateralized voxels within the entire nigrostriatal pathway (table S5), with focal points including the SN, suggesting that the joint activity of voxels within the SN contained sufficient information about the OGS in both the fMRI and the fPET datasets (Fig. 5, fig. S7, and table S5). Further support was provided by the ROI-MVPA analysis centered on the SN, which yielded high prediction accuracies: 82.41% ($P < 0.001$) for the fMRI data and 69.27% ($P < 0.001$) for the fPET data.

Although to a lesser extent, discriminative information maps were also identified in left-lateralized regions such as the thalamus, hypothalamus, nucleus accumbens, and amygdala (table S6), confirming that the classifiers were not merely detecting univariate differences between the stimulation and baseline conditions. This indicates that the multivariate analyses exhibited greater sensitivity in discriminating between the stimulation and baseline categories.

To summarize, although the univariate fMRI analysis revealed a minimal BOLD response in the SN, multivariate pattern analyses substantiated that hemodynamic and glucose uptake signal changes within the right SN remained predictive and capable of distinguishing between OGS and baseline trials.

Functional isolation of the striatum during OGS

Subsequent to the observation of a BOLD signal suppression during the OGS and a subsequent overshoot after stimulation cessation within the right striatum, nucleus accumbens, and amygdala (Fig. 2C), we carried out functional and molecular connectivity analyses to test whether the abovedescribed idiosyncratic signal changes could unveil a regulatory mechanism that would functionally isolate the striatum from other brain regions including areas upstream in the nigrostriatal pathway, in response to the OGS. We performed seed-based connectivity analyses (*29*) on both the fMRI and the fPET datasets to evaluate connectivity differences between OGS and baseline blocks.

Since the striatum receives axonal projections from SN dopaminergic neurons that corelease the two neurotransmitter γ-aminobutyric acid (GABA) and dopamine (*30*–*32*), possibly involved in the hypothesized isolation mechanism, we specifically sought to characterize connectivity differences in response to the OGS using the right striatum as the seed region. While the molecular connectivity analysis showed the expected strong metabolic coupling between the right striatum and upstream nigrostriatal pathway brain regions, such as the right thalamus, hypothalamus, midbrain, and SN during the OGS (compared to baseline), the functional connectivity analysis primarily revealed within-seed interactions (i.e., with voxels in the right striatum), extending to neighboring voxels in the nucleus accumbens and the amygdala. These results seem to evidence a metabolically active isolation mechanism, initiated by the OGS on areas receiving dopaminergic inputs, which could serve to functionally isolate the right striatum for areas upstream the nigrostriatal pathway (Fig. 6 and table S6).

Reduced SNc activity confirmed by c-fos immunohistochemistry

To understand the mismatch between hemodynamic and metabolic responses in the two main regions, we performed c-fos$^+$ stainings in the striatum and the SN. We found an increased c-fos expression in the right dorsal striatum of ChR2 rats compared to the left dorsal striatum and compared to ipsi- and contralateral dorsal striata of GFP rats (see Fig. 7A and fig. S4). However, no differences in c-fos expression levels were observed between the right and left SN (Fig. 7, B and C, and table S3). This result supports an inhibition of the neuronal activity in the SN during stimulation, a metabolically active process, resulting in high glucose demand.

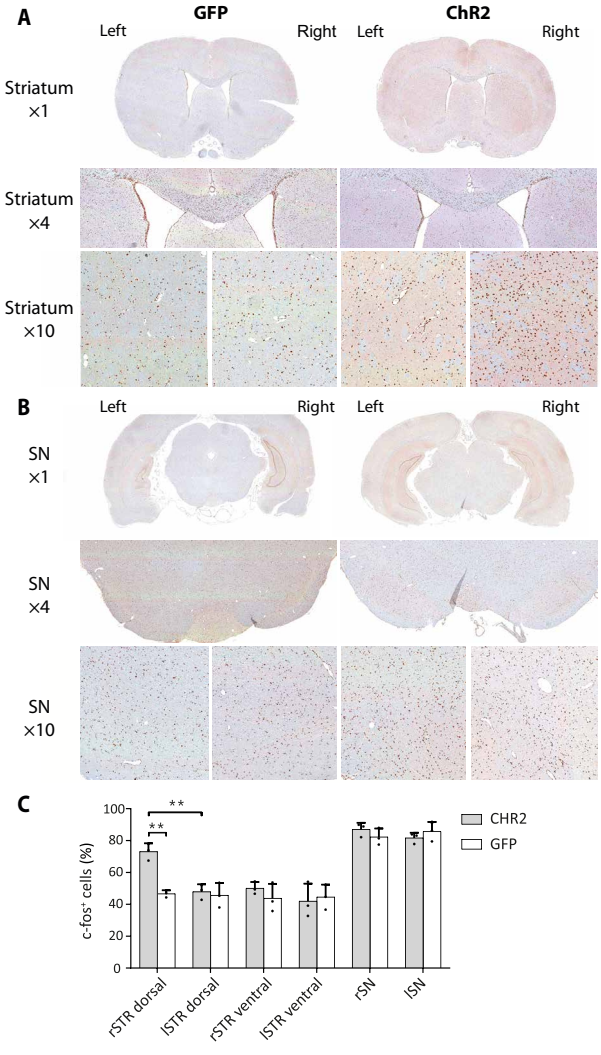

Fig. 7. c-fos immunohistochemical staining reveals increased neuronal activation in the striatum but not SN following OGS. (**A**) c-fos staining in one exemplary ChR2 and GFP rat is illustrated for one selected region of the dorsal striatum in ×1, ×4, and ×10 magnifications. A higher number of c-fos$^+$ cells were identified in the ×4 and ×10 magnifications of the right striatum of the exemplary ChR2 rat. (**B**) c-fos staining in one exemplary ChR2 and GFP rat is illustrated for one ROI of the SN in ×1, ×4, and ×10 magnifications. (**C**) The percentage of c-fos$^+$ cells is increased in the right dorsal striatum of the three selected ChR2-expressing rats compared to the left dorsal striatum ($P = 0.0036$, Welch's t test) of the ChR2-expressing rats and compared to the right dorsal striatum ($P = 0.0061$) of the three selected GFP-expressing rats. $^{**}P < 0.01$.

Exclusion of virus-induced neurotoxic effects via tyrosine hydroxylase staining

We further performed in vitro validation of neuronal integrity to exclude any viral- or stimulation-induced neurotoxicity in the SN and striatum. The tyrosine hydroxylase (TH) immunohistochemistry (IHC) in the SN revealed abundant TH$^+$ neurons and its projections but without qualitative differences between the right and left sides in both GFP- and ChR2-expressing rats (fig. S5). In addition, massive presence of TH$^+$ fibers was detected in the striatum, which is known to be a major postsynaptic target of the SN. In the striatum, the TH IHC did not reveal any qualitative differences in the dorsal/ventral and right/left striatum between GFP- and ChR2-expressing rats.

DISCUSSION

fMRI and fPET are two valuable imaging techniques used in neuroscience research to study neuronal activation. In this study, we used an OGS of the dopaminergic pathway using simultaneous BOLD-fMRI and [^{18}F]FDG-fPET imaging in the rat brain. The findings reveal important insights into both temporal and molecular aspects of brain function.

To enable within-group comparison of fPET data in rats, we used an [^{18}F]FDG bolus + constant infusion protocol. In this study, we validated the application of ICA as a data-driven approach for analyzing rat fPET data acquired during OGS in rats. By automatically sorting components according to spatial kurtosis (*21*, *22*), we identified the [^{18}F]FDG uptake map for the OGS component as the first kurtosis-ranked component. This was supported by a GLM-based approach, which identified consistent signal changes, thereby fostering efficient future studies by reducing the need for large control groups. Furthermore, we demonstrated the application of MVPA (*33*) on fMRI and fPET data, enabling the examination and comparison of distributed activity patterns to discern differences between conditions.

A distinct discovery of our study was that we observed a BOLD signal suppression during the stimulation and a subsequent overshoot after the cessation of the OGS within the right striatum, nucleus accumbens, and amygdala. Functional and molecular connectivity analyses provided evidence for a metabolically active isolation mechanism elicited in the aforementioned regions, which was modulated by the OGS. The fact that these brain areas are acknowledged recipients of dopaminergic inputs prompted us to suggest a potential role of dopamine in this mechanism.

Although MVPA showed that hemodynamic and glucose uptake signal changes within the right SN could discriminate between OGS and baseline trials, we observed only a minimal BOLD response in the SN in our univariate analysis when compared to fPET. To corroborate our observations, we conducted an ex vivo analysis of c-fos expression in both the striatum and the SNc. We found increased c-fos expression levels in the dorsal striatum, which receives input from the SNc, but we did not find discernible differences in the SNc. This occurred despite a high metabolic demand in the stimulated region. Dopamine release is modulated by numerous neuromodulators (*34*). One interpretation posits that OGS triggers the release of dopamine thereby activating dopamine D2 auto- and heteroreceptors and

inhibiting further activation-induced dopamine release (*35*, *36*). This process may curtail the maximum attainable BOLD signal increase during stimulation (*13*) and may be important to regulate neurotransmitter levels at the synapse. This control is essential for the effective operation of the dopaminergic system. Upon termination of the stimulation, the presynaptic autoinhibition is lifted, leading to the BOLD signal overshoot. Although autoreceptors have been known for many years, the complexity of mammalian central nervous system circuits makes it difficult to isolate this mechanism from other neurotransmitter effects. In addition, several studies have shown that GABA is coreleased from dopaminergic neurons (*30*, *31*) and that this corelease acts as an early responder to dampen phasic-to-tonic dopamine signaling via ionotropic GABA type A receptors (*32*). Other models propose the role of GABAergic interneurons in autoinhibition by providing local feedback inhibition (*37*, *38*). Our observations of a relatively low BOLD response and an overshot immediately following the cessation of stimulation align with the autoreceptor model.

A key feature of the basal ganglia architecture is the division of incoming information into two distinct pathways: the direct and indirect pathways (*39*). Neurons in the direct pathway predominantly express the D1 dopamine receptor, whereas neurons in the indirect pathway express the D2 dopamine receptor (*40*, *41*). These receptors have opposing effects when bound to dopamine, influencing intracellular G protein messengers and subsequent changes in cellular excitation.

The classic theory, known as the "Go/No-go" model, posits that the direct and indirect pathways of the basal ganglia work antagonistically to facilitate and inhibit action, respectively (*42*–*44*). Conversely, other models suggest that the direct pathway selects the desired action, while the indirect pathway inhibits other competing actions, thereby emphasizing the chosen action (*45*–*47*). Each theory is supported by various behavioral, physiological, and imaging studies. Nevertheless, the exact mechanisms by which the direct and indirect pathways of the basal ganglia operate together still remain controversial and not fully understood (*48*).

Since dopamine has been shown to have a higher affinity to the dopamine D2 receptor ($K_d = 25$ nM) (*49*) than for the dopamine D1 receptor ($K_d = 1.6$ μM) (*49*), it is often assumed that they respond differently to tonic and phasic dopamine release (*41*, *50*). PET/MRI studies have shown that the combination of both makes up the fMRI signal (*51*, *52*). According to this model, low-affinity D1 receptors detect phasic, high-amplitude dopamine increases, while D2 receptors detect low-amplitude tonic dopamine increases (*53*). The negative BOLD response observed in the primary motor cortex and S1 in our study aligns with this model and may be explained by an enhanced inhibition of thalamic output due to a predominance of indirect pathway activation, which reduces cortical excitation. However, recent findings also show an activation of D2 receptors during phasic dopamine release (*54*, *55*). The impairment of dopamine and GABA corelease may also explain involuntary movements, so called L-dopa–induced dyskinesia, a side effect of long-term L-dopa treatment, where corelease of GABA is not achieved and D2 autoreceptors are not present on serotonergic neurons that take up the L-dopa due to the loss of dopaminergic neuronal projections (*56*, *57*). Thus, therapeutic strategies in PD should focus on restoring dopaminergic and GABAergic autoreceptor function in the striatum.

Alongside the positive BOLD signals, we observed stimulation-induced negative BOLD responses. These were not associated with a relative decrease in [^{18}F]FDG in any brain region, a finding consistent with previous research in (*11*). While positive BOLD responses were accompanied by increased glucose metabolism, the authors observed that negative BOLD responses in regions of the default mode network did not show reduced glucose metabolism during a working memory task. Subsequent work demonstrated that this dissociation between negative BOLD response and glucose metabolism is dependent on the corresponding task-positive networks (*58*). Negative BOLD responses are considered to be a consequence of increased deoxyhemoglobin concentrations (*59*, *60*). These increases in deoxyhemoglobin occur during increased oxygen consumption compared to a constant cerebral blood flow or during decreased cerebral blood flow compared to a higher, stable, or only slightly reduced oxygen consumption. The precise physiological origin of the negative responses remains debated with theories including the "vascular steel" effect (*61*, *62*), the "vascular sharing" effect (*63*–*65*), and regional extremely high oxygen consumption resulting from strong neuronal activation that cannot be balanced by cerebral blood flow increases (*62*). In addition, neurotransmitter release might provoke neurovascular responses that can eventually affect the BOLD signal (*66*, *67*). A recent study further suggests that opioidergic neurotransmission contributes to negative BOLD-fMRI signals in the striatum (*68*). We hypothesize that neurotransmitter and vasoactive effects play a crucial role in the positive and negative responses, but further studies are needed to pinpoint the exact molecular mechanisms.

We further observed metabolic and hemodynamic changes in similar regions, yet differences were found in the spatial extent, location of the regional activation center, proportion of overlapping voxels, and significance of activated regions between the two modalities. For instance in the within-group approach, BOLD-fMRI revealed 15 activated brain regions and 9 regions with a negative BOLD response, while [^{18}F]FDG-fPET revealed 16 activated brain regions. Of these regions, nine showed activation in both modalities, with six regions having overlapping voxels. The observed discrepancies between the two modalities can be attributed to their distinct physiological readouts. While [^{18}F]FDG is a marker of glucose consumption (metabolic response), the BOLD signal is driven by localized changes in blood flow and blood oxygenation (hemodynamic response). Although several studies indicate the highest glucose consumption in neurons at the synaptic level, our data also support high glucose consumption at the soma. In contrast to PET, MRI enables in vivo imaging with higher spatial resolution, typically in the range of 0.27 mm by 0.27 mm in plane for the applied echo planar imaging–BOLD sequence. However, vascular effects are not confined to the activation site, and larger vessels contribute more to the BOLD signal. Consequently, there is a widespread effect that limits spatial resolution and may result in a mislocalization of activation centers (*69*).

Our findings, while primarily focused on understanding the broader impact of nigral activity on brain function, also have potential implications for the diagnosis and treatment of PD. The ability of [^{18}F]FDG-PET to capture metabolic changes across the entire brain, beyond the striatum, provides valuable insights into the systemic effects of nigral-striatal dysfunction, which are characteristic of PD. While traditional dopaminergic tracers such as fluoro–L-dopa and dihydrotetrabenazine are highly effective in visualizing dopaminergic pathways, they predominantly highlight striatal changes and may overlook the broader network disruptions that contribute

to the full spectrum of PD symptoms. Our results suggest that [^{18}F]FDG-fPET, by providing a more comprehensive view of brain metabolism, could complement existing diagnostic tools by identifying changes in regions such as the thalamus, amygdala, and cortex, which are also involved in the disease process. Furthermore, understanding the metabolic consequences of dopamine and potentially GABA release in these regions could inform the development of new therapeutic strategies aimed at modulating activity across these broader networks, rather than focusing solely on the nigrostriatal pathway. This could lead to more effective treatments that address both motor and nonmotor symptoms of PD, ultimately improving patient outcomes.

One notable limitation of our study relates to the utilization of anesthesia, a common element in preclinical imaging studies. Anesthesia has the potential to affect vascular and metabolic responses, which can subsequently lead to alterations in the responsiveness to neuronal stimulations. Although medetomidine anesthesia has been proposed for small animal fMRI experiments in earlier research (*70*–*72*), it may elevate blood glucose levels (*73*, *74*), reducing the uptake of [^{18}F]FDG into the brain (*74*, *75*). Isoflurane, often used in [^{18}F]FDG-PET experiments, can also substantially influence the BOLD signal owing to its vasodilatory effect (*76*–*79*). Thus, in an effort to optimize the methodological approach, we selected α-chloralose anesthesia. This choice is based on its suitability for both modalities and its strong functional-metabolic coupling effects, which induce robust fMRI-BOLD activations even after weak stimulations, making it appropriate for [^{18}F]FDG-fPET imaging (*80*–*82*). However, older studies in *Xenopus* oocytes suggest that α-chloralose may potentiate GABA-induced currents, presumable through an interaction with GABA type A receptors (*83*, *84*). Since GABA has been shown to be coreleased from dopaminergic nerve terminals, it may induce an enhanced modulation on GABAergic activity that may be less pronounced in a conscious state. In addition, an older study in rats did not find an influence of α-chloralose on dopamine content and metabolism in the rat striatum (*85*). In the context of our study, we strived to mitigate potential confounding effects through consistent anesthesia protocols and by contrasting our stimulations to resting state periods in the same animals. Future studies designed to explore these interactions would be very valuable.

The present study identified pronounced activations in regions within the basal ganglia circuitry, including the striatum, thalamus, and cortex. We also detected increased activation in areas such as the amygdala, septum, hippocampus, periaqueductal gray, and orbitofrontal cortex. These findings might be attributed to the partial stimulation of ventral tegmental area dopamine neurons (*1*). In addition, our study did not involve the use of TH- or dopamine transporter (DAT)–Cre rats for selective dopaminergic stimulation. This means that OGS may have incidentally extended to areas such as the SN pars reticulata, located beneath the SNc.

Another limitations of our study is the use of a relatively long and intense stimulation protocol, which was chosen on the basis of pilot experiments to optimize signal detection in our [^{18}F]FDG-PET imaging. While this approach allowed us to capture robust metabolic changes across multiple brain regions, the strong and sustained nature of the stimulation may not accurately reflect physiological conditions encountered in typical brain function. This could potentially lead to exaggerated responses that might not be representative of normal dopaminergic activity. In addition, the prolonged stimulation differs from the shorter protocols commonly used in fMRI studies, which may limit the direct comparability of our findings with those obtained from other imaging modalities. These factors should be considered when interpreting the generalizability of our results, and future studies may benefit from exploring a range of stimulation intensities and durations to better understand their effects on brain function and metabolism. Furthermore, our study did not directly address how these findings apply to the clinical diagnosis and treatment of PD, which may require additional research using disease-specific models and parameters.

In conclusion, our study sheds light on the intricacies of the dopaminergic pathway, providing insights into the relationship between BOLD signals and metabolic responses. By using simultaneous optogenetic BOLD-fMRI and [^{18}F]FDG-fPET imaging, we were able to observe a complex interaction involving both hemodynamic and metabolic processes. This integrated approach may help in identifying specific patterns of brain activation. One such example could include the effects of deep brain stimulations in patients with PD, in which targeting the classical regions has been shown to be insufficient for improving the entire spectrum of PD symptoms in addition to the observed side effects (*86*). Using simultaneous [^{18}F]FDG-PET/BOLD-fMRI during neuronal stimulations may help to identify target regions to improve motor and nonmotor symptoms in PD. The findings and the application of cutting-edge techniques in this research offer a roadmap for future investigations into brain function. While the present study unveils the potential of these methods and uncovers interesting aspects of the neuronal mechanisms, it also emphasizes the need for further detailed research to unravel the complexities of the mammalian central nervous system circuits. Our results not only enhance the current understanding of the brain's neurotransmitter systems but also pave the way for more focused and nuanced explorations, especially regarding the interactions between different neurotransmitters and their effect on overall brain functionality.

MATERIALS AND METHODS

Experimental timeline

Figure 1A shows a simplified time course of the experimental procedures. We randomly divided the rats into two groups and injected an adeno-associated virus (AAV) vector containing either ChR2 ($n = 21$) or AAV-GFP ($n = 15$) rats into the right SNc. Twelve weeks after viral vector injection, we implemented an optical fiber above the SNc and performed simultaneous [^{18}F]FDG-fPET/BOLD-fMRI scans. We started the laser stimulation 20 min after start of the fPET/fMRI acquisition using a block design with 3-min rest between the blocks. The stimulation protocol used in this study was based on a study by Bass and colleagues (*87*) in which maximal peaks for dopamine release were observed at 20-, 30-, and 40-Hz frequency with 20-, 10-, and 4-ms light pulse widths, respectively. To achieve robust, reliable, and reproducible [^{18}F]FDG-PET and BOLD-fMRI signal response, we used long stimulation durations and high power.

We divided each 10-min stimulation block into 60-s on and 15-s off stimulation phases. Light frequency within the on phases was 20 Hz with a duty cycle of 50% and a resulting pulse duration of 25 ms. After the acquisition, we performed an anatomical MRI, subsequently transcardially perfused the rats, and harvested the brains for in vitro validation. We performed fluorescence microscopy to

confirm ChR2–enhanced yellow fluorescent protein (eYFP) and enhanced GFP (eGFP) viral vector expression in the striatum and SNc (Fig. 1B).

Animals

We conducted all animal experiments in compliance with the European directives on the protection and use of laboratory animals (Council Directive 2010/63/UE), with the German animal protection law, and with approval of the official local authorities (Regierungspräsidium Tübingen, permit number R 6/17). Male Long-Evans ($n = 36$) rats were purchased from Charles River Laboratories (Calco, Lecco, Italy). All rats were maintained in our vivarium on a 12:12-hour light-dark cycle and were kept at a room temperature with 40 to 60% humidity. Rats had free access to a standard diet and tap water.

During the time course of the experiment, nine rats were excluded from the data analysis due to technical or experimental failures: fiber implantation ($n = 3$), PET insert ($n = 3$), and MR ($n = 3$). During the study, the frequency bandwidth was changed because of a gradient coil exchange: 3 GFP and 5 ChR2 rats were scanned with a frequency bandwidth of 166,666.7 Hz; 9 GFP and 13 ChR2 rats were scanned with a frequency bandwidth of 119,047.6 Hz.

Stereotaxic viral vector injection

Before the viral vector injections, we allowed the rats to adapt for at least 2 weeks in the animal facility. We anesthetized each rat ($n = 36{,}375 \pm 27$ g) with an intraperitoneal injection of a mixture (1 ml/kg) of fentanyl (0.005 mg/kg), midazolam (2 mg/kg), and medetomidine (0.15 mg/kg). The head was shaved, and the animal was placed into a stereotaxic frame. A central incision was made to expose bregma and lambda. A 5-ml Hamilton syringe needle (Hamilton Company, Reno, NV, USA) was enclosed by a glass capillary (inner diameter, 50 ± 5 μm; Hilgenberg GmbH, Malsfeld, Germany). Stock solutions of pAAV-hSyn-hChR2(H134R)-EYFP (#26973; AAV5, 1.7×10^{13} gene copies/ml) or pAAV-hSyn-EGFP (#50465; AAV5, 1.2×10^{13} gene copies/ml) (Addgene Inc., Watertown, MA, USA) were diluted to 8.5×10^{11} gene copies/ml using phosphate-buffered saline (PBS) (Gibco, Life Technologies Inc., Carlsbad, CA, USA). Two microliters were slowly injected (0.1 μl every 15 s) through a drill hole into the right SNc [mediolateral, −2.0 mm; anterior-posterior, −5.0 mm; dorsoventral, −7.2 mm; according to the stereotaxic atlas of Paxinos and Watson (*88*)]. To allow for diffusion of the virus into the tissue, the needle was left in place for 5 min. Before slowly retracting the needle from the brain (3.5 mm/min), it was withdrawn to −7.0 mm (dorsoventral) for another 2 min. The incision was closed by four to five stitches, and a subcutaneous antidote injection of atipamezol (0.75 mg/kg) and flumazenil (0.2 mg/kg) was administered.

Simultaneous [^{18}F]FDG-fPET/BOLD-fMRI with OGS

Optical setup

A 473-nm laser (MBL-III–473 nm–100 mW, PhotonTec Berlin GmbH, Berlin, Germany) with a maximum output power of 100 mW equipped with an FC/PC fiber coupler having a numerical aperture of 0.22 was used for OGSs. The laser was connected (FC/PC MM Fiber Connector, 230 μm, Stainless Steel, Thorlabs, Newton, NJ, USA) to an approximately 6-m-long optical fiber (TECS-Clad multimode optical fiber, Thorlabs, Newton, NJ, USA) with a glass fiber core of 200 μm and a numerical aperture of 0.39. The FC/PC connector was assembled and polished in-house using four different polishing sheets sequentially: silicon carbide lapping 5-μm grit, aluminum oxide lapping 3- and 1-μm grit, and calcinated alumina lapping 0.3-μm grit (Thorlabs, Newton, NJ, USA). The implantable end of the fiber was stripped for at least 2.5 cm, and a ceramic ferrule (2.5-mm multimode ceramic ferrule and 231-μm bore size, Thorlabs, Newton, NJ, USA) was glued (LOCTITE 454, Henkel AG & Co. KGaA, Dusseldorf, Germany) around the bare fiber end. After drying, the length of the protruding fiber was cleaved to a length of at least 8.2 mm. The laser was coupled to a power supply unit (PSU-III-LED, PhotonTec Berlin GmbH, Berlin, Germany) with transistor-transistor logic (TTL) modulation up to 1 kHz. It was driven by a stimulus generator (STG 2004, Multi Channel Systems MCS GmbH, Reutlingen, Germany) controlled by a flexible software (MC_Stimulus II, Multi Channel Systems MCS GmbH, Reutlingen, Germany). Fiber output power was measured using a fiber optic power meter (PM20A, Thorlabs, Newton, NJ, USA) before each single scan.

Animal preparation

AAV-injected rats ($n_{ChR2} = 21$, $n_{Ctrl} = 15$, 12 ± 1 weeks after surgery, 510 ± 36 g) were fasted overnight. Anesthesia was induced with 5% isoflurane evaporated in air in an induction chamber. After loss of the righting reflex, isoflurane was maintained at 2.5 to 3% evaporated in air at a flow rate of 0.8 liter/min. The head was shaved, and a blood sample was collected by puncturing the tail vein for glucose determination (124 ± 13 mg/dl). One tail vein catheter was placed on each side for anesthesia and tracer infusions. Endotracheal intubation was performed using a self-made cannula and an external light source for correct placement of the tube. The small animal ventilator (DC1 73-3629, Harvard Apparatus, Holliston, MA, USA) was set to 60 breaths/min with an inspiration duration of 60% of the ventilation cycle. The end inspiratory pressure was set to approximately 12-cm H_2O and the flow to 500 ml/min. During preparation and surgery, animals were warmed by a heating pad.

Optical fiber implantation

The rat was placed into a stereotaxic frame. A central incision was made to expose bregma and lambda. The optical fiber was inserted through a drilled hole into the right SNc (mediolateral, −2.0 mm; anterior-posterior, −5.0 mm; dorsoventral, −7.1 mm; according to the stereotaxic atlas of Paxinos and Watson). Superglue was applied to fixate the ceramic ferrule to the skull. Isoflurane levels were slowly reduced after an initial bolus of 16 mg of α-chloralose (Sigma-Aldrich Chemie GmbH, Taufkirchen, Germany), followed by another bolus containing 5 mg of α-chloralose and 0.25 mg of pancuronium bromide (Inresa Arzneimittel GmbH, Freiburg, Germany). A constant infusion of α-chloralose (20 mg/kg per hour) and pancuronium bromide (1 mg/kg per hour) was started and maintained during the whole time course of the experiment along with 0.5% isoflurane evaporated in air.

[^{18}F]FDG-fPET/BOLD-fMRI

[^{18}F]FDG was synthetized using [^{18}O]water and the $^{18}O(p,n)^{18}F$ nuclear reaction described elsewhere (*89*). Simultaneous fPET/fMRI experiments were performed on a small animal 7-T MRI system (ClinScan, Bruker BioSpin MRI GmbH, Ettlingen, Germany) equipped with a small-animal PET insert, as previously described (*90*). A linearly polarized radio frequency coil (Bruker BioSpin MRI GmbH, Ettlingen, Germany) with an inner diameter of 72 mm was

used for signal excitation and a planar single loop surface coil with an inner diameter of 20 mm (Bruker BioSpin MRI GmbH, Ettlingen, Germany) was used as receiver coil. Rats were placed on a water-heated bed (MedRes, Cologne, Germany), connected to the small animal ventilator (DC1 73-3629, Harvard Apparatus, Holliston, MA, USA) and to a feedback temperature control unit (MedRes, Cologne, Germany) set to 36.5°C. The temperature was constantly monitored by a rectal probe; oxygen saturation and heartbeat were monitored using a MR compatible pulse oximeter (Bruker BioSpin MRI GmbH, Ettlingen, Germany).

Localizer images were acquired to position the rat brain in the PET/MRI center of the field of view. B0 shimming was performed to optimize magnetic field homogeneity. After an isoflurane washout period of at least 1 hour, the PET insert and a T2*-weighted gradient echo planar imaging sequence (duration, 5700 s; echo time, 18 ms; repetition time, 2000 ms; voxel size, 0.27 mm by 0.27 mm by 1.00 mm; field of view, 25 mm by 19 mm; image dimensions, 92 pixels by 70 pixels by 20 pixels; slice thickness, 0.8 mm; slices, 20) covering the brain were started simultaneously. A total of 141 ± 8 MBq of [^{18}F]FDG were injected 30 s after the start of the fPET and fMRI acquisition using a bolus (167 μl/min for 1 min) plus constant infusion (6.7 μl/min for 93.5 min) protocol. Dynamic PET data were acquired for 95 min and saved as list-mode files. Laser stimulation was started 20 min after start of the simultaneous fPET/fMRI acquisition using a block design described above. Laser irradiance values of 20 ± 3 mW were measured in continuous mode before each fiber implantation using the fiber optic power meter.

At the end of the scan, an anatomical T2 TurboRARE sequence was acquired (echo time, 67 ms; repetition time, 1800 ms; rare factor, 28; averages, 1; field of view, 40 mm by 32 mm by 32 mm; image dimensions, 160 pixels by 128 pixels by 128 pixels; voxel size, 0.25 mm by 0.25 mm by 0.25 mm). To allow for maximal c-fos expression, the animal was transcardially perfused with 50 ml of PBS at room temperature, 50 ml of PBS cooled to 4°C, and 50 ml of 4.5% paraformaldehyde (SAV Liquid Production GmbH, Flintsbach am Inn, Germany) 90 min after the start of the first stimulation phase. A second blood sample was collected from an intrathoracic vein for glucose determination (86 ± 10 mg/dl) right before perfusion. The brain was surgically removed and fixed in 4.5% formalin (SAV Liquid Production GmbH, Flintsbach am Inn, Germany).

Imaging data analysis

Data preprocessing

fPET list-mode data were divided into 95× 1-min time frames. Sinograms were reconstructed into a dynamic fPET image using OSEM2D reconstruction algorithm. The dynamic brain fPET scans were converted into Neuroimaging Informatics Technology Initiative (NIfTI) format using PMOD software. fMRI and anatomical images were converted into NIfTI format using Bruker2NIfTI software (v1.0.20170707, Sebastiano Ferraris, University College London).

Data preprocessing was conducted as previously described (*5*) using Statistical Parametric Mapping 12 (SPM 12; Wellcome Trust Centre for Neuroimaging, University College London, London, UK) via MATLAB (The MathWorks, Natick, MA, USA) and Analysis of Functional NeuroImages (National Institute of Mental Health, Bethesda, Maryland, USA). In summary, realignment of fMRI and fPET data was performed in SPM. Binary masks were generated from average images and the anatomical MRI scans. With these, the brain was extracted from the fPET, anatomical reference, and fMRI image ("skull stripping") before coregistration of the fPET and fMRI to the anatomy. Spatial normalization was performed using parameters, which were calculated by comparing the anatomical reference to the Schiffer rat brain atlas (*91*). The normalized fMRI and fPET images were smoothed using a 1.5-mm by 1.5-mm by 1.5-mm Gaussian kernel toward the spatial resolution of the PET insert. A temporal high-pass filter with a cutoff frequency of 256 Hz was applied to the fMRI data, with the purpose of removing scanner-attributable low-frequency drifts in the fMRI time series. Although SPM's default high-pass cutoff is set to 128 Hz, we increased the cutoff frequency to 256 Hz, since this strategy has been proposed to improve the signal-to-noise ratio when using block lengths of more than 15-s off duration as is the case in the present study (*92*).

Extraction of mean time courses within an ROI was performed using MarsBar (*93*). The list of 54 selected ROIs, including abbreviations and volumes, is included in table S4.

fMRI statistical analysis

Data were analyzed using SPM version 12 (www.fil.ion.ucl.ac.uk/spm). A block design was used for the ChR2 and GFP groups (*92*), modeling each of the six 10-min stimulation blocks using a canonical hemodynamic response function that emulates the early peak at 5 s and the subsequent undershoot (*94*). The within-subject design matrix for the first level analysis included two regressors: OGS and baseline (3 min between stimulation blocks). Two contrast images per individual were calculated as follows: OGS > baseline and baseline > OGS.

Between-group approach. Single mean images for each contrast of interest (OGS > baseline and baseline > OGS) were first generated for each subject. Then, a two-sample *t* test was carried out to identify the regions that showed significant signal changes between the ChR2 and the GFP groups. Results were thresholded at $P < 0.001$ for voxel-level inference with a cluster-level threshold of $P < 0.05$ corrected for the whole-brain volume using FWE, which controls for the expected proportion of false-positive clusters. This threshold was also chosen for all subsequent fMRI and fPET analyses to ensure consistency and simplify the interpretation. Furthermore, this approach has been shown to provide control of the false-positive rate comparable to other software programs (*95*). Nevertheless, results also indicate significant findings after correction at $P < 0.05$ FWE voxel level, which is highly conservative.

Within-group approach. Single-subject voxel-wise statistical parametric maps for the aforementioned contrasts were obtained and subjected to group-level one-sample *t* tests. The significant map for the group random effects analysis was thresholded at $P < 0.001$ for voxel-level inference with a cluster-level threshold of $P < 0.05$ (FWE-corrected).

fPET statistical analysis

Between-group approach. [^{18}F]FDG-fPET images were first subjected to intensity normalization with reference to the cerebellum (*96*). A two-sample *t* test was used to compare changes in glucose metabolism induced by OGS during the last 10-min stimulation block (corresponding to fPET frames 86 to 95 = time window with onset at second 2551 with a duration of 600 s) between GFP and ChR2 rats. Results were thresholded at $P < 0.001$ for voxel-level inference with a cluster-level threshold of $P < 0.05$ (FWE-corrected).

Within-group GLM approach. Modeling of [^{18}F]FDG-fPET data with the GLM was done in MATLAB as described previously (*16*, *18*). Before the GLM, the signal-to-noise ratio of fPET data was increased

by application of a low-pass filter with a cutoff frequency of $^1/_5$ min (i.e., half the duration of the task block). The GLM is then used to separate task effects from baseline by construction of a design matrix that models task effects. This approach is most similar to conventional fMRI analyses (see within-group fMRI statistics above), thus yielding the term fPET. The design matrix included an OGS regressor and one for the baseline. We defined the OGS regressor as a ramp function with a slope of 1 kBq per frame when stimulation was active and zero otherwise. This is equivalent to the integral of a boxcar function used in fMRI task analyses. The baseline regressor accounts for the continuous uptake of the radioligand due to its irreversible kinetics. We defined it as the average of all gray matter voxels, excluding those voxels declared as activated with the fMRI within-group approach. This approach has been shown to be the best choice in terms of model fits (*18*), yielding comparable results to an independent baseline definition (*4*), and does not affect test-retest reliability (*97*). That is, each voxel's time course was modeled by two regressors, namely, the OGS time course and the baseline signal, thus isolating stimulation effects from the raw fPET time-activity curve. The resulting β values of the OGS regressor were then subject to group-level statistical analysis in SPM at $P < 0.001$ for voxel-level inference with a cluster-level threshold of $P < 0.05$ (FWE-corrected).

Within-group ICA approach. The data-driven ICA approach is a method for recovering underlying signals from linear mixtures of those signals, which draws upon higher-order signal statistics to estimate a set of components that are maximally independent from each other (*98*). ICA separates sources by maximizing their non-Gaussianity, and, therefore, non-Gaussianity is fundamental for ICA model estimation (*99*). One way to understand the connection between independence and non-Gaussianity is offered by the central limit theorem, which states that the distribution of a sum (or mixture) of random variables tends to be more Gaussian than the original random variables. This, in turn, implies that when the sources are made more non-Gaussian, they become more independent (or unmixed). The distance to a Gaussian can be approximated using measures of non-Gaussianity, such as skewness and kurtosis, the latter being widely used for estimating non-Gaussianity in ICA. ICA algorithms, including FastICA and Infomax, maximize independence by finding components that have either maximum or minimum kurtosis (*100*, *101*).

In the case of fPET, ICA first requires a preprocessing step to remove the global baseline signal before the unmixing stage. This technique is conducted to improve the sensitivity for an accurate inference of spatially independent components. Following the procedure described in (*17*, *19*), we first applied whole-brain normalization to obtain four-dimensional volumes that represented the dynamic relative [^{18}F]FDG uptake (time-activity) map (*96*). Two further preprocessing steps were implemented before the application of ICA: data reduction and whitening. Data reduction was performed by principal components analysis to capture most of the variability in the data (>99%) while reducing its dimensionality. Prewhitening was done to improve the convergence of the ICA algorithm and was achieved simultaneously with principal components analysis. To separate the independent components, we used the FastICA algorithm (*100*, *102*, *103*). We estimated 20 components per subject, as this number provided a reasonable trade-off between preserving most of the variance while considerably reducing the size of the data. Group-level spatial ICA was conducted using temporal concatenation, which is a widely used approach in group fMRI (*102*) and which has already been successfully applied to fPET data (*17*, *19*). The resulting components were sorted according to spatial kurtosis (i.e., a measure of the sparseness of a distribution) following the general framework presented by Lu and Rajapakse (*22*). ICA was implemented with the GIFT v4.0b (*102*) and CONN v22a (*104*) toolboxes in MATLAB v.R2019a (Natick, MA, USA).

While the GLM approach uses a model-based hypothesis, ICA is data-driven and does not require a priori assumptions on the form and shape of the expected [^{18}F]FDG-fPET response. On the other hand, the GLM is simpler to implement and interpret, whereas the ICA approach requires a posteriori selection of components, which can be challenging when the spatial distribution of the effects is unknown. Here, we overcome the need for a manual identification of task effects by automatically sorting components according to spatial kurtosis (*21*, *22*).

Percent-overlap-of-activation

To evaluate the percent overlap of activation between the fPET and fMRI results, we used the reliability measure proposed by Rombouts *et al.* (*105*) and Machielsen *et al.* (*106*), which is identical to the similarity coefficient proposed by Dice (*107*). According to this measure, the overlap of activation for any two replications (e.g., *k* and *m*) is established as in Eq. 1, where $V_{k,m}$ is the number of voxels identified as activated in both the *k*th and the *m*th replications and V_k and V_m denote the number of voxels identified as activated in the *k*th and the *m*th experiments, respectively

$$\omega_{k,m} = \frac{2V_{k,m}}{V_k + V_m} \quad (1)$$

Therefore, $\omega_{k,m}$ is a ratio of the number of voxels identified as activated in both replications to the average number of voxels identified as activated in each replication. Note that this measure spans from 0 (i.e., no overlap) to 1 (perfect overlap) within the identified brain activation.

Histology

TH and c-fos IHC

Perfused brains were fixated in 4.5% formalin (SAV Liquid Production GmbH, Flintsbach am Inn, Germany) and sectioned into three coronal parts (parts A, B, and C): One cut was performed approximately through the striatum, and the second one was performed through the SN. Then, the tissue was embedded in paraffin. Three rats from each group were selected on the basis of the previous fPET and fMRI results. For histology, 3- to 5-μm-thick sections were cut and stained with hematoxylin and eosin and correlated with the "Mouse Brain Atlas" (Allen Reference Atlas–Mouse Brain, available at https://atlas.brain-map.org/) to identify the sections containing the desired anatomical areas (striatum and SN). Adjacent to those sections, c-fos and TH IHC were performed on an automated immunostainer (Ventana Medical Systems Inc., Oro Valley, AZ, USA) according to the company's protocols for open procedures with slight modifications. The slides were stained with the antibodies c-fos (SC-52, Santa Cruz Biotechnology, Dallas, TX, USA) and TH (#22941, Immunostar, Hudson, WI, USA). Appropriate positive and negative controls were used to confirm the adequacy of the staining. All samples were scanned with the Ventana DP200 (Roche, Basel, Switzerland) and processed with the Image Viewer MFC Application. Final image preparation was performed with Adobe Photoshop CS6.

The neuronal activation, revealed by c-fos IHC, was bilaterally quantified in the selected rats in the dorsal and ventral striatum and in the SN. For this, three ROIs were selected in each target region. See fig. S6 for more details on the selected ROIs. The number of positive and negative cells was counted at a magnification of ×400. A test for significant differences between right and left ROIs within the group and a comparison of the ROIs between GFP- and ChR2-expressing rats was performed using a Welch's *t* test in Prism 9 (V. 9.3.1, GraphPad Software LLC, San Diego, CA, USA). No quantification of the TH IHC was performed.

GFP and YFP immunofluorescence staining

Adjacent to c-fos–, TH-, and hematoxylin and eosin–stained sections, a GFP/YFP staining was performed to control for AAV expression. Paraffin sections were rehydrated using a series of xylol and decreasing ethanol concentrations. Antigen retrieval was performed for 15 min at 95°C using universal antigen retrieval (R&D Systems Inc., Minneapolis, MN, USA). Sections were blocked in PBS containing 0.2% Triton X-100 and 5% bovine serum albumin and stained for GFP or YFP using an anti-GFP antibody (NB100-1614, Novus Biologicals, Biotechne, Wiesbaden Nordenstadt, Germany; 1:200) plus secondary anti-chicken Alexa Fluor 555 (A32932, Thermo Fisher Scientific Inc., Waltham, MA, USA; 1:200) together with 4′,6-diamidino-2-phenylindole (D1306, Thermo Fisher Scientific Inc., Waltham, MA, USA; 1:500). All antibodies were diluted in antibody diluent (IW-1000, IHC World LLC, Woodstock, MD, USA) and incubated for 1 hour at room temperature. Cover glasses were placed on top using antifade mounting medium (P36980, Thermo Fisher Scientific Inc., Waltham, MA, USA), and sections were acquired on a Leica DMi8 microscope interfaced with Leica LAS X software (Leica Microsystems CMS GmbH, Wetzlar, Germany). The images were further processed with ImageJ.

Supplementary Materials

This PDF file includes:

Supplementary Methods
Figs. S1 to S7
Tables S1 to S6
References

REFERENCES AND NOTES

1. B. Liss, J. Roeper, Individual dopamine midbrain neurons: Functional diversity and flexibility in health and disease. *Brain Res. Rev.* **58**, 314–321 (2008).
2. S. D. Jamadar, P. G. D. Ward, T. G. Close, A. Fornito, M. Premaratne, K. O'Brien, D. Stäb, Z. Chen, N. J. Shah, G. F. Egan, Simultaneous BOLD-fMRI and constant infusion FDG-PET data of the resting human brain. *Sci. Data* **7**, 363 (2020).
3. C. Y. Sander, H. D. Hansen, H. Y. Wey, Advances in simultaneous PET/MR for imaging neuroreceptor function. *J. Cereb. Blood Flow Metab.* **40**, 1148–1166 (2020).
4. A. Hahn, M. Breakspear, L. Rischka, W. Wadsak, G. M. Godbersen, V. Pichler, P. Michenthaler, T. Vanicek, M. Hacker, S. Kasper, R. Lanzenberger, L. Cocchi, Reconfiguration of functional brain networks and metabolic cost converge during task performance. *eLife* **9**, e52443 (2020).
5. T. M. Ionescu, M. Amend, T. Watabe, J. Hatazawa, A. Maurer, G. Reischl, B. J. Pichler, H. F. Wehrl, K. Herfert, Neurovascular uncoupling: Multimodal imaging delineates the acute effects of 3,4-methylenedioxymethamphetamine. *J. Nucl. Med.* **64**, 466–471 (2023).
6. T. M. Ionescu, M. Amend, R. Hafiz, B. B. Biswal, A. Maurer, B. J. Pichler, H. F. Wehrl, K. Herfert, Striatal and prefrontal D2R and SERT distributions contrastingly correlate with default-mode connectivity. *Neuroimage* **243**, 118501 (2021).
7. S. Marciano, T. M. Ionescu, R. S. Saw, R. Y. Cheong, D. Kirik, A. Maurer, B. J. Pichler, K. Herfert, Combining CRISPR-Cas9 and brain imaging to study the link from genes to molecules to networks. *Proc. Natl. Acad. Sci. U.S.A.* **119**, e2122552119 (2022).
8. K. Fischer, V. Sossi, A. von Ameln-Mayerhofer, G. Reischl, B. J. Pichler, Quantification of dopamine transporters in mice with unilateral 6-OHDA lesions using [^{11}C] methylphenidate and PET. *Neuroimage* **59**, 2413–2422 (2012).
9. K. Fischer, V. Sossi, A. Schmid, M. Thunemann, F. C. Maier, M. S. Judenhofer, J. G. Mannheim, G. Reischl, B. J. Pichler, Noninvasive nuclear imaging enables the in vivo quantification of striatal dopamine receptor expression and raclopride affinity in mice. *J. Nucl. Med.* **52**, 1133–1141 (2011).
10. N. Y. Lettfuss, K. Fischer, V. Sossi, B. J. Pichler, A. von Ameln-Mayerhofer, Imaging DA release in a rat model of L-DOPA-induced dyskinesias: A longitudinal in vivo PET investigation of the antidyskinetic effect of MDMA. *Neuroimage* **63**, 423–433 (2012).
11. L. J. Stiernman, F. Grill, A. Hahn, L. Rischka, R. Lanzenberger, V. Panes Lundmark, K. Riklund, J. Axelsson, A. Rieckmann, Dissociations between glucose metabolism and blood oxygenation in the human default mode network revealed by simultaneous PET-fMRI. *Proc. Natl. Acad. Sci. U.S.A.* **118**, e2021913118 (2021).
12. E. S. Boyden, F. Zhang, E. Bamberg, G. Nagel, K. Deisseroth, Millisecond-timescale, genetically targeted optical control of neural activity. *Nat. Neurosci.* **8**, 1263–1268 (2005).
13. M. Benoit-Marand, E. Borrelli, F. Gonon, Inhibition of dopamine release via presynaptic D2 receptors: Time course and functional characteristics in vivo. *J. Neurosci.* **21**, 9134–9141 (2001).
14. M. Villien, H.-Y. Wey, J. B. Mandeville, C. Catana, J. R. Polimeni, C. Y. Sander, N. R. Zürcher, D. B. Chonde, J. S. Fowler, B. R. Rosen, J. M. Hooker, Dynamic functional imaging of brain glucose utilization using fPET-FDG. *Neuroimage* **100**, 192–199 (2014).
15. H. F. Wehrl, M. Hossain, K. Lankes, C. C. Liu, I. Bezrukov, P. Martirosian, F. Schick, G. Reischl, B. J. Pichler, Simultaneous PET-MRI reveals brain function in activated and resting state on metabolic, hemodynamic and multiple temporal scales. *Nat. Med.* **19**, 1184–1189 (2013).
16. A. Hahn, G. Gryglewski, L. Nics, M. Hienert, L. Rischka, C. Vraka, H. Sigurdardottir, T. Vanicek, G. M. James, R. Seiger, A. Kautzky, L. Silberbauer, W. Wadsak, M. Mitterhauser, M. Hacker, S. Kasper, R. Lanzenberger, Quantification of task-specific glucose metabolism with constant infusion of ^{18}F-FDG. *J. Nucl. Med.* **57**, 1933–1940 (2016).
17. S. D. Jamadar, P. G. D. Ward, S. Li, F. Sforazzini, J. Baran, Z. Chen, G. F. Egan, Simultaneous task-based BOLD-fMRI and [18-F] FDG functional PET for measurement of neuronal metabolism in the human visual cortex. *Neuroimage* **189**, 258–266 (2019).
18. L. Rischka, G. Gryglewski, S. Pfaff, T. Vanicek, M. Hienert, M. Klobl, M. Hartenbach, A. Haug, W. Wadsak, M. Mitterhauser, M. Hacker, S. Kasper, R. Lanzenberger, A. Hahn, Reduced task durations in functional PET imaging with [^{18}F]FDG approaching that of functional MRI. *Neuroimage* **181**, 323–330 (2018).
19. S. Li, S. D. Jamadar, P. G. D. Ward, M. Premaratne, G. F. Egan, Z. Chen, Analysis of continuous infusion functional PET (fPET) in the human brain. *Neuroimage* **213**, 116720 (2020).
20. F. De Martino, F. Gentile, F. Esposito, M. Balsi, F. Di Salle, R. Goebel, E. Formisano, Classification of fMRI independent components using IC-fingerprints and support vector machine classifiers. *Neuroimage* **34**, 177–194 (2007).
21. E. Formisano, F. Esposito, N. Kriegeskorte, G. Tedeschi, F. Di Salle, R. Goebel, Spatial independent component analysis of functional magnetic resonance imaging time-series: Characterization of the cortical components. *Neurocomputing* **49**, 241–254 (2002).
22. W. Lu, J. C. Rajapakse, Eliminating indeterminacy in ICA. *Neurocomputing* **50**, 271–290 (2003).
23. C. H. Moritz, B. P. Rogers, M. E. Meyerand, Power spectrum ranked independent component analysis of a periodic fMRI complex motor paradigm. *Hum. Brain Mapp.* **18**, 111–122 (2003).
24. T. Davis, K. F. LaRocque, J. A. Mumford, K. A. Norman, A. D. Wagner, R. A. Poldrack, What do differences between multi-voxel and univariate analysis mean? How subject-, voxel-, and trial-level variance impact fMRI analysis. *Neuroimage* **97**, 271–283 (2014).
25. F. Pereira, T. Mitchell, M. Botvinick, Machine learning classifiers and fMRI: A tutorial overview. *Neuroimage* **45**, S199–S209 (2009).
26. A. Abraham, F. Pedregosa, M. Eickenberg, P. Gervais, A. Mueller, J. Kossaifi, A. Gramfort, B. Thirion, G. Varoquaux, Machine learning for neuroimaging with scikit-learn. *Front. Neuroinform.* **8**, 14 (2014).
27. N. Kriegeskorte, R. Goebel, P. Bandettini, Information-based functional brain mapping. *Proc. Natl. Acad. Sci. U.S.A.* **103**, 3863–3868 (2006).
28. T. E. Nichols, A. P. Holmes, Nonparametric permutation tests for functional neuroimaging: A primer with examples. *Hum. Brain Mapp.* **15**, 1–25 (2002).
29. K. J. Friston, Functional and effective connectivity: A review. *Brain Connect.* **1**, 13–36 (2011).
30. N. X. Tritsch, J. B. Ding, B. L. Sabatini, Dopaminergic neurons inhibit striatal output through non-canonical release of GABA. *Nature* **490**, 262–266 (2012).
31. N. X. Tritsch, W. J. Oh, C. Gu, B. L. Sabatini, Midbrain dopamine neurons sustain inhibitory transmission using plasma membrane uptake of GABA, not synthesis. *eLife* **3**, e01936 (2014).
32. J. C. Patel, A. D. Sherpa, R. Melani, P. Witkovsky, M. R. Wiseman, B. O'Neill, C. Aoki, N. X. Tritsch, M. E. Rice, GABA co-released from striatal dopamine axons dampens phasic dopamine release through autoregulatory $GABA_A$ receptors. *Cell Rep.* **43**, 113834 (2024).

33. T. M. Mitchell, R. Hutchinson, R. S. Niculescu, F. Pereira, X. Wang, M. Just, S. Newman, Learning to decode cognitive states from brain images. *Mach. Learn.* **57**, 145–175 (2004).
34. D. Sulzer, S. J. Cragg, M. E. Rice, Striatal dopamine neurotransmission: Regulation of release and uptake. *Basal Ganglia* **6**, 123–148 (2016).
35. C. P. Ford, The role of D2-autoreceptors in regulating dopamine neuron activity and transmission. *Neuroscience* **282**, 13–22 (2014).
36. A. Andrea, E. L.-O. José, R. Maria, M. Claudia De, F. W. Hopf, I. Ciro, H. Briac, J. Jacob, K. Chisato, W. Marc, G. C. Marc, B. Antonello, S. David, B. Emiliana, Dual control of dopamine synthesis and release by presynaptic and postsynaptic dopamine D2 receptors. *J. Neurosci.* **32**, 9023 (2012).
37. A. B. Nelson, N. Hammack, C. F. Yang, N. M. Shah, R. P. Seal, A. C. Kreitzer, Striatal cholinergic interneurons drive GABA release from dopamine terminals. *Neuron* **82**, 63–70 (2014).
38. T. Koos, J. M. Tepper, Inhibitory control of neostriatal projection neurons by GABAergic interneurons. *Nat. Neurosci.* **2**, 467–472 (1999).
39. J. W. Mink, The basal ganglia: Focused selection and inhibition of competing motor programs. *Prog. Neurobiol.* **50**, 381–425 (1996).
40. C. R. Gerfen, T. M. Engber, L. C. Mahan, Z. Susel, T. N. Chase, F. J. Monsma Jr., D. R. Sibley, D1 and D2 dopamine receptor-regulated gene expression of striatonigral and striatopallidal neurons. *Science* **250**, 1429–1432 (1990).
41. D. J. Surmeier, J. Ding, M. Day, Z. Wang, W. Shen, D1 and D2 dopamine-receptor modulation of striatal glutamatergic signaling in striatal medium spiny neurons. *Trends Neurosci.* **30**, 228–235 (2007).
42. R. L. Albin, A. B. Young, J. B. Penney, The functional anatomy of basal ganglia disorders. *Trends Neurosci.* **12**, 366–375 (1989).
43. M. R. DeLong, Primate models of movement disorders of basal ganglia origin. *Trends Neurosci.* **13**, 281–285 (1990).
44. A. V. Kravitz, B. S. Freeze, P. R. Parker, K. Kay, M. T. Thwin, K. Deisseroth, A. C. Kreitzer, Regulation of parkinsonian motor behaviours by optogenetic control of basal ganglia circuitry. *Nature* **466**, 622–626 (2010).
45. G. Cui, S. B. Jun, X. Jin, M. D. Pham, S. S. Vogel, D. M. Lovinger, R. M. Costa, Concurrent activation of striatal direct and indirect pathways during action initiation. *Nature* **494**, 238–242 (2013).
46. O. Hikosaka, Y. Takikawa, R. Kawagoe, Role of the basal ganglia in the control of purposive saccadic eye movements. *Physiol. Rev.* **80**, 953–978 (2000).
47. J. F. Keeler, D. O. Pretsell, T. W. Robbins, Functional implications of dopamine D1 vs. D2 receptors: A 'prepare and select' model of the striatal direct vs. indirect pathways. *Neuroscience* **282**, 156–175 (2014).
48. P. Calabresi, B. Picconi, A. Tozzi, V. Ghiglieri, M. Di Filippo, Direct and indirect pathways of basal ganglia: A critical reappraisal. *Nat. Neurosci.* **17**, 1022–1030 (2014).
49. E. K. Richfield, J. B. Penney, A. B. Young, Anatomical and affinity state comparisons between dopamine D1 and D2 receptors in the rat central nervous system. *Neuroscience* **30**, 767–777 (1989).
50. J. K. Dreyer, K. F. Herrik, R. W. Berg, J. D. Hounsgaard, Influence of phasic and tonic dopamine release on receptor activation. *J. Neurosci.* **30**, 14273–14283 (2010).
51. J. B. Mandeville, C. Y. M. Sander, B. G. Jenkins, J. M. Hooker, C. Catana, W. Vanduffel, N. M. Alpert, B. R. Rosen, M. D. Normandin, A receptor-based model for dopamine-induced fMRI signal. *Neuroimage* **75**, 46–57 (2013).
52. C. Y. Sander, J. M. Hooker, C. Catana, M. D. Normandin, N. M. Alpert, G. M. Knudsen, W. Vanduffel, B. R. Rosen, J. B. Mandeville, Neurovascular coupling to D2/D3 dopamine receptor occupancy using simultaneous PET/functional MRI. *Proc. Natl. Acad. Sci. U.S.A.* **110**, 11169–11174 (2013).
53. L. Hunger, A. Kumar, R. Schmidt, Abundance compensates kinetics: Similar effect of dopamine signals on D1 and D2 receptor populations. *J. Neurosci.* **40**, 2868–2881 (2020).
54. P. F. Marcott, A. A. Mamaligas, C. P. Ford, Phasic dopamine release drives rapid activation of striatal D2-receptors. *Neuron* **84**, 164–176 (2014).
55. C. Yapo, A. G. Nair, L. Clement, L. R. Castro, J. Hellgren Kotaleski, P. Vincent, Detection of phasic dopamine by D1 and D2 striatal medium spiny neurons. *J. Physiol.* **595**, 7451–7475 (2017).
56. S. Navailles, P. De Deurwaerdere, Imbalanced dopaminergic transmission mediated by serotonergic neurons in L-DOPA-induced dyskinesia. *Parkinsons Dis.* **2012**, 323686 (2012).
57. R. C. Sellnow, J. H. Newman, N. Chambers, A. R. West, K. Steece-Collier, I. M. Sandoval, M. J. Benskey, C. Bishop, F. P. Manfredsson, Regulation of dopamine neurotransmission from serotonergic neurons by ectopic expression of the dopamine D2 autoreceptor blocks levodopa-induced dyskinesia. *Acta Neuropathol. Commun.* **7**, 8 (2019).
58. G. M. Godbersen, S. Klug, W. Wadsak, V. Pichler, J. Raitanen, A. Rieckmann, L. Stiernman, L. Cocchi, M. Breakspear, M. Hacker, R. Lanzenberger, A. Hahn, Task-evoked metabolic demands of the posteromedial default mode network are shaped by dorsal attention and frontoparietal control networks. *eLife* **12**, e84683 (2023).
59. I. Vanzetta, A. Grinvald, Increased cortical oxidative metabolism due to sensory stimulation: Implications for functional brain imaging. *Science* **286**, 1555–1558 (1999).
60. D. Malonek, U. Dirnagl, U. Lindauer, K. Yamada, I. Kanno, A. Grinvald, Vascular imprints of neuronal activity: Relationships between the dynamics of cortical blood flow, oxygenation, and volume changes following sensory stimulation. *Proc. Natl. Acad. Sci. U.S.A.* **94**, 14826–14831 (1997).
61. T. A. Woolsey, C. M. Rovainen, S. B. Cox, M. H. Henegar, G. E. Liang, D. Liu, Y. E. Moskalenko, J. Sui, L. Wei, Neuronal units linked to microvascular modules in cerebral cortex: Response elements for imaging the brain. *Cereb. Cortex* **6**, 647–660 (1996).
62. N. Harel, S. P. Lee, T. Nagaoka, D. S. Kim, S. G. Kim, Origin of negative blood oxygenation level-dependent fMRI signals. *J. Cereb. Blood Flow Metab.* **22**, 908–917 (2002).
63. Y. Liu, H. Shen, Z. Zhou, D. Hu, Sustained negative BOLD response in human fMRI finger tapping task. *PLOS ONE* **6**, e23839 (2011).
64. A. Rodriguez-Baeza, F. Reina-De La Torre, M. Ortega-Sanchez, J. Sahuquillo-Barris, Perivascular structures in corrosion casts of the human central nervous system: A confocal laser and scanning electron microscope study. *Anat. Rec.* **252**, 176–184 (1998).
65. M. Moraschi, M. DiNuzzo, F. Giove, On the origin of sustained negative BOLD response. *J. Neurophysiol.* **108**, 2339–2342 (2012).
66. Y. Y. Shih, C. C. Chen, B. C. Shyu, Z. J. Lin, Y. C. Chiang, F. S. Jaw, Y. Y. Chen, C. Chang, A new scenario for negative functional magnetic resonance imaging signals: Endogenous neurotransmission. *J. Neurosci.* **29**, 3036–3044 (2009).
67. L. Edvinsson, J. McCulloch, J. Sharkey, Vasomotor responses of cerebral arterioles in situ to putative dopamine receptor agonists. *Br. J. Pharmacol.* **85**, 403–410 (1985).
68. D. H. Cerri, D. L. Albaugh, L. R. Walton, B. Katz, T. W. Wang, T. H. Chao, W. Zhang, R. J. Nonneman, J. Jiang, S. H. Lee, A. Etkin, C. N. Hall, G. D. Stuber, Y. I. Shih, Distinct neurochemical influences on fMRI response polarity in the striatum. *Nat. Commun.* **15**, 1916 (2024).
69. X. Yu, D. Glen, S. Wang, S. Dodd, Y. Hirano, Z. Saad, R. Reynolds, A. C. Silva, A. P. Koretsky, Direct imaging of macrovascular and microvascular contributions to BOLD fMRI in layers IV-V of the rat whisker-barrel cortex. *Neuroimage* **59**, 1451–1460 (2012).
70. N. Sirmpilatze, J. Baudewig, S. Boretius, Temporal stability of fMRI in medetomidine-anesthetized rats. *Sci. Rep.* **9**, 16673 (2019).
71. J. Grandjean, G. Desrosiers-Gregoire, C. Anckaerts, D. Angeles-Valdez, F. Ayad, D. A. Barrière, I. Blockx, A. B. Bortel, M. Broadwater, B. M. Cardoso, M. Célestine, J. E. Chavez-Negrete, S. Choi, E. Christiaen, P. Clavijo, L. Colon-Perez, S. Cramer, T. Daniele, E. Dempsey, Y. Diao, A. Doelemeyer, D. Dopfel, L. Dvořáková, C. Falfán-Melgoza, F. F. Fernandes, C. F. Fowler, A. Fuentes-Ibañez, C. Garin, E. Gelderman, C. E. Golden, C. C. Guo, M. J. Henckens, L. A. Hennessy, P. Herman, N. Hofwijks, C. Horien, T. M. Ionescu, J. Jones, J. Kaesser, E. Kim, H. Lambers, A. Lazari, S.-H. Lee, A. Lillywhite, Y. Liu, Y. Y. Liu, A. López-Castro, X. López-Gil, Z. Ma, E. MacNicol, D. Madularu, F. Mandino, S. Marciano, M. J. McAuslan, P. McCunn, A. McIntosh, X. Meng, L. Meyer-Baese, S. Missault, F. Moro, D. Naessens, L. J. Nava-Gomez, H. Nonaka, J. J. Ortiz, J. Paasonen, L. M. Peeters, M. Pereira, P. D. Perez, M. Pompilus, M. Prior, R. Rakhmatullin, H. M. Reimann, J. Reinwald, R. T. de Rio, A. Rivera-Olvera, D. Ruiz-Pérez, G. Russo, T. J. Rutten, R. Ryoke, M. Sack, P. Salvan, B. G. Sanganahalli, A. Schroeter, B. J. Seewoo, E. Selingue, A. Seuwen, B. Shi, N. Sirmpilatze, J. A. Smith, C. Smith, F. Sobczak, P. J. Stenroos, M. Straathof, S. Strobelt, A. Sumiyoshi, K. Takahashi, M. E. Torres-García, R. Tudela, M. van den Berg, K. van der Marel, A. T. van Hout, R. Vertullo, B. Vidal, R. M. Vrooman, V. X. Wang, I. Wank, D. J. Watson, T. Yin, Y. Zhang, S. Zurbruegg, S. Achard, S. Alcauter, D. P. Auer, E. L. Barbier, J. Baudewig, C. F. Beckmann, N. Beckmann, G. J. Becq, E. L. Blezer, R. Bolbos, S. Boretius, S. Bouvard, E. Budinger, J. D. Buxbaum, D. Cash, V. Chapman, K.-H. Chuang, L. Ciobanu, B. Coolen, J. W. Dalley, M. Dhenain, R. M. Dijkhuizen, O. Esteban, C. Faber, M. Febo, K. W. Feindel, G. Forloni, J. Fouquet, E. A. Garza-Villarreal, N. Gass, J. C. Glennon, A. Gozzi, O. Gröhn, A. Harkin, A. Heerschap, X. Helluy, K. Herfert, A. Heuser, J. R. Homberg, D. J. Houwing, F. Hyder, G. D. Ielacqua, I. O. Jelescu, H. Johansen-Berg, G. Kaneko, R. Kawashima, S. D. Keilholz, G. A. Keliris, C. Kelly, C. Kerskens, J. Y. Khokhar, P. C. Kind, J.-B. Langlois, J. P. Lerch, M. A. López-Hidalgo, D. Manahan-Vaughan, F. Marchand, R. B. Mars, G. Marsella, E. Micotti, E. Muñoz-Moreno, J. Near, T. Niendorf, W. M. Otte, P. Pais, W.-J. Pan, R. A. Prado-Alcalá, G. L. Quirarte, J. Rodger, T. Rosenow, C. S. Baptista, A. Sartorius, S. J. Sawiak, T. W. Scheenen, N. Shemesh, Y.-Y. I. Shih, A. Shmuel, G. Soria, R. Stoop, G. J. Thompson, S. M. Till, N. Todd, A. Van Der Linden, A. van der Toorn, G. A. van Tilborg, C. Vanhove, A. Veltien, M. Verhoye, L. Wachsmuth, W. Weber-Fahr, P. Wenk, X. Yu, V. Zerbi, N. Zhang, B. B. Zhang, L. Zimmer, G. A. Devenyi, M. M. Chakravarty, A. Hess, A consensus protocol for functional connectivity analysis in the rat brain. *Nat. Neurosci.* **26**, 673–681 (2022).
72. C. Grimm, N. Wenderoth, V. Zerbi, An optimized protocol for assessing changes in mouse whole-brain activity using opto-fMRI. *STAR Protoc.* **3**, 101761 (2022).
73. T. D. Ambrisko, Y. Hikasa, Neurohormonal and metabolic effects of medetomidine compared with xylazine in beagle dogs. *Can. J. Vet. Res.* **66**, 42–49 (2002).
74. C. Suzuki, M. Kosugi, Y. Magata, Conscious rat PET imaging with soft immobilization for quantitation of brain functions: Comprehensive assessment of anesthesia effects on cerebral blood flow and metabolism. *EJNMMI Res.* **11**, 46 (2021).
75. L. Laaksonen, M. Kallioinen, J. Långsjö, T. Laitio, A. Scheinin, J. Scheinin, K. Kaisti, A. Maksimow, R. E. Kallionpää, V. Rajala, J. Johansson, O. Kantonen, M. Nyman, S. Sirén,

K. Valli, A. Revonsuo, O. Solin, T. Vahlberg, M. Alkire, H. Scheinin, Comparative effects of dexmedetomidine, propofol, sevoflurane, and S-ketamine on regional cerebral glucose metabolism in humans: A positron emission tomography study. *Br. J. Anaesth.* **121**, 281–290 (2018).
76. K. Masamoto, M. Fukuda, A. Vazquez, S. G. Kim, Dose-dependent effect of isoflurane on neurovascular coupling in rat cerebral cortex. *Eur. J. Neurosci.* **30**, 242–250 (2009).
77. N. K. Logothetis, J. Pauls, M. Augath, T. Trinath, A. Oeltermann, Neurophysiological investigation of the basis of the fMRI signal. *Nature* **412**, 150–157 (2001).
78. F. Zhao, T. Jin, P. Wang, S. G. Kim, Isoflurane anesthesia effect in functional imaging studies. *Neuroimage* **38**, 3–4 (2007).
79. T. Maekawa, C. Tommasino, H. M. Shapiro, J. Keifer-Goodman, R. W. Kohlenberger, Local cerebral blood flow and glucose utilization during isoflurane anesthesia in the rat. *Anesthesiology* **65**, 144–151 (1986).
80. M. Ueki, G. Mies, K. A. Hossmann, Effect of alpha-chloralose, halothane, pentobarbital and nitrous oxide anesthesia on metabolic coupling in somatosensory cortex of rat. *Acta Anaesthesiol. Scand.* **36**, 318–322 (1992).
81. N. J. Maandag, D. Coman, B. G. Sanganahalli, P. Herman, A. J. Smith, H. Blumenfeld, R. G. Shulman, F. Hyder, Energetics of neuronal signaling and fMRI activity. *Proc. Natl. Acad. Sci. U.S.A.* **104**, 20546–20551 (2007).
82. C. Alonso Bde, T. Makarova, A. Hess, On the use of α-chloralose for repeated BOLD fMRI measurements in rats. *J. Neurosci. Methods* **195**, 236–240 (2011).
83. K. M. Garrett, J. Gan, Enhancement of γ-aminobutyric acid$_A$ receptor activity by α-chloralose. *J. Pharmacol. Exp. Ther.* **285**, 680–686 (1998).
84. E. Kumamoto, Y. Murata, Enhancement by lanthanide of general anesthetic-induced GABAA-receptor current in rat septal cholinergic neurons in culture. *J. Neurophysiol.* **75**, 2294–2299 (1996).
85. M. Massott, V. G. Longo, α-Chloralose and the central dopaminergic system. *J. Pharm. Pharmacol.* **30**, 667 (1978).
86. N. Montemurro, N. Aliaga, P. Graff, A. Escribano, J. Lizana, New targets and new technologies in the treatment of Parkinson's disease: A narrative review. *Int. J. Environ. Res. Public Health* **19**, 8799 (2022).
87. C. E. Bass, V. P. Grinevich, Z. B. Vance, R. P. Sullivan, K. D. Bonin, E. A. Budygin, Optogenetic control of striatal dopamine release in rats. *J. Neurochem.* **114**, 1344–1352 (2010).
88. G. Paxinos, C. Watson, *The Rat Brain in Stereotaxic Coordinates* (Academic Press, San Diego; 1998).
89. K. Hamacher, H. H. Coenen, G. Stöcklin, Efficient stereospecific synthesis of no-carrier-added 2-[^{18}F]-fluoro-2-deoxy-D-glucose using aminopolyether supported nucleophilic substitution. *J. Nucl. Med.* **27**, 235–238 (1986).
90. J. A. Disselhorst, D. F. Newport, A. M. Schmid, F. P. Schmidt, C. Parl, C. C. Liu, B. J. Pichler, J. G. Mannheim, NEMA NU 4-2008 performance evaluation and MR compatibility tests of an APD-based small animal PET-insert for simultaneous PET/MR imaging. *Phys. Med. Biol.* **67**, 045015 (2022).
91. W. K. Schiffer, M. M. Mirrione, A. Biegon, D. L. Alexoff, V. Patel, S. L. Dewey, Serial microPET measures of the metabolic reaction to a microdialysis probe implant. *J. Neurosci. Methods* **155**, 272–284 (2006).
92. R. Henson, "Chapter 15 - Efficient experimental design for fMRI" in *Statistical Parametric Mapping*, K. Friston, J. Ashburner, S. Kiebel, T. Nichols, W. Penny, Eds. (Academic Press, 2007), pp. 193–210.
93. M. Brett, J.-L. Anton, R. Valabregue, J.-B. Poline, "Region of interest analysis using an SPM toolbox" in *8th Internation Conference on Functional Mapping of the Human Brain*. (CD-ROM in NeuroImage, 2002), pp. 497.
94. K. J. Friston, E. Zarahn, O. Josephs, R. N. Henson, A. M. Dale, Stochastic designs in event-related fMRI. *Neuroimage* **10**, 607–619 (1999).
95. A. Eklund, T. E. Nichols, H. Knutsson, Cluster failure: Why fMRI inferences for spatial extent have inflated false-positive rates. *Proc. Natl. Acad. Sci. U.S.A.* **113**, 7900–7905 (2016).
96. F. J. López-González, J. Silva-Rodríguez, J. Paredes-Pacheco, A. Niñerola-Baizán, N. Efthimiou, C. Martín-Martín, A. Moscoso, Á. Ruibal, N. Roé-Vellvé, P. Aguiar, Intensity normalization methods in brain FDG-PET quantification. *Neuroimage* **222**, 117229 (2020).
97. L. Rischka, G. M. Godbersen, V. Pichler, P. Michenthaler, S. Klug, M. Klöbl, V. Ritter, W. Wadsak, M. Hacker, S. Kasper, R. Lanzenberger, A. Hahn, Reliability of task-specific neuronal activation assessed with functional PET, ASL and BOLD imaging. *J. Cereb. Blood Flow Metab.* **41**, 2986–2999 (2021).
98. M. J. McKeown, L. K. Hansen, T. J. Sejnowsk, Independent component analysis of functional MRI: What is signal and what is noise? *Curr. Opin. Neurobiol.* **13**, 620–629 (2003).
99. A. Hyvärinen, E. Oja, Independent component analysis: Algorithms and applications. *Neural Netw.* **13**, 411–430 (2000).
100. V. D. Calhoun, V. K. Potluru, R. Phlypo, R. F. Silva, B. A. Pearlmutter, A. Caprihan, S. M. Plis, T. Adalı, Independent component analysis for brain FMRI does indeed select for maximal independence. *PLOS ONE* **8**, e73309 (2013).
101. A. Hyvärinen, E. Oja, A fast fixed-point algorithm for independent component analysis. *Neural Comput.* **9**, 1483–1492 (1997).
102. V. D. Calhoun, T. Adali, G. D. Pearlson, J. J. Pekar, A method for making group inferences from functional MRI data using independent component analysis. *Hum. Brain Mapp.* **14**, 140–151 (2001).
103. A. Hyvärinen, Fast and robust fixed-point algorithms for independent component analysis. *IEEE Trans. Neural Netw.* **10**, 626–634 (1999).
104. A. Nieto-Castanon, *Handbook of fcMRI Methods in CONN* (Hilbert Press, 2020).
105. S. A. Rombouts, F. Barkhof, F. G. Hoogenraad, M. Sprenger, P. Scheltens, Within-subject reproducibility of visual activation patterns with functional magnetic resonance imaging using multislice echo planar imaging. *Magn. Reson. Imaging* **16**, 105–113 (1998).
106. W. C. Machielsen, S. A. Rombouts, F. Barkhof, P. Scheltens, M. P. Witter, FMRI of visual encoding: Reproducibility of activation. *Hum. Brain Mapp.* **9**, 156–164 (2000).
107. L. R. Dice, Measures of the amount of ecologic association between species. *Ecology* **26**, 297–302 (1945).
108. M. E. Weaverdyck, M. D. Lieberman, C. Parkinson, Tools of the trade multivoxel pattern analysis in fMRI: A practical introduction for social and affective neuroscientists. *Soc. Cogn. Affect. Neurosci.* **15**, 487–509 (2020).
109. T. J. Adkins, T. G. Lee, Reward modulates cortical representations of action. *Neuroimage* **228**, 117708 (2021).
110. L. Grosenick, B. Klingenberg, K. Katovich, B. Knutson, J. E. Taylor, Interpretable whole-brain prediction analysis with GraphNet. *Neuroimage* **72**, 304–321 (2013).
111. V. Michel, A. Gramfort, E. Eger, G. Varoquaux, B. Thirion, "A comparative study of algorithms for intra- and inter-subjects fMRI decoding" in *Machine Learning and Interpretation in Neuroimaging*, G. Langs, I. Rish, M. Grosse-Wentrup, B. Murphy, G. Langs, I. Rish, M. Grosse-Wentrup, B. Murphy, Eds. (Springer, 2012), pp. 1–8.
112. C. Allefeld, K. Görgen, J.-D. Haynes, Valid population inference for information-based imaging: From the second-level *t*-test to prevalence inference. *Neuroimage* **141**, 378–392 (2016).
113. R. Gilron, J. Rosenblatt, O. Koyejo, R. A. Poldrack, R. Mukamel, What's in a pattern? Examining the type of signal multivariate analysis uncovers at the group level. *Neuroimage* **146**, 113–120 (2017).
114. M. T. Todd, L. E. Nystrom, J. D. Cohen, Confounds in multivariate pattern analysis: Theory and rule representation case study. *Neuroimage* **77**, 157–165 (2013).
115. S. M. Helfinstein, T. Schonberg, E. Congdon, K. H. Karlsgodt, J. A. Mumford, F. W. Sabb, T. D. Cannon, E. D. London, R. M. Bilder, R. A. Poldrack, Predicting risky choices from brain activity patterns. *Proc. Natl. Acad. Sci. U.S.A.* **111**, 2470–2475 (2014).
116. K. Izuma, K. Shibata, K. Matsumoto, R. Adolphs, Neural predictors of evaluative attitudes toward celebrities. *Soc. Cogn. Affect. Neurosci.* **12**, 382–390 (2016).
117. J. Jiang, C. Summerfield, T. Egner, Visual prediction error spreads across object features in human visual cortex. *J. Neurosci.* **36**, 12746–12763 (2016).
118. J. Kim, J. Wang, D. H. Wedell, S. V. Shinkareva, Identifying core affect in individuals from fMRI responses to dynamic naturalistic audiovisual stimuli. *PLOS ONE* **11**, e0161589 (2016).
119. Q. Wang, B. Cagna, T. Chaminade, S. Takerkart, Inter-subject pattern analysis: A straightforward and powerful scheme for group-level MVPA. *Neuroimage* **204**, 116205 (2020).
120. E. Olivetti, S. Veeramachaneni, E. Nowakowska, Bayesian hypothesis testing for pattern discrimination in brain decoding. *Pattern Recognit.* **45**, 2075–2084 (2012).
121. K. H. Brodersen, J. Daunizeau, C. Mathys, J. R. Chumbley, J. M. Buhmann, K. E. Stephan, Variational Bayesian mixed-effects inference for classification studies. *Neuroimage* **76**, 345–361 (2013).
122. J. Stelzer, Y. Chen, R. Turner, Statistical inference and multiple testing correction in classification-based multi-voxel pattern analysis (MVPA): Random permutations and cluster size control. *Neuroimage* **65**, 69–82 (2013).
123. S. Whitfield-Gabrieli, A. Nieto-Castanon, Conn: A functional connectivity toolbox for correlated and anticorrelated brain networks. *Brain Connect.* **2**, 125–141 (2012).

Acknowledgments: We thank the technical assistants at the Werner Siemens Imaging Center (WSIC), University of Tuebingen for invaluable support during the experiments. We further thank A. Ohmayer and the Weigelin group at the WSIC for assistance with the fluorescence microscope. Furthermore, we thank J. Mannheim and A. Schmid for technical support, which ensured the reliable performance of the MRI and PET insert. Furthermore, we would like to acknowledge the contributions of X.-m. Chen and X. Yu, who were formerly affiliated at the Max Planck Institute for Biological Cybernetics in Tuebingen, Germany. Their assistance in establishing the optogenetic approach at our institute has been instrumental. **Funding:** We would like to acknowledge the financial support received for this research project from the following sources: fortüne program (University of Tübingen, F1351583), Carl Zeiss Foundation (0563-2.8/517), and Werner Siemens Foundation (to B.J.P.). **Author contributions:** Conceptualization: K.H., B.J.P., F.B., T.M.I., R.L., and L.Q.-M. Methodology: S.H., F.B., G.R., K.H., A.H., B.J.P., T.M.I., L.K., R.L., G.D., and L.Q.-M. Software: A.H., F.B., and T.M.I. Validation: S.H., K.H., F.B., and G.D. Formal analysis: S.H., A.H., F.B., and T.M.I. Investigation:

B.W., S.H., I.G.-M., G.D., and L.Q.-M. Resources: K.H., G.R., B.W., B.J.P., I.G.-M., and R.L. Data curation: K.H. Writing—original draft: S.H., K.H., and F.B. Writing—review and editing: G.R., K.H., B.W., B.J.P., T.M.I., L.K., and F.B. Visualization: S.H., K.H., F.B., I.G.-M., and L.Q.-M. Supervision: K.H. and R.L. Project administration: K.H. Funding acquisition: K.H. and B.J.P.
Competing interests: The authors declare that they have no competing interests. **Data and materials availability:** All data needed to evaluate the conclusions in the paper are present in the paper and/or the Supplementary Materials. Codes and fPET and fMRI imaging data are available on Dryad repository: DOI: 10.5061/dryad.1vhhmgr2r and https://doi.org/10.5281/zenodo.11522241.

Submitted 4 December 2023
Accepted 23 September 2024
Published 25 October 2024
10.1126/sciadv.adn2776

Science Advances
AAAS

Supplementary Materials for

Functional PET/MRI reveals active inhibition of neuronal activity during optogenetic activation of the nigrostriatal pathway

Sabrina Haas *et al.*

Corresponding author: Kristina Herfert, Kristina.herfert@med.uni-tuebingen.de

Sci. Adv. **10**, eadn2776 (2024)
DOI: 10.1126/sciadv.adn2776

This PDF file includes:

Supplementary methods.

Multivariate pattern analysis (MVPA) applied to fMRI and fPET data.
Multivariate pattern analysis (MVPA) allows to evaluate differences between conditions with higher sensitivity than conventional univariate analysis by focusing on the analysis and comparison of distributed patterns of activity (*24, 25*). MVPA is frequently framed within the context of "brain decoding" applications, where distinct representational content can be discerned from fMRI activity patterns after performing a "training" or "learning phase". In this perspective, MVPA tools are commonly denoted as classifiers or, in broader terms, learning machines. Multivariate methods, including machine learning classifiers, prove to be highly sensitive tools for gauging brain information due to their ability to detect complex, high-dimensional mappings between spatially distributed patterns of brain activity and stimuli (*33*). The two datasets (fMRI and fPET) were pre-processed using the same sets of operations (see details in Data Preprocessing subsection). For the MVPA analyses, and following (*108*) we used normalized (i.e., transformation into a common reference space) and spatially smoothed data in order to reveal signatures or "biomarkers" of the optogenetic stimulation that would generalize across individuals. We applied whole-brain normalization to the fPET data to obtain 4D volumes that represented the dynamic relative [^{18}F]FDG uptake (time-activity) map (*17, 19, 96*). Prior to trial extraction, fPET and fMRI time courses were standardized using z normalization. As training exemplars for each class, response values were estimated for the individual optogenetic stimulation and baseline trials. The estimated trial response was calculated as the mean of three-minute time-span measurement points (i.e., duration equal to the length of the baseline blocks) around the peak BOLD or glucose uptake response during the optogenetic stimulation blocks relative to the correspondent pre-stimulus baseline activity. Using this strategy for both the fMRI and fPET datasets allowed us to obtain the same number of exemplars in each class, 12 per subject (6 per condition).

MVPA at the whole-brain level analysis using Spacenet classifiers and Searchlight.
We conducted whole-brain analysis employing SpaceNet classifiers sourced from the nilearn python package (*26*). These classifiers leverage spatial priors and regularization techniques to generate sparse yet structured coefficient maps. When the classifier achieves high out-of-sample classification accuracy, the resulting coefficient maps can be construed as information maps, indicating voxels wherein the collective activity carries discriminative information about the respective class (*109-111*). The SpaceNet classifiers were fit using 5-fold cross-validation and validated using a left-out test set (20%). For whole-brain SpaceNet MVPA analysis we employed a single train-test split approach to train and validate the model instead of cross-validation with permutation testing. Unfortunately, conducting permutation testing with SpaceNet would demand considerable computational resources, estimated at approximately 1500 hours per subject. Consequently, while SpaceNet yields interpretable maps, evaluating its null distribution presents a significant challenge.
Considering the above-mentioned limitations of the SpaceNet classifiers, we further performed a searchlight decoding analysis (*27*). This approach involves sliding a spherical window (of 1mm radius for our analysis) throughout the entire brain to map local multivariate effects and conducting independent decoding analyses within each sphere. We utilized the searchlight

implementation provided by nilearn (*26*), enabling us to acquire single-fold accuracy maps necessary to perform inference.

Classically, the decoding performance (used to measure the ability of the classifier to distinguish patterns associated with the different conditions included in the paradigm) is estimated separately in each participant. These within-subject measurements are then combined at the group level, to provide population-based inference, analogous to the standard hierarchical approach employed in univariate activation analyses. Since several limitations of this group-level strategy have been brought forward (*112-114*), we here used a different classifier-based framework to assess multivariate effects. This approach, referred to by distinct names such as across-subject classification, subject-transfer decoding or inter-subject pattern analysis (*115-119*), directly operates at the group-level by exploiting data from all available individuals in a single analysis at the group level: considering the data from all available individuals, the decoding performance is evaluated using data from new participants, namely those who were not part of the classifier's training dataset. When performing across-subject classification, a cross-validation of the type leave-one-subject-out enables a quantitative evaluation of the results that allows drawing inferences about the entire population from which the participant group was sampled, including individuals for which no data was available (*115, 119*). Across-subject classification exhibits enhanced sensitivity for detecting weak distributed effects and facilitates interpretation compared to standard hierarchical MVPA approaches, which often require further scrutiny due to potential ambiguities. Importantly, across-subject classification enables the identification of group-wise invariants within functional neuroimaging patterns, rendering it an invaluable tool for discerning neuromarkers or brain signatures, and offering a versatile framework for population-level multivariate analyses (*119*).

For our searchlight analysis we therefore employed a leave-one-subject-out cross-validation approach, in which the model accuracy was repeatedly computed on the data from the left-out subject. The approach trains on (n - 1) chunks, and classifies the remaining chunk, and repeats this for every chunk, also called fold. We created one chunk for each subject: 16 chunks for the fPET data and 18 chunks for the fMRI data.

To perform statistical inference at the group level, it is common practice to employ a t-test on decoding accuracies: this test evaluates whether the null hypothesis of chance-level average accuracy can be rejected, indicating the presence of a multivariate difference between conditions at the group level. However, various criticisms have been raised in the literature upon this approach, including concerns about the statistical distribution of classification accuracies (*112, 120*), the non-directional nature of identified group-information (*113*), and the potential bias introduced by confounding factors (*114*). Consequently, alternative methods have been developed [see, for example, (*112, 120-122*). Here, we employed a permutation test (Nichols & Holmes, 2002) to address the aforementioned limitations. This method evaluates the significance of the average accuracy at the group level in a non-parametric manner. Additionally, a permutation test allowed us to keep computational cost within reasonable bounds, a requirement that other alternatives, such as those suggested by (*122*) might not fulfill. We utilized the implementation provided by the SnPM toolbox (*28*) to analyze the accuracy maps from single-fold (for the inter-subject cross-validation), conducting 1000 permutations and applying a significance threshold of $p < 0.05$, corrected for family-wise-error (FWE).

MVPA ROI analysis.
For conducting MVPA ROI analysis, we performed an initial feature selection by considering only those voxels within the right SN. Estimated responses across relevant voxels from the right SN formed the feature vectors used to train the classifier. We evaluated a Gaussian Naive Bayes classifier (GNB) on the fMRI and fPET datasets. Analogous to the searchlight analysis, to assess multivariate effects, we used an across-subject classification approach. A positive result in this framework implies that the model has learnt an implicit rule from the training data that yields statistically significant generalization power on data from new subjects (*119*). We employed a leave-one-subject-out cross-validation for the MVPA ROI analysis. We tested the statistical significance of the accuracy of prediction using a permutation test: assuming there is no class information in the data, the labels can be permuted without altering the expected accuracy using a given classifier and number of features (i.e., this would equal chance level) (*28*). We performed 1000 permutations of a leave-one-subject-out cross-validated MVPA, and evaluated a GNB classifier with default parameters in Scikit-learn (*26*).

Functional and molecular connectivity analyses.
We used connectivity measures in order to attain a depiction of the optogenetic stimulation effects on neural dynamics in our experiment. We performed seed-based connectivity analysis, on both the fMRI and fPET datasets, to evaluate connectivity differences between optogenetic stimulation and baseline blocks (*29*).
The striatum receives axonal projections from SN dopaminergic neurons and houses a large population of GABAergic neurons. Consequently, we used the right striatum as seed region and assessed connectivity differences in response to the optogenetic stimulation.
Preprocessing of the fMRI and fPET data was performed as already described (see details in Data Preprocessing subsection) using SPM12 and the CONN toolbox (*123*), running in MATLAB (2019a, MathWorks, Inc.). The preprocessing steps included slice-timing correction, motion correction, normalization (i.e., transformation into a common reference space) and spatial smoothing. Following the procedure described in (*17, 19*) we applied whole-brain normalization to the fPET data, in order to obtain 4D volumes that represented the dynamic relative [^{18}F]FDG uptake (time-activity) map (*96*) A temporal high-pass filter with a cut-off frequency of 256 Hz was further applied to the fMRI data, with the purpose of removing scanner attributable low frequency drifts in the fMRI time series (*92*).

Seed-based connectivity analyses for fPET and fMRI data.
Functional connectivity depicts the temporal correlation of regional timeseries and is conceptualized to represent dynamic interaction and information sharing between brain regions (*29*), therefore characterizing spatially segregated functional networks at global scales. We calculated functional connectivity for the fMRI and fPET datasets using the CONN toolbox (*123*) in the form of seed-to-voxel analyses for assessing effects at the whole-brain level. Temporal correlations for the right striatum seed were computed for all voxels in the brain using a general linear model (GLM) for the contrast OGS > baseline. The functional connectivity analyses produced seed-to-voxel parameter estimate images, which were entered into population-level analyses. We report results thresholded at voxel level $p < 0.001$ (uncorrected) and cluster level $p < 0.05$ (family-wise error [FWE] corrected for multiple comparisons) for a valid voxel-wise inference approach (*95*).

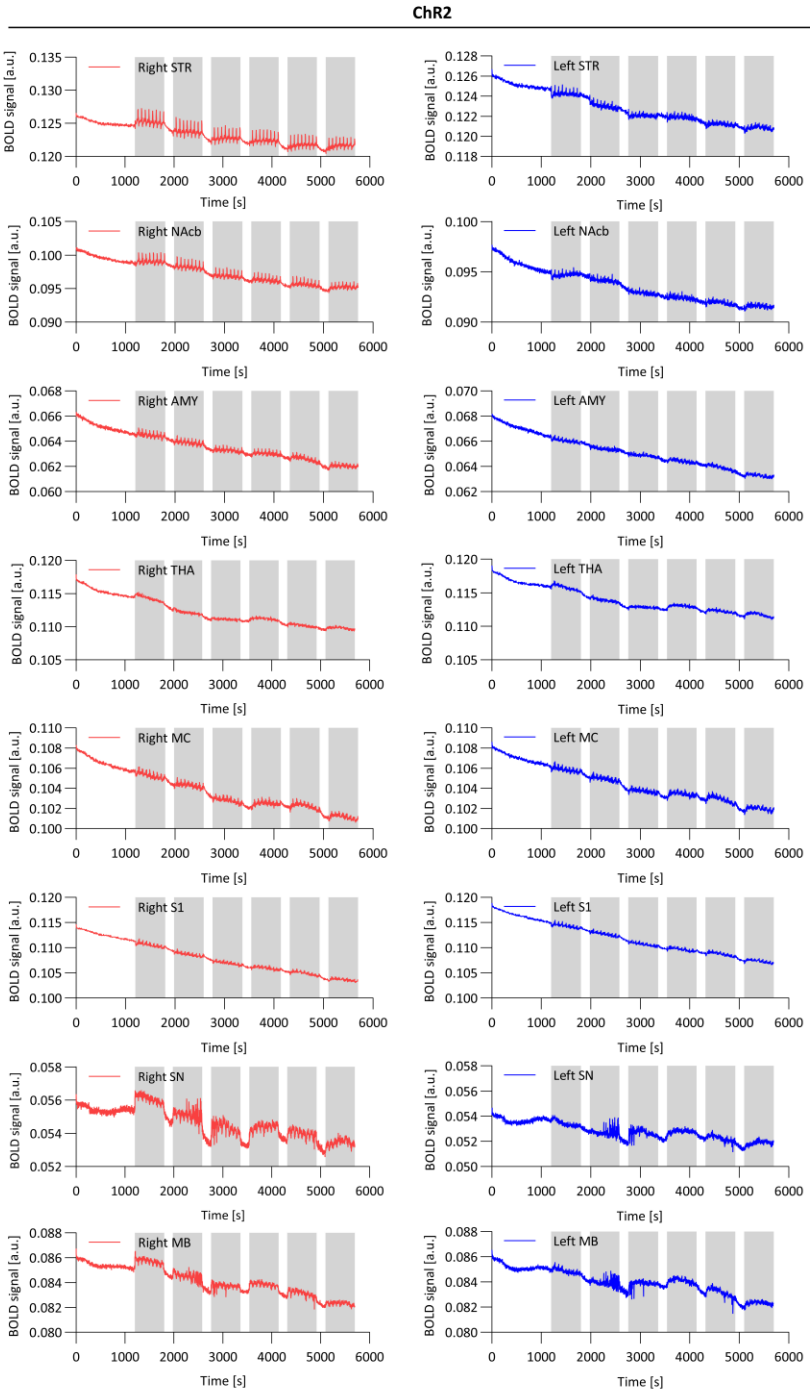

Fig. S1. BOLD-fMRI signal time courses of selected regions. Mean BOLD signal time courses over 95 minutes are shown for selected regions for ChR2 (n = 18) expressing rats. ChR2 expressing rats responded to stimulation (highlighted in grey) with positive BOLD signal changes in the right striatum, nucleus accumbens, amygdala, thalamus, midbrain and substantia nigra. Negative responses were obtained in the contralateral striatum, nucleus accumbens, amygdala and right and left cortical regions. Abbreviations: AMY, amygdala; MB, midbrain; MC, motor cortex; NAcb, nucleus accumbens; S1, somatosensory cortex; SN, substantia nigra; STR, striatum; THA, thalamus.

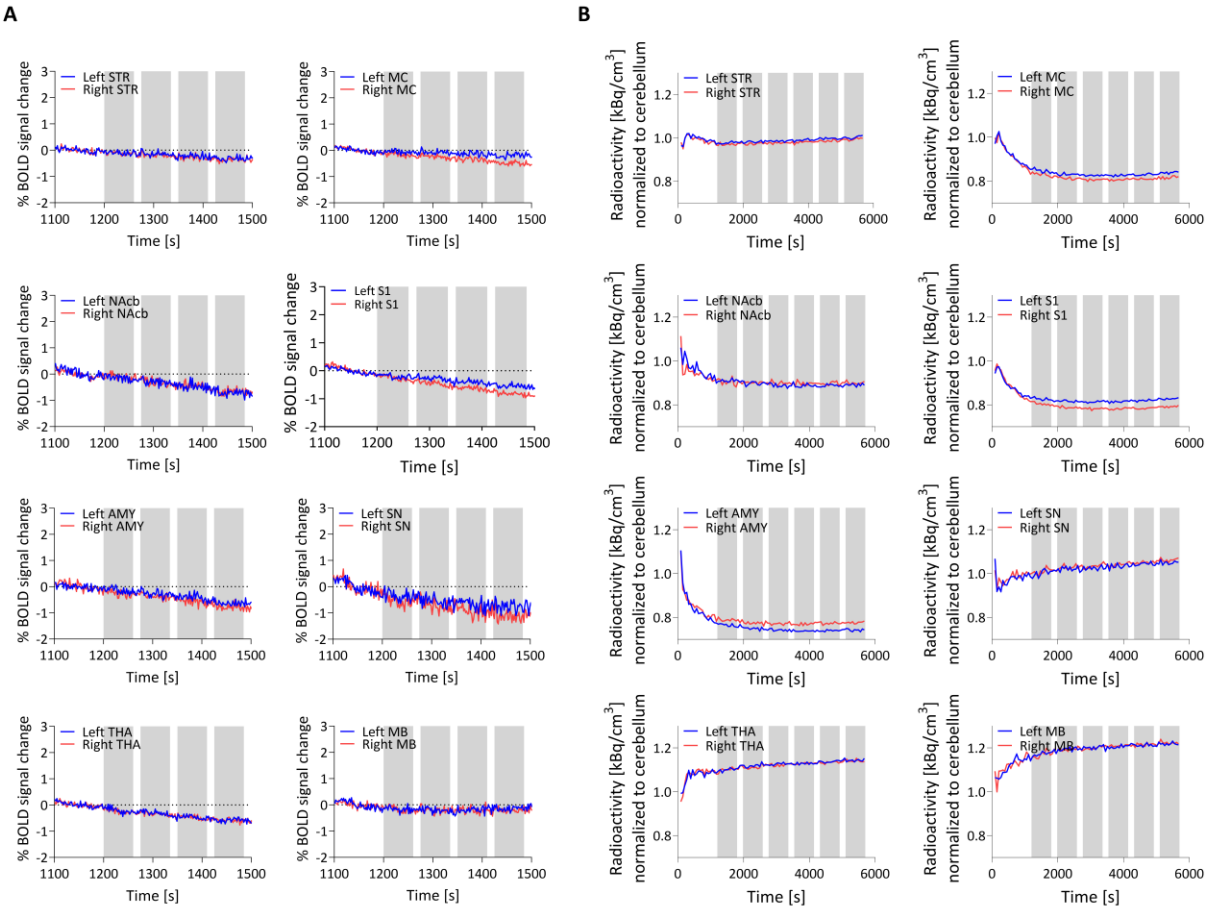

Fig. S2. %BOLD-fMRI signal changes and PET time activity curves in GFP rats. (**A**) Mean %BOLD signal changes over 400 seconds are shown for selected regions of GFP (n = 12) expressing rats. (**B**) Mean normalized [^{18}F]FDG time activity curves over 95 minutes are shown for selected regions of GFP (n = 14) expressing rats. In both modalities, GFP expressing rats did not respond to stimulation (highlighted in grey). Abbreviations: AMY, amygdala; MB, midbrain; MC, motor cortex; NAcb, nucleus accumbens; S1, somatosensory cortex; SN, substantia nigra; STR, striatum; THA, thalamus.

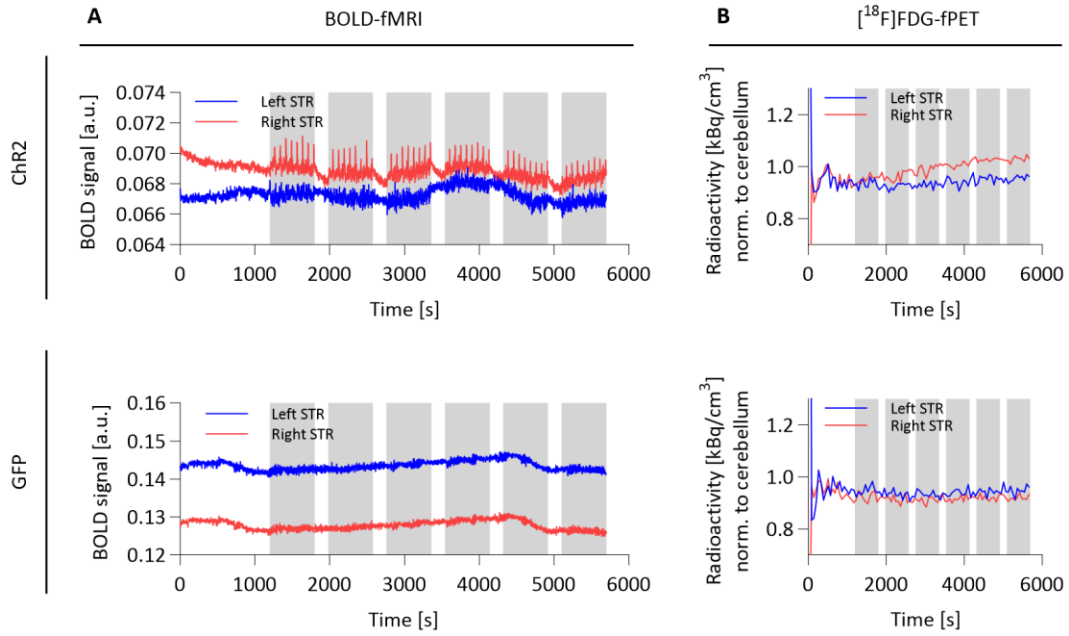

Fig. S3. [^{18}F]FDG-fPET and BOLD-fMRI activation on single animal level. (**A**) Mean BOLD signal time courses over 95 minutes are shown for the striatum for one exemplary ChR2 and GFP expressing rat. (**B**) Mean normalized time activity curves over 95 minutes are shown for the striatum of one exemplary ChR2 and GFP expressing rat. Grey bars indicate 10-minute stimulation blocks. Abbreviations: ChR2, channelrhodopsin-2; GFP, green fluorescent protein; STR, striatum.

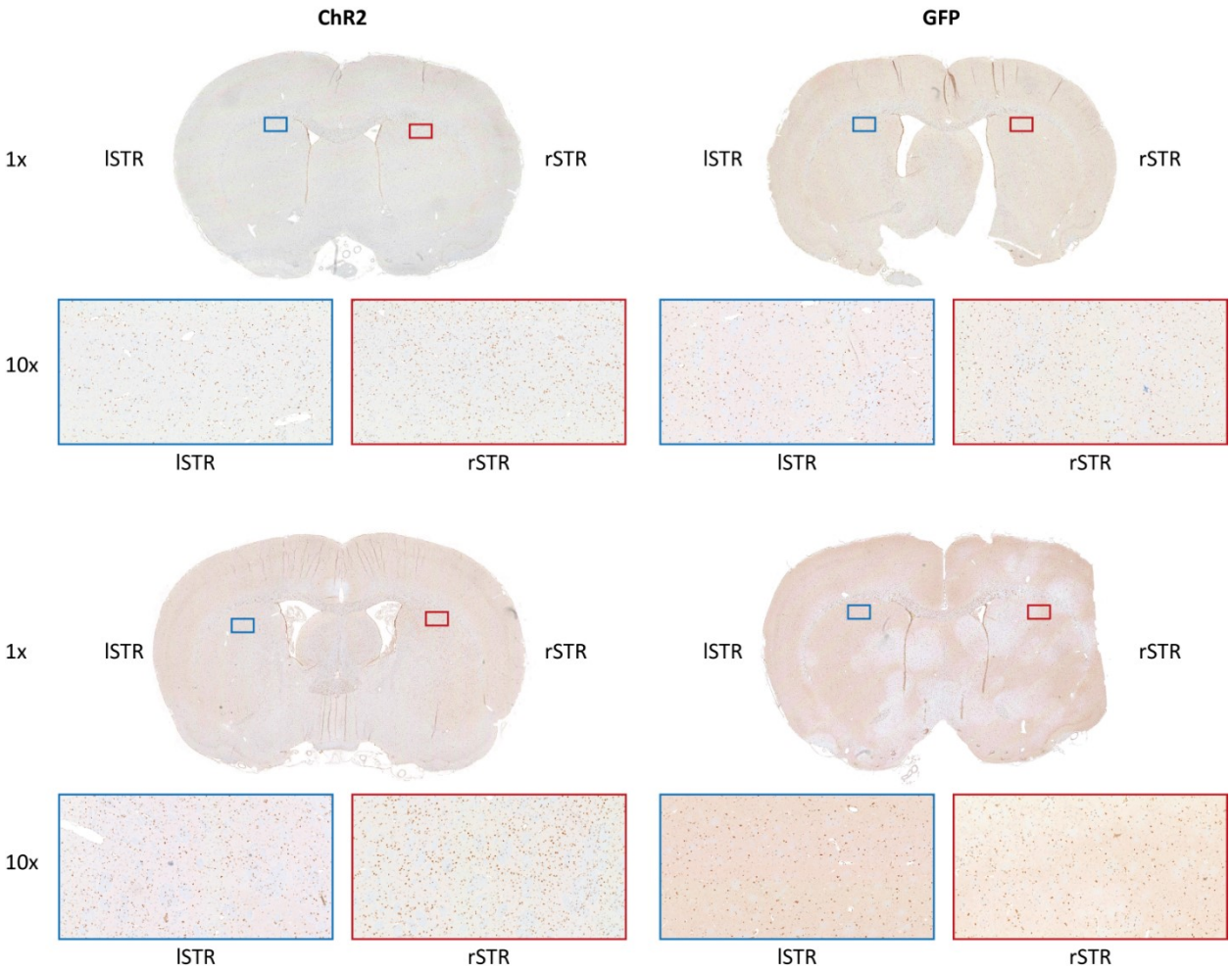

Fig. S4. c-fos immunohistochemical staining in the striatum. C-fos staining in the other two ChR2 and GFP rats not shown in Fig. 7 is shown for the dorsal striatum in 1× and 10× magnifications. A higher number of c-fos+ cells can be identified in the 10× magnification of the right striatum of the ChR2 rats. Abbreviations: ChR2, channelrhodopsin-2; GFP, green fluorescent protein; l, left; r, right; STR, striatum.

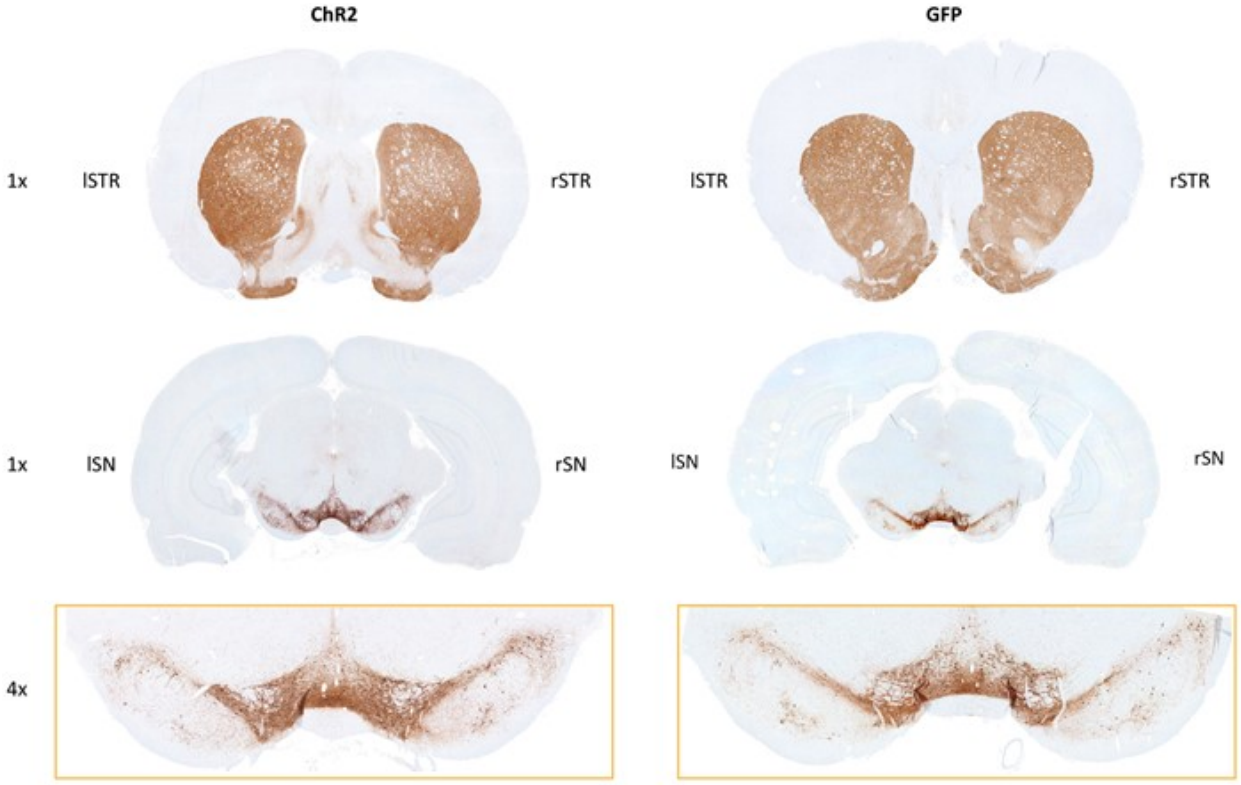

Fig. S5. Tyrosine hydroxylase immunohistochemical staining in the striatum and substantia nigra. Tyrosine hydroxylase staining in one exemplary ChR2 and one GFP rat is shown for the striatum in 1× and substantia nigra in 1× and 4× magnification. No qualitative left to right differences were identified in neither of the regions. Technical reasons are responsible for an uneven distribution of the staining. Abbreviations: ChR2, channelrhodopsin-2; GFP, green fluorescent protein; l, left; r, right; SN, substantia nigra; STR, striatum.

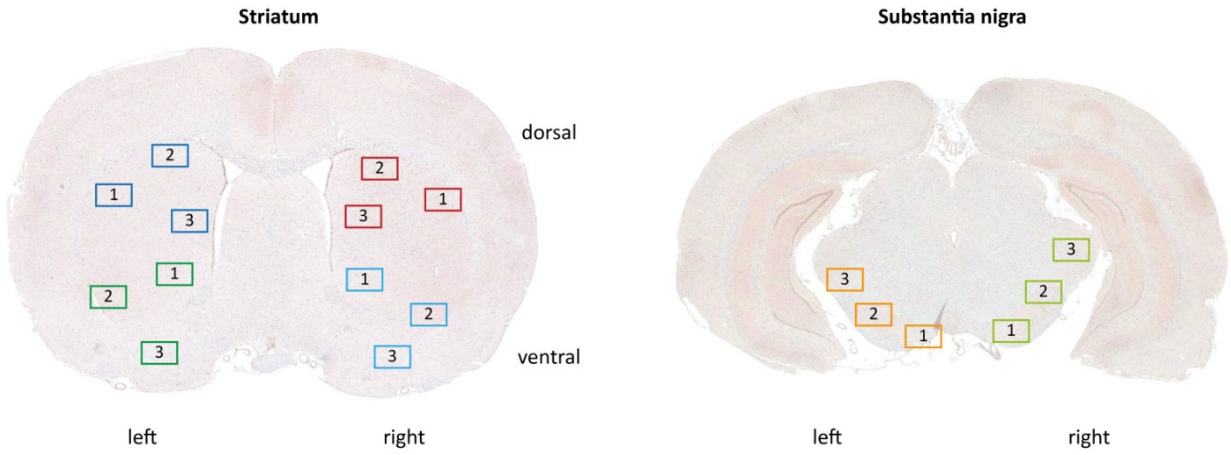

Fig. S6. Selected regions of interest for quantitative analysis of c-fos immunohistochemistry. Three regions of interest for c-fos quantification were drawn into the right and left, dorsal and ventral striatum and right and left substantia nigra of each selected rat.

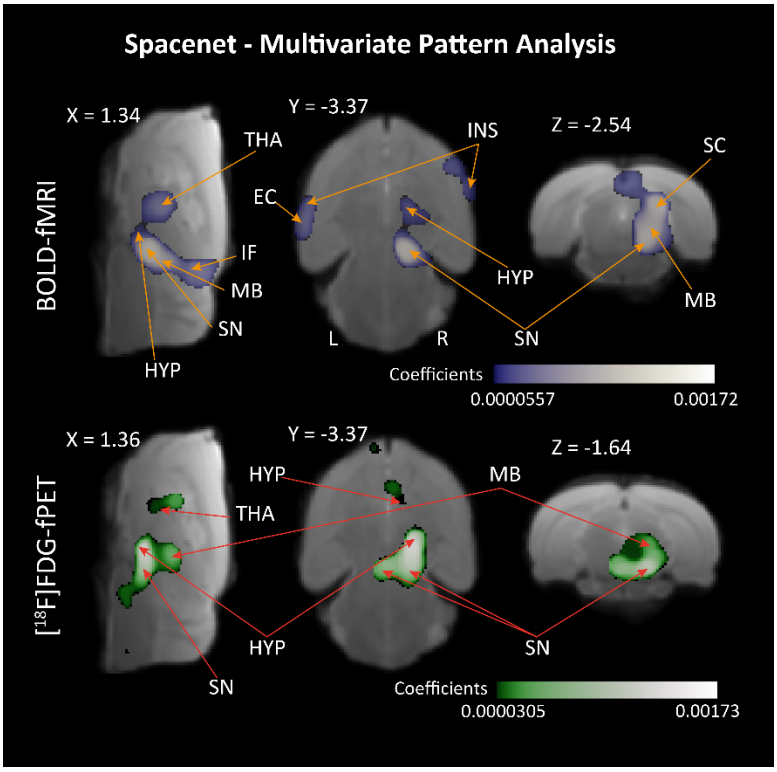

Fig. S7. Optogenetic stimulation coding at the whole-brain level using MVPA Spacenet classifiers. We trained multivariate classifiers to decode the optogenetic stimulation (vs. baseline) from patterns of hemodynamic responses or glucose uptake. The displayed results show group-level analysis of SpaceNet coefficient maps for the fMRI (top) and fPET (bottom) datasets, which can be interpreted as information maps specifying voxels whose joint signal changes contains information about the class (i.e., optogenetic stimulation). Abbreviations: AMY, amygdala; EC, entorhinal cortex; HYP, hypothalamus; INS, insular cortex; MB, midbrain; NAcb, nucleus accumbens; SC, superior colliculus; IC, inferior colliculus; SN, substantia nigra; STR, striatum; THA, thalamus; L, left; R, right.

Component	Kurtosis	Skeweness	Variability	Frequency
ICA_9 (OGS)	9.4702	1.5296	0.89649	0.0015126
ICA_7	6.1892	-1.1373	0.61559	0.0019337
ICA_5	6.0444	-0.029553	0.74643	0.0024379
ICA_1	5.9096	-0.92696	0.62911	0.0026374
ICA_3	5.5793	-1.6948	0.66834	0.0030253
ICA_6	5.1538	0.45623	0.71338	0.0029699
ICA_4	5.0307	0.20187	0.77642	0.002992
ICA_2	4.9093	0.3029	0.77882	0.0029532
ICA_11	4.8252	0.46421	0.81305	0.0027648
ICA_12	4.7691	0.42947	0.74488	0.0031804
ICA_18	4.5608	-0.071605	0.77426	0.0026208
ICA_16	4.1498	0.35611	0.92187	0.0031472
ICA_10	3.7893	0.17116	0.85876	0.0032524
ICA_13	3.4033	0.043359	0.86731	0.0030973
ICA_14	2.8282	0.045367	1.011	0.0031305
ICA_8	2.7453	0.034452	0.87565	0.0030862
ICA_20	2.6707	-0.013394	0.77546	0.0034574
ICA_15	2.5996	0.008139	0.80949	0.0029699
ICA_17	2.5655	-0.029454	0.77274	0.0032912
ICA_19	2.226	0.12018	0.79925	0.0028092

Table S1. Independent component analysis (ICA). Descriptive measures derived from the independent component's voxels values distribution for all 20 components (kurtosis sorted).

Brain region (ROI)	Distance activation centers [mm] BETWEEN	Distance activation centers [mm] WITHIN	Dice similarity coefficient BETWEEN	Dice similarity coefficient WITHIN
R AMY	5.0	5.0	-	-
R HIP posterior	2.2	-	-	-
R HYP	1.6	2.1	0.277	0.018
R MB	2.1	2.7	0.165	0
PAG	1.9	1.0	-	-
R SN	1.3	0.9	0.026	0
R S1	-	2.8	-	0.042
R INS	-	3.7	-	0.080
R NAcb		0.9	-	0.444
R STR	1.2	2.9	0.548	0.743
R THA	3.5	-	0.024	0.0221

Table S2. Distance of t-value peak location between fPET and fMRI and Dice similarity coefficient (between- and within-group analysis). Abbreviations: AMY, amygdala; HIP, hippocampus; HYP, hypothalamus; ICA, independent component analysis; L, left; MB, midbrain; PAG, periaqueductal gray; R, right; SN, substantia nigra; STR, striatum; THA, thalamus; NAcb, nucleus accumbens; INS, insular cortex; S1, somatosensory cortex.

	ChR2		GFP	
Brain region (ROI)	**Right**	**Left**	**Right**	**Left**
Dorsal striatum	73 ± 4.0%	48 ± 5.6%	47 ± 6.7%	46 ± 2.5%
Ventral striatum	50 ± 17%	42 ± 11%	44 ± 11%	45 ± 15%
Substantia nigra	87 ± 4.0%	82 ± 5.5%	82 ± 5.7%	86 ± 4.2%

Table S3. Percentage of c-fos+ cells. Abbreviations: ChR2, channelrhodopsin-2; GFP, green fluorescent protein; ROI, region of interest.

Brain region (ROI)	ROI volume [mm^3]	# voxels	Abbreviation
R/ L nucleus accumbens	7.9	993	NAcb
R/ L amygdala	21.1	2640	AMY
R/ L caudate putamen	43.5	5444	STR
R/ L auditory cortex	27.5	3440	AC
R/ L cingulate cortex	14.5	1810	Cg
R/ L entorhinal cortex	59.0	7377	EC
R/ L insular cortex	21.1	2641	INS
R/ L medial prefrontal cortex	6.3	788	mPFC
R/ L motor cortex	32.6	4076	MC
R/ L orbitofrontal cortex	18.9	2367	OFC
R/ L parietal cortex	7.6	954	PaC
R/ L retrosplenial cortex	18.9	2365	RS
R/ L somatosensory cortex	71.6	8950	S1
R/ L visual cortex	36.1	4517	V1
R/ L anterodorsal hippocampus	25.1	3133	HIP ant.
R/ L posterior hippocampus	9.8	1223	HIP post.
R/ L hypothalamus	18.4	2294	HYP
R/ L olfactory cortex	14.0	1751	OC
R/ L superior colliculus	7.1	892	SC
R/ L midbrain	11.4	1431	MB
R/ L ventral tegmental area/ substantia nigra	5.5	691	SN
R/ L cerebellum – grey matter	75.0	9374	CG
R/ L cerebellum – white matter	23.4	2938	CW
R/ L inferior colliculus	5.7	718	IC
R/ L thalamus	30.7	3839	THA
medulla	58.2	2944	Med
periaqueductal gray	9.9	1238	PAG
pituitary gland	5.8	733	PG
septum	9.4	1170	Sep

Table S4. Characteristics and abbreviations of selected regions of interest (Schiffer rat brain atlas)
Abbreviations: L, left; R, right; ROI, region of interest.

Region	Cluster Peak	Voxels	Max t-value (z-value)	Mean t (std.)	*p*-value (FWE)
Seed-based *molecular* connectivity (SBC)					
Midbrain R*	0.55 -2.8 -1.2	581	10.38 (5.54)	5.04 (0.99)	< 0.0001
Substantia nigra R*		510		5.22 (1.22)	cl.
Hypothalamus R		200		4.46 (0.55)	cl.
Substantia nigra L		10		3.99 (0.22)	cl.
Thalamus R		10		3.88 (0.15)	cl.
Seed-based *functional* connectivity (SBC)					
Striatum R*	4.52 -3.2 3.6	4949	18.81 (7.16)	8.11 (2.39)	< 0.0001
Amygdala R*		739		6.97 (1.74)	cl.
Nucleus Accumbens R*		586		6.45 (1.01)	cl.

Table S5. Functional and molecular connectivity. Results are shown at threshold $p < 0.001$ voxel-level uncorrected, $p < 0.05$ cluster-level FWE-corrected; * markings show brain regions with significant signal changes at voxel-level FWE-corrected $p < 0.05$). Results of group seed-based connectivity (SBC) analysis, with the right striatum as seed region for the contrast optogenetic stimulation vs. baseline. The regions described showed stronger positive functional/metabolic connectivity with the seed region during the optogenetic stimulation compared to baseline. Abbreviations: L, left; R, right; Cl., areas integrating the above detailed cluster-level p-value.

Region	Coordinates	Voxels	Mean t (std.)
fMRI - Searchlight			
Striatum R	5.4 -1.6 2	4442	5.48 (1.07)
Thalamus R	1.22 -2.8 1.6	1399	4.92 (0.89)
Midbrain R	0.55 -2.6 -2.8	1027	5.54 (1.37)
Substantia nigra R	0.11 -2.8 -1.6	512	4.85 (0.91)
Hypothalamus R	2.1 -3.2 4	320	4.49 (0.69)
Nucleus accumbens R	1.88 -2.4 7	123	6.61 (0.91)
Insular cortex R	6.28 -2 2.2	97	4.96 (1.01)
Substantia nigra L	-0.54 -2.8 -1.6	76	5.82 (1.59)
Amygdala R	5.4 -3.4 2.2	44	5.38 (1.07)
Hypothalamus L	-2.62 -4.47 1.61	41	4.59 (0.74)
Thalamus L	-0.97 -1.11 3.19	38	4.11 (0.43)
Nucleus accumbens L	-1.49 -3.37 6.18	27	4.76 (0.89)
fPET - Searchlight			
Hypothalamus R	0.11 -4 -1.4	740	5.07 (0.91)
Thalamus R	2.54 -2 0.99	671	5.16 (1.18)
Substantia nigra R	0.99 -3.6 -1.4	565	5.35 (1.11)
Midbrain R	2.1 -3.2 -2.8	425	4.84 (0.74)
Striatum R	2.54 -1.6 4.8	173	4.16 (0.40)
Substantia nigra L	-0.55 -2.8 -1.5	78	5.38 (0.70)
Amygdala R	3.42 -3.8 -1.2	20	4.22 (0.54)
Amygdala L	-3.56 -5.30 2.16	19	4.69 (0.95)
Hypothalamus L	-0.32 -3.2 0.99	18	4.38 (0.75)
Nucleus accumbens L		11	4.21 (0.33)
Thalamus L	-0.98 -2.4 -6.55	8	4.13 (0.30)

Table S6. Searchlight analysis. Regions where searchlight-based classification analysis discriminates between optogenetic stimulation vs. baseline trials (searchlight classification >60%, whole-brain cluster-corrected $p < 0.05$ via comparison with 1000 random permutations). Coordinates denote the 3D center of gravity of each region. Abbreviations: L, left; R, right.

REFERENCES AND NOTES

1. B. Liss, J. Roeper, Individual dopamine midbrain neurons: Functional diversity and flexibility in health and disease. *Brain Res. Rev.* **58**, 314–321 (2008).

2. S. D. Jamadar, P. G. D. Ward, T. G. Close, A. Fornito, M. Premaratne, K. O'Brien, D. Stäb, Z. Chen, N. J. Shah, G. F. Egan, Simultaneous BOLD-fMRI and constant infusion FDG-PET data of the resting human brain. *Sci. Data* **7**, 363 (2020).

3. C. Y. Sander, H. D. Hansen, H. Y. Wey, Advances in simultaneous PET/MR for imaging neuroreceptor function. *J. Cereb. Blood Flow Metab.* **40**, 1148–1166 (2020).

4. A. Hahn, M. Breakspear, L. Rischka, W. Wadsak, G. M. Godbersen, V. Pichler, P. Michenthaler, T. Vanicek, M. Hacker, S. Kasper, R. Lanzenberger, L. Cocchi, Reconfiguration of functional brain networks and metabolic cost converge during task performance. *eLife* **9**, e52443 (2020).

5. T. M. Ionescu, M. Amend, T. Watabe, J. Hatazawa, A. Maurer, G. Reischl, B. J. Pichler, H. F. Wehrl, K. Herfert, Neurovascular uncoupling: Multimodal imaging delineates the acute effects of 3,4-methylenedioxymethamphetamine. *J. Nucl. Med.* **64**, 466–471 (2023).

6. T. M. Ionescu, M. Amend, R. Hafiz, B. B. Biswal, A. Maurer, B. J. Pichler, H. F. Wehrl, K. Herfert, Striatal and prefrontal D2R and SERT distributions contrastingly correlate with default-mode connectivity. *Neuroimage* **243**, 118501 (2021).

7. S. Marciano, T. M. Ionescu, R. S. Saw, R. Y. Cheong, D. Kirik, A. Maurer, B. J. Pichler, K. Herfert, Combining CRISPR-Cas9 and brain imaging to study the link from genes to molecules to networks. *Proc. Natl. Acad. Sci. U.S.A.* **119**, e2122552119 (2022).

8. K. Fischer, V. Sossi, A. von Ameln-Mayerhofer, G. Reischl, B. J. Pichler, Quantification of dopamine transporters in mice with unilateral 6-OHDA lesions using [^{11}C]methylphenidate and PET. *Neuroimage* **59**, 2413–2422 (2012).

9. K. Fischer, V. Sossi, A. Schmid, M. Thunemann, F. C. Maier, M. S. Judenhofer, J. G. Mannheim, G. Reischl, B. J. Pichler, Noninvasive nuclear imaging enables the in vivo

quantification of striatal dopamine receptor expression and raclopride affinity in mice. *J. Nucl. Med.* **52**, 1133–1141 (2011).

10. N. Y. Lettfuss, K. Fischer, V. Sossi, B. J. Pichler, A. von Ameln-Mayerhofer, Imaging DA release in a rat model of L-DOPA-induced dyskinesias: A longitudinal in vivo PET investigation of the antidyskinetic effect of MDMA. *Neuroimage* **63**, 423–433 (2012).

11. L. J. Stiernman, F. Grill, A. Hahn, L. Rischka, R. Lanzenberger, V. Panes Lundmark, K. Riklund, J. Axelsson, A. Rieckmann, Dissociations between glucose metabolism and blood oxygenation in the human default mode network revealed by simultaneous PET-fMRI. *Proc. Natl. Acad. Sci. U.S.A.* **118**, e2021913118 (2021).

12. E. S. Boyden, F. Zhang, E. Bamberg, G. Nagel, K. Deisseroth, Millisecond-timescale, genetically targeted optical control of neural activity. *Nat. Neurosci.* **8**, 1263–1268 (2005).

13. M. Benoit-Marand, E. Borrelli, F. Gonon, Inhibition of dopamine release via presynaptic D2 receptors: Time course and functional characteristics in vivo. *J. Neurosci.* **21**, 9134–9141 (2001).

14. M. Villien, H.-Y. Wey, J. B. Mandeville, C. Catana, J. R. Polimeni, C. Y. Sander, N. R. Zürcher, D. B. Chonde, J. S. Fowler, B. R. Rosen, J. M. Hooker, Dynamic functional imaging of brain glucose utilization using fPET-FDG. *Neuroimage* **100**, 192–199 (2014).

15. H. F. Wehrl, M. Hossain, K. Lankes, C. C. Liu, I. Bezrukov, P. Martirosian, F. Schick, G. Reischl, B. J. Pichler, Simultaneous PET-MRI reveals brain function in activated and resting state on metabolic, hemodynamic and multiple temporal scales. *Nat. Med.* **19**, 1184–1189 (2013).

16. A. Hahn, G. Gryglewski, L. Nics, M. Hienert, L. Rischka, C. Vraka, H. Sigurdardottir, T. Vanicek, G. M. James, R. Seiger, A. Kautzky, L. Silberbauer, W. Wadsak, M. Mitterhauser, M. Hacker, S. Kasper, R. Lanzenberger, Quantification of task-specific glucose metabolism with constant infusion of ^{18}F-FDG. *J. Nucl. Med.* **57**, 1933–1940 (2016).

17. S. D. Jamadar, P. G. D. Ward, S. Li, F. Sforazzini, J. Baran, Z. Chen, G. F. Egan, Simultaneous task-based BOLD-fMRI and [18-F] FDG functional PET for measurement of neuronal metabolism in the human visual cortex. *Neuroimage* **189**, 258–266 (2019).

18. L. Rischka, G. Gryglewski, S. Pfaff, T. Vanicek, M. Hienert, M. Klobl, M. Hartenbach, A. Haug, W. Wadsak, M. Mitterhauser, M. Hacker, S. Kasper, R. Lanzenberger, A. Hahn, Reduced task durations in functional PET imaging with [^{18}F]FDG approaching that of functional MRI. *Neuroimage* **181**, 323–330 (2018).

19. S. Li, S. D. Jamadar, P. G. D. Ward, M. Premaratne, G. F. Egan, Z. Chen, Analysis of continuous infusion functional PET (fPET) in the human brain. *Neuroimage* **213**, 116720 (2020).

20. F. De Martino, F. Gentile, F. Esposito, M. Balsi, F. Di Salle, R. Goebel, E. Formisano, Classification of fMRI independent components using IC-fingerprints and support vector machine classifiers. *Neuroimage* **34**, 177–194 (2007).

21. E. Formisano, F. Esposito, N. Kriegeskorte, G. Tedeschi, F. Di Salle, R. Goebel, Spatial independent component analysis of functional magnetic resonance imaging time-series: Characterization of the cortical components. *Neurocomputing* **49**, 241–254 (2002).

22. W. Lu, J. C. Rajapakse, Eliminating indeterminacy in ICA. *Neurocomputing* **50**, 271–290 (2003).

23. C. H. Moritz, B. P. Rogers, M. E. Meyerand, Power spectrum ranked independent component analysis of a periodic fMRI complex motor paradigm. *Hum. Brain Mapp.* **18**, 111–122 (2003).

24. T. Davis, K. F. LaRocque, J. A. Mumford, K. A. Norman, A. D. Wagner, R. A. Poldrack, What do differences between multi-voxel and univariate analysis mean? How subject-, voxel-, and trial-level variance impact fMRI analysis. *Neuroimage* **97**, 271–283 (2014).

25. F. Pereira, T. Mitchell, M. Botvinick, Machine learning classifiers and fMRI: A tutorial overview. *Neuroimage* **45**, S199–S209 (2009).

26. A. Abraham, F. Pedregosa, M. Eickenberg, P. Gervais, A. Mueller, J. Kossaifi, A. Gramfort, B. Thirion, G. Varoquaux, Machine learning for neuroimaging with scikit-learn. *Front. Neuroinform.* **8**, 14 (2014).

27. N. Kriegeskorte, R. Goebel, P. Bandettini, Information-based functional brain mapping. *Proc. Natl. Acad. Sci.* **103**, 3863–3868 (2006).

28. T. E. Nichols, A. P. Holmes, Nonparametric permutation tests for functional neuroimaging: A primer with examples. *Hum. Brain Mapp.* **15**, 1–25 (2002).

29. K. J. Friston, Functional and effective connectivity: A review. *Brain Connect.* **1**, 13–36 (2011).

30. N. X. Tritsch, J. B. Ding, B. L. Sabatini, Dopaminergic neurons inhibit striatal output through non-canonical release of GABA. *Nature* **490**, 262–266 (2012).

31. N. X. Tritsch, W. J. Oh, C. Gu, B. L. Sabatini, Midbrain dopamine neurons sustain inhibitory transmission using plasma membrane uptake of GABA, not synthesis. *eLife* **3**, e01936 (2014).

32. J. C. Patel, A. D. Sherpa, R. Melani, P. Witkovsky, M. R. Wiseman, B. O'Neill, C. Aoki, N. X. Tritsch, M. E. Rice, GABA co-released from striatal dopamine axons dampens phasic dopamine release through autoregulatory $GABA_A$ receptors. *Cell Rep.* **43**, 113834 (2024).

33. T. M. Mitchell, R. Hutchinson, R. S. Niculescu, F. Pereira, X. Wang, M. Just, S. Newman, Learning to decode cognitive states from brain images. *Mach. Learn.* **57**, 145–175 (2004).

34. D. Sulzer, S. J. Cragg, M. E. Rice, Striatal dopamine neurotransmission: Regulation of release and uptake. *Basal Ganglia* **6**, 123–148 (2016).

35. C. P. Ford, The role of D2-autoreceptors in regulating dopamine neuron activity and transmission. *Neuroscience* **282**, 13–22 (2014).

36. A. Andrea, E. L.-O. José, R. Maria, M. Claudia De, F. W. Hopf, I. Ciro, H. Briac, J. Jacob, K. Chisato, W. Marc, G. C. Marc, B. Antonello, S. David, B. Emiliana, Dual control of

dopamine synthesis and release by presynaptic and postsynaptic dopamine D2 receptors. *J. Neurosci.* **32**, 9023 (2012).

37. A. B. Nelson, N. Hammack, C. F. Yang, N. M. Shah, R. P. Seal, A. C. Kreitzer, Striatal cholinergic interneurons drive GABA release from dopamine terminals. *Neuron* **82**, 63–70 (2014).

38. T. Koos, J. M. Tepper, Inhibitory control of neostriatal projection neurons by GABAergic interneurons. *Nat. Neurosci.* **2**, 467–472 (1999).

39. J. W. Mink, The basal ganglia: Focused selection and inhibition of competing motor programs. *Prog. Neurobiol.* **50**, 381–425 (1996).

40. C. R. Gerfen, T. M. Engber, L. C. Mahan, Z. Susel, T. N. Chase, F. J. Monsma Jr., D. R. Sibley, D1 and D2 dopamine receptor-regulated gene expression of striatonigral and striatopallidal neurons. *Science* **250**, 1429–1432 (1990).

41. D. J. Surmeier, J. Ding, M. Day, Z. Wang, W. Shen, D1 and D2 dopamine-receptor modulation of striatal glutamatergic signaling in striatal medium spiny neurons. *Trends Neurosci.* **30**, 228–235 (2007).

42. R. L. Albin, A. B. Young, J. B. Penney, The functional anatomy of basal ganglia disorders. *Trends Neurosci.* **12**, 366–375 (1989).

43. M. R. DeLong, Primate models of movement disorders of basal ganglia origin. *Trends Neurosci.* **13**, 281–285 (1990).

44. A. V. Kravitz, B. S. Freeze, P. R. Parker, K. Kay, M. T. Thwin, K. Deisseroth, A. C. Kreitzer, Regulation of parkinsonian motor behaviours by optogenetic control of basal ganglia circuitry. *Nature* **466**, 622–626 (2010).

45. G. Cui, S. B. Jun, X. Jin, M. D. Pham, S. S. Vogel, D. M. Lovinger, R. M. Costa, Concurrent activation of striatal direct and indirect pathways during action initiation. *Nature* **494**, 238–242 (2013).

46. O. Hikosaka, Y. Takikawa, R. Kawagoe, Role of the basal ganglia in the control of purposive saccadic eye movements. *Physiol. Rev.* **80**, 953–978 (2000).

47. J. F. Keeler, D. O. Pretsell, T. W. Robbins, Functional implications of dopamine D1 vs. D2 receptors: A 'prepare and select' model of the striatal direct vs. indirect pathways. *Neuroscience* **282**, 156–175 (2014).

48. P. Calabresi, B. Picconi, A. Tozzi, V. Ghiglieri, M. Di Filippo, Direct and indirect pathways of basal ganglia: A critical reappraisal. *Nat. Neurosci.* **17**, 1022–1030 (2014).

49. E. K. Richfield, J. B. Penney, A. B. Young, Anatomical and affinity state comparisons between dopamine D1 and D2 receptors in the rat central nervous system. *Neuroscience* **30**, 767–777 (1989).

50. J. K. Dreyer, K. F. Herrik, R. W. Berg, J. D. Hounsgaard, Influence of phasic and tonic dopamine release on receptor activation. *J. Neurosci.* **30**, 14273–14283 (2010).

51. J. B. Mandeville, C. Y. M. Sander, B. G. Jenkins, J. M. Hooker, C. Catana, W. Vanduffel, N. M. Alpert, B. R. Rosen, M. D. Normandin, A receptor-based model for dopamine-induced fMRI signal. *Neuroimage* **75**, 46–57 (2013).

52. C. Y. Sander, J. M. Hooker, C. Catana, M. D. Normandin, N. M. Alpert, G. M. Knudsen, W. Vanduffel, B. R. Rosen, J. B. Mandeville, Neurovascular coupling to D2/D3 dopamine receptor occupancy using simultaneous PET/functional MRI. *Proc. Natl. Acad. Sci. U.S.A.* **110**, 11169–11174 (2013).

53. L. Hunger, A. Kumar, R. Schmidt, Abundance compensates kinetics: Similar effect of dopamine signals on D1 and D2 receptor populations. *J. Neurosci.* **40**, 2868–2881 (2020).

54. P. F. Marcott, A. A. Mamaligas, C. P. Ford, Phasic dopamine release drives rapid activation of striatal D2-receptors. *Neuron* **84**, 164–176 (2014).

55. C. Yapo, A. G. Nair, L. Clement, L. R. Castro, J. Hellgren Kotaleski, P. Vincent, Detection of phasic dopamine by D1 and D2 striatal medium spiny neurons. *J. Physiol.* **595**, 7451–7475 (2017).

56. S. Navailles, P. De Deurwaerdere, Imbalanced dopaminergic transmission mediated by serotonergic neurons in L-DOPA-induced dyskinesia. *Parkinsons Dis.* **2012**, 323686 (2012).

57. R. C. Sellnow, J. H. Newman, N. Chambers, A. R. West, K. Steece-Collier, I. M. Sandoval, M. J. Benskey, C. Bishop, F. P. Manfredsson, Regulation of dopamine neurotransmission from serotonergic neurons by ectopic expression of the dopamine D2 autoreceptor blocks levodopa-induced dyskinesia. *Acta Neuropathol. Commun.* **7**, 8 (2019).

58. G. M. Godbersen, S. Klug, W. Wadsak, V. Pichler, J. Raitanen, A. Rieckmann, L. Stiernman, L. Cocchi, M. Breakspear, M. Hacker, R. Lanzenberger, A. Hahn, Task-evoked metabolic demands of the posteromedial default mode network are shaped by dorsal attention and frontoparietal control networks. *eLife* **12**, e84683 (2023).

59. I. Vanzetta, A. Grinvald, Increased cortical oxidative metabolism due to sensory stimulation: Implications for functional brain imaging. *Science* **286**, 1555–1558 (1999).

60. D. Malonek, U. Dirnagl, U. Lindauer, K. Yamada, I. Kanno, A. Grinvald, Vascular imprints of neuronal activity: Relationships between the dynamics of cortical blood flow, oxygenation, and volume changes following sensory stimulation. *Proc. Natl. Acad. Sci. U.S.A.* **94**, 14826–14831 (1997).

61. T. A. Woolsey, C. M. Rovainen, S. B. Cox, M. H. Henegar, G. E. Liang, D. Liu, Y. E. Moskalenko, J. Sui, L. Wei, Neuronal units linked to microvascular modules in cerebral cortex: Response elements for imaging the brain. *Cereb. Cortex* **6**, 647–660 (1996).

62. N. Harel, S. P. Lee, T. Nagaoka, D. S. Kim, S. G. Kim, Origin of negative blood oxygenation level-dependent fMRI signals. *J. Cereb. Blood Flow Metab.* **22**, 908–917 (2002).

63. Y. Liu, H. Shen, Z. Zhou, D. Hu, Sustained negative BOLD response in human fMRI finger tapping task. *PLOS ONE* **6**, e23839 (2011).

64. A. Rodriguez-Baeza, F. Reina-De La Torre, M. Ortega-Sanchez, J. Sahuquillo-Barris, Perivascular structures in corrosion casts of the human central nervous system: A confocal laser and scanning electron microscope study. *Anat. Rec.* **252**, 176–184 (1998).

65. M. Moraschi, M. DiNuzzo, F. Giove, On the origin of sustained negative BOLD response. *J. Neurophysiol.* **108**, 2339–2342 (2012).

66. Y. Y. Shih, C. C. Chen, B. C. Shyu, Z. J. Lin, Y. C. Chiang, F. S. Jaw, Y. Y. Chen, C. Chang, A new scenario for negative functional magnetic resonance imaging signals: Endogenous neurotransmission. *J. Neurosci.* **29**, 3036–3044 (2009).

67. L. Edvinsson, J. McCulloch, J. Sharkey, Vasomotor responses of cerebral arterioles in situ to putative dopamine receptor agonists. *Br. J. Pharmacol.* **85**, 403–410 (1985).

68. D. H. Cerri, D. L. Albaugh, L. R. Walton, B. Katz, T. W. Wang, T. H. Chao, W. Zhang, R. J. Nonneman, J. Jiang, S. H. Lee, A. Etkin, C. N. Hall, G. D. Stuber, Y. I. Shih, Distinct neurochemical influences on fMRI response polarity in the striatum. *Nat. Commun.* **15**, 1916 (2024).

69. X. Yu, D. Glen, S. Wang, S. Dodd, Y. Hirano, Z. Saad, R. Reynolds, A. C. Silva, A. P. Koretsky, Direct imaging of macrovascular and microvascular contributions to BOLD fMRI in layers IV-V of the rat whisker-barrel cortex. *Neuroimage* **59**, 1451–1460 (2012).

70. N. Sirmpilatze, J. Baudewig, S. Boretius, Temporal stability of fMRI in medetomidine-anesthetized rats. *Sci. Rep.* **9**, 16673 (2019).

71. J. Grandjean, G. Desrosiers-Gregoire, C. Anckaerts, D. Angeles-Valdez, F. Ayad, D. A. Barrière, I. Blockx, A. B. Bortel, M. Broadwater, B. M. Cardoso, M. Célestine, J. E. Chavez-Negrete, S. Choi, E. Christiaen, P. Clavijo, L. Colon-Perez, S. Cramer, T. Daniele, E. Dempsey, Y. Diao, A. Doelemeyer, D. Dopfel, L. Dvořáková, C. Falfán-Melgoza, F. F. Fernandes, C. F. Fowler, A. Fuentes-Ibañez, C. Garin, E. Gelderman, C. E. Golden, C. C. Guo, M. J. Henckens, L. A. Hennessy, P. Herman, N. Hofwijks, C. Horien, T. M. Ionescu, J. Jones, J. Kaesser, E. Kim, H. Lambers, A. Lazari, S.-H. Lee, A. Lillywhite, Y. Liu, Y. Y. Liu, A. López-Castro, X. López-Gil, Z. Ma, E. MacNicol, D. Madularu, F. Mandino, S. Marciano, M. J. McAuslan, P. McCunn, A. McIntosh, X. Meng, L. Meyer-Baese, S. Missault, F. Moro, D. Naessens, L. J. Nava-Gomez, H. Nonaka, J. J. Ortiz, J. Paasonen, L. M. Peeters, M. Pereira, P. D. Perez, M. Pompilus, M. Prior, R. Rakhmatullin, H. M. Reimann, J. Reinwald, R. T. de Rio, A. Rivera-Olvera, D. Ruiz-Pérez, G. Russo, T. J. Rutten, R. Ryoke, M. Sack, P.

Salvan, B. G. Sanganahalli, A. Schroeter, B. J. Seewoo, E. Selingue, A. Seuwen, B. Shi, N. Sirmpilatze, J. A. Smith, C. Smith, F. Sobczak, P. J. Stenroos, M. Straathof, S. Strobelt, A. Sumiyoshi, K. Takahashi, M. E. Torres-García, R. Tudela, M. van den Berg, K. van der Marel, A. T. van Hout, R. Vertullo, B. Vidal, R. M. Vrooman, V. X. Wang, I. Wank, D. J. Watson, T. Yin, Y. Zhang, S. Zurbruegg, S. Achard, S. Alcauter, D. P. Auer, E. L. Barbier, J. Baudewig, C. F. Beckmann, N. Beckmann, G. J. Becq, E. L. Blezer, R. Bolbos, S. Boretius, S. Bouvard, E. Budinger, J. D. Buxbaum, D. Cash, V. Chapman, K.-H. Chuang, L. Ciobanu, B. Coolen, J. W. Dalley, M. Dhenain, R. M. Dijkhuizen, O. Esteban, C. Faber, M. Febo, K. W. Feindel, G. Forloni, J. Fouquet, E. A. Garza-Villarreal, N. Gass, J. C. Glennon, A. Gozzi, O. Gröhn, A. Harkin, A. Heerschap, X. Helluy, K. Herfert, A. Heuser, J. R. Homberg, D. J. Houwing, F. Hyder, G. D. Ielacqua, I. O. Jelescu, H. Johansen-Berg, G. Kaneko, R. Kawashima, S. D. Keilholz, G. A. Keliris, C. Kelly, C. Kerskens, J. Y. Khokhar, P. C. Kind, J.-B. Langlois, J. P. Lerch, M. A. López-Hidalgo, D. Manahan-Vaughan, F. Marchand, R. B. Mars, G. Marsella, E. Micotti, E. Muñoz-Moreno, J. Near, T. Niendorf, W. M. Otte, P. Pais, W.-J. Pan, R. A. Prado-Alcalá, G. L. Quirarte, J. Rodger, T. Rosenow, C. S. Baptista, A. Sartorius, S. J. Sawiak, T. W. Scheenen, N. Shemesh, Y.-Y. I. Shih, A. Shmuel, G. Soria, R. Stoop, G. J. Thompson, S. M. Till, N. Todd, A. Van Der Linden, A. van der Toorn, G. A. van Tilborg, C. Vanhove, A. Veltien, M. Verhoye, L. Wachsmuth, W. Weber-Fahr, P. Wenk, X. Yu, V. Zerbi, N. Zhang, B. B. Zhang, L. Zimmer, G. A. Devenyi, M. M. Chakravarty, A. Hess, A consensus protocol for functional connectivity analysis in the rat brain. *Nat. Neurosci.* **26**, 673–681 (2022).

72. C. Grimm, N. Wenderoth, V. Zerbi, An optimized protocol for assessing changes in mouse whole-brain activity using opto-fMRI. *STAR Protoc.* **3**, 101761 (2022).

73. T. D. Ambrisko, Y. Hikasa, Neurohormonal and metabolic effects of medetomidine compared with xylazine in beagle dogs. *Can. J. Vet. Res.* **66**, 42–49 (2002).

74. C. Suzuki, M. Kosugi, Y. Magata, Conscious rat PET imaging with soft immobilization for quantitation of brain functions: Comprehensive assessment of anesthesia effects on cerebral blood flow and metabolism. *EJNMMI Res.* **11**, 46 (2021).

75. L. Laaksonen, M. Kallioinen, J. Långsjö, T. Laitio, A. Scheinin, J. Scheinin, K. Kaisti, A. Maksimow, R. E. Kallionpää, V. Rajala, J. Johansson, O. Kantonen, M. Nyman, S. Sirén, K. Valli, A. Revonsuo, O. Solin, T. Vahlberg, M. Alkire, H. Scheinin, Comparative effects of dexmedetomidine, propofol, sevoflurane, and S-ketamine on regional cerebral glucose metabolism in humans: A positron emission tomography study. *Br. J. Anaesth.* **121**, 281–290 (2018).

76. K. Masamoto, M. Fukuda, A. Vazquez, S. G. Kim, Dose-dependent effect of isoflurane on neurovascular coupling in rat cerebral cortex. *Eur. J. Neurosci.* **30**, 242–250 (2009).

77. N. K. Logothetis, J. Pauls, M. Augath, T. Trinath, A. Oeltermann, Neurophysiological investigation of the basis of the fMRI signal. *Nature* **412**, 150–157 (2001).

78. F. Zhao, T. Jin, P. Wang, S. G. Kim, Isoflurane anesthesia effect in functional imaging studies. *Neuroimage* **38**, 3–4 (2007).

79. T. Maekawa, C. Tommasino, H. M. Shapiro, J. Keifer-Goodman, R. W. Kohlenberger, Local cerebral blood flow and glucose utilization during isoflurane anesthesia in the rat. *Anesthesiology* **65**, 144–151 (1986).

80. M. Ueki, G. Mies, K. A. Hossmann, Effect of alpha-chloralose, halothane, pentobarbital and nitrous oxide anesthesia on metabolic coupling in somatosensory cortex of rat. *Acta Anaesthesiol. Scand.* **36**, 318–322 (1992).

81. N. J. Maandag, D. Coman, B. G. Sanganahalli, P. Herman, A. J. Smith, H. Blumenfeld, R. G. Shulman, F. Hyder, Energetics of neuronal signaling and fMRI activity. *Proc. Natl. Acad. Sci. U.S.A.* **104**, 20546–20551 (2007).

82. C. Alonso Bde, T. Makarova, A. Hess, On the use of α-chloralose for repeated BOLD fMRI measurements in rats. *J. Neurosci. Methods* **195**, 236–240 (2011).

83. K. M. Garrett, J. Gan, Enhancement of γ-aminobutyric acid$_A$ receptor activity by α-chloralose. *J. Pharmacol. Exp. Ther.* **285**, 680–686 (1998).

84. E. Kumamoto, Y. Murata, Enhancement by lanthanide of general anesthetic-induced GABAA-receptor current in rat septal cholinergic neurons in culture. *J. Neurophysiol.* **75**, 2294–2299 (1996).

85. M. Massott, V. G. Longo, α-Chloralose and the central dopaminergic system. *J. Pharm. Pharmacol.* **30**, 667 (1978).

86. N. Montemurro, N. Aliaga, P. Graff, A. Escribano, J. Lizana, New targets and new technologies in the treatment of Parkinson's disease: A narrative review. *Int. J. Environ. Res. Public Health* **19**, 8799 (2022).

87. C. E. Bass, V. P. Grinevich, Z. B. Vance, R. P. Sullivan, K. D. Bonin, E. A. Budygin, Optogenetic control of striatal dopamine release in rats. *J. Neurochem.* **114**, 1344–1352 (2010).

88. G. Paxinos and C. Watson, *The Rat Brain in Stereotaxic Coordinates*. (Academic Press, San Diego; 1998).

89. K. Hamacher, H. H. Coenen, G. Stöcklin, Efficient stereospecific synthesis of no-carrier-added 2-[^{18}F]-fluoro-2-deoxy-D-glucose using aminopolyether supported nucleophilic substitution. *J. Nucl. Med.* **27**, 235–238 (1986).

90. J. A. Disselhorst, D. F. Newport, A. M. Schmid, F. P. Schmidt, C. Parl, C. C. Liu, B. J. Pichler, J. G. Mannheim, NEMA NU 4-2008 performance evaluation and MR compatibility tests of an APD-based small animal PET-insert for simultaneous PET/MR imaging. *Phys. Med. Biol.* **67**, 045015 (2022).

91. W. K. Schiffer, M. M. Mirrione, A. Biegon, D. L. Alexoff, V. Patel, S. L. Dewey, Serial microPET measures of the metabolic reaction to a microdialysis probe implant. *J. Neurosci. Methods* **155**, 272–284 (2006).

92. R. Henson, "Chapter 15 - Efficient experimental design for fMRI" in *Statistical Parametric Mapping*, K. Friston, J. Ashburner, S. Kiebel, T. Nichols, W. Penny, Eds. (Academic Press, 2007), pp. 193–210.

93. M. Brett, J.-L. Anton, R. Valabregue, J.-B. Poline, “Region of interest analysis using an SPM toolbox” in *8th Internation Conference on Functional Mapping of the Human Brain*. (CD-ROM in NeuroImage, 2002), pp. 497.

94. K. J. Friston, E. Zarahn, O. Josephs, R. N. Henson, A. M. Dale, Stochastic designs in event-related fMRI. *Neuroimage* **10**, 607–619 (1999).

95. A. Eklund, T. E. Nichols, H. Knutsson, Cluster failure: Why fMRI inferences for spatial extent have inflated false-positive rates. *Proc. Natl. Acad. Sci. U.S.A.* **113**, 7900–7905 (2016).

96. F. J. López-González, J. Silva-Rodríguez, J. Paredes-Pacheco, A. Niñerola-Baizán, N. Efthimiou, C. Martín-Martín, A. Moscoso, Á. Ruibal, N. Roé-Vellvé, P. Aguiar, Intensity normalization methods in brain FDG-PET quantification. *Neuroimage* **222**, 117229 (2020).

97. L. Rischka, G. M. Godbersen, V. Pichler, P. Michenthaler, S. Klug, M. Klöbl, V. Ritter, W. Wadsak, M. Hacker, S. Kasper, R. Lanzenberger, A. Hahn, Reliability of task-specific neuronal activation assessed with functional PET, ASL and BOLD imaging. *J. Cereb. Blood Flow Metab.* **41**, 2986–2999 (2021).

98. M. J. McKeown, L. K. Hansen, T. J. Sejnowsk, Independent component analysis of functional MRI: What is signal and what is noise? *Curr. Opin. Neurobiol.* **13**, 620–629 (2003).

99. A. Hyvärinen, E. Oja, Independent component analysis: Algorithms and applications. *Neural Netw.* **13**, 411–430 (2000).

100. V. D. Calhoun, V. K. Potluru, R. Phlypo, R. F. Silva, B. A. Pearlmutter, A. Caprihan, S. M. Plis, T. Adalı, Independent component analysis for brain FMRI does indeed select for maximal independence. *PLOS ONE* **8**, e73309 (2013).

101. A. Hyvärinen, E. Oja, A fast fixed-point algorithm for independent component analysis. *Neural Comput.* **9**, 1483–1492 (1997).

102. V. D. Calhoun, T. Adali, G. D. Pearlson, J. J. Pekar, A method for making group inferences from functional MRI data using independent component analysis. *Hum. Brain Mapp.* **14**, 140–151 (2001).

103. A. Hyvärinen, Fast and robust fixed-point algorithms for independent component analysis. *IEEE Trans. Neural Netw.* **10**, 626–634 (1999).

104. A. Nieto-Castanon, *Handbook of fcMRI Methods in CONN* (Hilbert Press, 2020).

105. S. A. Rombouts, F. Barkhof, F. G. Hoogenraad, M. Sprenger, P. Scheltens, Within-subject reproducibility of visual activation patterns with functional magnetic resonance imaging using multislice echo planar imaging. *Magn. Reson. Imaging* **16**, 105–113 (1998).

106. W. C. Machielsen, S. A. Rombouts, F. Barkhof, P. Scheltens, M. P. Witter, FMRI of visual encoding: Reproducibility of activation. *Hum. Brain Mapp.* **9**, 156–164 (2000).

107. L. R. Dice, Measures of the amount of ecologic association between species. *Ecology* **26**, 297–302 (1945).

108. M. E. Weaverdyck, M. D. Lieberman, C. Parkinson, Tools of the trade multivoxel pattern analysis in fMRI: A practical introduction for social and affective neuroscientists. *Soc. Cogn. Affect. Neurosci.* **15**, 487–509 (2020).

109. T. J. Adkins, T. G. Lee, Reward modulates cortical representations of action. *Neuroimage* **228**, 117708 (2021).

110. L. Grosenick, B. Klingenberg, K. Katovich, B. Knutson, J. E. Taylor, Interpretable whole-brain prediction analysis with GraphNet. *Neuroimage* **72**, 304–321 (2013).

111. V. Michel, A. Gramfort, E. Eger, G. Varoquaux, B. Thirion, "A comparative study of algorithms for intra- and inter-subjects fMRI decoding" in *Machine Learning and Interpretation in Neuroimaging*, G. Langs, I. Rish, M. Grosse-Wentrup, B. Murphy, G. Langs, I. Rish, M. Grosse-Wentrup, B. Murphy, Eds. (Springer, 2012), pp. 1–8.

112. C. Allefeld, K. Görgen, J.-D. Haynes, Valid population inference for information-based imaging: From the second-level *t*-test to prevalence inference. *Neuroimage* **141**, 378–392 (2016).

113. R. Gilron, J. Rosenblatt, O. Koyejo, R. A. Poldrack, R. Mukamel, What's in a pattern? Examining the type of signal multivariate analysis uncovers at the group level. *Neuroimage* **146**, 113–120 (2017).

114. M. T. Todd, L. E. Nystrom, J. D. Cohen, Confounds in multivariate pattern analysis: Theory and rule representation case study. *Neuroimage* **77**, 157–165 (2013).

115. S. M. Helfinstein, T. Schonberg, E. Congdon, K. H. Karlsgodt, J. A. Mumford, F. W. Sabb, T. D. Cannon, E. D. London, R. M. Bilder, R. A. Poldrack, Predicting risky choices from brain activity patterns. *Proc. Natl. Acad. Sci. U.S.A.* **111**, 2470–2475 (2014).

116. K. Izuma, K. Shibata, K. Matsumoto, R. Adolphs, Neural predictors of evaluative attitudes toward celebrities. *Soc. Cogn. Affect. Neurosci.* **12**, 382–390 (2016).

117. J. Jiang, C. Summerfield, T. Egner, Visual prediction error spreads across object features in human visual cortex. *J. Neurosci.* **36**, 12746–12763 (2016).

118. J. Kim, J. Wang, D. H. Wedell, S. V. Shinkareva, Identifying core affect in individuals from fMRI responses to dynamic naturalistic audiovisual stimuli. *PLOS ONE* **11**, e0161589 (2016).

119. Q. Wang, B. Cagna, T. Chaminade, S. Takerkart, Inter-subject pattern analysis: A straightforward and powerful scheme for group-level MVPA. *Neuroimage* **204**, 116205 (2020).

120. E. Olivetti, S. Veeramachaneni, E. Nowakowska, Bayesian hypothesis testing for pattern discrimination in brain decoding. *Pattern Recognit.* **45**, 2075–2084 (2012).

121. K. H. Brodersen, J. Daunizeau, C. Mathys, J. R. Chumbley, J. M. Buhmann, K. E. Stephan, Variational Bayesian mixed-effects inference for classification studies. *Neuroimage* **76**, 345–361 (2013).

122. J. Stelzer, Y. Chen, R. Turner, Statistical inference and multiple testing correction in classification-based multi-voxel pattern analysis (MVPA): Random permutations and cluster size control. *Neuroimage* **65**, 69–82 (2013).

123. S. Whitfield-Gabrieli, A. Nieto-Castanon, Conn: A functional connectivity toolbox for correlated and anticorrelated brain networks. *Brain Connect.* **2**, 125–141 (2012).

b) Submitted publications included in the dissertation

[11C]MODAG 005 – a novel PET tracer targeting alpha-synuclein aggregates in the brain

Ran Sing Saw
Eberhard Karls University Tuebingen, Department of Preclinical Imaging and Radiopharmacy
Sabrina Buss
Eberhard Karls University Tuebingen, Department of Preclinical Imaging and Radiopharmacy
Felix Schmidt
MODAG GmbH
Sergey Ryazanov
Max Planck Institute for Multidisciplinary Sciences, Department of NMR-based Structural Biology
Andrei Leonov
Max Planck Institute for Multidisciplinary Sciences, Department of NMR-based Structural Biology
Laura Kuebler
Eberhard Karls University Tuebingen, Department of Preclinical Imaging and Radiopharmacy
Daniel Bleher
Eberhard Karls University Tuebingen, Department of Preclinical Imaging and Radiopharmacy
https://orcid.org/0000-0002-2216-2524
Ioannis Papadopoulos
Eberhard Karls University Tuebingen
Benjamin Roeben
Department of Neurology, Eberhard Karls University Tuebingen, 72076 Tuebingen, Germany
Fabian Schmidt
Werner Siemens Imaging Center, Department of Preclinical Imaging and Radiopharmacy, Eberhard Karls University Tuebingen, 72076 Tuebingen, Germany
Matthias Reimold
Nuclear Medicine and Clinical Molecular Imaging, Department of Radiology, Universityhospital Tuebingen, 72076 Tuebingen, Germany
Federica Bonanno
Eberhard Karls University Tuebingen, Department of Preclinical Imaging and Radiopharmacy
Ann-Kathrin Grotegerd
Eberhard Karls University Tuebingen
Viktoria Ruf
Ludwig Maximilians University, Center for Neuropathology and Prion Research
Bernadette Dahl
Eberhard Karls University Tuebingen

Christine Sandiego
Invicro
Kelly Henry
Invicro
Birgit Fehrenbacher
Eberhard Karls University Tuebingen
Martin Schaller
Eberhard Karls University Tuebingen
Philipp Kahle
Eberhard Karls University Tuebingen
Thomas Gasser
Department of Neurology, Eberhard Karls University Tuebingen, 72076 Tuebingen, Germany
Kathrin Brockmann
Department of Neurology, Eberhard Karls University Tuebingen, 72076 Tuebingen, Germany
Gerald Reischl
Werner Siemens Imaging Center, Department of Preclinical Imaging and Radiopharmacy, Eberhard Karls University Tuebingen, 72076 Tuebingen, Germany
Christian la Fougère
Nuclear Medicine and Clinical Molecular Imaging, Department of Radiology, Universityhospital Tuebingen, 72076 Tuebingen, Germany
Bernd Pichler
University of Tübingen https://orcid.org/0000-0001-6784-5524
Andreas Maurer
Eberhard Karls University Tuebingen https://orcid.org/0000-0003-2412-5361
Christian Griesinger
Max Planck Institute for Multidisciplinary Sciences, Department of NMR-based Structural Biology
Armin Giese
MODAG GmbH
Kristina Herfert
kristina.herfert@med.uni-tuebingen.de

Eberhard Karls University Tuebingen https://orcid.org/0000-0003-0231-7717

Article

Keywords:

Posted Date: March 21st, 2024

DOI: https://doi.org/10.21203/rs.3.rs-2189800/v1

Additional Declarations: Yes there is potential Competing Interest. A patent has been filed (PCT/EP2020/082778). Armin Giese, Felix Schmidt, Andrei Leonov and Sergey Ryazanov are employed by MODAG GmbH, which retains ownership of MODAG-005, Armin Giese and Christian Griesinger are shareholders of MODAG GmbH.

[^{11}C]MODAG-005 – a novel PET tracer targeting alpha-synuclein aggregates in the brain

Ran Sing Saw[1&], Sabrina Haas[1&], Felix Schmidt[2&], Sergey Ryazanov[3,2&], Andrei Leonov[3,2&], Laura Kuebler[1], Daniel Bleher[1], Ioannis Papadopoulos[1], Benjamin Roeben[4,7,8], Fabian Schmidt[1,5], Matthias Reimold[5], Federica Bonanno[1], Ann-Kathrin Grotegerd[1], Viktoria C. Ruf[6], Bernadette Dahl[7,8,9], Christine M. Sandiego[10], Kelly E. Henry[10], Birgit Fehrenbacher[11], Martin Schaller[11], Philipp J. Kahle[7,8], Thomas Gasser[4,7], Kathrin Brockmann[4,7,8], Gerald Reischl[1,12], Christian la Fougère[5,12], Bernd J. Pichler[1,12], Andreas Maurer[1,12], Christian Griesinger[3,13*], Armin Giese[2*], Kristina Herfert[1*]

[1]Werner Siemens Imaging Center, Department of Preclinical Imaging and Radiopharmacy, Eberhard Karls University Tuebingen, 72076 Tuebingen, Germany
[2]MODAG GmbH, 55234 Wendelsheim, Germany
[3]Department of NMR-based Structural Biology, Max Planck Institute for Multidisciplinary Sciences, 37077 Goettingen, Germany
[4] Department of Neurology, Eberhard Karls University Tuebingen, 72076 Tuebingen, Germany
[5] Nuclear Medicine and Clinical Molecular Imaging, Department of Radiology, Universityhospital Tuebingen, 72076 Tuebingen, Germany
[6] Ludwig Maximilians University, Center for Neuropathology and Prion Research, 81377 Munich, Germany
[7]Hertie Institute for Clinical Brain Research, Department of Neurodegenerative Diseases, Eberhard Karls University Tuebingen, 72076 Tuebingen, Germany
[8]German Center for Neurodegenerative Diseases, 72076 Tuebingen, Germany
[9]Graduate School of Cellular and Molecular Neuroscience, Eberhard Karls University Tuebingen, 72076 Tuebingen, Germany
[10]Invicro, LLC, 119 4th Avenue, Needham, MA 02494, United States of America
[11]Department of Dermatology, Eberhard Karls University Tuebingen, 72076 Tuebingen, Germany
[12]Cluster of Excellence iFIT (EXC 2180) "Image-Guided and Functionally Instructed Tumor Therapies", Eberhard Karls University Tuebingen, 72076 Tuebingen, Germany
[13]Cluster of Excellence “Multiscale Bioimaging: From Molecular Machines to Networks of Excitable Cells” (MBExC), University of Goettingen, 37075 Goettingen, Germany

&These authors contributed equally
*Corresponding authors, kristina.herfert@med.uni-tuebingen.de; giese@modag.net; cigr@mpinat.mpg.de

Synucleinopathies are neurodegenerative diseases characterized by the presence of brain inclusions containing the pathologically aggregated protein α-synuclein (αSYN). The development of a positron emission tomography tracer to detect aggregates of misfolded αSYN would revolutionize early diagnosis, disease monitoring and the evaluation of therapeutic efficacy. Here we present the development and preclinical *in vitro* and *in vivo* validation of [^{11}C]MODAG-005. *In vitro* binding experiments demonstrate subnanomolar binding affinity to recombinant αSYN fibrils as well as to αSYN inclusions in human brain tissue. Specific binding in multiple system atrophy (MSA) brain tissue was detected using autoradiography and microautoradiography, and was validated through immunostaining. *In vivo*, [^{11}C]MODAG-005 shows good brain penetration, rapid clearance from brain tissue and low metabolite formation in rodents and non-human primates. In addition, a pronounced binding and a good signal-to-noise ratio were achieved in an αSYN fibril-injected rat model and in an αSYN(A30P) transgenic mouse model in correlation to the pathological load. To validate its value for therapy development, we show target engagement of the drug candidate anle138b in the brain tissues from αSYN(A30P) mouse and MSA as well as *in vivo* in αSYN fibril-injected rats. Finally, our translational approach in a first-in-human patient with clinically established MSA, revealed a marked tracer binding in regions affected by αSYN pathology, particularly in the striatum, where the pattern corresponded with the neurodegeneration shown by dopamine transporter single-photon emission computed tomography.

Synucleinopathies, such as Parkinson’s disease (PD), dementia with Lewy bodies (DLB), and multiple system atrophy (MSA), are neurodegenerative diseases that pose a substantial threat to our aging society. A definitive diagnosis is currently only possible by post-mortem autopsy [1]. Their shared neuropathological hallmark is the presence of misfolded αSYN, which appears with a spatial distribution in the brain that depends on the stage and type of disease. The accumulation of pathological αSYN begins years before the onset of the first (motor) symptoms and would therefore be an excellent biomarker for early detection and monitoring of disease progression [2].

Positron emission tomography (PET) is a non-invasive imaging technology that traces a radioactively labelled molecule designed for a certain biological target *in vivo* [3]. In Alzheimer’s disease (AD), the

development of PET tracers targeting amyloid-β (Aβ) and tau aggregates has greatly advanced our understanding of the time course of aggregation and the regional spread of pathology, revolutionizing the early diagnosis of AD and the assessment of therapeutic effects. Several small molecules targeting αSYN aggregates have been developed over the past decade, with two of them being studied in human subjects [4-7]. Nonetheless, none of these molecules has been translated into clinical applications so far. Compared to Aβ and tau, researchers have encountered considerable challenges in their search for an αSYN PET tracer. This is mainly due to the low availability of the target in tissue, which requires a highly specific molecule with little to no background binding. In addition, misfolded αSYN contains β-sheet secondary structural elements that resemble those of other misfolded peptides and proteins, such as Aβ or tau, which are also found as co-pathologies. Fibril polymorphism is another challenge that further complicates the development of a specific and selective radiotracer due to the multiple conformations of αSYN fibrils, resulting in different morphologies and structures with altered stability and toxicity [8, 9]. Furthermore, since αSYN aggregates are, in contrast to Aβ, located intracellularly, a molecule that penetrates both, the blood–brain barrier and the cell membrane, is required. In addition, the highly complex structure of Lewy bodies, consisting of lipophilic organelles and membrane fragments, presents an additional barrier to αSYN fibril binding [10].

We have developed two prior radiolabeled αSYN-targeting tracers that are structurally derived from the lead compound anle138b (**Extended Data Fig. 1a**) [11]: anle253b (**Extended Data Fig. 1b**) and its successor MODAG-001 (**Extended Data Fig. 1c**) [12, 13]. We have also demonstrated from *in vitro* saturation binding assays that MODAG-001 exhibited high affinity for αSYN fibrils, showed a favorable *in vivo* pharmacokinetic profile, and was able to detect injected recombinant αSYN fibrils in rats [12]. In pigs, (d_3)-[^{11}C]MODAG-001 possessed excellent brain kinetics and a confirmed specific binding in an αSYN pig model *in vivo* [14]. However, in human brain tissue, no to very low binding was observed which is due to its high non-specific binding, lowering the signal-to-noise ratio (SNR) in the target tissue. Nonetheless, its high affinity and promising pharmacokinetic properties formed the basis for the development and testing of next-generation compounds with reduced non-specific binding.

Here, we report the development, preclinical evaluation and first-in-human study of an αSYN PET tracer candidate, [^{11}C]MODAG-005, the de-methylated form of [^{11}C]MODAG-001 (**Extended Data Fig. 1d**).

Results

In vitro fibril binding assays

A competition binding assay using [^{3}H]MODAG-001 as the reference compound was performed to evaluate the binding affinity of MODAG-005 towards αSYN fibrils and revealed a high binding affinity (K_i = 0.4 nM) for MODAG-005 (**Fig. 1a**).

In vitro binding affinity of [^{3}H]MODAG-005 to αSYN fibrils and selectivity over tau and $A\beta_{1-42}$ fibrils were determined using saturation binding assays (n = 3). Specific binding was highest towards αSYN fibrils (B_{max} = 6.6 ± 0.7 pmol/nmol total αSYN) compared to tau (B_{max} = 1.2 ± 0.2 pmol/nmol total tau) and $A\beta_{1-42}$ fibrils (B_{max} = 0.11 ± 0.03 pmol/nmol total $A\beta_{1-42}$) (**Fig. 1b**). [^{3}H]MODAG-005 showed a very high affinity towards αSYN fibrils (K_d = 0.2 ± 0.03 nM) with low non-specific binding (**Fig. 1c**). A 36-fold and >100-fold lower affinity was observed towards tau (K_d = 7.1 ± 0.7 nM) and $A\beta_{1-42}$ (K_d = 21 ± 7.7 nM) fibrils, respectively (**Fig. 1d,e**). MODAG-005 was further tested for off-target binding in a Cerep panel. Specific focus was put on monoamine oxidase B (MAO-B) as this was reported to be overexpressed in several proteinopathies [15]. The IC_{50} value for MAO-B was 0.8 µM.

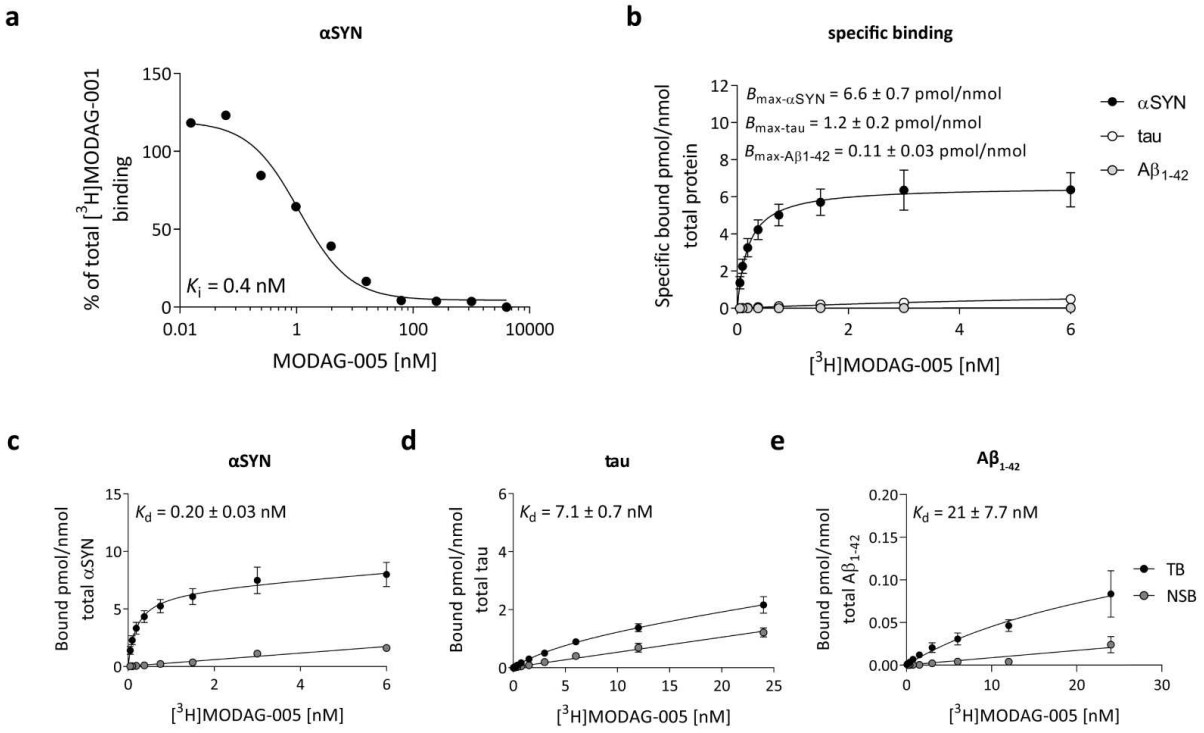

Fig. 1: [^{3}H]MODAG-005 in vitro binding experiments on recombinant human αSYN, tau, and synthetic human Aβ$_{1-42}$ fibrils. a, Competition binding experiment (n = 1, no replicates) with [^{3}H]MODAG-001 showed increased affinity of MODAG-005 to αSYN fibrils. **b**, Saturation binding experiments (n = 3, each in triplicates on the same fibril batch) revealed high binding specificity of [^{3}H]MODAG-005 to αSYN fibrils compared to tau and Aβ$_{1-42}$. **c**, **d**, and **e**, Non-linear regression of TB and NSB revealed a very high affinity towards αSYN fibrils (**c**), moderate affinity towards tau (**d**), and low affinity for Aβ$_{1-42}$ (**e**). Aβ$_{1-42}$, β-amyloid$_{1-42}$; αSYN, α-synuclein; NSB, non-specific binding; SB, specific binding; TB, total binding. The points in **b**, **c**, **d,** and **e** are represented as mean ± s.d..

Binding of [^{3}H]MODAG-005 in human and mouse brain tissue

Fig. 2 and **Extended Data Fig. 2** show [^{3}H]MODAG-005 autoradiography and αSYN pSer129 immunofluorescence microscopy images of the cerebellar cortex of two MSA cases and two control cases. In macroscopic autoradiography, both MSA cases showed a clear specific binding of [^{3}H]MODAG-005 in the white matter of the cerebellum and cerebellar nuclei, which was blocked by an excess of unlabeled MODAG-005 (**Fig. 2a, Extended Data Fig. 2a**). [^{3}H]MODAG-005 binding to αSYN pathology was confirmed by αSYN pSer129 immunofluorescence microscopy. For microscopic verification of [^{3}H]MODAG-005 binding to αSYN aggregates, microautoradiography and subsequent immunofluorescence microscopy were performed on the same brain section of MSA case 1. An extensive presence of silver grains was detected in the cerebellar white matter, indicating the binding of [^{3}H]MODAG-005. These silver grains colocalized with the αSYN pSer129 immunofluorescence signal, with similar distribution and size as αSYN pathology in the white matter. No specific binding, immunofluorescent signal and intense silver grains were observed in the control case (**Fig. 2b, Extended Data Fig. 2b**). Quantitative analysis of MSA and control cases showed increased specific binding in the cerebellar white matter of MSA (3.6 ± 1.4 pmol/mg, n = 2) compared to control (0.6 ± 0.2 pmol/mg, n = 2) (**Fig. 2c**).

To determine the binding affinity on MSA brain tissue sections, saturation binding autoradiography was performed. The Scatchard plot revealed one high- and one low-affinity binding site of [^{3}H]MODAG-005 (**Fig. 2d**). A K_d of 0.25 nM was determined for the high-affinity binding site (**Fig. 2e**), which is consistent with K_d values determined on recombinant human fibrils (**Fig. 1c**). The high-affinity binding site of [^{3}H]MODAG-005 remained after pre-blocking with selegiline (K_d = 1.3 nM) (**Extended Data Fig. 2c** and **d**). To confirm the absence of co-pathology in both MSA cases, pTau and Aβ staining was performed in addition to αSYN pSer129 (**Extended Data Fig. 3**).

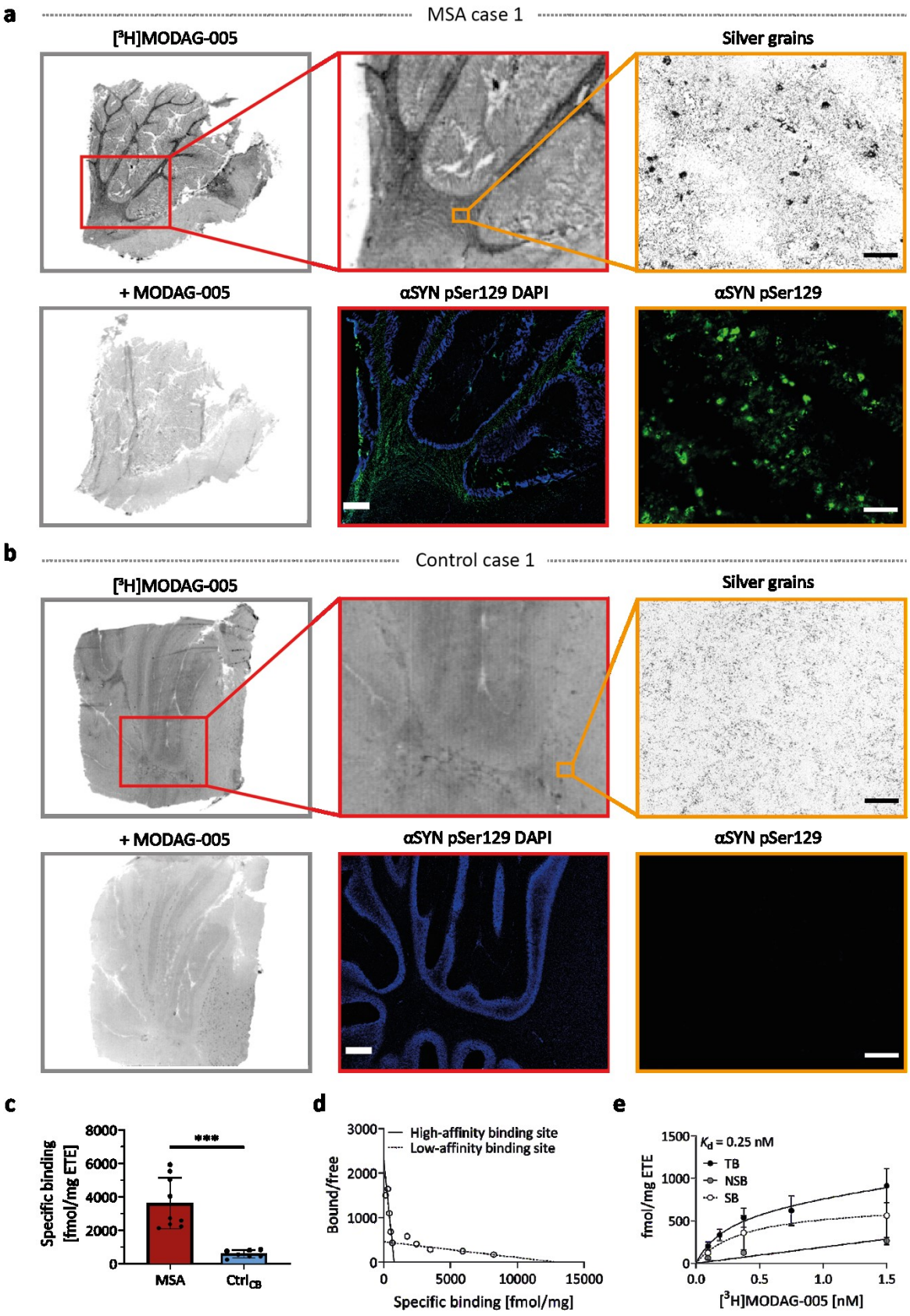

Fig. 2: [^{3}H]MODAG-005 binding to αSYN pathology in MSA brain tissue. a and **b**, Macroscopic autoradiography (3 nM [^{3}H]MODAG-005, with the addition of 3 µM unlabeled MODAG-005 for blocking), microautoradiography (30 nM [^{3}H]MODAG-005) and immunofluorescence microscopy verification of pathology in post-mortem human brain tissues of one exemplary MSA (**a**) and one exemplary healthy control case (**b**). Red boxes show higher magnification and immunofluorescence microscopy images of αSYN pSer129 (green) and DAPI (blue). Scale bars, 1 mm. Microautoradiography (silver grains) and subsequent

immunofluorescence microscopy of αSYN pSer129 (green) are shown in orange boxes. Scale bars, 50 µm. **c**, Quantification shows high specific binding of 3 nM [^{3}H]MODAG-005 in MSA compared to controls (p = 0.0003, n = 2 biological replicates, repeated measurements in each sample). **d** and **e**, Saturation binding autoradiography in MSA brain tissue revealed two binding sites (**d**) with a high affinity binding site (K_d = 0.25 nM) (**e**) in agreement with fibril binding assays (n = 1, repeated measurements in each sample) A K_d value of 31.9 nM was obtained for the low-affinity binding site. αSYN, α-synuclein; DAPI, 4′,6-diamidino-2-phenylindole; ETE, estimated tissue equivalent; MSA, multiple system atrophy; NSB, non-specific binding; SB, specific binding; TB, total binding. Data in **c** and **e** are represented as mean ± s.d.. In **c**, Shapiro-Wilk test indicated normal distribution and a two-way unpaired t-test with Welch's correction was used for the comparisons.

Furthermore, target engagement of the potential therapeutic compound anle138b was examined on human MSA brain tissues (**Fig. 3**). In macroscopic autoradiography, anle138b was able to block [^{3}H]MODAG-005 binding to αSYN pathology in the white matter of MSA tissue (**Fig. 3a**) with a K_i value of 25 nM as revealed by a competition experiment (**Fig. 3b**). Binding specificity of [^{3}H]MODAG-005 was further demonstrated by microautoradiography showing the colocalization of [^{3}H]MODAG-005 signals with αSYN aggregates as well as successful blocking by unlabeled MODAG-005 and anle138b (**Fig. 3c**). Furthermore, both the lack of colocalization between silver grains and MAO-B staining and the inability of selegiline to block tracer signal indicated that the detected signal of [^{3}H]MODAG-005 in MSA tissue was mainly specific and not due to MAO-B binding (**Fig. 3c**).

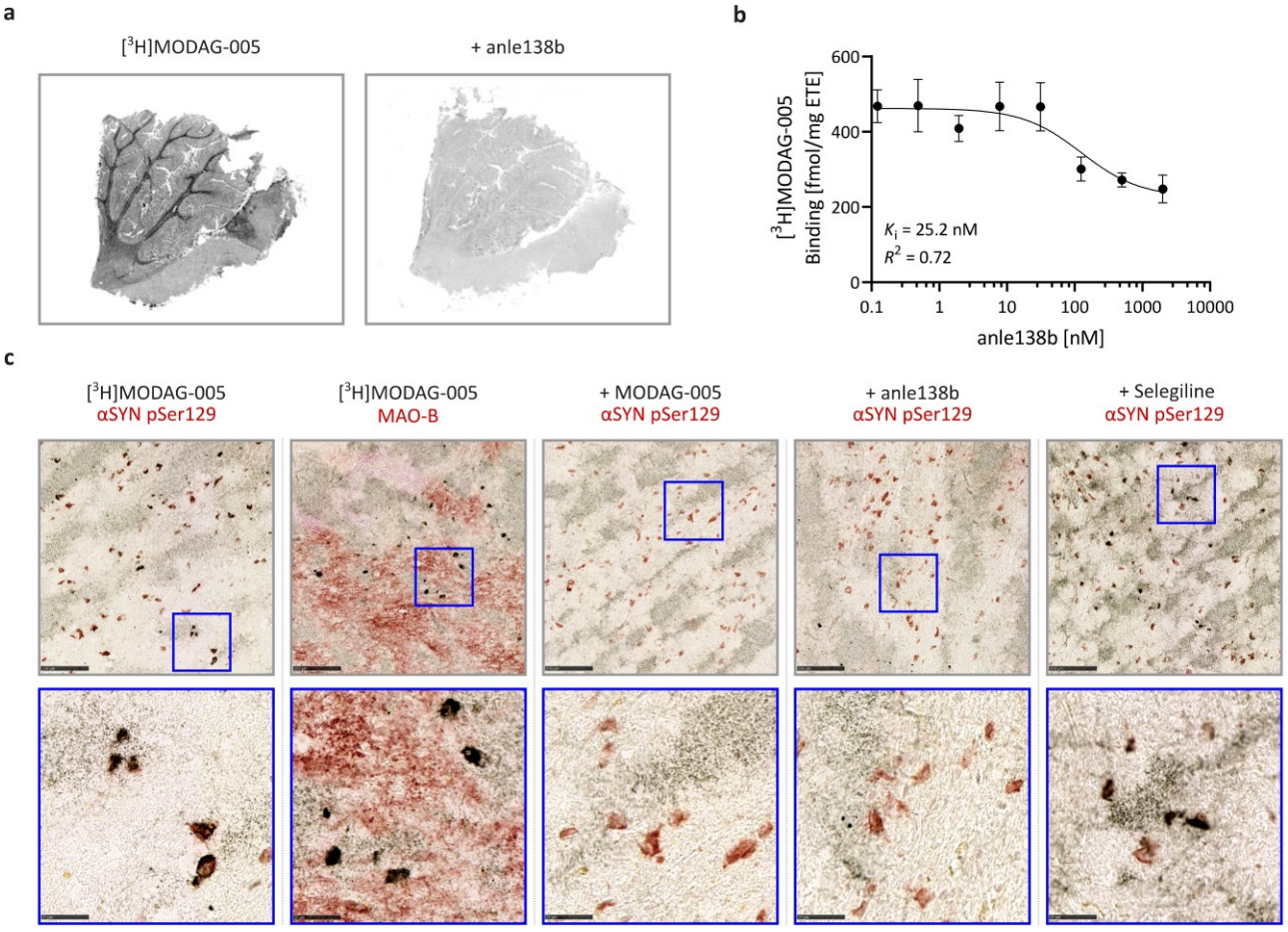

Fig. 3: [^{3}H]MODAG-005 autoradiography and microautoradiography demonstrated binding specificity and target engagement of anle138b in human MSA tissue. a, Autoradiography images show total binding of 3 nM [^{3}H]MODAG-005 (left) and non-specific binding after blocking with 3 µM anle138b (right) in human MSA case 1 brain tissue. **b**, Competition binding with anle138b in human MSA case 1 tissue revealed a K_i value of 25 nM (n = 1, repeated measurements in each sample). The K_i value was calculated based on the K_d value of [^{3}H]MODAG-005 at the high-affinity, low-capacity binding site. **c**, [^{3}H]MODAG-005 microautoradiography (60 nM) (silver grains) with αSYN pSer129 or MAO-B immunohistochemistry (red) shows the colocalization of tracer binding with αSYN pathology, but no colocalization with MAO-B expression. Tracer binding to αSYN aggregates was specific, as indicated by successful blocking (30 µM) with unlabeled MODAG-005 and anle138b, but not with selegiline. Images were taken from the white matter

of MSA case 1 and are shown in grey boxes (scale bar, 100 µm), further magnified images are shown in blue boxes (scale bar, 25 µm). αSYN, α-synuclein; ETE, estimated tissue equivalent; MAO-B, monoamine oxidase B; MSA, multiple system atrophy. Points in **b** are represented by mean ± s.d..

Fig. 4a shows [^{3}H]MODAG-005 autoradiography in the frontal cortex of one PD, one AD, one PSP, and one control case. Increased binding values for the PD (3.8 ± 0.3 pmol/mg), AD (4.0 ± 0.6 pmol/mg) and PSP (1.5 ± 0.8 pmol/mg) case compared to the control case (cortical grey matter: 1.1 ± 0.3 pmol/mg, subcortical white matter 0.1 ± 0.1 pmol/mg) are shown in **Fig. 4b**. Immunofluorescence microscopy images after staining for αSYN pSer129, tau and Aβ are shown in **Extended Data Fig. 4** and **Extended Data Table 1**. To examine the binding of [^{3}H]MODAG-005 to αSYN aggregates in PD, correlation analysis of autoradiography binding and αSYN pSer129 immunofluorescence microscopy was performed. The result indicated a moderate and significant correlation between the two signals (r = 0.56, p < 0.0001) (**Fig. 4c**). Off-target binding in AD brain tissue was further investigated using saturation binding autoradiography, which revealed two binding sites with K_d values of 2 nM and > 500 nM (**Supplementary Item 2**).

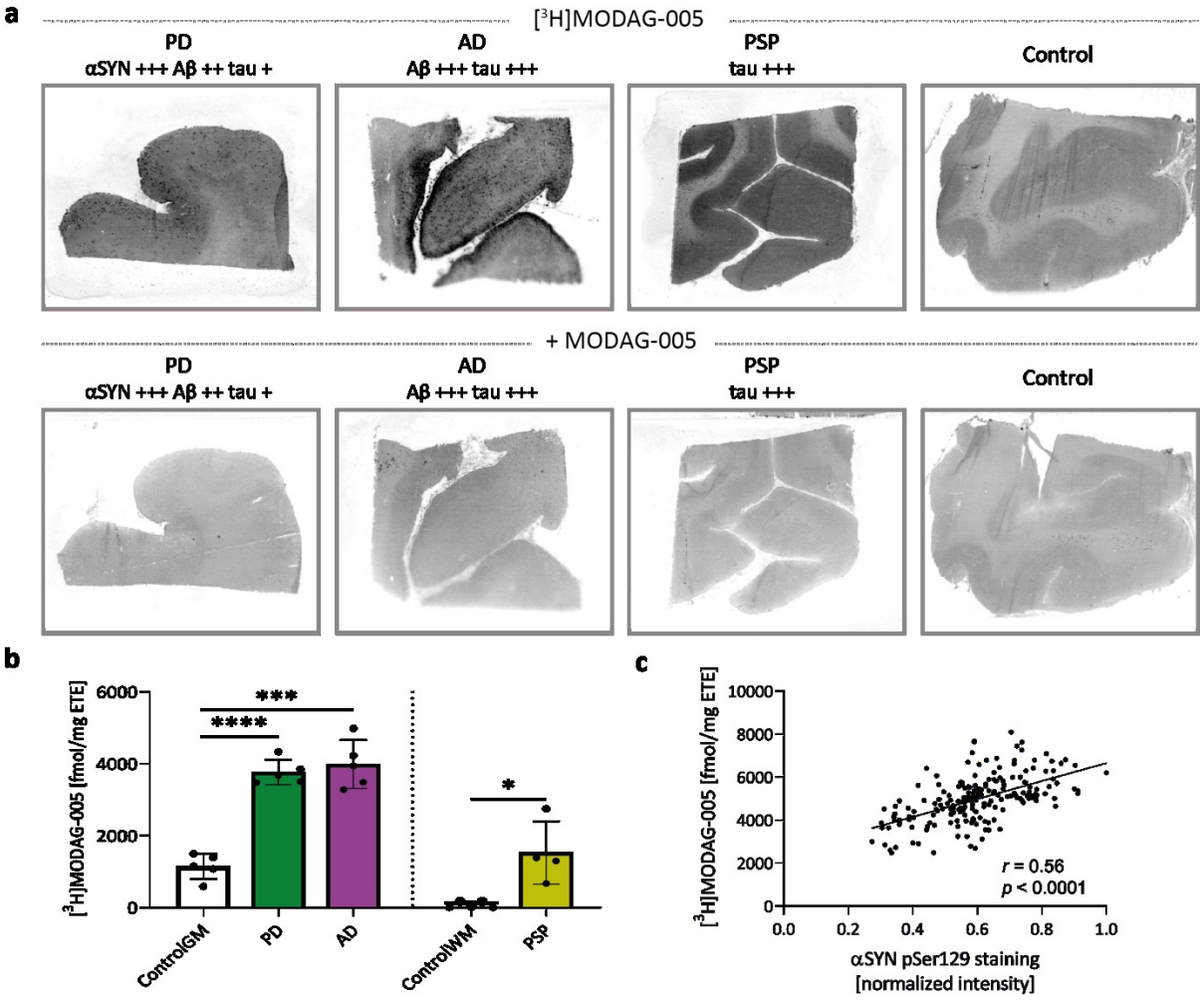

Fig. 4: [^{3}H]MODAG-005 binding in post-mortem human brain tissues of PD, AD and PSP cases. Autoradiography was performed with 3 nM [^{3}H]MODAG-005 and 3 µM unlabeled MODAG-005 for blocking. **a**, Autoradiography images of total binding (upper row) and non-specific binding after blocking with unlabeled MODAG-005 (lower row) in the frontal cortex of PD, AD, PSP, and control brain tissue. **b**, Quantification shows high binding in PD, AD, and PSP brain tissues compared to controls. **c**, In PD tissue, a moderate correlation was observed between [^{3}H]MODAG-005 binding and αSYN pSer129 immunofluorescence microscopy. The number of "+" symbols indicates an increasing degree of pathology. AD, Alzheimer's disease, αSYN, α-synuclein; ETE, estimated tissue equivalent; GM, grey matter; PD, Parkinson's disease; PSP, progressive supranuclear palsy; WM, white matter. Data in **b** are represented as mean ± s.d.. Data in **b** and **c** are from repeated measurements in each sample (n = 1). In **b**, Shapiro-Wilk test indicated normal distribution, Brown-Forsythe and Welch ANOVA with Dunnett's T3 multiple comparisons were used to compare ControlGM with PD and AD, and a two-way unpaired t-test with Welch's correction was used to

compare ControlWM with PSP. In **c**, the αSYN pSer129 staining intensity was normalized by the maximum intensity.

The binding of [^{3}H]MODAG-005 as well as target engagement of anle138b was further determined on brain tissue sections of the αSYN(A30P) mouse model of PD and age-matched wild-type mice (**Fig. 5a**). Quantitative analysis in brain regions (**Supplementary Item 3**) with positive αSYN pSer129 immunofluorescence signals revealed higher binding in the midbrain (2.0 ± 0.7 pmol/mg vs. 0.3 ± 0.5 pmol/mg), brainstem (1.2 ± 0.4 pmol/mg vs. 0.2 ± 0.5 pmol/mg), zona incerta (1.9 ± 0.5 pmol/mg vs. 0.2 ± 0.4 pmol/mg) and cerebellum (0.5 ± 0.7 pmol/mg vs. -0.1 ± 0.4 pmol/mg) compared to the age-matched control (**Fig. 5b**). In the cortex, no differences were observed (0.7 ± 0.5 pmol/mg vs. 0.6 ± 0.4 pmol/mg).

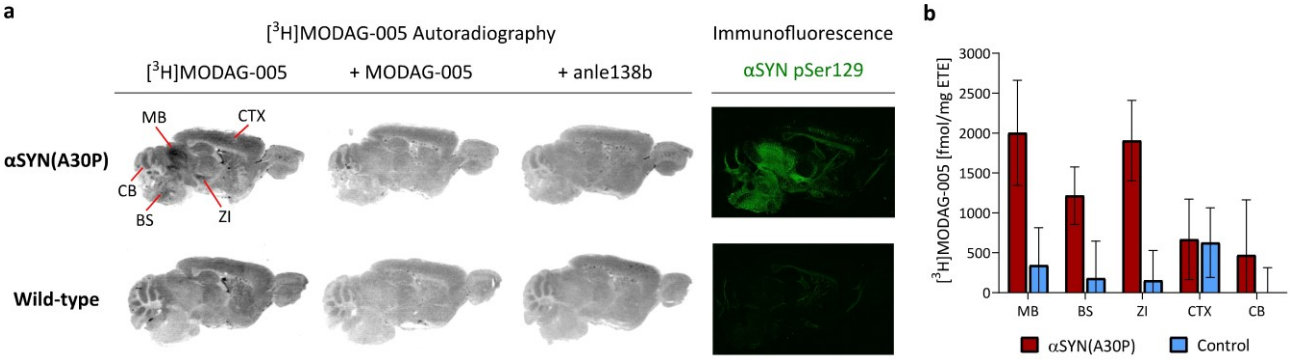

Fig. 5: [^{3}H]MODAG-005 binding and anle138b target engagement in the αSYN(A30P) mouse model of PD. Autoradiography was performed with 3 nM [^{3}H]MODAG-005 and 3 µM unlabeled MODAG-005 or anle138b for blocking. **a**, [^{3}H]MODAG-005 total binding, self-blocking and anle138b blocking in brain sections of an αSYN(A30P) mouse and an age-matched wild-type mouse is shown. Distribution of αSYN pathology was confirmed via immunofluorescence staining of αSYN pSer129 (green). **b**, Quantification (total binding minus self-blocking) revealed increased tracer binding in regions with αSYN pathology compared to the corresponding brain regions of age-matched wild-type mouse. αSYN, α-synuclein; BS, brainstem; CB, cerebellum; CTX, cortex; ETE, estimated tissue equivalent; MB, midbrain; ZI, *zona incerta.* Data in **b** are presented as mean ± s.d., obtained from repeated measurements in technical replicates (3 for [^{3}H]MODAG-005 and 2 [^{3}H]MODAG-005 + MODAG-005 for NSB). No statistical test was performed.

These findings led us to label MODAG-005 with carbon-11 to study its *in vivo* pharmacokinetics and radio-metabolite formation. The results of the radiolabeling are provided in the **Supplementary Item 4**.

Pharmacokinetic and metabolic profile in rodents

After the successful synthesis of [^{11}C]MODAG-005 (**Fig. 6a**), dynamic PET scans were performed in mice and rats. **Fig. 6b,c** shows whole body sagittal [^{11}C]MODAG-005 PET/MRI images and time-activity curves (TACs) of selected brain regions and peripheral organs from one exemplary mouse over time. Rapid brain uptake with a peak standardized uptake value (SUV) of 1.9 and a fast wash-out from the brain with clearance half-lives ranging from 5.5 to 6.7 minutes in the selected brain regions was observed. TACs of selected brain regions from one rat after injection of [^{11}C]MODAG-005 revealed SUVs up to 3.2 (**Extended Data Fig. 5a**) and a fast wash-out from the brain with clearance half-lives ranging from 3.1 to 6.1 minutes. [^{11}C]MODAG-005 radio-metabolite formation in the brain and plasma of mice (n = 3 per time-point) (**Fig. 6d**) and rats (n = 1 per time-point) (**Extended Data Fig. 5b**) was determined at 5 and 15 minutes after tracer injection. Quantitative analysis revealed one metabolite in the brain with 96 ± 1.1% and 79 ± 3.1% of the parent compound remaining at 5 minutes and 15 minutes after tracer injection, respectively. Analysis of the rats revealed one metabolite in the brain with 91% and 64% of the parent compound remaining at 5 minutes and 15 minutes after injection, respectively. **Extended Data Table 2** summarizes quantitative values of all radio-metabolites obtained in plasma and brain.

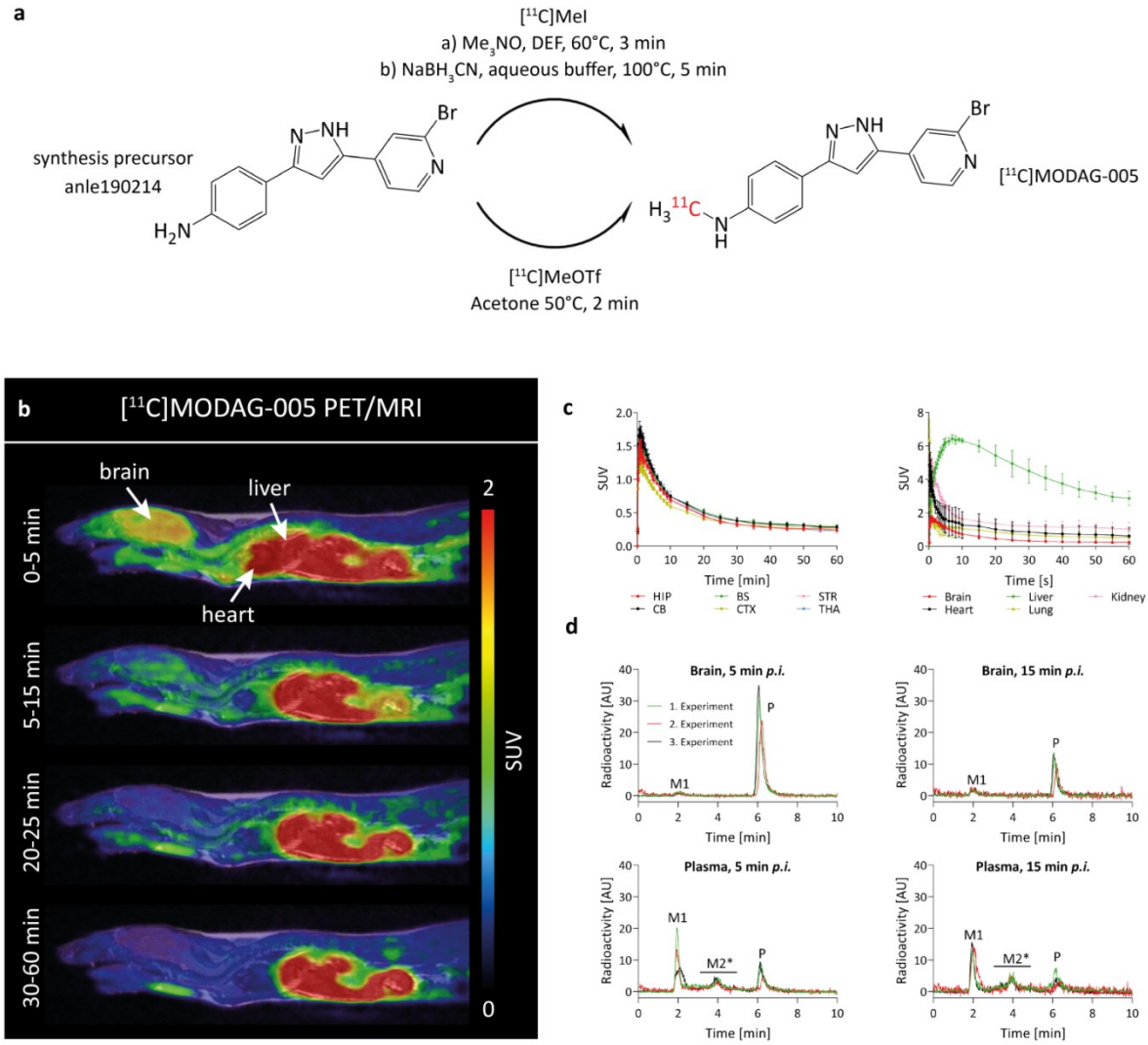

Fig. 6: Radiolabeling and *in vivo* characterization of [^{11}C]MODAG-005 in healthy mice. a, Radiolabeling of [^{11}C]MODAG-005 was performed by reductive methylation or direct methylation and resulted in radiochemical yields of 12.0 ± 2.2% or 11.8 ± 2.7% and molar activities of 49.2 ± 11.2 GBq/µmol or 209 ± 44 GBq/µmol (end of synthesis), respectively. **b**,**c left**, Exemplary whole body [^{11}C]MODAG-005 PET/MR images over time (n = 1) and mean TACs (n = 3) show high brain uptake (max. SUV = 1.9) and a fast washout from the brain in mice. **c right**, *In vivo* biodistribution in different organs is shown. **d**, Radiometabolite analysis (n = 3) revealed one metabolite present in the brain with 96 ± 1% and 79 ± 3% of the parent compound remaining at 5 and 15 minutes post tracer injection, respectively. In the blood plasma, additional metabolites M2* were detected. AU, arbitrary units; BS, brainstem; CB, cerebellum; CTX, cortex; HIP, hippocampus; MRI, magnetic resonance imaging; M1, metabolite 1; M2*, metabolite 2*; P, parent compound; PET, positron emission tomography; p.i., post injection; STR, striatum; SUV, standardized uptake value; TACs, time-activity curves; THA, thalamus. The points in **c** are represented as mean ± s.d..

Verification of binding to injected αSYN fibrils

To investigate whether we can detect [^{11}C]MODAG-005 binding to αSYN fibrils *in vivo*, rats were injected with αSYN fibrils into the right striatum; sham injection with buffer was performed on the contralateral side. Four days post injection, [^{11}C]MODAG-005 PET images were acquired, and brains were surgically extracted to confirm αSYN fibril location using thioflavin S staining and [^{3}H]MODAG-005 autoradiography. In addition, [^{11}C]MODAG-005 PET images were acquired from non-injected wild-type animals to exclude the possible contribution of blood–brain barrier leakage to increased tracer uptake because of intracranial injections. **7a** shows exemplary brain [^{11}C]MODAG-005 PET images of one αSYN fibril-injected rat and one non-injected rat summed up from 2.5 to 60 minutes. Increased tracer accumulation is seen at the αSYN fibril injection site. αSYN fibril location is confirmed by thioflavin S staining and *in vitro* [^{3}H]MODAG-005 autoradiography. Elevated tracer retention in the fibril-injected striatum compared to the sham-injected striatum was detected in TACs as well as in time-SUVR curves calculated using the cerebellum as the reference region (**Extended Data Fig. 6a, Fig. 7b**). Average SUVR showed increased tracer binding in the fibril-injected compared to the

sham-injected striatum of αSYN fibril-injected rats (1.18 ± 0.059 vs. 0.967 ± 0.041, $p = 0.0003$), but no difference between the right and left striatum of non-injected rats (0.97 ± 0.043 vs. 0.99 ± 0.071, $p = 0.542$) (**Fig. 7c**). Furthermore, **Extended Data Fig. 7** shows the improved SNR by a direct comparison of d_3-[^{11}C]MODAG-001 and [^{11}C]MODAG-005 PET images of αSYN fibril-injected rats at four days post injection.

To investigate and exclude that the elevated tracer binding was due to an inflammatory process and/or possible MAO-B binding, we performed immunohistochemistry of glial fibrillary acidic protein (GFAP) as a surrogate marker of astrogliosis and MAO-B. While stronger signals were observed in the fibril-injected striatum compared to the sham-injected striatum for both staining, the strongest astrogliosis and MAO-B expression were found in the cortex in both brain hemispheres (**Extended Data Fig. 6b**). In comparison, images from *in vivo* [^{11}C]MODAG-005 PET and *in vitro* [^{3}H]MODAG-005 autoradiography displayed a different pattern compared to the findings from GFAP and MAO-B immunohistochemistry, with no strong tracer binding in the areas surrounding the injection trajectory, where an inflammatory response and MAO-B upregulation were the highest (**Fig. 7a**).

In addition, PET data was further analyzed using different approaches to define the volumes of interest and an alternative reference region. **Extended Data Fig. 6c** shows the PET analysis performed using volumes of interest based on isocontour automatic detection set to 70% to include only the region with expected fibril localization. TACs and time-SUVR curves, as well as average SUVR, collectively illustrated a higher tracer retention in the fibril-injected striatum compared to the non-injected striatum (average SUVR = 1.66 ± 0.137 vs. 0.98 ± 0.163, $p = 0.0021$). Using the left, sham-injected striatum as the reference region, elevated tracer retention was detected in the fibril-injected striatum compared to the non-injected striatum (average SUVR = 1.24 ± 0.018 vs. 0.99 ± 0.054, $p = 0.003$) (**Fig. 7d**).

To determine the binding specificity of [^{11}C]MODAG-005 and to study the *in vivo* target engagement of anle138b in fibril-injected rats, two PET scans consisting of a baseline measurement with vehicle injection and a blocking measurement with anle138b administration were performed between three to four days after fibril injection in rats. Five minutes before tracer injection, vehicle or anle138b (1 mg/kg dose in the vehicle) was administered intravenously as a single bolus. Administration of anle138b successfully blocked tracer binding (average SUVR = 1.24 ± 0.018 at baseline vs. 0.99 ± 0.054 at blocking, $p = 0.028$, sham-injected striatum as reference region) (**Fig. 7e**). Similar results were obtained using the cerebellum as the reference region (**Extended Data Fig. 6d** and **e**): Average SUVR indicated a successful blocking by anle138b, which reduced tracer binding from 1.23 ± 0.01 to 1.15 ± 0.02 ($p = 0.04$) in the fibril-injected striatum (**Extended Data Fig. 6e**). In contrast, anle138b increased tracer signal in the sham-injected striatum from 0.96 ± 0.04 to 1.08 ± 0.03 ($p = 0.02$) (**Extended Data Fig. 6e**).

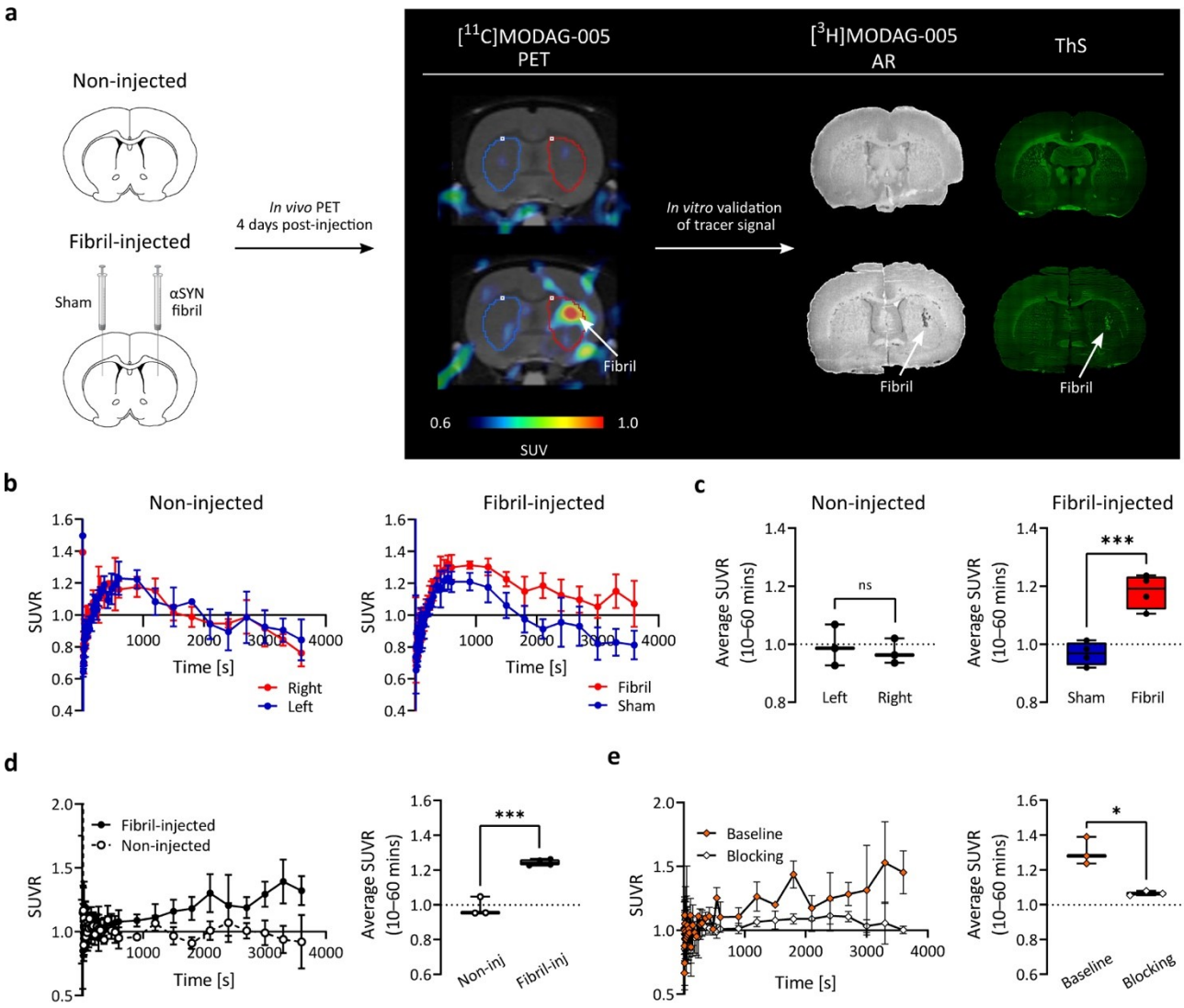

Fig. 7: *In vivo* characterization of [^{11}C]MODAG-005 in fibril-injected rats. a, Brain [^{11}C]MODAG-005 PET images (sum of 2.5 to 60 min) of one exemplary non-injected and one unilateral αSYN-fibril injected rat scanned four days post injection are shown. Increased tracer accumulation was observed in the fibril-injected right striatum, but not in the vehicle-injected left striatum and non-injected rat. The location of αSYN fibrils was confirmed by [^{3}H]MODAG-005 autoradiography and thioflavin S staining. **b**, **c**, PET analysis using the cerebellum as reference region for SUVR calculation. **b**, SUVR values over time did not differ in the striatum of non-injected rats, whereas they were increased in the right, αSYN fibril-injected striatum compared to the left, sham-injected striatum. **c**, A comparison of the average SUVR between the right and left striatum of non-injected rats (0.97 ± 0.043 vs. 0.99 ± 0.071, p = 0.542) and between the fibril- and sham-injected striatum of αSYN fibril-injected rats (1.18 ± 0.059 vs. 0.97 ± 0.041, p = 0.0003) is shown. **d**, **e**, PET analysis using the sham-injected, left striatum as the reference region for SUVR calculation. **d**, Time-SUVR curves and average SUVR showed increased tracer retention in the fibril-injected striatum compared to non-injected striatum (average SUVR = 1.24 ± 0.018 vs. 0.99 ± 0.054, p = 0.003). **e**, Time-SUVR curves and average SUVR showed a decreased tracer retention in the fibril-injected striatum with anle138b blocking compared to baseline (average SUVR = 1.24 ± 0.018 vs. 0.99 ± 0.054, p = 0.028). AR, autoradiography; αSYN, α-synuclein; fibril-inj, fibril-injected; non-inj, non-injected; PET, positron emission tomography; SUV, standardized uptake value; SUVR, standardized uptake value ratio; ThS, thioflavin S. Data are presented as mean ± s.d.. Box plots extend from the 25th to 75th percentiles with the median indicated in the middle of the box and the minimum to maximum values shown by the whiskers. An unpaired two-tailed t-test was used for comparisons. In **b** and **c**, n = 3 for non-injected rats and n = 4 for fibril-injected rats. In **d** and **e**, fibril-injected rats underwent both baseline and blocking scans (n = 3).

Evaluation of [^{11}C]MODAG-005 in αSYN(A30P) transgenic mouse model of PD

To study the ability of [^{11}C]MODAG-005 to detect intracellular αSYN aggregates *in vivo*, we performed PET imaging in the αSYN(A30P) transgenic mouse model of PD and age-matched wild-type mice (**Fig. 8**,

Extended Data Fig. 8). The presence and distribution of αSYN pathology were verified by immunohistochemistry of αSYN pSer129, which revealed the strongest pathology in the brainstem, midbrain and hypothalamic areas in αSYN(A30P) mice (**Fig. 8a**, **Extended Data Fig. 8a**). Immunohistochemistry further revealed a heterogeneity in the pathology load among αSYN(A30P) mice. **Extended Data Fig. 8b** shows in the x-axis the percentage of positive αSYN pSer129 immunohistochemistry in the brainstem of αSYN(A30P) mice with a large interindividual variation, which ranged from 0.2% to 12.4%. αSYN(A30P) mice with less than 1% positive staining signal were excluded from the main PET analysis shown in **Fig. 8b** and **Extended Data Fig. 8c**.

[^{11}C]MODAG-005 binding in individual brain regions was consistent with the αSYN pathology distribution. Elevated time-SUVR curves and average SUVR values reflected increased tracer retention in αSYN(A30P) compared to wild-type mice in the brainstem (1.16 ± 0.06 vs. 1.07 ± 0.07, $p = 0.004$), midbrain (0.94 ± 0.04 vs. 0.88 ± 0.06, $p = 0.03$) and hypothalamus (1.28 ± 0.13 vs. 1.15 ± 0.10, $p = 0.008$) (**Fig. 8b**). A moderate positive correlation was indicated between αSYN pSer129 immunohistochemistry and [^{11}C]MODAG-005 PET binding in the brainstem ($r = 0.47$, $p = 0.043$) (**Extended Data Fig. 8b**). On the other hand, no enhanced tracer binding was detected in the amygdala ($p = 0.20$), striatum ($p = 0.08$), thalamus ($p = 0.10$) and cerebellum ($p = 0.31$) (**Extended Data Fig. 8c**), where lower αSYN pathology load was detected (**Extended Data Fig. 8a**).

To investigate and exclude that the elevated tracer binding was due to potential off-target binding to MAO-B, we further performed immunohistochemistry and a qualitative scoring of MAO-B expression in the brainstem, midbrain, and hypothalamus (score 0–3, where 0 indicates no staining and 3 indicates relatively abundant staining) (**Extended Data Fig. 9**). Example of MAO-B immunohistochemistry images with their respective given score, as well as a larger magnification of the staining are displayed in **Extended Data Fig. 9a** and **b**, respectively. Our analysis revealed comparable average scores of MAO-B staining, ranging from 0 to 2 for all groups of αSYN(A30P) and wild-type mice, indicating no difference in MAO-B expression between the animal groups.

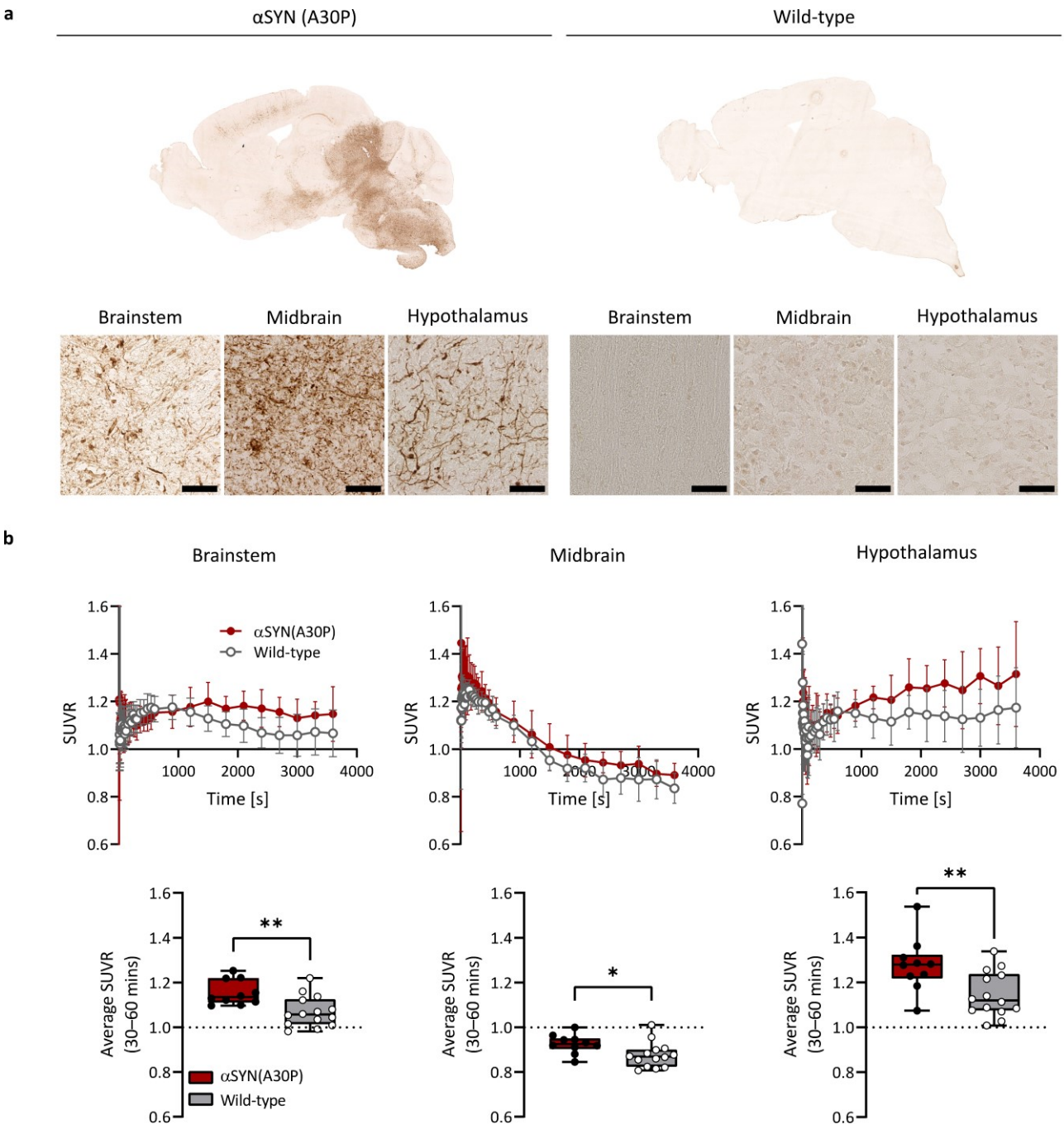

Fig. 8: *In vivo* characterization of [^{11}C]MODAG-005 in the αSYN(A30P) transgenic mouse model. a, Immunohistochemistry of αSYN pS129 in αSYN(A30P) and wild-type mouse brain. Exemplary whole-brain images as well as magnified images in brain regions with high pathology load such as the brainstem, midbrain, and hypothalamus are shown. Scale bar, 50 µm. **b**, [^{11}C]MODAG-005 PET time-SUVR curves and average SUVR comparison between αSYN(A30P) mice (n = 10) and wild-type mice (n = 14) are shown. SUVR values were calculated using the cortex as the reference region and averaged from 30 to 60 minutes. Time-SUVR curves showed higher tracer retention in αSYN(A30P) mice. Comparing the average SUVR values, increased tracer binding was detected in αSYN(A30P) mice compared to wild-type mice in the brainstem (1.16 ± 0.06 vs. 1.07 ± 0.07, p = 0.004), midbrain (0.94 ± 0.04 vs. 0.88 ± 0.06, p = 0.03) and hypothalamus (1.28 ± 0.13 vs. 1.15 ± 0.10, p = 0.008). Data points in time-SUVR curves are presented as mean ± s.d.. Box plots extend from the 25th to 75th percentiles with the median indicated in the middle of the box and the minimum to maximum values shown by the whiskers. Shapiro-Wilk test was used to test for a normal distribution. An unpaired two-tailed t-test was performed to compare the average SUVR values between both animal groups. αSYN, α-synuclein; SUVR, standardized uptake value ratio.

Characterization of [^{11}C]MODAG-005 in non-human primate brain

To evaluate the tracer characteristics in wild-type non-human primates (NHPs) without αSYN pathology, we performed dynamic *in vivo* PET imaging and plasma radio-metabolite analysis in two cynomolgus monkeys (NHP 1 and NHP 2). **Fig. 9a,b** and **Extended Data Fig. 10a,b** show a macaque MRI image as well as baseline and competition [^{11}C]MODAG-005 PET images of the brain summed up from 0–10 minutes and 90–120 minutes with respective TACs of selected brain regions over time. For visualization, images and TACs in units of kBq/cm^3 were converted to SUV in units of g/mL. At baseline, rapid brain uptake with a peak SUV of 3.7 and 6.1 for NHP 1 and NHP 2, respectively, and a fast wash-out from the brain with a clearance half-life of approximately 12 minutes (one-phase decay model from the peak) was identified (**Fig. 9b** and **Extended Data Fig. 10b**). After blocking with MODAG-005, we saw similar pharmacokinetic profile with peak SUVs of 4.7 and 4.2 for NHP 1 and NHP 2, respectively, and a clearance half-life of approximately 16 minutes. Total volume of distribution (V_T) and K_1 were estimated using a 2-tissue compartment model [16]. V_T is the activity ratio between tissue and plasma at equilibrium, and K_1 is the rate of tracer delivery from plasma to brain tissue. In the whole brain, V_T and K_1 were estimated to be 6.89 ± 1.58 mL/cm^3 and 0.49 ± 0.12 mL/cm^3/min, respectively. V_T at baseline and competition were compared, revealing little differences in NHP 1 (5.11–6.15 mL/cm^3 vs. 4.87–6.07 mL/cm^3) and some degree of lowered V_T in NHP 2 (7.76–9.81 mL/cm^3 vs. 5.03–6.58 mL/cm^3) (**Fig. 9c** and **Extended Data Fig. 10c**). On the other hand, little changes between K_1 at baseline and competition were noted for both NHP 1 (0.30–0.45 mL/cm^3/min vs. 0.36–0.63 mL/cm^3/min) and NHP 2 (0.49–0.89 mL/cm^3/min vs. 0.51–0.78 mL/cm^3/min) (**Fig. 9d** and **Extended Data Fig. 10d**).

[^{11}C]MODAG-005 radio-metabolite formation in the plasma of NHP 1 and NHP 2 was determined 5, 15, 30, 45, and 60 minutes after tracer injection (**Fig. 9e** and **Extended Data Table 3**). Quantitative analysis revealed two metabolites in the plasma with 74 ± 1.3%, 29 ± 0.3%, 18 ± 1.7%, 14 ± 1.0%, and 8.6 ± 1.0% of the parent compound remaining at 5, 15, 30, 45, and 60 minutes after tracer injection, respectively. Heart rate (BPM), body temperature, expired CO_2, respiration/min, pulse O_2%, % anesthetic gas, and oxygen (L/min) throughout the scans are summarized in **Supplementary Item 5**.

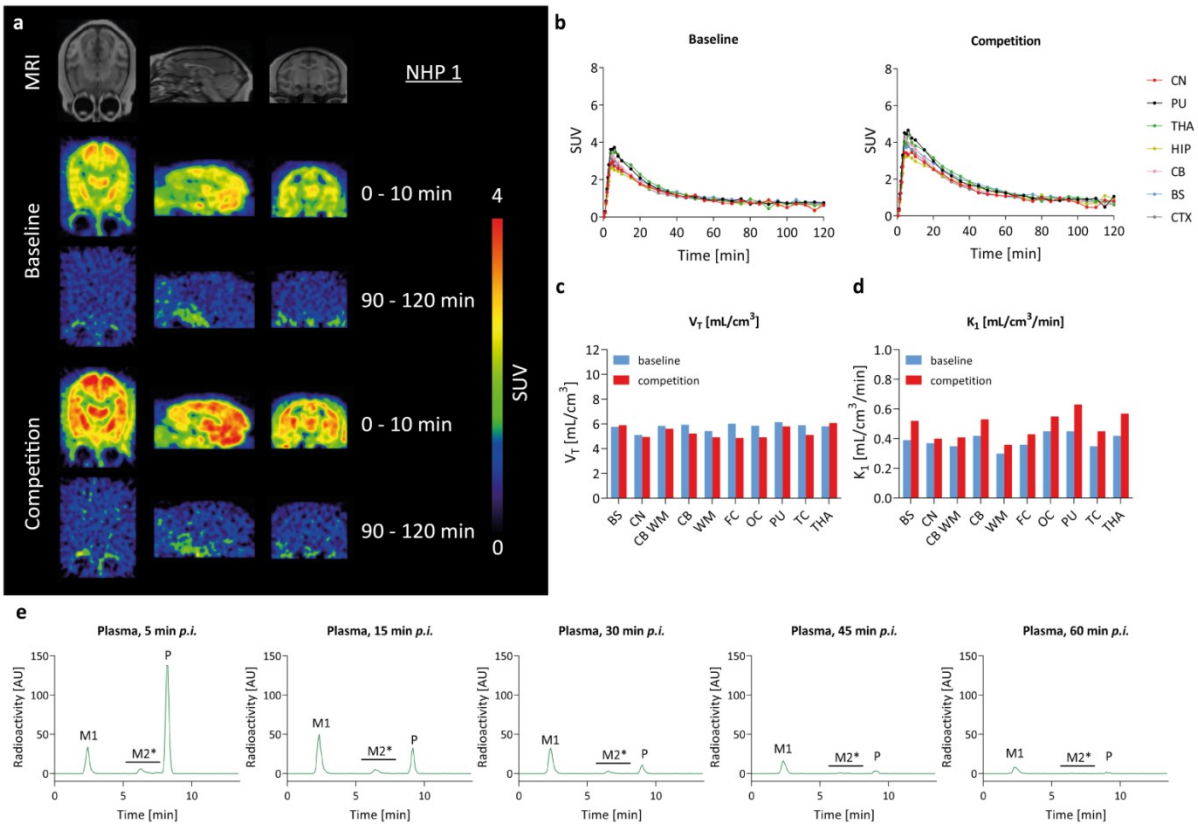

Fig. 9: *In vivo* characterization of [^{11}C]MODAG-005 in non-human primates (NHPs). a, Transversal, sagittal, and coronal (left to right) MRI of one exemplary cynomolgus monkey brain and [^{11}C]MODAG-005 PET images at baseline and after pre-injection of unlabeled MODAG-005 (sum of frame 0 to 10 and 90 to 120 minutes). **b**, TACs of different brain regions show high brain uptake with peak SUVs of 3.7 (baseline) and 4.7 (competition) followed by a fast clearance from the brain. **c**,**d**, Volume of distribution (V_T) and K_1 values estimated from a 2-tissue-compartment model at baseline and after competition with MODAG-005. **e**, Plasma radio-metabolites revealed the formation of two metabolites, with 70%, 24%, 16%, 12%, and 8% of

the parent compound remaining at 5, 15, 30, 45, and 60 minutes post tracer injection, respectively. For results in NHP2, see **Extended Data Fig. 10).**
AU, arbitrary units; BS, brainstem; CB, cerebellum; CB WM, cerebellar white matter; CN, caudate nucleus; CTX, cortex; WM, white matter; FC, frontal cortex; HIP, hippocampus; MRI, magnetic resonance imaging; M1, metabolite 1; M2*, metabolite 2*; OC, occipital cortex; P, parent compound; PET, positron emission tomography; p.i., post injection; PU, putamen; STR, striatum; SUV, standardized uptake value; TACs, time-activity curves; TC, temporal cortex; 2-TCM, two tissue compartment model; THA, thalamus.

[^{11}C]MODAG-005 - first in human

Following radiochemical development and preclinical evaluation, the radiochemical synthesis process for [^{11}C]MODAG-005 was transferred to a Good Manufacturing Practice (GMP) environment and further optimized to fulfill the requirements for a human application, in this case following the regulations of the German Medicinal Products Act ("Arzneimittelgesetz" AMG §13(2b)). After full disclosure, a first-in-human translational PET-scan with [^{11}C]MODAG-005 was performed on a high sensitive PET-scanner (Biograph Vision Quadra) in a patient diagnosed with an overlap syndrome of multiple system atrophy – parkinsonian type (MSA-P) and cerebellar type (MSA-C). The patient gave a written informed consent for both performing the PET scan with [^{11}C]MODAG-005 and further data-processing and evaluation. The diagnosis of overlapping MSA-C and MSA-P was based on clinical assessment, diagnostic MRI and Single-Photon-Emission Computed Tomography (SPECT) of the presynaptic dopamine transporter (DAT) with [^{123}I]FP-CIT.

Fig. 10a presents MRI data revealing advanced cerebellar and pontine atrophy including indication of the "Hot Cross Bun" sign, reflecting degeneration of pontocerebellar tracts. In line with these findings, [^{123}I]FP-CIT-SPECT images (**Fig. 10b**) show a strong presynaptic dopaminergic degeneration (reduced DAT availability) in the left and right striatum with a greater reduction on the right side. Notably, elevated [^{11}C]MODAG-005 retention was observed in brain regions anticipated to exhibit αSYN pathology, specifically in the caudate, putamen, thalamus, pons and cerebellar white matter. With respect to the striatum, this retention was slightly higher on the right side, mirroring the lateralization noted in the [^{123}I]FP-CIT-SPECT images. TACs of selected brain regions, including the occipital cortex as reference region due to its expected lack of pathology, are depicted in **Fig. 10c**.

The pharmacokinetic analysis, illustrated in **Fig. 10d,e**, reveals a rapid brain uptake of [^{11}C]MODAG-005 in the brain. The occipital cortex showed a peak SUV of 2.8 and a clearance half-life of 20 min. For comparison, peak SUV was 3.5 and and clearance half life was 10 min in the occipital cortex in the healthy NHP shown in **Fig. 9** and **Supplementary item 8.** In comparison to the MSA patient, no difference in tracer uptake was observed between the striatum and occipital cortex in the NHP as shown in **Fig. 9b,c**.

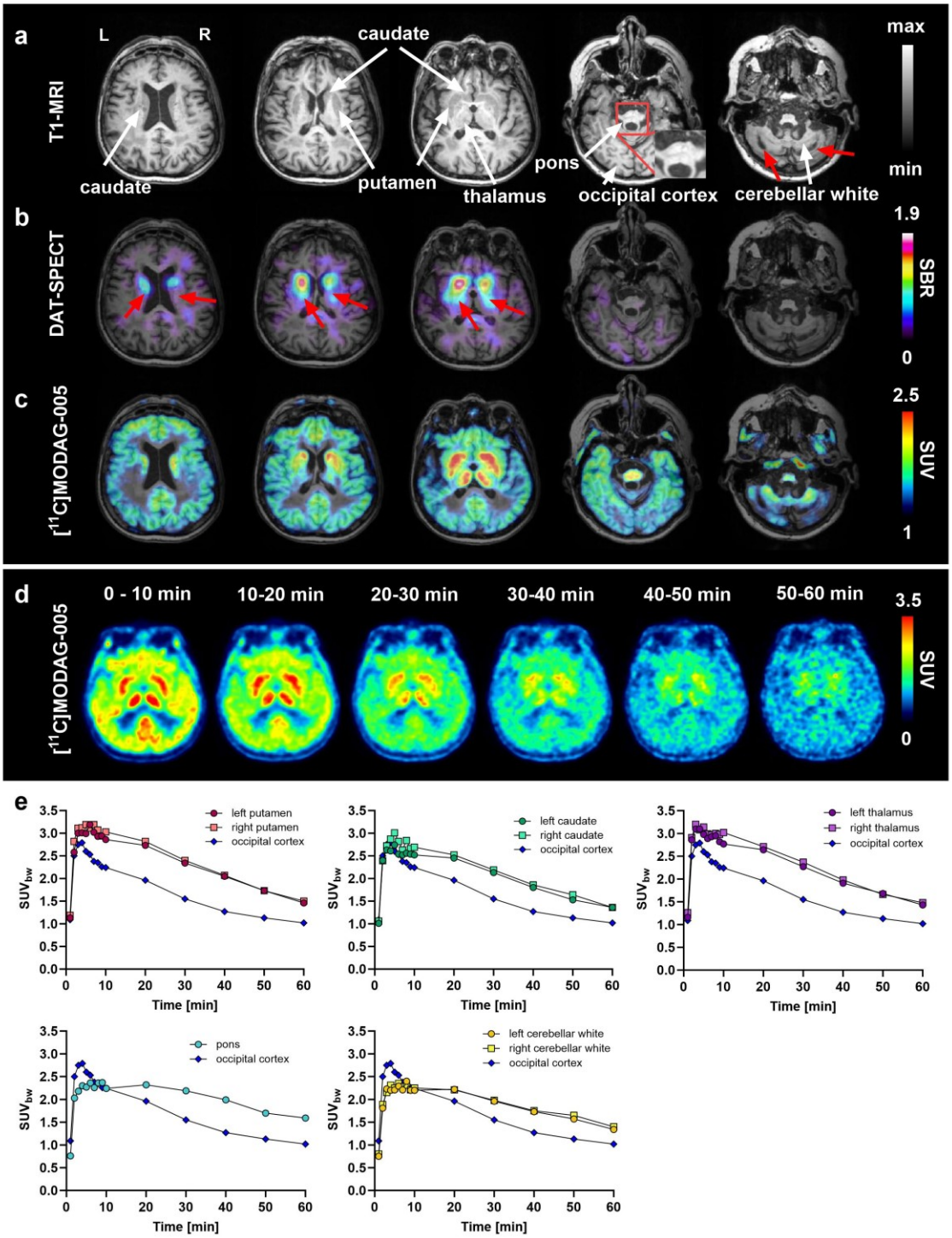

Fig. 10: [^{11}C]MODAG-005 first-in-human PET. a, Transversal MR scans of a patient clinically diagnosed with an overlap syndrome of MSA-P and MSA-C, highlighting advanced cerebellar and pontine atrophy including indication of the “Hot Cross Bun” sign reflecting degeneration of pontocerebellar tracts (indicated by red arrows and zoomed insert). White arrows indicate anatomical regions which show increased [^{11}C]MODAG-005 uptake. **b**, Dopamine transporter (DAT) SPECT images, revealing significant presynaptic dopaminergic degeneration in the bilateral striatum (caudate and putamen) with a more pronounced effect on the right side. **c**, [^{11}C]MODAG-005 PET images (sum of 20-60 min) illustrating elevated binding in the bilateral striatum. Additionally, increased binding is noted in the thalamus, pons and cerebellar white matter – regions associated with expected αSYN pathology. **d**,**e** The pharmacokinetic profile of [^{11}C]MODAG-005 in a representative slice (sum of all frames) and corresponding time-activity curves of selected brain regions, demonstrate rapid brain uptake (peak SUV: 2.8) and moderately fast clearance ($t_{1/2}$ = 20 min) from the occipital cortex, a region anticipated to be free of pathology. Conversely, regions expected to exhibit αSYN pathology show a prolonged tracer retention. MRI, magnetic resonance imaging; PET, positron emission

tomography; SBR, specific binding ratio; SUVbw, standardized uptake value (normalized to body weight); SPECT, single photon emission computer tomography; DAT, dopamine transporter.

Discussion

Pathological αSYN is the key hallmark in several major devastating neurodegenerative diseases, most prominently PD, DLB, and MSA. Its aggregation seems to be the central driver of their pathogenesis and inhibiting this process holds considerable promise as a therapeutic strategy, qualifying it as a main target for potential disease-modifying drugs, such as anle138b (emrusolmin) [11, 17], PD01A [18], BIIB054 [19] or RO7046015 [20].

Several PET radiotracers targeting neurodegeneration and their underlying metabolic processes have been successfully developed [21-23] and offer the possibility of a differential diagnosis late in the disease. However, pathology-specific early diagnosis is needed to modify and/or stop the disease and efficiently slow down its progression by therapy.
In contrast to αSYN aggregates, radiotracers for imaging the neuropathological hallmarks of AD and tauopathies have been developed [24-27]. The clinical assessment of amyloid burden using PET imaging has been playing a key role in the enrolment and outcome measurement of clinical trials to investigate the efficacy of anti-amyloid therapies [28-31].

The development of a non-invasive diagnostic tool for αSYN pathology is crucial and an αSYN PET tracer would be a game changer for basic research, early diagnosis, and therapy development. The emergence of different classes of αSYN ligands in the past decade is an encouraging reflection of the advances in αSYN PET tracer development. Yet, a tracer that combines all the desirable properties is still missing. A common challenge is the lack of detectable tracer binding to αSYN pathology in the human brain, despite their good affinity to αSYN fibrils [12, 32]. A number of recently developed αSYN ligands show promising *in vitro* binding. Yet, *in vivo* brain uptake and kinetics seems to require further optimization [33-35]. For other αSYN ligands, evaluation and data analysis in animal models was not unambiguously conclusive [36, 37]. While a few tracer candidates have been advanced to human studies, off-target binding seems to be an issue and bigger patient cohorts should be investigated for conclusive evaluation of the suitability of the tracer for human diagnosis [7, 38].

Herein, we aimed to develop an αSYN PET tracer, MODAG-005, based on the lead structure anle138b and its derivatives, anle253b and MODAG-001, and to perform a detailed evaluation to characterize its binding profile from *in vitro* with fibrils and brain tissues to *in vivo* in animal models. We demonstrated its high specificity and affinity in a subnanomolar range, which is superior to all respective published values of other tracer candidates published so far [5-7, 39, 40]. Our previous study reported [^{11}C]MODAG-001 as a new potential αSYN PET ligand [12], however, it failed to efficiently detect aggregated αSYN from human brain tissue and showed a high non-specific background binding.

Following the identification of the de-methylated MODAG-001 (MODAG-005) as a brain-penetrating metabolite, our next goal was to enhance the properties of MODAG-001 by removing a major metabolite that confounds kinetic modeling.The *in vitro* affinity of [^{3}H]MODAG-005 towards human αSYN fibrils was found to be improved by three-fold. Comparing [^{3}H]MODAG-005 to its predecessor, [^{3}H]MODAG-001, the selectivity of [^{3}H]MODAG-005 for αSYN over tau fibrils increased. Furthermore, it is >100-fold more selective for αSYN over $A\beta_{1-42}$ fibrils. MODAG-005 was further tested for potential off-target binding using the Cerep diversity panel comprising 71 target proteins (receptors, transporters, channels, enzymes) and a customized kinase panel comprising 159 different kinases. A special focus was put on MAO-B binding, as *in silico* analysis of different tau tracer candidates showed that they bind to the same region as the MAO-B inhibitor selegiline, i.e., the substrate entry site. Thus, IC_{50} values obtained in the Cerep assay should provide valid information on binding to the relevant site. The determined IC_{50} of 0.8 µM is considered to be of little relevance for MODAG-005 *in vivo* PET.

We further demonstrate the binding of [^{3}H]MODAG-005 to αSYN pathology of human brains. The ability of MODAG-005 to bind to αSYN inclusions in brain tissues of synucleinopathies, particularly with an unprecedented high affinity, indicates its potential for imaging the misfolded αSYN in human brains. Moreover, successful blocking and competition with anle138b in brain tissue from human MSA and the αSYN(A30P) mouse model provide evidence for the target engagement of anle138b as MODAG-005 competes for the same binding site. Using [^{3}H]MODAG-005, we confirmed the binding of anle138b to aggregated αSYN in human MSA brain tissue, determining a K_i of 25 nM.

Despite the presence of co-pathology in PD brain tissue, we detected a remarkable binding which correlates with αSYN immunofluorescence. A previous competition assay between MODAG-001 and SIL26 suggested that the two ligands likely target the same binding site [12, 41]. The latter was reported to bind to PD homogenates with a K_i value of 33.5 nM, pointing to the presence of a binding site for MODAG-001/MODAG-005 in αSYN aggregates from the PD brain. Further validation of tracer binding in PD brain tissue will be pursued in future work.

In line with the fibril binding assay, [^{3}H]MODAG-005 autoradiography also revealed non-selective binding in PD, AD, and PSP tissues. By nature, amyloid fibrils, such as Aβ, tau, and αSYN, share structural similarity between binding pockets as they form unique beta-sheet secondary structures [42]. Small molecule compounds might therefore bind all three amyloids to a certain extent. Even when a clean off-target profile was indicated *in vitro*, the tracer signal may still be confounded by disease-related off-target binding *in vivo*. For example, [^{18}F]ACI-12589 showed binding in other neurodegenerative diseases with an increased cortical retention in AD subjects correlated to areas of tau tracer [^{18}F]RO948 uptake despite the lack tau binding *in vitro* [7]. Hence, it is important to note that off-target binding remains a challenge for all current tracer candidates that have undergone thorough validation studies and thus merits further improvement in future development.

Our *in vitro* results showed a high concordance between binding to the type of recombinant αSYN fibrils used by us (K_d = 0.20 ± 0.03 nM) and αSYN aggregates in human brain tissue (K_d = 0.25 nM). This is particularly important for future screenings on recombinant fibrils, as screenings on tissue homogenates are challenging and the tissue is precious. A high-affinity binding site for [^{3}H]MODAG-005 remained in MSA tissue after selegiline blocking, indicating the specificity of αSYN binding.

Based on the promising *in vitro* binding in human tissues, MODAG-005 was labeled with carbon-11 for *in vivo* evaluation. *In vivo* [^{11}C]MODAG-005 PET studies in healthy mice and rats showed sufficient brain uptake and rapid clearance, which fulfils the pharmacokinetic requirements of a central nervous system PET tracer. Since [^{11}C]MODAG-005 is the de-methylated form of [^{11}C]MODAG-001, we were able to reduce the number of detectable radio-metabolites in the brain from two to one. While the presence of radiometabolite in the brain could confound kinetic modelling, analysis in human subjects will be required to confirm the metabolic profile of [^{11}C]MODAG-005, as lower species, such as rodents, have faster and more extensive metabolism compared to humans [43].

In the fibril injection model, [^{11}C]MODAG-005 was able to detect injected αSYN fibrils *in vivo.* Although αSYN fibrils are mainly located extracellularly, it is a suitable model to study and compare the binding kinetics of tracers to αSYN aggregates under physiological conditions. Despite the increase in astrogliosis and MAO-B expression which were associated with intracranial surgery and the injected fibril, immunohistochemistry revealed a different pattern of GFAP and MAO-B upregulation in the brain compared to *in vivo* [^{11}C]MODAG-005 PET images and *in vitro* [^{3}H]MODAG-005 autoradiography, thereby excluding the possibility that increased tracer signal was due to MAO-B off-target binding. A successful reduction of tracer binding after anle138b blocking indicated the binding specificity of [^{11}C]MODAG-005 and provided evidence for the *in vivo* target engagement of anle138b.

We demonstrated that [^{11}C]MODAG-005 has an improved image contrast compared to MODAG-001, showing a better signal in the fibril-injected striatum and lower background binding in the uninjected striatum. The removal of the methyl group increases the hydrophilicity of the molecule, thereby reducing its non-specific binding to the myelin/lipid-containing white matter brain structures [44] and, consequently increases the SNR of the tracer in tissue. The *in vivo* pharmacokinetics study of [^{11}C]MODAG-005 showed a good tracer uptake into the brain, demonstrating that the small increase in the hydrophilicity of MODAG-005 while improving the SNR in PET imaging, did not impair its ability to penetrate the blood-brain barrier. Taken together, one of the biggest downsides of MODAG-001 – its non-specific *in vivo* background binding – was addressed and improved with MODAG-005.

Furthermore, [^{11}C]MODAG-005 was investigated in *vivo* in the αSYN(A30P) mouse model of PD. This mouse model has intracellular Lewy body-like aggregates of the transgenic human αSYN with the A30P mutation that causes familial PD [45]. Compared to age-matched wild-type mice, enhanced binding of [^{11}C]MODAG-005 in αSYN(A30P) mice was demonstrated in brain regions with strong αSYN pathology, validated by immunohistochemistry and in line with literature reports [45, 46]. This increase in tracer binding was not caused by MAO-B, since its expression was similar in these brain regions regardless of pathology load. On the other hand, in brain regions with less αSYN pathology, [^{11}C]MODAG-005 could not distinguish between the two groups. Nevertheless, a correlation between the amounts of αSYN pSer129 and the degree

of [^{11}C]MODAG-005 binding in the brainstem indicated the tracer's potential to differentiate between individuals with different pathology loads and suggested the successful use of [^{11}C]MODAG-005 as an αSYN PET tracer for *in vivo* application.

In view of the promising results above, we proceeded to investigate the potential translation of [^{11}C]MODAG-005 to larger species by performing *in vivo* studies in healthy NHPs. Our tracer showed a rapid brain uptake and clearance, with peak SUVs of 3.7–6.1, which is high compared to tracers for Aβ ([^{11}C]PIB <2) [47] or tau (Tauvid ~2.3) [48] in their preclinical evaluation in NHPs. V_T values in NHP 1 were not reduced after competition with MODAG-005 pointing to low to no off-target binding in the healthy brains. For NHP 2, V_T was lower in competition compared to baseline values, which may be attributed to an increased heart rate observed during tracer injection at baseline affecting tracer uptake or low signal to noise in parent fraction measurements after 30 minutes for the baseline scan that may affect the arterial input function. A retest study would be helpful to assess test-retest reliability of V_T to determine if the change in V_T is meaningful. With a mean K_1 of 0.49 ± 0.12 mL/cm^3/min, the tracer exhibited excellent extraction from the plasma to the tissue. Competition increased K_1 values, which might be a result of blocked plasma protein binding, resulting in higher concentrations of [^{11}C]MODAG-005 in the brain. Radio-metabolite analysis indicates a similar metabolism in rodents and NHPs.

The first-in-human translational use of [^{11}C]MODAG-005 was performed for clinical and diagnostic investigation of a patient with the diagnosis of clinically established MSA according to the Movement Disorders Society clinical diagnostic criteria for MSA [49]. Clinically, the patient presented with an overlap syndrome of MSA-P and MSA-C. Absence of Aβ copathology was determined by analysis of cerebrospinal fluid (CSF) profiles of $A\beta_{1\_42}$, total-Tau and p181-Tau levels which were in the normal range. [^{11}C]MODAG-005 demonstrated rapid brain uptake achieving peak SUVs of 2.2-3.2, aligning with the aforementioned Aβ and tau tracers [47, 48]. Notably the tracers elimination half-life in the occipital coretex was prolonged compared to NHP, suggesting increased non-specific binding in human brain tissue. Despite this, [^{11}C]MODAG-005 exhibited pronounced retention in regions anticipated to exhibit αSYN pathology, particularly within the caudate putamen, corroborating significantly reduced DAT availability observed in earlier SPECT imaging.

The lateralization of tracer uptake, more pronounced on the right, mirrored the asymmetrical DAT loss observed in DAT imaging. Additionally, tracer accumulation in the cerebellum and pons was observed, aligning with the expected neuropathology and supporting the diagnostic accuracy of [^{11}C]MODAG-005. While the absence of a healthy control limits direct comparison, the comparison with NHP data, which showed no increased tracer uptake in analogous regions, provides indirect evidence of the tracer's specificity.

In the present study, we report a detailed *in vitro* and *in vivo* evaluation of MODAG-005. We obtained a clear macroscopic and microscopic evidence of tracer binding to glial cytoplasmic inclusions in MSA brain tissue with an unprecedented binding affinity, which is superior compared to affinities reported for other αSYN tracer candidates. Feasibility for *in vivo* imaging was consolidated through the successful identification of regions with high pathology in the αSYN(A30P) transgenic mouse model. We also presented evidence for a specific binding of MODAG-005 to αSYN pathology which was independent of MAO-B, as validated in brain tissue sections of human MSA, fibril-injected rat, and αSYN(A30P) mice. This investigation is crucial and has been discussed in αSYN tracer development [7], yet often not studied [40, 50]. We further applied MODAG-005 to confirm the target engagement of the potential therapeutic agent anle138b, both *in vitro* and *in vivo*. On the other hand, limitations of this work are the lack of an unambiguous tracer binding to LBs and LNs in human PD tissue due to the presence of concomitant pathology, as well as off-target binding to Aβ and tau aggregates. Both of these merits in-depth investigation or improvement in future work.

In conclusion, our results collectively indicate that [^{11}C]MODAG-005 is a promising tracer candidate for *in vivo* imaging of MSA patients. Its superior subnanomolar binding affinity to αSYN aggregates may provide an advantage over other tracers with lower binding. Furthermore, the present study demonstrated the potential application of [^{11}C]MODAG-005 to validate *in vivo* drug target engagement of novel αSYN-targeting therapeutic agents in clinical trials.

Methods

A competition screening of a compound library against [^{3}H]MODAG-001 was performed, which identified MODAG-005 to be a high-affinity binder to recombinant αSYN fibrils. After tritiation, the binding affinity and selectivity of [^{3}H]MODAG-005 were determined using saturation binding assays against αSYN, tau, and Aβ fibrils, and in animal and human brain slices. After ^{11}C-labeling, *in vivo* characterization of [^{11}C]MODAG-005

was performed in rodents and NHPs using PET imaging and metabolite analysis. Furthermore, *in vivo* binding was determined in rats intrastriatally injected with αSYN fibrils.

Precursor and standard synthesis of MODAG-005
The synthesis of MODAG-005 and its precursor for radiosynthesis is described in **Supplementary Item 6**. The calculated logP (clogP) and topological polar surface area (tPSA, [Å^2]) values shown in **Extended Data Fig. 1** were calculated by the Molinspiration property engine (v2021.10).

MODAG-005 tritiation
MODAG-005 was tritiated (RC Tritec AG, Teufen Switzerland), dissolved in EtOH, and stored at -80°C until further usage. The A_m was 2.96 GBq/µmol, and its radiochemical purity was > 98%, as determined via high-performance liquid chromatography (HPLC).

Fibril binding experiments
Expression, purification, and generation of sonicated human recombinant wild-type αSYN were performed using previously established protocols [12, 13]. Carrier-free recombinant human 4-repeat-tau (4R-tau) (Tau-441/2N4R-Tau), hereinafter referred as tau, was purchased lyophilized from Bio-Techne GmbH (Wiesbaden, Germany), and reconstituted in 50 mM Tris-buffer, pH 7.0. Fibrillation was induced by heparin under constant agitation and the generated fibrils were sonicated, as described previously [12, 51]. Sonicated $Aβ_{1-42}$ fibril batch 1 production was adapted from [41] and performed as described previously [12]. Sonicated $Aβ_{1-42}$ fibril batch 2 was produced analogous to batch 1 but with 96 hours incubation time and validated using thioflavin T (ThT) fluorescence assay, negative staining transmission electron microscopy, as described previously [12], as well as [^{3}H]Pittsburg compound B (PiB) saturation binding assay (**Supplementary Item 1**). Prior to binding experiments, the optimal concentration for the respective fibril type was determined by performing a concentration determination assay to prevent ligand depletion, as described in [12].

Binding experiments were conducted as previously described [12]. Briefly, for competition binding experiments, a fixed concentration of αSYN (15 nM) fibrils was incubated with 1 nM [^{3}H]MODAG-001 in low-binding plates (96-well micro test plate, ratiolab GmbH, Dreieich, Germany). Competition was induced by adding ten concentrations of a 1:4 serial dilution of unlabeled MODAG-005 (4 µM–0.02 nM) in 30 mM Tris-HCl, 10% ethanol, 0.05% Tween20, pH 7.4 (in the following referred to as EtOH-Tween buffer) in a total volume of 200 µL/well.

For [^{3}H]MODAG-005 saturation binding assays, a fixed concentration of αSYN (15 nM), tau (250 nM) or $Aβ_{1-42}$ (1 µM) fibrils was incubated with with decreasing concentrations of [^{3}H]MODAG-005 (6 nM/24 nM–0.05 nM) in EtOH-Tween buffer in a total volume of 200 µL/well. Co-incubation with 400 nM unlabeled MODAG-005 was used to determine non-specific binding of the radiotracer. For [^{3}H]PiB saturation binding assay, $Aβ_{1-42}$ (2.5 µM) fibrils was incubated with decreasing concentrations of [^{3}H]PiB (32 nM–0.06 nM) in 50 mM Tris-HCl, 10% EtOH, 0.1% BSA, 0.025% NaN_3, pH 7.4, in a total volume of 200 µL/well. Co-incubation with 400 nM unlabeled PiB was used to determine non-specific binding of the radiotracer.

Incubation at 45 rpm for two hours at 37°C was performed on a shaker (MaxQ™ 6000, orbit diameter 1.9 cm, Thermo Fisher Scientific Inc., Marietta, OH, USA). The plate was covered by removable sealing tape (PerkinElmer, Waltham, MA, USA) to prevent evaporation of the tracer solutions. A filtermat harvester (PerkinElmer, Waltham, MA, USA) was used to filter bound radioligands onto a glass fibre filtermat B (PerkinElmer, Waltham, MA, USA), which was pre-incubated with 5 mg/mL polyethyleneimine (Sigma Aldrich Chemie GmbH, Taufkirchen, Germany) only for αSYN and $Aβ_{1-42}$ fibrils. After harvesting, the filtermat was dried in the microwave, and melt-on scintillator sheets (MeltiLex™ B/HS, PerkinElmer, Waltham, MA, USA) were molten into the filtermat. After solidification at room temperature, the filter was placed in a MicroBeta sample bag (PerkinElmer, Waltham, MA, USA) and measured using the Wallac MicroBeta® TriLux liquid scintillation counter (PerkinElmer, Waltham, MA, USA). Radioactivity converted to bound pmol fibril per added nmol of total fibril was plotted against increasing [^{3}H]MODAG-005 or [^{3}H]PiB concentrations in nM. Data points were fitted using nonlinear regression analysis in GraphPad Prism (GraphPad Software, Inc., Version 7.03, La Jolla (CA), USA). Saturation binding assays were performed in triplicates and repeated in three independent experiments.

Off-target binding
A Cerep diversity panel and a customized kinase panel assay were performed by Eurofins Cerep in France with a specific focus on MAO-B binding. The compound enzyme inhibition effect was calculated as a % inhibition of control enzyme activity. Competition binding assays were performed using increasing concentrations of MODAG-005 and IC_{50} values were determined by non-linear regression analysis of the competition curves.

Human and mouse brain tissue
Post-mortem human brain tissue samples were provided as 10 µm sections by the Neurobiobank Muenchen (NBM, Munich, Germany), where cases were collected on the basis of written informed consent according to the guidelines of the ethics committee of the Ludwig-Maximilians-University Munich, Germany (# 345-13). **Extended Data Table 1** provides a summary of the subjects and controls from which brain tissues were obtained. For PD case, the disease duration was approximately 25–26 years, with the first symptoms appearing in the patient's mid-60s as tremor of the left hand. The disease progressed with exhibition of akinetic-rigid syndrome and camptocormia over time, as well as mild cognitive impairment ten years ante mortem, and dementia (PD with dementia) five years ante mortem. The use of human tissue samples for this study was approved by the ethics committee of the Faculty of Medicine at the University of Tuebingen (Ethics approval number: 813/2018BO2).

In addition, 20 µm sagittal mouse brain sections for autoradiography experiments were obtained from an αSYN(A30P) (B6.Cg-Tg(THY1-SNCA A30P)1734Sud/J) and an age-matched wild-type (male, 72 weeks) mouse. All tissues were stored at -80°C until further use.

***In vitro* (micro)autoradiography**
Post-mortem human and mouse brain sections were used for autoradiographic evaluation of [^{3}H]MODAG-005. After defrosting, the brain sections were pre-incubated in 30 mM Tris-HCl, 0.1% BSA, pH 7.4 (in the following referred to as BSA buffer) for 25 minutes at room temperature. For total binding, the sections were incubated in 3 nM [^{3}H]MODAG-005. For blocking, adjacent sections were co-incubated with 3 µM unlabeled MODAG-005 or anle138b.

For saturation binding experiments, brain sections were incubated with decreasing concentrations of [^{3}H]MODAG-005 (48 to 0.1 nM for MSA; 96 to 0.2 nM for AD). To determine non-specific binding, adjacent sections (for tracer concentrations 96 nM, 48 nM, 24 nM, and thereafter every second section) were co-incubated with 3 µM unlabeled MODAG-005. In the selegiline pre-blocking saturation experiment, MSA tissue sections were pre-incubated in 3 µM selegiline for one hour at room temperature and washed (three times for ten minutes) before tracer incubation (96 to 0.38 nM, with non-specific binding determined at every tracer concentration). For competition binding experiments, 1 nM [^{3}H]MODAG-005 was incubated with decreasing concentrations of unlabeled anle138b (2 µM to 0.03 nM).

In all experiments, brain sections were incubated at room temperature for one hour with subsequent washing in ice-cold BSA buffer (three times for ten minutes) followed by dipping for three seconds in ice-cold deionized water. The dried sections were then exposed to a phosphor imaging plate (BAS-IP TR2025, Fuji Imaging Plate, VWR, Denmark) with a tritium standard (ART-123 and ART-123A; American Radiolabelled Chemicals, St. Louis, MO, USA) for seven days and scanned in a phosphor imager (BAS 5000, FUJIFILM Life Science, Stamford, CT, USA).

For data quantification, ImageJ software (US National Institutes of Health, Bethesda, MD, USA) was used. Images were converted to 32-bit and the square math function for increasing the grey value range was applied. Regions of interest (ROIs) were drawn over the tritium standard to obtain a standard curve. ROIs were placed in the white matter of MSA, progressive supranuclear palsy (PSP), a neurodegenerative tauopathy with a predominance of 4R-tau isoforms [52], and control cases (cerebellum and frontal cortex), and in the grey matter of PD, AD, and control cases (frontal cortex). For the mouse brain sections, ROIs were placed in the midbrain, brainstem, zona incerta, cortex, and cerebellum (**Supplementary Item 3**), which are brain regions of expected αSYN pathology, and cross-validated with pSer129 αSYN immunofluorescence microscopy [45]. Specific binding was calculated by subtracting the non-specific binding from the total binding values. After interpolation from the standard curve, the specific binding values were divided by the A_m of the tracer and converted into fmol/mg.

Statistical analysis was performed using GraphPad Prism (Version 8.4.0). Comparisons were carried out using values obtained from repeated measurements in each sample (ROIs placed at different locations) to capture any difference in pathology and tracer binding across the tissue sections. Welch's t-test was used to compare the specific binding between MSA cases and controls (cerebellum - white matter), as well as PSP and control (frontal cortex – white matter). For comparison of AD and PD with control (frontal cortex – grey matter), Brown-Forsythe and Welch ANOVA with Dunnett's T3 multiple comparisons test was carried out. For the saturation binding experiment in MSA, a Scatchard plot was prepared in GraphPad Prism based on the calculated specific binding. Data points for the high-affinity binding site (0.09–1.5 nM) and the low-affinity binding site (3–48 nM) were determined by visual inspection. Subsequently, non-linear regression (saturation binding: one-site – total and non-specific binding) was performed independently for the two sites to

determine the respective K_d and B_{max} values. The lines in the Scatchard plot were drawn based on these values, where x-intercept = B_{max} and y-intercept = B_{max}/K_d. For the competition experiment with anle138b in MSA, non-linear regression (competitive binding: one-site-fit K_i) was used. For the autoradiography in mouse brain tissues, no statistical test was performed.

For microscopic investigation of tracer binding, microautoradiography was performed in two MSA cases and one control case, which were thawed and fixed in 4.5% paraformaldehyde (PFA, SAV Liquid Production GmbH, Flintsbach am Inn, Germany) for ten minutes at room temperature. Pre-incubation and washing steps were as above. Brain sections were incubated for one hour with 30 or 60 nM [^{3}H]MODAG-005. Adjacent tissue sections were additionally incubated with 30 µM unlabeled MODAG-005, anle138b, or selegiline for blocking. Subsequent procedures were performed in a safe light-illuminated dark room. The slides were dipped for five seconds into a 1:1 mixture of distilled water and Ilford K5 emulsion (Agar Scientific Ltd, Stansted, UK) molten in a 40°C water bath and left to dry in an upright position for two hours at room temperature. After drying, the slides were stored in the dark at 4°C for one to two weeks. For development, the slides were incubated for four minutes in Ilford Phenisol at 20°C, followed by one minute in Ilford Ilfostop and four minutes in Ilford Hypam (prepared according to manufacturer's instruction, Agar Scientific Ltd, Stansted, UK). The slides were then washed in running tap water for ten minutes and finally rinsed in distilled water.

Immunofluorescence

Immunofluorescence microscopy was carried out on the same brain sections after (micro)autoradiography. All sections were fixed with 4.5% PFA as above, when not performed prior to microautoradiography. For antigen retrieval, sodium citrate buffer (10 mM, pH 6.0, Sigma Aldrich Chemie GmbH, Darmstadt, Germany) was boiled and the brain sections to be stained for αSYN pSer129 and phospho-tau (pTau) were incubated at room temperature in the boiled buffer for 30 minutes; brain sections to be stained for $A\beta_{1\text{-}42}$ were incubated in 97% formic acid for ten minutes at room temperature. After washing, the sections were subsequently equilibrated in Tris-buffered saline (TBS) supplemented with 0.1% Triton X-100 and 1% BSA, pH 7.6 (in the following referred to as TBS-X) for ten minutes, before blocking in TBS supplemented with 0.3% Triton X-100 and 10% normal goat serum (Vector Laboratories, Linaris Biologische Produkte GmbH, Dossenheim, Germany) for 60 minutes at room temperature. Incubation with primary antibody was carried out overnight at 4°C with either mouse anti-phosphorylated αSYN pSer129 monoclonal antibody (1:5000 in TBS-X, pSyn#64; 015-25191, FUJIFILM Wako Chemicals Europe GmbH, Neuss, Germany), mouse anti-pTau (Ser202, Thr205) monoclonal antibody (1:500 in TBS-X, AT8, MN1020, Invitrogen, Rockford, IL, USA), or rabbit anti-$A\beta_{1\text{-}42}$ polyclonal antibody (1:200 in TBS-X, 218703, Synaptic Systems, Goettingen, Germany). After three times washing with TBS-X, the sections were incubated with secondary antibodies (1:250 in TBS-X) for one hour in the dark, using either goat anti-mouse Alexa Fluor 488 (A-11036, Invitrogen, Carlsbad, CA, USA), goat anti-mouse Alexa Fluor 647 (A32728, Invitrogen, Carlsbad, CA, USA), or goat anti-rabbit Alexa Fluor 568 (A-11036, Invitrogen, Carlsbad, CA, USA). After three washes following secondary antibody incubation, sections were stained with 3 nM 4′,6-diamidino-2-phenylindole (DAPI) (Invitrogen, Carlsbad, CA, USA) for five minutes and washed before being mounted on coverslips with ProLong Glass Antifade Mountant (Invitrogen, Carlsbad, CA, USA).

Whole-section images of the stained tissues were captured at 10 × magnification using Leica DMi8 microscope interfaced with Leica LAS X software (Leica Microsystems CMS GmbH, Wetzlar, Germany). The images were further processed with ImageJ. Background subtraction was performed with a rolling ball radius of 100 pixels for αSYN pSer129 and pTau staining, whereas a radius of 200 pixels was used for $A\beta_{1\text{-}42}$ staining.

For the correlative analysis of autoradiography and immunofluorescence microscopy in PD tissues, the immunofluorescence microscopy image was co-registered with the autoradiography image using the ImageJ plugin 'Big Warp'. Autoradiography images were processed and quantified as above. ROIs of 20 × 20 pixels were drawn covering the whole brain section. The same ROIs were applied for the co-registered immunofluorescence microscopy image. Mean grey values of the immunofluorescence microscopy image were measured and normalized by dividing them by maximum intensity. Correlation and linear regression analysis of the autoradiography and immunofluorescence microscopy were performed using GraphPad Prism software.

Immunohistochemistry

Immunohistochemistry of αSYN pS129, GFAP, and MAO-B was performed in brain tissue sections from human MSA cases, fibril-injected and non-injected rats, αSYN(A30P) and wild-type mice from *in vivo* PET study. Thawing, post-fixation (20 minutes) and antigen retrieval of the cryosections was performed as described in the immunofluorescence. Following antigen retrieval, the tissue sections underwent quenching

(1 mL quenching solution = 890 µL TBS, 100 µL methanol, and 10 µL 30% hydrogen peroxide) for 20 minutes to inhibit endogenous peroxidase. Following equilibration in buffer and one-hour blocking (0.3% Triton-X and 10% normal goat serum), mouse and rat tissues underwent an additional one-hour blocking step with goat F(ab) anti-mouse or anti-rat IgG (1:100 in TBS-X, ab6668 and ab7172, Abcam, Rozenburg, The Netherlands), respectively, to reduce background. Following F(ab) IgG blocking, tissues were washed for ten minutes in TBS-X. Incubation with primary antibody was carried out overnight at 4°C with either mouse anti-phosphorylated αSYN (pSer129) monoclonal antibody (1:5000 in TBS-X, pSyn#64; 015-25191, FUJIFILM Wako Chemicals Europe GmbH, Neuss, Germany), rabbit recombinant anti-GFAP antibody (1:1000 in TBS-X, EPR1034Y, Abcam, Rozenburg, The Netherlands) or rabbit polyclonal anti-MAO-B (1:2000 (for human tissue) or 1:2500 (for rodent tissue) in TBS-X, HPA002328, Atlas Antibodies, Bromma, Sweden). Following overnight incubation, tissues were washed three times with TBS-X and incubated with a secondary antibody (EnVision+/HRP Dual Link Rabbit/Mouse, K406189-2, Agilent, Waldbronn, Germany) for 30 minutes at room temperature. After washing, tissues were incubated with 3,3′-diaminobenzidine (1:50 in substrate buffer according to manufacturer's instruction, Agilent, Waldbronn, Germany) for up to ten minutes or NovaRED Substrate Kit (prepared according to manufacturer's instruction by Vector Laboratories, SK-4800, Biozol, Eching, Germany) for up to 20 minutes. Tissues were washed, dehydrated in an ethanol series, and cleared with Clear-Rite 3 (Epredia Netherlands B.V., DA Breda, Netherlands). Stained tissues were mounted with Eukitt quick-hardening mounting medium (Fluka Analytical, Munich, Germany) and scanned with a NanoZoomer 2.0 HT (Hamamatsu Photonics K.K., Hamamatsu, Japan) at 40 × magnification.

Semi-quantitative analysis by image thresholding was performed for the immunohistochemistry of αSYN pSer129 in the brainstem of aSYN(A30P) and wild-type mice from *in vivo* PET study. Stained tissues which presented with artifacts not feasible to be removed manually were excluded from analysis. All aSYN(A30P) mice (n = 14, 6–10 tissue sections per animal) and randomly selected wild-type mice (n = 5, 2 tissue sections per animal) were analyzed. ROI was drawn in the brainstem using QuPath (Version 0.4.2). Tissue border and any tissue artifacts were not included into the ROI to avoid staining artifacts. Images with the ROI were exported from QuPath to ImageJ with no pixel downsampling (resolution = 1) and subsequently converted to 8-bit images. A threshold of 0–120 was applied using the "Threshold" function of ImageJ to create binary images and the percentages positive area were measured. Furthermore, qualitative scoring was performed for the immunohistochemistry of MAO-B in aSYN(A30P) and wild-type mice from *in vivo* PET study. Two wild-type mice and two aSYN(A30P) mice were selected from each animal group based on the pathology load (> 5%, 1–5% and < 1% aSYN pSer129) determined by semi-quantitative analysis of aSYN pSer129 immunohistochemistry (4 tissue sections per animal). Staining in the brainstem, midbrain and hypothalamus was given a score from zero to three, where score zero depicted the absence of staining and score three represented the maximum staining which was observed across the stained tissues.

Radiosynthesis of [^{11}C]MODAG-005

Both the precursor anle190214 and the unlabeled reference compound were obtained as reported in "Precursor and Standard synthesis of MODAG-005". Radiolabeling was carried out by either reductive methylation with [^{11}C]CH_2O or direct methylation using [^{11}C]MeOTf [12, 53], to achieve highly selective labeling of the aniline nitrogen without loss of radioactivity through pyrazole-labelled side product formation, as well as a higher molar activity for *in vivo* binding experiments. All solvents and reagents were obtained by commercial suppliers with analytical grade and used without further purification.

Radiosynthesis by reductive methylation: [^{11}C]CO_2 was prepared by the bombardment of ^{14}N target gas containing 1% O_2 with 70 µA of 16.5 MeV protons on a PETtrace 890 cyclotron (GE Healthcare). No carrier added [^{11}C]CO_2 was delivered to the automatic synthesis module and [^{11}C]MeI was produced via the phase-gas conversion pathway [54]. Radiosynthesis, purification, and formulation were automated on Tracerlab FX MeI and Tracerlab FX M (GE Healthcare) radiochemical synthesizers Analytical HPLC was performed using an Infinity 1260 HPLC system (Agilent Technologies) equipped with a NaI(Tl) detector for radioactivity detection. Radiochemical and chemical purities of the radiolabeled compound as well as carrier content for calculation of molar radioactivity were determined by analytical radio-HPLC.

Briefly, [^{11}C]MeI was trapped in a solution of 1 mg anle190214 and 5 mg trimethylamine *N*-oxide in 350 µL diethyl formamide (DEF) and reacted for three minutes at 60°C. The Schiff-base intermediate was then reduced to [^{11}C]MODAG-005 by the addition of 1.2 mL 0.1 M citrate-phosphate buffer pH 5 containing 60 µL 2 M sodium cyanoborohydride in DEF and incubation for five minutes at 100°C. The product was purified by isocratic HPLC (Phenomenex Synergi Max-RP, 4 µm, 80 Å, 250 × 10 mm; 6 mL/min 55% acetonitrile in water; retention time seven minutes) and reformulated in 500 µL ethanol and 5 mL phosphate-buffered saline using a Sep-Pak Plus Light C18 cartridge (Waters, Eschborn, Germany). Radiochemical purity as well as carrier content for calculation of A_m were quantified by analytical HPLC (Phenomenex Luna Phenyl-Hexyl,

5 µm, 100 Å, 250 × 4.6 mm; 1.5 mL/min 30% acetonitrile). At the end of the synthesis (EOS), the radiochemical yield was 12.0 ± 2.2% and the A_m was 49.2 ± 11.2 GBq/μmol.

Radiosynthesis by direct methylation - method A: [^{11}C]MeI was obtained as above in "Radiosynthesis by reductive methylation". [^{11}C]MeOTf was generated by the reaction of the produced [^{11}C]MeI with silver triflate in an online flow-through process at 200°C under helium gas flow. The radiolabeling precursor anle190214 (1-2 mg, 3.17-6.35 µmoles) was dissolved in 500 µL of 2-butanone and the reaction vial was vortexed. No-carrier added [^{11}C]MeOTf was bubbled through the solution cooled to -20°C. The reaction mixture was heated to 75°C for two minutes. After cooling down to room temperature, the solution was diluted with 1.5 mL of H_2O and transferred to the HPLC system. The crude product purified by semi-preparative HPLC on a Synergi 4 µm Max-RP 80 Å, 250 × 100 mm column was eluted with an isocratic flow of 55% acetonitrile in water (flow rate: 6 mL/min) with a retention time of 6.5 minutes. Chromatograms were registered using an UV-detector (254 nm) and a Geiger-Müller tube. The HPLC fraction containing the purified product was diluted with 50 mL of water and loaded on a Sep-Pak Plus Light C18 cartridge, previously conditioned with 10 mL of ethanol and 10 mL of water. The cartridge was washed with 5 mL of water, and the product was eluted with 0.5 mL of ethanol and formulated with the addition of 5 mL of PBS. Radiochemical and chemical purities of the radiolabeled compound as well as carrier content for calculation of molar radioactivity were determined by analytical radio-HPLC.

At the EOS the radiochemical yield was 11.8 ± 2.7% and the A_m was 209 ± 44 GBq/μmol.

Another direct methylation method is presented in the **Supplementary Item 7** section.

Animals
Mouse and rat experiments were conducted in compliance with the European directives on the protection and use of laboratory animals (Council Directive 2010/63/UE) and with the German animal protection law and with the approval of the local authorities (Regierungspraesidium Tübingen (Germany), R3/19G). Nine female C57BL/6J mice (21 ± 1.7 g) and 13 female Sprague Dawley rats (307 ± 28.4 g) were obtained from Charles River Laboratories (Sulzfeld, Germany). Additionally, αSYN(A30P) transgenic mice (n = 14, 12 females and 2 males, 100 ± 10 weeks old, 30 ± 3.4 g), which express human αSYN with an A30P mutation under the Thy-1 promoter, and age-matched wild-type mice on the same C57BL/6J background (n = 14, 11 females and 3 males, 100 ± 11 weeks old, 32 ± 4.3 g), were bred in Hertie Institute for Clinical Brain Research (Tuebingen, Germany) and also kindly provided by Prof. Dr. Tiago Fleming Outeiro (University Medical Center Goettingen, Goettingen, Germany) (excluded n = 2 from each group, which died during the PET scan). All animals were maintained in our vivarium on a 12:12 hour light-dark cycle and were kept at a temperature of 22°C with 40-60% humidity with free access to a standard diet and tap water.

Macaque experiments were conducted in compliance with all applicable sections of the Final Rules of the Animal Welfare Act regulations (Code of Federal Regulations, Title 9), the Public Health Service Policy on Humane Care and Use of Laboratory Animals from the Office of Laboratory Animal Welfare, and the Guide for the Care and Use of Laboratory Animals from the National Research Council (OLAW, current edition) (NRC, current edition). Adult (> 5–6 years of age) male (n = 1, 6.0 kg, NHP 1) and female (n = 1, 6.4 kg, NHP 2) cynomolgus macaques (*Macaca fascicularis*) were maintained at Charles River Laboratories, Inc. (Mattawan, MI, USA, CRL Study No., 2579-100) on a 12:12 hour light-dark cycle. They were kept at temperatures of 18 to 29°C with 30–70% humidity with free access to a standard diet and tap water.

Patient
The first translational use of the [^{11}C]MODAG-05 was performed in a 70 year-old female patient clinically diagnosed with an overlap syndrome of MSA-P and MSA-C supported by findings on MRI and [^{123}I]FP-CIT SPECT imaging indicating advanced neurodegeneration.

The clinical syndrome of our patient was characterized by cerebellar gait and limb ataxia (unsteady gait and dysmetria), mixed hypokinetic-cerebellar dysarthria in combination with parkinsonism (left-sided bradykinesia, rigidity, marked postural instability), autonomic dysfunction (urinary urge and orthostatic hypotension) as well as lack of response to dopaminergic drug therapy, consistent with the diagnosis of clinically established MSA according to the Movement Disorder Society Criteria for the Diagnosis of Multiple System Atrophy [49].

The patient was referred to the experimental diagnostics unit since the patient presented with an overlap syndrome of MSA-P and MSA-C.

Absence of Aβ copathology was determined by cerebrospinal fluid (CSF) analysis of Aβ1-42, Aβ1-40, Aβ1-42/ Aβ1-40 ratio, phospho- and total Tau using a fully automated chemiluminescent enzyme immunoassay (CLEIA) with commercially available kits on the LUMIPULSE® G600II platform (Fujirebio Europe, Ghent, Belgium).

αSYN fibril injection into the rat brain

Stereotactic surgeries were performed as previously described [12]. Briefly, rats (n = 7) were intracranially injected with 4 µL of αSYN fibrils (30 µM) using a stereotaxic injector (Stoelting, Wood Lane, IL, USA) (0.4 µL every 60 seconds.) into the right striatum (medial-lateral = -3.4 mm, anterior-posterior = 0.0 mm, dorsoventral = -4.8 mm) according to the stereotaxic atlas of Paxinos and Watson [55]. A contralateral injection of 4 µL vehicle (50 mM Tris-buffer, 100 mM sodium chloride, 0.02% sodium azide, pH 7.0) served as negative control. PET imaging was performed either four days or between three to four days (for blocking study) post injection. Thioflavin S staining on coronal 30 µm cryosections of fibril-injected rats was performed as described in [12]. Images were captured using a Leica DMi8 microscope and FITC filter settings (excitation 460 nm–500 nm; emission 512 nm–542 nm). Autoradiography of the cryosections was performed as described above, using 3 nM [^{3}H]MODAG-005 and 3 µM unlabeled MODAG-005 for blocking.

***In vivo* PET and MRI analysis in mice and rats**

PET imaging was performed as described previously [12]. Mice and rats were anaesthetized with 1.5-1.7% isoflurane evaporated in 100% oxygen at a flow rate of 0.8 L/min. Their body temperature was maintained at 37°C using a feedback temperature control unit. Five seconds after the start of the PET acquisition, mice for the pharmacokinetic study (n = 3) were injected intravenously (i.v.) with 14 ± 0.7 MBq of [^{11}C]MODAG-005 (A_m = 37 ± 9.2 GBq/µmol at time of injection) and rats for the pharmacokinetic and fibril injection studies (four days post-injection) (n = 8) with 24 ± 3.0 MBq (A_m = 41 ± 6.8 GBq/µmol at time of injection) produced by reductive methylation. Dynamic PET data were acquired for 60 minutes and divided into 39 time frames (12×5 s, 6×10 s, 6×30 s, 5×60 s, and 10×300 s). For the blocking study in fibril-injected rats as well as the study in the αSYN(A30P) transgenic mouse model, animals were injected i.v. with 27 ± 1.6 MBq (A_m = 134 ± 33.6 GBq/µmol at time of injection) and 15 ± 0.9 MBq (A_m = 175 ± 82.4 GBq/µmol at time of injection) of [^{11}C]MODAG-005, respectively, which was produced by direct methylation method A. For the blocking study in fibril-injected rats, two PET scans between three to four days after fibril injection were performed, which consisted of a baseline measurement with vehicle injection (20% PEG-400 (Carl Roth GmbH, Karlsruhe, Germany) and 80% of 20% aqueous sulfobutyl ether β-cyclodextrin sodium (CycloLab Ltd., Budapest, Hungary)) and a blocking measurement with the administration of anle138b (1 mg/kg dose in the vehicle) as a single intravenously bolus five minutes before tracer injection. Dynamic 60-minute PET data were divided into 45 frames (10 × 2 s, 8 × 5 s, 6 ×10 s, 6 × 30 s, 5 × 60 s, 10 × 300 s). For attenuation correction, a 13-minute transmission measurement with a cobalt-57 point source was performed after the PET data acquisition.

Subsequently, animals were sacrificed under CO_2 and perfused with cold PBS. Brains were extracted and frozen immediately either in 2-methybutane cooled on dry ice (fibril-injected rats) or in TissueTek (mice). OSEM3D was used as data reconstruction algorithm. After the PET acquisition of mice in the pharmacokinetic study, whole-body anatomical magnetic resonance images were acquired on a 7T small animal magnetic resonance imaging (MRI) scanner (Bruker BioSpin GmbH, Ettlingen, Germany). Animals were kept under 1.5% isoflurane anesthesia evaporated in 100% oxygen at a flow rate of 0.8 L/min. Signal transmission and readout were performed using a linearly polarized radiofrequency coil with an inner diameter of 72 mm (Bruker BioSpin GmbH, Ettlingen, Germany). A localizer sequence was used to position the mice in the centre of the field of view. Anatomical images were acquired with a Turbo RARE T2 sequence (TR/TE 800 ms/35.1 ms, FoV 37.4 mm × 85.8 mm × 22.8 mm, Matrix 144 × 256 × 92).

Mouse PET scans were co-registered to the whole-body MRI scan. Based on the MRI anatomy, volumes of interest of the lung, liver, heart, brain, and kidneys were hand-drawn using PMOD software (version 3.2; PMOD Technologies, Zürich, Switzerland). The volumes of interest of different regions in the rat and mouse brain were extracted using the atlas provided by PMOD [56-58]. TACs were extracted and converted to SUVs, calculated as in **equation (1)**:

$$SUV\ (t) = \frac{radioactivity\ concentration\ (\frac{kBq}{mL})}{\frac{injected\ dose}{body\ weight}\ (\frac{kBq}{g})} \quad (1)$$

Additionally, the SUV ratio (SUVR) was calculated using the cerebellum or the left/sham-injected striatum as the reference region in the study in fibril-injected rats, and using the cortex as reference in the study in the αSYN(A30P) mouse model. SUVR values were calculated with **equation (2)**:

$$SUVR = \frac{radioactivity\ in\ target\ region}{radioactivity\ in\ referece\ region} \quad (2)$$

***In vivo* PET/MRI in non-human primates**

In vivo macaque experiments were performed at Charles River Laboratories, Inc. (Mattawan, MI, USA) under the sponsorship of inviCRO LLC (Needham, MA, USA). Macaques were initially sedated by intramuscularly administering 5-10 mg/kg of ketamine and maintained under 2.0% isoflurane evaporated in 100% oxygen at a flow rate of 2 L/min. Body temperature was maintained at 38°C. Heart rate (BPM), body temperature, expired CO_2, respiration/min, pulse O_2%, % anesthetic gas, and oxygen (L/min) were monitored at approximately 15-minute intervals throughout the time course of the scans. The brains were placed in the center of the FOV in a Siemens microPET Focus 220 scanner (Siemens, Knoxville, TN) in a head-first supine orientation. Macaques received a three-minute intravenous injection of either 6 mL of vehicle control at baseline or 1 mg/kg dose of MODAG-005 beginning five minutes prior to the injection of 127 MBq (m) or 57 MBq (f) of [^{11}C]MODAG-005 (A_m at time of injection = 33 ± 7 GBq/µmol) produced by direct methylation method B (**Supplementary Item 7**). Dynamic PET data were acquired for 120 minutes and divided into 33 time frames (6 × 30 s, 3 × 60 s, 2 × 120 s, and 22 × 300 s). Filtered back projection was used as data reconstruction algorithm at a 256 × 256 matrix. Following the PET acquisition, anatomical T_1-weighted images were acquired with a Philips Intera 1.5T MRI scanner using a focused-head 3D T_1FE (gradient spoiled) sequence. The PET data were rigidly co-registered to the MRI, and the MRI was normalized to the cynomolgus template; the combined transformations were used to map the PET volumes into cynomolgus template space to delineate volumes of interest (VOIs). Ten VOIs were extracted from the brain using the brain atlas in PMOD 3.802. TACs were extracted and converted to SUVs, calculated as in **equation (1)**.

Arterial blood sampling for activity measurements in blood and plasma and metabolite analysis (identified in bold italic) via a right inguinal (external iliac) or left internal iliac artery vascular access port was performed during the PET acquisition at 0.25, 0.75, 1.25, 1.75, 2.25, 3.25, 4, ***5***, ***10***, ***15***, ***30***, ***45***, ***60***, 90, and 120 minutes post tracer administration.

At least 14 days after the baseline scan, animals were re-scanned as above with 89 MBq (m) and 222 MBq (f) [^{11}C]MODAG-005 and in addition with a three-minute infusion of 1 mg/kg unlabeled MODAG-005 in the vehicle, five minutes before the start of the PET acquisition. Arterial blood sampling for metabolite analysis from the right inguinal (external iliac) or left internal iliac artery via the vascular access port was performed as above.

Volume of distribution (VT) and K1 values estimated from a 2-tissue-compartment model at baseline and after competition with MODAG-005.

***In vivo* PET, SPECT and MRI in humans**

For the diagnostic work-up of the neurodegenerative Parkinson syndrome a DAT SPECT (3 h. p.i. of 185 MBq [^{123}I]FP-CIT; Discovery 670 GE Healtcare) was performed 3 years before the patient presented again in our imaging department.

PET imaging was performed on a high sensitive Long-Field of-View PET/CT scanner (Biograph Vision Quadra Siemens Healthineers) after intravenous bolus injection of 49 MBq [^{11}C]MODAG-005 (A_m at time of injection 39 GBq/µmol). Dynamic PET data were acquired for 60 minutes and divided into 15 time frames (10 × 60 s, 5 × 600 s). OSEM 3D was used as the data reconstruction algorithm and attenuation correction was applied based on the CT. In addition, a clinical 3T-MRI (Siemens Magnetom Prisma Fit) was performed at the same day which included (T1- and T2-weighted sequences). The PET data were co-registered to the MRI, and VOIs (right and left caudate, putamen, thalamus, pons, cerebellar white matter and the occipital cortex) were drawn based on the anatomical information in the MR image. TACs were extracted and converted to SUVs, calculated as in **equation (1)**.

***Ex vivo* metabolite analysis in plasma and brain**

Metabolite analysis in mice and rats was performed as described previously [12]. Briefly, each anaesthetized mouse was injected with 204 ± 36.9 MBq of [^{11}C]MODAG-005 (A_m = 37 ± 11 GBq/µmol at time of injection), and each rat with 436 ± 2.7 MBq (A_m = 46 ± 0.8 GBq/µmol at time of injection) produced by reductive

methylation using a tail vein catheter. Five or 15 minutes post tracer injection, blood plasma samples were collected by heart puncture and the perfused brain of the mouse or right hemisphere of the rat was homogenized in phosphate-buffered saline. After sample preparation as described in [12], separation was achieved by reversed-phase radio-HPLC on a Luna C18(2) column (5 µm, 100 Å, 250 mm × 4.6 mm, Phenomenex, Aschaffenburg, Germany) with 0.1% trifluoroacetic acid in water/acetonitrile (70/30) and an isocratic flow of 1.5 mL/min. Data were decay corrected to the start-time-point of the first sample and analyzed as previously described using the peak analyzer function in Origin software (OriginLab Corporation, version 9.1G, Northampton, MA, USA) [12].

Plasma metabolite analysis in NHPs was performed from samples collected during the PET acquisition. An Agilent 1100 HPLC system, equipped with a coincidence detector for radioactivity and a diode array detector for UV that was set to 287 nm, was used. Plasma (500 µL) was diluted with a diluent solution (1.0 mL of 10 µg/mL cold MODAG-005 standard in water) and injected directly onto a Phenomenex Onyx monolithic column (10 × 100 mm), which was fitted with a 10×10 mm guard cartridge. The solvent A was 100 mM ammonium acetate, pH 8.0, and the solvent B was acetonitrile. The samples were analyzed using a gradient method. The parent compound HPLC retention time was identified by injection of 1 µL of [^{11}C]MODAG-005 mixed with 1.5 mL water containing 10 µg MODAG-005 and 5 µL DMSO. 50-200 µCi of a [^{11}C]MODAG-005 dose solution in a volume no greater than 0.25 mL was spiked into two 2.5 mL arterial blood samples, which were taken shortly before a dose injection, to measure *ex vivo* blood metabolism, and labelled as “Standard A”, and “Standard B”. Standard B was analyzed immediately post-processing from whole blood to plasma. Standard A was retained at room temperature and processed to plasma at the same time as the 120-minute post-injection sample. The *in vivo* metabolism of [^{11}C]MODAG-005 was analyzed from 3.5 mL arterial blood samples that were collected at 5, 15, 30, 45, and 60 minutes post injection. The whole blood samples were centrifuged at 1,300 × g for six minutes at 4°C to separate plasma, of which 500 µL was injected into the metabolite profiling HPLC system for analyzing the radio-metabolites.

Data were analysed as previously described [12] using the peak analyzer function in Origin software (OriginLab Corporation, version 9.1G, Northampton, MA, USA) with correction for radioactive decay within the respective run.

Reporting Summary. Further information on research design is available in the Nature Research Reporting Summary linked to this article.

Data availability

Data associated with the reported findings are available in the manuscript or **Supplementary Information**. All raw and analyzed PET and MRI datasets for the data analysis will be made available at the DRYAD repository upon publication.

References

1. Palermo, G, Del Prete, E, Bonuccelli, U, and Ceravolo, R, *Early autonomic and cognitive dysfunction in PD, DLB and MSA: blurring the boundaries between alpha-synucleinopathies.* J Neurol, 2020. **267**(12): p. 3444-3456.
2. Gomez-Tortosa, E, Newell, K, Irizarry, MC, Sanders, JL, and Hyman, BT, *alpha-Synuclein immunoreactivity in dementia with Lewy bodies: morphological staging and comparison with ubiquitin immunostaining.* Acta Neuropathol, 2000. **99**(4): p. 352-7.
3. Dupont, AC, Largeau, B, Guilloteau, D, Santiago Ribeiro, MJ, and Arlicot, N, *The Place of PET to Assess New Therapeutic Effectiveness in Neurodegenerative Diseases.* Contrast Media Mol Imaging, 2018. **2018**: p. 7043578.
4. Korat, Š, Bidesi, NSR, Bonanno, F, Di Nanni, A, Hoàng, ANN, Herfert, K, Maurer, A, Battisti, UM, Bowden, GD, Thonon, D, Vugts, D, Windhorst, AD, and Herth, MM, *Alpha-Synuclein PET Tracer Development-An Overview about Current Efforts.* Pharmaceuticals (Basel), 2021. **14**(9).
5. Matsuoka, K, Ono, M, Takado, Y, Hirata, K, Endo, H, Ohfusa, T, Kojima, T, Yamamoto, T, Onishi, T, Orihara, A, Tagai, K, Takahata, K, Seki, C, Shinotoh, H, Kawamura, K, Shimizu, H, Shimada, H, Kakita, A, Zhang, M-R, Suhara, T, and Higuchi, M, *High-Contrast Imaging of α-Synuclein Pathologies in Living Patients with Multiple System Atrophy.* 2022. **37**(10): p. 2159-2161.
6. Xiang, J, Tao, Y, Xia, Y, Luo, S, Zhao, Q, Li, B, Zhang, X, Sun, Y, Xia, W, Zhang, M, Kang, SS, Ahn, EH, Liu, X, Xie, F, Guan, Y, Yang, JJ, Bu, L, Wu, S, Wang, X, Cao, X, Liu, C, Zhang, Z, Li, D, and Ye, K, *Development of an α-synuclein positron emission tomography tracer for imaging synucleinopathies.* Cell, 2023. **186**(16): p. 3350-3367.e19.
7. Smith, R, Capotosti, F, Schain, M, Ohlsson, T, Vokali, E, Molette, J, Touilloux, T, Hliva, V, Dimitrakopoulos, IK, Puschmann, A, Jögi, J, Svenningsson, P, Andréasson, M, Sandiego, C, Russell,

DS, Miranda-Azpiazu, P, Halldin, C, Stomrud, E, Hall, S, Bratteby, K, Tampio L'Estrade, E, Luthi-Carter, R, Pfeifer, A, Kosco-Vilbois, M, Streffer, J, and Hansson, O, *The α-synuclein PET tracer [18F] ACI-12589 distinguishes multiple system atrophy from other neurodegenerative diseases.* Nat Commun, 2023. **14**(1): p. 6750.

8. Fares, MB, Jagannath, S, and Lashuel, HA, *Reverse engineering Lewy bodies: how far have we come and how far can we go?* Nature Reviews Neuroscience, 2021. **22**(2): p. 111-131.
9. Close, W, Neumann, M, Schmidt, A, Hora, M, Annamalai, K, Schmidt, M, Reif, B, Schmidt, V, Grigorieff, N, and Fändrich, M, *Physical basis of amyloid fibril polymorphism.* Nature Communications, 2018. **9**(1): p. 699.
10. Shahmoradian, SH, Lewis, AJ, Genoud, C, Hench, J, Moors, TE, Navarro, PP, Castano-Diez, D, Schweighauser, G, Graff-Meyer, A, Goldie, KN, Sutterlin, R, Huisman, E, Ingrassia, A, Gier, Y, Rozemuller, AJM, Wang, J, Paepe, A, Erny, J, Staempfli, A, Hoernschemeyer, J, Grosseruschkamp, F, Niedieker, D, El-Mashtoly, SF, Quadri, M, Van, IWFJ, Bonifati, V, Gerwert, K, Bohrmann, B, Frank, S, Britschgi, M, Stahlberg, H, Van de Berg, WDJ, and Lauer, ME, *Lewy pathology in Parkinson's disease consists of crowded organelles and lipid membranes.* Nat Neurosci, 2019. **22**(7): p. 1099-1109.
11. Wagner, J, Ryazanov, S, Leonov, A, Levin, J, Shi, S, Schmidt, F, Prix, C, Pan-Montojo, F, Bertsch, U, Mitteregger-Kretzschmar, G, Geissen, M, Eiden, M, Leidel, F, Hirschberger, T, Deeg, AA, Krauth, JJ, Zinth, W, Tavan, P, Pilger, J, Zweckstetter, M, Frank, T, Bahr, M, Weishaupt, JH, Uhr, M, Urlaub, H, Teichmann, U, Samwer, M, Botzel, K, Groschup, M, Kretzschmar, H, Griesinger, C, and Giese, A, *Anle138b: a novel oligomer modulator for disease-modifying therapy of neurodegenerative diseases such as prion and Parkinson's disease.* Acta Neuropathol, 2013. **125**(6): p. 795-813.
12. Kuebler, L, Buss, S, Leonov, A, Ryazanov, S, Schmidt, F, Maurer, A, Weckbecker, D, Landau, AM, Lillethorup, TP, Bleher, D, Saw, RS, Pichler, BJ, Griesinger, C, Giese, A, and Herfert, K, *[(11)C]MODAG-001-towards a PET tracer targeting alpha-synuclein aggregates.* Eur J Nucl Med Mol Imaging, 2020.
13. Maurer, A, Leonov, A, Ryazanov, S, Herfert, K, Kuebler, L, Buss, S, Schmidt, F, Weckbecker, D, Linder, R, Bender, D, Giese, A, Pichler, BJ, and Griesinger, C, *(11) C Radiolabeling of anle253b: a Putative PET Tracer for Parkinson's Disease That Binds to alpha-Synuclein Fibrils in vitro and Crosses the Blood-Brain Barrier.* ChemMedChem, 2019.
14. Raval, NR, Shalgunov, V, Nasser, A, Madsen, CA, Battisti, UM, Herth, MM, Jørgensen, LM, Plavén-Sigray, P, and Knudsen, GM, *Evaluation of the α-synuclein PET radiotracer (d3)-[11C]MODAG-001 in a protein deposition pig model.* Neuroscience Applied, 2022. **1**: p. 100016.
15. Harada, R, Furumoto, S, Kudo, Y, Yanai, K, Villemagne, VL, and Okamura, N, *Imaging of Reactive Astrogliosis by Positron Emission Tomography.* Front Neurosci, 2022. **16**: p. 807435.
16. Innis, RB, Cunningham, VJ, Delforge, J, Fujita, M, Gjedde, A, Gunn, RN, Holden, J, Houle, S, Huang, SC, Ichise, M, Iida, H, Ito, H, Kimura, Y, Koeppe, RA, Knudsen, GM, Knuuti, J, Lammertsma, AA, Laruelle, M, Logan, J, Maguire, RP, Mintun, MA, Morris, ED, Parsey, R, Price, JC, Slifstein, M, Sossi, V, Suhara, T, Votaw, JR, Wong, DF, and Carson, RE, *Consensus nomenclature for in vivo imaging of reversibly binding radioligands.* J Cereb Blood Flow Metab, 2007. **27**(9): p. 1533-9.
17. Levin, J, Sing, N, Melbourne, S, Morgan, A, Mariner, C, Spillantini, MG, Wegrzynowicz, M, Dalley, JW, Langer, S, Ryazanov, S, Leonov, A, Griesinger, C, Schmidt, F, Weckbecker, D, Prager, K, Matthias, T, and Giese, A, *Safety, tolerability and pharmacokinetics of the oligomer modulator anle138b with exposure levels sufficient for therapeutic efficacy in a murine Parkinson model: A randomised, double-blind, placebo-controlled phase 1a trial.* eBioMedicine, 2022. **80**: p. 104021.
18. Volc, D, Poewe, W, Kutzelnigg, A, Lührs, P, Thun-Hohenstein, C, Schneeberger, A, Galabova, G, Majbour, N, Vaikath, N, El-Agnaf, O, Winter, D, Mihailovska, E, Mairhofer, A, Schwenke, C, Staffler, G, and Medori, R, *Safety and immunogenicity of the α-synuclein active immunotherapeutic PD01A in patients with Parkinson's disease: a randomised, single-blinded, phase 1 trial.* Lancet Neurol, 2020. **19**(7): p. 591-600.
19. Lang, AE, Siderowf, AD, Macklin, EA, Poewe, W, Brooks, DJ, Fernandez, HH, Rascol, O, Giladi, N, Stocchi, F, Tanner, CM, Postuma, RB, Simon, DK, Tolosa, E, Mollenhauer, B, Cedarbaum, JM, Fraser, K, Xiao, J, Evans, KC, Graham, DL, Sapir, I, Inra, J, Hutchison, RM, Yang, M, Fox, T, Budd Haeberlein, S, Dam, T, and Investigators, S, *Trial of Cinpanemab in Early Parkinson's Disease.* N Engl J Med, 2022. **387**(5): p. 408-420.
20. Pagano, G, Taylor, KI, Anzures-Cabrera, J, Marchesi, M, Simuni, T, Marek, K, Postuma, RB, Pavese, N, Stocchi, F, Azulay, JP, Mollenhauer, B, López-Manzanares, L, Russell, DS, Boyd, JT, Nicholas, AP, Luquin, MR, Hauser, RA, Gasser, T, Poewe, W, Ricci, B, Boulay, A, Vogt, A, Boess, FG, Dukart, J, D'Urso, G, Finch, R, Zanigni, S, Monnet, A, Pross, N, Hahn, A, Svoboda, H, Britschgi, M, Lipsmeier, F, Volkova-Volkmar, E, Lindemann, M, Dziadek, S, Holiga, Š, Rukina, D, Kustermann, T, Kerchner, GA, Fontoura, P, Umbricht, D, Doody, R, Nikolcheva, T, and Bonni, A, *Trial of Prasinezumab in Early-Stage Parkinson's Disease.* N Engl J Med, 2022. **387**(5): p. 421-432.

21. Eidelberg, D, Moeller, JR, Dhawan, V, Spetsieris, P, Takikawa, S, Ishikawa, T, Chaly, T, Robeson, W, Margouleff, D, Przedborski, S, and et al., *The metabolic topography of parkinsonism.* J Cereb Blood Flow Metab, 1994. **14**(5): p. 783-801.
22. Breit, S, Reimold, M, Reischl, G, Klockgether, T, and Wüllner, U, *[(11)C]d-threo-methylphenidate PET in patients with Parkinson's disease and essential tremor.* J Neural Transm (Vienna), 2006. **113**(2): p. 187-93.
23. Volkow, ND, Ding, YS, Fowler, JS, Wang, GJ, Logan, J, Gatley, SJ, Schlyer, DJ, and Pappas, N, *A new PET ligand for the dopamine transporter: studies in the human brain.* J Nucl Med, 1995. **36**(12): p. 2162-8.
24. Klunk, WE, Engler, H, Nordberg, A, Wang, Y, Blomqvist, G, Holt, DP, Bergström, M, Savitcheva, I, Huang, GF, Estrada, S, Ausén, B, Debnath, ML, Barletta, J, Price, JC, Sandell, J, Lopresti, BJ, Wall, A, Koivisto, P, Antoni, G, Mathis, CA, and Långström, B, *Imaging brain amyloid in Alzheimer's disease with Pittsburgh Compound-B.* Ann Neurol, 2004. **55**(3): p. 306-19.
25. Jie, C, Treyer, V, Schibli, R, and Mu, L, *Tauvid™: The First FDA-Approved PET Tracer for Imaging Tau Pathology in Alzheimer's Disease.* Pharmaceuticals (Basel), 2021. **14**(2).
26. Barthel, H and Sabri, O, *Clinical Use and Utility of Amyloid Imaging.* 2017. **58**(11): p. 1711-1717.
27. Hashimoto, H, Kawamura, K, Igarashi, N, Takei, M, Fujishiro, T, Aihara, Y, Shiomi, S, Muto, M, Ito, T, Furutsuka, K, Yamasaki, T, Yui, J, Xie, L, Ono, M, Hatori, A, Nemoto, K, Suhara, T, Higuchi, M, and Zhang, MR, *Radiosynthesis, photoisomerization, biodistribution, and metabolite analysis of 11C-PBB3 as a clinically useful PET probe for imaging of tau pathology.* J Nucl Med, 2014. **55**(9): p. 1532-8.
28. Sevigny, J, Chiao, P, Bussière, T, Weinreb, PH, Williams, L, Maier, M, Dunstan, R, Salloway, S, Chen, T, Ling, Y, O'Gorman, J, Qian, F, Arastu, M, Li, M, Chollate, S, Brennan, MS, Quintero-Monzon, O, Scannevin, RH, Arnold, HM, Engber, T, Rhodes, K, Ferrero, J, Hang, Y, Mikulskis, A, Grimm, J, Hock, C, Nitsch, RM, and Sandrock, A, *The antibody aducanumab reduces Aβ plaques in Alzheimer's disease.* Nature, 2016. **537**(7618): p. 50-56.
29. Swanson, CJ, Zhang, Y, Dhadda, S, Wang, J, Kaplow, J, Lai, RYK, Lannfelt, L, Bradley, H, Rabe, M, Koyama, A, Reyderman, L, Berry, DA, Berry, S, Gordon, R, Kramer, LD, and Cummings, JL, *A randomized, double-blind, phase 2b proof-of-concept clinical trial in early Alzheimer's disease with lecanemab, an anti-Aβ protofibril antibody.* Alzheimer's Research & Therapy, 2021. **13**(1): p. 80.
30. Klein, G, Delmar, P, Kerchner, GA, Hofmann, C, Abi-Saab, D, Davis, A, Voyle, N, Baudler, M, Fontoura, P, and Doody, R, *Thirty-Six-Month Amyloid Positron Emission Tomography Results Show Continued Reduction in Amyloid Burden with Subcutaneous Gantenerumab.* The Journal of Prevention of Alzheimer's Disease, 2021. **8**(1): p. 3-6.
31. Salloway, S, Farlow, M, McDade, E, Clifford, DB, Wang, G, Llibre-Guerra, JJ, Hitchcock, JM, Mills, SL, Santacruz, AM, Aschenbrenner, AJ, Hassenstab, J, Benzinger, TLS, Gordon, BA, Fagan, AM, Coalier, KA, Cruchaga, C, Goate, AA, Perrin, RJ, Xiong, C, Li, Y, Morris, JC, Snider, BJ, Mummery, C, Surti, GM, Hannequin, D, Wallon, D, Berman, SB, Lah, JJ, Jimenez-Velazquez, IZ, Roberson, ED, van Dyck, CH, Honig, LS, Sánchez-Valle, R, Brooks, WS, Gauthier, S, Galasko, DR, Masters, CL, Brosch, JR, Hsiung, G-YR, Jayadev, S, Formaglio, M, Masellis, M, Clarnette, R, Pariente, J, Dubois, B, Pasquier, F, Jack, CR, Koeppe, R, Snyder, PJ, Aisen, PS, Thomas, RG, Berry, SM, Wendelberger, BA, Andersen, SW, Holdridge, KC, Mintun, MA, Yaari, R, Sims, JR, Baudler, M, Delmar, P, Doody, RS, Fontoura, P, Giacobino, C, Kerchner, GA, Bateman, RJ, Formaglio, M, Mills, SL, Pariente, J, van Dyck, CH, and the Dominantly Inherited Alzheimer Network–Trials, U, *A trial of gantenerumab or solanezumab in dominantly inherited Alzheimer's disease.* Nature Medicine, 2021. **27**(7): p. 1187-1196.
32. Verdurand, M, Levigoureux, E, Zeinyeh, W, Berthier, L, Mendjel-Herda, M, Cadarossanesaib, F, Bouillot, C, Iecker, T, Terreux, R, Lancelot, S, Chauveau, F, Billard, T, and Zimmer, L, *In Silico, in Vitro, and in Vivo Evaluation of New Candidates for alpha-Synuclein PET Imaging.* Mol Pharm, 2018. **15**(8): p. 3153-3166.
33. Akasaka, T, Watanabe, H, Kaide, S, Iikuni, S, Hasegawa, M, and Ono, M, *Synthesis and evaluation of novel radioiodinated phenylbenzofuranone derivatives as α-synuclein imaging probes.* Bioorg Med Chem Lett, 2022. **64**: p. 128679.
34. Kaide, S, Watanabe, H, Shimizu, Y, Iikuni, S, Nakamoto, Y, Hasegawa, M, Itoh, K, and Ono, M, *Identification and Evaluation of Bisquinoline Scaffold as a New Candidate for alpha-Synuclein-PET Imaging.* ACS Chem Neurosci, 2020. **11**(24): p. 4254-4261.
35. Kaide, S, Watanabe, H, Iikuni, S, Hasegawa, M, Itoh, K, and Ono, M, *Chalcone Analogue as New Candidate for Selective Detection of α-Synuclein Pathology.* ACS Chem Neurosci, 2022. **13**(1): p. 16-26.
36. Janssen, B, Tian, G, Lengyel-Zhand, Z, Hsieh, CJ, Lougee, MG, Riad, A, Xu, K, Hou, C, Weng, CC, Lopresti, BJ, Kim, HJ, Pagar, VV, Ferrie, JJ, Garcia, BA, Mathis, CA, Luk, K, Petersson, EJ, and Mach, RH, *Identification of a Putative α-synuclein Radioligand Using an in silico Similarity Search.* Mol Imaging Biol, 2023. **25**(4): p. 704-719.

37. Zhang, S, Zhu, R, Pan, B, Xu, H, Olufemi, MF, Gathagan, RJ, Li, Y, Zhang, L, Zhang, J, Xiang, W, Kagan, EM, Cao, X, Yuan, C, Kim, SJ, Williams, CK, Magaki, S, Vinters, HV, Lashuel, HA, Garcia, BA, James Petersson, E, Trojanowski, JQ, Lee, VM, and Peng, C, *Post-translational modifications of soluble α-synuclein regulate the amplification of pathological α-synuclein.* Nat Neurosci, 2023. **26**(2): p. 213-225.
38. Matsuoka, K, Ono, M, Takado, Y, Hirata, K, Endo, H, Ohfusa, T, Kojima, T, Yamamoto, T, Onishi, T, Orihara, A, Tagai, K, Takahata, K, Seki, C, Shinotoh, H, Kawamura, K, Shimizu, H, Shimada, H, Kakita, A, Zhang, MR, Suhara, T, and Higuchi, M, *High-Contrast Imaging of α-Synuclein Pathologies in Living Patients with Multiple System Atrophy.* Mov Disord, 2022.
39. Molette J., GE, Darmency V., *BICYCLIC COMPOUNDS FOR DIAGNOSIS AND THERAPY*, A.I. Sa, Editor. 2017.
40. Endo, H, Ono, M, Takado, Y, Matsuoka, K, Takahashi, M, Tagai, K, Kataoka, Y, Hirata, K, Takahata, K, Seki, C, Kokubo, N, Fujinaga, M, Mori, W, Nagai, Y, Mimura, K, Kumata, K, Kikuchi, T, Shimozawa, A, Mishra, SK, Yamaguchi, Y, Shimizu, H, Kakita, A, Takuwa, H, Shinotoh, H, Shimada, H, Kimura, Y, Ichise, M, Suhara, T, Minamimoto, T, Sahara, N, Kawamura, K, Zhang, M-R, Hasegawa, M, and Higuchi, M, *Imaging α-synuclein pathologies in animal models and patients with Parkinson's and related diseases.* 2023: p. 2020.10.23.349860.
41. Bagchi, DP, Yu, L, Perlmutter, JS, Xu, J, Mach, RH, Tu, Z, and Kotzbauer, PT, *Binding of the radioligand SIL23 to alpha-synuclein fibrils in Parkinson disease brain tissue establishes feasibility and screening approaches for developing a Parkinson disease imaging agent.* PLoS One, 2013. **8**(2): p. e55031.
42. Breydo, L and Uversky, VN, *Structural, morphological, and functional diversity of amyloid oligomers.* FEBS Lett, 2015. **589**(19 Pt A): p. 2640-8.
43. Pike, VW, *PET radiotracers: crossing the blood-brain barrier and surviving metabolism.* Trends Pharmacol Sci, 2009. **30**(8): p. 431-40.
44. Leung, CS, Leung, SS, Tirado-Rives, J, and Jorgensen, WL, *Methyl effects on protein-ligand binding.* J Med Chem, 2012. **55**(9): p. 4489-500.
45. Neumann, M, Kahle, PJ, Giasson, BI, Ozmen, L, Borroni, E, Spooren, W, Müller, V, Odoy, S, Fujiwara, H, Hasegawa, M, Iwatsubo, T, Trojanowski, JQ, Kretzschmar, HA, and Haass, C, *Misfolded proteinase K-resistant hyperphosphorylated alpha-synuclein in aged transgenic mice with locomotor deterioration and in human alpha-synucleinopathies.* J Clin Invest, 2002. **110**(10): p. 1429-39.
46. Schell, H, Hasegawa, T, Neumann, M, and Kahle, PJ, *Nuclear and neuritic distribution of serine-129 phosphorylated alpha-synuclein in transgenic mice.* Neuroscience, 2009. **160**(4): p. 796-804.
47. Schou, M, Varnäs, K, Sandell, J, Johnström, P, Cselenyi, Z, Svensson, S, Nakao, R, Amini, N, Bergman, L, Sumic, A, Gulyas, B, Lindström-Böö, E, Halldin, C, and Farde, L, *Synthesis, Radiolabeling, and In Vivo Pharmacokinetic Evaluation of the Amyloid Beta Radioligand [11C]AZD4694 in Nonhuman Primates.* Molecular Imaging and Biology, 2014. **16**(2): p. 173-179.
48. Drake, LR, Pham, JM, Desmond, TJ, Mossine, AV, Lee, SJ, Kilbourn, MR, Koeppe, RA, Brooks, AF, and Scott, PJH, *Identification of AV-1451 as a Weak, Nonselective Inhibitor of Monoamine Oxidase.* ACS Chemical Neuroscience, 2019. **10**(8): p. 3839-3846.
49. Wenning, GK, Stankovic, I, Vignatelli, L, Fanciulli, A, Calandra-Buonaura, G, Seppi, K, Palma, JA, Meissner, WG, Krismer, F, Berg, D, Cortelli, P, Freeman, R, Halliday, G, Höglinger, G, Lang, A, Ling, H, Litvan, I, Low, P, Miki, Y, Panicker, J, Pellecchia, MT, Quinn, N, Sakakibara, R, Stamelou, M, Tolosa, E, Tsuji, S, Warner, T, Poewe, W, and Kaufmann, H, *The Movement Disorder Society Criteria for the Diagnosis of Multiple System Atrophy.* Mov Disord, 2022. **37**(6): p. 1131-1148.
50. Xiang, J, Zhang, Z, and Ye, K, *A promising PET tracer candidate targeting α-synuclein inclusions.* Clin Transl Med, 2023. **13**(9): p. e1408.
51. Goedert, M, Jakes, R, Spillantini, MG, Hasegawa, M, Smith, MJ, and Crowther, RA, *Assembly of microtubule-associated protein tau into Alzheimer-like filaments induced by sulphated glycosaminoglycans.* Nature, 1996. **383**(6600): p. 550-3.
52. Whitwell, JL, Höglinger, GU, Antonini, A, Bordelon, Y, Boxer, AL, Colosimo, C, van Eimeren, T, Golbe, LI, Kassubek, J, Kurz, C, Litvan, I, Pantelyat, A, Rabinovici, G, Respondek, G, Rominger, A, Rowe, JB, Stamelou, M, Josephs, KA, and Group, ftMDS-ePS, *Radiological biomarkers for diagnosis in PSP: Where are we and where do we need to be?* 2017. **32**(7): p. 955-971.
53. Philippe, C, Haeusler, D, Mitterhauser, M, Ungersboeck, J, Viernstein, H, Dudczak, R, and Wadsak, W, *Optimization of the radiosynthesis of the Alzheimer tracer 2-(4-N-[11C]methylaminophenyl)-6-hydroxybenzothiazole ([11C]PIB).* Applied Radiation and Isotopes, 2011. **69**(9): p. 1212-1217.
54. Larsen, P, Ulin, J, Dahlstrøm, K, and Jensen, M, *Synthesis of [11C]iodomethane by iodination of [11C]methane.* Applied Radiation and Isotopes, 1997. **48**(2): p. 153-157.
55. Paxinos, G, Watson, CR, and Emson, PC, *AChE-stained horizontal sections of the rat brain in stereotaxic coordinates.* J Neurosci Methods, 1980. **3**(2): p. 129-49.

56. Ma, Y, Hof, PR, Grant, SC, Blackband, SJ, Bennett, R, Slatest, L, McGuigan, MD, and Benveniste, H, *A three-dimensional digital atlas database of the adult C57BL/6J mouse brain by magnetic resonance microscopy.* Neuroscience, 2005. **135**(4): p. 1203-15.
57. Mirrione, MM, Schiffer, WK, Fowler, JS, Alexoff, DL, Dewey, SL, and Tsirka, SE, *A novel approach for imaging brain-behavior relationships in mice reveals unexpected metabolic patterns during seizures in the absence of tissue plasminogen activator.* Neuroimage, 2007. **38**(1): p. 34-42.
58. Schiffer, WK, Mirrione, MM, Biegon, A, Alexoff, DL, Patel, V, and Dewey, SL, *Serial microPET measures of the metabolic reaction to a microdialysis probe implant.* J Neurosci Methods, 2006. **155**(2): p. 272-84.

Acknowledgements
We thank the technical assistants, Madhushree Pethe, Sophie Stotz and Marilena Poxleitner at the Werner Siemens Imaging Center (WSIC), University of Tuebingen for their support during experiments. We extend our appreciation to Anna Ohmayer, Gina Dunkel and the Weigelin group at the WSIC for their support with the fluorescence microscope. We further thank Prof. Dr. Tiago Fleming Outeiro from the University Medical Center Goettingen for providing us transgenic mice for the experiment.

This research project received funding from the European Union's Seventh Framework Programme (FP7/2007 2013, Multisyn) under REA grant agreement No. 602646, the European Union's Horizon 2020 Research and Innovative Programme under the Marie Skłodowska-Curie grant agreement No. 813528, the Michael J Fox Foundation for Parkinson's Research under grant No. MJFF16008, the Max Planck Society, and the Deutsche Forschungsgemeinschaft (DFG, German Research Foundation) under Germany's Excellence Strategy-EXC 2067/1-390729940.

Author contributions
R.S.S., S.H. – data acquisition and analysis, drafting of the manuscript

L.K., F.S., S.R., A.L., D.B., I.P., F.B., A.K.G. A.M.,– data acquisition and analysis, reviewed manuscript

B.J.P., C.G., A.G., K.H. - development and conceptual design, supervised experiments, drafting and reviewed manuscript

G.R. – optimization of radiochemical synthesis process to a GMP environment and optimization for human application, reviewed manuscript

C.M.S. - design, analysis, data interpretation, drafting macaque experiments

K.E.H. – design, supervision of macaque experiments, data interpretation, drafting macaque experiments and manuscript methods

V.C.R. – providing human post-mortem brain tissue, reviewed manuscript

B.R., K.B., T.G. – recruitment of the human patient, interpretation of clinical and imaging data, reviewed manuscript

C.L.F., M.R. – acquisition, analysis and interpretation of SPECT and PET clinical data, reviewed manuscirpt

B.D., P.K. – providing αSYN(A30P) and control mice, support with immunohistochemistry, reviewed manuscript

B.F., M.S. – providing electron microscopy support, reviewed manuscript

Competing interests
A patent has been filed (PCT/EP2020/082778) that includes MODAG-005.

Armin Giese, Felix Schmidt, Andrei Leonov and Sergey Ryazanov are employed by MODAG GmbH, which retains ownership of MODAG-005, Armin Giese and Christian Griesinger are shareholders of MODAG GmbH. The other authors declare no competing interests.

Inclusion and ethics

The questionnaire and methodology for this study were approved by the ethics committee of the Faculty of Medicine at the University of Tuebingen (Ethics approval number: 813/2018BO2).
All rodent experiments were conducted in compliance with the German animal protection law and with the approval of the local authorities (Regierungspräsidium Tübingen, R3/19G). Macaque experiments were conducted in compliance with all applicable sections of the Final Rules of the Animal Welfare Act regulations (Code of Federal Regulations, Title 9), the Public Health Service Policy on Humane Care and Use of Laboratory Animals from the Office of Laboratory Animal Welfare, and the Guide for the Care and Use of Laboratory Animals from the National Research Council (OLAW, current edition) (NRC, current edition).

All authors agree with the submitted version of the manuscript. The material submitted for publication has not been previously reported and is not under consideration for publication elsewhere.

Extended Data Figures

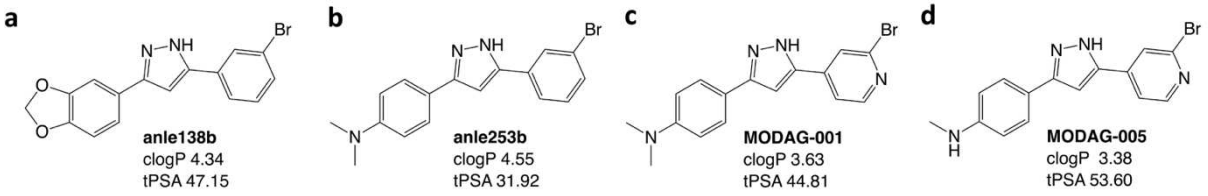

Extended Data Fig. 1: Chemical structures of anle138b (a), anle253b (b), MODAG-001 (c), and MODAG-005 (d) with their calculated logP and topological polar surface area [Å^2] values. clogP, calculated logP; tPSA, topological polar surface area.

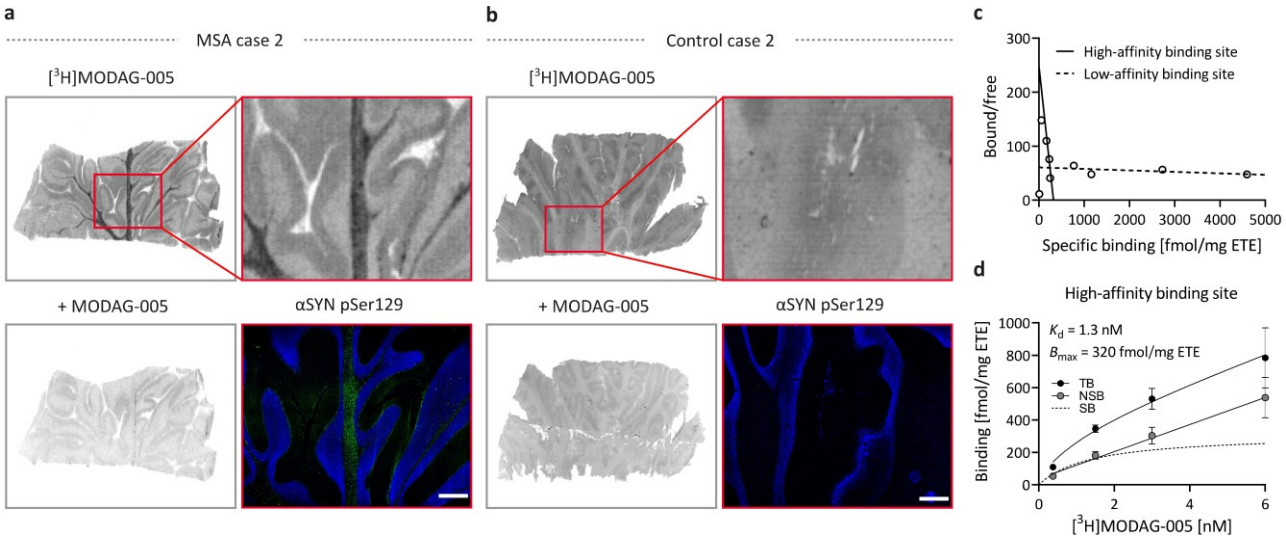

Extended Data Fig. 2: [^{3}H]MODAG-005 binding in MSA case 2 brain tissues. a, Autoradiographic images of total binding (3 nM) and after self-blocking (3 µM unlabeled MODAG-005) and immunofluorescence microscopy verification of pathology in post-mortem human cerebellar brain tissues of MSA case 2 and **b**, healthy control case 2. Red boxes show the total binding of autoradiography at higher magnification, with immunofluorescence microscopy images of αSYN pSer129 (green) and DAPI (blue). Scale bars,1 mm. **c** and **d**, A high-affinity binding site (K_d = 1.3 nM) remained after selegiline pre-blocking (3 µM for 1 hour) saturation binding autoradiography in MSA case 2 brain tissue (n = 1, repeated measurements in each sample). A K_d value of 364 nM was estimated for the low-affinity binding site (not shown). αSYN, α-synuclein; ETE, estimated tissue equivalent; MSA, multiple system atrophy; NSB, non-specific binding; SB, specific binding; TB, total binding. Data points in **d** are represented as mean ± s.d..

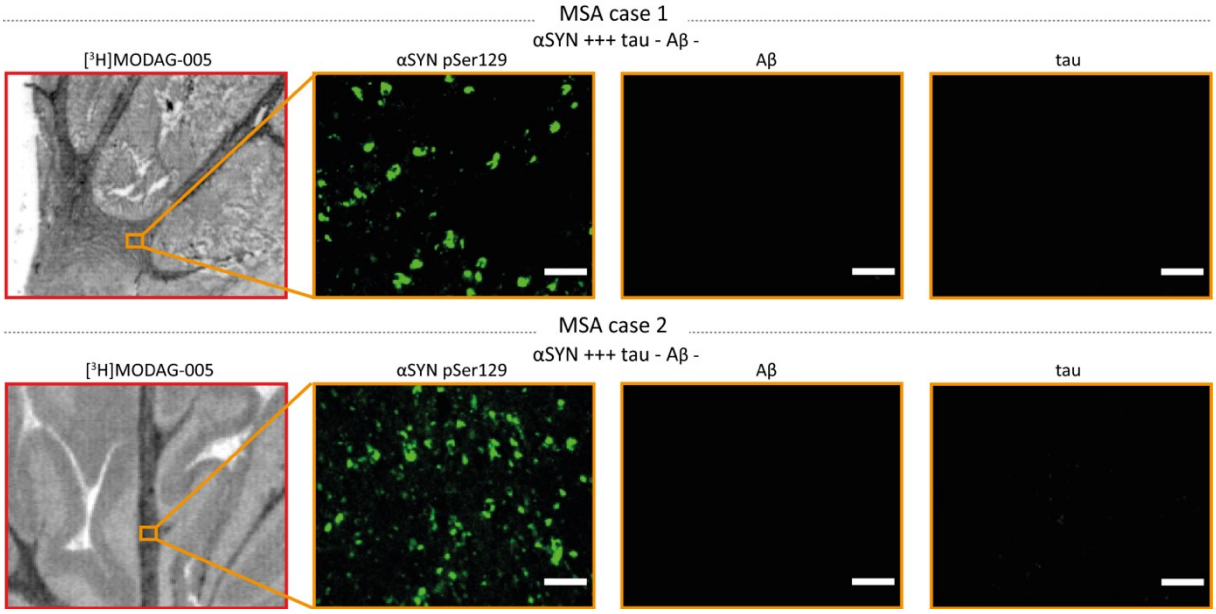

Extended Data Fig. 3: αSYN, Aβ and tau immunofluorescence microscopy on human MSA case 1 and 2 brain sections. αSYN pathology was confirmed using αSYN pSer129 staining (green). The absence of immunofluorescence microscopy for $A\beta_{1-42}$ and phosphorylated tau confirms tracer binding to αSYN in both MSA cases. The number of "+" symbols indicates an increasing degree of pathology; "-" symbolizes the absence of pathology. Scale bars, 50 µm. Aβ, β-amyloid; αSYN, α-synuclein; MSA, multiple system atrophy.

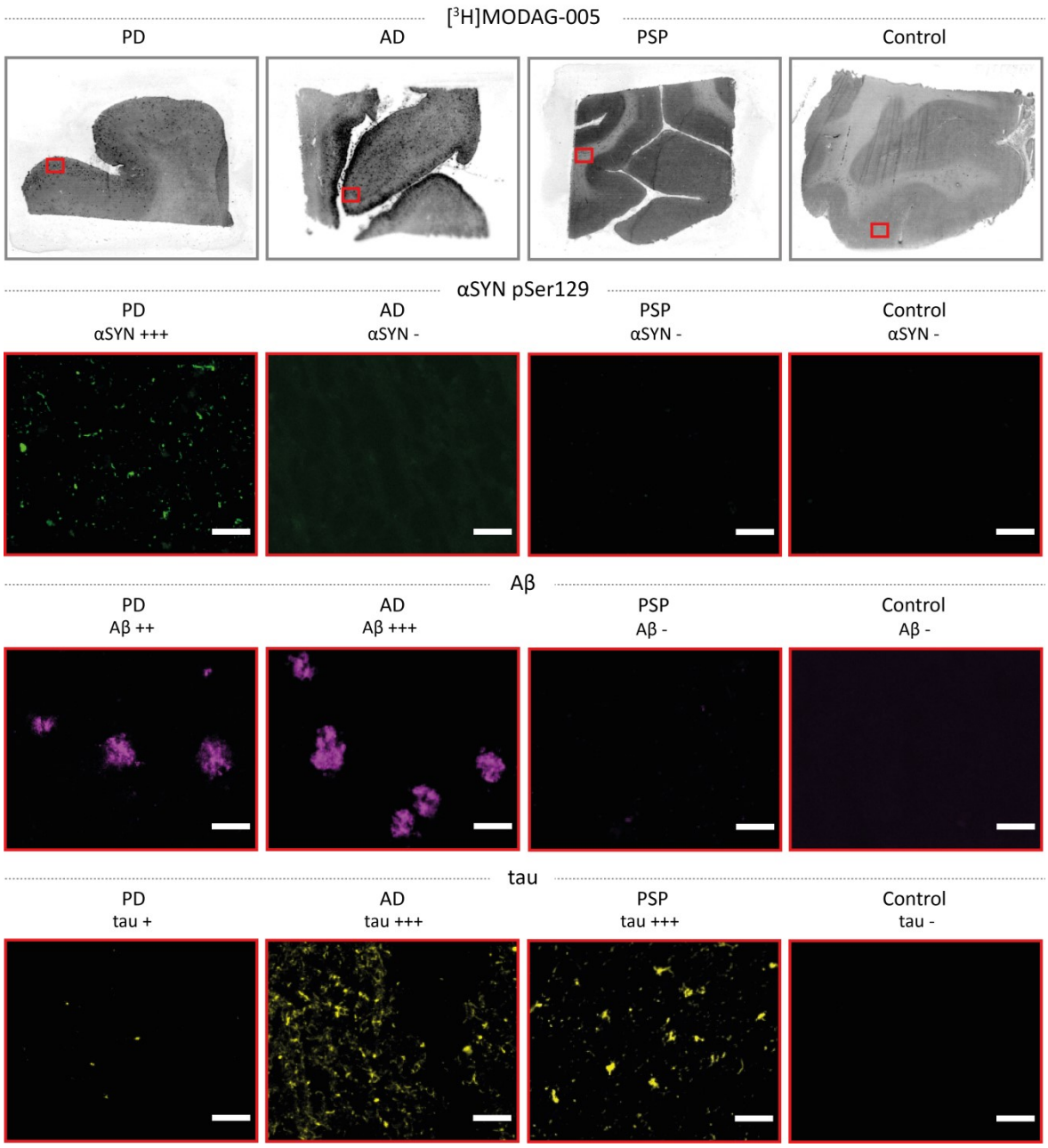

Extended Data Fig. 4: Confirmation of αSYN, Aβ and tau pathology on human brain sections using immunofluorescence microscopy. Antibodies against αSYN pSer129 (green), $Aβ_{1-42}$ (magenta) and phosphorylated tau (yellow) were used to verify the pathology. The number of "+" symbols indicates an increasing degree of pathology; "-" symbolizes the absence of pathology. Scale bars, 50 µm. AD, Alzheimer's disease; Aβ, β-amyloid; αSYN, α-synuclein; PD, Parkinson's disease; PSP, progressive supranuclear palsy.

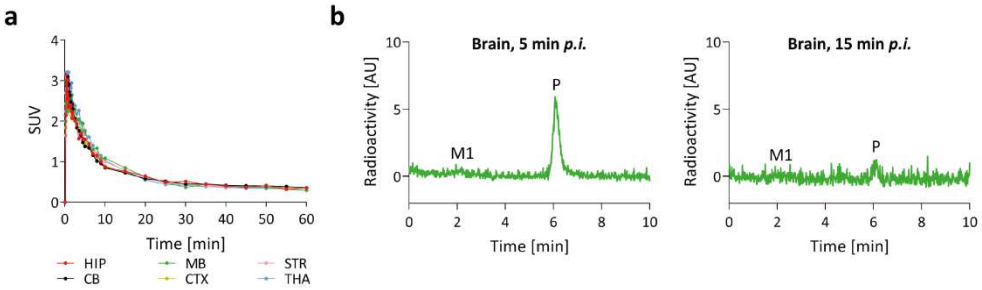

Extended Data Fig. 5: Pharmacokinetic and metabolic profile of [^{11}C]MODAG-005 in the rat brain. a, [^{11}C]MODAG-005 brain TACs show high uptake into the brain (max. SUV = 3.2) and fast clearance from the brain. **b**, Radio-metabolite analysis revealed one metabolite present in the brain with 91% and 64% of the parent compound remaining at five and 15 minutes post tracer injection, respectively. AU, arbitrary units; CB, cerebellum; CTX, cortex; HIP, hippocampus; MB, midbrain; M1, metabolite 1; P, parent compound; p.i., post injection; STR, striatum; SUV, standardized uptake value; THA, thalamus.

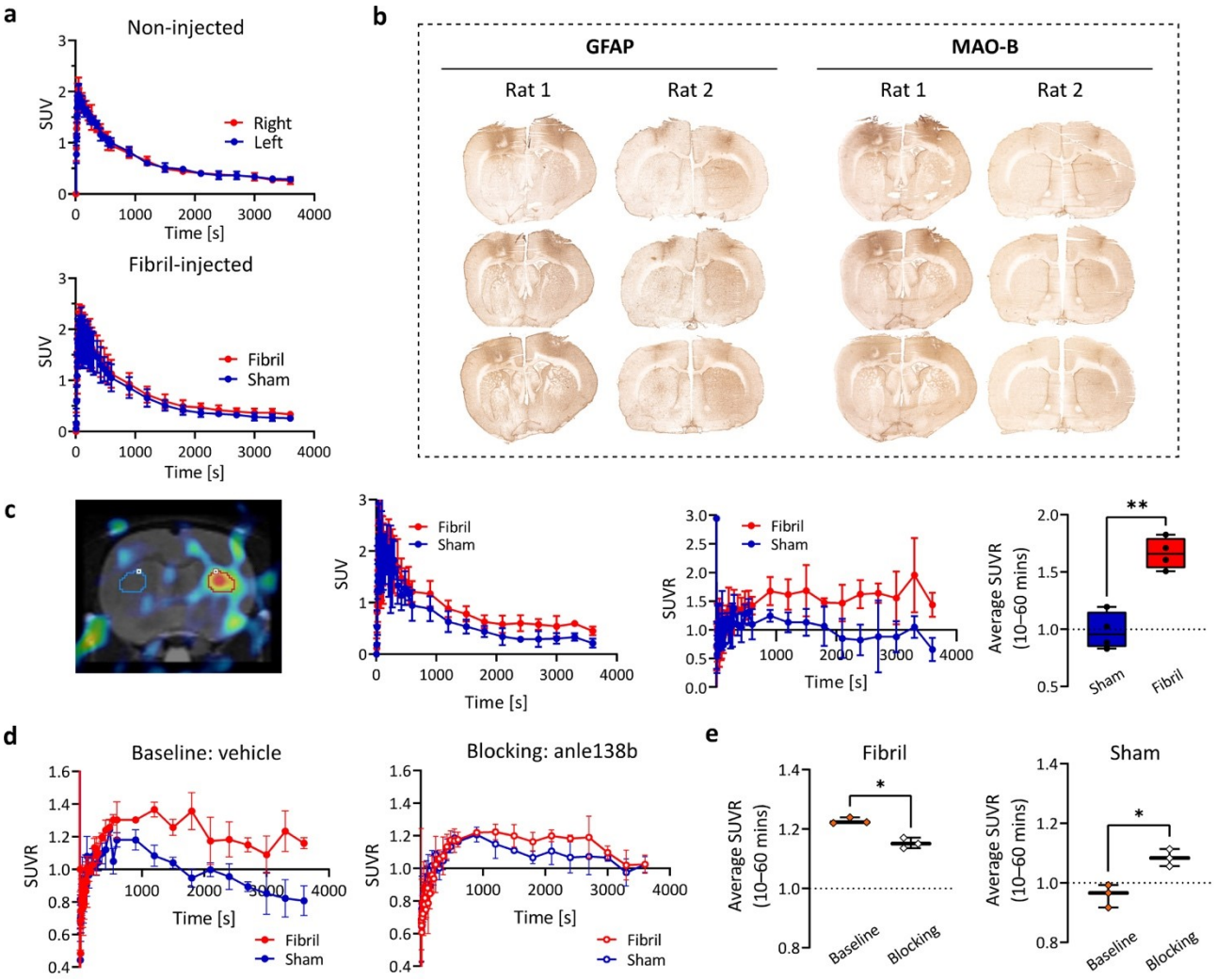

Extended Data Fig. 6: PET analysis of [^{11}C]MODAG-005 and immunohistochemistry assessment of GFAP and MAO-B expression in fibril-injected rats. a, TACs in the striatum of non-injected rats (n = 3) and fibril-injected rats (n = 4) are shown. A visible difference in [^{11}C]MODAG-005 retention between fibril-injected striatum and sham-injected striatum was detected, whereas no differences in the TACs between non-injected right and left striatum were observed. **b**, Immunohistochemistry of GFAP and MAO-B showed an increased astrogliosis and MAO-B expression in the fibril-injected striatum and, more prominently, along the injection trajectory in the cortex of both hemispheres (n = 2). **c**, PET analysis using VOI based on isocontour automatic detection set to 70%. An example PET/MR image is shown with VOI which were created surrounding the hotspot in the fibril-injected striatum (red) and subsequently mirror-reflected into the contralateral, sham-injected striatum (blue). TACs and time-SUVR curves as well as average SUVR with the cerebellum as the reference region revealed a higher tracer retention in the fibril-injected striatum compared to the non-injected striatum (average SUVR = 1.66 ± 0.137 vs. 0.98 ± 0.163, p = 0.0021). **d**, **e**, Fibril-injected rats underwent a baseline scan with vehicle administration and a blocking scan with anle138b administration. The cerebellum was used as the reference region for SUVR calculation. SUVR values over time showed a smaller difference between the fibril-injected and sham-injected striatum when blocked with anle138b. Average SUVR was decreased by anle138b blocking (from 1.23 ± 0.010 to 1.15 ± 0.018, p = 0.038) in the fibril-injected striatum, but increased in the sham-injected striatum (from 0.96 ± 0.038 to 1.08 ± 0.029, p = 0.019). GFAP, glial fibrillary acid protein; MAO-B, monoamine oxidase B; SUV, standardized uptake value; SUVR, standardized uptake value ratio; VOI, volume of interest. Data are presented as mean ± s.d.. Box plots extend from the 25th to 75th percentiles with the median indicated in the middle of the box and the minimum to maximum values shown by the whiskers. An unpaired two-tailed t-test was used in **c** and **e**. In **a** and **c**, n = 3 for non-injected rats and n = 4 for fibril-injected rats. In **d** and **e**, fibril-injected rats underwent both baseline and blocking scans (n = 3).

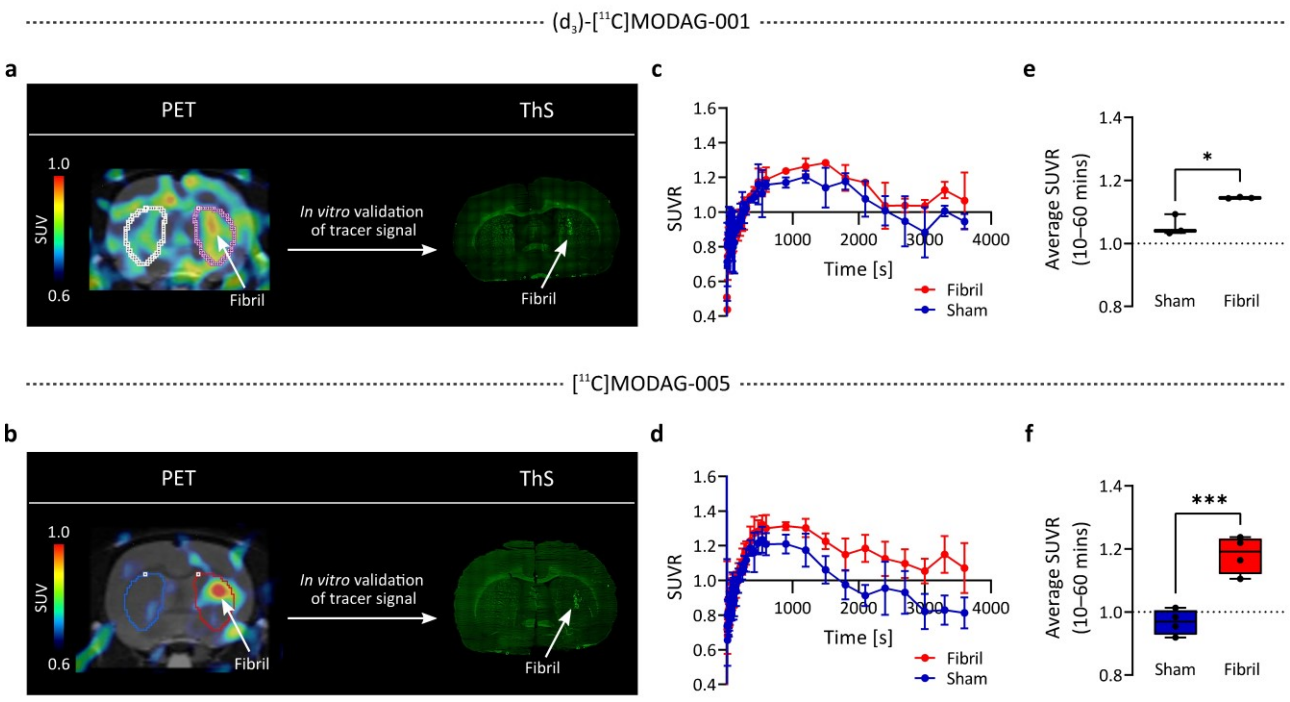

Extended Data Fig. 7: Comparison of (d_3)-[^{11}C]MODAG-001 and [^{11}C]MODAG-005 *in vivo*. **a**,**b**, (d_3)-[^{11}C]MODAG-001 and [^{11}C]MODAG-005 PET images (sum of 2.5 to 60 min) of exemplary αSYN fibril-injected rats four days post injection into the brain. **a-f**, Increased tracer binding was observed in the fibril-injected right striatum compared to the vehicle-injected left striatum for both tracers. **e**,**f**, An improved target-to-background ratio was observed for [^{11}C]MODAG-005 (1.18 ± 0.059 vs. 0.97 ± 0.041, p = 0.0003, n = 4) compared to (d_3)-[^{11}C]MODAG-001 (1.15 ± 0.002 vs. 1.06 ± 0.033, p = 0.0454, n = 3), via comparison of the average SUVR between the fibril-injected and sham-injected striatum. αSYN, α-synuclein; PET, positron emission tomography; SUV, standardized uptake value; SUVR, standardized uptake value ratio; ThS, thioflavin S. Data in **c**, **d**, **e** and **f** are represented as mean ± s.d.. In **e** and **f**, Shapiro-Wilk test indicated normal distribution and two-tailed paired t-tests were used for the comparisons.

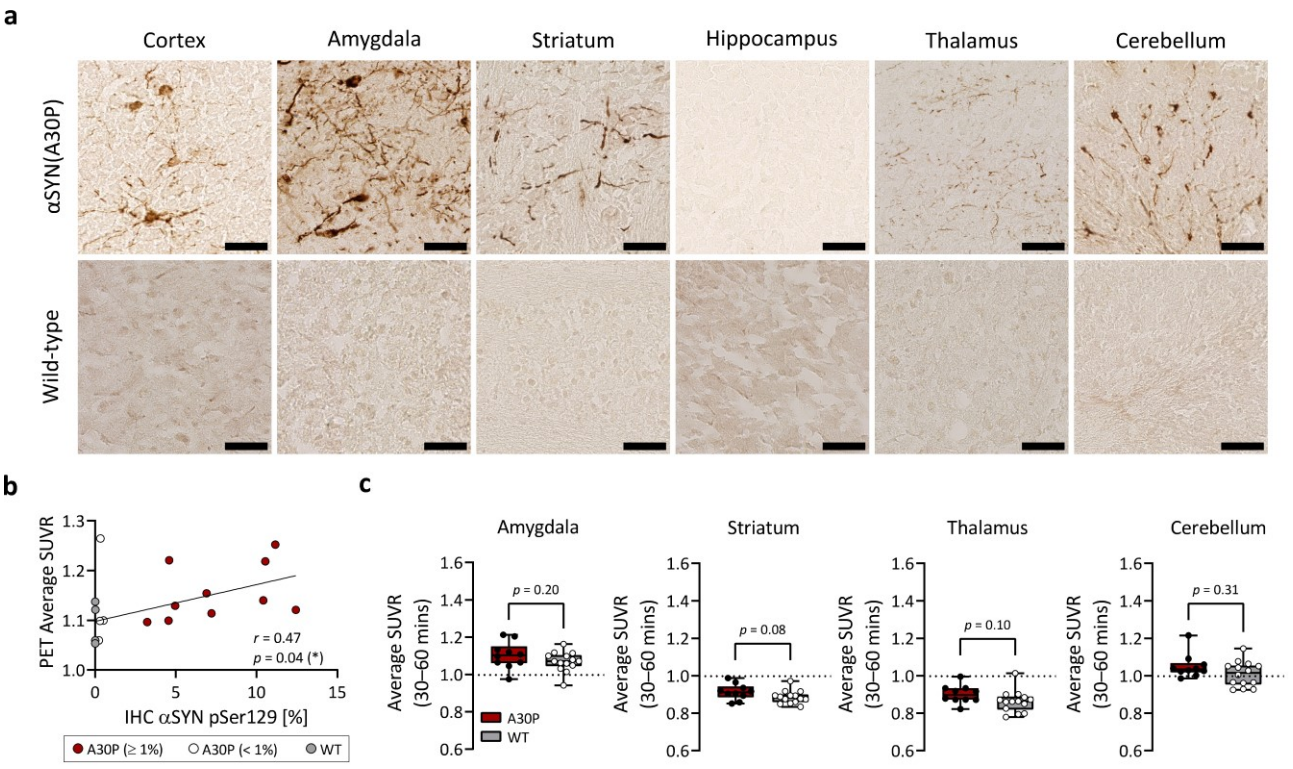

Extended Data Fig. 8: Evaluation of [^{11}C]MODAG-005 in the αSYN(A30P) transgenic mouse model and immunohistochemical validation. a, Immunohistochemistry of αSYN pS129 showed the presence of αSYN pathology in αSYN(A30P) mice in the cortex, amygdala, striatum, thalamus and cerebellum, but not in the hippocampus. No pathology was detected in wild-type mice. Scale bar, 50 µm. **b**, Data on the percentage of positive αSYN pSer129 immunohistochemistry (x-axis) in the brainstem of αSYN(A30P) mice revealed a large interindividual variation, ranging from 0.2% to 12.4%. Only αSYN(A30P) mice with ≥ 1% percentage of positive staining (red circles) were included in the main PET analysis, while αSYN(A30P) mice with < 1% (white circles) were excluded due to the lack of pathology. Wild-type mice (gray circles) showed no staining with a negligible positive signal in thresholded images (< 0.04%). Taking into account both groups, αSYN(A30P) mice (n = 14) and randomly selected wild-type mice (n = 5), a moderate positive correlation between αSYN pSer129 immunohistochemistry and [^{11}C]MODAG-005 PET binding in the brainstem was detected (r = 0.47, p = 0.043). **c**, Comparison of [^{11}C]MODAG-005 PET average SUVR calculated from 30 to 60 minutes showed no differences between the both groups in the amygdala (p = 0.20), striatum (p = 0.08), thalamus (p = 0.10) and cerebellum (p = 0.31). A30P, αSYN(A30P) mice; αSYN, α-synuclein; IHC, immunohistochemistry; PET, positron emission tomography; SUVR, standardized uptake value ratio; WT, wild-type mice. In **b**, data points are presented as the mean value of individual animals in immunohistochemistry pathology quantification from all A30P αSYN mice (n = 14, 6–10 tissue sections per animal) and randomly selected wild-type mice (n = 5, 2 tissue sections per animal). Only the wild-type mice with immunohistochemical quantification were included in the correlation analysis with PET imaging data. In **c**, box plots extend from the 25th to 75th percentiles with the median indicated in the middle of the box and the minimum to maximum values shown by the whiskers. Shapiro-Wilk test was used to test for normal distribution. An unpaired two-tailed t-test was performed to compare the average SUVR values between the two animal groups for all brain regions except in the cerebellum. Mann-Whitney test was performed for the cerebellum due to non-Gaussian distribution.

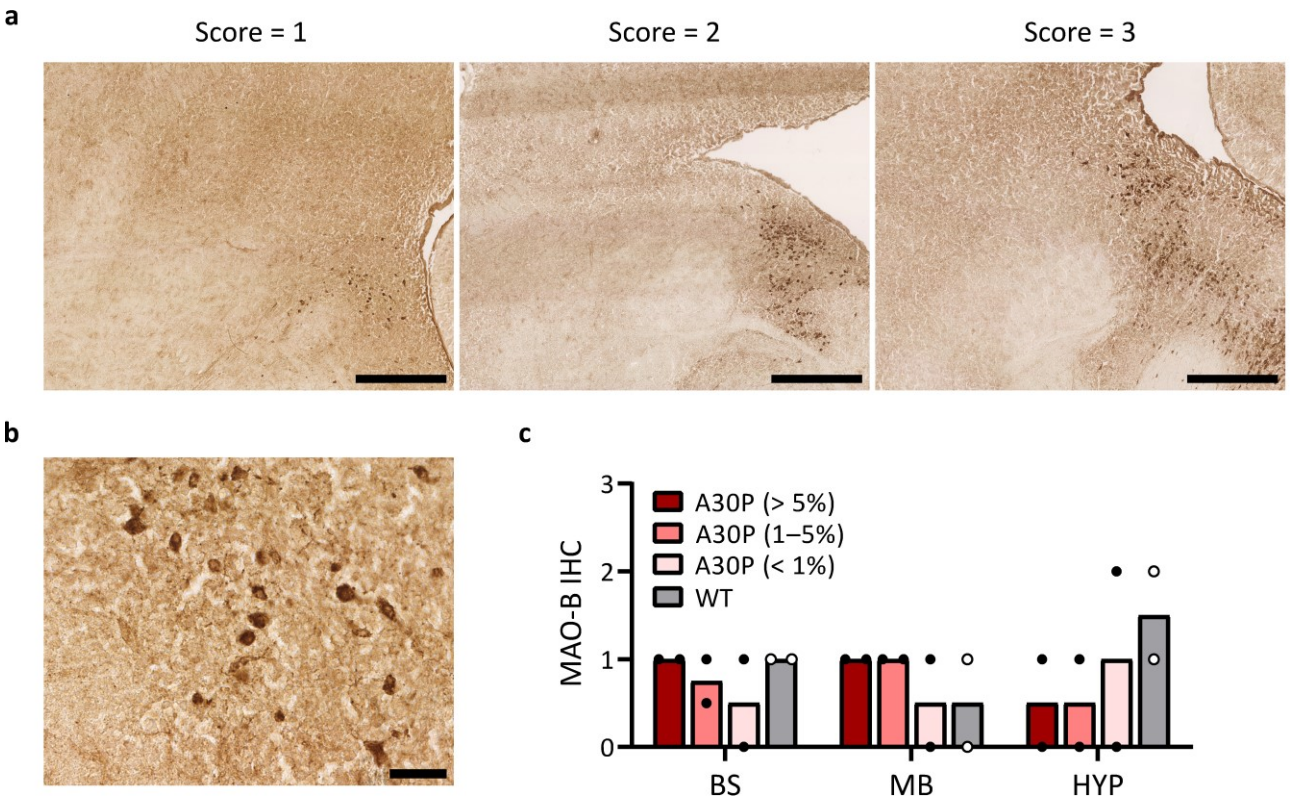

Extended Data Fig. 9: Immunohistochemistry analysis of MAO-B expression in αSYN(A30P) and wild-type mouse brain sections. αSYN(A30P) mice were assessed in three groups based on their αSYN pSer129 pathology load as determined previously (A30P > 5%, A30P = 1–5%, A30P < 1%). Qualitative scoring (score 0–3) was performed for the brainstem, midbrain and hypothalamus. **a**, Example of MAO-B immunohistochemistry images with their respective given score. Scale bar, 500 µm. **b**, MAO-B immunohistochemistry showed a staining diameter of approximately 10 µm. Scale bar, 50 µm. **c**, Analysis by qualitative scoring indicated a similar average scoring of MAO-B staining between score 0 to score 2 for all αSYN(A30P) and wild-type mouse groups (n = 2 per animal group, 4 tissue sections per animal). A30P, αSYN(A30P) mice; BS, brainstem; HYP, hypothalamus; IHC, immunohistochemistry; MB, midbrain.

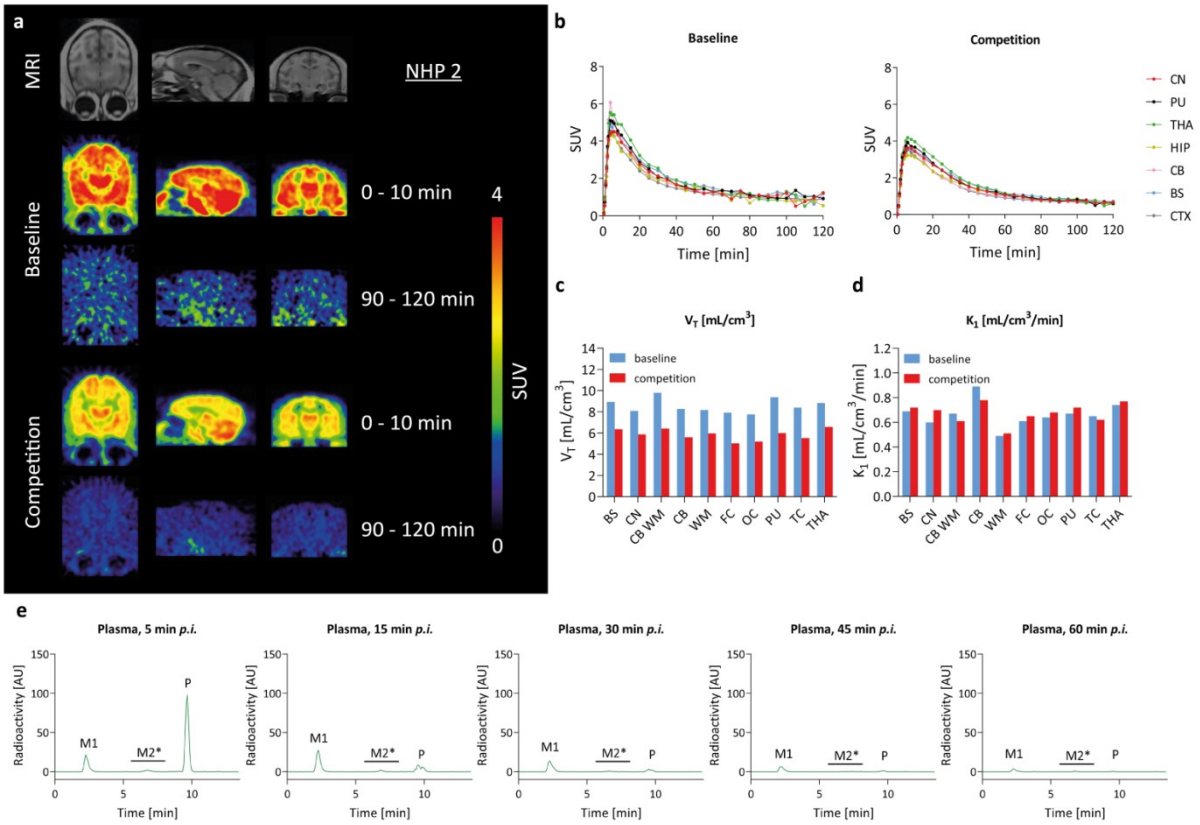

Extended Data Fig. 10: *In vivo* characterization of [^{11}C]MODAG-005 in non-human primates (NHPs). a, Transversal, sagittal and coronal (left to right) MRI of one exemplary cynomolgus monkey brain and [^{11}C]MODAG-005 PET images at baseline and after pre-injection of MODAG-005 (sum of frame 0 to 10 and 90 to 120 minutes). **b**, TACs of different brain regions show high brain uptake with peak SUVs of 6.1 (baseline) and 4.2 (competition) followed by a fast clearance from the brain. **c**,**d**, Volume of distribution (V_T) and K_1 values estimated from a 2-tissue-compartment model at baseline and after competition with MODAG-005. **e**, Plasma radio-metabolites revealed the formation of two metabolites, with 71%, 24%, 13%, 9% and 5% of the parent compound remaining at 5, 15, 30, 45, and 60 minutes post tracer injection, respectively. AU, arbitrary units; BS, brainstem; CB, cerebellum; CB WM, cerebellar white matter; CN, caudate nucleus; CTX, cortex; WM, white matter; FC, frontal cortex; HIP, hippocampus; MRI, magnetic resonance imaging; M1, metabolite 1; M2*, metabolite 2*; OC, occipital cortex; P, parent compound; PET, positron emission tomography; p.i., post injection; PU, putamen; STR, striatum; SUV, standardized uptake value; TACs, time-activity curves; TC, temporal cortex; 2-TCM, two tissue compartment model; THA, thalamus.

Extended Data Table 1: Overview of the human brain sections used in the autoradiography experiments and immunofluorescence microscopy validation.

Cases	Region	Age at death (years)	Sex	PMI (hour)	LBD (Braak)	AD (Braak & Braak)	AD (Thal)	Pathology		
								αSYN	Aβ	pTau
MSA1	CB	64	F	52	0	I	1	+++	-	-
MSA2	CB	54	M	71	0	0-I	0	+++	-	-
Control 1	CB	76	F	26	0	III	3	-	-	-
Control 2	CB	66	F	27-39	0	I	3	-	-	-
PD	FC	79	F	26	6	IV	3	+++	++	+
AD	FC	70	M	24	0	VI	5	-	+++	+++
PSP	FC	66	M	7	0	0	0	-	-	+++
Control 3	FC	64	F	39	0	0	0	-	-	-

The number of “+” symbols indicates an increasing degree of pathology in the particular region analyzed from low (+), moderate (++) to severe (+++) pathology; “-” symbolizes the absence of pathology. Aβ, β-

amyloid; αSYN, α-synuclein; AD, Alzheimer's disease; CB, cerebellum; Ctrl, control; F, female; FC, frontal cortex; LBD, Lewy body dementia; M, male; MSA, multiple system atrophy; PD, Parkinson's disease; PMI, post-mortem interval; PSP, progressive supranuclear palsy; pTau, phospho-Tau.

Extended Data Table 2: [^{11}C]MODAG-005 radio-metabolite quantification of brain and plasma samples at five and 15 minutes after injection in mice (n = 3 per time-point) and rats (n = 1 per time-point).

	M1 (t_R 2.0 min)		*M2* (t_R 3.9 min)*		*P (t_R 6.1 min)*	
Mice	***%***	***%ID/volume or weight***	***%***	***%ID/volume or weight***	***%***	***%ID/volume or weight***
Brain, 5 min	4.1 ± 1.1	0.5 ± 0.1$^{\#}$			96 ± 1.1	13 ± 6.0$^{\#}$
Brain, 15 min	21 ± 3.1	1.0 ± 0.2$^{\#}$			79 ± 3.1	4.3 ± 1.6$^{\#}$
Plasma, 5 min	40 ± 2.9	1.1 ± 0.4^{+}	32 ± 1.5	0.9 ± 0.4^{+}	29 ± 3.1	0.9 ± 0.4^{+}
Plasma, 15 min	44 ± 11	1.2 ± 0.4^{+}	33 ± 3.7	1.0 ± 0.4^{+}	22 ± 7.6	0.6 ± 0.2^{+}
Rats						
Brain, 5 min	9.0	0.3$^{\#}$			91	3.0$^{\#}$
Brain, 15 min	36	0.2$^{\#}$			64	0.3$^{\#}$
Plasma, 5 min	28	0.3^{+}	36	0.4^{+}	36	0.4^{+}
Plasma, 15 min	34	0.4^{+}	47	0.5^{+}	20	0.2^{+}

M1, metabolite 1; M2*, mixture of various metabolites; P, parent compound; t_R, retention time; %ID, % injected dose; $^{\#}$, per g brain tissue; $^{+}$, per plasma in one mL blood. Data are represented as mean ± s.d..

Extended Data Table 3: [^{11}C]MODAG-005 radio-metabolite quantification of plasma samples at 5, 15, 30, 45 and 60 minutes after injection in cynomolgus monkey (n = 2).

	M1 (t_R 2.3 min)	***M2* (t_R 6.6 min)***	***P (t_R 9.2 min)***
Cynomolgus monkey	***%***	***%***	***%***
Plasma, 5 min	19 ± 0.7	3.9 ± 1.0	74 ± 1.3
Plasma, 15 min	61 ± 1.6	6.9 ± 2.1	29 ± 0.3
Plasma, 30 min	70 ± 1.7	7.1 ± 0.9	18 ± 1.7
Plasma, 45 min	70 ± 1.4	7.5 ± 1.3	14 ± 1.0
Plasma, 60 min	67 ± 8.3	7.7 ± 3.2	8.6 ± 1.0

M1, metabolite 1; M2*, mixture of various metabolites; P, parent compound; t_R, retention time.

Supplementary Information

Supplementary Item 1

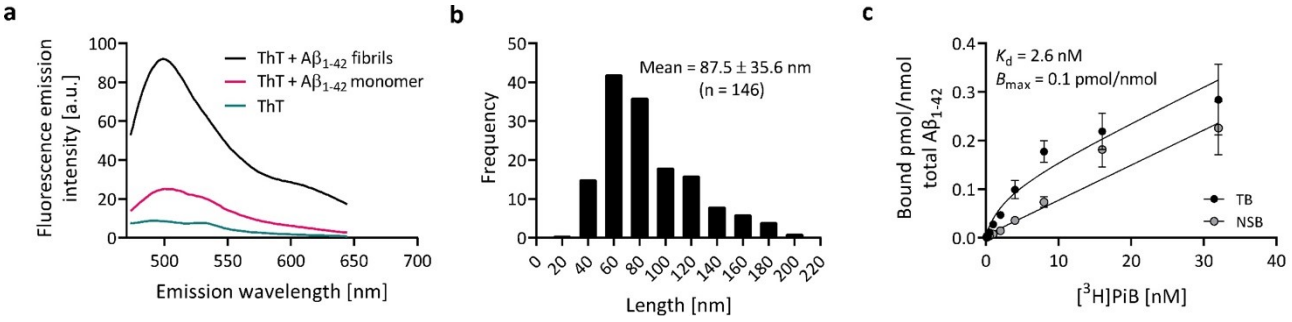

Characterization of Aβ$_{1-42}$ fibrils. a, Increase in ThT fluorescence emission spectrum in the presence of Aβ$_{1-42}$ fibrils compared to in the presence of monomers or ThT only. **b**, Length measurement and distribution of Aβ$_{1-42}$ fibrils were assessed from the negative stain electron microscopy images (mean length = 87.5 ± 35.6 nm). **c**, [^{3}H]PiB saturation binding assay confirmed good binding to Aβ$_{1-42}$ fibrils, with a K_d of 2.6 nM and a B_{max} of 0.1 pmol/nmol. Aβ$_{1-42}$, β-amyloid$_{1-42}$; NSB, non-specific binding; SB, specific binding; TB, total binding; ThT, thioflavin T. The points in **c** are presented as mean ± s.d..

Supplementary Item 2

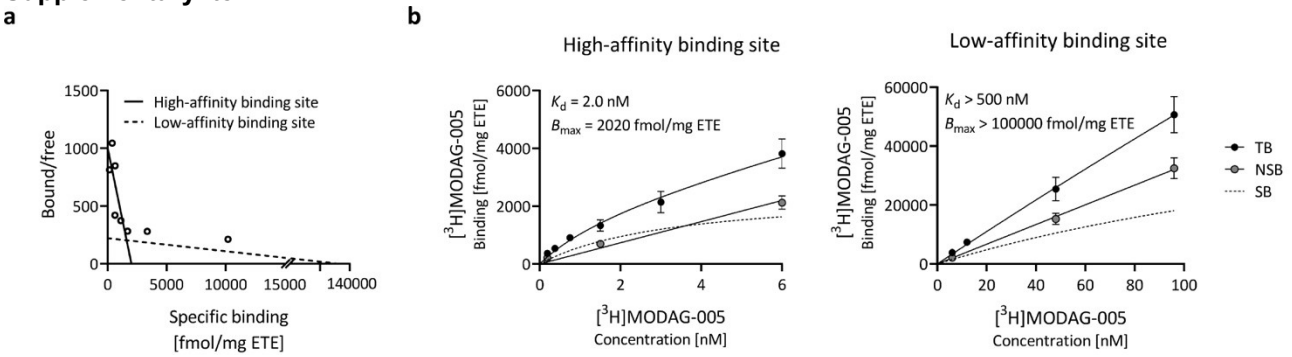

[^{3}H]MODAG-005 binding in AD brain tissue. Saturation binding autoradiography was performed in AD brain tissue (n = 1, repeated measurements in each sample). **a**, Scatchard plot revealed two binding sites in AD tissue. **b**, Saturation binding curves of high-affinity binding site and low-affinity binding site show K_d values of 2 nM and > 500 nM, respectively. ETE, estimated tissue equivalent; NSB, non-specific binding; SB, specific binding; TB, total binding. Data points in **b** are represented as mean ± s.d..

Supplementary Item 3

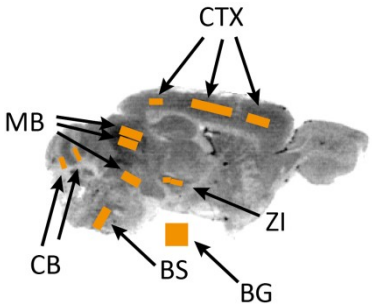

ROI definition for [^{3}H]MODAG-005 quantification in the αSYN(A30P) mouse model of PD. Abbreviations: BG, background; BS, brainstem; CB, cerebellum; CTX, cortex; MB, midbrain; ROI, region of interest; ZI, *zona incerta.*

Supplementary Item 4

^{11}C-labeling of MODAG 005

The radiolabeling of MODAG-005 was first approached by reductive methylation We observed the formation of [^{11}C]MODAG-005 with decay-corrected radiochemical yields of 12.0 ± 2.2% (from trapped MeI to formulated tracer) in a total synthesis time of 27.6 ± 0.9 minutes (from end of MeI trapping to end of

formulation) (**Fig. 6a**). The obtained A_m at the end of the synthesis was relatively low (49.2 ± 11.2 GBq/µmol). The synthesis thus required further optimization for successful imaging of low-abundant targets such as αSYN aggregates for *in vivo* studies.

To obtain a higher A_m, the radiosynthesis of [^{11}C]MODAG-005 was performed by direct methylation with [^{11}C]MeOTf. We achieved a decay-corrected radiochemical yield of 11.8 ± 2.7% (from trapped MeI to formulated tracer) and a A_m of 209 ± 44 GBq/*µ*mol. The radiolabeling of [^{11}C]MODAG-005 with higher A_m was used for follow-up rodent studies not presented in this study (method A).

For the *in vivo* studies in macaque, the direct methylation synthesis route, established in the Department of Preclinical Imaging and Radiopharmacy (Tuebingen, Germany), was adapted at Invicro-London and further adapted at Charles River. The direct methylation method B achieved a decay-corrected radiochemical yield of 3.7 ± 2.3% (from trapped MeI to formulated tracer) and a A_m of 89.3 ± 14 GBq/µmol.

Supplementary Item 5

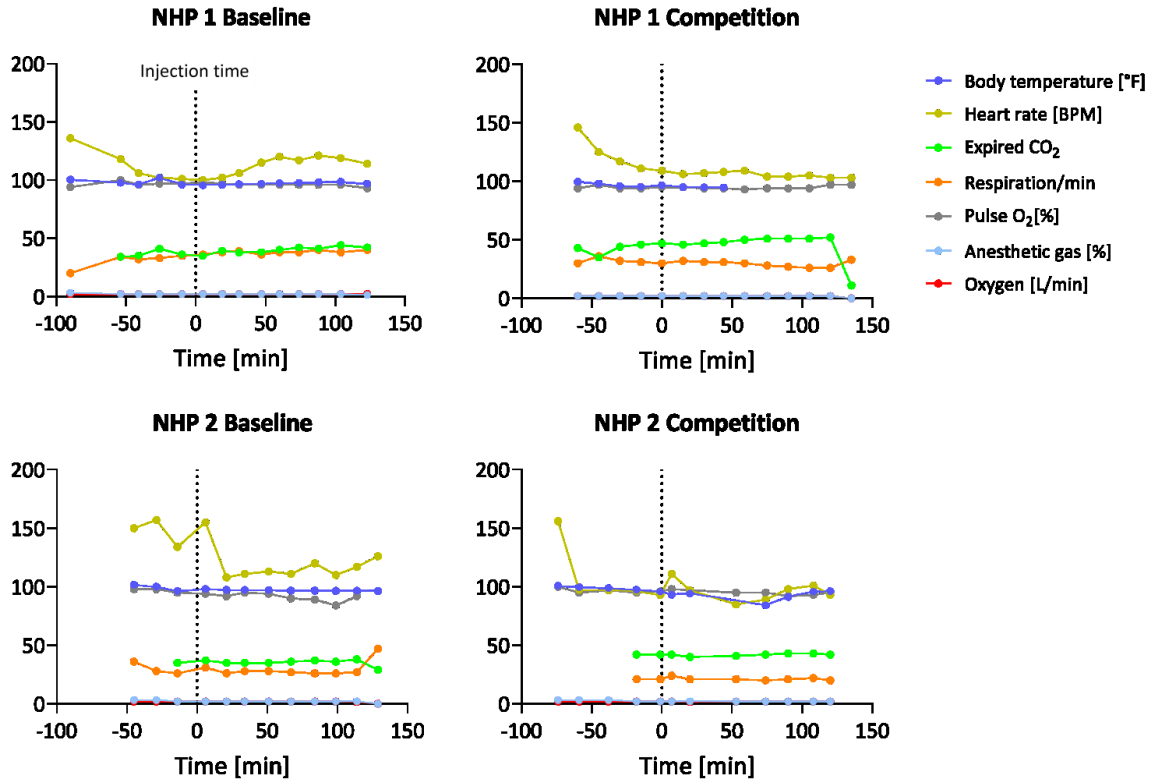

Macaque vitals. Monitoring of heart rate (BPM), body temperature (°F), expired CO_2, respiration/min, pulse O_2 (%), anesthetic gas (%), and oxygen (L/min) throughout the NHP PET scans.

Supplementary Item 6
Compound synthesis
All starting materials and solvents were of commercial grade and used as received unless noted otherwise. Thin layer chromatography (TLC): Macherey-Nagel precoated sheets, 0.25 mm ALUGRAM® SIL G/UV254 plates, detection with UV and/or by charring with 10% w/w ethanolic phosphomolybdic acid reagent followed by heating at 200°C. Flash column chromatography was performed by using Merck silica gel 60 (0.063-0.100 mm). Analytical HPLC was performed by using a Waters HPLC system with a Waters 996 Photodiode Array Detector. All separations involved a mobile phase of 0.1% trifluoroacetic acid (TFA) (v/v) in water and 0.1% TFA in acetonitrile. Unless otherwise specified, a gradient of 50% CH_3CN /50% H_2O → 100% CH_3CN in 30 minutes was used. HPLC was performed by using a reversed-phase (RP) column Eurospher RP 18, 100 Å, 5 µm, 250 × 4.6 mm at a flow rate of 1 mL/min. Electrospray ionization mass spectrometry (ESI-MS) and liquid chromatography/mass spectrometry (LC/MS) analyses were obtained by using a Waters Micromass ZQ 4000 mass spectrometer in conjunction with the Waters HPLC apparatus described above. NMR spectra were recorded by using a 400 MHz Bruker Avance spectrometer (Bruker AG, Rheinstetten, Germany) equipped with a TXI HCN z-gradient probe. All spectra were processed by using TOPSPIN 3.1 (Bruker AG, Karlsruhe, Germany). ^{1}H-NMR chemical shifts (δ) are reported in parts per million (ppm) relative to DMSO-d_5

as an internal standard. Data are reported as follows: chemical shift, multiplicity (s = singlet, bs = broad singlet, d = doublet, dd = doublet of doublets, ddd = doublet of doublet of doubletts), coupling constants (J, given in Hz), integration. ^{13}C-NMR chemical shifts (δ) are reported in parts per million (ppm) relative to DMSO-d_6 as an internal standard. The following experiments were used to record the resonances of the compounds: ^{1}H-1D, ^{13}C-1D-NMR spectra and ^{13}C-APT (attached proton test with a single J-evolution time of 1/145 seconds, spectra are processed such that quaternary and methylene groups have positive sign and methyl and methine groups negative sign). To resolve the overlap of resonances and recover undetectable resonances in ^{1}H and APT spectra, 2D-[^{13}C,^{1}H]-HSQC (heteronuclear single quantum coherence), 2D-[^{13}C, ^{1}H]-HMBC (heteronuclear multiple bond correlation) and 2D-NOESY were recorded for some compounds. The synthesis of the precursor anle190214 is depicted in the following figure.

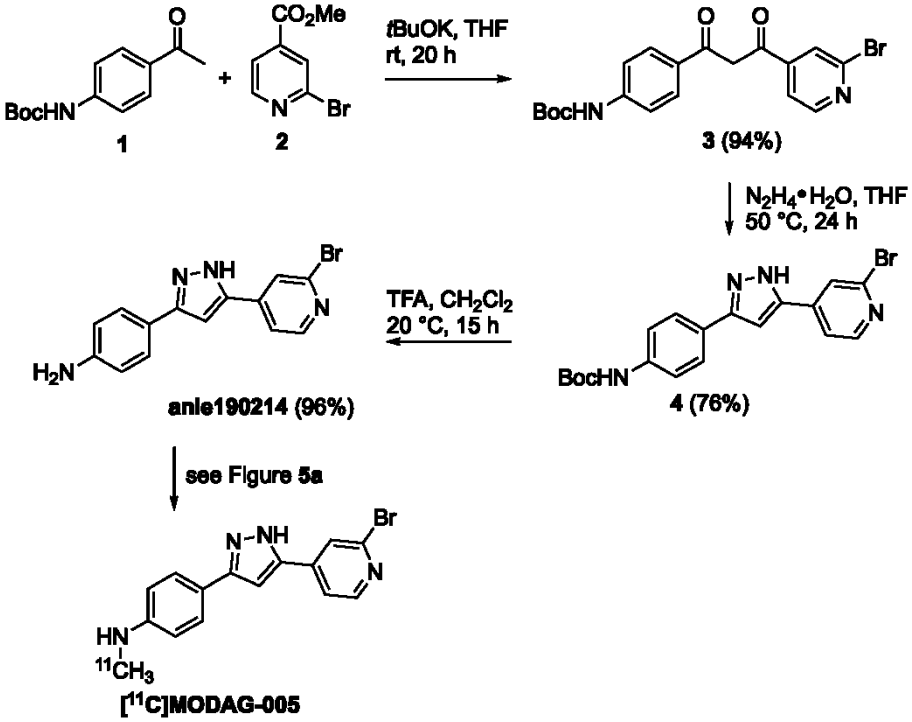

Experimental procedures and characterization data of compounds

MODAG-005: 4-[5-(2-Bromopyridin-4-yl)-1*H*-pyrazol-3-yl]-*N*-methylaniline was synthesized as described previously [12].

tert-Butyl {4-[3-(2-bromopyridin-4-yl)-3-oxopropanoyl]phenyl}carbamate **3**
A solution of potassium *tert*-butoxide (FW 112.21, 583 mg, 5.2 mmol) in THF (10.4 mL) was added to a stirred solution of *tert*-butyl *N*-(4-acetylphenyl)carbamate **1** (FW 235.28, 941 mg, 4 mmol) and methyl 2-bromopyridine-4-carboxylate **2** (FW 216.03, 1.04 g, 4.8 mmol) in THF (15 mL). The reaction mixture was stirred for 20 h. A 10 µL aliquot was sampled, quenched with 1M phosphate buffer pH 7, extracted with EtOAc and analyzed by TLC and LC-MS. About 95% conversion of ketone was observed. The mixture was poured into 1M phosphate buffer pH 7 (15 mL) and ice water (15 mL), and stirred at 0°C for 30 min. The resulting yellow solid was filtered off, washed with water (3 × 10 mL) and air dried to give 1.57 g (3.74 mmol, 94%) of crude product, which was used for the next step w/o purification. LC-MS: sample 0.5 mg/mL in CH_3CN; 10 µL injection volume; column: Eurospher RP18 100 Å, 5µm, 250 × 4.6 mm, solvents: water (+0.1% TFA, A) and CH_3CN (+0.1% TFA, B), gradient: B 50% → 100% in 30 min, detector UV 260 nm, peak RT 22.9 min, mass 419.2 (100%), 421.2 (98%), $[M+H]^+$). TLC (SiO_2, *n*-hexane:EtOAc = 2:1), R_f = 0.7.

tert-Butyl {4-[5-(2-bromopyridin-4-yl)-1*H*-pyrazol-3-yl]phenyl}carbamate **4**
To a solution of the *tert*-butyl {4-[3-(2-bromopyridin-4-yl)-3-oxopropanoyl]phenyl}carbamate **3** (1.57 g, 3.74 mmol) in THF (20 mL) was added hydrazine monohydrate (388 µL, 400 mg, 8 mmol). After being stirred at 50°C for 24 h the reaction mixture was cooled to room temperature and concentrated under reduced pressure. A mixture *n*-hexane/EtOAc = 2/1 (16 mL) was added, the mixture was stored 2 h at room temperature, then 15 h at 4°C. The resulting solid was filtered off, washed with *n*-hexane and vacuum dried. The crude product was purified by flash chromatography on silica gel (*n*-hexane/EtOAc = 1/1) to afford 1.18 g (2.84 mmol, 76%) of title product as beige solid. ^{1}H NMR (400 MHz, DMSO-d6, two rotamers, main form) δ

= 13.63 (bs, 1H), 9.53 (s, 1H), 8.41 (d, *J* = 5.1 Hz, 1H), 8.02 (s, 1H), 7.86 (d, *J* = 5.1, Hz, 1H), 7.69 (d, *J* = 8.6 Hz, 2H), 7.57 (d, *J* = 8.6 Hz, 2H), 7.35 (s, 1H), 1.49 (s, 9H). ^{13}C NMR (100.6 MHz, DMSO-d6, two rotamers, main form) δ = 152.8, 150.9, 147.6, 144.2, 142.3, 139.2 (2C), 125.8 (2C), 123.2, 122.6, 119.2, 118.4 (2C),100.6, 79.4, 28.2 (3C). LC MS (RP18-100 Å, gradient 50% CH_3CN /50% H_2O $\rightarrow$ 100% CH_3CN in 30 min), RT 14.6 min and mass 415.3 (100%), 417.3 (98%), $[M+H]^+$. TLC (SiO_2, *n*-hexane/EtOAc = 1/1) R_f 0.56, m.p.: 230-235°C (dec).

4-[5-(2-bromopyridin-4-yl)-1*H*-pyrazol-3-yl]aniline **anle190214**
To a suspension of *tert*-butyl {4-[5-(2-bromopyridin-4-yl)-1*H*-pyrazol-3-yl]phenyl}carbamate **4** (FW 415.28, 1.18 g, 2.84 mmol) in CH_2Cl_2 (21 mL) trifluoroacetic acid (2.8 mL, 4.14 g, 36.4 mmol) was added. The mixture was stirred at room temperature for 15 h and concentrated in vacuum. 1M phosphate buffer pH 7 (20 mL) was added, the resulting precipitate was filtered off, washed with water (2×10 mL) and air dried to give 859 mg (2.73 mmol, 96%) of product as a yellow-orange colored solid. ^{1}H NMR (400 MHz, DMSO-d6) δ = 13.22 (bs, 1H), 8.39 (d, *J* = 5.2 Hz, 1H), 8.01 (d, *J* = 0.8 Hz, 1H), 7.83 (dd, *J* = 5.2, 1.4 Hz, 1H), 7.47 (ddd, *J* = 7.5, 1.7, 0.9 Hz, 2H), 7.19 (s, 1H), 6.64 (ddd, *J* = 7.5, 1.7, 0.9 Hz, 2H), 5.49 (bs, 2H). ^{13}C NMR (100.6 MHz, DMSO-d6) δ = 150.8, 149.2, 146.4, 146.1, 143.8, 142.2, 126.3 (2C), 123.0, 119.0, 116.8, 113.9 (2C), 99.2. LC MS (RP18-100Å, gradient 0% CH_3CN /100% H_2O $\rightarrow$ 100% CH_3CN in 30 min), RT 14.8 min and mass 315.2 (98%), 317.2 (100%), $[M+H]^+$. TLC (SiO_2, *n*-hexane/EtOAc = 1/1) R_f 0.25, m.p.: >300°C.

Supplementary Item 7
Radiosynthesis by direct methylation - method B
$[^{11}C]CO_2$ was produced via a $^{14}N[p,\alpha]^{11}C$ nuclear reaction on a Siemens RDS-111 cyclotron, using 1% O_2 in N_2 as the target gas, using a Havar HP target.

No carrier-added $[^{11}C]CO_2$ was delivered to Tracerlab FX_2MeI (GE Healthcare) and $[^{11}C]MeI$ was produced *via* the phase-gas conversion pathway [54]. $[^{11}C]MeI$ passed through a silver triflate column, packed with a mixture of silver triflate and Carbosphere, at 200°C to generate $[^{11}C]MeOTf$, which bubbled into a reactor vessel pre-charged with a solution of anle190214 (2–3 mg) in anhydrous acetone (500 µL) held at -20°C. Radiosynthesis, purification and formulation were automated on EZ Modular Lab radiochemical synthesizers (Eckert & Ziegler GmbH).

The reaction mixture was heated to 50°C for three minutes, and then diluted with 1.7 mL of the preparative HPLC eluent. $[^{11}C]$MODAG-005 was purified by semi-preparative HPLC on an Agilent SB-phenyl column (5 µm, 9.4 × 250 mm) with 55% of 95/5 of acetonitrile/H_2O and 45% 50 mM aqueous ammonium acetate solution at a flow rate of 8 mL/min, which was eluted at seven minutes. The quality control of a dose solution was performed with an analytical HPLC on an Agilent SB-phenyl column (5 µm, 4.6 × 150 mm) with acetonitrile/50 mM aq. ammonium acetate (45/55) at a flow rate of 1.5 mL/min $[^{11}C]$MODAG-005 was eluted at 4.3 minutes, which was confirmed by co-injection of a MODAG-005 standard solution, and the radiochemical purity of a dose solution was >98%. At the end of the synthesis the radiochemical yield (decay-corrected) was 3.7 ± 2.3% and the molar activity (A_m) was 89.3 ± 14 GBq/μmol (End of synthesis).

Supplementary item 8

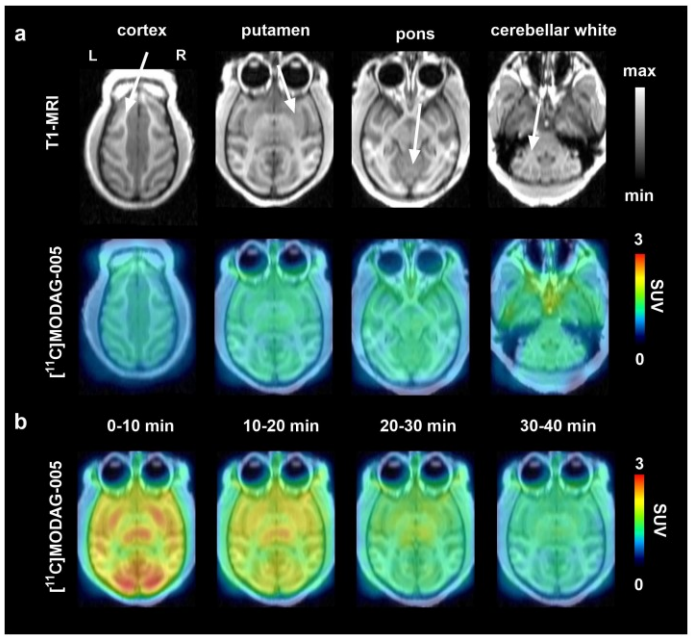

[^{11}C]MODAG-005 pharmacokinetic profile in the non-human primate brain. a, T1-weigthed MR images of a healthy cymologous monkey and corresponding [^{11}C]MODAG-005 PET images (sum of all frames) illustrating homogeneous tracer distribution in all brain regions. **b**, The pharmacokinetic profile of [^{11}C]MODAG-005 in a representative slice demonstrates fast tracer clearence and no tracer retention in any brain regions. MRI, magnetic resonance imaging; SUV, standardized uptake value (normalized to body weight).

References

1. Kuebler, L., *et al*., [^{11}C]MODAG-001-towards a PET tracer targeting alpha-synuclein aggregates. *Eur. J. Nucl. Med. Mol. Imaging*, 2020.
2. Larsen, P., Ulin, J., Dahlstrom, K. and Jensen, M., Synthesis of [11C]iodomethane by iodination of [11C]methane. *Appl. Radiat. Isot.*, 1997. **48**(2): p. 153-157.

Eidesstattliche Erklärung

Ich erkläre hiermit, dass ich die zur Promotion eingereichte Arbeit mit dem Titel: *Imaging of Biomarkers and Brain Circuits Involved in Parkinson's Disease* selbstständig verfasst, nur die angegebenen Quellen und Hilfsmittel benutzt und wörtlich oder inhaltlich übernommene Stellen (alternativ: Zitate) als solche gekennzeichnet habe. Ich erkläre, dass die Richtlinien zur Sicherung guter wissenschaftlicher Praxis der Universität Tübingen (Beschluss des Senats vom 25.5.2000) beachtet wurden. Ich versichere an Eides statt, dass diese Angaben wahr sind und dass ich nichts verschwiegen habe. Mir ist bekannt, dass die falsche Abgabe einer Versicherung an Eides statt mit Freiheitsstrafe bis zu drei Jahren oder mit Geldstrafe bestraft wird.

_____ _____

Ort und Datum Unterschrift